Doctoral Dissertation

博士論文

Formation and Evolution of High-Redshift Galaxies Using Cosmological Simulations and Multi-Wavelength Observations

（宇宙論的シミュレーションと多波長放射モデルで探る高赤方偏移銀河の形成と内部構造）

A Dissertation Submitted for the Degree of Doctor of Philosophy
May 2025

令和 7 年 5 月 博士（理学）申請

Department of Physics, Graduate School of Science,
The University of Tokyo

東京大学大学院 理学系研究科 物理学専攻

Yurina Nakazato

仲里 佑利奈

Abstract

Understanding the nature of galaxies formed within the first billion years of the Universe is crucial to unravel the processes of cosmic reionization and the formation of the first galaxies. Recent high-sensitivity observations with the James Webb Space Telescope (JWST), operational since 2022, have spectroscopically identified numerous distant galaxies via rest-frame UV and optical emission lines. Particularly, the detection of galaxies at redshift $z > 10$ has significantly advanced, continually updating the frontier of the most distant galaxies. To date, more than 1,300 galaxies at $z > 6$ (cosmic age < 1 Gyr) have been confirmed, providing an opportunity for statistical investigations of their physical properties. Simultaneously, the Atacama Large Millimeter/submillimeter Array (ALMA) has enabled the detection of rest-frame far-infrared (FIR) emission lines and dust re-emission from these high-redshift galaxies. Multi-wavelength emission characteristics thus hold key insights into the star formation (mass assembly) history and galaxy kinematics. To provide theoretical interpretations and complementary insights for these cutting-edge observations, this study employs cosmological galaxy formation simulations coupled with comprehensive multi-wavelength emission modeling.

JWST's high spatial resolution has unveiled previously unresolved internal structures in galaxies at $z > 6$, revealing clumpy morphologies. While local galaxy clumps primarily form through violent disk instabilities or minor mergers, the formation mechanisms for clumps in high-redshift galaxies, which often lack well-developed disks, remain unclear. To clarify this, we used large-scale, high-resolution cosmological zoom-in simulations (FirstLight), investigating the nature and formation of clumps during the epoch of reionization. By computing observable optical emission line intensities ([OIII] 5007Å) from simulated galaxies and developing an algorithm to identify clumps based on their observational luminosities, we directly compared our identified clumpy galaxies with observations. Applying this method to 62 simulated galaxies across 4,000 snapshots, we demonstrated for the first time that clumps observed in high-redshift galaxies predominantly originate from major galaxy mergers. During mergers, gas compression induces the formation of multiple clumps, which coalesce into a single massive galaxy within tens of Myrs, indicating that observed clumpy structures are temporary morphologies. Additionally, the predicted number density of clumpy structures aligns well with observed major merger frequencies at high redshift.

While JWST primarily observes emission from ionized gas, ALMA captures emission from both ionized and neutral gas ([OIII] 88 μm, [CII] 158 μm). The synergy between JWST and ALMA thus provides a comprehensive view of the multi-phase interstellar medium (ISM) in star-forming regions of high-redshift galaxies. Observational studies have reported [OIII] 88μm/[CII] 158μm line ratios at high redshift exceeding those of local star-forming galaxies by factors of 10–100. Although various simulations attempted to reproduce these ratios, insufficient spatial resolution and simplified radiation modeling have typically prevented successful explanations. Here, by utilizing a novel radiation-hydrodynamics simulation (RAMSES-RT) achieving 0.1 pc spatial resolution, we constructed detailed line emission models at the cell level. This unprecedented resolution allowed accurate modeling of ionized bubble structures previously unresolved by other studies, successfully reproducing the high observed [OIII] /[CII] ratios. Moreover, we analytically showed that the [OIII] /[CII] ratio scales with the density and mass ratio of ionized to neutral gas, quantitatively explaining the redshift evolution of this line ratio for the first time.

With ongoing high-redshift observations by JWST and ALMA, it is increasingly important to establish comprehensive multi-wavelength emission models that bridge theoretical predictions and observational data. This thesis provides a comprehensive treatment of multi-wavelength emission processes from rest-frame UV to FIR, thoroughly investigating clumpy morphologies and ISM properties. These results enhance our understanding of the dynamical and chemical characteristics of high-redshift galaxies and the formation history of cosmic structures in the early Universe.

Contents

List of Figures

List of Tables

Chapter 1

Introduction

Our universe began with the Big Bang approximately 13.8 billion years ago. The initial state was characterized by extremely high density and temperature, with the gas existing as plasma. As the temperature of the universe decreased due to cosmic expansion, Thomson scattering between photons and electrons ceased, and most free electrons were captured by protons to form hydrogen atoms by $z \sim 1100$. This epoch is referred to as recombination, as also shown in Figure 1.1. The subsequent formation of large-scale structures occurred via a bottom-up scenario.

According to the standard cosmological model ΛCDM, mini-halos with masses of $M_{\rm halo} = 10^{5-6}\,M_\odot$, collapsing at $z \sim 20-30$ are the formation sites of the first stars (Population III stars; Yoshida et al., 2003). Pop III stars form in primordial gas with zero metallicity, where metal cooling is absent, and the gas temperature only decreases to about 200 K via hydrogen molecules (Yoshida et al., 2006, 2012). This leads to a large Jeans mass ($M_{\rm J} \propto T^{3/2}$), resulting in massive stars with masses of approximately 10–100 $M_\odot$, characterized by a top-heavy initial mass function (IMF; e.g., Hosokawa et al., 2011; Hirano et al., 2014, 2015). These massive stars have short lifetimes of a few million years, ending either as core-collapse supernovae (SNe) or directly collapsing into black holes (BHs), forming seeds for supermassive black holes in the center of galaxies (e.g., Inayoshi et al., 2020). SNe enrich the surrounding gas to metallicities of $Z \sim 10^{-5} - 10^{-3}\,Z_\odot$ (Chiaki and Yoshida, 2022).

As the halo mass further increases to $M_{\rm halo} \sim 10^8\,M_\odot$, the virial temperature rises to $T_{\rm vir} \sim 10^4\,{\rm K}$. The gas then cools primarily via Lyman-alpha emission, followed by additional cooling through metal-line emission (Omukai et al., 2008). This process enables the formation of second-generation stars, known as Population II stars, whose assembly is generally categorized as the first galaxies (Bromm and Yoshida, 2011). Hierarchical mergers and cold gas accretion (Dekel et al., 2009b) lead to further growth, with galaxies reaching halo masses of $M_{\rm halo} \gtrsim 10^{10}\,M_\odot$ by $z \sim 6-10$. At this stage, the virial temperature becomes sufficiently high ($T_{\rm vir} \gtrsim 3\times10^4\,{\rm K}$), activating collisional excitation and ionization cooling from helium and metals (see Section 2.3). These high-redshift galaxies have stellar masses of $M_* \gtrsim 10^8\,M_\odot$, which are observable by ALMA and JWST (see Chapter 4).

It is crucial to reveal the formation and evolution of such first objects for a comprehensive understanding of the star formation history of the Universe. During this period, the Universe consisted exclusively of primordial gas composed predominantly of hydrogen and helium (with trace amounts of lithium) produced by Big Bang nucleosynthesis, and no BHs existed[1]. However, after the emergence of stars, ionizing photons emitted from the first galaxies drove cosmic reionization, which represents the last and largest phase transition at $z \simeq 5-10$, during which the IGM transitioned from a neutral state to one that is fully ionized. In addition, elements heavier than helium were synthesized via stellar nucleosynthesis and enriched the surrounding interstellar medium (ISM) through supernova explosions, simultaneously producing dust. At high redshift,

[1]Beyond the ΛCDM model allows the existence of Primordial Black Hole (PBH).

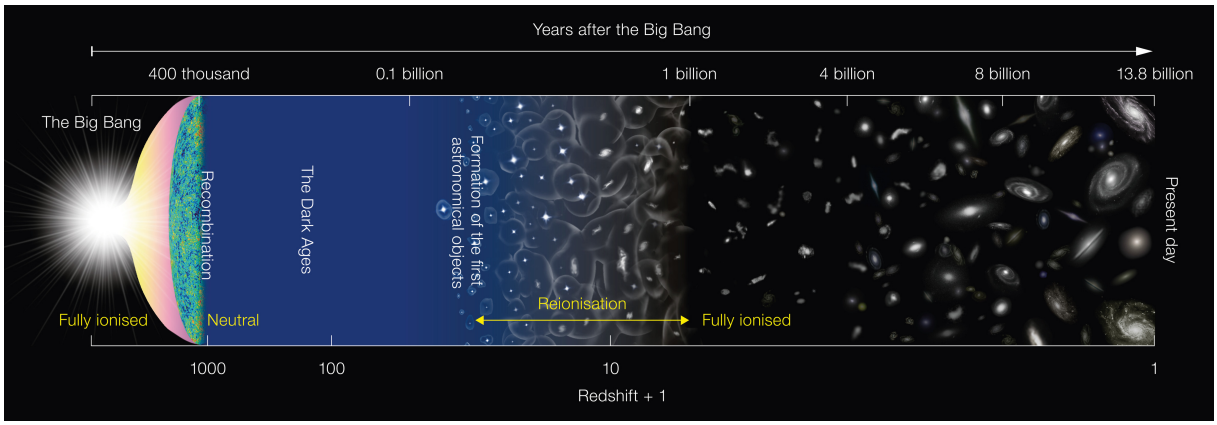

Figure 1.1: Schematic diagram of the history of the universe, which illustrates the major milestones in cosmic evolution since the Big Bang, approximately 13.8 billion years ago. The diagram is not to scale. The first major phase transition, known as recombination, occurred at $z \sim 1100$, when the universe became neutral and no sources of photons existed—an epoch referred to as the "dark ages." The formation of the first stars took place at redshifts from $z \sim 20$ to 30, followed by the emergence of the first galaxies at $z \simeq 10 - 15$. These galaxies emitted large amounts of ionizing photons, triggering the second phase transition: reionization, which occurred at $z \sim 5 - 10$. Image credit: NAOJ.

Type II supernovae are considered the primary contributors to dust production (Mancini et al., 2015). Understanding dust physics is crucial, because accurate measurements of star formation histories require tracing dust-obscured star formation, which can be estimated through UV attenuation and IR re-emission. Recent ALMA observations have detected numerous dusty galaxies at high redshifts, suggesting that approximately 30% of star formation at $z \sim 7$ is obscured (e.g., Fudamoto et al., 2021; Algera et al., 2023). Additionally, black holes formed through core-collapse or direct collapse evolve into supermassive black holes (SMBHs) at the centers of galaxies. Understanding the co-evolutionary processes of galaxies and supermassive black holes (SMBHs), including their feedback mechanisms, is particularly important in light of the recent discovery of new AGN populations identified by JWST, such as the so-called "little red dots." Therefore, understanding the formation and evolution of these *first objects* is crucial for elucidating the subsequent formation of metals, dust, and black holes, as well as the mechanisms driving cosmic reionization.

Furthermore, stellar mass assembly (i.e., star formation histories), metal enrichment, and the emergence of black holes and dust in the high-redshift universe significantly affect the subsequent evolution of the cosmic star formation rate density (SFRD), which is a key observable for understanding the history of galaxy formation. In galaxies that host supermassive black holes at their centers, star formation activity can be regulated or sustained by AGN feedback. This feedback can influence the redshift evolution of the SFRD, including the observed peak at $z \sim 2$. Dust is also crucial, as it absorbs UV photons emitted by stars and re-emits the energy in the infrared. The left panel of Figure 1.2 shows the SFRD measured at different wavelengths: far-UV (1500 Å) and far-infrared (8–1000 μm). This illustrates that at lower redshifts ($z \lesssim 2$), a significant fraction of star formation activity is obscured by dust. Therefore, correcting for dust attenuation is essential for deriving the intrinsic star formation activity. This attenuation is commonly calibrated using the IRX–$\beta_{\rm UV}$ relation (e.g., Meurer et al., 1999); see also Chapters 4 and 7. Dust-obscured star formation in the high-redshift universe is only now beginning to be constrained observationally.

Therefore, understanding the formation processes, star formation activity, and interstellar medium (ISM) properties of high-redshift galaxies within the first billion years of the universe is of great importance. These objects are increasingly observable with JWST and ALMA.

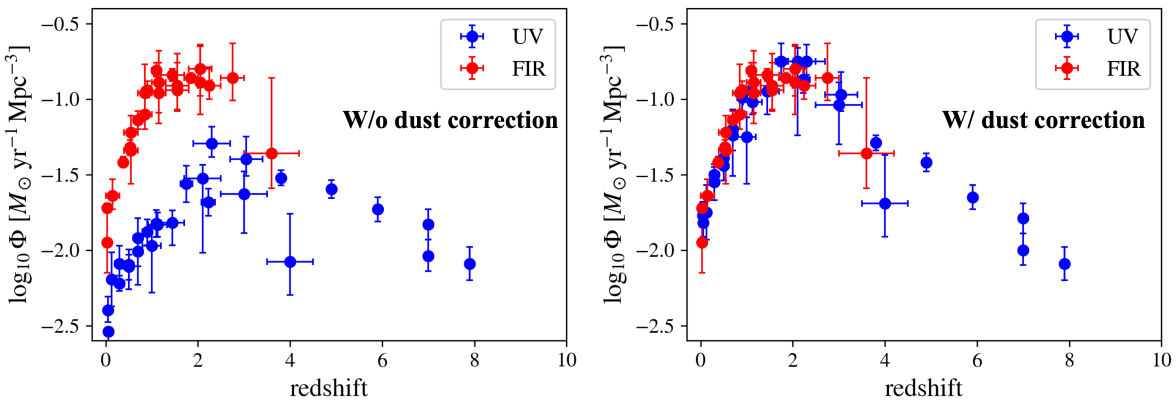

Figure 1.2: The observed star formation rate density (SFRD) as a function of redshift. Red points indicate measurements from rest-frame FIR observations, while blue points represent rest-frame FUV measurements. The left panel shows the SFRD derived from FUV (uncorrected for dust attenuation) and FIR data. The right panel shows the same data, but with dust attenuation corrections applied. The data is taken from Table 1 of Madau and Dickinson (2014).

Currently, three galaxies at $z = 14$ have been reported (Carniani et al., 2024; Naidu et al., 2025), one of which (GS-z14-0) has been observed in [OIII] 88μm emission with ALMA (Carniani et al., 2025; Schouws et al., 2024). To date, more than 1300 galaxies at $z > 6$ have been spectroscopically confirmed (Adamo et al., 2024a; Roberts-Borsani et al., 2024), highlighting the importance of statistically characterizing their physical properties. High spatial resolution imaging with JWST has revealed complex internal structures in high-redshift galaxies, including prominent clumpy morphologies (e.g., Harikane et al., 2025a). Complementary to these findings, ALMA observations continue to provide valuable insights through detections of far-infrared emission lines and dust continuum, enabling detailed studies of the multi-phase ISM and star formation processes in the early universe.

To interpret the aforementioned cutting-edge observational results and to provide complementary theoretical insights, it is essential to utilize cosmological simulations to track the formation and evolution of high-redshift galaxies. However, simulations solve N-body of dark matter particles and hydrodynamics of gas, and thus do not directly output observable quantities such as line and continuum information. Emission line calculations require consistent solutions of rate equations and energy equations across multiple ionization states of elements and transitions for various levels. Performing these calculations on-the-fly during simulations are computationally expensive, and are usually performed through post-processing approaches using photoionization codes (Dopita and Sutherland, 1996; Ferland et al., 1998). Moreover, an accurate treatment of dust attenuation and re-emission requires solving a six-dimensional radiative transfer equation, which consists of three spatial dimensions, two angular dimensions for scattering, and one frequency dimension. Even simulations incorporating on-the-fly radiative transfer typically rely on post-processing using Monte Carlo radiative transfer codes (Baes et al., 2011; Narayanan et al., 2021) and obtain dust emissions.

In this thesis, we develop multi-wavelength emission models for nebular emission lines and dust attenuation/re-emission, applying these models to zoom-in cosmological simulations. We explore the star formation histories, dynamical evolution, and physical properties of the interstellar medium in high-redshift galaxies. Our theoretical predictions and interpretations provide crucial insights into the latest JWST and ALMA observations.

The thesis consists of eight chapters, comprehensively examining star formation and ISM properties in galaxies at $z \geq 6$ using multi-wavelength radiative models and large-scale simulations. Chapter 2 outlines the basic galaxy formation theory, including cosmological structure formation and star formation processes. Chapter 3 reviews emission line mechanisms from ion-

ized and neutral hydrogen gas and dust attenuation and re-emission mechanisms. Chapter 4 surveys recent multi-wavelength observational discoveries of high-redshift galaxies, emphasizing the importance of connecting these observations to theoretical models. Chapter 5 describes general suites of galaxy formation simulations and reviews recent cosmological simulation studies that focus on $z \gtrsim 6$ galaxies in comparison with the latest JWST and ALMA observations. Chapters 6-8 detail original research outcomes: Chapter 6 explores clumpy structures at $z = 6-9$ using JWST observations and simulations, Chapter 7 examines dust absorption and re-emission distributions, and Chapter 8 investigates physical origins of high-[OIII] 88μm /[CII] 158μm line ratio at high-redshift galaxies using sub-parsec radiative transfer simulations. Finally, Chapter 9 summarizes the thesis and discusses prospects.

Chapter 2

Galaxy Formation Theory

2.1 Standard Cosmological Model

Understanding the formation and evolution of galaxies requires a robust theoretical framework that describes how structures grow under the influence of gravity, cosmic expansion, and astrophysical processes. In this chapter, we review the foundations of the standard cosmological model, focusing on the large-scale structure and dynamics of the universe within the framework of general relativity. We start by summarizing the basic cosmological principles and introducing the Friedmann–Lemaître–Robertson–Walker (FLRW) metric, which describes an isotropic and homogeneous expanding universe.

2.1.1 The Friedmann–Lemaître–Robertson–Walker metric

The infinitesimal interval $\mathrm{d}s^2$ is defined at each point in a local inertial frame as:

$$\mathrm{d}s^2 = g_{\mu\nu}\mathrm{d}x^\mu \mathrm{d}x^\nu = g_{00}c^2\mathrm{d}t^2 + 2cg_{0i}\mathrm{d}t\mathrm{d}x^i + g_{ij}\mathrm{d}x^i\mathrm{d}x^j, \quad (\mu,\nu = 0,1,2,3,\ i,j = 1,2,3), \quad (2.1)$$

where $\mathrm{d}x^\mu$ is an infinitesimal coordinate displacement in four-dimensional spacetime, and $g_{\mu\nu}$ is the metric tensor.

Let us assume that the universe is isotropic and homogeneous on large length-scales exceeding tens of mega-parsecs, implying there are no privileged locations. This assumption is called the cosmological principle. From this principle, the coordinates t and x^i are orthogonal, and thus the metric tensor satisfies $g_{i0} = g_{0i} = 0$. The proper time for a fundamental observer coincides with the cosmic time, and the infinitesimal interval $\mathrm{d}s^2$ reduces to $\mathrm{d}s^2 = -c^2\mathrm{d}t^2$ when $\mathrm{d}x^i = 0$. Hence, we obtain $g_{00} = -1$. The assumption of uniformity requires that space expands (or contracts) with time, and the spatial part of the metric tensor can be expressed as $g_{ij} = a^2(t)\gamma_{ij}$. Here, $a(t)$ is the scale factor, representing the relative size of the universe at cosmic time t. With the above considerations, $\mathrm{d}s^2$ can be written as:

$$\mathrm{d}s^2 = -c^2\mathrm{d}t^2 + a^2(t)\gamma_{ij}\mathrm{d}x^i\mathrm{d}x^j. \quad (2.2)$$

Let us work in polar coordinates, in which the angular directions $\mathrm{d}\phi$, $\mathrm{d}\theta$ and the radial direction $\mathrm{d}r$ are mutually orthogonal. Thus, we can express the spatial metric γ_{ij} by separating these variables as follows;

$$\gamma_{ij}\mathrm{d}x^i\mathrm{d}x^j = W(r)\mathrm{d}r^2 + r^2(\mathrm{d}\theta^2 + \sin^2\theta\mathrm{d}\phi^2) \quad (2.3)$$

$$\therefore \quad \mathrm{d}s^2 = -c^2\mathrm{d}t^2 + a(t)[W(r)\mathrm{d}r^2 + r^2(\mathrm{d}\theta^2 + \sin^2\theta\mathrm{d}\phi^2)]. \quad (2.4)$$

In order to determine the function $W(r)$ explicitly, we introduce the scalar curvature R, defined

as the trace of the Ricci tensor $R_{\alpha\beta}$;

$$
\begin{aligned}
R \equiv R^{\mu}_{\mu} &= g^{\alpha\beta} R_{\alpha\beta} && (2.5)\\
&= g^{00} R_{00} + g^{ij} R_{ij} && (2.6)\\
&= -R_{00} + \frac{\gamma_{ij}}{a^2}\left(\tilde{R_{ij}} + \frac{1}{c^2}(a\ddot{a} + 2\dot{a}^2)\gamma_{ij}\right) && (2.7)\\
&= \frac{3}{c^2}\frac{\ddot{a}}{a} + \frac{3}{c^2}\left(\frac{\ddot{a}}{a} + 2\left(\frac{\dot{a}}{a}\right)^2\right) + \frac{1}{a^2}\gamma_{ij}\tilde{R_{ij}} && (2.8)\\
&= \frac{6}{c^2}\frac{\ddot{a}}{a} + \frac{6}{c^2}\left(\frac{\dot{a}}{a}\right)^2 + \frac{1}{a^2}\left[\frac{\tilde{R^{rr}}}{W(r)} + \frac{\tilde{R^{\theta\theta}}}{r^2} + \frac{\tilde{R^{\phi\phi}}}{r^2\sin^2\theta}\right] && (2.9)\\
&= \frac{6}{c^2}\frac{\ddot{a}}{a} + \frac{6}{c^2}\left(\frac{\dot{a}}{a}\right)^2 + \frac{1}{a^2}\left[\frac{W'}{rW^2} + \frac{2}{r^2}\left(\frac{rW'}{2W^2} + 1 - \frac{1}{W}\right)\right]. && (2.10)
\end{aligned}
$$

Here we introduce two shorthand notations for differentiation: $\cdot \equiv \frac{\mathrm{d}}{\mathrm{d}t}$ for differentiation with respect to cosmic time t, and $' \equiv \frac{\mathrm{d}}{\mathrm{d}r}$ for differentiation with respect to the radial coordinate r. The Ricci tensor associated with the spatial metric γ_{ij} is denoted as $\tilde{R_{ij}}$. Since the third term in Eq. (2.10) must be independent of position (reflecting spatial homogeneity), the expression inside the square brackets can be replaced by introducing a constant spatial curvature parameter K;

$$\frac{2W'}{rW^2} + \frac{2}{r^2}\left(1 - \frac{1}{W}\right) = 6K. \tag{2.11}$$

Solving Eq.(2.11), we obtain

$$W(r) = \frac{1}{1 - Kr^2}. \tag{2.12}$$

Thus, the metric for an isotropic and homogeneous universe is given by

$$\mathrm{d}s^2 = -c^2\mathrm{d}t^2 + a(t)^2\left[\frac{\mathrm{d}r^2}{1 - Kr^2} + r^2(\mathrm{d}\theta^2 + \sin^2\theta\mathrm{d}\phi^2)\right]. \tag{2.13}$$

This metric is known as the Friedmann–Lemaître–Robertson–Walker (FLRW) metric. The spatial curvature parameter K determines the geometry (curvature) of the universe. Usually, the scale factor is normalized at the present cosmic time t_0 as $a(t_0) = 1$.

The two coordinate systems defined by the vectors $\boldsymbol{r}$ and $\boldsymbol{x}$, which are related by $\boldsymbol{r} = a(t)\boldsymbol{x}$, are called the proper coordinates and the comoving coordinates, respectively. The proper coordinate system expands with time following the expansion of the universe through the scale factor $a(t)$, while the comoving coordinate system subtracts out the effect of cosmic expansion and remains fixed relative to the expanding universe.

2.1.2 Friedmann Equation

This subsection derives the equation describing the time evolution of the scale factor $a(t)$ from the FLRW metric. The Einstein equation is written as

$$R_{\mu\nu} - \frac{1}{2}g_{\mu\nu}R + \Lambda g_{\mu\nu} = \frac{8\pi G}{c^4}T_{\mu\nu}. \tag{2.14}$$

We consider an ideal fluid[1], for which the energy-momentum tensor is given by

$$T_{\mu\nu} = (\rho_{\mathrm{E}} + P)u_\mu u_\nu + P g_{\mu\nu}, \tag{2.15}$$

[1] A viscosity term works as an anisotropic effect.

where $u_\mu, \rho_{\rm E}, P$ are the four-velocity of matter, energy density of matter, and pressure of matter, respectively. Substituting Eq.(2.15) into the Einstein equation (Eq. 2.14), the (0,0) component is written as

$$\frac{3}{c^2}\left(\frac{\dot{a}}{a}\right)^2 + \frac{3}{c^2}\frac{K}{a^2} - \Lambda = \frac{8\pi G}{c^4}\rho_{\rm E} \tag{2.16}$$

$$\therefore \quad \left(\frac{\dot{a}}{a}\right)^2 = \frac{8\pi G}{3c^2}\rho_{\rm E} - \frac{Kc^2}{a^2} + \frac{\Lambda c^2}{3}. \tag{2.17}$$

This equation is called the Friedmann equation. For the spatial (i, j) components, we obtain

$$-\frac{1}{c^2}\left(2\frac{\ddot{a}}{a} + \left(\frac{\dot{a}}{a}\right)^2 + \frac{c^2K}{a^2}\right)g_{ij} + \Lambda g_{ij} = \frac{8\pi G}{c^4}P g_{ij} \tag{2.18}$$

$$\therefore \quad \frac{\ddot{a}}{a} = -\frac{1}{2}\left[\left(\frac{\dot{a}}{a}\right)^2 + \frac{c^2K}{a^2}\right] + \frac{\Lambda c^2}{2} - \frac{4\pi G}{c^2}P \tag{2.19}$$

$$\therefore \quad \frac{\ddot{a}}{a} = -\frac{4\pi G}{3c^2}(\rho_{\rm E} + 3P) + \frac{\Lambda c^2}{3} \quad \text{(substituting Eq.(2.17) into Eq. (2.19))} \tag{2.20}$$

$$\therefore \quad \ddot{a} = -\frac{G}{a^2}\frac{4\pi}{3}\left(\frac{\rho_{\rm E}}{c^2} + \frac{3P}{c^2} - \frac{\Lambda c^2}{4\pi G}\right)a^3. \tag{2.21}$$

Equation (2.21) can be regarded as the equation of motion for a uniformly dense sphere with radius a. The first term on the right-hand side (RHS) represents the contribution of mass of matter, the second term shows that the effective gravity increases with pressure, and the third term is the cosmological constant representing "repulsion" of the universe.

2.1.3 Equation of State of the Universe

Differentiating the Friedmann equation, Eq.(2.17) with respect to time t yields

$$\frac{\ddot{a}}{a} = \frac{4\pi G}{3c^2}\left(\frac{a}{\dot{a}}\dot{\rho_{\rm E}} + 2\rho_{\rm E}\right) + \frac{\Lambda c^2}{3} \tag{2.22}$$

Comparing this result with Eq.(2.20), we obtain

$$\dot{\rho_{\rm E}} = -3\frac{\dot{a}}{a}(\rho_{\rm E} + P), \tag{2.23}$$

which describes the evolution of the energy density of matter.
Two equations, Eq.(2.17) and Eq.(2.21), contain three variables $\rho_{\rm E}, P, a$. Therefore, an additional equation, often referred to as an equation of state (EoS), is required to close the system. By introducing a constant parameter w, we consider a generalized EoS $P = w\rho_{\rm E}$. From Eq. (2.23), we have

$$\rho_{\rm E} \propto a(t)^{-3(1+w)}, \tag{2.24}$$

where $w = 0, 1/3, -1$ correspond to matter, radiation, and dark energy, respectively. In the following, we consider these specific cases separately.
(i) Non-relativistic matter with negligible pressure (collisionless particles)
Equation (2.23) is rewritten as

$$\dot{\rho_{\rm E}} = -3\frac{\dot{a}}{a}\rho \quad \rightarrow \quad \frac{\rho_{\rm E}}{c^2} = \rho_{\rm m} \sim mn(t) \propto a^{-3}, \tag{2.25}$$

where $\rho_{\rm m}$ is the mass density of matter, and $n(t)$ is the number density of matter particles each with mass m. Equation (2.25) indicates that the total mass in a comoving volume is conserved.

(ii) Relativistic matter (radiation)
Substituting $P = \rho_{\rm E}/3$ into Eq.(2.23), we obtain

$$\dot{\rho_{\rm E}} = -4\frac{\dot{a}}{a}\rho_{\rm E} \quad \rightarrow \quad \rho_{\rm E} \propto a^{-4} \tag{2.26}$$

This relationship reflects a constant number density ($\propto a^{-3}$) combined with the increase of wavelength of a photon proportional to the cosmic expansion ($\propto a^{-1}$).

(iii) Cosmological constant
Substituting $P = -\rho_{\rm E}$ into Eq.(2.23), we find

$$\dot{\rho_{\rm E}} = 0 \quad \rightarrow \quad \rho_{\rm E} \propto \text{const.} \tag{2.27}$$

Here we define

$$\rho_\Lambda = \frac{\Lambda c^4}{8\pi G}, \quad P_\Lambda = -\frac{\Lambda c^4}{8\pi G}. \tag{2.28}$$

Thus, the Einstein equation (Eq.(2.14)) can be rewritten as

$$R_{\mu\nu} - \frac{1}{2}g_{\mu\nu}R = \frac{8\pi G}{c^4}(T_{\mu\nu} + T_{\Lambda\,\mu\nu}), \tag{2.29}$$

where $T_{\Lambda\,\mu\nu}$ is described by ρ_Λ and P_Λ. In this description, the cosmological constant can be regarded as *fluid* satisfying the EoS $\rho_\Lambda = -P_\Lambda$.

2.1.4 Cosmological Parameter

We summarize the basic parameters that characterize an isotropic and homogeneous cosmological model. In the following, the subscript 0 denotes the value at the present epoch.

2.1.4.1 Hubble Constant

Hubble's law is given by

$$v_0 = H_0 d_0, \tag{2.30}$$

where v_0 and d_0 represent the recession velocity and distance to a galaxy, respectively. The proportionality constant H_0 is called the Hubble constant, defined as $H_0 \equiv \left.\frac{\dot{a}}{a}\right|_{t=t_0}$, and determines the expansion rate of the present-day universe.

The dimensionless Hubble constant h is defined by normalizing H_0 to 100 $\mathrm{km\,s^{-1}\,Mpc^{-1}}$ as

$$h = \frac{H_0}{100\ \mathrm{km\,s^{-1}\,Mpc^{-1}}} \tag{2.31}$$

2.1.4.2 Density Parameter

The Friedmann equation (Eq. 2.17) at the present epoch ($t = t_0$) is written as

$$H_0^2 = \frac{8\pi G}{3c^2}\rho_{\rm E,0} - Kc^2 + \frac{\Lambda c^2}{3}. \tag{2.32}$$

Let us first consider a flat, matter-dominated universe, i.e., $K = 0$, $\Lambda = 0$, and $\rho_{\rm E} \propto a^{-3}$, known as the Einstein–de Sitter universe. In this case, the energy density is dominated by non-relativistic matter, and Eq. (2.32) simplifies to

$$\rho_{\rm E,crit0} = \frac{3H_0^2c^2}{8\pi G} \tag{2.33}$$

$$\therefore \ \rho_{c0} \equiv \frac{\rho_{\rm E,crit0}}{c^2} = \frac{3H_0^2}{8\pi G} \sim 1.88 \times 10^{-29} h^2\ \mathrm{g\,cm^{-3}}, \tag{2.34}$$

where ρ_{c0} is defined as the critical density.

Next, we consider a more general case, called a Friedmann universe, in which radiation, matter, and a cosmological constant coexist, and non-zero curvature is allowed. By normalizing each energy density to the critical density, we define dimensionless density parameters as

$$\Omega_{m0} \equiv \frac{\rho_{m0}}{\rho_{c0}} = \frac{8\pi G\rho_{m0}}{3H_0^2c^2}, \quad \Omega_{r0} \equiv \frac{\rho_{r0}}{\rho_{c0}} = \frac{8\pi G\rho_{r0}}{3H_0^2c^2}, \quad \Omega_{\Lambda 0} \equiv \frac{\rho_{\Lambda 0}}{\rho_{c0}} = \frac{\Lambda c^2}{3H_0^2}. \tag{2.35}$$

Equation (2.32) becomes

$$\frac{Kc^2}{H_0^2} = \Omega_{m0} + \Omega_{r0} + \Omega_{\Lambda 0} - 1. \tag{2.36}$$

Thus, the Friedmann equation at $t = t$ is rewritten by introducing the Hubble parameter $H \equiv \frac{\dot{a}}{a}|_{t=t}$, and using the relations $\rho_m \propto a^{-3}$ ($\rho_r \propto a^{-4}$);

$$H^2 = H_0^2\left(\frac{\Omega_{r0}}{a^4} + \frac{\Omega_{m0}}{a^3} + \frac{1-\Omega_{r0}-\Omega_{m0}-\Omega_{\Lambda 0}}{a^2} + \Omega_{\Lambda 0}\right). \tag{2.37}$$

In the special case of a flat universe ($K = 0$), the density parameters satisfy the constraint $\Omega_m + \Omega_r + \Omega_\Lambda = 1$. From Eqs. (2.25), (2.26), and (2.27), the evolution of each density parameter can be expressed as follows,

$$\Omega_r = \frac{\Omega_{r0}}{\Omega_{r0} + \Omega_{m0}a + \Omega_{\Lambda 0}a^4}, \quad \Omega_m = \frac{\Omega_{m0}\,a}{\Omega_{r0} + \Omega_{m0}a + \Omega_{\Lambda 0}a^4}, \quad \Omega_\Lambda = \frac{\Omega_{\Lambda 0}\,a^4}{\Omega_{r0} + \Omega_{m0}a + \Omega_{\Lambda 0}a^4} \tag{2.38}$$

Figure 2.1 shows the evolution of the density parameters as a function of the scale factor $a(t)$.

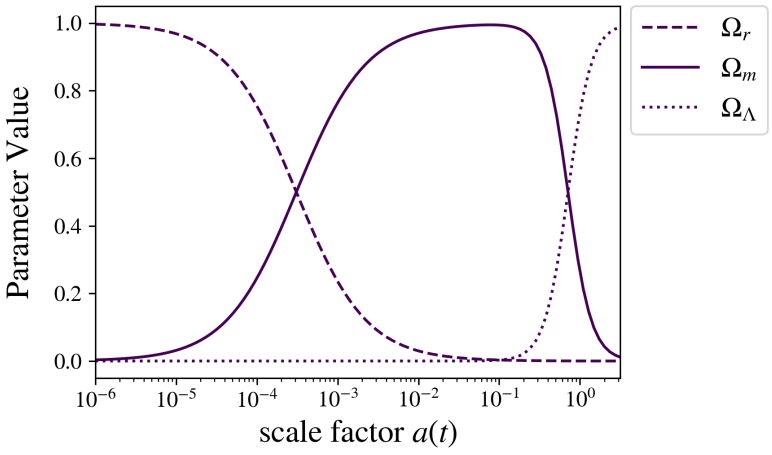

Figure 2.1: Evolution of the density parameters Ω_r, Ω_m, and Ω_Λ as a function of the scale factor $a(t)$. The present-day values adopted here are $\Omega_{r0} = 8.05 \times 10^{-5}$, $\Omega_{m0} = 0.27$, and $\Omega_{\Lambda 0} = 0.73$ (Komatsu et al., 2009).

From Figure 2.1, the matter-dominated phase roughly corresponds to the redshift range of $0.5 < z < 3000$. At intermediate redshifts ($z \sim 10-500$), the contributions from radiation, dark energy, and curvature are negligible ($\Omega_{r0} \approx \Omega_{\Lambda 0} \approx K \approx 0$). Thus, Eq. (2.37) simplifies to

$$H^2 = H_0^2\frac{\Omega_{m0}}{a^3} \tag{2.39}$$

$$\therefore a = \left(\frac{3}{2}H_0 t\right)^{2/3} \tag{2.40}$$

Since non-relativistic matter satisfies $\rho \propto a^{-3}$ (Eq. 2.25), the energy density at cosmic time t is given by

$$\rho_{\rm E} = \rho_m = \frac{\rho_{m0}}{a^3} = \frac{c^2}{6\pi G t^2}. \tag{2.41}$$

2.1.5 Redshift

The wavelength λ of a photon emitted by an object at time t is stretched by cosmic expansion. This phenomenon is called redshift. The parameter quantifying the degree of this wavelength shift is also called the redshift, and is defined as

$$z = \frac{\lambda_0 - \lambda}{\lambda}. \tag{2.42}$$

By normalizing the scale factor to unity at the present epoch, $a(t_0) = 1$, we have the following simple relationship between the scale factor a and redshift z:

$$a = \frac{1}{z+1} \tag{2.43}$$

Observational estimates of the present-day density parameters allow us to trace the time evolution of the expansion (or contraction) of the universe. However, to fully understand the formation and evolution of non-linear structures in the universe, it is necessary to consider the evolution of density perturbations.

2.2 Structure formation

Non-relativistic matter can form large-scale cosmological structures starting from initially small fluctuations. In contrast, relativistic components (such as radiation) possess a streaming length too large to allow efficient structure formation. Here, we consider an expanding universe as the background spacetime and treat matter as an ideal fluid. Thus, physical properties of matter can be determined by density ρ, pressure P, and velocity $\boldsymbol{v}$.

The continuity equation and the Euler equation (fluid equation), written in flat, non-expanding spatial coordinates $\boldsymbol{r}$, are given by

$$\frac{\partial \rho}{\partial t} + \nabla \cdot (\rho \boldsymbol{v}) = 0 \tag{2.44}$$

$$\frac{\partial \boldsymbol{v}}{\partial t} + (\boldsymbol{v} \cdot \nabla) = -\frac{\nabla P}{\rho} - \nabla \phi, \tag{2.45}$$

which considers hydrodynamic pressure and gravitational interactions.

Next, we consider the equations in comoving coordinates $\boldsymbol{x}$. The coordinates $\boldsymbol{r}$ and $\boldsymbol{x}$ are related as follows;

$$\boldsymbol{r} = a\boldsymbol{x} \tag{2.46}$$

$$\dot{\boldsymbol{r}} = \dot{a}\boldsymbol{x} + a\dot{\boldsymbol{x}} \tag{2.47}$$

The first term on the RHS of the second equation indicates that matter at rest in the comoving coordinate is in motion in the proper coordinate. Thus we can replace $\boldsymbol{v} \to \boldsymbol{v} + \dot{a}\boldsymbol{x}$ and fluid equations in the comoving coordinate are written as[2]

$$\begin{aligned} &\frac{\partial \rho}{\partial t} + 3\frac{\dot{a}}{a}\rho + \frac{1}{a}\nabla \cdot (\rho \boldsymbol{v}) = 0 \\ &\frac{\partial \boldsymbol{v}}{\partial t} + \frac{\dot{a}}{a}\boldsymbol{v} + \frac{1}{a}(\boldsymbol{v} \cdot \nabla)\boldsymbol{v} = -\frac{1}{a}\nabla\Phi - \frac{1}{a\rho}\nabla P \\ &\Delta\Phi = 4\pi G a^2(\rho_{\rm tot} - \bar{\rho}_{\rm tot}) \end{aligned} \tag{2.49}$$

[2]The gravitational potential in the comoving coordinate is $\Phi = \phi + \frac{1}{2}a\ddot{a}|\boldsymbol{x}|^2$. Note that partial differentiation is also replaced:

$$\left.\frac{\partial}{\partial t}\right|_r \to \left.\frac{\partial}{\partial t}\right|_x - \frac{\dot{a}}{a}\boldsymbol{x} \cdot \nabla_x, \quad \nabla_r \to \frac{1}{a}\nabla_x \tag{2.48}$$

The density and pressure fluctuations, $\delta(\boldsymbol{x},t)$ and $\delta p(\boldsymbol{x},t)$ are defined as follows;

$$\delta(\boldsymbol{x},t) = \frac{\rho(\boldsymbol{x},t)-\bar{\rho}(t)}{\bar{\rho}(t)} \tag{2.50}$$

$$\delta p(\boldsymbol{x},t) = p(\boldsymbol{x},t)-\bar{p}(t) \tag{2.51}$$

Thus, Eq.(2.49) can be rearranged as

$$\frac{\partial\delta}{\partial t}+\frac{1}{a}\Delta\cdot[(1+\delta)\boldsymbol{v}]=0 \tag{2.52}$$

$$\frac{\partial\boldsymbol{v}}{\partial t}+\frac{\dot{a}}{a}\boldsymbol{v}+\frac{1}{a}(\boldsymbol{v}\cdot\Delta)\boldsymbol{v}=-\frac{1}{a}\Delta\Phi-\frac{\Delta(\delta p)}{a\bar{\rho}(1+\delta)}. \tag{2.53}$$

$$\left(\frac{\partial}{\partial t}+2\frac{\dot{a}}{a}\right)(2.52)\rightarrow\frac{\partial^2\delta}{\partial t^2}+\frac{\partial}{\partial t}\left[\frac{1}{a}\Delta\cdot[(1+\delta)\boldsymbol{v}]\right]+\frac{2\dot{a}}{a}\frac{\partial\delta}{\partial t}+\frac{2\dot{a}}{a^2}\Delta\cdot[(1+\delta)\boldsymbol{v}]=0 \tag{2.54}$$

$$-\frac{1}{a}\Delta\cdot(2.53)\rightarrow-\frac{1}{a}\frac{\partial}{\partial t}-\frac{\dot{a}}{a^2}\Delta\cdot\boldsymbol{v}-\frac{1}{a^2}\Delta\cdot[(\boldsymbol{v}\cdot\Delta)\boldsymbol{v}]=\frac{1}{a^2}\frac{1}{a^2}\Delta\Phi+\frac{\Delta(\delta p)}{a^2\bar{\rho}(1+\delta)} \tag{2.55}$$

2.2.1 Linear Growth of Density Fluctuations

The third term on the left-hand side of Eq. (2.55) is a non-linear term, which we neglect in the linear approximation. We get

$$\begin{aligned}\frac{\partial^2\delta}{\partial t^2}+\frac{2\dot{a}}{a}\frac{\partial\delta}{\partial t}-\frac{\Delta(\delta p)}{a^2\bar{\rho}}&=\frac{1}{a^2}\Delta\Phi\\&=\frac{4\pi G}{c^2}(\bar{\rho}_{\mathrm{E,tot}}\delta_{\mathrm{tot}}+3\delta p_{\mathrm{tot}}),\end{aligned} \tag{2.56}$$

where, $\bar{\rho}\mathrm{E,tot}$ is the total energy density of the fluid, and δtot represents the corresponding total density fluctuation. In the linear approximation, pressure fluctuations can be expressed in terms of density fluctuation $\delta\rho$ and entropy fluctuation δS as follows

$$\delta p=\left(\frac{\partial p}{\partial\rho}\right)_s\delta\rho+\left(\frac{\partial p}{\partial S}\right)_\rho\delta S, \tag{2.57}$$

where S is the entropy per unit mass and the sound speed is defined as $c_s^2\equiv\left(\frac{\partial p}{\partial\rho}\right)_s$. Thus, Eq.(2.56) is rewritten as

$$\frac{\partial^2\delta}{\partial t^2}+\frac{2\dot{a}}{a}\frac{\partial\delta}{\partial t}-\left(4\pi G\bar{\rho}\delta+\frac{c_s^2}{a^2}\Delta\delta\right)=\left(\frac{\partial p}{\partial S}\right)_\rho\frac{\Delta(\delta S)}{a^2\bar{\rho}}+\frac{4\pi G}{c^2}\left[\bar{\rho}_{\mathrm{tot}}\delta_{\mathrm{tot}}-\bar{\rho}\delta+3(\delta p_{\mathrm{tot}}-\delta p)\right] \tag{2.58}$$

If we assume a self-gravitational system with $\delta S=0$, we can neglect the RHS;

$$\frac{\partial^2\delta}{\partial t^2}+\frac{2\dot{a}}{a}\frac{\partial\delta}{\partial t}-\left(4\pi G\bar{\rho}\delta+\frac{c_s^2}{a^2}\Delta\delta\right)=0. \tag{2.59}$$

Taking the Fourier transform $\delta(\boldsymbol{x},t)\rightarrow\tilde{\delta}(\boldsymbol{k},t)$, we obtain

$$\frac{\partial^2\tilde{\delta}}{\partial t^2}+2\frac{\dot{a}}{a}\frac{\partial\tilde{\delta}}{\partial t}-\left(4\pi G\bar{\rho}-\frac{c_s^2k^2}{a^2}\right)\tilde{\delta}=0. \tag{2.60}$$

The second term acts as “friction” due to cosmic expansion, while the third term serves as a potential term. This linear equation implies that each Fourier mode with a different k evolves

independently. When $\left(4\pi G\bar{\rho} - \frac{c_s^2 k^2}{a^2}\right) < 0$, density fluctuations δ do not grow, but rather oscillate with damping and approach zero. Conversely, when $\left(4\pi G\bar{\rho} - \frac{c_s^2 k^2}{a^2}\right) > 0$, gravitational attraction dominates over pressure, allowing density fluctuations to grow and finally leading to gravitational collapse. There is the critical wavenumber $k_{\rm J} \equiv \dfrac{a\sqrt{4\pi G\bar{\rho}}}{c_s}$, which is called Jeans scale.

From here, we focus on the evolution of dark matter fluctuations in linear theory. Dark matter is collisionless, and therefore we set the sound speed $c_s = 0$. In this case, fluctuations can grow for wavenumbers satisfying $k < k_{\rm J}$, and the evolution equation for dark matter fluctuations becomes

$$\ddot{\delta} + 2\frac{\dot{a}}{a}\dot{\delta} - 4\pi G\bar{\rho}\delta = 0. \tag{2.61}$$

Considering an Einstein–de Sitter universe, in which $\dot{a}/a = 2/3t$ and $\rho = 1/6\pi G t^2$ (from Eq.2.41), we can rewrite Eq.(2.61) as

$$\ddot{\delta} + \frac{4}{3t}\dot{\delta} - \frac{2}{3t^2}\delta = 0. \tag{2.62}$$

The solution is expressed by the superpositions of two solutions,

$$\delta = At^{2/3} + Bt^{-1}. \tag{2.63}$$

The first and second terms are known as the "growing mode" and the "decaying mode", respectively. Typically, we focus only on the growing mode, indicating that density fluctuations evolve as $\delta \propto t^{2/3}$, which is proportional to the scale factor a during the matter-dominated epoch.

2.2.2 Non-linear Model for Spherical Collapse

The linear approximation discussed in the previous section is valid only when the density fluctuation satisfies $\delta \ll 1$. However, as δ increases, nonlinear effects must be taken into account in structure formation. In the present-day universe, density fluctuations evolve non-linearly on scales $\lesssim 10\ h^{-1}$, Mpc. To illustrate non-linear evolution, we first consider a simple spherical collapse model. Suppose that we have a sphere with mass M, constant density, and radius r. For simplicity, we place this sphere in an Einstein–de Sitter universe. The equation of motion for this sphere is given by

$$\ddot{r} = -\frac{GM(<r)}{r^2}. \tag{2.64}$$

From energy conservation, we have

$$\frac{1}{2}\dot{r}^2 - \frac{GM(<r)}{r} = E(=\text{const.}) \tag{2.65}$$

The cases of $E < 0$ and $E > 0$ correspond, respectively, to a bound solution (where r contracts after expansion) and an unbound solution (where r expands indefinitely). Integrating Eq. (2.65), we can express r and t parametrically in terms of a parameter θ as follows

$$\begin{cases} r = (GM)^{1/3}A^2(1-\cos\theta) \\ t = A^3(\theta - \sin\theta) \end{cases} \qquad (E<0) \tag{2.66}$$

$$\begin{cases} r = (GM)^{1/3}A^2(\cosh\theta - 1) \\ t = A^3(\sinh\theta - \theta) \end{cases} \qquad (E>0), \tag{2.67}$$

where A is constant. The density inside the sphere is $\rho = \dfrac{3M}{4\pi r^3}$ and the mean density of the Einstein-de Sitter universe is $\bar{\rho} = \dfrac{1}{6\pi G t^2}$. Therefore, the density fluctuation is defined as

$$\delta \equiv \frac{\rho}{\bar{\rho}} - 1 = \begin{cases} \dfrac{9}{2}\dfrac{(\theta - \sin\theta)^2}{(1-\cos\theta)^3} - 1 & (E < 0) \\ \dfrac{9}{2}\dfrac{(\sinh\theta - \theta)^2}{(\cosh\theta - 1)^3} - 1 & (E > 0) \end{cases} \tag{2.68}$$

Equations (2.66), (2.67), and (2.68) are plotted in Figure 2.2.

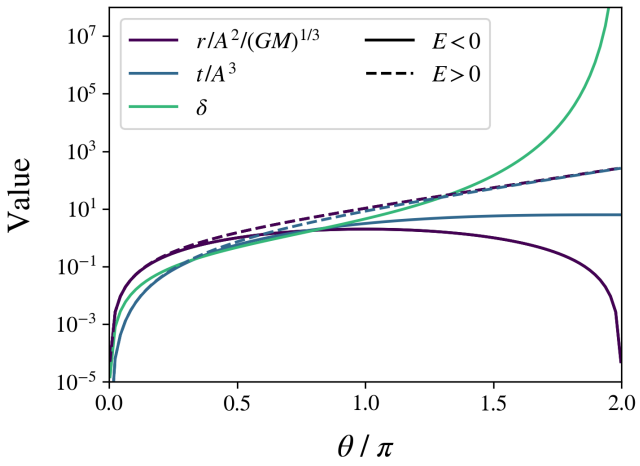

Figure 2.2: Radius r (purple), time t (blue), over density δ(green) as a function of θ. Solid and dashed lines represent the bound ($E < 0$) and unbound ($E > 0$) cases, respectively.

For the unbound solution ($E > 0$), the radius expands monotonically, and the density remains lower than the average density. In contrast, for the bound solution ($E < 0$), the sphere initially expands but eventually collapses.

The turning point from expansion to contraction corresponds to the maximum radius, occurring at $\theta = \pi$. At this turning point, the time, radius, and density fluctuation are given by

$$t_{\rm turn} = \pi A^2, \quad r_{\rm turn} = 2(GM)^{1/3}A^2, \quad \delta_{\rm turn} = \frac{9\pi^2}{16} - 1. \tag{2.69}$$

The point where $r \to 0$ is a collapse point and corresponds to $\theta = 2\pi$. Time at the collapsing point is

$$t_{\rm coll} = 2t_{\rm turn} = 2\pi A^2. \tag{2.70}$$

At the time of collapse, the density fluctuation diverges, $\delta \to \infty$.

2.2.3 Virial Equilibrium in a Spherical Model

In reality, the density does not diverge infinitely. Instead, a sphere is gravitationally bound and reaches virial equilibrium. For a gravitationally bound system in equilibrium, the total energy E and the potential energy U satisfy the following relationship,

$$E = \frac{1}{2}\langle U \rangle, \tag{2.71}$$

Consider a sphere of uniform density that is gravitationally bound and in equilibrium. Its density can be expressed in terms of its mass M and radius R as $\rho = \dfrac{3M}{4\pi R^3}$. The mass enclosed within

a radius r $(0 < r < R)$ is $\frac{4\pi r^3}{3}\rho$, and the mass of a thin shell located between radii r and $r + dr$ is $4\pi r^2 \rho dr$. Thus, the gravitational potential energy of the sphere is calculated by integrating over the entire volume,

$$U = -\int_0^R \frac{G}{r}\frac{4\pi r^3}{3} \cdot 4\pi r^2 dr = -\int_0^R \frac{G}{r}\frac{Mr^3}{R^3}\frac{3Mr^2 dr}{R^3} = -\frac{3}{5}\frac{GM^2}{R}. \tag{2.72}$$

We now follow the non-linear collapse of a sphere with uniform density using the virial theorem. The non-linear growth of a spherically symmetric model has already been described in Section 2.2.2. A sphere has the maximum radius $R_{\rm turn}$ at the turning point, and the total energy is

$$E = U = -\frac{3}{5}\frac{GM^2}{R_{\rm turn}}. \tag{2.73}$$

After reaching this turning point, the sphere begins to contract. While in Section 2.2.2 we assumed velocity dispersion could be neglected, in reality, velocity dispersion provides support against gravitational collapse, and the sphere eventually settles into virial equilibrium. The potential energy in virial equilibrium is expressed as

$$U_{\rm vir} = -\frac{3}{5}\frac{GM^2}{R_{\rm vir}}. \tag{2.74}$$

According to the virial theorem $E = \frac{1}{2}U_{\rm vir}$, and the virial radius is given by

$$R_{\rm vir} = \frac{1}{2}R_{\rm turn}. \tag{2.75}$$

The time to reach virial equilibrium can be considered the same as the time to reach the collapse point, $t_{\rm coll}$. Thus, the density fluctuation at $t = t_{\rm coll}$ is

$$\delta_{\rm coll} = \frac{\rho}{\bar{\rho}} - 1 = \frac{3M}{4\pi R_{\rm vir}^3}\frac{1}{\frac{1}{6\pi G t_{\rm coll}^2}} - 1 \tag{2.76}$$

$$= 18\pi^2 - 1 \simeq 178. \tag{2.77}$$

For baryons, we consider an ideal gas consisting of N molecules with an average molecular weight μ, uniformly distributed within a sphere of radius $R_{\rm vir}$, assuming the gas is in virial equilibrium. The total kinetic energy of the gas is

$$E = \frac{1}{2}N\mu m_{\rm H}\langle v^2\rangle, \tag{2.78}$$

where $m_{\rm H}$ and $\langle v^2\rangle$ are proton mass and the mass-weighted mean square velocity of the molecules, respectively. From Eq.(2.71) and (2.74), $\langle v^2\rangle$ is re-write using the gas total mass $M_{\rm gas} = N\mu m_{\rm H}$,

$$M_{\rm gas}\langle v^2\rangle = \frac{3}{5}\frac{GMM_{\rm gas}}{R_{\rm vir}} \tag{2.79}$$

$$\therefore \langle v^2\rangle = \frac{3}{5}\frac{GM}{R_{\rm vir}}, \tag{2.80}$$

where M is the total masses within $R_{\rm vir}$. When the gas is in thermal equilibrium, energy is equally partitioned among the molecules as ;

$$\frac{1}{2}\mu m_{\rm H}\langle v^2\rangle = \frac{3}{2}k_{\rm B}T. \tag{2.81}$$

The temperature T defined by Eq.(2.81) is called the virial temperature;

$$T_{\rm vir} = \frac{\mu m_{\rm H}\langle v^2\rangle}{3k_{\rm B}} = \frac{GM\mu m_{\rm H}}{5k_{\rm B}R_{\rm vir}} = \frac{\mu m_{\rm H}}{5k_{\rm B}}V_{\rm c}^2, \tag{2.82}$$

where the second equality follows from the assumption of a uniform sphere. Here, $V_{\rm c}$ is known as the circular velocity, defined as $V_{\rm c} \equiv \sqrt{GM/R_{\rm vir}}$.

In summary, a halo with mass $M_{\rm h}$ collapsing at redshift z has a virial radius ($R_{\rm vir}$), circular velocity ($V_{\rm circ}$), and virial temperature ($T_{\rm vir}$) given by

$$R_{\rm vir} = 0.784\, h^{-1}{\rm kpc} \left(\frac{M_{\rm h}}{10^8 h^{-1} M_\odot}\right)^{1/3} \left(\frac{\Delta_{\rm c}}{18\pi^2}\right)^{-1/3} \left(\frac{1+z_{\rm vir}}{10}\right)^{-1} \tag{2.83}$$

$$V_{\rm circ} = \sqrt{\frac{GM}{R_{\rm vir}}} = 23.4\ {\rm km\,s^{-1}} \left(\frac{M_{\rm h}}{10^8\ h^{-1} M_\odot}\right)^{1/3} \left(\frac{\Delta_c}{18\pi^2}\right)^{1/6} \left(\frac{1+z_{\rm vir}}{10}\right)^{1/2} \tag{2.84}$$

$$T_{\rm vir} = \frac{\mu m_{\rm p} {V_{\rm circ}}^2}{2k_{\rm B}} = 1.98\times 10^4\ {\rm K} \left(\frac{\mu}{0.6}\right) \left(\frac{M_{\rm h}}{10^8\ h^{-1} M_\odot}\right)^{2/3} \left(\frac{\Delta_c}{18\pi^2}\right)^{1/3} \left(\frac{1+z_{\rm vir}}{10}\right). \tag{2.85}$$

2.3 Gas Cooling/ Heating

After the system reaches virial equilibrium, the gas can further contract by radiative cooling, while the dark matter halo cannot. The evolution of the gas is described by the continuity equation, the Euler equation, and the energy equation;

$$\frac{\partial \rho}{\partial t} + \nabla\cdot(\rho \boldsymbol{v}) = 0 \tag{2.86}$$

$$\frac{\partial \boldsymbol{v}}{\partial t} + (\boldsymbol{v}\cdot\nabla)\boldsymbol{v} = -\nabla\Phi - \frac{\nabla P}{\rho} \tag{2.87}$$

$$\frac{\partial}{\partial t}\left[\rho\left(\frac{v^2}{2}+\mathcal{E}\right)\right] + \nabla\cdot\left[\rho\left(\frac{v^2}{2}+\frac{P}{\rho}+\mathcal{E}\right)\right] - \rho\boldsymbol{v}\cdot\nabla\Phi = \mathcal{H}-\mathcal{C}, \tag{2.88}$$

where ρ, P, v and $\mathcal{E}$ are gas mass density, pressure, velocity, and specific internal energy of the fluid, respectively. The gravitational potential Φ follows the Poisson equation,

$$\Delta\Phi = 4\pi G \rho_{\rm tot}, \tag{2.89}$$

where $\rho_{\rm tot}$ represents the mass density for matters (=baryons+dark matters). Here, $\mathcal{H}$ and $\mathcal{C}$ are heating and cooling rates per unit volume, and the following processes contribute to these terms.

2.3.1 Compton Cooling (Inverse Compton Scattering)

When low-energy photons ($\nu_{\rm p}$) pass through hot but non-relativistic ionized gas (plasma) with temperature $T_{\rm e}$ (i.e., $h\nu_{\rm p} \equiv k_{\rm B}T_\gamma \ll k_{\rm B}T_{\rm e} \ll m_{\rm e}c^2$), the gas is cooled through the inverse Compton scattering. The volume emissivity (=cooling rate per unit volume) is written as

$$\mathcal{C}_{\rm comp} = \frac{4k_{\rm B}T_{\rm e}}{m_{\rm e}c^2} c\sigma_{\rm T} n_{\rm e} a_{\rm r} T_\gamma^4, \tag{2.90}$$

where $\sigma_{\rm T}$ and $a_{\rm r}$ are the Thomson cross-section and the radiation constant, respectively. The corresponding cooling timescale is written as the ratio of internal energy[3] and the cooling rate;

$$t_{\rm Comp} = \frac{3n_{\rm e}k_{\rm B}T_{\rm e}}{\mathcal{C}_{\rm Comp}} = \frac{3m_{\rm e}c}{4\sigma_{\rm T}a_{\rm r}T_\gamma^4}. \tag{2.91}$$

This cooling timescale is independent of the gas density and temperature. If we consider the Cosmic Microwave Background (CMB) as the radiation source, its temperature is given by $T_\gamma =$

[3]The internal energy per unit volume is $\mathcal{E} = (3/2)n_{\rm gas}k_{\rm B}T$, with gas density defined as $n_{\rm gas} = n_{\rm H} + n_{\rm He} + n_{\rm e}$. Assuming the primordial gas composition, we have $n_{\rm He} = n_{\rm H}/12$ and $n_{\rm e} = 2n_{\rm He} + n_{\rm H} = 7n_{\rm H}/6$, leading to $n_{\rm gas} = 27n_{\rm e}/14$. Thus, $\mathcal{E} \simeq 3n_{\rm e}k_{\rm B}T_{\rm e}$.

$2.7(1+z)$, K. Comparing the Compton cooling timescale to the Hubble time ($t = \frac{2}{3H_0}(1+z)^{-3/2}$, from Eq. 2.40), we obtain

$$\frac{t_{\rm comp}}{t} = 250(1+z)^{-5/2}\left(\frac{H_0}{70\,{\rm km\,s^{-1}\,Mpc^{-1}}}\right). \tag{2.92}$$

This indicates that Compton cooling due to the CMB becomes important (i.e., $t_{\rm Comp}/t \lesssim 1$) at high redshifts, typically for $z \gtrsim 8$.

2.3.2 Radiative Cooling

When the gas temperature exceeds $T_{\rm gas} > 10^6$, K for primordial gas (or a few $\times 10^7$, K for metal-enriched gas), the gas becomes fully ionized through collisional ionization. In such highly ionized gas, free-free radiation (bremsstrahlung) is the dominant cooling mechanism. The volume emissivity per unit frequency is given by (Rybicki and Lightman, 1986);

$$\epsilon_{\rm ff}(\nu) = \frac{32\pi}{3}\frac{{\rm Z}^2 q_{\rm e}^6}{m_{\rm e}^2 c^4}\left(\frac{2\pi m_{\rm e}c^2}{3k_{\rm B}T_{\rm e}}\right)^{1/2} n_{\rm i} n_{\rm e} g(\nu,T)\exp\left(-\frac{h_{\rm P}\nu}{k_{\rm B}T_{\rm e}}\right) \tag{2.93}$$

$$= 6.8\times10^{-38}{\rm Z}^2\frac{n_{\rm i}n_{\rm e}}{T^{1/2}}g(\nu,T)\exp\left(-\frac{h_{\rm P}\nu}{k_{\rm B}T_{\rm e}}\right)\,{\rm erg\,s^{-1}\,cm^{-3}\,Hz^{-1}}, \tag{2.94}$$

where $g(\nu,T)\sim 1$ is the velocity-averaged Gaunt factor. Here, Z is the charge number of an ion, $n_{\rm i}$ is the ion number density, $q_{\rm e}$ is the electron charge, and $h_{\rm P}$ is Planck's constant. Integrating over frequency, the total volume emissivity of free-free radiation is

$$\mathcal{C}_{\rm ff} = \int \epsilon_{\rm ff}(\nu){\rm d}\nu \tag{2.95}$$

$$= 1.4\times10^{-19}T_{\rm e}^{1/2}\left(\frac{n_{\rm e}}{1\,{\rm cm^{-3}}}\right)^2\,{\rm erg\,s^{-1}\,cm^{-3}}. \tag{2.96}$$

Here, we assume fully ionized hydrogen gas (Z = 1 and $n_{\rm e} = n_{\rm i}$). For a fully ionized primordial gas mixture, Eq. (2.96) should be multiplied by a factor of 8/7.

As the temperature decreases, collisional ionization, recombination, and collisional excitation become significant mechanisms for gas cooling. Collisional ionization removes the kinetic energy from the gas equivalent to the ionization potential. Some ions subsequently recombine with free electrons, and during recombination, electrons cascade down through progressively lower energy levels. The corresponding recombination-line photons are emitted, radiatively cooling the gas.

Collisional excitation produces two types of emission lines: permitted lines and forbidden lines. At gas temperatures $T \gtrsim 10^4\,{\rm K}$, collisional excitation from the ground state ($n = 1$) to the first excited state ($n = 2$), corresponding to an energy gap of $10.2\,{\rm Z}^2\,{\rm eV}$, occurs. The subsequent Lyα radiation cools the gas. For atomic hydrogen, the volume emissivity of Lyα emission is expressed as[4]

$$\mathcal{C}_{\rm H} = 7.5\times10^{-19}{\rm erg\,s^{-1}\,cm^{-3}}\times\frac{1}{1+(T/10^5\,{\rm K})^{1/2}}\exp\left(-\frac{118348}{T}\right)n_{\rm e}n_{\rm H^0}, \tag{2.97}$$

where $n_{\rm H^0}$ denotes the number density of neutral hydrogen atoms. For gas temperatures $T \lesssim 10^4\,{\rm K}$, radiative cooling through permitted transitions becomes inefficient. Cooling is dominated by collisional excitation of fine-structure levels, producing forbidden-line emission. The physics of forbidden-line emission is discussed in Chapter 3.

[4]The Lyα cooling rate from collisional excitation can be derived similarly to the volume emissivity for forbidden lines described in Section 3.2.2, assuming a two-level system.

The cooling processes discussed above, including bremsstrahlung, have volume emissivities proportional to $n_{\rm i} n_{\rm e}$. Thus, we define the cooling function $\Lambda(T)$, with units of [erg s^{-1} cm^3], as

$$\Lambda(T) \equiv \frac{\mathcal{C}_{\rm tot}}{n_{\rm H}^2}, \tag{2.98}$$

where $\mathcal{C}_{\rm tot}$ includes bremsstrahlung, collisional ionization, recombination, and collisional excitation. Figure 2.3 shows cooling functions for different metallicities. In all cases, bremsstrahlung dominates at temperatures $T \geq 10^7, {\rm K}$, with $\Lambda(T) \propto T^{1/2}$, as derived in Eq. (2.96). For primordial gas at $T < 10^{5.5}\,{\rm K}$, most atoms recombine and collisional excitation becomes efficient. The two peaks at $T \sim 1.3 \times 10^4\,{\rm K}$ and $T \sim 10^5\,{\rm K}$ for primordial gas result from Lyα cooling by H^0 and He^+, respectively. Additional peaks at $T > 10^5\,{\rm K}$ for metal-enriched gas are due to permitted-line emission from collisionally excited metal ions.

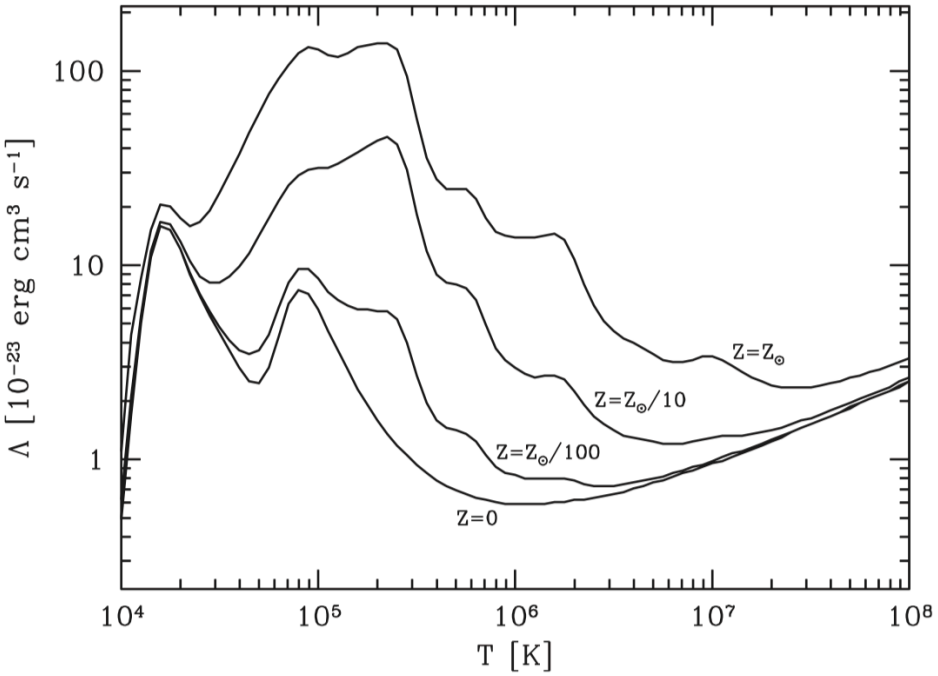

Figure 2.3: Cooling functions for primordial gas, and for gases with metallicities $Z/Z_\odot = 0.01, 0.1$ and 1.0, as indicated. The figure is taken from (Mo et al., 2010).

Note that the cooling functions described above are valid for gas in collisional ionization equilibrium (CIE) and do not account for external radiation sources. In HII regions around massive stars, photoionization dominates over collisional ionization. Additionally, the assumption of CIE fails when the cooling timescale becomes significantly shorter than the recombination timescale. This situation often occurs in diffuse, hot gas, such as galactic halos, leading to gas that is over-ionized relative to the CIE assumption (Gnat and Sternberg, 2007). Conversely, if the heating timescale is much shorter than the collisional ionization timescale, the gas becomes under-ionized compared to the CIE scenario. Strong shocks from supernova explosions provide a typical example of this condition.

2.3.3 Photoelectric Heating

As mentioned previously, external radiation fields can cause photoionization. The portion of photon energy exceeding the ionization potential is converted into kinetic energy, thus heating

the gas. The volume heating rate for each ion, with units of [erg s^{-1} cm^{-3}], is given by

$$\mathcal{H}_{\rm i} = n_{\rm i} \int_{\nu_i}^{\infty} \frac{4\pi J(\nu)}{h_{\rm P}\nu} \sigma_{\rm photo,i}(\nu)(h_{\rm p}\nu - h_{\rm p}\nu){\rm d}\nu, \tag{2.99}$$

where $J(\nu)$ and $\sigma_{\rm photo,i}(\nu)$ represent the intensity of the radiation field and the photoionization cross-section for ion species i, respectively. In addition to photoionization heating, other processes such as photoelectric heating by dust and photodissociation of H_2 by ultraviolet (UV) photons also contribute significantly to gas heating.

When the gas density and temperature is high, cooling process works effectively, and gas sphere contracts. However, the cooling timescale is longer than the dynamical timescale ($\simeq$ free-fall time scale, see Section 2.4.2), the gas sphere with mass $M_{\rm gas}$, radius R keeps virial equiriblium within a dark matter halo with $M_{\rm DM}$, and the temperature is inverse to virial radius (see Eq.2.82), which implies that temperature increases as the gas sphere contracts. The cooling timescale for primordial gas ($n_{\rm gas} = (27/12)n_{\rm H}$)is written as

When the gas density and temperature are high, the cooling processes become effective, and the gas sphere contracts. However, if the cooling timescale is longer than the dynamical timescale ($\simeq$ free-fall timescale, see Section 2.4.2), the gas sphere with mass $M_{\rm gas}$ and radius R remains in virial equilibrium within a dark matter halo of mass $M_{\rm DM}$. The cooling timescale for the primordial gas ($n_{\rm gas} = (27/12)n_{\rm H}$) is expressed as

$$t_{\rm cool} = \frac{\frac{3}{2}n_{\rm gas}k_{\rm B}T}{n_{\rm H}^2\Lambda(T)} \simeq 1.5\times10^9\,{\rm yr}\left(\frac{T}{10^6\,{\rm K}}\right)\left(\frac{n_{\rm H}}{10^{-3}\,{\rm cm^{-3}}}\right)^{-1}\left(\frac{\Lambda(T)}{10^{-23}\,{\rm erg\,s^{-1}\,cm^3}}\right)^{-1}. \tag{2.100}$$

The dynamical time scale is written as

$$t_{\rm dyn} = \sqrt{\frac{3\pi}{16G\rho_{\rm tot}}} = \sqrt{\frac{3\pi f_{\rm gas}}{32G\rho_{\rm gas}}} \sim 3.0\times10^9\,{\rm yr}\, f_{\rm gas}^{1/2}\left(\frac{n_{\rm H}}{10^{-3}\,{\rm cm^{-3}}}\right)^{-1/2}, \tag{2.101}$$

where $\rho_{\rm tot} = \rho_{\rm DM}+\rho_{\rm gas}$ within the halo and $f_{\rm gas}$ is the gas fraction defined as $f_{\rm gas} = M_{\rm gas}/M_{\rm tot} = M_{\rm gas}/(M_{\rm gas}+M_{\rm DM})$. The gas sphere in virial equilibrium satisfies

$$2\cdot\frac{3}{2}\frac{M_{\rm gas}}{\mu m_{\rm p}}k_{\rm B}T = \frac{3}{5}\frac{GM_{\rm tot}M_{\rm gas}}{R} \tag{2.102}$$

$$\therefore M_{\rm gas} = \left(\frac{5k_{\rm B}}{\mu m_{\rm p}G}\right)^{3/2}\left(\frac{3}{4\pi\mu m_{\rm p}}\right)^{1/2} T^{3/2}\, f_{\rm gas}^{3/2}\, n_{\rm H}^{-1/2} \tag{2.103}$$

$$\simeq 8.4\times10^{12}\,M_\odot\left(\frac{T}{10^6\,{\rm K}}\right)^{1/2} f_{\rm gas}^{3/2}\left(\frac{n_{\rm H}}{10^{-3}\,{\rm cm^{-3}}}\right)^{-1/2}. \tag{2.104}$$

Thus, by determining the combination of $n_{\rm H}$ and T that satisfies $t_{\rm cool} < t_{\rm dyn}$, we can obtain the corresponding gas (halo) mass. The typical threshold gas mass is approximately $M_{\rm gas} \sim 10^{12}\,M_\odot$ for cooling rates with solar metallicity.

2.4 Star formation

2.4.1 Jeans Instability

When the cooling timescale becomes significantly shorter than the dynamical timescale as described above, the gas continues to contract and eventually reaches the Jeans instability. Here, we examine the gravitational stability of a self-gravitating gas by adding small perturbations.

Consider an arbitrary quantity Q in an equilibrium state, which experiences small fluctuations Q_1, such that $Q = Q_0 + Q_1$ and $|Q_1| \ll Q_0$. We assume that the perturbation Q_1 can be described by a plane-wave solution of the form $Q_1 \propto e^{i(kx-\omega t)}$. In the initial equilibrium

state, the gas pressure, density, and velocity are P_0, ρ_0, and $\boldsymbol{v}_0 = 0$, respectively. When small perturbations are added adiabatically, these physical quantities become $\rho = \rho_0 + \rho_1$ and $\boldsymbol{v} = \boldsymbol{v}_1$. Substituting these into Eqs. (2.86), (2.87), and (2.89), and ignoring second-order terms, we obtain

$$\frac{\partial \rho_1}{\partial t} + \rho_0 \nabla \cdot \boldsymbol{v_1} = 0 \tag{2.105}$$

$$\frac{\partial \boldsymbol{v_1}}{\partial t} = -\frac{c_s^2}{\rho_0}\nabla \rho_1 - \nabla \Phi_1 \tag{2.106}$$

$$\Delta \Phi_1 = 4\pi G \rho_1, \tag{2.107}$$

where c_s is the sound speed. Performing a Fourier transform of the equations above, we obtain

$$-i\omega\tilde{\rho_1} + \rho_0 \cdot ik\tilde{v_1} = 0 \tag{2.108}$$

$$-i\omega\tilde{v_1} = -\frac{c_s^2}{\rho_0} ik\tilde{\rho_1} - ik\tilde{\Phi_1} \tag{2.109}$$

$$(ik)^2\tilde{\Phi_1} = 4\pi G\tilde{\rho_1} \tag{2.110}$$

In matrix form, these equations can be expressed as

$$\underbrace{\begin{pmatrix} -i\omega & i\rho_0 k & 0 \\ i\frac{kc_s^2}{\rho_0} & -i\omega & ik \\ -4\pi G & 0 & -k^2 \end{pmatrix}}_{\boldsymbol{A}} \underbrace{\begin{pmatrix} \rho_1 \\ v_1 \\ \Phi_1 \end{pmatrix}}_{\boldsymbol{x}} = \begin{pmatrix} 0 \\ 0 \\ 0 \end{pmatrix} \tag{2.111}$$

Thus, we have $\boldsymbol{A} \cdot \boldsymbol{x} = 0$. For a non-trivial solution $\boldsymbol{x} \neq \boldsymbol{0}$, $\boldsymbol{A}$ requires

$$\mathrm{dot}\boldsymbol{A} = (\omega^2 + 4\pi G\rho_0 - c_s^2 k^2)k^2 = 0 \tag{2.112}$$

$$\therefore\ \omega^2 = c_s^2 k^2 - 4\pi G\rho_0 \tag{2.113}$$

Equation (2.113) is known as the dispersion relation, which defines the critical Jeans wavenumber k_J is $k_\mathrm{J} = \frac{4\pi G\rho_0}{c_s}$.

When $k > k_\mathrm{J}$, we have $\omega^2 > 0$, and the system remains stable. Conversely, when $k < k_\mathrm{J}$, we have $\omega^2 < 0$, and the system becomes unstable, with perturbations growing exponentially. The threshold wavelength for gravitational instability is the Jeans length;

$$\lambda_\mathrm{J} = \frac{2\pi}{k_\mathrm{J}} = c_s\sqrt{\frac{\pi}{G\rho_0}}. \tag{2.114}$$

If the perturbation wavelength exceeds the Jeans length (λ_J), self-gravity dominates over pressure support. The Jeans mass, corresponding to a sphere with radius equal to half the Jeans length λ_J, is given by

$$M_\mathrm{J} = \frac{4\pi}{3}\left(\frac{\lambda_J}{2}\right)^3 \rho_0 = \frac{\pi}{6}\frac{c_s^3}{G^{3/2}\rho^{1/2}} \propto T^{3/2}\rho^{-1/2} \tag{2.115}$$

Once perturbations occur, pressure fluctuations generate sound waves that propagate through the cloud. The characteristic timescale for these sound waves to cross the cloud and re-establish pressure equilibrium is known as the sound crossing time;

$$t_\mathrm{sc} = \frac{\lambda_\mathrm{J}}{c_s}. \tag{2.116}$$

Jeans instability can also be discussed by comparing the sound crossing time (t_sc) with the free-fall time (t_ff), the gravitational collapse timescale explained in the next section. When $t_\mathrm{sc} < t_\mathrm{ff}$,

pressure effectively stabilizes the cloud against gravitational collapse. Conversely, if $t_{\rm sc} > t_{\rm ff}$, gravitational perturbations grow unabated, resulting in the cloud collapse.

It is important to note that this Jeans analysis assumes contradictory initial conditions. The unperturbed state assumes constant density and pressure ($\rho_0, p_0 = \text{const.}$) and zero initial velocity ($\boldsymbol{v}_0 = 0$). Substituting these conditions into the equation of motion (Eq.2.87) requires $\nabla\Phi_0 = 0$. However, the Poisson equation (Eq.2.89) cannot be satisfied unless $\rho_0 = 0$. This contradiction is referred to as the Jeans swindle.

2.4.2 Runaway Collapse

When the mass of a gas clump exceeds the Jeans mass ($M > M_{\rm J}$), gravitational collapse begins. The characteristic timescale for this gravitational collapse is known as the free-fall time. Here, we consider a spherical gas cloud with no pressure gradient, influenced solely by self-gravity. The cloud initially has a uniform density, and at $t = 0$, a shell within the cloud at radius $r = a$ is at rest (velocity $v = 0$). At a later time t, the radius of this shell is denoted as $R(t) = af(t, a)$, where $0 \leq f \leq 1$. The equation of motion for the shell at time t is

$$\frac{d^2R}{dt^2} = a\ddot{f} = -\frac{GM(<a)}{R^2} = -G\frac{1}{(af)^2}\frac{4\pi a^3}{3}\rho(0) \tag{2.117}$$

$$\therefore \ddot{f} = -\frac{4\pi G\rho(0)}{3f^2}. \tag{2.118}$$

In Eq.(2.118), the function f is independent of the initial radius a, indicating that a homogeneous gas sphere, regardless of its initial size, contracts simultaneously toward its center if collapse begins at the same initial time. Integrating Eq.(2.118) with respect to time, we obtain

$$\beta + \frac{1}{2}\sin(2\beta) = t\left(\frac{8\pi G\rho(0)}{3}\right)^{1/2} \quad (f = \cos^2\beta) \tag{2.119}$$

As f changes from $f = 1$ (initial state) to $f = 0$ (collapse to the center), the corresponding parameter β evolves from 0 to $\frac{\pi}{2}$. Substituting $\beta = \frac{\pi}{2}$ into Eq.(2.118), we obtain the free-fall timescale

$$t_{\rm ff} = \left(\frac{3\pi}{32G\rho(0)}\right)^{1/2}, \tag{2.120}$$

which represents the time it takes for a self-gravitating system to collapse from rest to an infinite density under its gravity. Eq.(2.120) indicates that higher-density inner regions collapse more rapidly than lower-density outer regions. Consequently, the central region contracts faster, forming a dense core while leaving behind an envelope. This phenomenon is known as runaway collapse.

Larson (1969) numerically calculated the collapse of an isothermal, spherical gas cloud with an initially uniform density distribution. They found that the density profile of the resulting envelope follows a power law of approximately $\rho \propto r^{-2}$. Even in the presence of pressure gradients, the central region collapses approximately on the free-fall timescale. The size of the central density peak roughly corresponds to the Jeans length, which scales as $\rho^{-1/2}$ (see Eq. 2.114).

The power-law density distribution of the envelope can be roughly explained as follows;

$$\frac{\lambda_J}{c_s} \sim t_{\rm ff} \sim \frac{1}{\sqrt{G\rho}} \tag{2.121}$$

$$\therefore \ \rho \propto \frac{c_s}{r^2} \propto \frac{T}{r^2}. \tag{2.122}$$

A more detailed derivation is presented in Larson (1969).

Chapter 3

Physics of Inter Stellar Medium

As mentioned in Section 2.4, gas cooling in dense regions triggers gravitational instability, leading to a runaway collapse and initiating star formation. Subsequently, massive stars born through this process end their short lifetimes (within tens of millions of years) as supernovae (SNe), significantly enriching their surroundings with heavy elements. This metal enrichment enables more efficient gas cooling through metal-line radiation, thus facilitating the formation of the next-generation stars. Additionally, the ionizing photons emitted by these young stellar populations ionize the surrounding gas, producing characteristic nebular emission lines that are observable with current telescopes such as JWST and ALMA. The metal enrichment by supernovae also leads to the formation of dust grains, crucial for interpreting multi-wavelength observations of high-redshift galaxies.

Figure 3.1 schematically summarizes these processes, highlighting the connections among star formation, metal enrichment, nebular emission, and dust formation, all of which are essential for understanding the chemical evolution of galaxies.

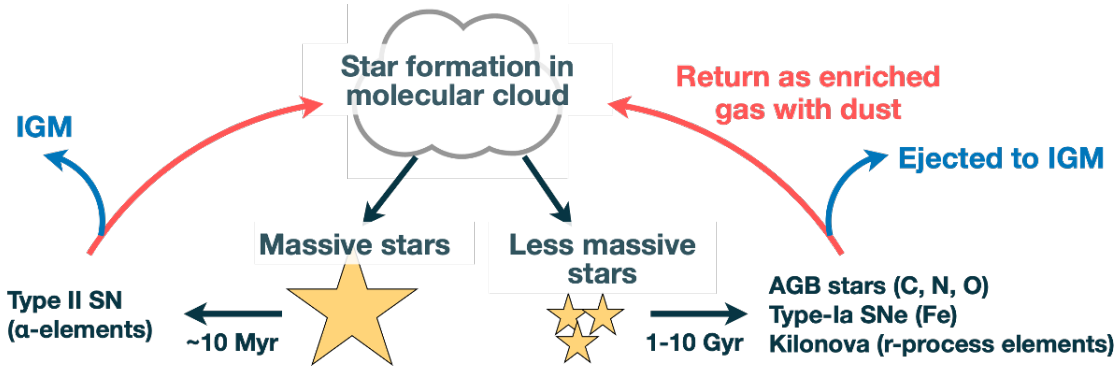

Figure 3.1: Schematic illustration of the metal enrichment process in galaxies.

The left path for massive stars may be important in high-redshift galaxies i.e., low-metallicity environments. This is because stellar mass is thought to scale with cloud mass (Jeans mass), which is proportional to $T_{\rm cloud}^{3/2}$ (Eq.(2.115)). Lower metallicity implies fewer available coolants, leading to higher cloud temperatures ($T_{\rm cloud}$) compared to environments with higher metallicity [1].

[1]The evolutionary paths for stars depend strongly on their ZAMS masses. High-mass stars typically evolve from the Main Sequence through stages such as Red Supergiants, Blue Supergiants, Luminous Blue Variables, and Wolf-Rayet stars, ultimately ending their lives as core-collapse supernovae (CCSN). On the other hand, mid- and low-mass stars evolve from the Main Sequence to the Red Giant Branch, then proceed to the Asymptotic Giant Branch (AGB), followed by the Thermal Pulsing-AGB phase, and eventually become Planetary Nebulae, leaving behind White Dwarfs.

Here we summarize the production timescales for four major elements: oxygen, nitrogen, carbon, and iron. Immediately following star formation, core-collapse supernovae (CCSNe) dominate the enrichment of the interstellar medium, primarily supplying oxygen and carbon within the first 30–40 Myr. After about 30 Myr, Type Ia supernovae begin to contribute significantly, enriching the environment predominantly with iron. Nitrogen enrichment occurs on slightly longer timescales (∼40 Myr after star formation), primarily through stellar winds from asymptotic giant branch (AGB) stars. Metallicity (Z) is defined as the total **mass fraction** of all elements heavier than helium relative to the baryon mass as

$$Z \equiv \frac{M_{\rm metal}}{M_{\rm baryon}}. \tag{3.1}$$

The solar metallicity is typically taken as $Z_\odot = 0.02$ (Anders and Grevesse, 1989). The metallicity of stars is commonly expressed using the iron-to-hydrogen abundance ratio;

$$[{\rm Fe/H}] = \log(M_{\rm Fe}/M_{\rm H}) - \log(M_{\rm Fe}/M_{\rm H})_\odot \tag{3.2}$$

$$= \log(N_{\rm Fe}/N_{\rm H}) - \log(N_{\rm Fe}/N_{\rm H})_\odot. \tag{3.3}$$

For gas-phase metallicities, the oxygen-to-hydrogen **number ratio** is frequently used;

$$12 + \log({\rm O/H}) \equiv 12 + \log(N_{\rm O}/N_{\rm H}). \tag{3.4}$$

The adopted solar oxygen abundance varies between studies, for example, $12+\log({\rm O/H})_\odot = 8.6$ in Asplund et al. (2009), and 8.9 in Woosley and Weaver (1995).

3.1 Star-forming Regions in a Galaxy

Star-forming regions generally consist of three main components: HII regions, photodissociation regions (PDRs), and molecular gas regions, as illustrated in Figure 3.2. These regions are primarily composed of ionized hydrogen, neutral hydrogen atoms, and molecular hydrogen, respectively. Heavier elements (metals) are also present in these regions. Emission lines from metals are crucial for studying the characteristics of star-forming regions. The detailed mechanisms behind metal-line emissions are discussed in Section 3.2.

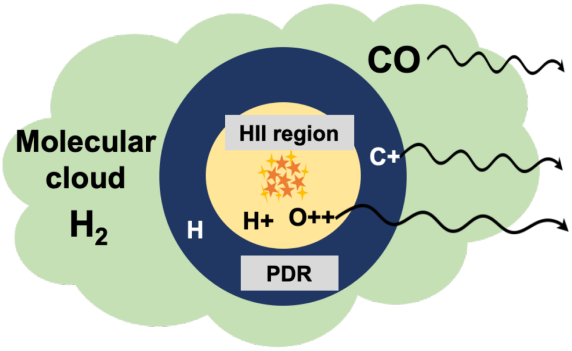

Figure 3.2: Illustration of star-forming regions. HII regions, PDRs, and molecular clouds are located progressively further from the central stars.

3.1.1 HII Regions

Massive stars, such as O-type and B-type stars, emit ionizing photons with energies $h\nu > 13.6$ eV. These photons ionize the surrounding gas, creating regions known as HII regions.

We define the recombination rate $N_{\rm rec}$ [cm^{-3}sec^{-1}] as the number of recombinations per unit volume per unit time.

$$N_{\rm rec} = n_{\rm p} n_{\rm e} \langle \sigma_{\rm e} v_{\rm e} \rangle = n_{\rm p} n_{\rm e} \alpha(T), \tag{3.5}$$

where σ_e is the cross-section for electron capture and $\langle \sigma_e v_e \rangle$ is a velocity-averaged value

$$\langle \sigma_e v_e \rangle = \int_{-\infty}^{\infty} \sigma_e f(v_e) v_e dv. \tag{3.6}$$

Since hydrogen is the dominant component, we approximate $n_p \sim n_e$. Therefore, Eq. (3.5) can be rewritten as

$$N_{rec} = \alpha(T) n_e^2 = \alpha(T) x^2 n_H^2 \quad \left(x \equiv \frac{n_e}{n_H} \right), \tag{3.7}$$

where n_H is the total number density of hydrogen atoms (both ionized and neutral), and x is the ionization fraction.

Let us assume that the gas is *optically thick*[2], meaning that no ionizing photons escape from the nebula. Additionally, we assume this condition holds within a spherical region of radius R_S. Integrating N_{rec} over the spherical region, we obtain the balance equation as follows,

$$Q_0 = \int N_{rec} dV = \frac{4\pi}{3} R_S^3 \epsilon x^2 n_H^2 \alpha(T), \tag{3.8}$$

where Q_0 is the ionizing photon number per unit time emitted from the source stars. In Eq.(3.8), we introduce filling factor ϵ (Gutiérrez and Beckman, 2008), which is defined as

$$\epsilon \equiv \frac{\text{(volume occupied by the clumps)}}{\text{(total volume of HII region)}}. \tag{3.9}$$

Real HII regions do not have perfectly spherical shapes but rather complex morphologies, consisting of highly dense, fully ionized gas clumps surrounded by otherwise nearly empty regions (e.g., Osterbrock and Flather, 1959). Hence, ϵ characterizes the inhomogeneous structure of HII regions.

Let us assume that the gas within R_S is totally ionized ($x = 1$) and that the case B approximation is valid. A gas is optically thick[3] to all Lyman Series photons and ionizing photons with $h\nu > 13.6$ eV. Such photons are immediately absorbed by other atoms nearby ("on-the-spot approximation"). Then, Eq.(3.8) becomes

$$Q_0 = \frac{4\pi}{3} R_S^3 n_{HII}^2 \epsilon \alpha_B, , \tag{3.10}$$

where n_{HII} is the density of HII region, and α_B is effective recombination coefficient for hydrogen atoms. The coefficient α_B is given by

$$\alpha_B \left(H^0, T \right) = \alpha_A \left(H^0, T \right) - \alpha_1 \left(H^0, T \right) \tag{3.11}$$

$$= \sum_{n=2}^{\infty} \alpha_n \left(H^0, T \right) \tag{3.12}$$

$$= 2.6 \times 10^{-13} \left(\frac{T_e}{10^4 \text{ K}} \right)^{-0.85} \text{ cm}^3 \text{s}^{-1}. \tag{3.13}$$

Here, α_n denotes the recombination coefficient for free-bound transitions to energy level n. Using Eq.(3.10), the size of the HII region, R_S, can be derived as follows;

$$R_S = \left(\frac{3Q_0}{4\pi n_{HII}^2 \epsilon \alpha_B} \right)^{1/3} \tag{3.14}$$

$$= 5.4 \left(\frac{n_{HII}}{10^2 \text{ cm}^{-3}} \right)^{-2/3} \left(\frac{Q_0}{5 \times 10^{49} \text{ s}^{-1}} \right)^{1/3} \text{ pc (for } T_e = 10^4 \text{ K}, \ \epsilon = 1), \tag{3.15}$$

[2] In this sentence, optically thick *globally*.
[3] In this sentence, "optically thick" is meant *locally*.

which is called Strömgren radius.

The ionization parameter U is defined as the ratio of the number density of ionizing photons to that of hydrogen atoms. It quantifies the ionization state within an HII region and serves as an indicator of star formation activity, as ionizing photons are primarily produced by young, massive stars. Since the ionization parameter varies spatially, a volume-averaged ionization parameter is typically expressed by assuming a spherical HII region with uniform density (Panuzzo et al., 2003):

$$\langle U \rangle = \int_0^{R_\mathrm{S}} \frac{U(r) 4\pi r^2}{\frac{4\pi}{3} R_\mathrm{S}^3} \, \mathrm{d}r, \text{ where } U(r) = \frac{Q(r)}{4\pi r^2 n_\mathrm{HII} c}. \tag{3.16}$$

Here $Q(r)$ is the number of ionizing photons passing through a spherical shell of radius r per unit time,

$$Q(r) = \#(\text{total ionizing photons from the source}) - \#(\text{photons absorbed within } r) \tag{3.17}$$

$$= Q_0 - \frac{4\pi}{3} r^3 n_\mathrm{HII}^2 \epsilon \alpha_\mathrm{B}. \quad (\because \text{ Eq. (3.10)}) \tag{3.18}$$

Substituting Eq.(3.10) and the Strömgren radius (Eq. (3.15)) into Eq.(3.16), we obtain

$$\langle U \rangle = \int_0^{R_\mathrm{S}} \left(\frac{Q_0}{4\pi r^2 n_\mathrm{HII} c} - \frac{r n_\mathrm{HII} \alpha_\mathrm{B} \epsilon}{3c} \right) \frac{3r^2 \, \mathrm{d}r}{R_\mathrm{S}^3} \tag{3.19}$$

$$= \frac{3Q_0}{4\pi n_\mathrm{HII} c} \left(\frac{4\pi n_\mathrm{HII}^2 \alpha_\mathrm{B} \epsilon}{3Q_0} \right)^{2/3} - \frac{n_\mathrm{HII} \alpha_\mathrm{B} \epsilon}{4c} \left(\frac{3Q_0}{4\pi n_\mathrm{HII}^2 \alpha_\mathrm{B} \epsilon} \right)^{1/3} \tag{3.20}$$

$$= \frac{3\alpha_\mathrm{B}^{2/3}}{4c} \left(\frac{3Q\epsilon^2 n_\mathrm{HII}}{4\pi} \right)^{1/3} \tag{3.21}$$

$$= 1.0 \times 10^{-2} \left(\frac{n_\mathrm{HII}}{10^2 \text{ cm}^{-3}} \right)^{1/3} \left(\frac{Q_0}{5 \times 10^{49} \text{ s}^{-1}} \right)^{1/3} \quad (\text{for } T_\mathrm{e} = 10^4 \text{ K}, \ \epsilon = 1). \tag{3.22}$$

The radius that satisfies $\langle U \rangle = U(r)$ can be derived from the equation $x^3 + (9/4)x^2 - 1 = 0$, where $x \equiv r/R_\mathrm{S}$. The solution to this equation is $r \sim 0.6 R_\mathrm{S}$.

3.1.2 Photodissociation Regions (PDR)

Photons with energies below 13.6 eV reach outside HII region. Hydrogen molecules are photodissociated and exist as neutral hydrogen atoms, and we call such regions photodissociation regions, short for PDR. In PDR, carbon is first ionized (first ionization potential: 11.26 eV), and oxygen exists as neutral atoms (first ionization potential: 13.62 eV). Fine-structure lines such as [CII] 158 μm and [OI] 63 μm are emitted from PDR and their emissivity depends on the incident radiation field G within the Habing band (6 - 13.6 eV) and the gas number density n. In reality, these properties have various distributions and HI gases have two-phase states; warm neutral medium (WNM, $T \sim 10^4$ K, $n_\mathrm{H} \sim 0.1$ cm^{-3}) and cold neutral medium (CNM, $T \sim 10^2$ K, $n_\mathrm{H} \sim 10^1 - 10^2$ cm^{-3}) as illustrated in Figure 3.3.

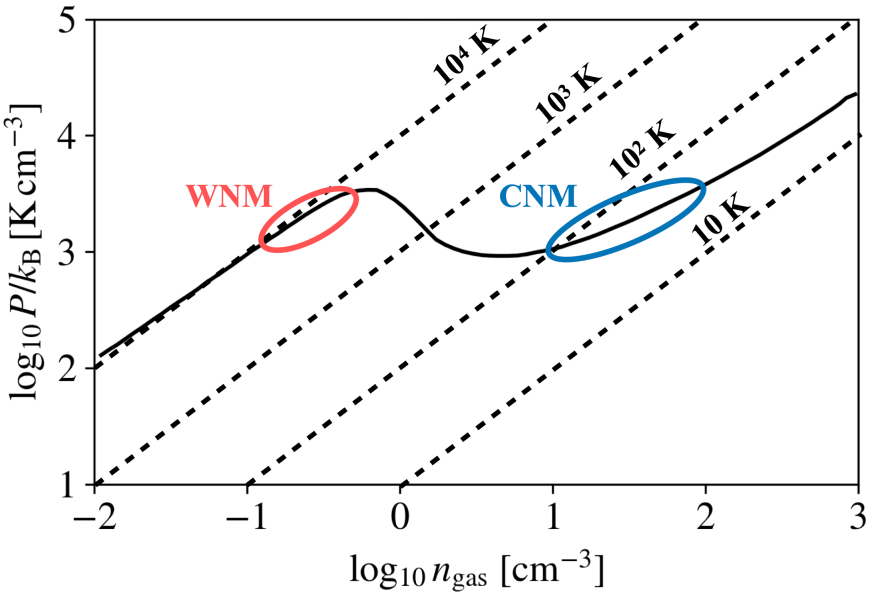

Figure 3.3: Phase diagram in HI region. Points on the black solid line satisfy radiative equilibrium between heating and cooling. The phase diagram is for an absorbing column of 10^{19} cm^{-2} in Wolfire et al. (1995). The dashed lines indicate constant temperatures.

3.1.3 Molecular Gas Regions

Molecular hydrogen (H_2) gas regions are found beyond the PDR. Among the three regions, molecular gas has the highest density ($10^2 - 10^5$ cm^{-3}) and the lowest temperature (typically a few tens of Kelvin). Under typical conditions, molecular gas regions have high internal pressure, undergo self-gravitationally collapse, and can lead to star formation. Due to their very low temperature, emission lines from H_2 are difficult to observe directly because the lowest excitation energy of H_2 corresponds to an excitation temperature of 512 K. Instead, CO emission lines are commonly used as effective tracers of molecular gas regions.

3.2 Radiative Processes

3.2.1 Selection Rules and Forbidden Lines

Emission lines arising from electric dipole radiation are termed permitted lines and must satisfy the following selection rules;
1. $\Delta L = 0, \pm 1$(but $L' = 0 \to L = 0$ is forbidden)
2. $\Delta J = 0, \pm 1$
3. $\Delta S = 0$,
where L is the orbital angular momentum, S is the spin quantum number, and J is the total angular momentum, i.e., $J = L + S$. However, even when transitions by electric dipole radiation are forbidden, transitions by magnetic dipole or electric quadrupole radiation are permitted. These transitions can occur in low-density environments, where collisional de-excitation is unlikely to occur. The corresponding emission lines are called forbidden lines and are generally denoted by brackets around the ion, such as [OIII] or [CII].

Also, there are the other emission lines coined semi-forbidden lines, which are electric dipole radiation but with changes of $\Delta S = \pm 1$. The semi-forbidden lines are denoted by] around the ion, such as CIII].

3.2.2 Collisionally Excited Line Emission and Critical Density

Collisionally excited line emissions, such as [OII] , [OIII] , and [NII] , play a crucial role in radiative processes within nebulae. The abundance of these ions is small relative to hydrogen (e.g., $N_{\rm O}/N_{\rm H} \sim 10^{-3.2}$, $N_{\rm N}/N_{\rm H} \sim 10^{-4.0}$ for solar abundance (Grevesse and Sauval, 1998). However, their excitation potential of a few electron volts, and thus can be dominant radiation in a diffuse nebula. The details are described in Seaton (1954, 1960); Osterbrock and Ferland (2006).

We consider a two-level system, as illustrated in Figure 3.4. Here, X_{21} represents the transition coefficient from the upper level (2) to the lower level (1). The Einstein coefficient for radiative de-excitation is denoted by $A_{21}[\mathrm{s}^{-1}]$, and the collisional de-excitation rate per unit volume per unit time is represented by $q_{21}[\mathrm{cm}^3\,\mathrm{s}^{-1}]$.

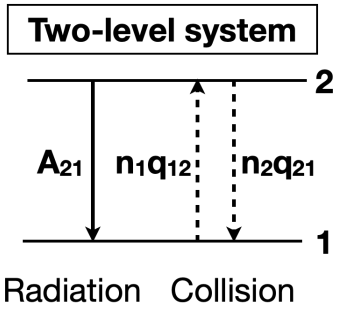

Figure 3.4: Transitions in a two-level system via radiation (solid arrows) and collisions (dashed arrows). The quantities $n_1 q_{12}$, A_{21}, and $n_2 q_{21}$ represent the excitation and de-excitation rates per unit time.

We calculate the collisional excitation and de-excitation rates q_{12}, q_{21}. The relationship between q_{12} and q_{21} is derived using the principle of detailed balance, which states that an elementary process (such as collisional excitation) is in equilibrium with its reverse process (collisional de-excitation) in a microscopic system in thermal equilibrium. In thermal equilibrium, we have

$$\begin{aligned}&(\text{rate of collisional excitation with velocities } u_1 \sim u_1 + \mathrm{d}u_1)\\ &= (\text{rate of collisional de-excitation with velocities } u_2 \sim u_2 + \mathrm{d}u_2).\end{aligned}$$

We can express this by using the collisional cross-section σ and Maxwell-Boltzmann velocity distribution $f(u) = \dfrac{4}{\sqrt{\pi}}\left(\dfrac{m}{2k_{\rm B}T}\right)^{3/2} u^2 \exp\left(-\dfrac{mu^2}{2k_{\rm B}T}\right)$ as follows,

$$n_{\rm e} n_1 u_1 \sigma_{12}(u_1) f(u_1) \mathrm{d}u_1 = n_{\rm e} n_2 u_2 \sigma_{21}(u_2) f(u_2) \mathrm{d}u_2 \tag{3.23}$$

$$\therefore \frac{n_2}{n_1} = \frac{u_1 \mathrm{d}u_1}{u_2 \mathrm{d}u_2} \frac{\sigma_{12}(u_1)}{\sigma_{21}(u_2)} \frac{f(u_1)}{f(u_2)} \tag{3.24}$$

$$= \frac{\sigma_{12}(u_1)}{\sigma_{21}(u_2)} \frac{u_1^2}{u_2^2} \exp\left[-\frac{m}{2k_{\rm B}T}\left(u_1^2 - u_2^2\right)\right] \tag{3.25}$$

Here, u_1 and u_2 have the following relationship;

$$\frac{1}{2}mu_1^2 = \chi + \frac{1}{2}mu_2^2, \tag{3.26}$$

where χ is the excitation potential.

In thermal equilibrium, the Boltzmann distribution between the two levels gives

$$\frac{n_2}{n_1} = \frac{\omega_2}{\omega_1} \exp\left(-\frac{\chi}{k_{\rm B}T}\right), \tag{3.27}$$

where ω_i is a statistical weight. From Eq. (3.25) and Eq. (3.27), we obtain the relation;

$$\omega_2 u_2^2 \sigma_{21}(u_2) = \omega_1 u_1^2 \sigma_{12}(u_1). \tag{3.28}$$

When $\frac{1}{2}mu_1^2 > \chi$, the collisional excitation can occur and its cross-section σ_{12} scales as $\sigma_{12} \propto u^{-2}$ due to electronic repulsion as follows (Hebb and Menzel, 1940),

$$\sigma_{12}(u_1) = \frac{\pi\hbar^2}{m^2 u_1^2}\frac{\Omega(1,2)}{\omega_1}, \tag{3.29}$$

where $\Omega(1,2)$ is the collision strength, a quantum mechanically determined quantity. The cross-section of collisional de-excitation σ_{21} is also calculated by Eq.(3.28) and Eq.(3.29),

$$\sigma_{21}(u_2) = \frac{\pi\hbar^2}{m^2 u_2^2}\frac{\Omega(1,2)}{\omega_2}. \tag{3.30}$$

Finally, the collisional de-excitation rate per unit time per unit volume is

$$q_{21} = \int_0^\infty u_2 \sigma_{21} f(u_2) \mathrm{d}u_2 \tag{3.31}$$

$$= \left(\frac{2\pi}{k_\mathrm{B}T}\right)^{1/2} \frac{\hbar^2}{m^{3/2}} \frac{\Upsilon_{(1,2)}}{\omega_2} \quad \left(\Upsilon_{(1,2)} \equiv \int_0^\infty \Omega_{(1,2)} \exp\left(-\frac{mv_2^2}{2k_\mathrm{B}T_\mathrm{e}}\right) d\left(\frac{mv_2^2}{2k_\mathrm{B}T_\mathrm{e}}\right)\right) \tag{3.32}$$

$$= \frac{8.629 \times 10^{-6}}{T^{1/2}} \frac{\Upsilon(1,2)}{\omega_2} \ [\mathrm{cm^3\,sec^{-1}}], \tag{3.33}$$

where $\Upsilon_{(1,2)}$ is the average collisional strength $\Omega_{(1,2)}$. The cross-section of collisional excitation is also calculated in the same way,

$$q_{12} = \frac{n_2}{n_1} q_{21} = \frac{8.629 \times 10^{-6}}{T^{-1/2}} \frac{\Upsilon_{(1,2)}}{\omega_1} \exp\left(-\frac{\chi}{k_\mathrm{B}T}\right) \ [\mathrm{cm^3\,sec^{-1}}] \tag{3.34}$$

Since electrons can be excited by collision[4] and be de-excited by collision or radiation, the balance equations are

$$n_\mathrm{e} n_1 q_{12} = n_\mathrm{e} n_2 q_{21} + n_2 A_{21} \tag{3.35}$$

$$\therefore \frac{n_2}{n_1} = \frac{n_\mathrm{e} q_{12}}{A_{21}\left[1 + \frac{n_\mathrm{e} q_{21}}{A_{21}}\right]}, \tag{3.36}$$

The Einstein coefficient A_{21} is determined by quantum physics, while the collisional excitation and de-excitation rates q_{12} and q_{21} are calculated using Eq.(3.34) and Eq.(3.33), respectively. The density at which collisional de-excitation and radiative de-excitation occur at equal rates is termed the *critical density*, defined as;

$$n_\mathrm{crit} \equiv \frac{A_{21}}{q_{21}}. \tag{3.37}$$

From Eq.(3.36), the volume emission rate ϵ_{12} [$\mathrm{erg\,s^{-1}\,cm^{-3}}$] is

$$\epsilon_{21} = n_2 A_{21} h_\mathrm{P} \nu_{21} = n_\mathrm{e} n_1 q_{12} \frac{1}{1 + \dfrac{n_\mathrm{e}}{n_\mathrm{crit}}} h_\mathrm{P} \nu_{21}. \tag{3.38}$$

[4]Electrons are primary collision particles in HII regions.

When the electron density is very low ($n_{\rm e} \ll n_{\rm crit}$), collisional de-excitation can be neglected;

$$\epsilon_{21} = n_2 A_{21} h_{\rm P} \nu_{21} = n_{\rm e} n_1 q_{12} h_{\rm P} \nu_{21} \tag{3.39}$$

$$= n_{\rm e} n_1 \nu_{21} \frac{8.629 \times 10^{-6}}{T^{1/2}} \frac{\Upsilon_{(1,2)}}{\omega_1} \exp\left(-\frac{\chi}{k_{\rm B} T}\right) \tag{3.40}$$

We see that the emission rate is proportional to $n_{\rm e} n_1$ in the low-density limit, implying that ϵ_{21} becomes maximum around $n_{\rm e} = n_{\rm crit}$.

In the high-density limit ($n_{\rm e} \gg n_{\rm crit}$), collisional de-excitation is dominant and Eq.(3.38) becomes

$$\epsilon_{21} = n_2 A_{21} h_{\rm P} \nu_{21} \tag{3.41}$$

$$= n_1 \frac{n_2}{n_1} A_{21} h_{\rm P} \nu_{21} \tag{3.42}$$

$$= n_1 \frac{\omega_2}{\omega_1} \exp\left(-\frac{\chi}{k_{\rm B} T}\right) A_{21} h_{\rm P} \nu_{21}. \quad (\because \text{Boltzmann distribution}) \tag{3.43}$$

We see that $\epsilon_{12} \propto n_1$ at given temperature T, and the emission rate is much smaller than that of low-density ($n_{\rm e} < n_{\rm crit}$) case because $n_1 \ll n_{\rm e}$.

In practice, ions often have multiple energy levels. For example, ions whose configurations are $2p^q$ or $3p^q$ ($q = 2, 3, 4$) have five levels. The thermal equilibrium at level i is expressed as

$$\sum_{j \neq i} n_j n_{\rm e} q_{ji} + \sum_{j>i} n_j A_{ji} = \sum_{j \neq i} n_i n_{\rm e} q_{ij} + \sum_{j<i} n_i A_{ij} \quad \left(\sum_j n_j = n\right) \tag{3.44}$$

From Eq.(3.44), we derive the critical density for multi-level systems as;

$$n_c(i) = \frac{\sum_{j<i} A_{ij}}{\sum_{j \neq i} q_{ij}}. \tag{3.45}$$

Note that we have to consider both collisional and radiative excitation rates in the multiple systems.

The left panel of Figure 3.5 shows the volume emissivity (ϵ) of [OIII] 5007Å as a function of electron density. The middle panel indicates $\epsilon \propto n_{\rm e}^2$ ($n_{\rm e}$) in low(high)-density limit as shown in Eq.(3.40) and Eq.(3.43). The volume of HII region satisfies $V \propto n_{\rm e}^{-2}$ and the total luminosity decreases as $L \propto n_{\rm e}^{-1}$ in high-density limit as shown in the right panel of Figure 3.5.

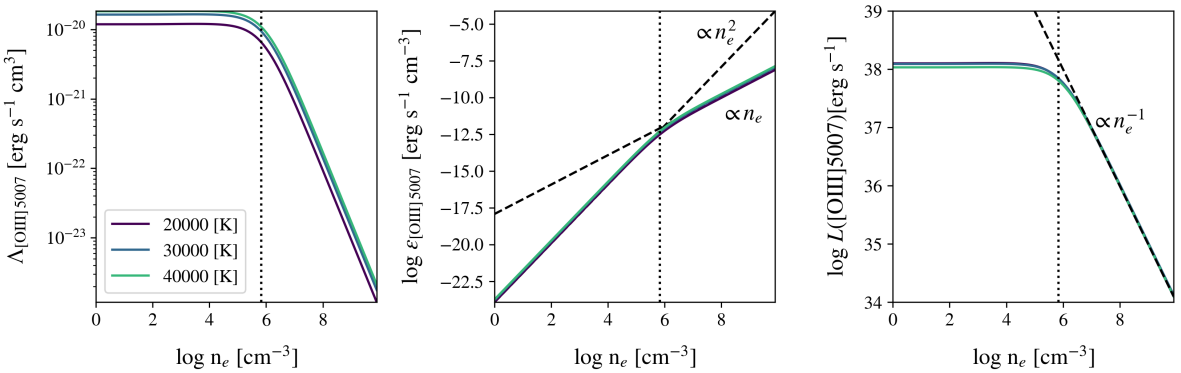

Figure 3.5: (Left) Cooling rate of [OIII] 5007 Å. (Middle) Volume emissivity of [OIII] 5007 Å. Emissivity is calculated from $\epsilon = n_{\rm e} n_{\rm O^{++}} \Lambda$ by assuming $n_{\rm O^{++}} = 10^{-4} n_{\rm e}$. (Right) Total luminosity of [OIII] 5007Å from HII region. Luminosity is calculated from $L = \epsilon \times V = \epsilon \times Q_0 / (n_{\rm e}^2 \alpha_{\rm B})$ by assuming $Q_0 = 5 \times 10^{49}\,{\rm s}^{-1}$. The dotted vertical lines represent the critical density of [OIII] 5007 Å.

Table 3.1 summarizes the critical densities and excitation temperatures for emission lines particularly important in diffuse nebulae. Ions whose ionization potentials ($E_{\rm ion}$) exceed 13.6 eV can exist only in HII regions, and thus mainly collide with free electrons. In contrast, ions with ionization potentials below 13.6 eV can exist in both HII regions and PDRs, mainly colliding with free electrons and neutral hydrogen atoms, respectively. Note that the [SII] 6717Å and 6731Å lines have ionization potentials below 13.6 eV but relatively high excitation temperatures ($T_{\rm exc} > 10^4$ K). This indicates that these lines primarily originate from the edges of HII regions rather than from PDRs. On the other hand, the [CII] 158μm line also has a low ionization potential, but its lower excitation temperature (~ 100 K) suggests it originates from both HII regions and PDRs.

Table 3.1: Properties of significant forbidden lines from HII regions. 'config': electron configurations, $E_{\rm ion}$: ionization potential, $n^{\rm e}_{\rm crit}$: critical density with colliders of electrons (hydrogen atoms) at the temperature of 10^4 K. $T_{\rm exc}$: excitation energy from the ground state ($\equiv E_{j0}/k_{\rm B}$). Values are adopted from Osterbrock and Ferland (2006) and Draine (2011).

ion	config	$E_{\rm ion}$[eV]	transition $(u-l)$	wavelength	$T_{\rm exc}$[K]	$n^{\rm e}_{\rm crit}$ [cm^{-3}]
CII	$2p^1$	11.3	$^2P_{3/2} - ^2P_{1/2}$	158 μm	91.2	50
NII	$2p^2$	14.5	$^3P_2 - ^3P_0$	122 μm	188	310
			$^3P_1 - ^3P_0$	205 μm	70	80
			$^1D_2 - ^3P_1$	6548 Å	2.20×10^4	6.60×10^4
			$^1D_2 - ^3P_2$	6584 Å	2.20×10^4	6.60×10^4
NIII	$2p^1$	29.6	$^2P_{3/2} - ^2P_{1/2}$	57 μm	302	1.50×10^3
OII	$2p^3$	13.6	$^2D_{5/2} - ^4S_{3/2}$	3727 Å	3.86×10^4	3.40×10^3
			$^2D_{3/2} - ^4S_{3/2}$	3729 Å	3.86×10^4	1.50×10^4
OIII	$2p^2$	35.1	$^3P_2 - ^3P_1$	52 μm	441	3.60×10^3
			$^3P_1 - ^3P_0$	88 μm	163	5.10×10^2
			$^1S_0 - ^1D_2$	4363 Å	6.12×10^4	2.78×10^7
			$^1D_2 - ^3P_1$	4959 Å	2.91×10^4	6.80×10^5
			$^1D_2 - ^3P_2$	5007 Å	2.91×10^4	6.80×10^5
NeIII	$2p^4$	41	$^1S_0 - ^1D_2$	3343 Å	8.02×10^4	1.37×10^8
			$^1D_2 - ^3P_1$	3968 Å	3.72×10^4	9.50×10^6
			$^1D_2 - ^3P_2$	3869 Å	3.72×10^4	9.50×10^6
SII	$2p^3$	10.4	$^2D_{5/2} - ^4S_{3/2}$	6717 Å	2.14×10^4	1.57×10^3
			$^2D_{3/2} - ^4S_{3/2}$	6731 Å	2.14×10^4	1.49×10^4
SIII	$2p^2$	23.3	$^3P_2 - ^3P_1$	18 μm	1.20×10^3	1.31×10^4
			$^3P_1 - ^3P_0$	33μm	429	4.22×10^3
			$^1S_0 - ^1D_2$	6312 Å	3.91×10^4	1.52×10^7

3.3 Nebula diagnostics by line ratios

As derived in Section 3.2.2, the emission rate of a radiative transition from an upper level j to a lower level i ($j > i$) is given by

$$\epsilon_{ji} = E_{ji} A_{ji} n_j, \tag{3.46}$$

$$A_{ji} = \frac{1}{(2L_j+1)(2S_j+1)} \sum_{J_j, J_i} (2J_j+1)\, A\left(L_j, S_j, J_j \to L_i, S_i, J_i\right), \tag{3.47}$$

where E_{ji} is the transition energy, n_j is the number density of particles in the upper level, and A_{ji} is the Einstein A coefficient averaged over the fine-structure levels of the upper term and

summed over those of the lower term. In what follows, we describe several commonly used emission-line diagnostics for inferring the physical conditions of ionized gas.

3.3.1 Electron Temperature Estimation

Hydrogen recombination lines are relatively insensitive to both the electron temperature (T_e) and electron density (n_e), as their emissivities are primarily governed by radiative cascades determined by the Einstein coefficients. Table 3.2 summarizes the emissivities of selected hydrogen lines relative to Hβ, assuming the Case B approximation.

Table 3.2: Hydrogen emission line intensities relative to Hβ, denoted as $X/\mathrm{H}\beta \equiv j_X/j_{\mathrm{H}\beta}$. The Case B approximation and low-density limit are assumed. Values are adopted from Osterbrock and Ferland (2006).

	Temperature [K]	2,500	5,000	10,000	20,000
	$4\pi j_{\mathrm{H}\beta}/(n_e n_p)$ [erg s^{-1} cm^{-3}]	2.70×10^{-25}	1.54×10^{-25}	8.30×10^{-26}	4.21×10^{-26}
Lyman series	Lyα/Hβ	33.0	32.5	32.7	34.0
Balmer series	Hα/Hβ	3.42	3.10	2.86	2.69
	Hγ/Hβ	0.439	0.458	0.470	0.485
	Hδ/Hβ	0.237	0.250	0.262	0.271
Paschen series	Pα/Hβ	0.684	0.562	0.466	0.394
	Pβ/Hβ	0.267	0.241	0.216	0.196

In contrast to hydrogen recombination lines, forbidden emission lines of metal species serve as more sensitive diagnostics of T_e in HII regions. Accurate determination of the electron temperature is essential for deriving gas-phase metallicities, as discussed in Section 3.3.3. Electron temperature is typically inferred from the ratio of line intensities originating from transitions between levels with significantly different excitation energies within the same ion. In this study, we adopt the classical formulation introduced by Seaton (1954, 1960) to derive T_e from these emission line ratios.

The electron configurations of the relevant ions are of the form $2p^q$ or $3p^q$ with $q = 2, 3, 4$, and we denote the energy levels by $n = 3, 2, 1$ as illustrated in Figure 3.6.

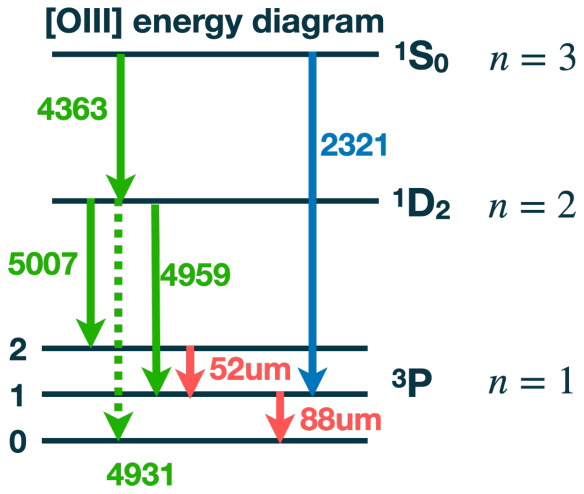

Figure 3.6: [OIII] energy diagram. Blue, green and red arrows indicate UV, optical and FIR emission lines, respectively. [OIII] 4931Å is emitted only by an electric-quadrupole transition and its emission is weak.

In equilibrium, the population of each level is determined by the balance between collisional excitations, de-excitations, and radiative transitions. For a three-level system, the population equations for levels $n = 2$ and $n = 3$ are written as

$$(n = 2) \quad n_1 q_{12} + n_3 (A_{32} + C_{32}) = n_2 (A_{21} + C_{21} + C_{23}) \tag{3.48}$$

$$(n = 3) \quad n_1 C_{13} + n_2 C_{23} = n_3 (A_{31} + A_{32} + C_{31} + C_{32}), \tag{3.49}$$

where C_{ji} denotes the collisional transition rate (per unit time) from level j to i, given by

$$C_{ji} \equiv n_{\rm e} q_{ji}, \tag{3.50}$$

with q_{ji} being the rate coefficient per unit volume, as defined in Eq. (3.33). By eliminating n_1 from Eqs. (3.48) and (3.49), the level population ratio n_2/n_3 can be expressed as

$$\frac{n_2}{n_3} = \frac{C_{12}}{C_{13}} \left\{ \frac{(A_{31} + C_{31}) + (A_{32} + C_{32})\,[1 + C_{13}/C_{12}]}{(A_{21} + C_{21}) + (C_{12}C_{23}/C_{13})\,[1 + C_{13}/C_{12}]} \right\}. \tag{3.51}$$

Using Eq. (3.50) and the definition of q_{ji}, the ratio C_{13}/C_{12} simplifies to

$$\frac{C_{13}}{C_{12}} = \frac{n_{\rm e} q_{13}}{n_{\rm e} q_{12}} = \frac{\Upsilon_{(1,3)}}{\Upsilon_{(1,2)}} \exp\left(-\frac{E_{32}}{kT_2}\right). \tag{3.52}$$

In the low-density limit, collisional de-excitation from the upper level $n = 3$ is negligible compared to spontaneous radiative transitions. Thus, we assume

$$\frac{\Upsilon_{(1,3)}}{\Upsilon_{(1,2)}} \ll 1,\ A_{31} \gg C_{31},\ A_{32} \gg C_{32} \Rightarrow \frac{C_{13}}{C_{12}} \ll 1. \tag{3.53}$$

Under these conditions, Eq. (3.51) reduces to a simpler form:

$$\frac{n_2}{n_3} = \frac{C_{12}}{C_{13}} \left\{ \frac{A_{31} + A_{32}}{A_{21} + C_{21}(C_{31} + C_{32})/C_{31}} \right\}. \tag{3.54}$$

The emissivity ratio of the two transitions, $\epsilon_{21}/\epsilon_{3i}$, is then expressed as

$$\frac{\epsilon_{21}}{\epsilon_{3i}} = \frac{E_{21} A_{21} n_2}{E_{3i} A_{3i} n_3} = \frac{E_{21} A_{21}}{E_{3i} A_{3i}} \frac{C_{12}}{C_{13}} \left\{ \frac{A_{31} + A_{32}}{A_{21} + C_{21}(C_{31} + C_{32})/C_{31}} \right\} \tag{3.55}$$

$$= \left[\frac{E_{21}}{E_{3i}} \frac{\Upsilon_{(1,2)}}{\Upsilon_{(1,3)}} \exp\left(\frac{E_{32}}{kT_{\rm e}}\right) \frac{A_{31} + A_{32}}{A_{3i}} \right] \frac{1}{1 + \frac{C_{21}}{A_{21}} \frac{C_{31} + C_{32}}{C_{31}}} \tag{3.56}$$

$$= [\cdots] \cdot \frac{1}{1 + \frac{n_{\rm e}}{A_{21}} \frac{q_{21}(q_{31} + q_{32})}{q_{31}}} = [\cdots] \cdot \frac{1}{1 + \frac{n_{\rm e}}{T^{1/2}} \frac{\Upsilon_{(1,2)}}{A_{21}\omega_2} \left(\frac{\Upsilon_{(3,1)} + \Upsilon_{(3,2)}}{\Upsilon_{(3,1)}} \right)} \tag{3.57}$$

$$= \frac{K_1 \exp\left(\frac{E_{32}}{kT_{\rm e}}\right)}{1 + K_2 \frac{n_{\rm e}}{T_{\rm e}^{1/2}}}, \tag{3.58}$$

where K_1 and K_2 are constants depending on the atomic structure of the ion.

For the [O III] line ratio with $i = 2$, the constants are given by

$$\frac{\epsilon_{21}}{\epsilon_{32}} = \frac{j_{4959} + j_{5007}}{j_{4363}} = \frac{7.90 \exp\left(3.29 \times 10^4 / T_{\rm e}\right)}{1 + 4.5 \times 10^{-4} n_{\rm e} / T_{\rm e}^{1/2}}. \tag{3.59}$$

Other ions with similar electron configurations (np^2), such as [N II], [Ne III], and [S III], exhibit comparable behavior and can also be used as electron temperature diagnostics. The

Table 3.3: Values of K_1, K_2, E_{32} for line ratios of [OIII], [NII], [NeIII], [SIII], adopted from Osterbrock and Ferland (2006).

ion	λ_{21} [Å]	λ_{32} [Å]	K_1	K_2	E_{32}/k_B
[OIII]	4959+5007	4363	7.90	4.5×10^{-4}	3.29×10^4
[NII]	6548+6583	5755	8.23	4.4×10^{-3}	2.50×10^4
[NeIII]	3869+3968	3343	13.7	3.8×10^{-5}	4.30×10^4
[SIII]	9532+9069	6312	5.44	3.5×10^{-4}	2.28×10^4

corresponding values of K_1, K_2, and E_{32} are summarized in Table 3.3. The dependence of the line ratios on T_e at a typical electron density of $n_e = 100$ cm^{-3} is shown in Figure 3.7.

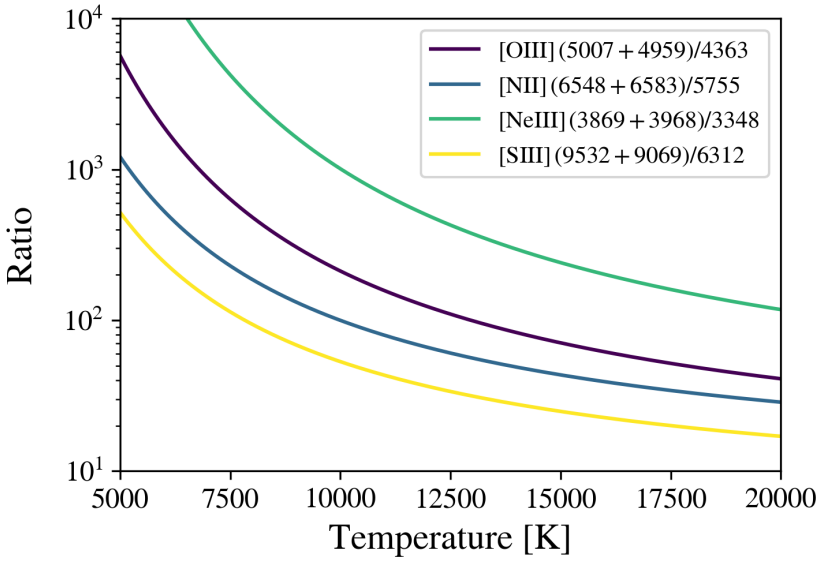

Figure 3.7: Line ratio as a function of electron temperature with the electron density of $n_e = 100$ cm^{-3}.

3.3.2 Density estimation

The electron density n_e can be derived using line ratios of transitions from levels with similar excitation energies but different critical densities. In particular, we focus on transitions within the same ion that share a common lower level, differing primarily in total angular momentum.

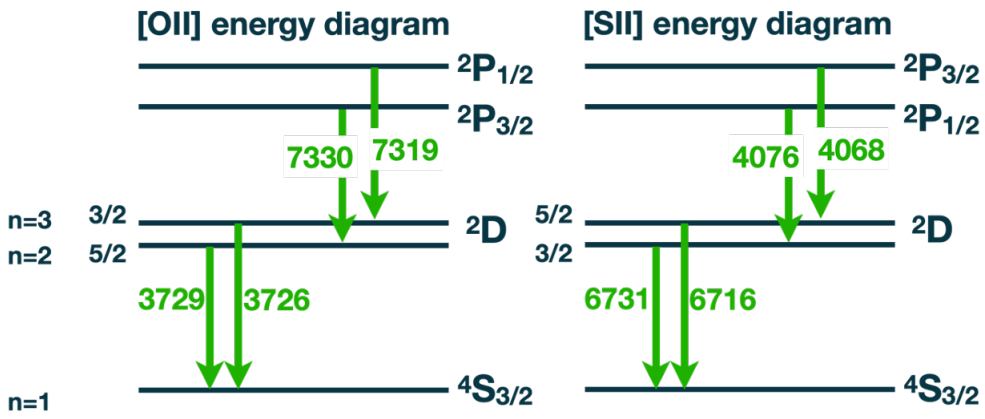

Figure 3.8: The first five energy diagram of OII and SII, which have np^3 configuration. Note that only the main optical emission lines are drawn as green arrows.

Figure 3.8 illustrates the first five energy levels of [OII] and [SII], both of which have an electron configuration of np^3. The optical transitions indicated by green arrows arise from closely spaced levels $^2D_{3/2}$ and $^2D_{5/2}$, which have nearly identical excitation energies. Consequently, their population ratio is largely insensitive to electron temperature, making their line ratio an effective diagnostic of electron density due to their different critical densities.

Denoting the levels $^2D_{3/2}$, $^2D_{5/2}$, and $^4S_{3/2}$ as levels 3, 2, and 1 respectively, the intensity ratio of the two emission lines is written using Eq. (3.38) as[5]

$$\frac{j_{21}}{j_{31}} = \frac{\epsilon_{21}}{\epsilon_{31}} = \frac{q_{12}h\nu_{21}}{1+\frac{n_\mathrm{e}}{n_{\mathrm{crit},21}}} \frac{1+\frac{n_\mathrm{e}}{n_{\mathrm{crit},31}}}{q_{13}h\nu_{31}} \tag{3.60}$$

$$= \frac{q_{12}\nu_{21}n_{\mathrm{crit},21}}{q_{13}\nu_{31}n_{\mathrm{crit},31}} \cdot \frac{n_{\mathrm{crit},31}+n_\mathrm{e}}{n_{\mathrm{crit},21}+n_\mathrm{e}} \equiv a\frac{b+n_\mathrm{e}}{c+n_\mathrm{e}} \tag{3.61}$$

Solving for n_e as a function of the observed line ratio $R \equiv j_{21}/j_{31}$ gives

$$n_\mathrm{e}(R) = \frac{cR-ab}{a-R}. \tag{3.62}$$

In the low-density limit, where collisional de-excitation is negligible, the line ratio simplifies to

$$\frac{j_{21}}{j_{31}} = \frac{\epsilon_{21}}{\epsilon_{31}} \sim \frac{q_{12}h\nu_{21}}{q_{13}h\nu_{31}} \tag{3.63}$$

$$= \frac{\omega_2}{\omega_1}\exp\left(-\frac{E_{21}}{kT}\right)E_{21} \cdot \frac{\omega_1}{\omega_3}\exp\left(+\frac{E_{31}}{kT}\right)E_{31} \tag{3.64}$$

$$= \frac{\omega_2}{\omega_3}\exp\left(\frac{E_{32}}{kT}\right) \cdot \frac{E_{21}}{E_{31}} \sim \frac{\omega_2}{\omega_3}, \tag{3.65}$$

where ω_i is the statistical weight of level i, and the final approximation holds for $E_{32} \ll kT$ and $E_{32} \ll E_{21}$. This is valid because the collisional excitation strengths and energy separations are nearly equal for the two transitions. For [OIII], the low-density limit yields

$$\frac{j_{\lambda3729}}{j_{\lambda3726}} \to 1.5. \quad \text{(low density limit)} \tag{3.66}$$

In the high-density limit ($n_\mathrm{e} \to \infty$), the level populations approach thermal equilibrium, and the ratio becomes

$$\frac{j_{21}}{j_{31}} \to \frac{q_{12}n_{\mathrm{crit},21}}{q_{13}n_{\mathrm{crit},31}} = \frac{\omega_2}{\omega_3} \cdot \frac{A_{21}}{A_{31}}. \tag{3.67}$$

[5] In these $D_{3/2} - S_{3/2}$, $D_{5/2} - S_{3/2}$ transitions, we can treat them as two-level systems.

Thus, for [OII] , the high-density limit gives

$$\frac{j_{\lambda 3729}}{j_{\lambda 3726}} \to \frac{3}{2} \cdot \frac{3.6 \times 10^{-5}}{1.6 \times 10^{-4}} = 0.34. \qquad \text{(high-density limit)} \tag{3.68}$$

Figure 3.9 shows the dependence of [OII] and [SII] optical line ratios on electron density at $T_e = 10^4$ K.

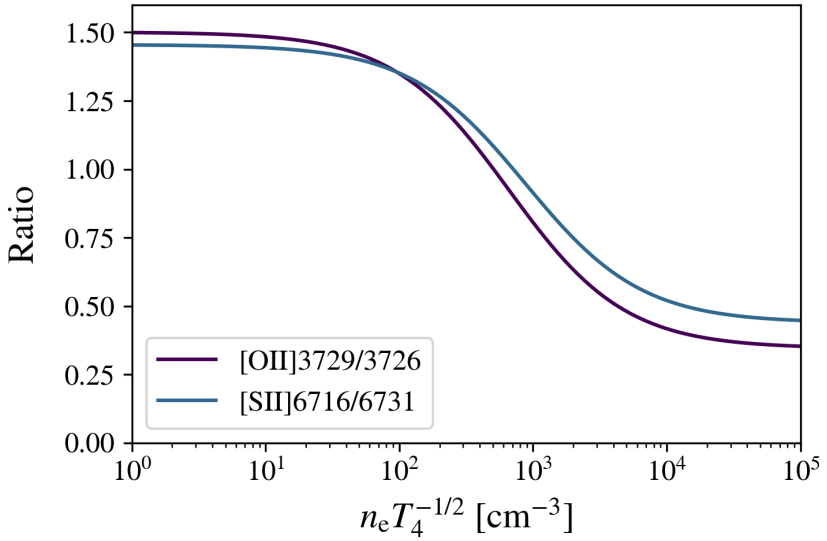

Figure 3.9: Line ratio as a function of electron density at $T_e = 10^4$ K.

In the far-infrared, the [OIII] $52, \mu$m/$88, \mu$m line ratio also serves as a sensitive probe of n_e. The levels involved in these transitions are $^3P_2$, $^3P_1$, and $^3P_0$, denoted as levels 2, 1, and 0, respectively. The line ratio is given by

$$\frac{j_{52}}{j_{88}} = \frac{j_{21}}{j_{10}} = \frac{n_2 A_{21} h\nu_{21}}{n_1 A_{10} h\nu_{10}}. \tag{3.69}$$

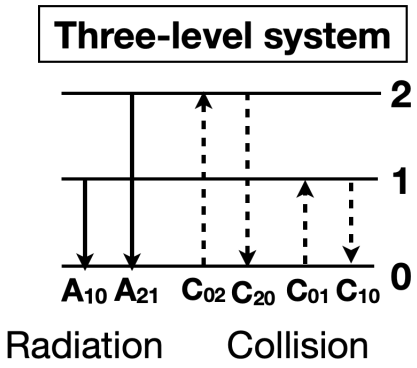

Figure 3.10: Transition through radiation (solid) and collision (dashed) in three-level systems.

Assuming a three-level system and neglecting radiative cascades from higher levels (Figure 3.10), the equilibrium level populations satisfy

$$(n = 2) \quad C_{02} n_0 + C_{12} n_1 = (C_{20} + A_{20} + C_{21} + A_{21})\, n_2 \tag{3.70}$$

$$(n = 1) \quad C_{01} n_0 + (C_{21} + A_{21})\, n_2 = (C_{10} + A_{10} + C_{12})\, n_1 \tag{3.71}$$

Eliminating n_0 from the above two equations, we obtain

$$\frac{n_2}{n_1} = \frac{C_{02}\left(C_{10}+A_{10}\right)+C_{02}C_{12}+C_{12}C_{01}}{C_{01}\left(C_{20}+A_{20}\right)+C_{01}\left(C_{21}+A_{21}\right)+\left(C_{21}+A_{21}\right)C_{02}}. \tag{3.72}$$

In Eq. (3.69), under the low-density limit, second-order terms in C (i.e., $O(C^2)$) can be neglected. In this case, the population ratio simplifies to

$$\frac{n_2}{n_1} \sim \frac{C_{02}A_{10}}{C_{01}\left(A_{20}+A_{21}\right)+A_{21}C_{02}} \sim \frac{C_{02}A_{10}}{(C_{01}+C_{02})A_{21}} \qquad (\because A_{20} \ll A_{21}). \tag{3.73}$$

Therefore, the FIR line ratio becomes

$$\frac{j_{52}}{j_{88}} = \frac{j_{21}}{j_{10}} \sim \frac{C_{02}A_{10}}{(C_{01}+C_{02})A_{21}} \cdot \frac{A_{21}h\nu_{21}}{A_{10}h\nu_{10}} = \frac{q_{20}\exp(-E_{21}/kT)}{q_{10}+q_{20}\exp(-E_{21}/kT)} \cdot \frac{E_{21}}{E_{10}}. \quad \text{(low density limit)} \tag{3.74}$$

In the high-density limit, where collisional transitions dominate over radiative ones, the system approaches thermal equilibrium. The level populations then follow the Boltzmann distribution, and the emission line ratio becomes

$$\frac{j_{52}}{j_{88}} = \frac{j_{21}}{j_{10}} \sim \frac{\omega_2}{\omega_1}\exp\left(-\frac{E_{21}}{kT}\right) \cdot \frac{A_{21}E_{21}}{A_{10}E_{10}}. \qquad \text{(high density limit)} \tag{3.75}$$

The collisional excitation and de-excitation rates, C_{ij} (for $i > j$) and C_{ji}, scale as $n_{\rm e}/T_{\rm e}^{1/2} \times \exp(-E_{ji}/kT_{\rm e})$ and $n_{\rm e}/T_{\rm e}^{1/2}$, respectively. Therefore, the [OIII] 52μm /88μm line ratio can be characterized as a function of $n_{\rm e}T_4^{-1/2}$, where $T_4 \equiv T_{\rm e}/10^4$K, as shown in Figure 3.11.

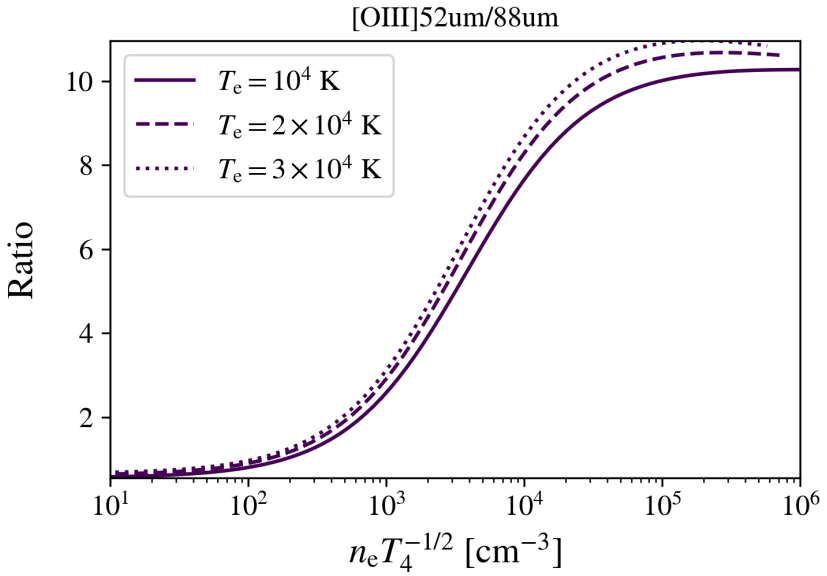

Figure 3.11: Line ratio [OIII] 52μm /88μm as a function of $n_{\rm e}\,T_4^{-1/2}$ with different electron temperatures of $T_{\rm e} = 10^4$ (solid), 2×10^4 (dashed), and 3×10^4 K (dotted).

3.3.3 Metallicity Estimation

3.3.3.1 Direct Method for Electron Temperature Measurement

In HII regions, oxygen atoms are ionized and the oxygen abundance relative to hydrogen can be written as

$$\frac{\rm O}{\rm H} = \frac{\rm O^+}{\rm H^+} + \frac{\rm O^{++}}{\rm H^+}. \tag{3.76}$$

The abundance O^{++}/H^+ is derived from the line ratio of [OIII] to Hβ. The emissivity of the [OIII] $\lambda\lambda$5007, 4959 lines is calculated using Eq. (3.40) as

$$\epsilon_{\lambda5007} + \epsilon_{\lambda4959} = \frac{4}{3}\epsilon_{\lambda5007} = \frac{4}{3} n_e n_2 q_{32} h\nu_{32} \propto n_e n(O^{++}) T_e^{-1/2} \exp\left(-\frac{E_{32}}{kT_e}\right), \tag{3.77}$$

where the ratio $\epsilon_{\lambda5007} : \epsilon_{\lambda4959} = 3 : 1$ is set by quantum mechanical selection rules (Storey and Zeippen, 2000).

The emissivity of Hβ is expressed as

$$\epsilon_{H\beta} = n_e\, n_p\, \alpha^{\rm eff}_{H\beta}\, E_{H\beta} \propto n_e n(H^+) T_e^{-1}. \tag{3.78}$$

Combining these expressions, the line ratio becomes

$$\frac{\epsilon_{\lambda5007} + \epsilon_{\lambda4959}}{\epsilon_{H\beta}} = C_1 \frac{n(O^{++})}{n(H^+)} T_e^{1/2} \exp\left(-\frac{E_{32}}{kT_e}\right), \tag{3.79}$$

where the coefficient C_1 is determined by atomic parameters and is only weakly dependent on temperature.

The abundance O^+/H^+ is derived in the same manner using the [OII] $\lambda\lambda$3726, 3729 lines:

$$\frac{\epsilon_{\lambda3726} + \epsilon_{\lambda3729}}{\epsilon_{H\beta}} = C_2 \frac{n(O^+)}{n(H^+)} T_e^{1/2} \left[\exp\left(-\frac{E_{\lambda3726}}{kT_e}\right) + \exp\left(-\frac{E_{\lambda3729}}{kT_e}\right)\right]. \tag{3.80}$$

From Eqs. (3.79) and (3.80), the total oxygen abundance is obtained as

$$\frac{O}{H} = \frac{\epsilon_{\lambda3727}}{\epsilon_{H\beta}} \times D_1(T_e) + \frac{\epsilon_{\lambda5007} + \epsilon_{\lambda4959}}{\epsilon_{H\beta}} \times D_2(T_e), \tag{3.81}$$

where the electron temperature T_e is determined via the method described in Section 3.3.1.

However, detection of the auroral line [OIII] λ4363 is challenging due to its weak intensity at low temperatures. Since this line can only be efficiently emitted in high-T_e environments, direct estimation of T_e is often limited to low-metallicity systems.

3.3.3.2 Strong-Line Method

As an alternative to the T_e-based method, metallicity can be estimated using strong-line diagnostics, which rely on bright emission lines such as [OIII], [OII], Hβ, or [NII] and Hα.

A widely used indicator is the $R23$ index, defined as

$$R23 \equiv \frac{[\text{OII}]\,\lambda3727 + [\text{OIII}]\,\lambda4959{,}5007}{\text{H}\beta_{\lambda4861}}. \tag{3.82}$$

It has been empirically established that R_{23} correlates with gas-phase metallicity (e.g., Pagel et al., 1979; McGaugh, 1991; Nagao et al., 2006; Maiolino et al., 2008; Curti et al., 2017, 2020). Note, however, that $R23$ is a double-valued function of metallicity and must be interpreted with care. Additionally, since the involved lines span a wide range of wavelengths, dust extinction can significantly affect the ratio, and proper correction is essential.

Another useful diagnostic is the $N2$ index,

$$N2 \equiv \frac{[\text{NII}]\,\lambda6584}{\text{H}\alpha_{\lambda6563}}, \tag{3.83}$$

which benefits from the proximity of the two lines in wavelength, making it less sensitive to dust attenuation. Unlike $R23$, the $N2$ index is a monotonic function of metallicity.

However, [NII] λ6584 tends to be extremely faint in low-metallicity environments. This is because nitrogen is predominantly synthesized in asymptotic giant branch (AGB) stars, which begin to contribute only after $\sim$40 Myr following a star formation episode, as will be discussed in the next section.

3.4 Dust Physics

From the discussions in the previous sections, we introduced that star-forming regions consist of multi-phase gas, and all gas phases with non-zero metallicity contain dust. Dust is a small solid particle, typically less than 0.1 μm in size. Although the total dust mass typically accounts for less than 1% of the total ISM gas mass, dust particles have interaction cross-sections for continuum radiation 10^4 times larger than gas particles. Thus, dust efficiently absorbs the rest-UV and optical emission from stars and re-emits it as infrared radiation. Consequently, understanding dust physics is crucial for interpreting dust-obscured star formation histories in the early Universe (see Chapter 4 for an observational overview).

In this section, we first summarize how dust is produced, destroyed, and grows in the early Universe. We then review its composition, size distribution, and optical properties. Finally, we outline the Monte Carlo techniques commonly employed to model radiative transfer through dusty media.

3.4.1 Dust Production and Evolution

At least within HII regions, the optical properties of dust and the dust-to-gas mass ratio are roughly similar to those found in the general interstellar medium. This leads to three fundamental questions: How are dust particles initially formed? How long can they survive? And how are they eventually destroyed? Considerable research has been dedicated to addressing these questions, and the main findings are summarized here. This section is based on Schneider and Maiolino (2024).

First, let us consider the formation of dust particles. In the early Universe, a primary dust production site is the ejecta from Type II supernovae (SNe). Immediately after a massive star explodes, metal-enriched gas is expelled at velocities of several thousand $\mathrm{km\,s^{-1}}$, and its initial temperature exceeds $10^8\,\mathrm{K}$, too hot to produce dust. A few hundred days after the explosion, however, the gas cools to a few thousand Kelvin due to radiative cooling and expansion. During this phase, certain atoms combine to form molecules such as CO and SiO, and dust nucleation begins within the SN ejecta. Dust grains nucleate according to classical nucleation theory, and subsequently, these molecules collide and coagulate, growing into larger dust grains. About 10^3–10^4 years after the explosion, a reverse shock interacts with this dust, destroying small grains ($\lesssim 0.2\,\mu$m) through sputtering, a process in which impinging atoms or ions erode dust grains by collision. Finally, the surviving larger grains ($> 0.2\,\mu$m) are mixed into the interstellar medium (ISM).

Both theoretical and experimental studies indicate that dust grains, once formed, can grow through the accretion of individual atoms from the interstellar gas. However, initial dust formation via atomic collisions alone is not possible, even at the highest densities found in gaseous nebulae.

The other major production site is AGB stars. AGB stars represent the late evolutionary stage of low-mass stars in the mass range $0.8 - 8\,M_\odot$, consisting of helium and hydrogen shell burning surrounding a degenerate carbon-oxygen core. These stars experience pulsations near their surfaces, causing continuous mass loss at rates of roughly $\sim 10^{-4} - 10^{-7}\,M_\odot, \mathrm{yr}^{-1}$. Atmospheric shock waves driven by stellar pulsations propagate through the stellar atmosphere, lifting gas above the stellar surface and creating dense, cool layers favorable for solid particle formation (e.g., Hoefner et al., 1998). The ejected gas cools a few au away from the stellar surface, allowing molecules such as CO, SiO, and C_2H_2 to form, with molecular abundances determined by the local C/O ratio. As the temperature drops to around 1000–1500 K, these molecules collide and coagulate, forming seed nuclei. Metals present in the surrounding gas then accrete onto these seed nuclei, facilitating dust grain growth. These grains absorb optical radiation from the star and are subsequently blown out by radiation pressure. The resulting dust grain size distribution typically ranges from $0.01 - 0.1\,\mu$m.

In addition to AGB stars and core-collapse supernovae, massive stars can also contribute to dust formation during their late evolutionary stages, particularly in the red supergiant (RSG) and Wolf–Rayet (WR) phases. RSGs represent the evolved helium-burning stage of massive O/B stars with initial masses $\lesssim 40\,M_\odot$. The duration of the RSG phase depends on the initial stellar mass. For instance, it lasts approximately 0.4 Myr for a $25\,M_\odot$ star and about 2 Myr for a $10\,M_\odot$ star (Meynet and Maeder, 2003). RSGs have low surface temperatures and drive slow, dense stellar winds, leading to favorable conditions for dust formation. The estimated dust formation rate in RSGs is $\sim 3 \times 10^{-8}\,M_\odot\,\mathrm{yr}^{-1}\,\mathrm{kpc}^{-2}$, which corresponds to roughly 1 % of the dust production rate of AGB stars. WR stars are the evolved descendants of RSGs that have lost their hydrogen envelopes. They exhibit strong, fast stellar winds ($\sim 1000 - 3000\,\mathrm{km\,s}^{-1}$) capable of destroying pre-existing dust grains produced in the preceding RSG phase. For single WR stars, surface temperatures are too high ($\gtrsim$ 30,000 K) to allow dust formation. However, in binary systems, gas can cool effectively in wind-wind interaction regions, enabling dust to form. Despite dust formation during these massive-star phases, much of the newly formed dust may be subsequently destroyed during the supernova explosion. UV flashes from supernovae can evaporate grains, and shock waves from the explosion can sputter or completely destroy dust particles, as observed in the supernova remnant Cas A (e.g., Dwek et al., 2008).

In summary, the primary sites of dust formation are supernova ejecta and the stellar surfaces of AGB stars. Since the evolutionary timescale for massive stars to explode as supernovae is about 4-40 Myrs, whereas low-mass stars require more than 300 Myrs to reach the AGB phase, the dominant dust formation channel in the high-redshift Universe (at $z > 6$) is thought to be Type II supernovae (Mancini et al., 2015).

However, the amount of stellar-produced dust is insufficient to explain the observed dust masses in galaxies. Subsequent dust growth via accretion in the ISM plays an important role in significantly increasing the dust mass. Metals present in the cold neutral medium of PDRs and molecular clouds accrete onto dust grain surfaces through weak electrostatic (van der Waals) forces, increasing grain sizes.

Dust grains can also be destroyed by several processes, including erosion by FUV photons with $E > 5.6\,\mathrm{eV}$ and grain–grain or gas–grain collisions. When dust grains are exposed to strong FUV radiation fields, erosion can occur through photodesorption and photodissociation, which break down C–C and C–H bonds. Small grains such as PAHs are particularly susceptible to destruction by FUV radiation. Furthermore, shocks in the turbulent ISM can cause collisions between dust grains, leading to shattering or vaporization. The typical threshold velocity for such grain–grain collisions is $\sim 10\,\mathrm{km\,s}^{-1}$.

3.4.2 Dust Composition

Dust composition and its size distribution in the interstellar medium (ISM) have been investigated indirectly through observations of elemental depletion patterns, extinction curves, polarization, and infrared spectral features.

In the absence of dust, the gas-phase elemental abundances in the local ISM would be expected to resemble the solar abundance. However, absorption line measurements have revealed that elements such as C, Mg, Si, and Fe are underabundant in the gas phase (i.e., depleted), indicating that a substantial fraction of them is incorporated into dust grains (e.g., Jenkins, 2009). In a typical diffuse interstellar cloud, about 2/3 of carbon and more than 90% of Mg, Si, and Fe are believed to reside in solid grains.

The extinction curve also provides information on the dust composition. Extinction is the combined effect of dust absorption and scattering. It is measured by comparing the spectra of two similar stars, one of which is reddened while the other is unaffected by dust. Assuming that the extinction tends to zero at infinite wavelengths ($\lambda \to \infty$), one can determine the wavelength dependence of the dust attenuation. The extinction A_λ at wavelength λ in magnitudes is defined

as

$$A_\lambda\,[\mathrm{mag}] \equiv 2.5\log_{10}\left(F_{0,\lambda}/F_\lambda\right), \tag{3.84}$$

where F_λ is the observed flux and $F_{0,\lambda}$ is the intrinsic stellar flux without dust. The extinction in magnitudes is related to the optical depth by

$$A_\lambda\,[\mathrm{mag}] = 2.5\log_{10} e^{\tau_\lambda} = 1.086\tau_\lambda. \tag{3.85}$$

Figure 3.12 shows the extinction curves in the Milky Way. Because photons with $\lambda \leq 1000\,\text{Å}$ are absorbed by atomic hydrogen, the extinction curve is shown up to $\lambda^{-1} = 10\,\mu\mathrm{m}^{-1}$. These extinction curves vary from sightline to sightline. The slope in the optical regime is characterized by the dimensionless ratio:

$$R_V \equiv \frac{A_V}{A_B - A_V} \equiv \frac{A_V}{E(B-V)}, \tag{3.86}$$

where A_B and A_V are the extinctions measured in the B(4405Å) and V(5470Å) photometric bands, and $E(B-V) \equiv A_B - A_V$ is the *redding*. The average value in the diffuse Milky Way is $R_V \simeq 3.1$, although there are variations depending on the environment.

The extinction curves also exhibit a prominent bump at $\lambda^{-1} = 4.6\,\mu\mathrm{m}^{-1}$, corresponding to $\lambda = 2175\,\text{Å}$. This feature is well described by a Drude (Lorentzian) profile:

$$C_{\mathrm{abs}} = \frac{4\pi q^2}{mc}\frac{\gamma}{4(\omega-\omega_0)^2+\gamma^2}, \tag{3.87}$$

where q is the charge of the dust grain, m is the grain mass, ω is the radiation frequency, and ω_0 is the natural (resonant) frequency of the dust particle. Here, the damping constant γ is defined as $\gamma = \frac{2}{3}\frac{\omega_0^2 q^2}{mc^3}$. The Full Width Half Maximum (FWHM) is equal to γ. While the central wavelength is nearly identical across different sightlines, the feature width varies considerably (Fitzpatrick and Massa, 1986). The extinction peak is widely attributed to aromatic carbonaceous materials, most likely a cosmic mixture of PAH molecules (e.g., Joblin et al., 1992; Li and Draine, 2001). The feature arises from the $\pi \to \pi^*$ electronic transition in sp^2-bonded carbon sheets.

Infrared extinction features also offer clues to dust composition. In Figure 3.13, the Milky Way ISM shows strong absorption at 9.7 μm and 18 μm , which are attributed to Si-O stretching and Si-O-Si bending modes in silicate minerals, respectively. Another broad feature at 3.4 μm arises from C-H stretching modes in hydrocarbons (Pendleton and Allamandola, 2002). In dense molecular clouds, additional absorption features due to ices, such as H_2O, NH_3, and CO_2, can also be seen.

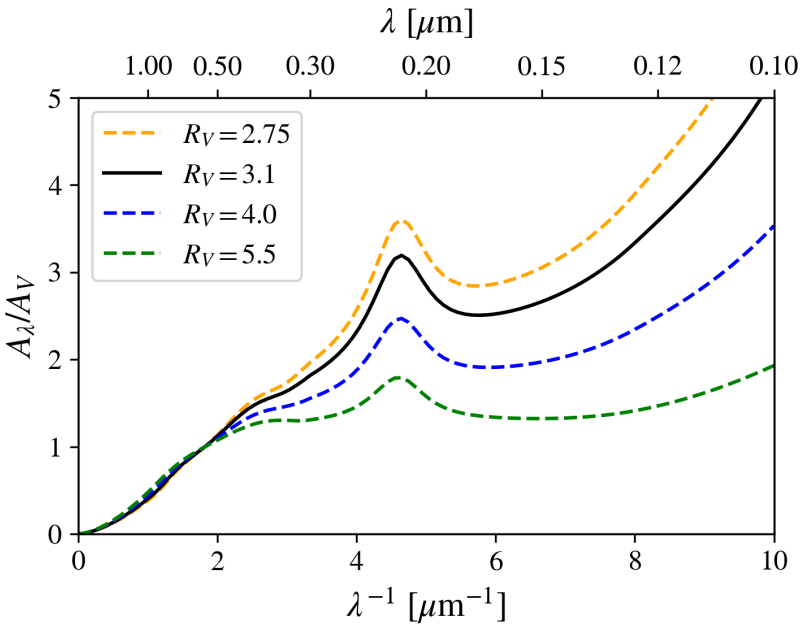

Figure 3.12: Interstellar extinction curves of the Milky Way with different R_V ($R_V = 2.75, 3.1, 4.0, 5.5$). Here $R_V = 3.1$ is the average value. The MW extinction curves are plotted using the CCM fitting functions (Cardelli et al., 1989).

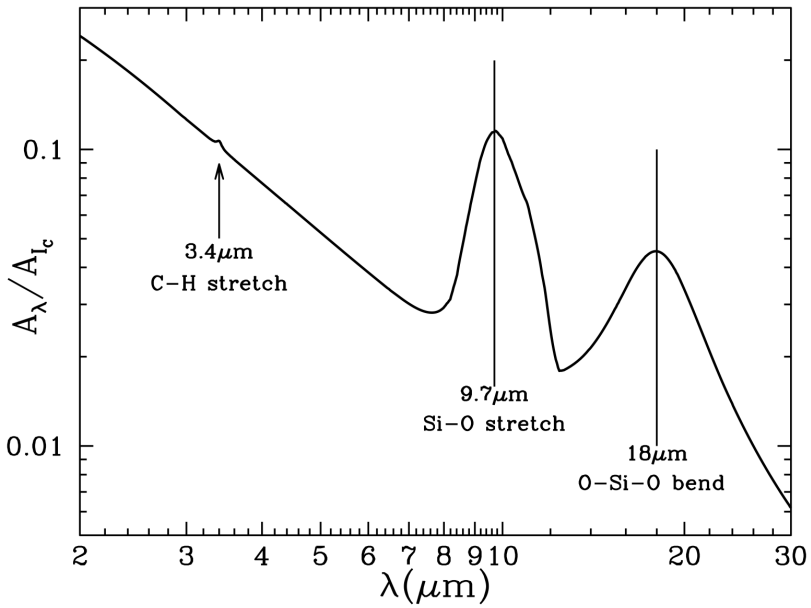

Figure 3.13: Extinction curve relative to the extinction at 8020Å. The extinction bumps at $\lambda = 9.7$, $18\,\mu$m are originated from silicate. This figure is taken from Draine (2011).

The IR emission spectrum also provides valuable information on dust composition. As shown in Figure 3.14, strong features at 3.3, 6.2, 7.7, 8.6, and 11.3 μm are now widely identified as vibrational modes of PAHs (e.g., Leger and Puget, 1984; Allamandola et al., 1985), and these features are seen in a wide range of Galactic and extragalactic environments (Draine and Li, 2007).

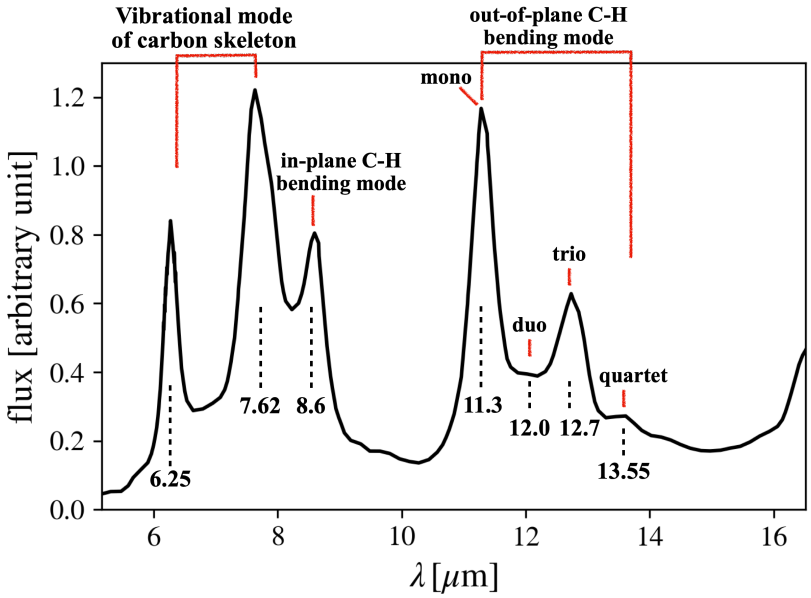

Figure 3.14: The PAH emission spectrum between 5 μm and 15 μm observed in the reflection nebula NGC7023 (Cesarsky et al., 1996). Each emission feature is labeled with a black dashed line. Above each feature, the corresponding emission mechanism is indicated.

3.4.3 Grain Size Distribution

A comprehensive model for interstellar dust must specify both the composition and the geometry (size and shape) of the grains. To reproduce the observed polarization of starlight, a fraction of grains must be non-spherical and magnetically aligned.

Grains absorb and scatter light most effectively when their size is comparable to the wavelength, i.e., $\lambda \sim 2\pi a$. Therefore, the wavelength dependence of extinction places strong constraints on the grain size distribution. The observed extinction curve, which extends down to $\sim 1000\,\text{AA}$ and scales approximately as λ^{-1}, requires the presence of grains with $a \lesssim 0.015\,\mu$m to account for UV extinction.

One model of grain size distribution is the MRN distribution (Mathis et al., 1977), which assumes two types of grains, amorphous silicates and carbonaceous materials, and assumes a power-law size distribution:

$$\mathrm{d}n/\mathrm{d}a \propto a^{-3.5} \quad (0.005\,\mu\text{m} \leq a \leq 0.25\,\mu\text{m}). \tag{3.88}$$

This distribution successfully reproduces the extinction curve from the near-infrared to the ultraviolet.

As noted in Section 3.4.2, PAHs are now understood to be an essential component. Weingartner and Draine (2001) extended the grain models to include amorphous silicates, graphite, and PAHs. Their model assumes power-law distributions for large grains and log-normal distributions for PAHs and very small ($a \lesssim 0.005\,\mu$m) carbonaceous grains. The resulting size distribution for the Milky Way is shown in Figure 3.15.

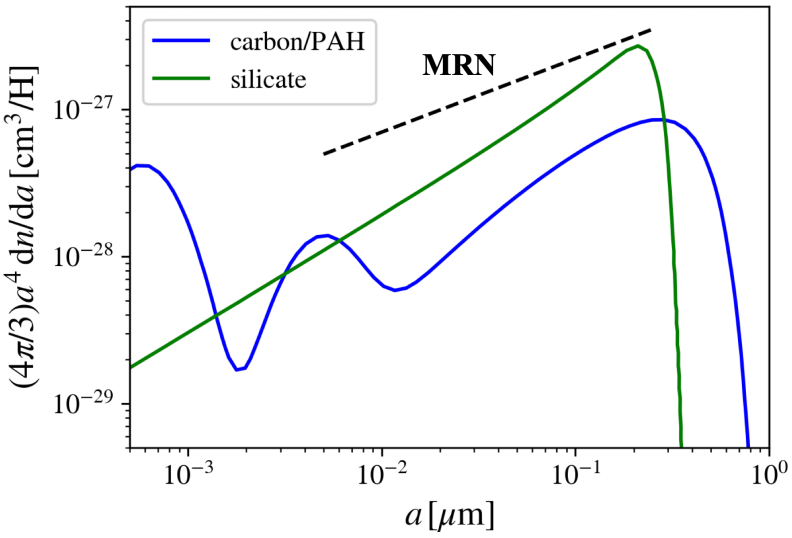

Figure 3.15: Size distributions for carbonaceous-silicate grain models for Milky Way dust with $R_V = 3.1$ derived by Weingartner and Draine (2001). The black dashed line indicates the slope of MRN distribution (Mathis et al., 1977).

Polarization of starlight also constrains the size of aligned grains. Although stellar light is initially unpolarized, passage through aligned, non-spherical dust grains produces linear polarization. The Serkowski law describes the polarization spectrum in the Milky Way, which peaks at $\lambda_{\max} \approx 0.55\,\mu$m. This corresponds to a characteristic grain size of $a = \lambda_{\max}/2\pi \approx 0.1\,\mu$m. Furthermore, the polarization decreases toward the UV ($\lambda < 0.3\,\mu$m), implying that the small grains dominating UV extinction ($a \lesssim 0.05\,\mu$m) are either spherical or poorly aligned with magnetic fields.

Finally, it is worth noting that while most of the mass in the ISM dust is in larger grains, most of the surface area, which is relevant for processes like accretion and photoelectric heating, is in small grains.

3.4.4 Absorption and Scattering Cross Sections

In order to describe the absorption and scattering properties of dust grains, we need to understand the electromagnetic response functions, i.e., how dust particles respond to incident electric and magnetic fields. Since the magnetization timescale is much longer than the oscillation period of the incident electromagnetic waves (1/frequency), magnetization effects can be neglected. Thus, we assume a magnetic permeability $\mu \sim 1$ and only focus on the electric field response. The electric field within a dielectric medium (i.e., a dust particle) is represented as a plane wave, $E(x,t) \propto e^{ikx-i\omega t}$, where k is the wavenumber, and ω is the angular frequency. We introduce the dielectric function $\epsilon(\omega) = \epsilon_1 + i\epsilon_2$ and the complex refractive index $m(\omega)$, defined as $m(\omega) = \sqrt{\epsilon(\omega)}$. The real part $\mathrm{Re}(m)$ and the imaginary part $\mathrm{Im}(m)$ correspond to the refractive index and the absorption index, respectively. From Maxwell's equations, the wavenumber k can be expressed as

$$k = \frac{m(\omega)\omega}{c}. \tag{3.89}$$

The electric field is then expressed as follows,

$$E \propto e^{ikx-i\omega t} = \exp\left[-\mathrm{Im}(m)\frac{\omega x}{c} + i\left(\frac{\omega \mathrm{Re}(m)x}{c} - \omega t\right)\right] \tag{3.90}$$

$$= \exp\left[-\mathrm{Im}(m)\frac{2\pi x}{\lambda} + i\left(\frac{2\pi \mathrm{Re}(m)x}{\lambda} - \omega t\right)\right], \tag{3.91}$$

where λ is a vacuum wavelength of incident radiation $\lambda \equiv 2\pi c/\omega$. Its amplitude decreases as

$$|E|^2 \propto \exp\left(-\frac{2\omega x}{c}\mathrm{Im}(m)\right). \tag{3.92}$$

When the grain size is much smaller than the wavelength of the incident radiation (the Rayleigh limit, $x < a \ll \lambda$), the electric field depends only on time, as $E \propto e^{-i\omega t}$. Assuming the external electric field is uniformly distributed, a dipole moment $\boldsymbol{P}$ is induced in the grain. The grain response is expressed through its atomic polarizability α, satisfying $\boldsymbol{P} = \alpha \boldsymbol{E}$. The absorbed energy per unit time, $P_{\rm abs}$, and the incident radiation flux, F, are given by

$$P_{\rm abs} = \frac{\omega}{2}\mathrm{Im}(\alpha)|E_0|^2 \tag{3.93}$$

$$F = \frac{c}{8\pi}|E_0|^2. \tag{3.94}$$

Therefore, the absorption cross-section is

$$C_{\rm abs} = \frac{P_{\rm abs}}{F} = \frac{4\pi\omega}{c}\mathrm{Im}(\alpha). \tag{3.95}$$

For scattering the scattered power is,

$$P_{\rm sca} = \frac{\omega^4}{3c^3}|\mathbf{P}|^2 = \frac{\omega^4}{3c^3}|\alpha E_0|^2. \tag{3.96}$$

The corresponding scattering cross-section is

$$C_{\rm sca} = \frac{P_{\rm sca}}{F} = \frac{8\pi}{3}\left(\frac{\omega}{c}\right)^4 |\alpha|^2. \tag{3.97}$$

The polarizability α is expressed as

$$\alpha = a^3 \frac{\epsilon - 1}{\epsilon + 2} \tag{3.98}$$

For an insulator, the dielectric function ϵ can be described as the response of a bound electron undergoing forced oscillation;

$$\epsilon = 1 + \frac{\omega_{\rm p}^2}{\omega_0^2 - \omega^2 - i\gamma\omega}, \tag{3.99}$$

where $\omega_{\rm p}$ and ω_0 are the plasma angular frequency and resonance angular frequency, respectively. In the Rayleigh limit, i.e., when $\omega_0^2 - \omega^2 \simeq \omega_0^2$ and $\omega_0^2 \gg |-i\gamma\omega|$, Eq. (3.99) is approximated as

$$\epsilon \simeq 1 + \frac{\omega_{\rm p}^2}{\omega_0^2} + \frac{i\omega_{\rm p}^3\omega\gamma}{\omega_0^4}. \tag{3.100}$$

Comparing to $\epsilon = \epsilon_1 + i\epsilon_2$, we obtain $\epsilon_1 = \epsilon_0$ and $\epsilon_2 = A\omega$, where ϵ_0 and A are constants. From Eqs. (3.95) and (3.97), we have

$$C_{\rm sca} = \frac{128\pi^5 a^6}{3\lambda^4}\left|\frac{\epsilon - 1}{\epsilon + 2}\right|^2 = \frac{128\pi^5 a^6}{3\lambda^4}\frac{(\epsilon_0 - 1)^2 + (A\omega)^2}{(\epsilon_0 + 2)^2 + (A\omega)^2} \simeq \frac{128\pi^5 a^6}{3\lambda^4}\frac{(\epsilon_0 - 1)^2}{(\epsilon_0 + 2)^2} \propto \lambda^{-4} \tag{3.101}$$

$$C_{\rm abs} = \frac{8\pi^2 a^3}{\lambda}\mathrm{Im}\left|\frac{\epsilon - 1}{\epsilon - 2}\right| = \frac{8\pi^2 a^3}{\lambda}\frac{3A\omega}{(\epsilon_0 + 2)^2 + (A\omega)^2} \simeq \frac{48\pi^3 a^3}{\lambda^2}\frac{Ac}{(\epsilon_0 + 2)^2} \propto \lambda^{-2} \tag{3.102}$$

For conductors, ϵ is described as the Drude model as

$$\epsilon = 1 - \frac{\omega_{\rm p}^2}{\omega^2 + i\omega\gamma} \tag{3.103}$$

$$\simeq 1 + \frac{\omega_{\rm p}^2 i}{\gamma\omega} \quad \text{(For Rayleigh limit)} \tag{3.104}$$

We then obtain $\epsilon_1 = 1$ and $\epsilon_2 = 4\pi\sigma_0/\omega$, where σ_0 is the conductivity defined as $\sigma_0 \equiv \omega_{\rm p}^2/4\pi\gamma$. Using Eqs.(3.95) and (3.97), the scattering and absorption cross-sections are derived as follows;

$$C_{\rm sca} = \frac{128\pi^5 a^6}{3\lambda^4}\left|\frac{\epsilon-1}{\epsilon+2}\right|^2 = \frac{128\pi^5 a^6}{3\lambda^4}\frac{\left(\frac{4\pi\sigma_0}{\omega}\right)^2}{3^2+\left(\frac{4\pi\sigma_0}{\omega}\right)^2} \simeq \frac{128\pi^5 a^6}{3\lambda^4} \tag{3.105}$$

$$C_{\rm abs} = \frac{8\pi^2 a^3}{\lambda}{\rm Im}\left|\frac{\epsilon-1}{\epsilon-2}\right| = \frac{8\pi^2 a^3}{\lambda}\frac{3\cdot\frac{4\pi\sigma_0}{\omega}}{1+\left(\frac{4\pi\sigma_0}{\omega}\right)^2} \simeq \frac{12\pi^3 c a^3}{\sigma_0\lambda^2}. \tag{3.106}$$

For both insulator and conductor cases in the Rayleigh limit, the ratio of scattering to absorption cross-sections is given by $C_{\rm sca}/C_{\rm abs} \propto a^3/\lambda^2$, satisfying the condition $C_{\rm sca}/C_{\rm abs} \ll 1$. In this regime, extinction is dominated by absorption, and thus we have $C_{\rm ext} \sim C_{\rm abs} \propto \lambda^{-2}$.

In the above discussion, we assume the Rayleigh limit, i.e., $a \ll \lambda$. However, this assumption becomes invalid in the UV–optical regime, where the spatial variation of the electric field can no longer be neglected (see Eq. 3.91). Mie (1908) derived an analytical solution for electromagnetic scattering and absorption by spherical grains, known as Mie theory. This theory describes the electric field using spherical harmonics and Bessel functions. The Mie coefficients are obtained by applying appropriate boundary conditions at the grain surface. Consequently, the absorption and scattering cross-sections are expressed as functions of the dimensionless size parameter $x = 2\pi a/\lambda$ and the complex refractive index m.

For grains with a small absorption index (${\rm Im}(m) \ll 1$), the extinction efficiency factor defined as $Q_{\rm ext} \equiv Q_{\rm abs} + Q_{\rm sca} \simeq Q_{\rm sca}$ exhibits significant oscillations arising from interference effects. In contrast, for grains with a large absorption index (${\rm Im}(m) \gtrsim 1$), such interference effects are suppressed, and thus, the oscillations do not appear.

As the size parameter x becomes large ($x \gg 1$), $Q_{\rm ext}$ asymptotically approaches 2, and thus, the extinction cross-section becomes $C_{\rm ext} = 2\pi a^2$. Geometrically, one might expect the cross-sectional area of a grain, πa^2, to represent an upper limit for extinction. However, this apparent paradox can be resolved by taking into account diffraction effects: light rays grazing the grain' s edge undergo diffraction, contributing to additional forward scattering. This leads to a total extinction cross-section twice the geometric area.

3.4.5 Dust Temperatures

Dust grains absorb stellar radiation primarily in the ultraviolet and optical regimes, and re-emit this energy thermally in the infrared as blackbody radiation—more precisely, as modified (graybody) emission due to their wavelength-dependent emissivity. The shape and peak of the emission spectrum are determined by the dust temperature. Observationally, this thermal emission is very important, as it allows us to estimate both the temperature and the mass of dust in galaxies or interstellar regions. Understanding the dust temperature is therefore essential for interpreting infrared observations and constraining the energy balance within the interstellar medium.

Absorption of UV/optical radiation from stars is the primary heating source for dust grains. Although collisional heating can contribute significantly in very dense environments, we neglect this effect here. The heating rate is then written as

$$\left(\frac{{\rm d}E}{{\rm d}t}\right)_{\rm abs} = \int {\rm d}\lambda\, u_{\lambda,*} c \cdot Q_{\rm abs}(a,\lambda)\pi a^2 \tag{3.107}$$

$$= \langle Q_{\rm abs}\rangle_* \pi a^2 c \int {\rm d}\lambda u_{\lambda,*} \tag{3.108}$$

where $u_{\lambda,*}$ is the stellar energy density per unit wavelength [erg cm^{-3} A^{-1}]. Here we define a spectrally averaged absorption cross-section as follows

$$\langle Q_{\rm abs}\rangle_* \equiv \frac{\int {\rm d}\lambda u_{\lambda,*} Q_{\rm abs}}{\int {\rm d}\lambda\, u_{\lambda,*}}. \tag{3.109}$$

Once the spectrum of the incident radiation is specified, we can determine $\langle Q_{\rm abs}\rangle_*$.

The heated grain cools via thermal emission, which can be approximated as blackbody radiation with temperature $T_{\rm d}$. The cooling rate is then given by

$$\left(\frac{{\rm d}E}{{\rm d}t}\right)_{\rm emis} = \int {\rm d}\lambda\, 4\pi B_\lambda(T_{\rm d}) C_{\rm abs}(a,\lambda). \tag{3.110}$$

Here, we introduce the Plank-averaged emission frequency,

$$\langle Q_{\rm abs}\rangle_{T_{\rm d}} \equiv \frac{\int {\rm d}\lambda B_\lambda(T_{\rm d})\, Q_{\rm abs}}{\int {\rm d}\lambda\, B_\lambda(T_{\rm d})}. \tag{3.111}$$

Substituting Eq.(3.111) into Eq.(3.110), we re-write the cooling rate as

$$\left(\frac{{\rm d}E}{{\rm d}t}\right)_{\rm emis} = 4\pi a^2 \langle Q_{\rm abs}\rangle_{T_{\rm d}} \sigma_{\rm SB} T_{\rm d}^4 \quad \left(\because \int {\rm d}\lambda B_\lambda(T_{\rm d}) = \frac{\sigma_{\rm SB}}{\pi} T_{\rm d}^4\right), \tag{3.112}$$

where $\sigma_{\rm SB}$ is Stefan-Boltzmann constant. From Eqs.(3.102) and (3.106), $Q_{\rm abs}$ is written as power-law with λ in the ayleigh limit. By setting $Q_{\rm abs}(\lambda) = Q_0(\lambda/\lambda_0)^{-\beta}$, Eq.(3.111) is re-written as

$$\langle Q_{\rm abs}\rangle_{T_{\rm d}} = \frac{15}{\pi^4} Q_0 \Gamma(\beta+4)\zeta(\beta+4)\left(\frac{\lambda_0 k_{\rm B} T_{\rm d}}{h_{\rm P} c}\right)^\beta, \tag{3.113}$$

where $\Gamma(t)$ and $\zeta(t)$ are the gamma function and zeta function, respectively. Equations (3.102) and (3.106) indicate that dust re-emission in the infrared regime satisfies the Rayleigh limit and follows $Q_{\rm abs} \propto \lambda^{-2}$, i.e., $\beta \simeq 2$.

From energy balance, we have

$$4\pi a^2 \langle Q_{\rm abs}\rangle_{T_{\rm d}} \sigma_{\rm SB} T_{\rm d}^4 = \pi a^2 \langle Q_{\rm abs}\rangle_* u_* c \tag{3.114}$$

$$\therefore 4\pi a^2 \frac{15}{\pi^4} Q_0 \Gamma(\beta+4)\zeta(\beta+4)\left(\frac{\lambda_0 k_{\rm B} T_{\rm d}}{h_{\rm P} c}\right)^\beta \sigma_{\rm SB} T_{\rm d}^4 = \pi a^2 \langle Q_{\rm abs}\rangle_* u_* c \tag{3.115}$$

$$\therefore T_{\rm d} = \left(\frac{h_{\rm P} c}{k_{\rm B}\lambda_0}\right)^{\beta/(4+\beta)} \left[\frac{\pi^4 \langle Q_{\rm abs}\rangle_* c}{60\Gamma(\beta+4)\zeta(\beta+4) Q_0 \sigma_{\rm SB}}\right]^{1/(\beta+4)} u_*^{1/(\beta+4)}. \tag{3.116}$$

If the spectral shape of the interstellar radiation field (ISRF) remains unchanged, the mean absorption efficiency factor $\langle Q_{\rm abs}\rangle_*$ can be treated as a constant. The radiation energy density u_* is usually expressed in terms of the dimensionless scaling parameter U, which represents the intensity of the local radiation field normalized to that of the MW interstellar radiation field (ISRF). Assuming the spectral shape of MW ISRF (Mathis et al., 1983), the dust temperature is

$$T_{\rm d} \sim 16.4\,{\rm K}\left(\frac{a}{0.1\,\mu{\rm m}}\right)^{-1/15} U^{1/6} \quad (\text{silicate } 0.01 \le a\,[\mu{\rm m}] \le 1) \tag{3.117}$$

$$\sim 22.3\,{\rm K}\left(\frac{a}{0.1\,\mu{\rm m}}\right)^{-1/40} U^{1/6}. \quad (\text{graphite } 0.005 \le a\,[\mu{\rm m}] \le 0.15) \tag{3.118}$$

The observed re-emission is the combination of re-emission from various grain populations, which is written as

$$j_\lambda = \sum_i \int {\rm d}a \frac{{\rm d}n_i}{{\rm d}a} \int {\rm d}T \left(\frac{{\rm d}P}{{\rm d}T}\right)_{i,a} C_{\rm abs}(\lambda, i, a) B_\lambda(T), \tag{3.119}$$

where ${\rm d}n_i/{\rm d}a$ represents the number density distribution of grain type i in the size interval $[a, a+{\rm d}a]$, and $({\rm d}P_i/{\rm d}T)$ is the temperature distribution function of the grains. Large grains

typically reach thermal equilibrium with the radiation field, thus exhibiting a nearly constant temperature distribution function, approximated by a delta function $\delta(T - T_{\rm d})$. On the other hand, small grains such as graphite and PAHs undergo stochastic heating due to their small heat capacities. For these very small grains, the absorption of even a single UV/optical photon can significantly elevate their temperature. Consequently, these small grains do not settle into thermal equilibrium, but instead experience rapid temperature fluctuations, stochastically emitting radiation at temperatures far exceeding the equilibrium temperature.

3.4.6 Observational Diagnostics of Dust

Dust plays a central role in shaping the observed spectral energy distributions (SEDs) of galaxies, through both absorption and scattering of stellar light and subsequent re-emission in the infrared. In this section, we focus on observational diagnostics that constrain the amount, distribution, and properties of dust in galaxies, particularly through the UV attenuation law and the relation between infrared excess and UV spectral slope.

3.4.6.1 Extinction/ Attenuation Law

It is essential to clearly distinguish between the concepts of *extinction* and *attenuation*. Extinction refers to the combined absorption and scattering (removal from the line of sight) of light by dust. The light is provided by a background point source (star, quasar), and the dust is an entirely foreground source. Since the source is a background point, the observed extinction depends solely on the optical properties and column density of dust, and is independent of the spatial distribution or geometry of the foreground dust layer.

Attenuation, in contrast, refers to the net effect of dust in a complex geometrical distribution, where radiation sources are embedded within the dust at various depths, including positions both in front of and behind the dust. Because both the radiation sources and the dust have extended distributions, their relative geometry significantly influences the net absorbed and scattered radiation, the latter now including scattering into the line of sight. Dust scattering into the line of sight tends to produce a greyer overall attenuation compared to the case where only scattering out of the line of sight occurs, resulting in an observed SED that is relatively bluer than in the case of pure extinction, and vice versa. This situation is typically encountered when studying galaxies or extended regions within galaxies.

Moreover, the relative distributions of dust and stars significantly affect the resulting attenuation. Here we consider two simplified geometric models: a distant uniform dust screen and a well-mixed slab, as illustrated in Figure 3.16. In the case of the uniform dust screen, the attenuation behaves similarly to extinction for a single background star, and the attenuated intensity is expressed as:

$$I_\nu = I_{\nu,0}\, e^{-\tau_\nu}, \tag{3.120}$$

where I_ν ($I_{\nu,0}$) is the attenuated (intrinsic) intensity, and τ_ν is the optical depth. In contrast, for the well-mixed geometry where dust and stars are homogeneously distributed, the attenuated intensity becomes:

$$I_\nu = I_{\nu,0}\, \frac{1 - e^{-\tau_\nu}}{\tau_\nu} \equiv I_{\nu,0} e^{-\tau_{\rm eff,\nu}}, \tag{3.121}$$

where $\tau_{\rm eff,\nu}$ is the effective optical depth, incorporating the averaged effect of scattering into the line of sight (Mathis et al., 1983). In this case, the optical depth from an external observer to stars located close to the surface of the slab is smaller than in the foreground screen case, resulting in an observed spectral energy distribution (SED) that is relatively bluer. Figure 3.17 shows the obscuration rate $f_{\rm obs} \equiv I/I_0$ and the effective optical depth as a function of optical depth.

Additionally, clumpiness within the dusty medium increases its transparency compared to a uniform dust distribution, as photons can escape through regions with lower dust column density(e.g., Gordon et al., 1997; Inoue, 2005; Inoue et al., 2020). Likewise, the clumpiness in the stellar distribution also affects attenuation. Some attenuation models also incorporate different treatments for stellar populations of varying ages. For instance, young stars are generally assumed to be embedded in denser clouds and thus experience stronger attenuation compared to older stellar populations. Such models predict a flattening of the ultraviolet (UV) bump feature in the attenuation curve (Granato et al., 2000).

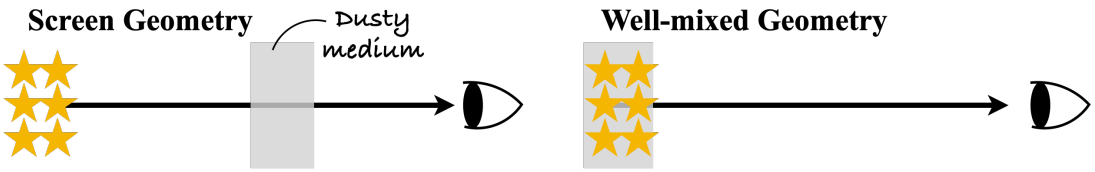

Figure 3.16: Schematic illustrations of stellar and dusty medium distributions. The left and right panels show a distant uniform screen geometry and a well-mixed geometry, respectively. There are also considerations of additional geometries, such as a clumpy medium and a close uniform screen geometry, where scattered light contributes significantly to the observed radiation.

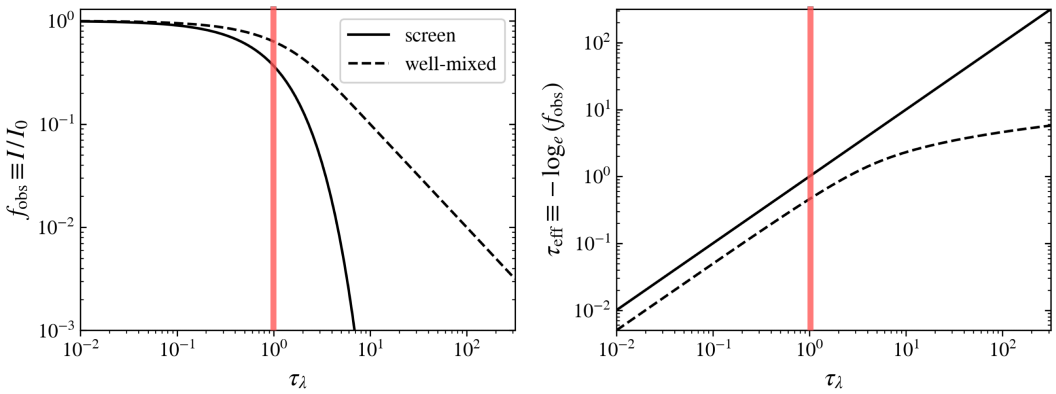

Figure 3.17: Dust obscuration (left) and effective optical depth (right) as a function of optical depth. The uniform screen and well-mixed cases are shown by the black solid and dashed lines, respectively. The red lines indicate the case of $\tau_\lambda = 1$.

The extinction curve is derived from observations of individual stars, as described in Section 3.4.2. Extinction curves have so far been measured for the Milky Way (MW), M31, the Small Magellanic Cloud (SMC), and the Large Magellanic Cloud (LMC) (Cardelli et al., 1989; Bianchi et al., 1996; Fitzpatrick, 1999; Gordon et al., 2003). These galaxies are unique in that individual stars can be resolved, allowing the determination of extinction properties from the foreground dust. Figure 3.18 shows extinction curves for the MW (with $R_V = 3.1$), LMC, and SMC. The MW and LMC curves exhibit a prominent bump at 2175 Å, implying the presence of small carbonaceous grains or polycyclic aromatic hydrocarbons (PAHs), as discussed in Section 3.4.2. In contrast, the extinction curve for the SMC lacks this 2175 Å bump and instead shows a nearly linear, steep rise with increasing λ^{-1}. This suggests that dust grains in the SMC are smaller than those in the Galactic diffuse interstellar medium, possibly due to either more efficient dust destruction or limited grain growth in the lower metallicity environment ($\sim 1/3\, Z_\odot$).

Especially, extinction curves could be approximated by a seven-parameter function of λ,

$$A_\lambda / A_{\lambda_{\rm ref}} \approx f(\lambda; R_{\rm V}, C_1, C_2, C_3, C_4, \lambda_0, \gamma). \tag{3.122}$$

At wavelength of $\lambda = 3030\,\text{Å} - 3.5\,\mu\text{m}$, the function depends only on λ and a single parameter of R_V. The parameters C_3, λ_0, γ determine the slope and curvature of the 2175 Å bump, and the C_1, C_2 determine the slope and curvature of the continuous extinction at $\lambda < 3030\,\text{AA}$. Cardelli et al. (1989) showed that if the single quantity R_v is known, it is possible to estimate the values of the other six parameters $(C_{1-4}, \lambda, \gamma)$ so that the optical-UV extinction can be approximated by a one-parameter family of curves, i.e., $A_\lambda / A_{\lambda_\text{ref}} \approx f(\lambda; R_\text{V})$. Figure 3.12 shows the Milky Way extinction curves for several R_V values, each corresponding to a different line of sight. Significant variations in the optical/UV regions of the curve reflect differences in the dust grain size distribution along those sightlines.

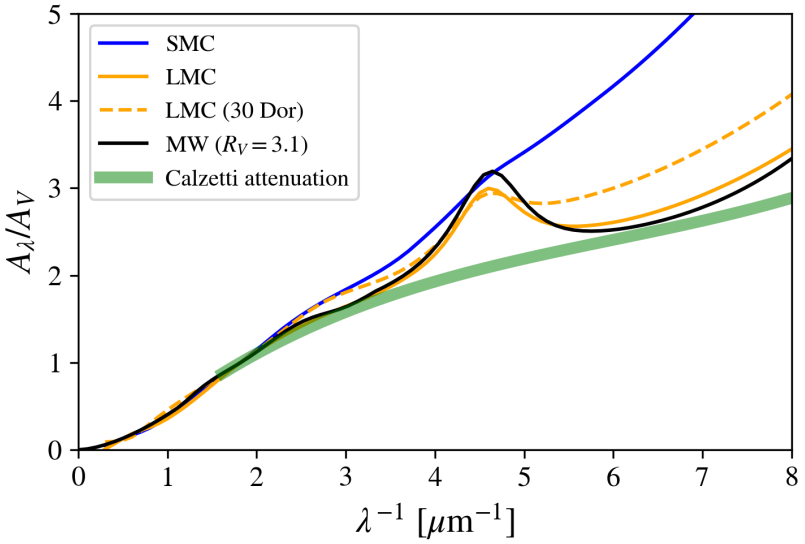

Figure 3.18: Extinction curves and the Calzetti attenuation curve (Calzetti et al., 2000). The solid blue and black lines show extinction curves for the SMC(Bar region) and MW, respectively, plotted using the fitting functions provided by Gordon et al. (2003) and Cardelli et al. (1989). The orange lines represent extinction curves for the LMC; the dashed orange line specifically corresponds to the region around 30 Doradus, where bursty star formation activity occurs, accompanied by supershell structures. The solid green line denotes the Calzetti curve, plotted using Eq.(3.124).

As we focus on more distant galaxies, we no longer obtain their extinction curves, but attenuation curves, which include geometrical effects of stars/dusts distribution and scattering. Calzetti et al. (1994) selected UV-bright starburst galaxies and empirically obtained the following attenuation law, known as Calzetti's attenuation law:

$$f_\text{int}(\lambda) = f_\text{obs}(\lambda) \times 10^{0.4 k_\text{e}(\lambda) E_\text{gas}(B-V)}, \tag{3.123}$$

where $f_\text{int}(\lambda)(f_\text{obs}(\lambda))$ is an intrinsic (observed) flux, and $E_\text{gas}(B-V)$ is a color excess for ionized nebulae. The obscuration curve is given by Calzetti et al. (2000),

$$\begin{aligned} k_\text{e}(\lambda) &= 1.17\left(-1.857 + \frac{1.040}{\lambda}\right) + 1.78 \;\; (\text{for } 0.63\,\mu\text{m} \le \lambda \le 2.20\,\mu\text{m}) \\ k_\text{e}(\lambda) &= 1.17\left(-2.156 + \frac{1.509}{\lambda} - \frac{0.198}{\lambda^2} + \frac{0.011}{\lambda^3}\right) + 1.78 \;\; (\text{for } 0.12\,\mu\text{m} \le \lambda \le 0.63\,\mu\text{m}). \end{aligned} \tag{3.124}$$

The $k_\text{e}(\lambda)$ contains a variety of effects, extinction proper, scattering, and the geometrical distribution of the dust relative to the emitters and entire stellar populations. Regarding the color excess, the reddening of the ionized gas is about twice that of the stellar continuum, expressed

quantitatively as

$$E_{\rm star}(B-V) = 0.44 E_{\rm gas}(B-V). \tag{3.125}$$

The color excess $E_{\rm gas}(B-V)$ can be derived from the Balmer decrement, defined as the line ratio of hydrogen Balmer series lines, typically Hα and Hβ. These emission lines originate from dusty ionized gas regions, while the stellar continuum primarily arises from gas with significantly less dust, resulting in a larger color excess for the gas as expressed by Eq.(3.125). Using Eq.(3.123), the observed line ratio of two Balmer lines H_i and H_j can be expressed as follows;

$$\frac{f_{\rm int}(\lambda_{\rm H_i})}{f_{\rm int}(\lambda_{\rm H_j})} = \frac{f_{\rm obs}(\lambda_{\rm H_i})}{f_{\rm obs}(\lambda_{\rm H_j})} \times 10^{0.4(A(\lambda_{\rm H_i})-A(\lambda_{\rm H_j}))} \tag{3.126}$$

$$\therefore A(\lambda_{\rm H_i}) - A(\lambda_{\rm H_j})) = 2.5 \left[\log_{10}\left(\frac{f_{\rm int}(\lambda_{\rm H_i})}{f_{\rm int}(\lambda_{\rm H_j})}\right) - \log_{10}\left(\frac{f_{\rm obs}(\lambda_{\rm H_i})}{f_{\rm obs}(\lambda_{\rm H_j})}\right)\right] \tag{3.127}$$

$$\therefore E_{\rm gas}(B-V) = \frac{2.5}{k(\lambda_{\rm i}) - k(\lambda_{\rm j})} \left[\log_{10}\left(\frac{f_{\rm int}(\lambda_{\rm H_i})}{f_{\rm int}(\lambda_{\rm H_j})}\right) - \log_{10}\left(\frac{f_{\rm obs}(\lambda_{\rm H_i})}{f_{\rm obs}(\lambda_{\rm H_j})}\right)\right]. \tag{3.128}$$

The intrinsic line ratio is uniquely determined by assuming case B with little dependence on temperature and electron densities.

Also, Calzetti law has $R_V \equiv A_{\rm V}/E_{\rm star}(B-V) = 4.05$ (Calzetti et al., 2000). As seen in Figure 3.18, there is no 217, Å bump in the Calzetti law. Two possible explanations for this absence are geometrical effects or intrinsic properties of the underlying extinction curves, which themselves may not exhibit the UV bump.mp.

3.4.6.2 IRX–β Relation

The infrared excess (IRX)–UV slope (β) relation provides a widely used empirical diagnostic for estimating dust attenuation solely from UV observations. First introduced by Meurer et al. (1999) for local UV-bright starburst galaxies, the IRX–β relation connects the total dust-reprocessed radiation, quantified as the ratio $L_{\rm IR}/L_{\rm UV}$, with the slope β of the UV continuum defined by $f_\lambda \propto \lambda^\beta$. This technique is particularly valuable for studies of high-redshift galaxies, where infrared observations are often unavailable or sensitivity-limited. Using the IRX–β relation, we can estimate the dust-attenuated UV luminosity and the re-emitted infrared luminosity, and finally derive the total star formation rate (SFR) by assuming energy balance between dust absorption and emission. The inferred SFR thus provides a robust measure to calibrate the cosmic SFR density evolution accurately (e.g., Madau and Dickinson, 2014).

The IRX–$\beta_{\rm UV}$ relation for local starburst galaxies was first investigated by Meurer et al. (1999) and Calzetti et al. (2000), known as the Calzetti IRX–$\beta_{\rm UV}$ relation. Takeuchi et al. (2012) later modified this relation by accounting for aperture effects in UV photometry. Observations indicate that the SMC exhibits lower IRX values compared to the Calzetti relation (e.g., Mao et al., 2014). Herschel and ALMA studies have shown that galaxies at $z \sim 2-5$ generally follow either the Calzetti or the SMC IRX–$\beta_{\rm UV}$ curves (e.g., Fudamoto et al., 2017; Koprowski et al., 2018; McLure et al., 2018; Reddy et al., 2018). However, at $z > 5$, some galaxies show significantly lower IRX values than these relations (e.g., Capak et al., 2015; Bouwens et al., 2016; Barisic et al., 2017), suggesting a significant evolution of dust properties from $z \sim 0$ to $z > 5$. There are several possible explanations for the origin of these low IRX values in high-redshift galaxies. A key uncertainty is that the dust temperature ($T_{\rm dust}$) is not directly measured in most galaxies at $z > 5$, as highlighted by multiple studies (e.g., Bouwens et al., 2016; Faisst et al., 2017; Behrens et al., 2018). Since these galaxies are typically observed in only a single FIR band, their dust temperatures are usually assumed to match those of local galaxies to estimate their IR luminosities.

The way to get IRX-β curves is as follows. Meurer et al. (1999) defined ${\rm IRX_{M99}}$ as

$${\rm IRX_{M99}} \equiv \frac{F_{\rm FIR}}{F_{1600}} = \frac{F_{\rm Ly\alpha} + \int_{912}^{\infty} f_{\lambda,0}(1 - 10^{-0.4A_\lambda}\,{\rm d}\lambda)}{F_{1600,0}\,10^{-0.4A_{1600}}} \left(\frac{F_{\rm FIR}}{F_{\rm dust,bol}}\right), \tag{3.129}$$

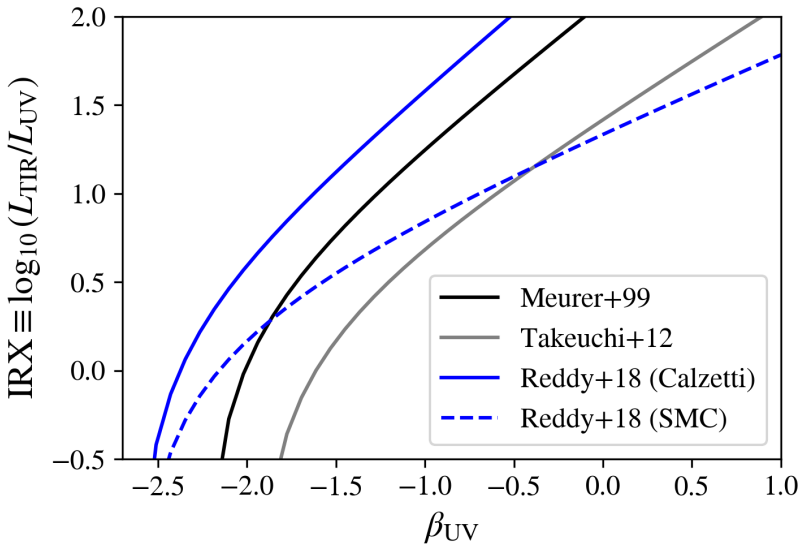

Figure 3.19: IRX–β relations derived from different observations and theoretical models. The black line shows the IRX–β relation for local UV starburst galaxies from Meurer et al. (1999), applying total IR luminosity corrections from Calzetti et al. (2000). The gray line corresponds to the same galaxy samples but with photometric aperture corrections applied (Takeuchi et al., 2012). Both the black and gray lines adopt the same stellar bolometric correction factor $\mathrm{BC}(1600)_*$, derived using STARBURST99 (Leitherer et al., 1999), assuming a Salpeter IMF, constant star formation history, and solar metallicity. The blue lines are derived using BPASS SED models (Eldridge et al., 2017), assuming a constant star formation history of 100 Myr with nebular emission, a double power-law IMF, and low stellar metallicity of $Z = 0.14, Z\odot$ (Reddy et al., 2018). The solid and dashed blue lines correspond to attenuation curves assuming Calzetti attenuation and SMC extinction laws, respectively.

where $F_{\rm FIR}$ is the flux of between 42-122 μm , and F_{1600} is UV flux. Here, $F_{{\rm Ly}\alpha}$ is Lyman-α flux produced by the recombination cascade. Here we assume that ionizing photons with $\lambda < 912\,$Å are not absorbed by dust. The total flux of dust emission is expressed as $F_{\rm dust,bol}$, and A_λ is obtained assuming attenuation curves. The flux $f_{\lambda,0}$ is the intrinsic flux. Since the dominant radiation from massive stars is UV photons, Eq.(3.129) is approximated as

$$\mathrm{IRX_{M99}} \approx (10^{0.4A_{1600}} - 1)\frac{F_{{\rm Ly}\alpha} + \int_{912}^{\infty} f_{\lambda,0}\,\mathrm{d}\lambda}{F_{1600}}\left(\frac{F_{\rm FIR}}{F_{\rm dust,bol}}\right) \tag{3.130}$$

$$= (10^{0.4A_{1600}} - 1)\frac{\mathrm{BC}(1600)_*}{\mathrm{BC(FIR)_{dust}}}. \tag{3.131}$$

Here

$$\mathrm{BC}(1600)_* = \frac{F_{{\rm Ly}\alpha} + \int_{912}^{\infty} f_{\lambda,0}\,\mathrm{d}\lambda}{F_{1600}},\ \ \mathrm{BC(FIR)_{dust}} = \frac{F_{\rm dust,bol}}{F_{\rm FIR}}. \tag{3.132}$$

The value $\mathrm{BC}(1600)_*$ is calculated assuming stellar SED models and star formation histories. In Meurer et al. (1999), $\mathrm{BC}(1600)_* = 1.66$ was adopted. The bolometric dust correction $\mathrm{BC(FIR)_{dust}}$ was obtained empirically from observations as $\mathrm{BC(FIR)_{dust}} = 1.4$. The attenuation A_{1500} and UV slope β have a linear relationship $A_{1600} = 4.43 + 1.99\beta$ for the observed starburst galaxies. Therefore, we obtain

$$\log_{10}(\mathrm{IRX_{M99}}) = \log_{10}(10^{0.4(4.43+1.99\beta)} - 1) + 0.076. \tag{3.133}$$

Currently, IRX adopts total IR luminosity, and Eq.(3.133) is corrected as

$$\mathrm{IRX} = \mathrm{IRX_{M99}} \times \frac{F_{\rm TIR}}{F_{\rm FIR}}, \tag{3.134}$$

where $F_{\rm TIR}/F_{\rm FIR}$ is corrected following Calzetti et al. (2000). Figure 3.19 shows the IRX–β relations. Meurer et al. (1999) and Takeuchi et al. (2012) adopted the same bolometric corrections but used different A_{1600}–β relations. Reddy et al. (2018) employed a lower-metallicity stellar SED, which yields a harder spectrum and smaller β values. Even when the same BC(1600)$*$ value is adopted, differences in the assumed attenuation curves alter the resulting $A1600$–β relation. Therefore, the IRX–β relation depends on both the attenuation curves and the intrinsic stellar SEDs. When comparing galaxy samples with similar stellar populations, the observed scatter in IRX–β can be interpreted primarily as resulting from differences in the attenuation curves.

3.4.7 Radiative Transfer with Dust

The radiative transfer equation is generally expressed as

$$\boldsymbol{n}\cdot\boldsymbol{\nabla} I(\boldsymbol{x},\boldsymbol{n},\lambda) = -\kappa(\boldsymbol{x},\lambda)\rho(\boldsymbol{x})I(\boldsymbol{x},\boldsymbol{n},\lambda) + j(\boldsymbol{x},\boldsymbol{n},\lambda). \tag{3.135}$$

The left-hand side of Eq. (3.135) represents the change in intensity as radiation propagates an infinitesimal distance ds from position $\boldsymbol{x}$ in direction $\boldsymbol{n}$, which can be written as $\frac{\mathrm{d}I}{\mathrm{d}s}(\boldsymbol{x},\boldsymbol{n},\lambda)$. The right-hand side accounts for the loss of radiation intensity due to absorption and scattering by the medium, and for emission from the medium itself at position $\boldsymbol{x}$ toward direction $\boldsymbol{n}$. Here, $\rho(\boldsymbol{x})$ is the mass density, and $\kappa(\boldsymbol{x},\lambda)$ is the mass extinction coefficient of the medium ($\kappa_{\rm ext} = \kappa_{\rm sca} + \kappa_{\rm abs}$). The three-dimensional dust radiative transfer equation can thus be expressed as

$$\frac{\mathrm{d}I}{\mathrm{d}s}(\boldsymbol{x},\boldsymbol{n},\lambda) = -\kappa_{\rm ext}(\boldsymbol{x},\lambda)\rho(\boldsymbol{x})I(\boldsymbol{x},\boldsymbol{n},\lambda) + j_*(\boldsymbol{x},\boldsymbol{n},\lambda) + j(\boldsymbol{x},\lambda) \tag{3.136}$$

$$+ \kappa_{\rm sca}(\boldsymbol{x},\lambda)\rho(\boldsymbol{x})\int_{4\pi}\Phi(\boldsymbol{n},\boldsymbol{n'},\boldsymbol{x},\lambda)I(\boldsymbol{x},\boldsymbol{n'},\lambda)\,\mathrm{d}\Omega' \tag{3.137}$$

Regarding the terms on the right-hand side of Eq. (3.137), the first term describes absorption by dust. The second term represents the primary emission, which typically originates from stars but may also include nebular emission (continuum and emission lines) or radiation from active galactic nuclei (AGN). The third term accounts for dust re-emission, which significantly contributes at wavelengths $\lambda > 1\,\mu$m. The fourth term represents scattering of radiation originally propagating in direction $\boldsymbol{n}'$, scattered at position $\boldsymbol{x}$, and redirected into direction $\boldsymbol{n}$. Here, $\Phi(\boldsymbol{n}, \boldsymbol{n}', \boldsymbol{x}, \lambda)$ is the scattering phase function, satisfying the normalization condition $\int_{4\pi} \Phi(\boldsymbol{n}, \boldsymbol{n}', \boldsymbol{x}, \lambda), \mathrm{d}\Omega = 1$. Dust consists of various grain types differing in chemical composition, size, and shape, each having distinct absorption and scattering coefficients, $\kappa_{\mathrm{abs},i}(\lambda)$, and $\kappa_{\mathrm{sca},i}(\lambda)$. Introducing ω_i as the fraction of the total number density contributed by type i dust, we obtain

$$\kappa_{\mathrm{XX}}(\boldsymbol{x}, \lambda) = \sum_i \omega_i(\boldsymbol{x}) \kappa_{\mathrm{XX},i}(\lambda) \quad (\mathrm{XX} = \mathrm{abs,\ sca,\ ext}) \tag{3.138}$$

$$\Phi(\boldsymbol{n}, \boldsymbol{n}', \boldsymbol{x}, \lambda) = \frac{\sum_i \omega_i(\boldsymbol{x}) \kappa_{\mathrm{sca},i} \Phi_i(\boldsymbol{n}, \boldsymbol{n}', \lambda)}{\sum_i \omega_i(\boldsymbol{x}) \kappa_{\mathrm{sca},i}(\lambda)}. \tag{3.139}$$

The dust re-emission is written as

$$j_{\mathrm{d}}(\boldsymbol{x}, \lambda) = \sum_i \omega_i(\boldsymbol{x}) \kappa_{\mathrm{abs},i}(\lambda) \rho(\boldsymbol{x}) B(T_i(\boldsymbol{x}), \lambda) \tag{3.140}$$

$$= \sum_i \omega_i(\boldsymbol{x}) \kappa_{\mathrm{abs},i}(\lambda) \rho(\boldsymbol{x}) \left[\int_0^\infty P_i(T, \boldsymbol{x}) B(T, \lambda) \mathrm{d}T \right], \tag{3.141}$$

where $B(T, \lambda)$ is the Planck function and T_i is the equilibrium temperature for dust type i. Eq.(3.140) is valid for large grains because they reach thermal equilibrium and emit as modified blackbodies. However, when we consider the small grains such as PAHs, we need to include stochastic heating effect as Eq.(3.141). Here $P_i(T, \boldsymbol{x})$ is the temperature distribution for dust grains as introduced in Section 3.4.5. This temperature distribution depends not only on the grain type but also on the intensity and hardness of the radiation field in which it is embedded.

The above discussion is valid for unpolarized light. Photons scattered by dust are naturally polarized. Polarized radiation is generally expressed by Stokes vector $\boldsymbol{S} = (I, Q, U, V)$, where I is the total specific intensity, Q and U are the linearly polarized intensity, and V is the circularly polarized intensity. The corresponding radiative transfer equation is written by replacing I with $\boldsymbol{S}$, and Φ with Mueller matrix $\boldsymbol{M}(\boldsymbol{n}, \boldsymbol{n}', \boldsymbol{x}.\lambda)$, which described the changes in the Stockes vector when radiation is scattered from propagation direction $\boldsymbol{n}'$ to a new direction $\boldsymbol{n}$.

To summarize, Eq. (3.137) is a six-dimensional differential equation involving three-dimensional (3D) spatial position $\boldsymbol{x}$, two-dimensional (2D) direction $\boldsymbol{n}$, and one-dimensional (1D) wavelength λ. Solving this equation numerically is computationally expensive. For instance, if each dimension of the six-dimensional phase space is discretized into 100 grid points, the intensity vector would contain 10^{12} entries, demanding significant computational resources and memory usage. Generally, two main numerical approaches are employed for solving dust radiative transfer in 3D simulations: ray-tracing and Monte Carlo methods. The ray-tracing method involves emitting rays from radiation sources and calculating the extinction of intensity I along each ray using the relation $I \to I \times e^{-\tau}$. At each interaction point, scattering and re-emission processes are considered, and the resulting intensities are integrated along the line-of-sight. On the other hand, the Monte Carlo method involves generating numerous photon packets and stochastically simulating the propagation, absorption, scattering, and re-emission processes for each packet. Specifically, the Monte Carlo approach includes the following four processes.

Step 1: Generation of Photon Packets

Firstly, we prepare N photon packets that have an energy of $L = \dfrac{L_{\mathrm{tot}}(\lambda)}{N}$, where $L_{\mathrm{tot}}(\lambda)$ is the total luminosity of the source at wavelength λ. Photon packets are emitted from the radiation

source, with position, direction, and wavelength randomly selected according to the following probability distribution function (PDF);

$$p(\boldsymbol{x}, \boldsymbol{n})\mathrm{d}\boldsymbol{x}\mathrm{d}\boldsymbol{n} = \frac{j_*(\boldsymbol{x}, \boldsymbol{n}, \lambda)\mathrm{d}\boldsymbol{x}\mathrm{d}\boldsymbol{n}}{L_{\mathrm{tot}}(\lambda)}. \tag{3.142}$$

Generally, stellar radiation and dust re-emission are isotropic and satisfy $p(\boldsymbol{n})\,\mathrm{d}\boldsymbol{n} = \dfrac{\mathrm{d}\boldsymbol{n}}{4\pi}$.

Step 2: Determination of the Interaction Point
Next, the optical depth is randomly sampled as $\tau = -\log_{\mathrm{e}}(R)$, where R is a uniformly distributed random number in the interval $(0, 1)$. The path length of the photon packet is then determined by $s = \dfrac{\tau}{\kappa_\lambda}$, where κ_λ is determined by the dust types.

Step3: Determination of Absorption and Scattering
The position is updated from $\boldsymbol{x}$ to $\boldsymbol{x}+s\boldsymbol{n}$. At this new position, we determine whether scattering or absorption occurs. Using a uniformly distributed random number R, we compare it to the albedo $\omega \equiv \kappa_{\mathrm{sca}}/\kappa_{\mathrm{ext}}$, with scattering occurring if $R \leq \omega$, and absorption if $R > \omega$.

Step 4-1: Scattering Case
When scattering occurs, we determine a new propagation direction n with the probability distribution of

$$p(\boldsymbol{n}) = \frac{\Phi(\boldsymbol{n}, \boldsymbol{n'}, \boldsymbol{x}, \lambda)}{4\pi}. \tag{3.143}$$

Steps 2 to 4-1 are repeated until the photon packet either escapes from the system or is absorbed.

Step 4-2: Absorption Case
If absorption occurs, the absorbed luminosity at each wavelength is stored within the corresponding spatial grid.

After performing the above calculations for all wavelengths, the accumulated absorbed luminosity is used to calculate the mean intensity $J(\boldsymbol{x}, \lambda)$ and the corresponding dust re-emission $j_{\mathrm{d}}(\boldsymbol{x}, \lambda)$. The newly computed emission term $j_{\mathrm{d}}(\boldsymbol{x}, \lambda)$ is recalculated as a secondary source, and this process is repeated until $j_{\mathrm{d}}(\boldsymbol{x}, \lambda)$ converges.

Several Monte Carlo codes are available for performing three-dimensional dust radiative transfer calculations, including SKIRT(Baes et al., 2011), SUNRISE(Jonsson et al., 2010), and POWDERDAY(Narayanan et al., 2021). Other codes are summarized in Table 1 of Salim and Narayanan (2020). In Chapter 7, we utilize the SKIRT code for post-processing radiative transfer calculations.

Chapter 4

Latest High Redshift Observations in JWST and ALMA Era

4.1 Historical Context and Motivation for High-redshift Studies

Galaxy surveys at high-redshift ($z \gtrsim 6$) represent the frontier of extragalactic astronomy. As discussed in Chapter 1, understanding the formation, evolution, and ISM properties of these galaxies is essential, as it provides critical insights into cosmic reionization and the star formation history at Cosmic Dawn (e.g., Dayal and Ferrara, 2018).

Prior to the 2020s, our understanding of high-redshift galaxies was primarily based on deep imaging and spectroscopy conducted using the Hubble Space Telescope (HST) and the Subaru Telescope. These observations provided extensive samples of Lyman-α emitters (LAEs) and Lyman-break galaxies (LBGs) out to $z \sim 8$ (e.g., Furusawa et al., 2016; Maiolino et al., 2015; Matsuoka et al., 2018; Pentericci et al., 2016; Ouchi et al., 2013; Sobral et al., 2015). However, cosmic reionization is ongoing at $z \gtrsim 8$, causing Lyman-α photons to be scattered significantly by neutral hydrogen atoms in the intergalactic medium (IGM). Currently, only two galaxies have been detected in Lyα emission at $z > 10$ (GN-z11:Bunker et al. (2023), and JADES-GS-z13-1-LA:Witstok et al. (2025)), while other confirmed Lyα emitters reside at $z \lesssim 8.5$ (see Figure 3 of Kageura et al., 2025). Therefore, alternative emission lines, which are neither absorbed nor scattered by the IGM, are crucial to confirm the galaxy redshifts at $z \gtrsim 8$.

The Atacama Large Millimeter/submillimeter Array (ALMA) has opened a new observational window by detecting rest-frame far-infrared (FIR) lines from high-redshift galaxies in the epoch of reionization (EoR). The most notable among these lines are [CII] 158μm and [OIII] 88μm . While the [CII] line has traditionally served as a standard tracer of star formation in nearby galaxies, several bright LAEs at high redshift resulted in non-detections of [CII] (e.g., Ouchi et al., 2013; Ota et al., 2014; Schaerer et al., 2015), implying that the ISM conditions in high-redshift galaxies may differ substantially from those in local star-forming galaxies. In contrast, the [OIII] 88μm line is often among the brightest FIR lines in galaxies with low metallicities (Cormier et al., 2012; Madden et al., 2013). Inoue et al. (2014) theoretically predicted that high-redshift galaxies could be strong [OIII] emitters, and indeed, the [OIII] line was successfully detected at $z = 7.2$ by ALMA for the first time (Inoue et al., 2016a). Since then, galaxies in the EoR have been increasingly spectroscopically confirmed by [OIII] 88μm (e.g., Hashimoto et al., 2018; Laporte et al., 2017; Tamura et al., 2019; Hashimoto et al., 2019; Carniani et al., 2017; Wong et al., 2022; Witstok et al., 2022; Harikane et al., 2020; Tadaki et al., 2022).

The James Webb Space Telescope (JWST; Gardner et al., 2006), which began science operations in July 2022, has opened a new era of high-redshift galaxy studies. JWST offers photometric and spectroscopic sensitivities more than an order of magnitude greater than those of its predecessors, as illustrated in Figure 4.1. By combining multiple photometric bands from NIRCam, two-color diagrams can efficiently select high-z galaxy candidates via the dropout

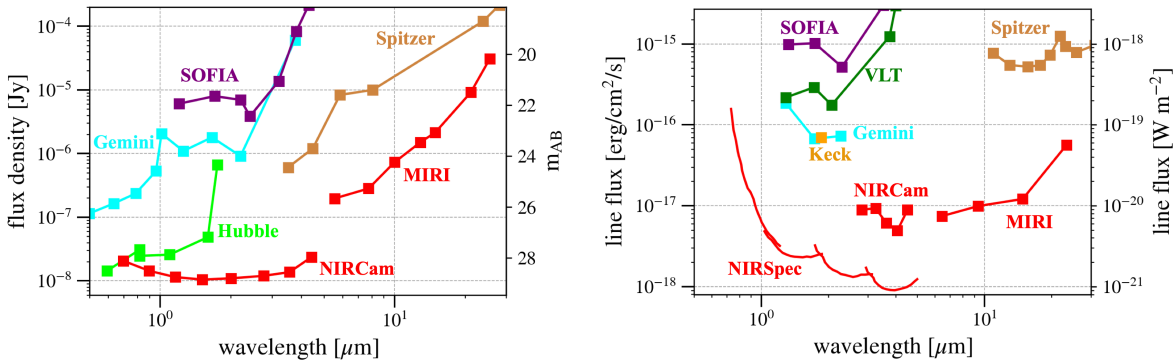

Figure 4.1: Sensitivity of photometric (left) and spectroscopic (right) instruments. Plots are the faintest flux for a point source that can be detected at SNR=10 in a 10,000 sec integration with JWST instruments. We also plot the other instruments for comparison. The figure is reproduced from the plots from https://www.stsci.edu/jwst/about-jwst/history/historical-sensitivity-estimates.

technique (e.g., Naidu et al., 2022; Harikane et al., 2023). Subsequent NIRSpec[1] observations then provide secure redshift confirmations through detections of Lyman breaks or rest-frame UV/optical emission lines. Prior to JWST, the highest spectroscopically confirmed galaxy was MACS1149-JD1 at z=9.11, observed via [OIII] 88μm (Hashimoto et al., 2018)[2]. JWST is now routinely identifying galaxies at $z \geq 10$. The latest observations have reported galaxies as distant as $z = 14.44$ (Naidu et al., 2025).

4.2 ALMA Observations of Galaxies at $z > 6$

Rest-frame FIR emission lines detected by ALMA not only enable the spectroscopic confirmation of distant galaxies but also provide insight into their multi-phase ISM. In particular, highly ionized lines such as [OIII] 88μm mostly trace HII regions associated with recent star formation (Cormier et al., 2012; Vallini et al., 2017; Arata et al., 2020), whereas [CII] 158 μm originates from a variety of environments, though mainly from photodissociation regions (PDRs; Stacey et al., 2010; Gullberg et al., 2015; Vallini et al., 2015; Lagache et al., 2018; Cormier et al., 2019). In addition, CO emission lines are accessible to ALMA, which traces molecular gas and directly traces star-forming sites. However, CO emission line detection remains limited to submillimeter galaxies (SMGs) or quasars up to $z \sim 6$ (Ono et al., 2022).

Ratios between FIR emission lines serve as powerful diagnostics of ISM properties. For example, the [OIII] 52μm /[OIII] 88μm ratio probes electron densities. However, detecting [OIII] 52μm remains challenging with current ALMA bands, despite its intrinsically higher luminosity compared to [OIII] 88μm . Several attempts to detect this line at high redshift have resulted only in upper limits (e.g., Killi et al., 2023; Zavala et al., 2024, , Ren et al. in prep.). Very recently (May 2025), (Harikane et al., 2025b) have reported the first detection of [OIII] 52μm in a $z > 6$ galaxy and confirmed electron density with [OIII] 52μm /[OIII] 88μm as $n_{\rm e,FIR} = 500\,{\rm cm}^{-3}$, which is four times lower than that estimated by [OII] doublet (see also Section 4.4).

Emission line ratios between different ions, as well as ratios between lines from the same ion, offer valuable diagnostics for probing the multi-phase ISM. The line ratio [OIII] /[CII], in particular, provides insight into the ISM ionization state, given their substantially different

[1]NIRCam Wide Field Slitless Spectroscopy (WFSS) also facilitates rapid spectroscopic confirmation for larger galaxy samples.

[2]GN-z11 was initially reported at $z \approx 11$ (Oesch et al., 2016), but subsequent JWST/NIRSpec observations revised its redshift to $z = 10.6$ (Bunker et al., 2023).

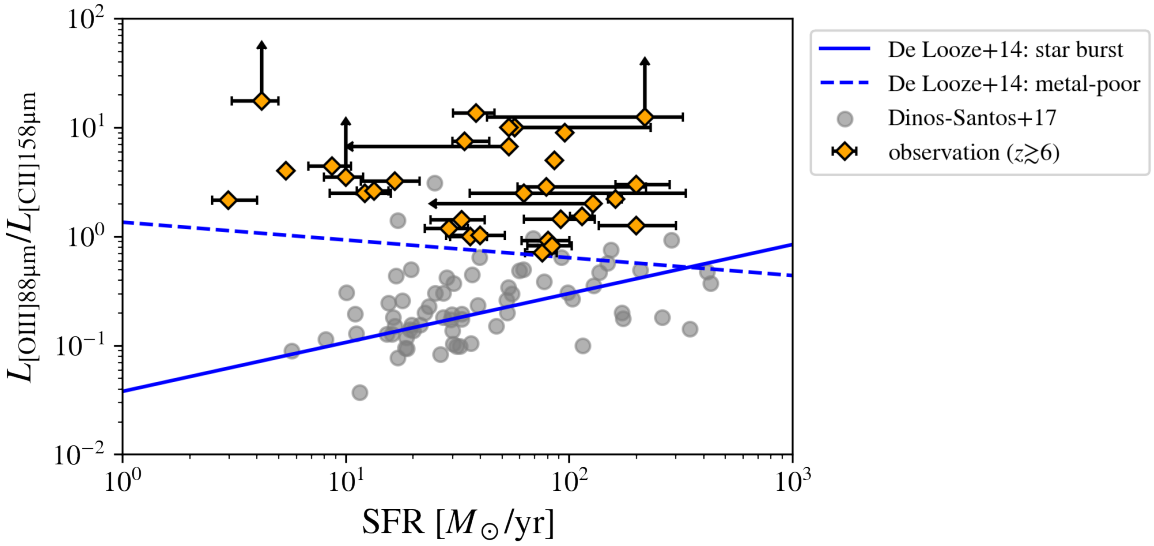

Figure 4.2: The [OIII] /[CII] luminosity ratio versus star formation rate. The orange plots with error bars are observations for $z \gtrsim 6$ galaxies(Hashimoto et al., 2019; Laporte et al., 2019; Tamura et al., 2019; Bakx et al., 2020; Hashimoto et al., 2018; Carniani et al., 2017; Maiolino et al., 2015; Harikane et al., 2020; Wong et al., 2022; Witstok et al., 2022; Algera et al., 2024; Schouws et al., 2024, 2025; Bakx et al., 2024; Fujimoto et al., 2024b). The $z \sim 0$ GOALS (U)LIRGs from Díaz-Santos et al. (2017) are shown as grey dots, and the local relations for starburst and dwarf galaxies from De Looze et al. (2014) are indicated by blue solid and dashed lines.

ionization potentials ([OIII] : 35.1 eV; [CII] : 11.2 eV). Observed high-redshift galaxies commonly exhibit high [OIII] /[CII] ratios ($\sim 3-20$), whereas local ($z \sim 0$) ULIRGs typically show much lower ratios ([OIII] /[CII] $\sim 0.04-1$), as illustrated in Figure 4.2. Although several cosmological simulations have attempted to reproduce and clarify the origin of the elevated [OIII] /[CII] ratios at high redshift, a definitive explanation remains elusive. This is because the ratio is influenced by multiple interrelated factors, including chemical abundances, ionization parameter, covering fractions, CMB attenuation, and observational biases.

In addition to FIR emission lines, ALMA provides essential insights into dust properties through continuum observations. Dust continuum emission has already been detected in certain galaxies at $z \gtrsim 6.5$ (e.g., Watson et al., 2015; Laporte et al., 2017; Bowler et al., 2018; Laporte et al., 2019; Witstok et al., 2022; Schouws et al., 2022; Inami et al., 2022). The Reionization Era Bright Emission Line Survey (REBELS; Bouwens et al., 2022b) has provided the first statistically significant perspective on dust and ISM characteristics in the UV-selected galaxies above $z \gtrsim 6.5$. Inami et al. (2022) reported dust detections in at least 40% of REBELS sources, suggesting dust is prevalent even among UV-bright, high-redshift galaxies. Indeed, at $z = 7$, a significant fraction ($\sim 30\%$) of cosmic star formation may be obscured by dust (see also Algera et al., 2023; Barrufet et al., 2023).

Dust plays a crucial role in obscuring star formation in high-redshift galaxies and significantly impacts cosmic reionization by absorbing ionizing photons (e.g., Hayes et al., 2011; Katz et al., 2017). Additionally, dust influences the chemical balance within galaxies, providing surfaces for H_2 formation, thereby enhancing star formation (Gould and Salpeter, 1963; Hirashita and Ferrara, 2002). However, the mechanisms that produce substantial amounts of dust within a few hundred million years after the Big Bang remain actively debated topics in theoretical and observational research (e.g., Vijayan et al., 2019; Sommovigo et al., 2020). At present, most dust detections at $z \gtrsim 7$ rely on single-wavelength continuum measurements, requiring uncertain

extrapolations of dust mass and IR luminosity from only a single data point (e.g., Bowler et al., 2018; Inami et al., 2022; Schouws et al., 2022; Witstok et al., 2022). While novel theoretical frameworks have been developed to infer dust properties (such as mass and temperature) from single-band continuum observations (e.g., Inoue et al., 2020; Sommovigo et al., 2021; Fudamoto et al., 2023), larger observational samples are essential for validating these approaches and assessing their reliability.

A key observational goal is therefore to constrain dust temperature $T_{\rm dust}$. Multi-band ALMA observations enable us to disentangle dust temperature and mass, since IR luminosity scales as $L_{\rm IR} \propto M_{\rm dust} T_{\rm dust}^{\beta+4}$, where $\beta \sim 1.5-2$ (see Eq. 3.112). Therefore, even small uncertainties in dust temperature translate into considerable variations in inferred dust mass and IR luminosity (Hodge and da Cunha, 2020; Bakx et al., 2021). Accurate measurements of dust temperature are essential for reliably assessing dust-obscured star formation and refining our understanding of dust enrichment mechanisms in the high-redshift Universe. Observationally, several groups have reported that dust temperatures may be higher at higher redshifts (e.g., Schreiber et al., 2018; Laporte et al., 2019; Bakx et al., 2020; Viero et al., 2022). Physically, such elevated temperatures may result from more compact galaxy morphologies (van der Wel et al., 2014; Fudamoto et al., 2022), leading to high star-formation rate surface densities (e.g., Schreiber et al., 2018). Additionally, galaxies with smaller dust reservoirs are exposed to more intense stellar radiation per dust grain, resulting in higher dust heating efficiencies (Sommovigo et al., 2022). However, multi-band ALMA observations at $z \gtrsim 6-7$ remain limited, frequently affected by non-detections, modest signal-to-noise ratios, or selection biases toward warmer and thus intrinsically brighter sources. Therefore, obtaining larger datasets of galaxies with well-constrained dust temperature measurements is crucial for a comprehensive understanding of dust-obscured star formation during the epoch of reionization.

In addition to probing ISM properties, ALMA enables detailed studies of gas dynamics due to its high velocity resolution ($\sim 10\,{\rm km\,s^{-1}}$). This resolution is significantly better than that of JWST/NIRSpec ($\Delta v \sim 111\,{\rm km\,s^{-1}}$) or MIRI(LRS)/NIRSpec(prism) ($\Delta v \sim 3000\,{\rm km\,s^{-1}}$). Typical galaxies observed at $z \gtrsim 6$ have circular velocities in the range of $100-200\,{\rm km\,s^{-1}}$, making ALMA particularly well-suited for investigating kinematic structures such as rotating disks and outflows.

Since [CII] emission primarily arises from neutral gas, which typically represents the dominant gas phase within galaxies, it is frequently used to trace gas motions. Galaxies at high redshift often experience frequent mergers and turbulent gas accretion (Conselice et al., 2008; Dekel et al., 2009b). Therefore, their gas dynamics are generally expected to be dispersion-dominated. However, several galaxies have been reported to host cold, rotating disks as revealed by [CII]-based velocity maps (e.g., Rizzo et al., 2020, 2021; Tsukui and Iguchi, 2021; Lelli et al., 2021; Parlanti et al., 2023; Roman-Oliveira et al., 2023; Neeleman et al., 2023; Fujimoto et al., 2024a). Furthermore, extended kinematic features indicative of galaxy interactions, such as bridges, have also been identified via [CII] observations in merging systems (e.g., Izumi et al., 2024; Zanella et al., 2024; Posses et al., 2024; Telikova et al., 2024). Outflowing gas components have similarly been probed through [CII] emission (e.g., Herrera-Camus et al., 2021; Ginolfi et al., 2020; Birkin et al., 2025), potentially driving extended [CII] halos as proposed by recent studies (Fujimoto et al., 2019; Ikeda et al., 2025; Solimano et al., 2024).

4.3 JWST Observations of Galaxies at $z > 6$

JWST has observed rest-frame optical emission lines at high-redshift galaxies for the first time. So far, JWST has spectroscopically identified over 1,300 galaxies at $z > 6$ (Adamo et al., 2024a; Roberts-Borsani et al., 2024), exceeding by more than a factor of 20 the sample confirmed before JWST launched (see Figure 2 of Adamo et al., 2024a).

Specifically, JWST discovers $z > 10$ galaxies for the first time, and currently, around 30

galaxies are confirmed at $z > 10$. Such discoveries allow us to investigate the UV luminosity function beyond $z \gtrsim 10$, revealing unexpectedly luminous galaxies compared to previous theoretical predictions (e.g., Finkelstein et al., 2022; Bouwens et al., 2022a). Several new scenarios have thus been proposed to explain these bright UVLFs such as (i) increasing star formation efficiencies (SFE) (e.g., Dekel et al., 2023; Li et al., 2024; Ceverino et al., 2024; Inayoshi et al., 2022), (ii) stochastic bursty star formation (e.g., Pallottini and Ferrara, 2023a; Shen et al., 2023; Mason et al., 2023; Sun et al., 2023; Gelli et al., 2024; Sugimura et al., 2024), (iii) increasing the light-to-mass ratio (L/M_*) via a top-heavy IMF (e.g., Haslbauer et al., 2022; Trinca et al., 2024; Cueto et al., 2024; Hutter et al., 2025; Yung et al., 2024; Jeong et al., 2025; Lu et al., 2025; Mauerhofer et al., 2025), and (iv) dusty outflow(e.g., Ferrara et al., 2023; Ferrara, 2024; Ferrara et al., 2025; Fiore et al., 2023; Ziparo et al., 2023; Nakazato and Ferrara, 2024). Even modified ΛCDM models can explain the observed UVLF such as *blue* power-spectrum at small-scale (Hirano and Yoshida, 2024) via primordial BH (Liu and Bromm, 2022; Huang et al., 2024; Zhang et al., 2024), or primordial magnetic fields (Parashari and Laha, 2023; Ralegankar et al., 2024).

JWST observations not only enable the spectroscopic identification of galaxies at high redshift but also provide essential constraints on the physical properties of their ISM through diagnostic emission-line ratios. For example, the ratios among rest-frame optical emission lines such as [OIII] 5007Å, 4959Å, and Hβ enable the estimation of gas-phase oxygen abundances (i.e., metallicities; Nakajima et al. 2023; Curti et al. 2023). In particular, galaxies exhibiting auroral lines like [OIII] 4363Å allow direct measurements of electron temperatures (Morishita et al., 2024). Using these lines, the mass–metallicity relation has recently been constrained at $z = 4 - 10$ for the first time (Morishita et al., 2024; Laseter et al., 2024).

JWST has also detected rest-frame UV emission lines and reported non-solar abundance patterns in high-redshift galaxies. Ratios among emission lines such as CIII]1907,1909Å, OIII]1666Å, and NIV]1483, 1486Å suggest unusual C/O and N/O abundance ratios compared to those observed in local galaxies (Cameron et al., 2023; D'Eugenio et al., 2024; Topping et al., 2024b). Recently, some high-redshift galaxies have been identified as "N-emitters", showing super-solar N/O abundances based on highly-ionized UV emission lines (e.g., NIV]; Isobe et al. 2023b).

By measuring emission line ratios of different ionization stages of oxygen, JWST enables the construction of the O32-R23 diagram, where O32 $\equiv$ [OIII] 5007Å/[OII] 3727, 3729Å and $R23 \equiv$ ([OIII] 4959, 5007Å + [OII] 3727, 3729Å)/Hβ. It is well established that O32 mainly traces the ionization parameter, whereas R23 is strongly correlated with metallicity (e.g., Nakajima and Ouchi, 2014). JWST has extended this diagnostic to EoR galaxies, providing deeper insights into ISM conditions within HII regions at cosmic dawn.

Furthermore, JWST enables the estimation of electron densities via ratios of collisionally excited emission lines arising from the same ion but with closely spaced excitation energies, such as [OII] 3729/3727Å, [SII] 6733/6718Å, CIII]1909/CIII]1907, and NIV]1483/NIV]1486. Electron densities measured from these ratios at high redshift are found to range from 500 to $10^4, \mathrm{cm}^{-3}$ (e.g., Isobe et al., 2023a; Topping et al., 2025; Harikane et al., 2025b; Scholtz et al., 2024; Marconcini et al., 2024), over an order of magnitude higher than typical local galaxy values derived from [OII] and [SII] lines (Kashino et al., 2017; Mingozzi et al., 2022; Davies et al., 2021; Sanders et al., 2016).

In addition to its unprecedented sensitivity, JWST offers remarkable spatial resolution, providing new insights into the internal structures of high-redshift galaxies. Typical spatial resolutions are $\sim$ 1" for ground-based telescopes (e.g., Keck in seeing-limited mode), $\sim$ 0.2" for HST, and $\sim$ 0.07" for JWST. Such capabilities have revealed that some $z > 6$ galaxies consist of multiple sub-components previously unresolved in pre-JWST observations (e.g., Harikane et al., 2025b; Hainline et al., 2024a; Chen et al., 2023). Furthermore, combining JWST' s high spatial resolution with gravitational lensing magnification, stellar clusters with masses of $M_* = 10^{6-7} M_\odot$ have been resolved down to parsec scales at $z = 6 - 10$ (e.g., Adamo et al., 2024b; Mowla et al., 2024; Vanzella et al., 2023a). Such observations suggest these clusters could

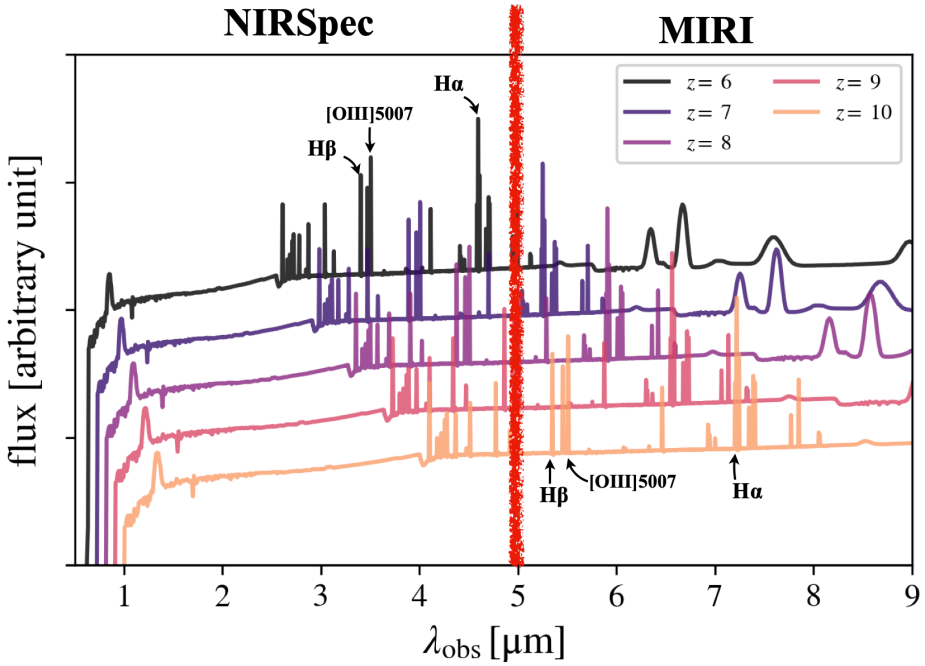

Figure 4.3: SED models for galaxies at $z = 6, 7, 8, 9$, and 10, generated using the FSPS stellar population synthesis code (Conroy et al., 2009; Conroy and Gunn, 2010). The strong emission lines labeled are Hβ, [OIII] 5007Å, and Hα. The thick red line marks the 5 μm boundary between the NIRSpec (0.6-5 μm) and MIRI (5-28 μm) coverage.

be potential proto-globular clusters, providing fundamental clues to characterize clustered star formation in the early Universe, including their cluster mass functions, formation efficiencies, and survival rates.

4.4 Synergetic Insights from JWST and ALMA

Combining JWST and ALMA observations provides comprehensive constraints on both the physical conditions and the kinematics of the multi-phase ISM in high-redshift galaxies. Physical conditions can be investigated through emission-line ratios spanning from optical to FIR wavelengths, while gas kinematics are probed via ALMA moment-1 maps and integral field unit (IFU) spectroscopy from JWST. Figure 4.4 illustrates the panchromatic spectral energy distribution (SED) of a typical star-forming galaxy at $z = 7$. JWST probes emission lines from the rest-frame UV to optical, whereas ALMA detects FIR emission lines and dust continuum emission from large grains at rest wavelengths of $\lambda_{\rm rest} \gtrsim 40\,\mu$m. The planned space mission PRIMA (the PRobe far-Infrared Mission for Astrophysics; Moullet et al., 2023) will further extend observations to mid-infrared wavelengths, detecting emission from Polycyclic Aromatic Hydrocarbons (PAHs), continuum emission from small dust grains, and mid-IR fine-structure lines such as [NeII]13 μm and [NeIII]16 μm .

Taking ratios of rest-frame optical emission lines observed with JWST to rest-frame FIR emission lines detected by ALMA enables investigations into ISM conditions that JWST alone cannot probe. For instance, by combining electron temperatures measured from the [OIII] 4363Å line with the [OIII] 88/[OIII] 5007 line ratio, electron densities in the FIR-emitting gas ($n_{\rm e,FIR}$) can be estimated (Harshan et al., 2024; Fujimoto et al., 2024b). Recently, Harikane et al. (2025b) reported that these $n_{\rm e,FIR}$ values are systematically lower than electron densities derived from rest-frame UV and optical emission lines, suggesting the existence of a multi-phase ionized gas structure. Furthermore, they noted that assuming a single-phase ionized gas model based solely on electron temperatures from the [OIII] 4363Å line could lead to underestimating gas-phase

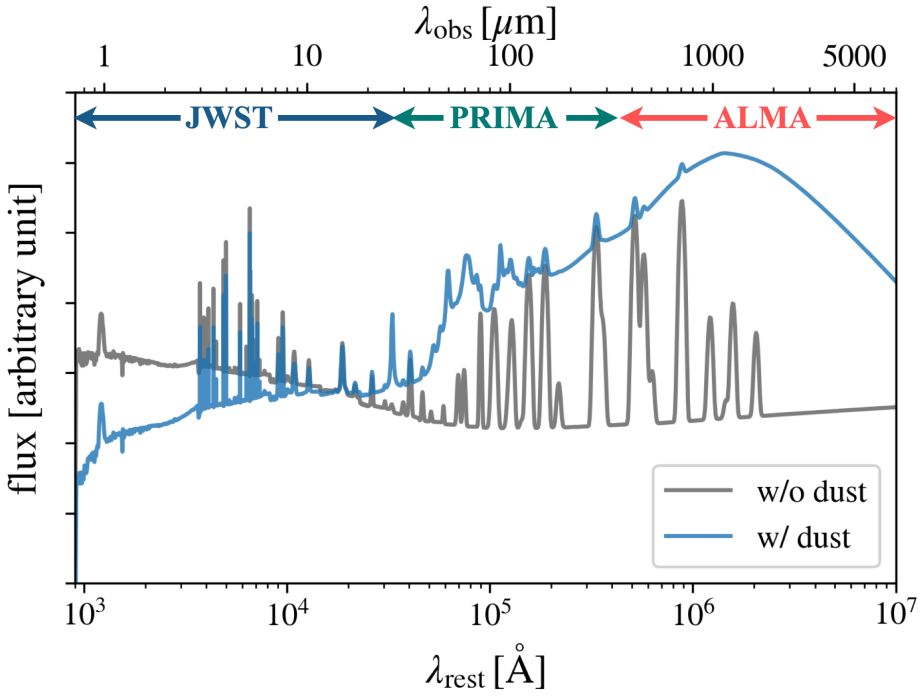

Figure 4.4: Mock SEDs of star-forming galaxies at $z = 7$, generated using the FSPS stellar population synthesis code (Conroy et al., 2009; Conroy and Gunn, 2010). The blue (gray) lines indicate the SEDs with (without) dust attenuation. The observational wavelength coverage of JWST, PRIMA, and ALMA is indicated by arrows at the top of the figure.

metallicities by up to 0.8 dex.

From a theoretical perspective, line-ratio diagrams utilizing synergies between JWST and ALMA have also been explored (Nakazato et al., 2023). Figure 4.5 shows line-ratio diagrams combining rest-frame optical and FIR [OIII] emission lines. These diagrams are sensitive to gas-phase metallicity and electron density ($n_{\rm e,FIR}$). The upper panel specifically targets galaxies for which [OIII] 52 μm emission has been detected, whereas the lower panel can be broadly applied to galaxies at $z = 6 - 12$.

Moreover, panchromatic SEDs obtained by combining JWST and ALMA data significantly improve the accuracy of the derived galaxy properties through a comprehensive SED fitting (e.g., Sugahara et al., 2025). As discussed in Section 4.2, [CII] , OI, and CO emissions are also available by ALMA. Combining these emissions and JWST-detected emissions, we can understand multi-phase ISM from HII regions, photodissociation regions, and molecular clouds, and kinematics in each phase (Fujimoto et al., 2024b; Fudamoto et al., 2025).

4.5 Remaining Open Questions and Challenges

So far, there are several scientific cases for high-redshift galaxies. Among them, this thesis focuses on the interstellar medium (ISM) properties of galaxies at $z \geq 6$. In particular, I will address the following topics throughout the thesis: (i) Formation and evolution of clumpy structures (**kinematics, morphologies**), (ii) Nature of dust formation and evolution at high redshift (**dust physics**), and (iii) The origin of high [OIII] /[CII] ratios (**multi-phase ISM properties**).

In light of the observational trends described above, this thesis employs cosmological zoom-in simulations coupled with detailed emission-line modeling of multi-phase gas and dust. Zoom-in simulations enable us to spatially resolve the internal structures of high-redshift galaxies and

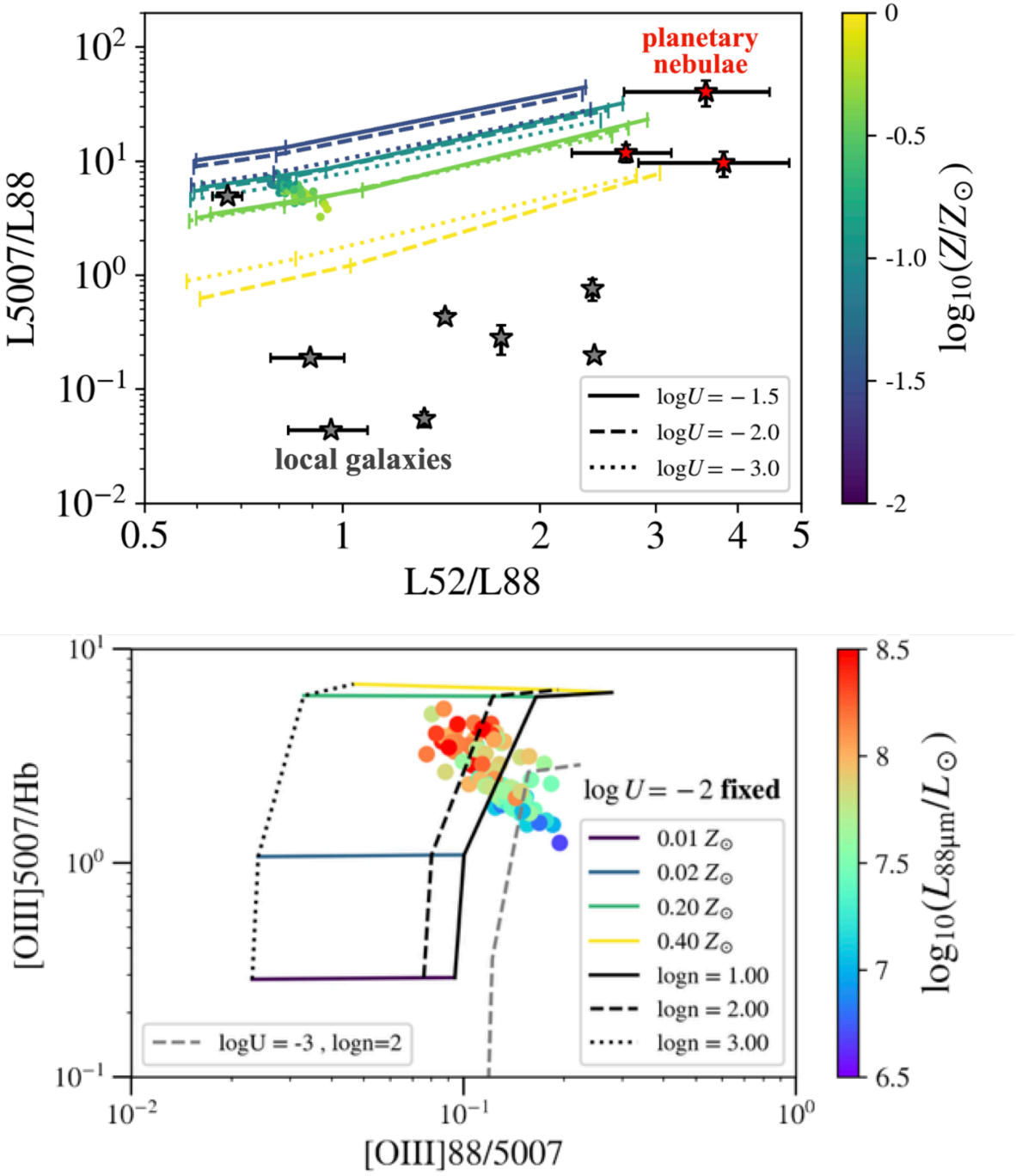

Figure 4.5: Top: The line luminosity ratio [OIII] 5007Å/[OIII] 88μm versus [OIII] 52μm /[OIII] 88μm . Solid circles represent simulated galaxies from the FirstLight simulations at $z = 7$, with colors indicating gas metallicity. Gray star symbols denote local galaxies from Moustakas and Kennicutt (2006) and Brauher et al. (2008), while red star symbols represent local planetary nebulae from Dinerstein et al. (1985). The CLOUDY model results are shown as lines color-coded by metallicity ($\log(Z/Z_\odot) = -1.30, -0.70, -0.40, 0.0$). Solid, dashed, and dotted lines correspond to ionization parameters of $\log U = -1.5, -2, -3$, respectively. The tick marks on each CLOUDY model line represent the gas densities of the HII region of $\log n_{\rm HII}, [{\rm cm}^{-3}] = 1, 2, 3$ from left to right. Bottom: An example demonstrating the diagnostic capability of line-ratio diagrams based on CLOUDY calculations. Degeneracies with parameters such as electron temperature or ionizing radiation strength can be resolved by fully modeling all available emission lines (including several oxygen transitions and auroral lines in some cases) and by performing spectrophotometric SED-fitting techniques. For comparison, galaxies at $z \sim 10$ from the FirstLight simulations are plotted, color-coded by their [OIII] 88μm line luminosity. The top panel is adapted from Nakazato et al. (2023).

investigate their detailed ISM properties (see Chapter 5). By comparing simulation results with recent JWST and ALMA observations, we aim to elucidate the physical origins of the observed emission-line ratios, dust content, and morphological characteristics of galaxies before and during the Epoch of Reionization.

A significant advantage of simulations is their ability to track the formation and evolution of galaxies over cosmic time, whereas observations typically capture galaxies at a single evolutionary snapshot. Tracking time evolution allows us to better understand star formation histories and the feedback processes that shape observed galaxy properties. Furthermore, simulations provide fully three-dimensional spatial distributions (x, y, z-coordinates), whereas observational data are limited to two spatial dimensions (x, y) along with one-dimensional wavelength information. This detailed spatial information enables simulations to clearly distinguish between different morphological features such as disks and mergers. Observationally limited spatial resolution at high redshifts sometimes misinterprets velocity gradients arising from mergers as signatures of rotating disks (e.g., Rizzo et al., 2022), leading to potential misunderstandings about the redshift evolution of galaxy disk structures.

Moreover, simulations can resolve internal structures within galaxies that remain inaccessible to current observations[3]. Accurately interpreting the emission properties of observed galaxies requires resolving distributions of key physical parameters, including gas density, temperature, metallicity, stellar mass surface density, mass-weighted stellar age, and radiation fields. To facilitate direct comparisons between multi-wavelength observational results and simulations, it is essential to develop robust emission-line and dust attenuation/re-emission models based on the simulated data. This approach allows us to pinpoint the physical origins of observed morphologies and ISM properties of high-redshift galaxies, ultimately accelerating our understanding of galaxy formation processes and the sources and mechanisms driving cosmic reionization.

The results of this study are expected to significantly enhance our comprehensive understanding of the dynamical and chemical properties of high-redshift galaxies, thereby providing valuable insights into the history of structure formation, star formation in the early Universe.

[3]Recent JWST observations with gravitational lensing reveal pc-scale stellar clusters (e.g., Adamo et al., 2024b).

Chapter 5

Galaxy Formation Simulation

In order to interpret the latest high-redshift observational results introduced in Chapter 4, there are several theoretical approaches: analytical calculations, semi-analytical models, and numerical simulations.

The first approach involves describing galaxy formation using theoretical models and approximate formulations. For example, halo formation can be described using Press-Schechter theory and spherical collapse models; star formation is modeled via cooling criteria and the Kennicutt-Schmidt relation; and feedback processes are treated using simplified models such as the Eddington limit. This approach helps us understand which physical processes are dominant in galaxy formation, and the computational cost is very low.

The second approach uses halo merger trees derived from N-body simulations or Press-Schechter theory, and models galaxy evolution through simplified analytic recipes. These include gas accretion, star formation, supernova and AGN feedback, metal enrichment, and dust evolution. This method is called the semi-analytical approach. Its primary advantage is computational efficiency compared to full N-body + hydrodynamical simulations. This enables the generation of galaxy samples that are orders of magnitude larger than those produced by cosmological simulations and allows rapid exploration of parameter and model space (e.g., adding new physics and assessing their impacts). Major disadvantages are that they lack morphological and spatial information of galaxies, and rely on simplified models.

The third approach, full numerical simulations (N-body + hydro), is the most physically realistic, as it directly solves the coupled equations governing dark matter, gas dynamics, cooling, star formation, and feedback processes. However, it is computationally expensive and often difficult to re-run with varying parameters.

In what follows, we review galaxy formation simulations.

5.1 Galaxy Formation Simulations

There are two types of galaxy formation simulations: cosmological simulations and isolated simulations. Both simulations solve the dynamics of dark matter and gas by integrating the following five basic equations:

$$\boxed{\text{Poisson eq.}} \quad \nabla^2\Phi = 4\pi G\rho_{\rm tot} \tag{5.1}$$

$$\boxed{\text{Continuity eq.}} \quad \frac{\partial\rho_{\rm gas}}{\partial t} + \nabla\cdot(\rho_{\rm gas}\boldsymbol{v}) = \mathcal{S}_{\rho_{\rm gas}} \tag{5.2}$$

$$\boxed{\text{Euler eq.}} \quad \frac{\partial\boldsymbol{v}}{\partial t} + (\boldsymbol{v}\cdot\nabla)\boldsymbol{v} = -\frac{\nabla P_{\rm tot}}{\rho_{\rm gas}} - \nabla\Phi + \mathcal{S}_{\boldsymbol{v}} \tag{5.3}$$

$$\boxed{\text{Energy eq.}} \quad \frac{\partial E}{\partial t} + \nabla\cdot[(E + P_{\rm thermal})\boldsymbol{v}] = -\rho_{\rm gas}\boldsymbol{v}\cdot\nabla\Phi + (\Gamma - \Lambda) + \mathcal{S}_E \tag{5.4}$$

$$\boxed{\text{Equation of State}} \quad P_{\rm thermal} = (\gamma - 1)\rho_{\rm gas}\varepsilon \quad (E = \rho_{\rm gas}(\varepsilon + \boldsymbol{v}^2)), \tag{5.5}$$

where $\rho_{\rm gas}$, $\boldsymbol{v}$, and P denote the gas mass density, gas velocity, and gas pressure, respectively. The total gas energy density is given by $E = \rho_{\rm gas}(\epsilon + \boldsymbol{v}^2)$, where ϵ is the internal energy per unit mass of the gas. The total mass density is expressed as $\rho_{\rm tot}$, including contributions from gas, stars, and dark matter. The adiabatic index is denoted by γ. Here Γ and Λ represent the heating rate from stellar winds and supernova feedback, and the cooling rate due to metal-line radiation, respectively, as explained in Section 2.3. The terms $\mathcal{S}_{\rho_{\rm gas}}$, $\mathcal{S}_{\boldsymbol{v}}$, and $\mathcal{S}_E$ are source and sink terms determined by star formation and stellar mass loss processes.

In addition to the hydrodynamical equations, the advection of metals produced in stars and released into the gas via supernovae, stellar winds, and evolved stars is solved self-consistently:

$$\frac{\partial \rho_{Z_i}}{\partial t} + \nabla \cdot (\rho_{Z_i} \boldsymbol{v}) = \mathcal{S}_{Z_i,\rm FD} + \mathcal{S}_{Z_i,\rm ML} + \mathcal{S}_{Z_i,\rm SF}, \tag{5.6}$$

where FD, ML, and SF stand for feedback, mass loss, and star formation, respectively. Z_i represents two types of metals originating from Type II and Type Ia supernovae ($i = \rm SNII, SNIa$), and ρ_{Z_i} is the mass density of the ejected metals.

The main sub-grid physics considered in these simulations include star formation, feedback from stellar winds, supernovae, and AGN, metal enrichment, and the UV background. The detailed implementations vary between simulations. The specific models adopted in the FirstLight and RAMSES-RT simulations are described in Chapters 6 and 8, respectively.

In general, there are two types of galaxy formation simulations: isolated simulations and cosmological simulations. In isolated simulations, the mass and density profiles of galaxy components—such as the dark matter halo, gas, disk, and bulge—are manually specified as initial conditions, and the subsequent evolution is followed. The computational cost is relatively low compared to cosmological simulations. Therefore, isolated simulations are advantageous for testing various sub-grid physics, such as feedback models (e.g., Hopkins et al., 2011; Agertz et al., 2013; Rosdahl et al., 2015), or for comparing different simulation codes, as in the AGORA project (Kim et al., 2014).

They are also useful for studying specific dynamical processes with high spatial resolution, such as galaxy mergers, by explicitly setting the initial positions, velocities, and spin orientations of two galaxies (e.g., Renaud et al., 2013, 2015; Fensch et al., 2017; Maji et al., 2017). In the following, we focus on cosmological simulations.

5.1.1 Cosmological Simulations

Cosmological simulations follow galaxy formation by setting cosmological parameters as initial conditions. First, we specify the cosmological parameters and compute the linear growth of density fluctuations to obtain the density power spectrum $P(\boldsymbol{k}, z)$ at an initial redshift $z = z_{\rm init}$. Based on the obtained power spectrum, a random Gaussian field is generated in Fourier space[1].

By applying an inverse Fourier transform, we obtain the initial density field in real space. From this, we compute the displacement vector and determine the initial positions $\boldsymbol{x}$ using the Zel'dovich approximation[2]:

$$\boldsymbol{x} = \boldsymbol{q} + D_+(z)\boldsymbol{\Phi}, \tag{5.9}$$

where $\boldsymbol{q}$ is the Lagrangian coordinate and D_+ is the linear growth factor. The initial velocity is then given by $\boldsymbol{v} = a\dot{D}_+\boldsymbol{\Phi}$, where a is the scale factor. Figure 5.1 illustrates the initial condition generation for cosmological simulations.

[1]The initial overdensity field satisfies the following relations:

$$\langle \delta(\boldsymbol{x}) \rangle = 0 \tag{5.7}$$

$$\langle \delta(\boldsymbol{k}) \delta^*(\boldsymbol{k'}) \rangle = P(\boldsymbol{k}) \delta^{\rm D}(\boldsymbol{k} - \boldsymbol{k'}), \tag{5.8}$$

where $\delta^{\rm D}$ is the Dirac delta function.

[2]Simulations typically consider second-order perturbation theory (2LPT).

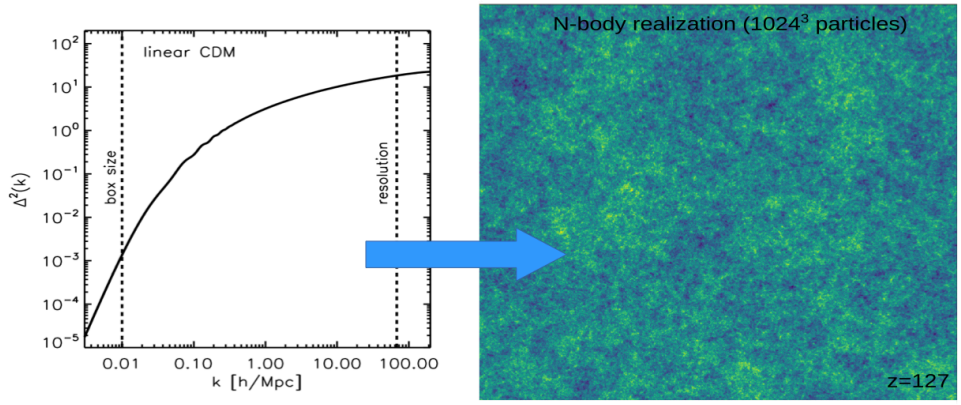

Figure 5.1: Illustration of the initial conditions for an N-body simulation. The left panel shows the dimensionless linear power spectrum for cold dark matter. The vertical dashed lines indicate the modes corresponding to the simulation's box size and resolution scale. The right panel shows the dark matter density field at $z = 127$, generated based on the power spectrum shown in the left panel. The initial conditions for gas are also produced in the same way. The side length of the simulated region is 40 cMpc/h. This figure is adapted from Zavala and Frenk (2019).

After preparing the initial density and velocity fields at $z = z_{\rm init}$, the simulation evolves them self-consistently under gravity and hydrodynamics based on the above five basic equations (5.2) - (5.5).

There are mainly two types of cosmological simulations: full-box (non-zoom-in) and zoom-in simulations. In full-box simulations, we follow the evolution of all galaxies within the simulation volume. This allows us to study the large-scale galaxy distribution, which is useful for line-intensity mapping and statistical analyses such as scaling relations and luminosity functions. However, full-box simulations typically have limited spatial resolution ($\Delta x_{\rm min} \sim 200\,{\rm pc}$, see Table 5.1), making it difficult to resolve low-mass galaxies or the internal structures of galaxies.

In contrast, zoom-in simulations focus on individual galaxies at higher resolution. We first run a low-resolution dark matter-only simulation from $z = z_{\rm init}$ to $z = z_{\rm end}$, identify specific(massive) halos, and determine their Lagrangian regions, which are the initial positions of the particles that form each target halo. We then regenerate the initial conditions for dark matter and gas with higher resolution in these regions, while the surrounding regions are simulated at lower resolution. For each of the selected target halos, a hydrodynamical + N-body simulation is carried out individually. The concept of zoom-in simulations is illustrated in Figure 5.2.

With their high spatial (and temporal) resolution, zoom-in simulations allow us to follow detailed galaxy formation processes and internal structures. This makes it easier to directly compare simulated galaxies with individual observed galaxies. However, their main disadvantage is that statistical analyses are limited, as only a small number of selected progenitors are followed. Moreover, zoom-in simulations do not allow the study of large-scale spatial distributions of galaxies.

Table 5.1 summarizes the properties of recent cosmological simulations targeting $z > 6$ galaxies. Figure 5.3 shows the relation between simulation box size and dark matter particle mass for each simulation listed in Table 5.1. Simulations that appear in the upper-right region of the plot correspond to rare, massive objects resolved with high resolution. Depending on the specific science goal for high-redshift galaxies, it is important to choose appropriate simulations.

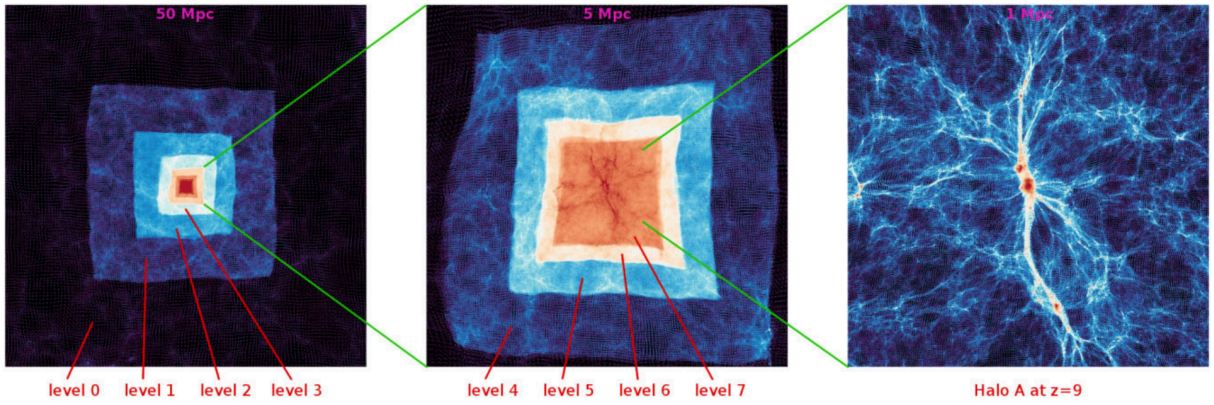

Figure 5.2: Illustration of the zoom-in technique. Some zoom-in simulations employ multiple resolution layers. From left to right, the side lengths of the projected regions are 50 Mpc, 5 Mpc, and 1 Mpc, respectively. This figure is adapted from Ricotti et al. (2022).

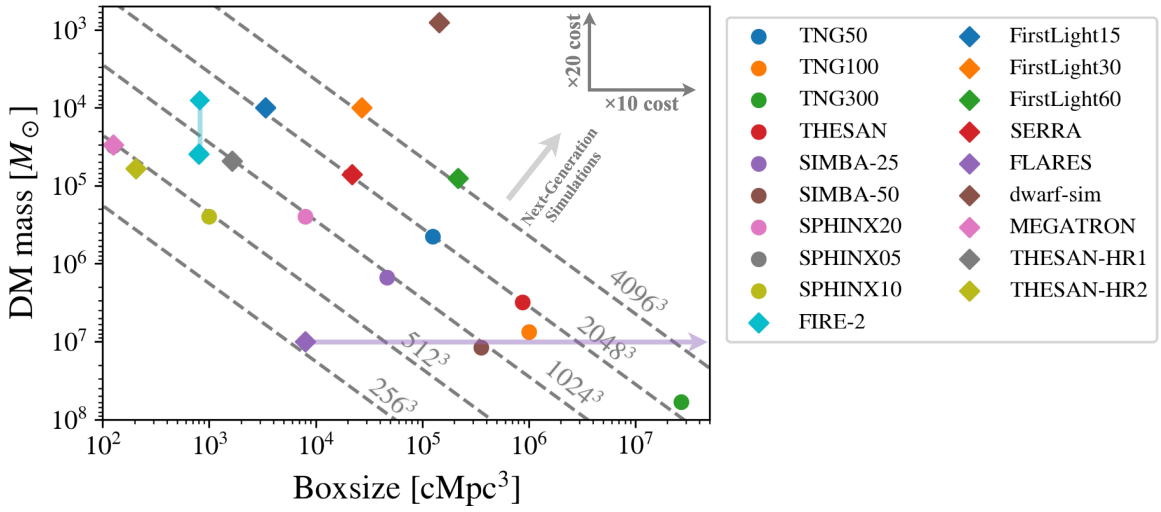

Figure 5.3: Comparison with recent cosmological simulations. Circles and diamonds represent non zoom-in and zoom-in simulations, respectively. The x-axis shows the simulation boxsize, and the y-axis shows the dark matter particle mass. To achieve a simulation with ten times larger box size at the same resolution, approximately ten times more computational cost is required. Similarly, achieving ten times higher mass resolution at fixed box size demands about twenty times more computational cost because both the number of particles and the number of time steps increase. Moving toward the upper right corner represents the frontier of next-generation high-resolution cosmological volume simulations, which is an extraordinarily demanding computational challenge.

Table 5.1: Summary of recent cosmological simulations focusing on high-redshift galaxies listed in Table 5.1. The fifth column indicates whether each simulation includes on-the-fly radiative transfer. A direct comparison of spatial resolution is difficult, as these simulations employ a variety of numerical methods, such as SPH (Smoothed Particle Hydrodynamics), moving mesh, AMR (Adaptive Mesh Refinement), and MFM (Meshless Finite Mass). Instead, we compare the dark matter particle mass listed in the third column. The fifth column "RT" indicates whether the simulations incorporate on-the-fly radiative transfer (RT).

Name	Box size [cMpc]	DM mass [$M_\odot$]	# samples	RT	Reference
Non-zoom-in simulations					
Illustris TNG	50, 100, 300	4.5×10^5, 7.5×10^6, 5.9×10^7	2×10^3, 10^4, 4×10^5 ($M_* \gtrsim 10^9\ M_\odot$ at $z = 0$)	×	Pillepich et al. (2019)
THESAN	95.5	3.1×10^6	$\sim 10^3$ ($M_* \gtrsim 10^9\ M_\odot$ at $z = 6$)	◯	Shen et al. (2024)
SIMBA	36, 71	1.5×10^6, 1.2×10^7	—	×	Wu et al. (2020)
SPHINX20	20	2.5×10^5	276 (SFR $\gtrsim 0.3\ M_\odot$/yr)	◯	Katz et al. (2023b); Rosdahl et al. (2022)
SPHINX	5, 10	3.1×10^4, 2.5×10^5	~ 500, 3000 ($M_\mathrm{h} \gtrsim 10^8\ M_\odot$ at $z = 6$)	◯	Rosdahl et al. (2018)
Zoom-in simulations					
FIRE-2	—	650–3.9×10^4	23	×	Ma et al. (2018b, 2019, 2020)
FirstLight	15, 30, 60	1×10^4, 1×10^4, 8×10^4	632	×	Ceverino et al. (2017)
SERRA	28	7.2×10^4	209	◯	Pallottini et al. (2022)
FLARES	20 (overdense, 3 cGpc)	1.0×10^7	$\sim 2 \times 10^3$ ($M_* \gtrsim 10^9\ M_\odot$ at $z = 6$)	×	Lovell et al. (2021b)
Dwarf galaxy sim	52.5	800	1	◯	Sugimura et al. (2024)
MEGATRON	5	3.0×10^4	1	◯	Katz et al. (2024)
THESAN-HR	11.8, 5.9	4.8×10^5, 6.0×10^4	14	◯	Kannan et al. (2025); Shen et al. (2024)

5.2 Baryonic Physics

To model the galaxy population, the hydrodynamical equations need to be augmented by a variety of astrophysical processes, such as gas cooling, star formation, stellar feedback, AGN feedback, magnetic fields, cosmic rays, dust physics, and so on. Most of these processes are implemented through effective, so-called subresolution models, which are necessary due to the limited numerical resolution of simulations. Here, we review two of the most important physical processes: star formation and stellar feedback.

5.2.1 Star Formation Recipe

In cosmological galaxy formation simulations, the parameters defining the onset of star formation (the temperature and density thresholds) and the star formation efficiency per free-fall time ($\epsilon_{\rm ff}$) play a crucial role. In large-volume simulations, the limited spatial resolution motivates relatively low density thresholds of $n_{\rm H} \sim 0.1$–$1\,{\rm cm}^{-3}$ and efficiencies of $\epsilon_{\rm ff} \sim 0.01$–$1$ per free-fall time (e.g., Springel and Hernquist, 2003; Schaye and Dalla Vecchia, 2008), which have been shown to reproduce the observed Kennicutt–Schmidt relation (Kennicutt, 1998a). Some zoom-in simulations with much higher resolution often adopt higher thresholds, $n_{\rm H} \gtrsim 10$–$10^2\,{\rm cm}^{-3}$ (e.g., Pallottini et al., 2022; Katz et al., 2024). Regarding the local star formation efficiency $\epsilon_{\rm ff}$, some simulations adopt more physically motivated values based on molecular gas fractions (e.g., FIRE-2; Hopkins et al., 2018; Gnedin and Kravtsov, 2011). Moreover, the latest high-resolution simulations, adopting results from cloud–scale studies, often use much higher thresholds ($n_{\rm H} \gtrsim 10^4\,{\rm cm}^{-3}$) and variable $\epsilon_{\rm ff}$ as a function of cloud metallicity, mass, and gas density (e.g., He et al., 2019; Garcia et al., 2023; Sugimura et al., 2024). The stellar component is created by converting gas into collisionless particles with stochastic probabilities at each timestep.

5.2.2 Stellar Feedback Models

Stellar feedback is an essential component of galaxy formation models, regulating the conversion of gas into stars, shaping the interstellar medium (ISM), and driving galactic-scale outflows. In cosmological simulations, feedback is implemented through subgrid prescriptions that capture the unresolved energy, momentum, and metal injection from stars into the surrounding gas.

The primary channels of stellar feedback are as follows:

1. **Supernova (SN) feedback**: Both Type II and Type Ia SNe inject thermal energy, momentum, and heavy elements into the ISM. Implementations include thermal energy deposition (e.g., Okamoto et al., 2010), momentum injection (e.g., Oppenheimer and Davé, 2006), and delayed cooling schemes to overcome numerical overcooling, as pointed out by White and Frenk (1991) and Navarro and Benz (1991). Implementation styles vary. Some models deposit energy and momentum directly into neighboring gas cells or particles (thermal or momentum mode), while others temporarily decouple wind particles from hydrodynamics to mimic unresolved breakout from dense regions (e.g., Pillepich et al., 2018). Momentum-boosting factors are sometimes applied to capture the terminal momentum of SN remnants unresolved at the simulation resolution.

2. **Radiative feedback**: Young, massive stars emit copious ionizing and non-ionizing radiation. Feedback channels include:

   - Photoionization heating, which raises gas temperatures to $\sim 10^4\,{\rm K}$.
   - Photoelectric heating on dust grains, important in neutral regions.
   - Direct radiation pressure from UV/optical photons.
   - Infrared (IR) multiple scattering, potentially boosting momentum injection in dusty, high-density environments.

3. **Stellar winds**: OB star winds and asymptotic giant branch (AGB) winds contribute to early gas removal and enrichment before the onset of SNe. These winds are often implemented as continuous mass and energy injection tied to stellar evolution tracks.

The parameters of stellar feedback models can either be chosen based on physical arguments or require a calibration procedure. The former approach is often used in zoom-in simulations; for instance, SN energy values, event frequencies, and stellar wind energies are derived from an assumed IMF and stellar SEDs. The latter approach is common in large-volume simulations (e.g., IllustrisTNG, EAGLE), where subresolution models are less detailed compared with those of zoom-in simulations. Calibration typically involves exploring the parameter space of the effective models through a large number of smaller-volume simulations. The resulting parameters are selected by comparing the simulated galaxy population with key observables, such as the star formation rate density (SFRD) as a function of cosmic time, the galaxy stellar mass function(SMF) at $z = 0$, and the present-day stellar-to-halo mass relation (e.g., Vogelsberger et al., 2014).

5.3 Recent Theoretical Interpretations with JWST/ALMA Observations

As discussed in Chapter 4, observations with JWST and ALMA have dramatically advanced our understanding of galaxy formation at $z \gtrsim 6$, providing statistical samples as well as spatially resolved views of individual galaxies. In this section, I review recent simulation-based works that aim to explain and reproduce these high-redshift observations.

5.3.1 Statistical Properties of Galaxy Populations

Recent cosmological simulations have made it possible to statistically investigate various galaxy properties at high redshift, such as the ultraviolet and infrared luminosity functions (UVLF, IRLF), the mass–metallicity relation (MZR), the size–mass relation, dust statistics, and galaxy kinematics. While some studies utilize large non-zoom-in cosmological simulations that follows all galaxies within the box, zoom-in simulations with sufficient sample sizes (e.g., more than 100 halos) can also provide statistically meaningful results. Moreover, recent techniques enable the estimation of number densities from zoom-in simulations by applying volume corrections or combining simulations with different zoom-in regions and box sizes. Table 5.2 summarizes recent simulation-based statistical studies for each key observable.

The UVLF, especially at $z \simeq 9$–15, has received particular attention due to JWST's discovery of UV-luminous galaxies in this epoch. To interpret these findings, large-volume simulations are essential, along with appropriate treatment of dust attenuation, which can significantly alter the observed UV fluxes.

The advent of NIRCam slitless spectroscopy has enabled the detection of rest-frame optical emission-line galaxies at specific redshifts, leading to observational constraints on the luminosity functions of lines such as Hα and [OIII] 5007 Å. Hα is a direct tracer of recent star formation ($\lesssim$ 10 Myr, Kennicutt, 1998b), so its luminosity function can inform the distribution of star formation rates (SFRs) across the galaxy population and constrain the cosmic SFR density. [OIII] 5007 Å, which traces high-ionization regions around young massive stars, is often stronger than Hα in low-metallicity, high-redshift galaxies, offering complementary insights into their star-forming conditions.

Metallicity constraints at $z > 6$ have become possible only recently thanks to JWST, based on emission-line diagnostics using rest-frame optical lines. These include both the T_e-based direct method and the strong-line method (see Section 3.3.3). Comparisons between simulations and observations can reveal the metal enrichment history of early galaxies and provide constraints on the implemented feedback and chemical evolution models.

The size–mass relation provides a probe of galaxy structural evolution, offering insights into whether galaxy growth proceeds inside-out or outside-in, the role of stellar and AGN feedback, and the epoch at which galaxies transition from compact to extended morphologies.

Dust-related statistics, including dust attenuation corrections for UV continuum and line emission and the infrared luminosity function, are crucial for interpreting observed spectral energy distributions (SEDs). Some simulations track dust mass on the fly and investigate the redshift evolution of dust-to-gas and dust-to-metal ratios. However, many cosmological simulations instead assume a fixed dust distribution and dust-to-metal mass ratio, and calculate dust properties based on these assumptions. In particular, recent theoretical studies have focused on dust temperature, infrared luminosity, the IRX–$\beta_{\rm UV}$ relation, and the $\beta_{\rm UV}$–$M_{\rm UV}$ relation, although these quantities are typically analyzed only in a galaxy-integrated manner.

5.3.2 Individual Galaxy Properties and Internal Structures

Zoom-in simulations with resolutions of ∼0.1-30 pc or better enable detailed studies of internal galaxy structures and are especially suitable for tracing the formation and evolution of individual high-z galaxies. Table 5.3 summarizes recent simulation works that focus on spatially resolved galaxy structures or individual star formation histories (SFHs). Except for SPHINX20, which uses a small box but achieves 11 pc resolution without zoom-in techniques, all of these simulations are of the zoom-in type.

In terms of morphologies, simulations have been used to interpret clumpy and disk-like galaxies observed by JWST. Some studies select simulated galaxies that match the observed redshift, stellar mass, and SFR of individual targets, and investigate their formation pathways, SFHs, and morphological evolution (e.g., Tanaka et al., 2024; Kiyota et al., 2025; Rodighiero et al., 2024b; Fujimoto et al., 2024b). Others generate mock observations from simulations, process them through synthetic pipelines, and compare them directly with actual observations (e.g., Costantin et al., 2023; Rizzo et al., 2022).

In the context of ALMA observations, simulations have been used to predict rest-frame FIR emission. The [OIII] 88 μm line, originating in ionized gas, can be modeled by assigning Strömgren spheres around young stellar particles even without on-the-fly radiative transfer as shown in Table 5.3. However, the [CII] 158 μm line, which arises from photodissociation regions (PDRs), requires detailed modeling of the UV radiation field and thus demands on-the-fly or post-processed radiative transfer.

Dust physics in simulations is often limited to galaxy-integrated quantities such as the IRX–$\beta_{\rm UV}$ relation, and spatially resolved distributions of dust grain sizes remain underexplored (see also Chapter 7). While some low-redshift studies have investigated line-of-sight dust attenuation effects (e.g., Cochrane et al., 2019), few high-redshift simulations have examined similar phenomena (Cochrane et al., 2024), possibly because inclination effects are expected to be small due to the compactness and lower dust content of early galaxies.

Simulated SFHs are also used to quantify the degree of burstiness in high-z star formation, including stochastic variations in SFRs. Some works have even investigated the emergence of quiescent galaxies at $z \gtrsim 6$ (e.g., Gelli et al., 2023).

As illustrated above, even when using the same set of simulation data, we can obtain valuable insights into a wide range of scientific topics by changing the focus of which observables are compared with the latest JWST and ALMA data.

5.4 Outlook for Galaxy Formation Simulations

Recent observations of high-redshift galaxies have revolutionized our understanding of early galaxy formation, revealing a wealth of new physical insights, as introduced in Chapter 4. However, many of the observed features remain challenging to reproduce simultaneously and

Table 5.2: Summary of recent cosmological simulation studies focusing on $z \gtrsim 6$ galaxies and key statistical observational results.

Topic	Simulation	Reference	Comment
UVLF	FIRE-2	Ma et al. (2019)	
	FIREbox-HR	Feldmann et al. (2025)	
	FLARES	Wilkins et al. (2023b)	
	FirstLight	Ceverino et al. (2024)	empirical dust correction
	MilleniumTNG	Kannan et al. (2023)	
	IllustrisTNG	Vogelsberger et al. (2020)	
Emission line LF	IllustrisTNG	Hirschmann et al. (2023)	also taking line ratio diagnostics
	FLARES	Wilkins et al. (2023a)	
	SPHINX20	Katz et al. (2023c)	
	THESAN	Kannan et al. (2022)	
	BLUETIDES	Wilkins et al. (2020)	CLOUDY
MZR	IllustrisTNG	Torrey et al. (2019)	
	FIRE-2	Ma et al. (2016)	
	FirstLight	Langan et al. (2020) Nakazato et al. (2023)	
	FLARES	Wilkins et al. (2023c)	
	THESAN	Garaldi et al. (2024)	
Size–Mass relation	IllustrisTNG	Pillepich et al. (2018)	
	FLARES	Roper et al. (2022) Punyasheel et al. (2025)	
	THESAN	Shen et al. (2024)	
	BLUETIDES	Marshall et al. (2022)	
	SIMBA	Wu et al. (2020)	
	FIRE-2	Ma et al. (2018a)	
Dust statistics	dusty gadget	Graziani et al. (2020)	on-the-fly
	gadget3-osaka	Aoyama et al. (2018)	on-the-fly
	FLARES	Vijayan et al. (2022)	
	FirstLight	Mushtaq et al. (2023)	post-process RT
	THESAN	Kannan et al. (2025)	
	CROC	Esmerian and Gnedin (2022)	post-process
	SIMBA	Li et al. (2019)	
	MassiveFIRE	Liang et al. (2019, 2021)	post-process RT (SKIRT)
	FIRE-2	Ma et al. (2019)	post-process RT (SKIRT)
	SERRA	Pallottini et al. (2022)	post-process RT (SKIRT)
Kinematics	SERRA	Kohandel et al. (2024)	disk galaxies
	FirstLight	Nakazato et al. (2024)	clumpy galaxies
	VELA	Mandelker et al. (2017)	clumpy galaxies

Table 5.3: Summary of recent cosmological simulation studies focusing on individual $z \gtrsim 6$ galaxies and their comparison with key observational results.

Topic	Simulation	References	Comments
Morphologies	SERRA	Kohandel et al. (2024)	disk galaxies
		Kohandel et al. (2019), Gelli et al. (2020)	merging galaxies
	VELA	Mandelker et al. (2017)	clumpy galaxies
	FirstLight	Nakazato et al. (2024)	clumpy galaxies
	THESAN-ZOOM	McClymont et al. (2025a)	galaxy size
Dwarf galaxies/ stellar clusters	SIEGE	Kimm et al. (2016) Calura et al. (2022, 2025) Garcia et al. (2023, 2025)	
	Sugimura et al. (2024)		
Emission lines/ (rest-optical)	FirstLight	Ceverino et al. (2021)	
	FLARES	Wilkins et al. (2023a)	
	Katz et al. (2018)	Katz et al. (2019)	massive EoR galaxies
	Katz et al. (2023a)	Katz et al. (2023a)	focusing on pop III
Emission lines/ (rest-FIR)	FirstLight	Nakazato et al. (2023)	[OIII] 88μm
	SERRA	Kohandel et al. (2023, 2025)	[OIII] 88μm
	SERRA	Pallottini et al. (2022)	[OIII] 88μm , [CII] 158μm
	Katz et al. (2018)	Katz et al. (2019)	[OIII] 88μm , [CII] 158μm
	SPHINX20	Katz et al. (2022)	[OIII] 88μm , [CII] 158μm
	Shimizu et al. (2014)	Moriwaki et al. (2018)	[OIII] 88μm
	PONOS	Schimek et al. (2024)	[OIII] 88μm , [CII] 158μm
	Yajima et al. (2017)	Arata et al. (2020)	[OIII] 88μm , [CII] 158μm
	Sugimura et al. (2024)	Nakazato et al. (2025) (Chapter 8)	[OIII] 88μm , [CII] 158μm
Dust	SERRA	Behrens et al. (2018)	SKIRT
	FirstLight	Chapter 6	SKIRT
	Yajima et al. (2017)	Arata et al. (2019)	ART^2
SFH	SERRA	Gelli et al. (2023), Pallottini and Ferrara (2023b)	quench galaxies stochastic burstiness
	Pallottini et al. (2017)	Pallottini et al. (2017)	
	FirstLight	Ceverino et al. (2018)	
	THESAN-ZOOM	McClymont et al. (2025b)	
	THESAN-ZOOM	Shen et al. (2025)	focusing on SFE

self-consistently in simulations, particularly across the wide range of physical scales from the interstellar medium (ISM) to the intergalactic medium (IGM). In this section, I outline promising directions for future galaxy formation simulations that aim to bridge this gap.

5.4.1 On-the-Fly Radiative Transfer in Massive Galaxies

Simulations with on-the-fly radiative transfer (RT) for massive galaxies ($M_* \gtrsim 10^8\,M_\odot$) are expected to become increasingly important. Resolving ionized gas structures in such systems requires spatial resolutions with a few parsecs or even sub-parsec scales. While some zoom-in cosmological simulations have already achieved sub-pc resolution with on-the-fly RT (e.g., Sugimura et al., 2024), these are mostly limited to the formation of low-mass, star-cluster-scale first galaxies ($M_* \sim 10^{5-6}\,M_\odot$). In contrast, current zoom-in simulations for more massive galaxies detectable by JWST typically resolve ∼10–20 pc, which is usually larger than the HII regions and might be insufficient to capture ionization structures accurately (see Table 5.1).

Sub-pc scale on-the-fly RT simulations of massive galaxies would allow us to resolve both ionized and neutral gas within galaxies, and provide direct access to electron density and temperature, which are observationally measured using emission line ratios, such as the [OII] doublet, [OIII] 88μm /5007Å for electron density, and [OIII] 4363/5007Å for electron temperature. These simulations can be used to study how individual galaxies evolve in emission-line diagnostic diagrams (e.g., O32–R23 plane) over cosmic time, as well as the spatial distributions of these quantities within a single snapshot.

In addition, such simulations will offer predictions for the escape fraction of ionizing photons ($f_{\rm esc}$), which cannot be directly measured in $z \gtrsim 6$ galaxies due to IGM absorption. For example, observable line ratios such as O32 and C43 have been proposed as $f_{\rm esc}$ tracers (e.g., Nakajima and Ouchi, 2014; Schaerer et al., 2022) using 1D radiative transfer calculations. Correlations between such emission lines and $f_{\rm esc}$ for simulated galaxies could be tested and calibrated for application to future observations. These simulations will also produce spatially resolved maps of electron density and temperature, providing insights into the internal structure of high-z galaxies that are recently been studied observationally via IFU surveys (e.g., Venturi et al., 2024; Kiyota et al., 2025). In particular, they can provide a theoretical mechanism of formation of multiphase ionized gas that has been recently revealed by joint JWST and ALMA observations (e.g., Usui et al., 2025; Harikane et al., 2025b, , see also Section 4.4).

Furthermore, on-the-fly RT enables a self-consistent treatment of radiation pressure over multiple cells, allowing studies of radiatively driven outflows. This mechanism may play a key role in explaining the emergence of UV-bright galaxies at $z > 10$, as suggested by recent JWST results (see Section 4.3).

5.4.2 BH Injection and AGN Feedback Models at $z \gtrsim 4$

At redshifts $z \gtrsim 4$, the contribution of black hole (BH) feedback has generally been considered negligible due to the small BH masses and their low number densities. As a result, most cosmological simulations in this epoch do not include BH feedback. At lower redshifts, however, AGN feedback is known to play an important role in quenching star formation, and models such as IllustrisTNG and SIMBA incorporate AGN feedback accordingly. These implementations are calibrated to reproduce global relations such as the stellar mass functions and the cosmic star formation rate density (SFRD) at $z \sim 0$ (e.g., IllustrisTNG:Weinberger et al. (2018), EAGLE:Schaye et al. (2015), SIMBA:Davé et al. (2019)). However, the tuned parameter values are often chosen empirically rather than being derived from physically motivated assumptions, reflecting the intrinsic complexity of modeling AGN feedback in a self-consistent manner. The need to revisit BH feedback at high redshift has been renewed by recent JWST observations, which have revealed a novel population of compact red sources known as "Little Red Dots" (LRDs). These objects represent a unique class of active galactic nuclei (AGNs) with distinctive

properties, potentially marking a critical phase in the formation and growth of early BHs, as discussed in Section 4.3.

Analytical studies suggest that LRDs consist of a black hole accreting near the Eddington limit (Inayoshi et al., 2024; Pacucci and Narayan, 2024), embedded within a massive, optically thick envelope with a characteristic temperature of 5000–7000 K (e.g., Kido et al., 2025; Liu et al., 2025). The super-Eddington accretion scenario naturally explains the observed weakness in X-ray and radio emission and the low variability of LRDs. Meanwhile, the optically thick envelope accounts for the red optical continuum and distinct spectral features such as a V-shaped continuum and Balmer breaks (Inayoshi and Maiolino, 2025).

It is becoming essential to investigate whether such objects can be reproduced in simulations. Because the structure around BHs in LRDs is expected to exist on sub-parsec scales, dedicated high-resolution simulations of individual BHs are necessary as a first step. Based on the physical insights gained from such simulations, the next challenge is to incorporate LRDs into galaxy-scale and cosmological simulations to investigate their formation, evolution, and impact on their host galaxies. It is also important to quantify the extent to which the blue side of the observed spectrum (rest-UV) is contributed by the host galaxy, as opposed to the emission from the central black hole and its surrounding envelope.

Implementing LRDs in galaxy formation simulations also opens a pathway to study the co-evolution between central BHs and their host galaxies, including the BH-tellar mass relation and the influence of BH feedback on star formation. Moreover, by modeling LRDs in non zoom-in cosmological simulations, it will be possible to assess whether the simulated number density of LRDs is consistent with that inferred from JWST observations.

5.4.3 Dust Evolution

In future studies, it will be increasingly important to incorporate dust formation, destruction, and grain size evolution into cosmological simulations. At present, however, implementing detailed dust physics in large-scale simulations remains technically challenging. Most current cosmological simulations do not compute dust properties on the fly. As a result, assumptions must be made regarding the spatial distribution, composition, and total mass of dust. These assumptions inevitably introduce uncertainties when interpreting dust-related observables.

Historically, in the past decade, physically motivated one-zone models have been used to study the evolution of dust grains and their size distributions (e.g., Lisenfeld and Ferrara, 1998; Dwek, 1998; Hirashita, 1999). These models have been incorporated into cosmological simulations (e.g., Aoyama et al., 2017, 2020). In these implementations, the dust size distribution is typically approximated using a two-size model, while only isolated galaxy simulations can consider the additional size distributions (e.g., Romano et al., 2022; Matsumoto et al., 2024). However, this simplification limits the ability to track variations in dust attenuation curves, such as the strength of the 2175 Å bump and the possible transition from SMC-like to MW-like curves inferred from high-redshift galaxy observations.

To provide theoretical insights into the observed diversity and evolution of dust attenuation curves, future cosmological simulations should aim to resolve the full dust size distribution by employing finely sampled size bins (e.g., 20–30 bins covering the 0.001–1 μm range). This would require on-the-fly treatment of key dust processes such as coagulation, accretion, shattering, and sputtering. Importantly, coagulation and accretion predominantly occur in cold, dense molecular clouds, while shattering and sputtering take place in hot, diffuse media. Thus, cosmological simulations must either achieve the spatial resolution necessary to resolve molecular clouds (i.e., $< 0.1\,\mathrm{pc}$), or implement physically motivated subgrid models to capture these multi-phase dust processes.

With such modeling in place, post-processing radiative transfer calculations can be performed to quantify dust attenuation and re-emission. This would enable predictions of redshift evolution in attenuation curves, spatial variations in dust grain sizes within galaxies, and the evolution

of size distributions across a statistical sample of simulated galaxies. Mock UV–IR spectral energy distributions (SEDs) could then be generated for direct comparison with observations from JWST and ALMA, providing a powerful testbed for models of high-redshift dust physics.

5.4.4 Chemical Abundances

Most current galaxy formation simulations treat all metals as a single quantity, without distinguishing individual chemical elements. Only a limited number of simulations have implemented element-by-element tracking of chemical abundances. For example, the simulations by Arata et al. (2020) and THESAN-ZOOM simulations (Kannan et al., 2025) follow the abundances of seven individual metal elements (N, O, Ne, Mg, Si, and Fe) for each gas or star particle. This enables a detailed investigation of the contributions of Type Ia and Type II supernovae, as well as asymptotic giant branch (AGB) stars, to the evolution of elemental abundances.

Similarly, the MEGATRON simulations (Katz et al., 2024) track the same set of elements and include yields from additional sources such as pair-instability supernovae (PISNe), which are thought to originate from Population III stars, and hypernovae (HNe) from massive Population II stars ($m_* \geq 25\,M_\odot$). Furthermore, MEGATRON calculates the ionization states of each element on the fly during the simulation, enabling a more realistic prediction of emission lines.

As discussed in Section 4.3, recent JWST observations have revealed a population of high-redshift galaxies with prominent nitrogen emission lines in the rest-frame ultraviolet. These so-called "N emitters" exhibit super-solar N/O abundance ratios, inferred from strong [NIII] and [NIV] emission lines. Theoretical interpretations suggest that such N enrichment may arise from very massive stars (VMS) (Nagele and Umeda, 2023; Marques-Chaves et al., 2024) or nitrogen-rich winds from Wolf–Rayet (WR) stars(Kobayashi and Ferrara, 2024; Watanabe et al., 2024; Fukushima and Yajima, 2024). However, it is worth noting that the classification of N emitters to date is largely based on UV emission lines. In some cases, galaxies identified as N emitters in the UV do not show elevated N/O ratios when derived from optical [NII] /[OII] line ratios (Ji et al., 2024). This highlights the importance of combining accurate abundance tracking with proper modeling of ionized regions and the ionization states of individual metal species in simulations.

In addition to nitrogen-rich galaxies, several carbon-rich systems have also been reported at high redshift. Some of these exhibit low overall metallicity (as traced by oxygen abundance) but super-solar C/O ratios (D'Eugenio et al., 2024; Nakajima et al., 2025; Scholtz et al., 2025). Such abundance patterns are difficult to explain with conventional stellar yields and may require contributions from Population III stars. Indeed, theoretical studies suggest that C-enhanced yields from normal Pop III stars or VMSs may be necessary to reproduce these observations(Vanni et al., 2023).

To address these questions, future simulations should aim to incorporate detailed chemical evolution models that include the contributions of Population III stars (both normal popIII stars and VMS), as well as metal yields from WR stellar winds. Element-by-element abundance tracking will enable simulations to investigate whether N emitters arise naturally without selection bias from UV line-diagnostics, and to study the evolution of N/O and C/O abundance ratios across cosmic time. This will be crucial for interpreting the physical origins of chemically peculiar galaxies observed by JWST.

5.4.5 Stellar Clusters at $z > 6$

Most of the simulation-based predictions discussed so far have focused on relatively massive galaxies ($M_* \gtrsim 10^8\,M_\odot$) that are detectable without gravitational lensing. However, thanks to the high sensitivity of JWST combined with lensing magnification, compact stellar clusters at $z \geq 6$ with effective radii of less than ∼10 pc and stellar masses of $M_* = 10^{5-6}\,M_\odot$ have begun to be discovered (e.g., Vanzella et al., 2023a, also see Section 4.3). Some of these clusters also

exhibit exceptionally high stellar surface densities of $\Sigma_* = 10^{5-6}\,M_\odot\,\mathrm{pc}^{-2}$(e.g., Adamo et al., 2024b).

These high-z stellar clusters are significantly denser and more compact than typical young star clusters in the local Universe, as well as than Galactic globular clusters (GCs). This offset is expected, as the physical conditions for star formation in galaxies during the epoch of reionization (EoR) are much more extreme. Such dense, compact stellar systems are considered promising candidates for proto-globular clusters, which may evolve into local GCs through several dynamical processes over a Hubble time, such as (i) mass loss due to stellar evolution, (ii) relaxation through two-body interactions, and (iii) the formation and dynamical influence of stellar-mass black holes.

Mass loss due to stellar evolution leads to adiabatic expansion of star clusters under the assumption of virial equilibrium. For example, a reduction of 50% in mass results in approximately a factor of 2 increase in the cluster radius, and consequently, a decrease in stellar density by roughly a factor of 8 (Gieles et al., 2021). Relaxation processes accelerated by the presence of stellar-mass black holes also contribute to structural evolution. Furthermore, external tidal fields can affect the long-term survival of these bound stellar systems.

Theoretical studies of stellar cluster formation have traditionally been carried out using isolated simulations (e.g., Fujii et al., 2021; Fukushima et al., 2020; Fukushima and Yajima, 2021; Menon et al., 2023, 2024). More recently, several efforts have begun to explore high-redshift stellar cluster formation in cosmological settings (e.g., Garcia et al., 2023, 2025; Calura et al., 2025, 2022). However, due to computational limitations, it remains difficult to trace the full evolution of these clusters down to $z = 0$ and to determine whether they can truly survive to become local GCs.

Future simulations should aim to follow the long-term dynamical evolution of such compact stellar systems across cosmic time to address key questions: Do these stellar clusters survive to become globular clusters? How universal is their high surface density at high redshift? In what environments do they preferentially form? Addressing these questions requires statistically significant samples and high-resolution simulations capable of resolving such compact systems within a cosmological context.

In addition to stellar clusters, gravitational lensing has also enabled the detection of low-mass galaxies with $M_* \sim 10^7\ M_\odot$ at $z \gtrsim 6$ (e.g., Asada et al., 2023; Fujimoto et al., 2024b; Asada et al., 2024). Some of these are observed as multiple-component systems. Owing to their low masses, such galaxies are expected to undergo frequent major mergers, leading to high clumpy fractions. Observations further suggest that these systems are in a bursty phase of star formation, characterized by elevated ratios of Hα emission to UV continuum flux.

Given that low-mass galaxies dominate the galaxy population in number, it is crucial to investigate them statistically in simulations. Doing so will allow us to quantify their contribution to cosmic reionization, particularly through their ionizing photon production and escape efficiencies.

Chapter 6

Clumpy Galaxy Formation in the Epoch of Reionization

6.1 Introduction

Recent observations by the James Webb Space Telescope (JWST) have significantly advanced our understanding of galaxy formation and evolution in the early Universe. A number of high-z galaxies have been observed so far, and the record of the most distant galaxies has been renewed (e.g., Curtis-Lake et al., 2023; Wang et al., 2023; Arrabal Haro et al., 2023; Harikane et al., 2024; Carniani et al., 2024). For galaxies at $z \gtrsim 9.5$, strong rest-frame optical emission lines such as [OIII] 5007 Å are outside the range of JWST NIRSpec. Additionally, because of the vast distance, these galaxies appear typically to be compact single-component systems (e.g., Ono et al., 2023; Tacchella et al., 2023). Thus, it is difficult to obtain detailed information on kinematics and internal structure.

Galaxies at $z = 6 - 9$ are promising targets for detailed studies on clump formation and evolution using emission lines. NIRCam has a resolution of 0.03"/pixel for long wavelength (2.4-5.0 μm), corresponding to $\sim$ 150 pc/pixel at $z = 8$ [1]. NIRSpec Integral Field Unit (IFU) has a pixel scale of 0.05"[2], corresponding to $\sim$ 250 pc/pixel at $z = 8$. Gravitational lensing with magnification μ increases the effective spatial resolution by $\sqrt{\mu}$, allowing detailed studies of internal structure of galaxies (e.g., Hsiao et al., 2023; Bradač et al., 2023; Álvarez-Márquez et al., 2023; Jones et al., 2024c; Hashimoto et al., 2023; Morishita et al., 2023; Meštrić et al., 2022; Claeyssens et al., 2023; Fujimoto et al., 2024a).

Especially, recent JWST photometry observations have reported a large number of galaxies at $z > 6$ that contain star-forming clumps and /or elongated structures with a scale of $\sim$ 100 pc in the rest-UV and optical wavelengths (e.g., Hainline et al., 2024a; Chen et al., 2023; Huertas-Company et al., 2024; Tacchella et al., 2023; Baker et al., 2023; Lines et al., 2025; Kiyota et al., 2025; Claeyssens et al., 2025; Morishita et al., 2025). A prominent example is JADES-GN-189.18051+62.18047, which consists of five clumps, and four of them are located within a small region of $\sim$ 7 kpc.

Some NIRSpec IFU observations also discovered merging systems of star-forming galaxies and core regions of proto-clusters at $z > 6$ with the strong detection of [OIII] 5007 Å (e.g., Hashimoto et al., 2023; Jones et al., 2024c; Arribas et al., 2024; Venturi et al., 2024). Hashimoto et al. (2023) and Jones et al. (2024c) found over four components within a $\sim$ 11 kpc regions. While these observations suggest a rapid assembly of high redshift galaxies, it remains largely unknown how the compact clumpy systems emerge in the early epochs.

[1] NIRCam has a pixel scale of 0.063"/pixel on the sky, but the post-process image data reduction allows the grid resolution 0.03" per pixel (Kashino et al., 2023; Matthee et al., 2023).

[2] NIRSpec IFU elements are 0.1"/pixel on the sky, but the combination of dithering and drizzle weighting allows sub-sampling of the detector pixels with 0.05" (Jones et al., 2024a,b,c; Hashimoto et al., 2023).

Clump formation at lower redshift $z = 0 - 4$ have been widely investigated both by observations (Genzel et al., 2011; Tadaki et al., 2014; Guo et al., 2015; Elmegreen et al., 2013) and theoretical studies (Oklopčić et al., 2017; Ceverino et al., 2010; Bournaud and Elmegreen, 2009; Agertz et al., 2009; Romeo et al., 2010; Romeo and Agertz, 2014). They have proposed two major mechanisms for clump formation: violent disk instability (VDI) and mergers.

The former is driven by, for example, cold gas accretion flowing along the cosmic web (Dekel et al., 2009b; Ceverino et al., 2010; Dekel and Krumholz, 2013; Rodriguez-Gomez et al., 2016), and the local disk instability is regulated by the Toomre parameter Q (Toomre, 1964). This is originally defined as $Q \equiv \sigma_{\rm r}\kappa/\pi G\Sigma$ for an infinitesimally thin gas disk, where $\sigma_{\rm r}, \kappa, G, \Sigma$ are the radial velocity dispersion, the epicyclic frequency, the gravitational constant, and gas surface density. Clumps formed in massive disk galaxies have been studied by cosmological simulations (Agertz et al., 2009; Ceverino et al., 2010; Mandelker et al., 2014, 2017; Buck et al., 2017; Ceverino et al., 2023; Inoue et al., 2016b; Genel et al., 2012) as well as isolated disk models (Tamburello et al., 2017; Faure et al., 2021; Bournaud et al., 2014; Bournaud and Elmegreen, 2009; Hopkins et al., 2012). Observations also identified clumps induced by VDI with significant rotations (e.g., Genzel et al., 2006, 2008). The fate of formed clumps (survival and disruption) has often been discussed from theory and observations (Dekel et al., 2009b; Renaud et al., 2014; Elmegreen et al., 2007).

The later competitive mechanism is mergers. Galaxy mergers cause significant gas density perturbations and even promote star formation (e.g., Di Matteo et al., 2008), and thus may be another promising formation path for clumps. Such clumpy galaxies via mergers are often discussed with a major-merger rate or a pair fraction. Numerical simulations suggest that the galaxy merger rate may increase at higher redshifts (e.g., Genel et al., 2008, 2009; Fakhouri and Ma, 2009; Hopkins et al., 2010; Rodriguez-Gomez et al., 2015).

Since observations cannot measure the rate directly, they instead quantify pair fractions (e.g., Tasca et al., 2014; Ribeiro et al., 2017; López-Sanjuan et al., 2013), which has been statistically investigated at lower redshift $z \lesssim 6$ with a large samples by HST. Ribeiro et al. (2017) argued that the obtained pair fraction infers a major merger fraction of $\sim$20 % over the redshift range $2 < z < 6$.

In addition to a pair fraction, a clumpy fraction $f_{\rm clumpy}$ has also been investigated to evaluate the contribution of merger and VDI (e.g., Guo et al., 2015; Shibuya et al., 2016; Ribeiro et al., 2017). Ribeiro et al. (2017) found that a clumpy fraction increases from 35 to 50 percent from z = 2-6, while Shibuya et al. (2016) reported the opposite trend and suggested that VDI is the main origin of clumps. The clumpy fraction may also depend on stellar mass (Guo et al., 2015), making it difficult to understand the redshift evolution.

While clumpy galaxies at $z > 7$ are newly observed by JWST in multiwavelength and their stellar mass and size are statistically investigated (e.g., Meštrić et al., 2022; Claeyssens et al., 2023), the redshift evolution of clumpy fractions and constraints on the formation scenario are not well understood. For numerical simulations, large-scale cosmological simulations such as Illustris TNG (Pillepich et al., 2018), THESAN (Shen et al., 2024), FLARES (Roper et al., 2022), BLUETIDES (Marshall et al., 2022), and SIMBA (Wu et al., 2020) have a minimum resolution of a few hundred pc, making it hard to resolve internal structures of galaxies at high redshift.

Zoom-in simulations can achieve better resolution, and clumpy structures are also reported (Barrow et al., 2017; Ma et al., 2018c; Katz et al., 2019; Arata et al., 2020; Gelli et al., 2020, 2021; Kohandel et al., 2020; Kimm et al., 2016; Calura et al., 2022). However, their samples are often limited to only a few galaxies, and there are few theoretical studies at $z > 6$ that qualitatively and statistically discuss the formation of clumps and their fates, their physical properties, and the clumpy fractions.

In this paper, we use the FirstLight simulation suite, which achieves a very high resolution of 17 pc and provides a large sample size to allow robust statistical analysis. We use outputs

for 62 simulated galaxies with 4092 snapshots in $z = 6 - 9$. Our main objective is to study the properties of galaxy clumps at the epoch of reionization, and their formation and evolution.

In our previous study (Nakazato et al., 2023), we devised a physical model of HII regions and calculated the luminosity of emission lines for the same FirstLight galaxy samples. The resulting relation between the star formation rate and [OIII] luminosity is consistent with recent observations (e.g., Hashimoto et al., 2018; Tamura et al., 2019; Harikane et al., 2020). We use the same model to characterize clumpy galaxies that are bright in rest-frame optical emission lines such as [OIII] 5007 Å.

This chapter is organized as follows. In Section 6.2, we introduce the numerical simulation and describe the method to calculate line luminosities and define clumps. In Section 6.3, we discuss in detail the formation and evolution of a few clumpy systems. Summary and conclusions are given in Section 6.4. Throughout this paper, we assume a set of parameters in ΛCDM cosmology with $\Omega_{\rm m} = 0.307$, $\Omega_{\rm b} = 0.048$, $h = 0.678$ and $\sigma_8 = 0.823$ from *Planck13* results (Planck Collaboration et al., 2014).

6.2 Method

6.2.1 Zoom-in Simulation:FirstLight

The simulations used in this work were first presented in Ceverino et al. (2017). We perform a cosmological zoom-in simulation for massive galaxies comparable to the observed ones. We use the simulation code ART, which adopts an Adaptive Mesh Refinement (Kravtsov et al., 1997; Kravtsov, 2003; Ceverino and Klypin, 2009).

6.2.1.1 Cosmological Initial Conditions

We begin by running a low-resolution (128^3 particles) dark matter (DM) only simulation in a cosmological box with a side length of 40 comoving Mpc/h. Initial conditions are generated with MUSIC (Hahn and Abel, 2011) at $z = 150$ using a Planck cosmology (Planck Collaboration et al., 2014). Dark matter halos are identified using the Bound-Density-Maxima (BDM) halo finder (Klypin and Holtzman, 1997). We selected all dark matter halos with a maximum circular velocity greater than $V_{\rm circ} = 178\,{\rm km\,s^{-1}}$ at $z = 5$, resulting in a sample of 62 halos. For each of them, we perform zoom-in simulations targeting the Lagrangian region defined by the initial positions of dark matter particles that reside within a spherical region of radius $2R_{\rm vir}$ centered on each identified halo at $z = 5$. The zoom-in initial conditions are constructed with a dark matter particle mass of $8 \times 10^4\,M_\odot$. All simulations are evolved down to $z = 5.5$.

6.2.1.2 Refinement

Grid refinement occurs on-the-fly in the simulation. When a cell contains more than eight particles for both DM and star particles, it is flagged for refinement. In addition to the above criteria, cells are flagged so that Jeans lengths are resolved by $N_{\rm J}$ cells. We set $N_{\rm J} = 7$ for cells with Δx (Ceverino et al., 2010), where Δx is the cell size. The smallest cells have a physical size of $\Delta x_{\rm min} = 31\,{\rm pc}(7/1 + z)$.

6.2.1.3 Star Formation

Stars form in high-density ($\rho > \rho_{\rm th}$) and low-temperature ($T < T_{\rm th}$) gas cells. In our simulations, we adopt thresholds of $\rho_{\rm th} = 0.035\,M_\odot\,{\rm pc^{-3}}$ ($n_{\rm th} = 1\,{\rm cm^{-3}}$) and $T_{\rm th} = 10^4\,{\rm K}$. Ceverino et al. (2014) showed that over 90% of stars form at $T < 10^3\,{\rm K}$, and more than 50% form at $T < 300\,{\rm K}$. When the above conditions are satisfied, stellar particles are formed as single stellar populations (SSPs), each characterized by an initial mass function (IMF), age, and metallicity. We adopt a Chabrier IMF (Chabrier, 2005) in the mass range of 0.1–100 $M_\odot$.

Stars are formed at discrete time intervals of $\Delta t_{\rm SF} = 5\,{\rm Myr}$, a value determined by computational constraints[3]. During each time step, star formation in a gas cell occurs stochastically with the following probability:

$$P = \min\left(0.2, \sqrt{\frac{\rho_{\rm gas}}{1000\rho_{\rm th}}}\right). \tag{6.1}$$

This prescription ensures that gas cells with higher densities are more likely to form stars, leading to a globally enhanced star formation efficiency (Ceverino et al., 2024). The maximum probability of 0.2 is introduced to avoid forming an excessive number of star particles in a single time interval.

The star formation rate associated with an individual stellar particle is proportional to the gas mass, expressed as $\dot{m}_* = m_{\rm gas}\Delta t_{\rm SF}/\tau$, with $\tau = 12\,{\rm Myr}$. The value of τ is calibrated to reproduce the observed Kennicutt–Schmidt relation (Kennicutt, 1998a). Indeed, Figure A1 of Ceverino et al. (2014) demonstrates the relationship between star formation surface density and gas surface density in several 1 kpc^2 regions within galaxies, which is consistent with the Kennicutt–Schmidt law (Kennicutt, 1998a).

Cooling rates are calculated assuming equilibrium (either collisional or photoionization) for each metal species. The net cooling rates for atomic hydrogen, helium, and metals are interpolated from precomputed CLOUDY tables (Ferland et al., 1998). The simulations assume an ideal monoatomic gas with an adiabatic index $\gamma = 5/3$.

6.2.1.4 UV Background Radiation

As the cosmic star formation rate density increases, the intergalactic medium is gradually filled with ultraviolet background (UVB) radiation (Haardt and Madau, 1996), which heats the gas and alters the ionization states of both primordial and metal-enriched gas. We use the redshift-dependent UVB model of Haardt and Madau (1996). For gas cells with $n_{\rm gas} > 0.1\,{\rm cm}^{-3}$, the UVB intensity is significantly suppressed to $5.9 \times 10^9\,{\rm erg\,s^{-1}\,cm^{-2}\,Hz^{-1}}$ to mimic partial self-shielding in dense gas.

6.2.1.5 Stellar and Radiative Feedback

In the FirstLight simulations, we incorporate the following stellar feedback mechanisms: supernovae (SNe) and stellar winds, radiation pressure on dust grains that absorb UV photons, and infrared (IR) radiation pressure via a subgrid model.

For feedback from SNe and stellar winds, we include both thermal and momentum components. These act as heating sources, with the total heating rate given by

$$\Gamma = \frac{1}{V}\sum_i M_i \Gamma'(t_{{\rm age},i}), \tag{6.2}$$

where M_i and $t_{{\rm age},i}$ are the mass and age of each stellar particle, respectively. The specific heating rate Γ' depends on the feedback type, which varies with stellar age.

Stellar winds are driven by massive stars with $M \geq 5\ M_\odot$ during the first 6 Myr of stellar evolution (Lamers and Cassinelli, 1999). We implement thermal feedback as a constant heating rate over 40 Myr, which corresponds to the lifetime of the lightest stars that end as core-collapse supernovae (SNII)[4]. The constant heating rate is set to $\Gamma' = 1.18 \times 10^{34}\ {\rm erg\,s^{-1}}\,M_\odot^{-1}$, which corresponds to a total energy injection of $E_{\rm SNII} = 2 \times 10^{51}$ erg from stellar winds and supernova

[3] Although the star formation time step is 5 Myr, the gas dynamics are computed with a maximum time resolution of 10^4 years.

[4] In the first few Myr, stellar winds from massive stars such as OB main-sequence and Wolf-Rayet stars dominate the energy injection. Later, core-collapse supernovae contribute. Both processes result in comparable momentum injection (Agertz et al., 2013).

explosions of massive stars with $M > 8\ M_\odot$.

After 40 Myr, thermal feedback is provided by AGB stars, although their injection rate is six orders of magnitude lower than that during the first 40 Myr.

We also include thermal feedback from Type Ia supernovae (SNIa), assuming a characteristic timescale of 1 Gyr. The event rate is three orders of magnitude lower than that of core-collapse SNe, and the specific heating rate is given by

$$\Gamma'_{\rm SNIa}(t_{\rm age}) = E_{\rm SNIa} \times \frac{{\rm d}N_{\rm SNIa}}{{\rm d}t\,{\rm d}M}(t_{\rm age}), \tag{6.3}$$

where $E_{\rm SNIa} = 10^{51}$ erg is the energy per SNIa, and the event rate is expressed as

$$\frac{{\rm d}N_{\rm SNIa}}{{\rm d}t\,{\rm d}M}(t_{\rm age}) = \frac{f_{\rm SNIa}}{1.75 t_{\rm peak}} e^{-x^2}\sqrt{x}, \quad x = \frac{t_{\rm peak}}{t_{\rm age}}, \tag{6.4}$$

with $f_{\rm SNIa}$ denoting the number of SNIa events per solar mass (derived from the assumed IMF), and $t_{\rm peak} = 1$ Gyr being the peak of the delay-time distribution. The heating rate Γ' from SNIa is thus approximately three orders of magnitude lower than that from SNII.

In addition to thermal energy feedback, we include momentum injection from the (unresolved) expansion of gaseous shells driven by SNe and stellar winds (Ostriker and Shetty, 2011). A total momentum of $3\times10^5\ M_\odot\,{\rm km\,s^{-1}}$ is injected per massive star with $M > 8\,M_\odot$, distributed uniformly over 40 Myr. This corresponds to the typical lifetime of stars that end as Type II SNe. The resulting IMF-averaged specific momentum is $3.75 \times 10^3\,{\rm km\,s^{-1}}$. The momentum injection is implemented as a non-thermal pressure component, similarly to radiation pressure.

For radiation pressure, we adopt the "RadPre_IR" model described in Ceverino et al. (2014). This model includes both direct radiation pressure and that from reprocessed IR radiation, but excludes photoionization and photoheating effects. Among the models explored in Ceverino et al. (2014), RadPre_IR provides the strongest radiative feedback. The resulting pressure is added as a non-thermal component to the total gas pressure in regions where ionizing photons from young stars are produced and trapped. We summarize the two types of radiation pressure below.

(i) Radiation Pressure on Dust

A fraction of the UV radiation from young stars is absorbed by dust grains, imparting outward momentum to the gas (e.g., Murray et al., 2005; Yajima et al., 2017). Assuming an isotropic radiation field, the radiation pressure is given by $P_{\rm rad} = \frac{4\pi}{3c} I$, where I is the radiation intensity, and the pressure equals one-third of the radiation energy density. The intensity is calculated as $I = \Gamma' m_* / (4\pi R^2)$, where Γ' is the ionizing luminosity per unit stellar mass. This yields $P_{\rm rad} = \Gamma' m_* / (R^2 c)$, with R set to half the cell size of neighboring cells. This approximation is accurate within a factor of a few. Ceverino et al. (2014) showed that variations in Γ' by up to a factor of four do not significantly affect the results.

Only stellar particles with ages $\lesssim 5\,{\rm Myr}$ contribute to radiation pressure, as the number of ionizing photons declines sharply after this time due to the death of massive stars (e.g., Xiao et al., 2018). We use the SSP code STARBURST99 (Leitherer et al., 1999) to compute Γ', adopting $\Gamma' = 10^{36}\,{\rm erg\,s^{-1}}\,M_\odot^{-1}$ as the time-averaged luminosity during the first 5 Myr.

Radiation pressure is applied only to gas cells that contain young stellar particles ($\leq 5\,{\rm Myr}$) and have hydrogen column densities above $10^{21}\,{\rm cm^{-2}}$. Assuming a UV opacity of $\kappa_{\rm UV} \sim 10^3\,{\rm cm^2\,g^{-1}}$ (Thompson et al., 2005), gas mixed with dust becomes optically thick at $N_{\rm H} \gtrsim 10^{20}\,{\rm cm^{-2}}$. To ensure efficient trapping of ionizing radiation, we adopt a threshold of $N_{\rm H,thres} = 10^{21}\,{\rm cm^{-2}}$[5].

(ii) Infrared Radiation

We also include the enhancement of radiation pressure due to reprocessed IR photons. These

[5]This threshold is appropriate for high-redshift galaxies, where dust content is lower and gas is more transparent.

photons undergo multiple scattering events in dusty regions, thereby increasing momentum transfer to the gas (Agertz et al., 2013; Hopkins et al., 2011; Murray et al., 2010). The total radiation pressure, including the contribution from infrared (IR) radiation, can be expressed as $P_{\rm rad,IR} = (1+\tau_{\rm IR})P_{\rm rad}$, where $\tau_{\rm IR}$ represents the optical depth in the IR regime. We assume that gas becomes optically thick to IR radiation above a density threshold of $n_{\rm gas} = 300\,{\rm cm}^{-3}$, yielding $\tau_{\rm IR} = n_{\rm gas}/300\,{\rm cm}^{-3}$.

To summarize, thermal and kinetic feedback from SNe and stellar winds primarily affect diffuse gas, while radiation pressure from stellar UV photons becomes dominant in moderately dense gas ($\sim 100\,{\rm cm}^{-3}$), and IR radiation pressure becomes significant in even denser regions ($\gtrsim 300\,{\rm cm}^{-3}$).

6.2.1.6 Numerical Resolution and Pressure Floor

In our simulations, we impose a pressure floor on the condensing gas in galaxies to prevent artificial fragmentation. It is known that fragmentation can occur if the local Jeans length $\lambda_{\rm J}$ is not well resolved by computational grids with a cell size $\Delta x_{\rm min}$. Truelove et al. (1997) show that artificial fragmentation can be prevented if the Jeans length is always resolved by at least four resolution elements (i.e., $N_{\rm J} \equiv \lambda_{\rm J}/\Delta x_{\rm min} = 4$). Ceverino et al. (2010) suggest a more stringent criteria of $N_{\rm J} = 7$ by running long-term cosmological simulations.

In our simulations, we set an effective pressure floor at

$$P_{\rm floor} = \frac{G\rho_{\rm gas}^2 N_{\rm J}^2 \Delta x_{\rm min}^2}{\pi\gamma}, \tag{6.5}$$

with $N_{\rm J} = 7$. We assume a ratio of specific heats of $\gamma = 5/3$ for monoatomic gas and $\rho_{\rm gas}$ is the gas mass density. The pressure in the Euler equation is replaced by Eq. (6.5) when its pure thermal pressure contribution has a lower value. Artificial fragmentation is effectively prevented by implementing the pressure floor, which is meant to model crudely non-thermal contributions such as local turbulence in the ISM.

Figure 6.1 shows a phase diagram for a snapshot of a clumpy system at $z = 7.2$ (see Figure 8.4). Gray dashed lines show the temperature threshold (horizontal, $T_{\rm crit} = 10^4\,{\rm K}$) and density threshold (vertical, $n_{\rm crit} = 1\,{\rm cm}^{-3}$) for star formation. The black dashed line in the left panel shows the following relationship calculated from Eq. (6.5),

$$T_{\rm J} = \frac{m_{\rm p}}{k_{\rm B}}\frac{P_{\rm floor}}{\rho_{\rm gas}} = 35\,{\rm K}\left(\frac{n_{\rm gas}}{1\,{\rm cm}^{-3}}\right)\left(\frac{N_{\rm J}}{7}\right)^2\left(\frac{\Delta x_{\rm min}}{17\,{\rm pc}}\right)^2, \tag{6.6}$$

where $m_{\rm p}$, $k_{\rm B}$ and $n_{\rm gas}$ are proton mass, Boltzmann constant, and gas number density, respectively. Note that there are gas cells below the black dashed line, on which the pressure floor is imposed in the simulation. Our pressure implementation prevents artificial fragmentation but it also prevents the growth of structures below ~ 100 pc scales. Previous simulations with the same implementation and resolution have already investigated low-redshift clumps (Mandelker et al., 2014, 2017; Inoue et al., 2016b; Inoue and Yoshida, 2019; Ceverino et al., 2023).

6.2.1.7 Metal Enrichment

The metal enrichment of from SNII and SNIa is considered separately because both supernova time-scales and release metal yields are quite different.

Single stellar particles release SNII metals in the first 40 Myrs as explained in section 6.2.1.5. The total mass of heavy elements from SNII is $F_{Z,{\rm SNII}}M_\star$, where $M_\star$ is the mass of the stellar population and $F_{Z,{\rm SNII}}$ is the metal mass fraction averaged over the IMF $\psi(m)$ within the range of $[m_{\rm min}, m_{\rm max}]$;

$$F_{Z,{\rm SNII}} = \frac{\int_8^{m_{\rm max}} m\psi(m) f_{Z,{\rm SNII}}(m){\rm d}m}{\int_{m_{\rm min}}^{m_{\rm max}} m\psi(m){\rm d}m}, \tag{6.7}$$

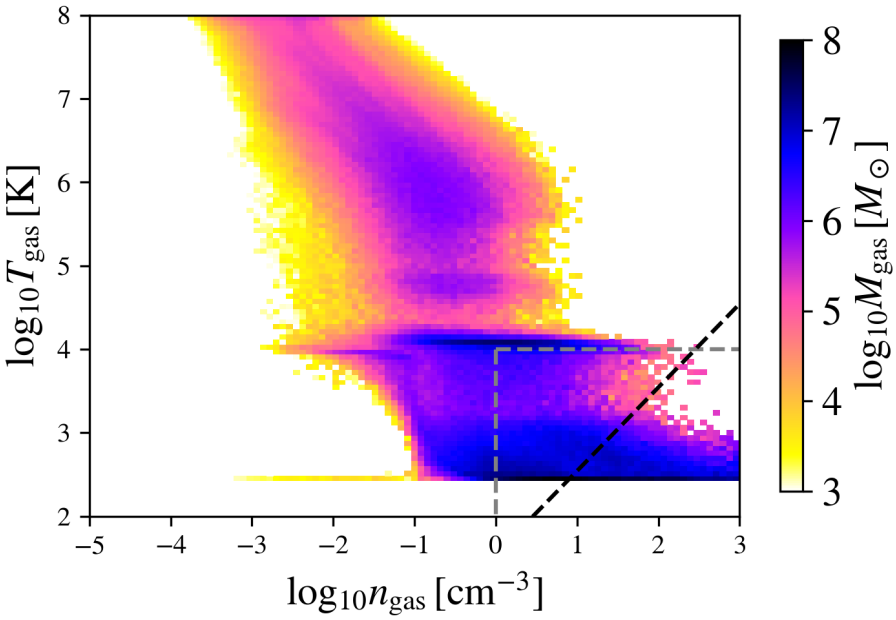

Figure 6.1: Temperature-density phase diagram for a clumpy system FL958 at $z = 7.2$. The color bar shows the gas mass within each bin $(\Delta \log_{10} n_{\rm gas}, \Delta \log_{10} T_{\rm gas}) = (0.08, 0.06)$. Gray dashed lines show the temperature threshold (horizontal) and density threshold (vertical) for star formation. The black dotted line shows the threshold of Eq. (6.6). We plot all of the gas cells inside a cube with a side length of 10 kpc. The figure is taken from Nakazato et al. (2024).

where $f_{Z,\rm SNII}(m)$ is the mass fraction in metals from a Type-II SNe of a star with mass m and is modeled as the following by Woosley and Weaver (1995), $f_{Z,\rm SNII}(m) = \min(0.2, 0.01m - 0.06)$. For a single SNIa, we set a fixed mass of ejected metal of 1.3 $M_\odot$ for $3 - 8$ $M_\odot$ stars.

6.2.1.8 Stellar Mass Loss

A stellar population loses mass through SNe and stellar winds from massive stars, WR or AGB stars. Stellar mass loss events inject mass, momentum, energy and metals to the surrounding gas. We introduce mass loss rate $f_{\rm loss}(t_{\rm age})$ as a function of the age of a single stellar population $t_{\rm age}$ provided by Jungwiert et al. (2001);

$$f_{\rm loss}\left(t_{\rm age}\right) \equiv -\frac{M_\star(\dot{t}_{\rm age})}{M_\star(t_{\rm age}=0)} = \frac{c_0}{t_{\rm age}+T_0}, \tag{6.8}$$

where coefficients have the constant values of $c_0 = 0.05$ and $T_0 = 5$ Myr. Therefore, the stellar particle mas at age of t_1 is obtained by integrating Eq.(6.8),

$$\int_0^{t_1} f_{\rm loss}(t){\rm d}t = \frac{M(t_1)-M(0)}{M(0)} = \int_0^{t_1} \frac{c_0}{t_{\rm age}+T_0}{\rm d}t \tag{6.9}$$

$$\therefore M(t_1) = \left[1 - c_0 \log\left(\frac{t_1+T_0}{T_0}\right)\right] M(0). \tag{6.10}$$

For example, the stellar particle with age $t_1 = 40$ Myr has a mass of $M(40\ {\rm Myr}) = 0.89\ M(0)$, which indicates that 10% of the stellar mass is lost during the first 40 Myr by SNII and stellar winds from massive stars.

6.2.1.9 Runaway Stars

We also include the effect of runaway stars, which are primarily OB-type massive stars (Blaauw, 1961) that are ejected from their birth sites due to velocity kicks, typically following the su-

pernova explosion of a binary companion. In our simulations, we assign a velocity kick of $\sim 10\,\mathrm{km\,s^{-1}}$ to 30% of newly formed stellar particles to account for this effect.

6.2.1.10 Stellar Mass Distributions of Galaxy Samples

Our 62 galaxy samples have stellar masses greater than $\sim 10^{10} M_\odot$ at $z = 5$. The maximum resolution in the zoom-in hydro simulations, particularly valid in dense clumps, enables the simulations to resolve gas densities of $\sim 10^3\,\mathrm{cm^{-3}}$ with temperatures of $\sim 300\,\mathrm{K}$. We store a total of 66 snapshots between $z = 9.5$ and $z = 5.5$ for each galaxy, with a space of the cosmic expansion parameter $\Delta a = 0.001$, corresponding to $7 - 10$ Myr [6]. The frequent output timing is sufficient to follow dynamics during galaxy mergers that occur on the tidal timescale of 10-100 Myrs (Renaud et al., 2013). Figure 6.2 shows the stellar mass evolution (left panel) and cumulative stellar mass distribution (right panel) for our 62 simulated massive galaxies. In the left panel, each galaxy exhibits diverse star formation histories. Even galaxies with similar stellar masses at $z \simeq 9$ evolve significantly differently by $z = 6$, resulting in substantial stellar mass differences, as highlighted by the orange (most massive) and blue (least massive) lines. By $z = 6$, the most massive galaxy is approximately 100 times more massive than the least massive one.

The right panel of Figure 6.2 compares our cumulative stellar mass distribution with other cosmological simulations (Moriwaki et al., 2018; Pallottini et al., 2019; Olsen et al., 2017). Our sample is selected to include more massive galaxies, resulting in a larger number of high-mass galaxies and fewer low-mass galaxies compared to the other simulation samples. Therefore, our simulation results are particularly suitable for comparison with observations of galaxies with stellar masses $M_* \gtrsim 10^{8-10.5}\,M_\odot$ at $z = 6 - 9$.

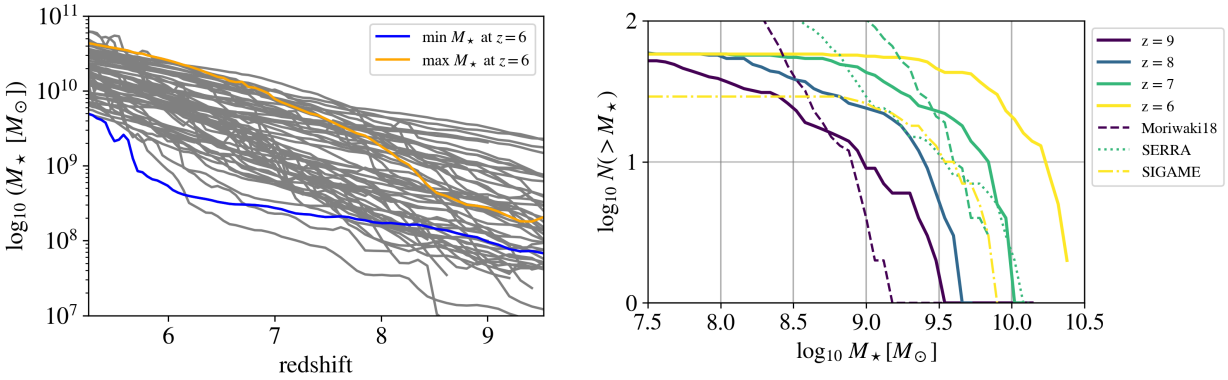

Figure 6.2: (Left) Stellar mass histories of the main galaxies from $z = 9.5$ to $z = 5.5$. Those galaxies have a large circular velocity of $V_c > 178$ km/s at $z = 5$. An orange (blue) line traces the evolution of a galaxy which has the maximum (minimum) stellar mass at $z = 6$. (Right) Cumulative distribution of stellar mass for massive galaxy samples ($V_{\rm max} > 187$ km/s) in FirstLight simulation. Dashed lines are results from Moriwaki et al. (2018) (purple and green), a green dotted line and a yellow dashdot line are results from SERRA simulation (Pallottini et al., 2022) and SÍGAME simulation Olsen et al. (2017), respectively. Each color represents different redshifts.

6.2.2 Line luminosity Calculation

We calculate the luminosities of emission lines from HII regions for the simulated galaxies and clumps. We adopt essentially the same model as Nakazato et al. (2023) and assume that each stellar particle is surrounded by a spherical HII region (e.g. Panuzzo et al., 2003; Hirschmann

[6] The time step width in the simulation is much shorter than this, being typically 1000 years.

et al., 2017, 2022). The shcematic pictures of our line calculation for each galaxy is described in Figure 6.3.

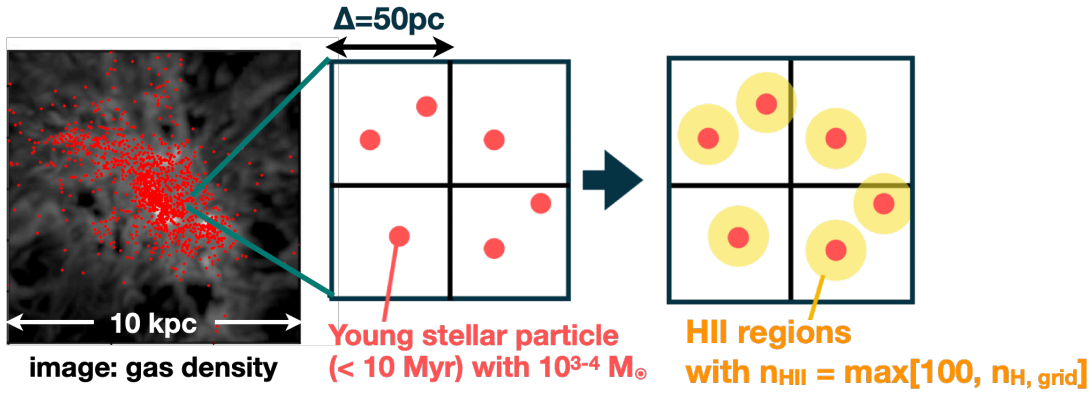

Figure 6.3: A simple cartoon of the modeling of HII regions. Left: Gas number density distribution with gray colormap and stellar particles younger than 10 Myr with red dots. One side length of the region is $0.3R_{\rm vir}$. Middle: an enlargement of the grids, which have a side length of 100 pc. Each grid contains several stellar particles. Right: HII regions around stellar particles as yellow circles. We assume spherical HII regions with a Strömgren radius.

We generate a table of a set of emission lines using CLOUDY (Ferland et al., 2013). As an input stellar SEDs, we adopt a single star model of BPASS (Eldridge et al., 2017). According to Eldridge et al. (2017), these SEDs are similar to other ones such as Starburst 99 (Leitherer et al., 1999), GALAXEV (Bruzual and Charlot, 2003), and Maraston (2005) at the age of $<$ 1 Gyrs. Note that BPASS binary star model can enhance the number of ionizing photons by a factor of up to $\sim$ 10 at the age of $<$ 10 Myr, leading to the [OIII] flux increase up to $\sim$ 1.2 times higher than that of the single model (Ceverino et al., 2021). The input parameters for CLOUDY are gas metallicity $Z_{\rm gas}$, ionization parameter U, and gas density in HII regions $n_{\rm HII}$. The adopted values of the parameters are listed in Table 6.2. In our table, we normalize the emission line luminosity for each stellar particle ($L_{{\rm line},i}$) by Hβ luminosity as

$$L_{{\rm line},i} = (1 - f_{\rm esc}) C_{\rm line}(Z_{\rm gas}, U, n_{\rm HII}) L_{\rm H\beta}^{\rm caseB}. \tag{6.11}$$

Here $f_{\rm esc}$ is the escape fraction and we assume $f_{\rm esc} = 0.1$, a value suggested by both radiation hydrodynamics simulations (Yajima et al., 2011; Kimm and Cen, 2014; Wise et al., 2014; Trebitsch et al., 2017; Xu et al., 2016), and observations (e.g., Nakajima et al., 2020) for high-z galaxies. Since individual HII regions are not resolved in our simulations, we assume that the gas density of a HII region is given by

$$n_{\rm HII} = \begin{cases} 100\,{\rm cm^{-3}} & (n_{\rm gas,grid} < 100\,{\rm cm^{-3}}) \\ n_{\rm gas,grid} & (n_{\rm gas,grid} \geq 100\,{\rm cm^{-3}}), \end{cases} . \tag{6.12}$$

where $n_{\rm gas,grid}$ is the gas number density of a grid with a size of $\Delta = 50\,{\rm pc}$. Our motivation for using a variable HII region density comes from the need to account for grid-to-grid density variations in our simulations. Setting a fixed HII region density at a typical value of $100\,{\rm cm^{-3}}$ (Osterbrock and Ferland, 2006; Hirschmann et al., 2017, 2022) could lead to unrealistic conditions where the grid density exceeds this value. To address this, we adopt a model with a variable HII region density if $n_{\rm gas,grid} > 100\,{\rm cm^{-3}}$[7]. Our model results in a higher global-averaged HII region density in high-z ($z > 6$) simulated galaxies compared to typical local HII regions.

[7] Nakazato et al. (2023) assumed the fixed HII density as $n_{\rm HII} = 100\,{\rm cm^{-3}}$. We also have checked the dependency of [OIII] 5007 Å luminosity on the density model and found that the value changes within only $\lesssim 1$ %.

This trend is also supported by recent JWST observations (e.g., Isobe et al., 2023a; Fujimoto et al., 2024b; Abdurro'uf et al., 2024).

A volume-averaged ionization parameter is written as

$$\langle U \rangle = \frac{3\alpha_{\rm B}^{2/3}}{4c} \left(\frac{3Q\epsilon^2 n_{\rm HII}}{4\pi} \right)^{1/3}. \tag{6.13}$$

The volume-filling factor of the gas ϵ is defined by

$$\epsilon = \frac{\text{(volume occupied by the clumps)}}{\text{(total volume of HII region)}} \equiv \frac{n_{\rm gas,grid}}{n_{\rm HII}}, \tag{6.14}$$

where $n_{\rm gas,grid}$ is the gas number density in each grid. In rare cases where the volume-averaged gas density exceeds the adopted hydrogen density in the ionized regions ($\epsilon > 1$), we set the filling factor to unity. Note that a larger $n_{\rm gas,grid}$ at fixed $n_{\rm HII}$ implies a larger filling factor ϵ, i.e., more compact gas clumps around the ionizing source. To calculate the ionization photon production rate Q, we use the value from Binaly Polulationi and Spectral Synthesis (BPASS) model (Byrne et al., 2022).

We compute the production rate of ionizing photons Q of the simulated galaxies using publicly available tables from BPASS. All physical properties we have selected are summarized in Table 6.1.

Table 6.1: BPASS table. We select the same population and IMF for all stellar particles. The rest four parameters are chosen for each stellar particle.

population	single stellar population
IMF	$\alpha_1 = -1.3,\ \alpha_2 = -2.35,\ M_1 = 0.5,\ M_{\rm max} = 300\ M_\odot$
[α/Fe]	$\Delta(\log(\alpha/{\rm Fe})) = -0.2, +0.0, +0.2, +0.4, +0.6$
metallicity ($Z_\star$)	10^{-5}, 10^{-4}, 10^{-3}, 0.002, 0.004, 0.008, 0.01, 0.02($Z_\odot$), 0.03, 0.04
Age	50 logarithmic bins in [1 Myr, 100 Gyr]; $10^{(6+0.1n)}$ $n = 0 - 50$
Mass	Fixed stellar particle mass of $10^6\ M_\odot$ in BPASS data

Our simulations adopt the stellar initial mass function modeled by broken power laws as

$$N(M < M_{\rm max}) \propto \int_{0.1}^{M_1} \left(\frac{M}{M_\odot} \right)^{\alpha_1} {\rm d}M + M_1^{\alpha_1} \int_{M_1}^{M_{\rm max}} \left(\frac{M}{M_\odot} \right)^{\alpha_2} {\rm d}M \tag{6.15}$$

We re-assign all of young stellar age in order to remove the time step effect of a star formation process in the simulations. This is because our simulations produce new stellar particles with a times step of $\Delta t_{\rm SF} = 5$ Myr as explained in section 6.2.1.3 and each galaxy usually has only two kinds of stellar age younger than 10 Myr. Most emission lines from HII regions are originated from young less than 10 Myr. For BPASS SED of a single stellar population, the number of ionizing photons will decrease over 2 dex from age 1 Myr to 10 Myr (Xiao et al., 2018), which might change the emissivity of each line for 2 dex from Eq. (6.11) and Eq. (6.16).

Then, we re-assign the stellar age as follows.

1. Consider stellar particle younger than 15 Myr. Notate three stellar ages T_1, T_2, T_3 ($T_1 < T_2 < T_3$) [Myr].
2. Reassign stellar age ramdomly within the range of $[T_3, T_2]$, $[T_2, T_1]$, and $[T_1, 1]$ Myr, respectively.

After re-assigning stellar age, we calculate ionizing photon rate Q for each young stellar particle (< 10 Myr).

We generate a library of emission lines using CLOUDY (Ferland et al., 2013). The library covers a wide range of gas metallicity $Z_{\rm gas}$, ionization parameter U as given in Table 6.2. We adopt SEDs from BPASS single stellar population with the same set of $Z_{\rm gas}$. For each case of $Z_{\rm gas}$, we input the corresponding stellar spectrum into the code because of $Z_\star \sim Z_{\rm gas}$. We assume the plane-parallel geometry for all the calculations. Notice that CLOUDY codes set the abundance of elements to be the solar one by default. The electron temperatures in the nebulae are calculated in the code with energy balance between heating and cooling rates. Especially, metal element works as a coolant and ionization parameter works as a heating source. Notice that when we substitute the ionization parameter to the CLOUDY Table 6.2, we use the value $U_{\rm inner}$ at the inner surface of HII region. For plane-parallel case, $U_{\rm inner}$ is twice $\langle U \rangle$. The library lists the line luminosity, $L_{\rm line}$, normalized by the Hβ line luminosity with the case-B approximation (Dopita and Sutherland, 2003). We look for the line ratio table $C_{\rm line}$ with the three parameters $Z_{\rm gas}$, U, $n_{\rm HII}$ which are closest to those of the target stellar particles in our simulation.

parameter	values
$\log_{10}\ Z_{\rm gas}$	0.001, 0.004, 0.008, 0.02 ($Z_\odot$), 0.04
$\log_{10}\ U$	-4.0, -3.9, ..., -1.1, -1.0
$\log_{10}\ (n_{\rm HII}/{\rm cm}^{-3})$	2.0 (fixed)

Table 6.2: The parameters used to calculate the line luminosities with CLOUDY.

Since the obtained values from cloudy are normalized to Hβ luminosities ($L_{\rm H\beta}$), we calculate $L_{\rm H\beta}$ for each stellar particle as

$$L_{nn'}^{\rm caseB} = 4\pi j_{nn'} V = h\nu_{nn'} \left(\frac{\alpha_{nn'}^{\rm eff}}{\alpha_{\rm B}} \right) Q, \tag{6.16}$$

where $j_{\rm H\beta}$ is the Hβ emission rate per unit volume per unit time per unit solid angle, and $\alpha_{\rm H\beta}^{\rm eff}$ is an effective recombination coefficient $V = Q/(n_{\rm HII}^2 \alpha_{\rm B})$ is a volume of HII region and $\alpha_{nn'}^{\rm eff}$ is an effective recombination coefficient. Here $h\nu_{nn'}$ is a transition energy $n = 4 \to n' = 2$, i.e., $h\nu_{\rm H\beta} = 2.55$ eV. The effective recombination coefficient for Hβ line is $\alpha_{\rm H\beta}^{\rm eff} = 3.72 \times 10^{-13}$ cm^3/s for $T_{\rm e} = 10^4$ K. We finally obtain the line luminosity for each grid as $L_{\rm line,grid} = \sum_i^N L_{{\rm line},i}$, where N is the number of stellar particles that the grid contains.

In our previous study (Nakazato et al., 2023; Mushtaq et al., 2023), we find that the magnitude of dust attenuation at rest-frame 5007 Å is approximately $A_{5007}\,[{\rm mag}] = 0.08, 0.24, 0.7$ for individual *galaxies* with $M_*/M_\odot = 10^8, 10^9, 10^{10}$, respectively. Thus, we expect that dust attenuation affects the line luminosity of a small clump by a factor of a few. We further discuss this issue of dust attenuation in Section 6.4.

6.2.3 Clump Finder

In order to compare the properties of the simulated clumpy galaxies with observations, we identify clumps in two-dimensional "images" using projection along a random line of sight (z-axis) of a cube with a fixed side length of 10 kpc. The size is larger than the main central galaxy, and is close to a field of view of NIRSpec IFU at $z = 8$. We assign masses of gas, stars, and dark matter to a uniform grid with $\Delta = 50$ pc by using a cloud-in-cell interpolation also employed in Mandelker et al. (2014, 2017) and Ceverino et al. (2023). The value is about three times the maximum AMR resolution. We first mark grids that contain young (< 10 Myr) stars with their surface mass density ($\Sigma_{M_*({\rm young})}$) greater than $10^{8.5}\,M_\odot{\rm kpc}^{-2}$, corresponding to the surface SFR density of $10^{1.5} M_\odot{\rm yr}^{-1}{\rm kpc}^{-2}$. We then identify candidate groups by running a Friends-of-Friends finder with linking length Δ to the marked grids. Groups with at least 16 grids ($N_{\rm grid}$)

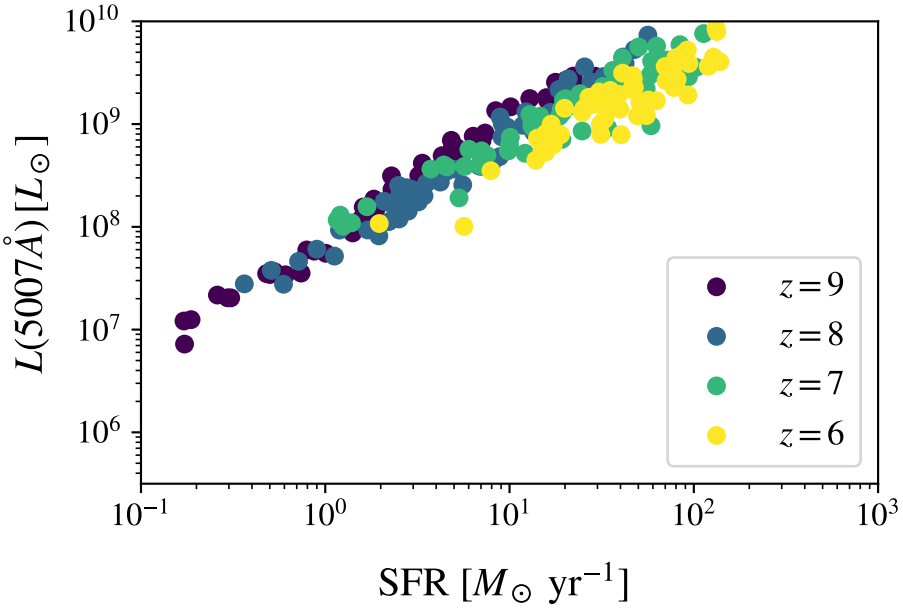

Figure 6.4: The [OIII] 5007 Å luminosity vs. SFR for our 62 simulated galaxies at $z = 9$ (purple), 8 (blue), 7 (green), and 6 (yellow). This figure is taken from Nakazato et al. (2024).

are identified as clumps. The threshold grouping number of grids corresponds to the minimum radius of clump $R_{\rm min} = \sqrt{N_{\rm grid}\Delta^2/\pi} = 113\,{\rm pc}$. The threshold surface stellar mass density and the minimum number of grids are chosen to ensure that the identified clumps are resolved by observations by NIRSpec IFU and NIRCam with the line flux of $F_{\rm [OIII]} \gtrsim 10^{-18}\,{\rm erg\,s^{-1}\,cm^{-2}}$ at $z = 8$. The details of threshold determination are described in the next section 6.2.3.1. We have also checked the effect of line of sight by changing inclination, and it does not change the number of clumps.

6.2.3.1 Parameter Determination

We set three parameters for our clump finder; grid size (Δ), threshold surface mass density of young stellar population ($\Sigma_{M_*({\rm young})}$), and the minimum number of grids ($N_{\rm grid}$). We assume that a HII region exists around each stellar particle. The grid size is set to be larger than the typical Strömgren radius for each stellar particle in our line emission model. The Strömgren radius $R_{\rm s}$ is given by

$$R_{\rm s} = \left(\frac{3Q_0}{4\pi n_{\rm HII}^2 \alpha_{\rm B}}\right)^{1/3} = 5.4\,{\rm pc}\left(\frac{n_{\rm HII}}{10^2\,{\rm cm^{-3}}}\right)^{-2/3}\left(\frac{Q_0}{5\times10^{49}\,{\rm s^{-1}}}\right)^{1/3}, \tag{6.17}$$

where $n_{\rm HII}$ is the gas density in HII regions and Q_0 is the number of ionizing photons per unit time. The electron temperature is $T_{\rm e} = 10^4\,{\rm K}$, and a filling factor of $\epsilon = 1$ is assumed. The value of Q_0 depends on stellar age, mass, and spectrum, which means the value varies to simulation resolutions and model SEDs. We have checked the distribution of Q_0 values for all stellar particles in our simulations and obtained the median (maximum) value of $Q_0 = 5\times10^{50}$ (5×10^{52}) ${\rm s^{-1}}$, and the corresponding Strömgren radius is $R_{\rm s} \sim 15\,(54)\,{\rm pc}$ for $n_{\rm HII} = 100\,{\rm cm^{-3}}$. We thus set $\Delta = 50\,{\rm pc}$.

To determine the threshold of surface young stellar mass density ($\Sigma_{M_*({\rm young})}$), we consider the relationship between $L_{\rm [OIII]\,5007\mathring{A}}$ and star formation rate (SFR). This relationship is implied from pre-JWST observations that have shown the tight correlation between [OIII] 88 μm and SFR at $z > 6$ (e.g., Harikane et al., 2020; Moriwaki et al., 2018; Katz et al., 2019; Pallottini et al., 2022; Kohandel et al., 2023). There are still few statistical investigations of [OIII] 5007

Å emitters at $z > 6$ (Matthee et al., 2023; Meyer et al., 2024), but lower-redshift ($z \lesssim 2$) galaxies are already reported to have tight correlation between [OIII] 5007 Å and SFR by both observations and simulations (e.g., Villa-Vélez et al., 2021; Hirschmann et al., 2023). Figure 6.4 shows the [OIII] 5007 Å luminosity against SFR for our galaxy samples. It is approximated as[8]

$$L_{[\mathrm{OIII}]\,5007\text{Å}} \sim 6 \times 10^7 \left(\frac{\mathrm{SFR}}{M_\odot \mathrm{yr}^{-1}}\right) L_\odot = 6 \times \left(\frac{M_{*(\mathrm{young})}}{M_\odot}\right) L_\odot, \tag{6.18}$$

where $M_{*(\mathrm{young})}$ is the mass of very young (< 10 Myrs) stars, and the instantaneous SFR is estimated as $(M_{*(\mathrm{young})}/10^7)\, M_\odot\, \mathrm{yr}^{-1}$. The flux limit to detect a clump by [OIII] 5007Å line is $\sim 3 \times 10^{-18}\, \mathrm{erg\,s^{-1}\,cm^{-2}}$, which corresponds to signal-to-noise ratio of $S/N > 5$ with an exposure time of $\sim 10^4$ sec (Hashimoto et al., 2018; Jones et al., 2024c; Arribas et al., 2024; Matthee et al., 2023). The corresponding luminosity is $L_{[\mathrm{OIII}]\,5007\text{Å}} \sim 6 \times 10^7\, L_\odot$ at $z = 8$. Substituting this into Eq.(6.18), we obtain $M_{*,(\mathrm{young})} \sim 10^7\, M_\odot$ for a "detectable" clump.

We set the minimum radius to be $R_{\mathrm{clump}} \sim 100$ pc, which can be resolved by recent JWST NIRCam/NIRSpec IFU observations (e.g. Chen et al., 2023; Hainline et al., 2024a; Hashimoto et al., 2023; Harikane et al., 2025a). We therefore set the threshold grid grouping number as $N_{\mathrm{grid}} = 16$, corresponding to $R_{\mathrm{clump}} = \sqrt{N_{\mathrm{grid}}\Delta^2/\pi} = 113\,\mathrm{pc}$, where one grid area is $\Delta^2 = 50^2\,\mathrm{pc}^2$. The minimum clump size is around seven times larger than the minimum AMR resolution of 17 pc. We emphasize that our identified clumps correspond to unlensed observed clumps. Strong lensing can enhance the resolution up to the ~ 10 pc level (e.g. Adamo et al., 2024b; Bradley et al., 2024; Mowla et al., 2024).

For this minimum clumps to have "detectable" luminosity, i.e., to have young stellar mass of $M_{*(\mathrm{young})} \gtrsim 10^7\, M_\odot$, each grid should have a surface stellar mass density of $\Sigma_{M_{*(\mathrm{young})}} \geq 10^7/16\, M_\odot \mathrm{grid}^{-1} = 10^{8.5}\, M_\odot \mathrm{kpc}^{-2}$. This value also corresponds to the surface SFR density of $\Sigma(\mathrm{SFR}) \geq 1/16\, M_\odot \mathrm{yr}^{-1}\,\mathrm{grid}^{-1} = 10^{1.5}\, M_\odot \mathrm{yr}^{-1}\mathrm{kpc}^{-2}$. Figure 6.5 shows schematic pictures of our clump identification algorithm. By running Friends-of-Friends after picking up the pixels, we identify four clumps.

6.2.4 Abundance Matching

FirstLight simulation provides a velocity-selected sample of massive galaxies with $\log V_{\mathrm{circ}}\,[\mathrm{km/s}] \geq 2.3$ at $z = 5$. The output of the zoom-in simulations contains the galaxies and their progenitors but not other smaller galaxies in a cosmological volume. In order to estimate the comoving number density of low mass galaxies, we use the circular velocity function of Bolshoi N-body simulation, which has a larger volume of $(250\,h^{-1}\mathrm{cMpc})^3$ (Klypin et al., 2011, 2016; Rodríguez-Puebla et al., 2016). Figure 6.6 compares the velocity functions at $z = 9 - 6$ obtained from FirstLight (solid lines) with those from the Bolshoi simulation (dashed lines). The latter can be well approximated by

$$n(>V) = AV^{-3} \exp\left(-\left[\frac{V}{V_0}\right]^\alpha\right), \tag{6.19}$$

[8]Our linear fitted line for each redshift is

$$\begin{aligned}
\log_{10} L_{[\mathrm{OIII}]}\,[L_\odot] &= 1.16 \times \log_{10} \mathrm{SFR} + 7.89 \quad (z = 9)\\
\log_{10} L_{[\mathrm{OIII}]}\,[L_\odot] &= 1.16 \times \log_{10} \mathrm{SFR} + 7.74 \quad (z = 8)\\
\log_{10} L_{[\mathrm{OIII}]}\,[L_\odot] &= 0.87 \times \log_{10} \mathrm{SFR} + 7.97 \quad (z = 7)\\
\log_{10} L_{[\mathrm{OIII}]}\,[L_\odot] &= 0.97 \times \log_{10} \mathrm{SFR} + 7.67 \quad (z = 6).
\end{aligned}$$

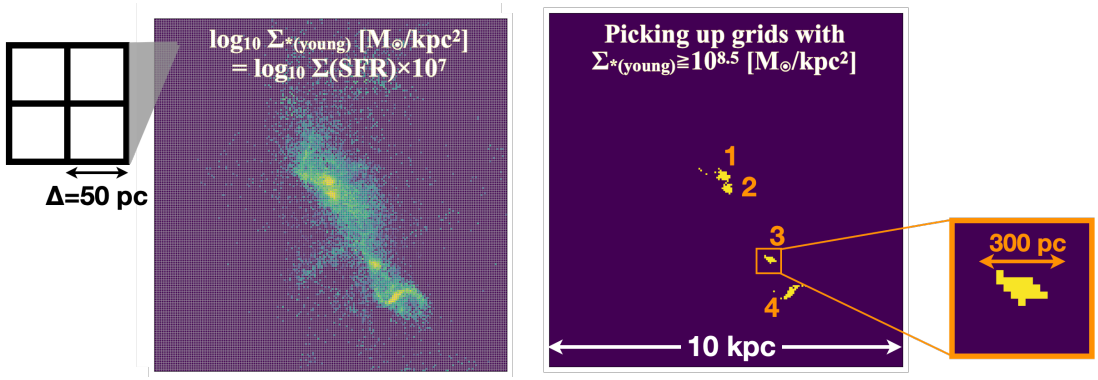

Figure 6.5: Schematic pictures of a clump finder. Left: The distribution of surface density of young (< 10 Myr) stellar particles. We overlaid gray grids with one side length of 50 pc. Right: Pixel distribution after picking up pixels with $\Sigma_{*(\mathrm{young})} \geqq 10^{8.5}\,M_\odot/\mathrm{kpc}^2$. Our clumpy identification algorithms identifies clumps with the radius over 113 pc (see Section 6.2.3.1).

where

$$A = 1.52 \times 10^4\,\sigma_8^{-3/4}(z)\,(h^{-1}\,\mathrm{Mpc/kms^{-1}})^{-3}, \tag{6.20}$$

$$\alpha = 1 + 2.15\,\sigma_8^{4/3}(z), \tag{6.21}$$

$$V_0 = 3300\frac{\sigma_8^2(z)}{1 + 2.5\sigma_8^2(z)}\,\mathrm{kms}^{-1}, \tag{6.22}$$

as derived in Klypin et al. (2011).

We reconstruct the halo and galaxy abundances in the following manner. We configure 20 velocity bins logarithmically scaled. In each bin, we calculate the ratio of the number density of the Bolshoi and FirstLight simulations, $R_i = n(> V_{\mathrm{circ}})_{,\mathrm{Bolshoi}}/n(> V_{\mathrm{circ}})_{,\mathrm{FL}}$. For each snapshot subscripted i, we compute the circular velocity ($V_{\mathrm{circ},i}$) of the galaxy and count the total number of galaxies within a velocity bin. We then use the ratio R_i as a weighting factor to derive the "true" number of single (clumpy) systems at a given redshift as

$$N_{\mathrm{single(clumpy)}}(z_{\mathrm{bin}}) = \sum_{i}^{\#\mathrm{snap}(z_{\mathrm{bin}})} \Theta R_i, \tag{6.23}$$

where Θ is set to 1 when snapshot i is single (clumpy) system and otherwise 0. Here $\#\mathrm{snap}(z_{\mathrm{bin}})$ represents the number of snapshots in each redshift bin. Dividing the number by the volume of the FirstLight simulation, i.e., $(40\,\mathrm{cMpc}/h)^3$, we obtain the number density of the single or clumpy systems at each redshift in Figure 6.14.

6.3 Result

6.3.1 Projection of Physical Properties for Simulated Clumpy Galaxies

Figure 6.7 and 6.8 shows projected maps for three examples of identified clumpy galaxies. Two, four, and three clumps are identified in these outputs as bright components. The clumps trace the distribution of young stars but also that of dense gas with $n_{\mathrm{gas}} \gtrsim 100\,\mathrm{cm}^{-3}$. Tail features can also be seen in [OIII] emission, similar to the recent galaxies observed by JWST (e.g., Hashimoto et al., 2023; Sugahara et al., 2025; Parlanti et al., 2025; Jones et al., 2024c). The distribution of the stars older than 100 Myrs appears more diffuse than the young stellar population. The underlying dark matter distribution shows signatures of mergers, which will be explained in

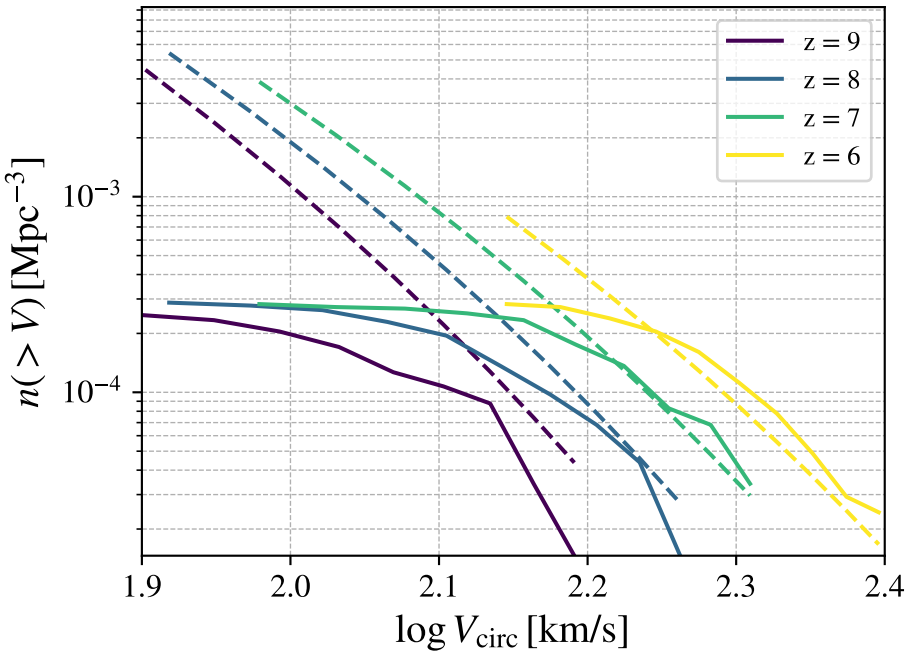

Figure 6.6: Velocity function of halos at z =9(purple), 8(blue), 7(green), and 6(yellow). Solid lines are obtained from FirstLight 62 samples, and dashed lines are from the Bolshoi simulation using the same cosmological parameter (Klypin et al., 2011).

detail in Section 6.3.3. Some clumps (e.g., clump C in Figure 6.7) are located off-center. The clumps are separated with $\sim 0.1-4$ kpc distances, similarly to the clumps at $z \simeq 6-8$ studied by Chen et al. (2023), with typical separations of $\sim$ 0.3 - 4.3 kpc. Such close clumps are also found in other JWST observations at $z > 6$; the JADES (Hainline et al., 2024a), EIGER (Matthee et al., 2023) and CANUCS (Asada et al., 2024) surveys. Figure 6.8 shows the similar projection map as the same as Figure 1.7, but for old stellar population (> 100 Myr), dark matter, and mass-weighted stellar age. Interestingly, old stellar distributions are different the young stellar distributions. For instance, FL958 has three main young stellar components in Figure 6.7, but has two old stellar components. This distinct distribution is also reflected in stellar age distributions, where we see spatial separations. Similar features are are found by JWST MIRI observations (e.g., Colina et al., 2023). Interestingly, even though our clump identification is based on bright [OIII] emitters, some clumps have old stellar age above 200 Myrs as shown in the right bottom clumps of FL958 in Figure 6.8. This clump might represent a recent rejuvenation of star formation, a scenario suggested by observations showing the coexistence of a Balmer break and bright emission lines such as [OIII] 5007Å(e.g., Witten et al., 2025; Kuruvanthodi et al., 2024).

The stellar age distributions in the right-most panels show a clear difference in the distribution of young and old components. Interestingly, similar features are found by JWST MIRI observations (e.g., Colina et al., 2023). Very recent observations report rejuvenate of star formation in high-redshift galaxies, i.e., co-existence of Balmer break and strong emission lines such as [OIII] 5007Å(Witten et al., 2025). The panels in the middle row focus on the galaxy FL957, which contains the highest number of clumps at $z > 6$. To see if those clumps are gravitationally bound or not, we have estimated the virial parameter (Bertoldi and McKee, 1992), $\alpha_{\rm vir} \equiv 5\sigma^2_{\rm clump} R_{\rm c}/GM$, where $\sigma_{\rm clump}$ and $R_{\rm c}$ are velocity dispersion within a clump and clump radius. All clumps have $\alpha \sim 0.2$, which indicates that these clumps are gravitationally bound.

The four-clump feature motivates us to compare it with the recent observation by Hashimoto et al. (2023), who spectroscopically studied the core of the most distant protocluster at $z = 7.88$,

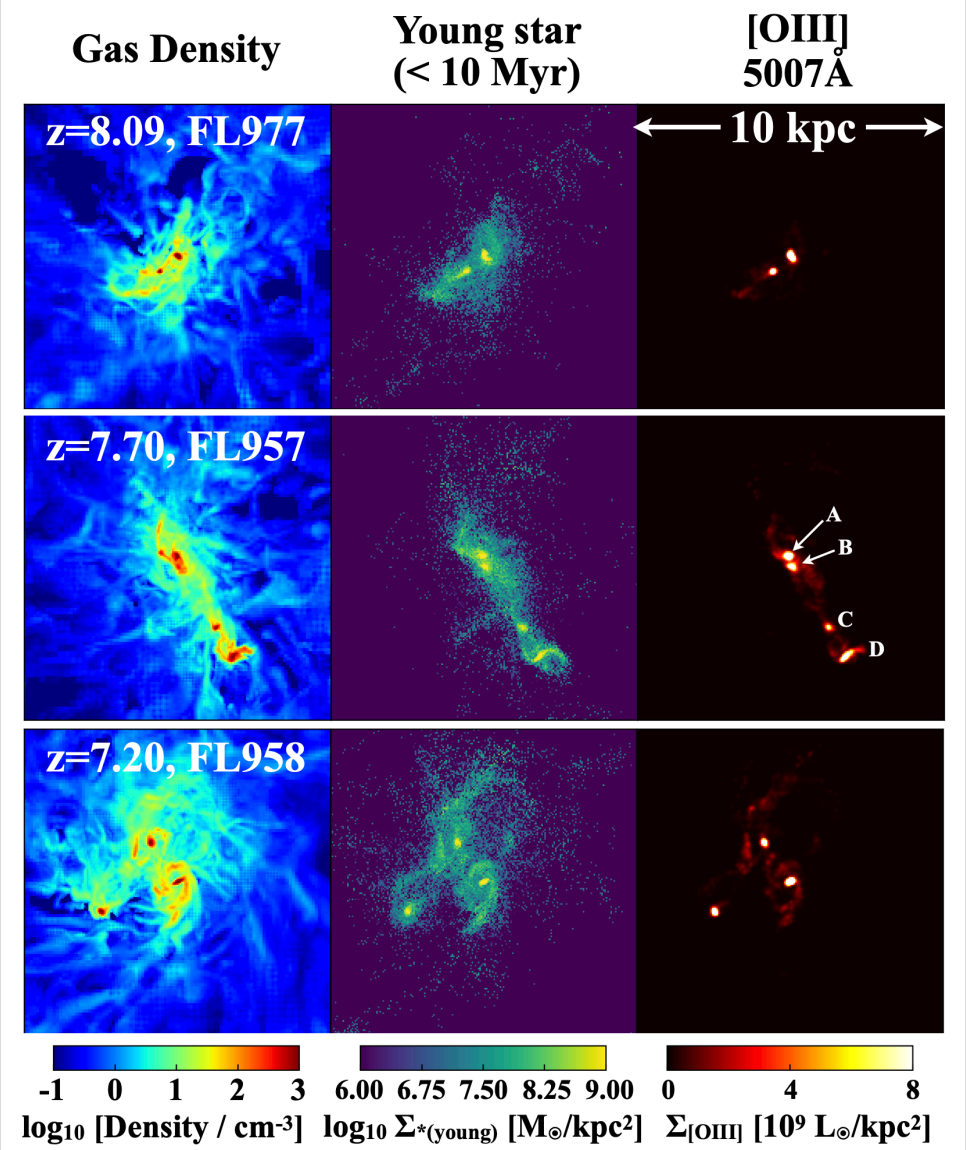

Figure 6.7: Three simulated clumpy galaxies at $z = 9.00$ (top, ID=FL977), $z = 7.70$ (middle, ID=FL957), and $z = 7.20$ (bottom, ID=FL958). Each column from left to right represents the averaged gas density, surface stellar mass density of young (< 10 Myr) population, [OIII] 5007 Å line flux, respectively. Each panel has a side length of 10 proper kpc and the same size of projected depth. This figure is taken from Nakazato et al. (2024).

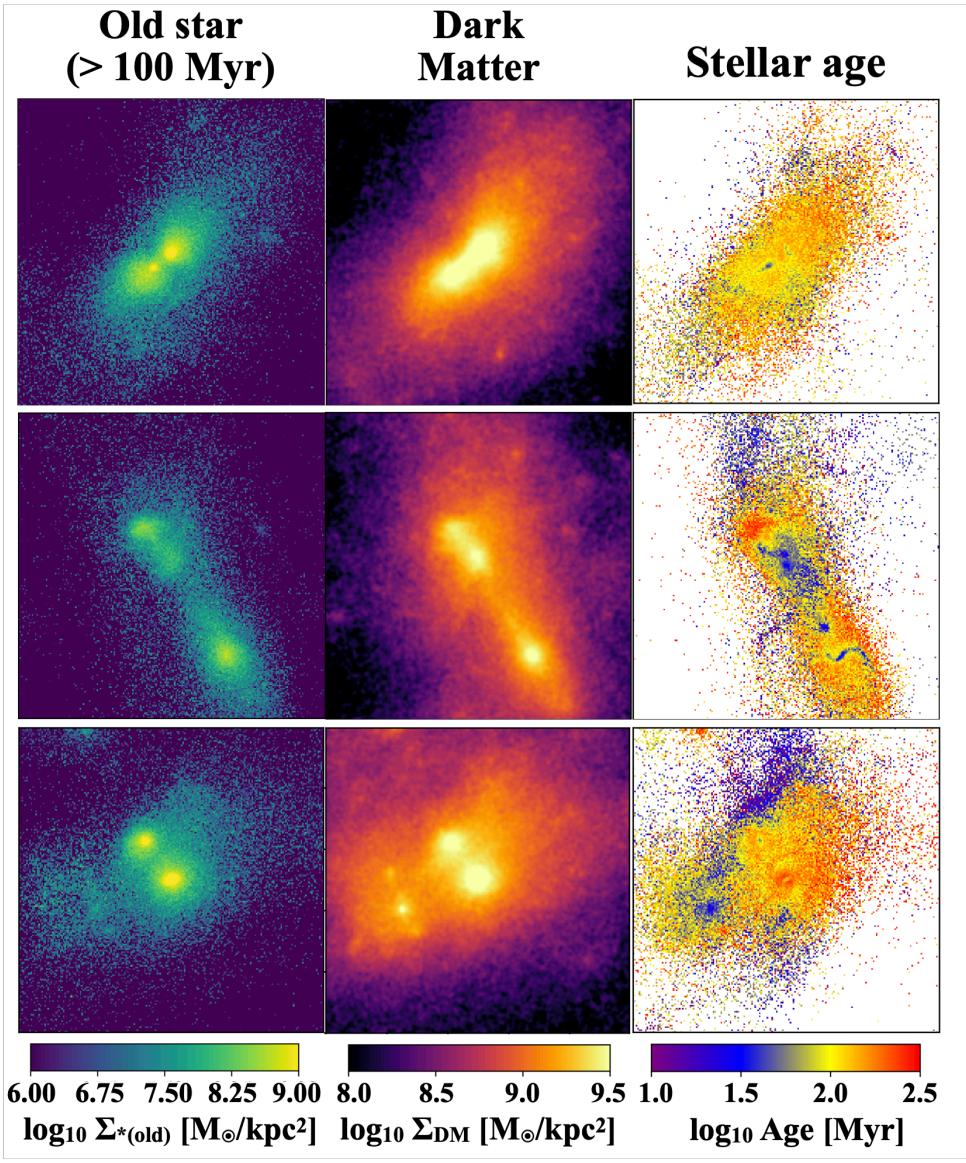

Figure 6.8: The same as Figure 6.7 but each column from left to right represents the surface mass density of old (> 100 Myr) stellar population and dark matter, and mass-weighted stellar age, respectively. This figure is taken from Nakazato et al. (2024).

	$M_{*,(\mathrm{young})}$ $[M_\odot]$	$M_{*,(\mathrm{all})}$ $[M_\odot]$	SFR $[M_\odot/\mathrm{yr}]$	$L_{[\mathrm{OIII}]\,5007\text{Å}}$ $[L_\odot]$	R_c [pc]	Age [Myr]
A	8.32×10^7	1.32×10^8	8.32	1.10×10^9	157	39
B	4.62×10^7	1.87×10^8	4.62	5.59×10^8	138	27
C	2.45×10^7	3.76×10^7	2.45	2.85×10^8	116	34
D	8.49×10^7	3.32×10^8	8.49	9.14×10^8	155	30

Table 6.3: Summary of properties of FL957 at $z = 7.70$, which contains four clumps within 10×10 kpc region. Note that $M_{*,(\mathrm{young})}$ refers to stellar masses younger than 10 Myrs and $M_{*,(\mathrm{all})}$ are stellar masses for all ages. A clump radius R_c in the 5th column is obtained as $R_\mathrm{c} = \sqrt{\Delta^2 N_\mathrm{grid}/\pi}$.

	# of clumps	$M_{*,(\mathrm{all})}$ $[M_\odot]$	$n_\mathrm{gas,clump}$ $[\mathrm{cm}^{-3}]$	Age [Myr]	R_c [pc]
single system	1503	5.2×10^9	283	134	234
clumpy system (total)	751	2.5×10^9	241	108	180
clumpy system (< 50 Myr)	182	2.7×10^8	269	35	142
clumpy system (> 50 Myr)	569	3.2×10^9	232	131	192
(single + clumpy) system	2254	4.3×10^9	269	125	216

Table 6.4: Summary of physical properties of galaxies we identify in single systems and clumpy systems. The clumps in clumpy systems are further categorized into two groups: those with ages younger than 50 Myr and older than 50 Myr. The last row of the table lists the average values for both systems. We see that old clumps (> 50 Myr) in clumpy systems have similar properties to ones in single systems, as discussed in section 6.3.2.

A2744-z7p9OD, with JWST NIRSpec integral field spectroscopy. The core region contains four clumps which are detected by [OIII] 5007 Å in a region of $\sim 11 \times 11$ kpc. Table 6.3 summarizes the clump properties. We find that the stellar mass, SFR, and [OIII] luminosities are similar to the observed clumps (see Table 1 in Hashimoto et al. (2023)). These properties are typical for clumps younger than 50 Myrs identified in the multiple systems, as shown in Table 6.4, which is discussed in the next section. We discuss that such properties are different from clumps older than 50 Myr in Section 6.3.2. In Sections 6.3.3 and 6.3.4, we show the formation and evolution of multi-clump systems.

6.3.2 Distributions of Clump Properties

Our clump finder identifies 2254 clumps in total. Of these, 1503 clumps are single systems, i.e., galaxies with one clump, often appearing as proto-bulge components. The remaining 751 clumps are in 325 clumpy systems. Table 6.4 summarizes the physical properties of the clumps. Figure 6.9 shows the distribution of the clump age weighted by stellar mass for single and multi-clump objects. The distribution for single systems has a peak at ~ 200 Myr, while the clumps in clumpy systems have a peak at ~ 90 Myr. Based on the age distribution, we can separate them into two types of clumps: clumps younger than 50 Myr and clumps older than 50 Myr, which are indicated by blue and red histograms, respectively.

Table 6.4 also shows the properties of clumps younger than 50 Myr and older than 50 Myr, respectively. We see that old clumps have similar stellar mass, age, and clump size to the clumps identified in single systems. Young clumps are smaller and their stellar mass is ten times lower than older clumps. Figure 6.10 shows the distributions of three properties for different systems: single systems with one clump ($N_\mathrm{clump} = 1$, black solid line), and young and old clumps in clumpy systems ($N_\mathrm{clump} \geqq 2$, red and blue). The probability distributions are normalized to the total number of clumps in each of the three systems.

The left panel of Figure 6.10 refers to the gas fraction ($f_\mathrm{gas} \equiv M_\mathrm{gas}/M_\mathrm{baryon}$) of individual clumps. Single systems have a distribution in the range of $f_\mathrm{gas} \sim 0.4 - 0.95$ and have the peak

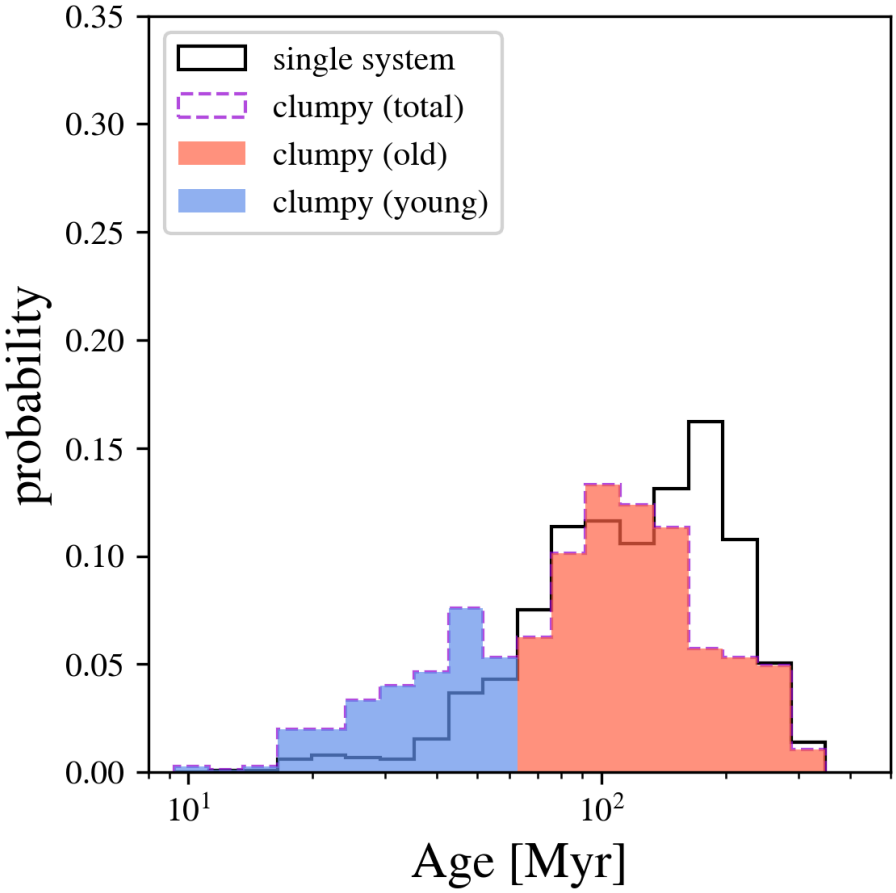

Figure 6.9: The distribution of mass-weighted clump ages. Black and dashed-purple histograms represent single systems (detected one central clump, i.e., proto-bulge) and clumpy systems, respectively. The histograms are normalized by the total number of clumps for each system. We divide the clumpy system into clumps younger than 50 Myrs (blue) and those older than 50 Myrs (red). This figure is taken from Nakazato et al. (2024).

at roughly $f_{\rm gas} \sim 0.85$. While clumps younger than 50 Myrs concentrate on the value of 0.95, clumps older than 50 Myrs have almost the same distribution as single systems.

The middle panel of Figure 6.10 refers to the surface mass density ratio of baryon and dark matter. Single systems have a peak at $\Sigma_{\rm baryon}/\Sigma_{\rm DM} \sim 10$, and the clumps older than 50 Myr have almost the same distribution and peak value. The shape of the distribution of clumps younger than 50 Myr is similar to the old ones, but the peak is shifted to a 0.5 dex larger value. This implies that over 50% of young clumps are formed off-center of their host dark matter halos, i.e., in a baryonic-rich environment.

The right panel of Figure 6.10 refers to the sSFR of individual clumps. The peak of the distribution for single systems is at sSFR $\sim 6\,{\rm Gyr}^{-1}$, while the peaks for old and young clumps are at ~ 10 and $55\,{\rm Gyr}^{-1}$, respectively. The sSFR values of single systems and old (> 50Myr) clumps in clumpy systems are similar to that of main-sequence galaxies at $z \sim 6$, sSFR $\sim 6\,{\rm Gyr}^{-1}$ (Popesso et al., 2023). However, young clumps in clumpy systems have over 9 times larger sSFR than that of main-sequence galaxies, and such large values are also seen in observed merging galaxies at $z > 6$ (e.g., Sugahara et al., 2025).

From the three physical properties in Figure 6.10, we see that clumps older than 50 Myr tend to have the same properties as single systems. On the other hand, clumps younger than 50 Myr are located in baryonic-rich environments. They are also gas-rich and in the process of bursty star formation. This indicates a different formation path for young clumps.

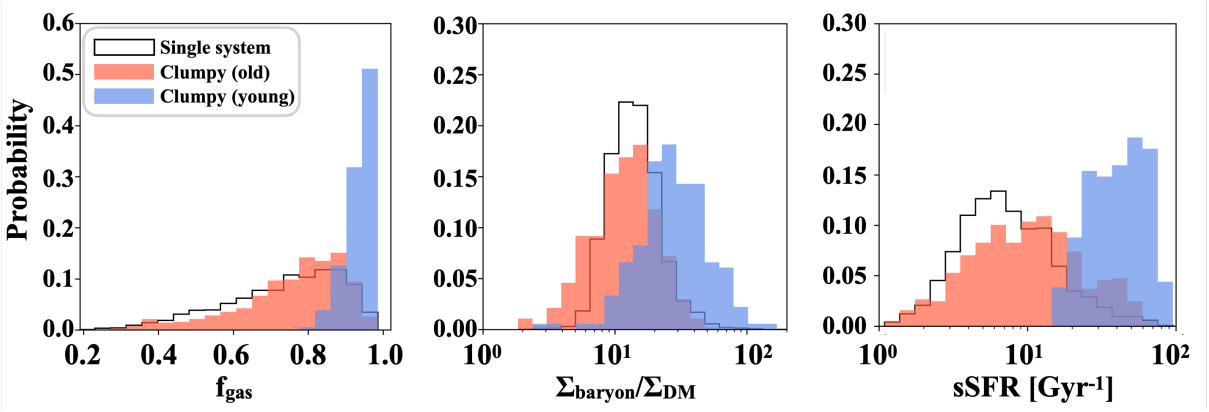

Figure 6.10: The probability distribution of the gas fraction, baryon-to-dark matter mass ratio, and specific star formation rate for our clump samples. The histograms with black solid lines are for single systems, and we color the histograms for clumps depending on their age. The distributions are normalized to the total number of clumps in each of the colored types. This figure is taken from Nakazato et al. (2024).

6.3.3 Clump Formation Induced by Merger

In this section, we study the formation of clumps during a merger. The top panels of Figure 6.11 show the time evolution of dark matter distribution around FL957, and the bottom panels represent gas density distribution in the same central region of 10 kpc. At $z = 8.01$, we see two dark matter halos, one in the center of the panel and the other one in the right bottom. The two galaxies experience the first pericenter passage at $z = 7.85$, which enhances the tidal compression of the surrounding gas and forms dense clumps. After the first passage ($z = 7.70$), we identify four clumps and this number is larger than that of merging halos. These clumps are formed off-center from the halos. Tail structures coming from clumps are formed by tidal effects during the galaxy interaction [9]. The formation of clumps triggered by galaxy merger has been investigated by isolated simulations which initially set an Antennae-like galaxy merger (e.g., Renaud et al., 2013, 2014, 2015). These previous studies have found that the first two pericenter passages increase compressive (curl-free) turbulence and lead to clumpy morphologies and bursty star formation with a timescale of 10-30 Myr. Their results are consistent with our findings from cosmological simulations at high redshift. Unlike the isolated simulations, which set initial parameters for galaxies and their orbits to reproduce the morphology and kinematics of merging galaxies (e.g., Renaud et al., 2013, 2015; Fensch et al., 2017; Maji et al., 2017), our cosmological simulations naturally demonstrate the formation of clumps due to mergers occurring at high redshift. Our simulations can also investigate statistics by connecting to a major merger rate density (see section 6.3.5).

We estimate the mass of a perturber that generates clumps based on the 0th-order approach of a spherical collapse model for a homogeneous sphere (Steidel et al., 1998; Overzier, 2016). A merger-induced clump is formed if the mass is

$$M_{\rm clump} = \bar{\rho}\delta \times V_{\rm clump} \gtrsim M_{\rm min}, \tag{6.24}$$

where $M_{\rm min}$ is the minimum baryon mass of the observable clump we define. Here, $\bar{\rho}$, δ, $V_{\rm clump}$ are the mean gas density around the progenitor, typical overdensity induced by the merger, and volume of the formed clump. Assuming that the perturber compresses the surrounding gas contained in a volume with its size $\sim R_{\rm per}$, the formed clump mass is re-written as

$$M_{\rm clump} = 2 \times 10^8\, M_\odot \left(\frac{\bar{\rho}\delta}{250\,{\rm cm}^{-3}}\right)\left(\frac{R_{\rm per}}{200\,{\rm pc}}\right)^3. \tag{6.25}$$

[9]The movie of clump formation is obtained here. The movie shows the time evolution of gas (left) and dark matter (right) densities from $z = 8.5$ to $z = 7.0$.

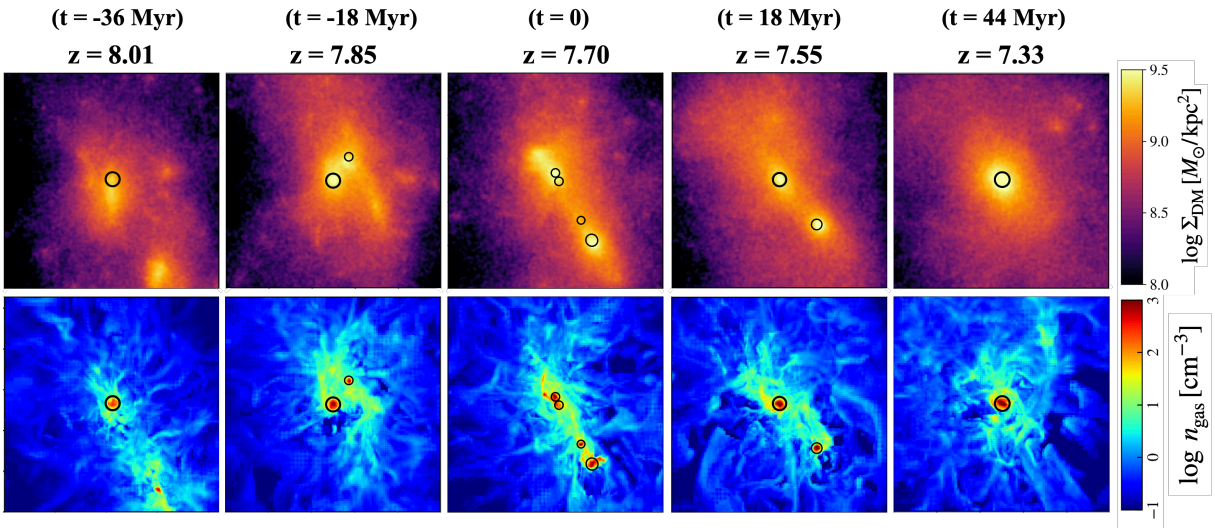

Figure 6.11: Time evolution of dark matter density (top) and gas density distribution (bottom) from $z = 8.01$ to $z = 7.33$. The side and projected lengths are 10 kpc for both projections. The black circles represent the location of the identified clumps. We set $t = 0$ at $z = 7.70$, when the galaxy consists of four luminous clumps. This figure is taken from Nakazato et al. (2024).

We normalize the relevant quantities by typical values found in our simulations (Table 6.4). For example, $\bar{\rho}\delta \sim 250\,\mathrm{cm}^{-3}$. The minimum mass of a clump that emits [OIII] lines bright enough to be observed is derived based on the young stellar mass criteria $M_{*(\mathrm{young}),\mathrm{min}} = 10^7\,M_\odot$ in section 6.2.3.1,

$$M_{\mathrm{min}} \sim \frac{M_{*(\mathrm{young}),\mathrm{min}}}{1 - f_{\mathrm{gas}}} = 10^8\,M_\odot \left(\frac{1 - f_{\mathrm{gas}}}{0.1}\right)^{-1}, \tag{6.26}$$

where f_{gas} is the gas fraction defined in section 6.3.2. Young clumps have $f_{\mathrm{gas}} \sim 0.9$ (Figure 6.10). Substituting equations (6.25) and (6.26) into Eq.(6.24), we obtain the characteristic size of the baryonic "wake" induced by merger encounter (perturber) as $R_{\mathrm{per}} \gtrsim 150 - 200\,\mathrm{pc}$. The mass ratio $q \equiv M_{\mathrm{center}}/M_{\mathrm{per}}$ largely determines the subsequent morphological evolution and the mode of triggered star formation. We assume the central one is more massive, i.e., $M_{\mathrm{center}} \geq M_{\mathrm{per}}$. Considering that the central object in the system has a typical size of $R_{\mathrm{center}} \simeq 200 - 230\,\mathrm{pc}$ as listed in Table 6.4 and assuming that both objects have similar gas densities, we estimate the mass ratio to be $q = (R_{\mathrm{center}}/R_{\mathrm{per}})^3 = 1 - 3.6$. We thus argue that bright clumpy galaxies in optical emission lines at $z > 6$ can be formed by a major merger.

6.3.4 Clump Fate

Figure 6.11 also follows the subsequent evolution of the clumpy system. A further 18 Myr after the formation of the four clumps, Clump B and C merge with clump A and D resulting in two clumps, which finally merge into a single system 26 Myrs later.

Figure 6.12 shows the redshift evolution of the number of clumps for the three galaxies shown in Figure 6.7. Clumpy structures are observed temporarily and finally merge into the center of the system 30-40 Myr after the multiple systems are formed, whose evolution is seen in other galaxy samples. The typical timescale is the crossing time during the merger:

$$t_{\mathrm{cross}} = \frac{d}{v - v_{\mathrm{center}}} \sim 50\,\mathrm{Myr} \left(\frac{d}{3\,\mathrm{kpc}}\right) \left(\frac{v - v_{\mathrm{center}}}{60\,\mathrm{km/s}}\right)^{-1}, \tag{6.27}$$

where d and v_{center} are the separation and the velocity of the central object. The derived crossing timescale is consistent with the merger timescale in Figure 6.11, and roughly the same order

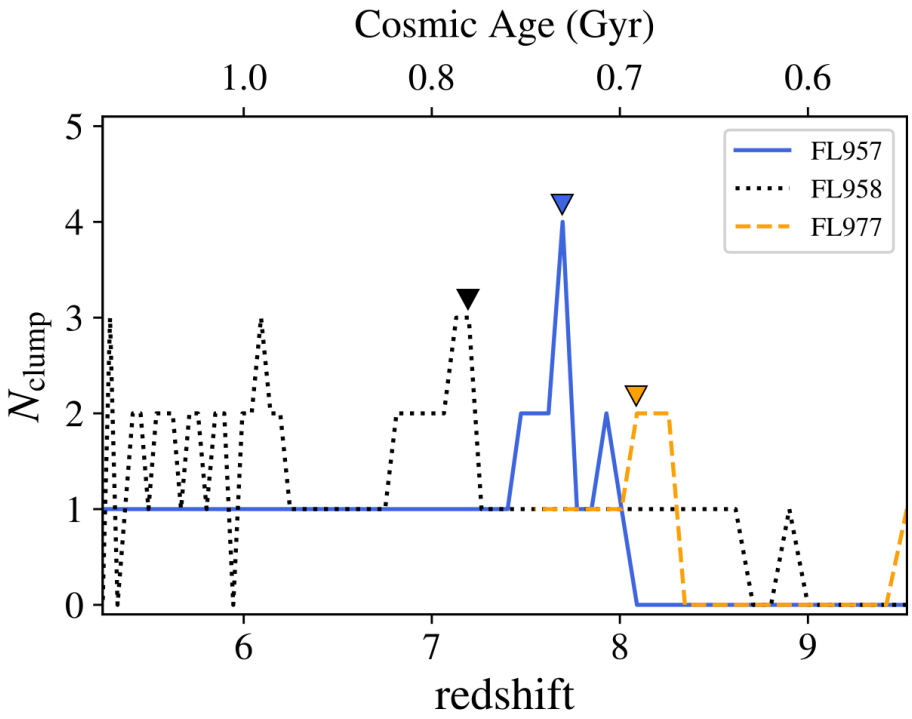

Figure 6.12: Time evolution of clump number as a function of redshift for the three galaxies shown in Figure 6.7. The inverted triangles represent the redshifts in Figure 6.7. $N_{\rm clump} = 0$ represents that clumps are too faint to be identified by the clump finder. This figure is taken from Nakazato et al. (2024).

of the orbital (dynamical) timescale of this system in a 10 kpc region, $t_{\rm orb} \sim t_{\rm dyn} \sim 25\,{\rm Myr}$. Therefore, we see that clumpy systems which are bright in rest-frame optical emission lines are temporary structures and finally merge into one massive galaxy within ~ 50 Myr.

Notice that the two galaxy systems (FL957, FL977) in Figure 6.12 are identified as $N_{\rm clump} = 0$ at $z \sim 9$. This implies that these galaxies are too faint to be identified as an [OIII] bright object at $z \sim 9$. As noted in Section 6.2, our clump identification is based on surface SFR density and the threshold value is 30 $M_\odot\,{\rm yr}^{-1}\,{\rm kpc}^{-2}$ (corresponding to 1 $M_\odot\,{\rm yr}^{-1}$ per clump). However, a lensing effect enables us to identify clumpy features even at $z \gtrsim 9$ as the recent observations report triply lensed galaxies at $z = 10.17$ (Hsiao et al., 2023, 2024).

We check other clumpy galaxies evolutions and the formed clumps are ended in merger into the central component within a few tens of Myrs.

Since our simulations end at $z = 5$, we cannot follow the further evolution to the present day. Some galaxies form clumps via disk instabilities at $z < 6$, outside the redshift range investigated here. Such clumps still exist at the final snapshot, $z = 5$, but most probably they migrate to the center or they are disrupted due to feedback. Due to our limited resolution, we cannot exclude the possibility that the densest regions of the clumps formed proto-globular clusters that may survive all these events. Future modeling will be required to follow their evolution.

6.3.5 Number Abundance of Clumpy Galaxies

Figure 6.13 represents the fraction of clump number at each redshift. Around 90% of galaxies at $z = 8 - 6$ are observed as a single system ($N_{\rm clump} = 1$). From Table 6.3 and 6.4, we see that both observable clumpy galaxies tend to have stellar masses of $M_* \gtrsim 10^9\,M_\odot$ in their systems, even though our clump definition sets a minimum clump mass of $M_* \geq M_{*({\rm young}),{\rm min}} = 10^7\,M_\odot$. Our sample galaxies at $z \geq 8.5$ have small stellar masses of $M_* \lesssim 10^9\,M_\odot$, resulting in that all of our samples at $8.5 \leq z \leq 9$ are identified as a single system. At these high-redshifts, the

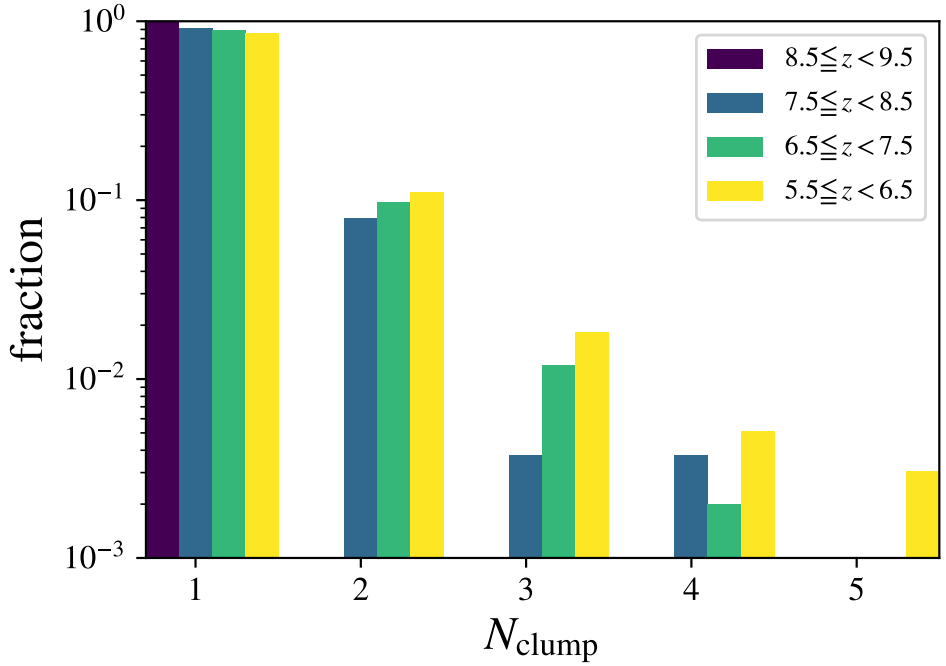

Figure 6.13: The fraction of each clump number at $z \sim 9$ (purple), $z \sim 8$ (blue), $z \sim 7$ (green), and $z \sim 6$ (yellow). The clump number $N_{\rm clump}$ is referred to as the number of clumps in the galaxy system within 10 kpc ×10 kpc region. This figure is taken from Nakazato et al. (2024).

corresponding UV magnitude is $M_{\rm UV} \gtrsim -19.7$ [10]. Galaxies at $z \lesssim 8$ are bright ($M_{\rm UV}$ < - 19.7) and multiple clumps are identified, which are formed by mergers. This trend is interestingly consistent with the recent JWST observations of Chen et al. (2023), who find that luminous $z \simeq 6-8$ galaxies with $M_{\rm UV} < -20.7$ tend to have 3-4 clumps and fainter galaxies with $M_{\rm UV} > -20.7$ tend to be a single system. The fraction of galaxies with three or more clumps ($N_{\rm clump} \geqq 3$) is $\sim$ 0.5 - 1%. Since the third/forth components are formed by tidal debris, the multi-clump formation efficiency might be affected by the orbit of mergers. (Renaud et al., 2009) follow a merger system in a non-cosmological simulations and find that protograde configurations can form tidal tails but retrograde configuration does not form tails because of less tidal torques.

We also evaluate whether some physical processes such as AGN feedbacks and cosmic rays can suppress the formation of clump. Since these processes are not considered in our simulations, we roughly estimate their effects in the following discussions. or AGN feedback, the timescale is assumed to be roughly the same as BH growth timescales, i.e., Salpeter timescale

$$t_{\rm Sal} = \frac{M_{\rm BH}}{\dot{M}_{\rm Edd}} = \frac{\sigma_{\rm T} c \epsilon_{\rm R}}{4\pi G m_{\rm p}} = 45\,{\rm Myr}\left(\frac{\epsilon_{\rm R}}{0.1}\right), \tag{6.30}$$

where $\sigma_{\rm T}, \epsilon_{\rm R}$ are the cross section of Thomson scattering and the radiative efficiency. The average clump gas density in our simulation is $\sim 250\,{\rm cm}^{-3}$, and the corresponding free-fall time scale is

$$t_{\rm ff} = \sqrt{\frac{3\pi}{32}}\frac{1}{\sqrt{G\rho}} \sim 3.2\,{\rm Myr}\left(\frac{n_{\rm gas}}{250\,{\rm cm}^{-3}}\right)^{-1/2}. \tag{6.31}$$

[10] We use the scaling relation between stellar mass and UV magnitude obtained from Ceverino et al. (2017, 2019) as follows,

$$M_{\rm UV} = \frac{\log_{10} M_* - 6}{\alpha_*} + M_*^* \ ({\rm for}\ z = 6-7), \tag{6.28}$$

$$M_{\rm UV} = \frac{\log_{10} M_* - 6}{\alpha_*} + M_*^* - 1 \ ({\rm for}\ z = 8-9), \tag{6.29}$$

where $\alpha_* = -0.394 \pm 0.002$ and $M_*^* = -12.13 \pm 0.03$.

Therefore, the clump formation (star formation in clumps) can occur before the AGN feedback becomes dominant. For cosmic rays (CR) feedback, CR loses the energy by Coulomb and ionization interactions and heats the thermal gas (Enßlin et al. (2007)), which leads to increasing of effective pressure of gas and suppressing star formation. Jubelgas et al. (2008) perform cosmological simulations including CR physics, and calculate the contribution of the CR pressure to the total pressure ($P_{\rm CR}/(P_{\rm CR}+P_{\rm thermal})$). We compare their results at $z=6$ and find that the CR pressure contribution can be expected to be less than 10% for our clump gas density($\sim 250\,{\rm cm}^{-3}$), which implies CR does not affect the star formation in the formed clumps.

We do not find any clumpy systems formed by violent disk instability (VDI) through cold accretion until $z\sim 6$. This is because VDI requires a massive disk with a large disk mass fraction (Dekel et al., 2009b; Ceverino et al., 2010). We identify some disk-like galaxies at $z=8-9$, but the stellar masses are $\lesssim 5\times10^9\,M_\odot$ and have smoothed disk. Specifically, two galaxies with five clumps are seen in a massive system; the total stellar mass in the field is $M_*\sim 10^{10}\,M_\odot$ at $z\sim 5.5$. The clumps in such a massive system are expected to be formed via violent disk instability as same as lower-redshift galaxies (Mandelker et al., 2014, 2017; Ceverino et al., 2023; Inoue et al., 2016b).

Figure 6.14 shows the number density of clumpy galaxies. As described in Section 6.2.1, our study employs zoom-in simulations and we need to correct for incompleteness in the number count of clumpy galaxies. We use the results of a larger boxsize N-body simulation (Klypin et al., 2011) (refer to Appendix 6.2.4 for details). The number density of single systems is $(1-3)\times10^{-4}\,{\rm cMpc}^{-3}$ at $z=6-9$. We identify all the simulated galaxies at $z=9$ as single systems and the number density is consistent with the UVLF at $M_{\rm UV}\sim-20$ (Harikane et al., 2023). At $z=6-8$, we estimate the number density to be $(1-5)\times10^{-5}\,{\rm cMpc}^{-3}$, and this value is enough to be observed by recent JWST surveys. The EIGER survey (Kashino et al., 2023) conducted deep JWST/NIRCam wide-field slitless spectroscopic observations and identified 117 [OIII] emitters at $z=5.33-6.93$ (Matthee et al., 2023). They found that $\sim$ 1% of their observed [OIII] emitters are closely separated within <1" (corresponding to $\lesssim 6$ kpc at $z\sim6$). They also derived the [OIII] luminosity function at $z\sim6$. We integrate it within the luminosity range for their samples and obtain the number density of their observed [OIII] emitters, $n_{\rm [OIII]}=10^{-2.8}\,{\rm cMpc}^{-3}$. Thus, we can estimate the number density of clumpy systems of their observed [OIII] emitters as $\sim 0.01\times n_{\rm [OIII]}=1.6\times10^{-5}\,{\rm cMpc}^{-3}$, consistent with our theoretical abundance of clumpy galaxies at $z=6-8$.

We can also derive the merger rate density from the clumpy systems within a 10 kpc $\times$ 10 kpc region following Mo et al. (2010). Under the assumption that these pairs will merge on a time scale $\tau_{\rm mrg}$, the merger rate density is related to the clumpy factor $f_{\rm clumpy}\equiv$ (# of clumpy systems with $N_{\rm clump}\geqq 2$)/(# of total systems), according to

$$\begin{aligned}\dot{n}_{\rm mrg}&=\frac{1}{\langle N_{\rm clump}\rangle}\frac{f_{\rm clumpy}n_{\rm gal}}{\tau_{\rm mrg}}\\&=6.3\times10^{-5}\,{\rm cMpc}^{-3}\,{\rm Gyr}^{-1}\left(\frac{f_{\rm clumpy}}{0.1}\right)\left(\frac{n_{\rm gal}}{10^{-4}\,{\rm cMpc}^{-3}}\right)\left(\frac{\tau_{\rm mrg}}{80\,{\rm Myr}}\right)^{-1},\end{aligned}\tag{6.32}$$

where $\langle N_{\rm clump}\rangle$ is the averaged clump number among clumpy systems. The factor $1/\langle N_{\rm clump}\rangle$ takes into account the fact that a multi-clump system ends in a single merger. Figure 6.13 shows that $\sim$ 80 - 90% of clumpy systems consist of two clumps, and we thus adopt $\langle N_{\rm clump}\rangle=2$. We obtain the clumpy factor from Figure 6.14 as $f_{\rm clumpy}\sim0.1-0.2$ and see that the value does not change very much at $z=6-9$, which is consistent with the recent JWST observation results (Duan et al., 2025). For the comoving number density of galaxies population $n_{\rm gal}$, we obtain $n_{\rm gal}\sim10^{-4}\,{\rm cMpc}^{-3}$ with $M_*\gtrsim10^9M_\odot$ [11] from Figure 6.14. The value also does not change largely within a factor of 1-2. We adopt the crossing timescale (Eq. (6.27)) as the merger

[11]This stellar mass is for a galaxy system within 10 kpc $\times$ 10kpc, not each clump stellar mass.

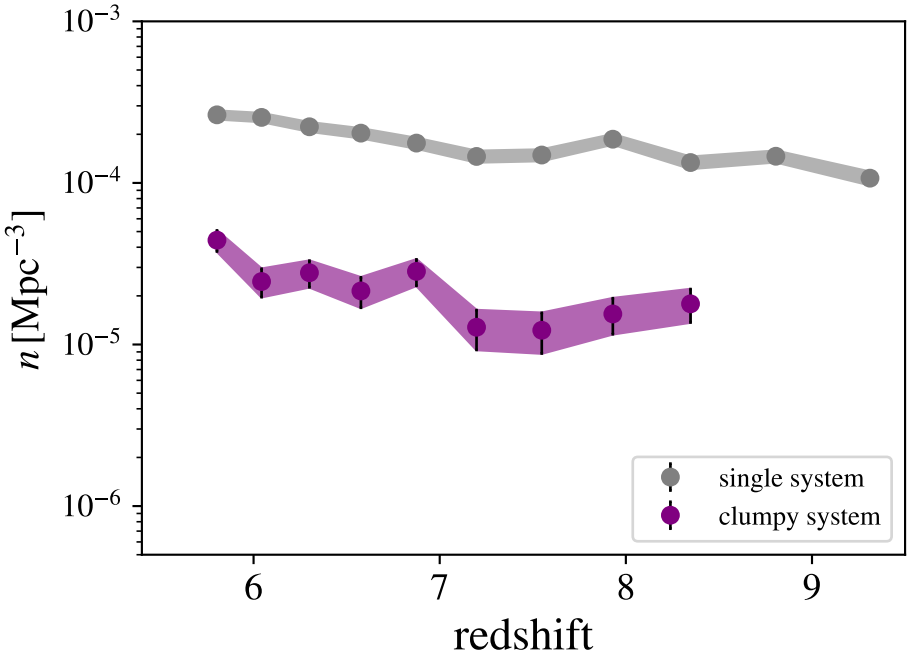

Figure 6.14: The number density of clumpy galaxies as a function of redshift. The gray and purple plots represent single systems and clumpy systems, respectively. The error bars are calculated from Poisson errors, $\sqrt{N}/V_{\rm box}$, where N is the number of clumpy galaxies and $V_{\rm box}$ is the comoving volume of the simulation box. This figure is taken from Nakazato et al. (2024).

timescale $\tau_{\rm mrg}$. In our case, we take into account a galaxy pair located within a 10 kpc $\times$ 10 kpc region, i.e., the separation of $d \sim 5$ kpc, which gives $\tau_{\rm mrg} \sim 80\,$Myr. The merging timescale is also seen in the top panels of Figure 6.11. Adopting this merger as a typical case, we obtain the merger rate density of $\dot{n}_{\rm mrg} = 6.3 \times 10^{-5}\,{\rm cMpc^{-3}\,Gyr^{-1}}$. This value is roughly consistent with the results from Millennium Simulation at $z > 6$ (fig.2 in Kitzbichler and White, 2008). We also compare our merger rate density with that of Illustris simulations. Rodriguez-Gomez et al. (2015) derive the major merger rate $\sim 1\,{\rm Gyr^{-1}}$ for the descendant stellar masses of $\sim 10^9\,M_\odot$ at $z = 6 - 9$. From the stellar mass function at $z > 6$ of Illustris simulations (Genel et al., 2014), the corresponding number density of the descendant mass is $\sim 10^{-4}\,{\rm cMpc^{-3}}$. Therefore, the major merger rate density is $\sim 10^{-4}\,{\rm cMpc^{-3}\,Gyr^{-1}}$, which is in good agreement with our values. These consistencies infer that clumpy galaxies, which are bright in rest-frame optical emission lines, can be linked to major mergers.

6.4 Discussion & Summary

We have studied formation of clumpy galaxies in the epoch of reionization observable in rest-frame optical emission lines. The clumps we identify are bright in [OIII] 5007Å and have radii of $\sim$ 150 - 200 pc, which can be resolved by JWST. We have shown that the observable large clumps are formed by major mergers. The clumps are categorized into two types: proto-bulges dominated by stellar populations older than 50 Myr and off-centered clumps dominated by younger stellar populations. The latter type of clump is formed from gas debris in tidal tails induced by the mergers. The merger-driven clumps tend to have a high gas fraction of over 90%, trigger bursty star formation with sSFR $\sim 20 - 100\,{\rm Gyr^{-1}}$, and produce young stellar components. The clumpy galaxies account for $\sim 10\%$ of the population, and the fraction remains roughly constant from $z = 9$ to $z = 6$. We also find that the clumpy systems are short-lived, ending in a merger with a companion(s) within a few tens of Myrs. The number density of clumpy systems is estimated to be $(1 - 5) \times 10^{-5}\,{\rm cMpc^{-3}}$, which is large enough to be observed

in recent JWST surveys (Matthee et al., 2023).

Formation of clumpy galaxies at $z \lesssim 4$ has been studied in detail (Mandelker et al., 2014, 2017; Buck et al., 2017; Ceverino et al., 2023; Inoue et al., 2016b). Especially, Mandelker et al. (2014) study clump formation in 29 galaxy samples at $z = 1-4$. They define clumps as baryonic overdensities in three dimensions.

They find that 70% of the clumps are formed *in situ* by violent disk instability while the remaining 30% are formed *ex situ* by minor mergers. In the present paper, we study clump formation at $z = 6-9$ using high-resolution simulations.

We define the clumps as [OIII] bright objects based on the threshold surface star formation rate so that they can be observed by JWST with a reasonable exposure time. We find that most of the observable clumps are formed by mergers of galaxies with roughly the same baryonic mass. A sufficiently large "perturber" comparable to the central object with size ~ 200 pc can generate gas wakes and overdensities to form large, bright clumps. Interestingly, we do not identify any VDI-driven clumps at $z > 6$ in our simulations. There are two possibilities for no VDI-driven clumps at $z > 6$; resolution limits or less disk fractions. For the former factor, Mayer et al. (2025) recently reproduce VDI-driven clumps with less massive galaxies ($M_* \sim 10^8\,M_\odot$) at $z = 7$ in their simulation. The sizes of formed clumps are a few pc, which are consistent with Toomre wavelength (Boley et al., 2010). The clump size is smaller than both our simulation resolution. However, such clumps are also smaller than the minimum size of our defined clumps, and are not be observed without lensing effects and the derived clumpy fraction will not be affected. The latter factor indicates that violent disk instability (VDI) might less likely to occur in low-mass galaxies because the disk mass itself is small (Dekel et al., 2009b).

In the VDI case, even when it occurs, clumps contain only 1-2 % of the mass of the central object (Ceverino et al., 2010), rendering them too faint to be detected through current observations. Our result suggests a change of the mode of clump formation from the predominantly merger-driven scenario in the early universe to VDI at low redshifts at $z \lesssim 4-5$.

There are still some caveats in our study. Firstly, we define clumps by adopting a constant threshold of surface star formation rate density. The constant value is motivated to identify observable clumps, but at the same time, we might miss clumps in low-mass galaxies at $z \sim 9$. Such unidentified low-mass clumps might correspond to proto-globular clusters. Recent JWST photometric observations in gravitational lens fields have found young stellar cluster candidates with $M_* = 10^5-10^6\,M_\odot$ at $z = 6-10$ (Vanzella et al., 2022, 2023a; Adamo et al., 2024b; Bradley et al., 2024; Mowla et al., 2024). The star clusters are also very small in size with effective radii of less than 1 pc (Adamo et al., 2024b), which our simulations cannot resolve. Some cosmological simulations focus on the formation of dwarf galaxies and stellar clusters at $z > 6$ and have sub-pc scale resolution (Ma et al., 2018a,b; Calura et al., 2022; Garcia et al., 2023; Sugimura et al., 2024; Garcia et al., 2025), allowing one to study the formation of smaller-scale structures.

Second, our clump identification is based on rest-frame optical emission lines. Statistics of high-z ($z > 6$) clumpy galaxies have been conducted from rest-frame UV observation by HST (e.g., Shibuya et al., 2016; Bowler et al., 2017, 2022; Meštrić et al., 2022). Some samples have also been observed by ALMA, and they have offsets between FIR emission regions and UV emission regions (Carniani et al., 2017). Recent JWST multi-band photometry or IFU observations enable us to perform multiwavelength studies of clumpy galaxies, from the rest-UV to NIR. The number of clumps is often reported to have spatial offsets between UV, optical, and NIR wavelengths (Colina et al., 2023; Bik et al., 2023; Kalita et al., 2024; Rodighiero et al., 2024a), while Treu et al. (2023) find no dramatic morphology changes across multi-bands. We note that multi-component observations at high redshift ($z > 6$) are more challenging than at lower redshift (e.g. $z \sim 2-3$, Meštrić et al., 2022; Zanella et al., 2024), where galaxy morphologies are most of the times less disturbed and present clearer features. Our study focuses on young giant clumps that are bright in [OIII] because rest-optical emission lines are less affected by dust attenuation than UV emission. These lines trace dense star-forming regions that are gravitationally bound and exist

as physical components (Claeyssens et al., 2023; Matthee et al., 2023). Clumps identified in UV-bands are expected to be heavily attenuated by dust in dense clouds of $n_{\rm gas} \geq 100\,{\rm cm}^{-3}$ (Figure 8.4). To detect UV clumps in the simulated galaxies and compare them with the current multiwavelength observations, we need to conduct post-processed three-dimensional radiative transfer calculation (e.g., SKIRT, Baes et al., 2011; Camps and Baes, 2020).

We have found that a clumpy system contains different stellar/clump populations: old ($>$ 50 Myr) clumps at the center of dark matter halos, and young ($<$ 50 Myr) off-centered clumps. The latter type of clumps originates from dense gas clouds that are formed in tidal tails during mergers. Observationally, it would be interesting to identify old clumps with ages of a few hundred Myrs. As shown in Figure 6.7 and 6.8, there are spatial offsets between the young ($\lesssim$ 50 Myr) and old ($\sim$ 300 Myr) components. Those old components are not detected as a clump based on our criteria. Recent JWST observations show that some clumps are detected in rest-frame optical emission lines and continuum, while others are detected only in continuum (e.g., Hashimoto et al., 2023). Detailed radiative transfer calculations would also enable us to understand the cause of the spatial offsets between young stellar populations and dust continuum emitting regions as seen in recent observations at $z > 6$ by ALMA (Tamura et al., 2023).

Emission line flux ratios provide crucial information on clump properties such as the ISM electron density, metallicity, and ionization parameters. For instance, Yang et al. (2023) use a zoom-in simulation to show that the ratio of $F_{\rm [OIII]\,5007\,\text{Å}}/F_{\rm [OII]\,3727\,\text{Å}}$ can be used to trace stellar populations younger than several Myr. The ratio is taken by some NIRSpec IFU/NIRISS observations to evaluate the ionization state and metalicity gradients in each pixel (Arribas et al., 2024; Saxena et al., 2024; Tripodi et al., 2024; Rodríguez Del Pino et al., 2024; Wang et al., 2022; Venturi et al., 2024). Line ratios are also measured for $z \sim 4$ lensed galaxies to determine and produce resolved dust-to-gas ratio maps (Birkin et al., 2023). Applying the same method to clumpy galaxies at higher redshift will enable us to characterize young and old clumps and to test the merger-driven scenario we propose here.

Furthermore, several Lyα emitters at $z \gtrsim 6$ are reported to be clumpy systems (e.g., MACS0416-Y1, SXDF-NB1006-2, BDF3299), indicating that clumps are distributed three-dimensionally and that such a distribution facilitates the escape of LyC and Lyα photons. Indeed, Witten et al. (2024) found that nine of their target galaxies at $z > 7$ exhibit clumpy structures in NIRCam photometry. Since the Lyα escape fraction correlates with the LyC escape fraction (Choustikov et al., 2024; Begley et al., 2024; Izotov et al., 2022), a large number of LyC photons can escape from such clumpy systems and contribute to the cosmic reionization.

Also, as shown in Figure 6.11, clumpy systems eventually merge into the central galaxy and evolve into massive single galaxies. After clumps fully merge, some galaxies in the FirstLight simulations develop extended, gas-rich disks, potentially contributing to the formation of the highest-redshift (cold-) disk galaxies, which have recently been observed with JWST and ALMA (Rowland et al., 2024). We conclude that by quantifying the contribution of environmental effects, such as galaxy mergers, to star formation histories and cosmic reionization, we can also gain insights into the subsequent dynamical evolution of galaxies.

Chapter 7

Spatially Resolved Dust Properties in Clumpy Galaxies

7.1 Introduction

Understanding when, where, and how dust forms in galaxies in the early Universe is crucial for accurately tracing the star formation history and galaxy evolution at high redshifts. The chemical composition, grain size distribution, and spatial geometry of dust relative to stellar populations all critically influence the dust attenuation curves of galaxies. Precisely determining these attenuation properties enables the reconstruction of intrinsic spectral energy distributions (SEDs) from observed attenuated SEDs, directly contributing to our understanding of the cosmic star formation rate (SFR) density evolution (e.g., Madau and Dickinson, 2014). As introduced in Chapter 4, dust-obscured star formation at high-redshift Universe is particularly helpful to understand galaxy evolution over cosmic time(Bouwens et al., 2016; Fudamoto et al., 2021; Algera et al., 2023; Barrufet et al., 2023; Zavala et al., 2021; Mitsuhashi et al., 2024).

Recent observational advances, particularly with the James Webb Space Telescope (JWST) in the rest-frame UV/optical and ALMA in the far-infrared (FIR), have opened new opportunities for studying dust properties in high-redshift galaxies. JWST observations are now enabling studies of dust attenuation curves through detailed SED fitting, revealing that approximately 20–30 % of high-z galaxies exhibit attenuation curves with pronounced UV bumps (Witstok et al., 2023; Markov et al., 2023, 2025; Ormerod et al., 2025; Fisher et al., 2025). These bumps imply the presence of polycyclic aromatic hydrocarbons (PAHs) or small carbonaceous grains (Li et al., 2024; Lin et al., 2025; Nanni et al., 2025). Meanwhile, ALMA continuum observations at FIR wavelengths, fitted with modified blackbody spectra, facilitate measurements of dust mass, dust temperature, and total IR luminosity. These quantities can then be combined to derive the IRX–β relation, defined as the relation between the infrared excess (IRX $\equiv L_{\rm IR}/L_{\rm UV}$) and the UV spectral slope ($\beta_{\rm UV}$) as introduced in Section 3.4.6.2. Historically, the IRX–$\beta_{\rm UV}$ relation was first introduced as a canonical relationship by Meurer et al. (1999), becoming widely used for correcting the total star formation activity in galaxies lacking direct infrared (IR) measurements (e.g., Overzier et al., 2011; Bouwens et al., 2007, 2009). However, it is known that local Ultra-Luminous Infrared Galaxies (ULIRGs) deviate significantly from this canonical relation, showing systematically higher IRX values and bluer UV slopes (Goldader et al., 2002). Recent ALMA observations of high-z galaxies reveal substantial scatter in their IRX–$\beta_{\rm UV}$ distributions (Fudamoto et al., 2020b,a; Capak et al., 2015; Barisic et al., 2017; Faisst et al., 2017; Bowler et al., 2024; Hashimoto et al., 2019; Bowler et al., 2022; Sugahara et al., 2025; Mitsuhashi et al., 2024), with examples of galaxies exhibiting either extremely high IRX values and blue slopes, similar to local ULIRGs, or low IRX values with redder slopes. These findings challenge the notion of a single "canonical" IRX–$\beta_{\rm UV}$ relation applicable across cosmic time.

Additionally, observational techniques now allow for detailed examinations of internal dust

distributions within galaxies at high redshifts. JWST high-resolution photometry using NIRCam enables pixel-by-pixel SED fitting to generate maps of visual attenuation (A_V)(e.g., Abdurro'uf et al., 2023; Giménez-Arteaga et al., 2023, 2024; Sun et al., 2024; Tanaka et al., 2024; Lines et al., 2025). NIRSpec integral field unit (IFU) observations allow construction of Balmer decrement maps through Hα/Hβ ratios (e.g., Parlanti et al., 2025; Ishikawa et al., 2025, , Mawatari et al. in prep.). Several recent JWST observations have reported that galaxies in the Epoch of Reionization (EoR) commonly exhibit clumpy morphologies (e.g., Chen et al., 2023; Hainline et al., 2024b; Shibuya et al., 2024; Lines et al., 2025; Harikane et al., 2025a). These observations highlight the importance of understanding how internal variations in dust properties and star formation influence integrated galaxy-scale measurements.

Galaxy clumps at high-z generally form via two primary mechanisms: mergers (ex-situ scenario) and violent disk instabilities (VDI, in-situ scenario) as discussed in Section 6.1. In Chapter 6, we conclude that approximately 10–20% of massive galaxies ($M_\star > 10^9\,M_\odot$) at high redshifts could be identified observationally as merger-driven clumpy systems (Nakazato et al., 2024). The observed clumpy fraction at EoR galaxies also supports the merger-driven clumps (e.g., Duan et al., 2025; Matthee et al., 2023). As galaxies evolve to massive gas-rich disks with $M_* \gtrsim 5 \times 10^9\,M_\odot$, VDI can produce 100 pc-scale clumps through gas accretion(e.g., Mandelker et al., 2025; Nakazato et al., 2024; Ceverino et al., 2010; Dekel et al., 2009b). While such internal variations could potentially affect integrated galaxy observables such as IRX-$\beta_{\rm UV}$ relations, previous theoretical studies based on cosmological simulations have mostly focused on integrated galaxy scales (e.g., Liang et al., 2021; Vijayan et al., 2022; Behrens et al., 2018; Mushtaq et al., 2023; Ma et al., 2019; Narayanan et al., 2018), which might overlook the detailed internal distributions. To clarify the impact of internal galaxy structures, it is therefore essential to quantitatively analyze dust attenuation and re-emission at sub-galactic scales and track their time evolution with short time bins.

In this chapter, we use zoom-in cosmological simulations FirstLight Ceverino et al. (2017) and quantitatively examine both the time evolution and internal dust properties in EoR galaxies. We specifically focus on three key areas: (i) time evolution of galaxy-integrated dust properties (UV slope, IRX, dust temperature) relative to SFR, (ii) the differences in dust properties between individual clumps and the integrated galaxy, (iii) distinctions in dust characteristics resulting from the two primary clump-formation pathways (merger-driven and VDI-driven). We utilize the IRX–$\beta_{\rm UV}$ relation as a diagnostic tool to interpret observed differences in dust and stellar geometries.

The remainder of this chapter is structured as follows. Section 7.2 details our cosmological zoom-in simulation suits and post-processed dust radiative transfer (RT) setup using SKIRT (Baes et al., 2011). In Section 7.3, we present spatial distributions and redshift evolution of physical properties, and show differences between the properties of individual clumps and those of the integrated galaxy. Section 7.4 introduces a toy model to interpret integrated and clump-specific IRX–β distributions in terms of star-dust geometry, applying these insights to observations. Finally, Section 7.5 summarizes our main conclusions and provides future prospects.

7.2 Method

7.2.1 FirstLight Zoom-in Simulations

We use the same zoom-in cosmological simulations, FirstLight (Ceverino et al., 2017), as in Chapter 6. The detailed settings for the initial conditions, star formation recipes, and subgrid physics are described in Section 8.2.1.

7.2.2 Post-processing Radiative Transfer

Dust attenuation and re-emission in our simulated galaxies are computed using the post-processing radiative transfer (RT) code SKIRT (Baes et al., 2011; Camps and Baes, 2020). SKIRT is an open-source, three-dimensional Monte Carlo dust RT code that consistently calculates dust temperatures by accounting for both absorption and anisotropic scattering processes. The general principles and procedures underlying the 3D Monte Carlo dust radiative transfer method are described in detail in Section 3.4.7.

To perform the RT calculations, we specify the stellar emission properties (Section 7.2.2.1), dust spatial distribution (Section 7.2.2.2), and adopted dust composition and grain-size distributions (Section 7.2.2.3) as input parameters.

7.2.2.1 Stellar Emission

The spatial distribution of stellar emission is determined by the positions of stellar particles in our hydrodynamical simulations. SKIRT supports directly importing data files that contain the necessary information on these stellar particles.

We construct the SEDs of individual stellar particles using single stellar population (SSP) models from BPASS (Eldridge et al., 2017), based on the mass, age, and metallicity of each star cluster. Each stellar particle is treated as a single starburst. Among the BPASS models, we adopt a Chabrier IMF with an upper mass limit of $300\,M_{\odot}$.

For stellar particles younger than 15 Myr, we reassign their ages. This adjustment is because our simulations form stellar particles with a fixed time step of $\Delta t_{\rm SF} = 5\,$Myr, while the simulation output times are not synchronized with this interval (see Section 6.2.1.3). We therefore re-assign the stellar ages as described in Section 6.2.2. Specifically, for stellar particles younger than 15 Myr with age stamps at T_1, T_2, and T_3 ($T_1 < T_2 < T_3$), we randomly sample new ages within each interval. For example, for a star with age T_1, we randomly draw a new age within $[1, T_1]$ Myr and assign it as the updated age.

We note that we consider only the stellar continuum and do not include nebular continuum emission. Although recent JWST observations suggest that nebular emission may dominate the UV continuum in some systems (e.g., Cameron et al., 2024), such spectra can be reproduced by models with a large number of very hot stars (e.g., Wolf-Rayet stars) with effective temperatures of $T_{\rm eff} \gtrsim 10^5\,$K. Inoue (2011) calculate the contribution of the nebular continuum and demonstrate that stellar continuum dominates for metallicities of $\log(Z/Z_{\odot}) = -0.7$ under a constant star formation rate over 10 Myr. Based on this, we expect that the nebular continuum does not significantly affect the UV slopes $\beta_{\rm UV}$ or the IR re-emission calculated in the following analysis.

The SED (including both stellar and dust emission) is sampled using 150 logarithmically spaced wavelength bins, covering the range from 0.1 to $1000\,\mu$m . To ensure good convergence, a total of 10^7 photon packets per wavelength bin are emitted from the stars in each calculation. The numerical convergence with respect to the number of photon packets and the wavelength binning is verified in Section 7.2.4.

The radiative transfer calculations are iterated until the IR re-emission luminosity converges within 3%, or until a maximum of seven iterations is reached. An octree structure is used to construct the dust grid, where cells are recursively subdivided until each contains less than 10^{-6} of the total dust mass. The highest grid level corresponds to a cell width of $\sim 4.9\,$pc, approximately one-fourth of the minimal cell size in the hydrodynamical simulation.

7.2.2.2 Dust Spatial Distribution

The spatial distribution of dust is imported from the hydrodynamical simulation by assuming that it scales with the metal distribution, using a constant dust-to-metal ratio defined as DTM = $M_{\rm dust}/M_{\rm metal}$. The choice of DTM sets the overall normalization of the extinction curve.

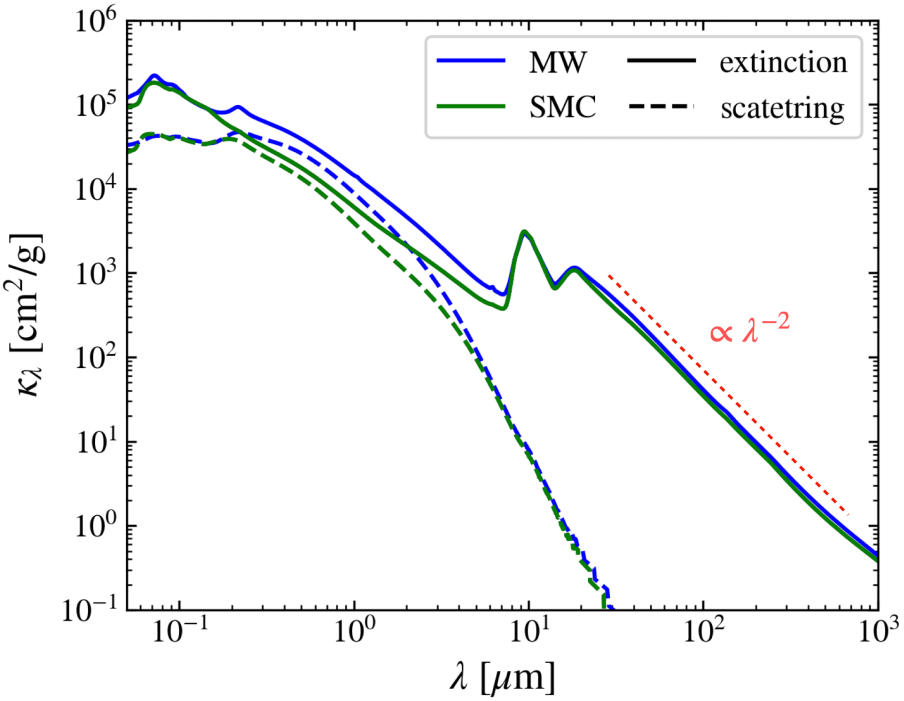

Figure 7.1: Dust opacity curve of the Weingartner and Draine (2001) dust model that is used for analysis in this work. Blue and green lines represent the opacity curve for the MW and SMC grain size distribution model, respectively. The solid and dashed lines show the extinction (= absorption + scattering) and scattering. In the mid- and far-IR ($> 30\,\mu$m), dust opacity scales with wavelength as $\kappa_\lambda \propto \lambda^{-2}$.

We adopt a fixed value of DTM = 0.4, which is commonly used for the Milky Way and similarly assumed in various high-redshift simulation studies (e.g., Behrens et al., 2018; Lovell et al., 2021a; Mushtaq et al., 2023). Although the value of DTM can influence the RT outputs, including the dust-to-gas mass ratio, dust temperature, and infrared luminosities, it remains poorly constrained in high-redshift observations (e.g., Wiseman et al., 2017), and theoretical models predict a wide range of values (e.g., Asano et al., 2013; Aoyama et al., 2017; Toyouchi et al., 2025). The implications of adopting a time-dependent DTM are discussed in Section 7.4.3.

7.2.2.3 Dust Absorption, Scattering, and Re-emission

The size distribution and composition of dust grains determine their absorption and scattering properties (e.g., Draine et al., 2014). We adopt the dust models developed by Weingartner and Draine (2001), which reproduce the observed extinction curves of the Milky Way (MW) and the Small Magellanic Cloud (SMC). The grain size distributions of graphite, silicate, and PAH components for the MW and SMC are sampled using 10/10/10 and 10/10/0 bins, respectively.

Figure 7.1 presents the dust opacity curves from UV to far-infrared (FIR) wavelengths based on the MW and SMC dust models from Weingartner and Draine (2001). Both dust absorption and scattering contribute significantly to opacity in the UV and optical regimes. At wavelengths longer than $\sim 30, \mu$m, dust absorption dominates the total opacity, scaling approximately as $\kappa \propto \lambda^{-\beta}$, where the dust emissivity spectral index is $\beta = 2$. The MW opacity curve exhibits a characteristic small bump at $\lambda \sim 0.22, \mu$m (the well-known 2175 AA UV bump), while the IR peaks at $\lambda = 9.7$ and $18\,\mu$m arise from silicate grains due to the Si–O stretching and bending vibrational modes, respectively (see Section 3.4.2).

The exact nature of dust grains in high-redshift galaxies remains an open question. Recent JWST observations have investigated the dust attenuation curves in galaxies at $z > 4$ (Fisher

et al., 2025; Ormerod et al., 2025; Witstok et al., 2023; Markov et al., 2023, 2025), and found that 20–25% of the REBELS and JADES samples exhibit evidence for the 2175 Å bump. This feature is often attributed to polycyclic aromatic hydrocarbons (PAHs) (Li et al., 2024; Lin et al., 2025; Nanni et al., 2025), as seen in the MW extinction curve (Cardelli et al., 1989), but absent in that of the SMC (Gordon et al., 2003). We therefore adopt both the MW and SMC dust models for comparison, and use the MW model as the default.

We include the self-absorption of dust emission, which becomes important in dense regions with high optical depth. The impact of self-absorption is examined in Section 7.2.4. Our simulations also account for transient heating processes, which are critical for computing non-local thermal equilibrium (NLTE) dust emission from stochastically heated small grains and PAH molecules (Camps and Baes, 2015).

SKIRT outputs an *indicative* dust temperature for each cell ($T_{\rm cell}$), defined as the mass-weighted equilibrium temperature ($T_{\rm eq}$). The equilibrium temperature of each dust species in a cell is computed by solving the radiative balance equation:

$$\int_0^\infty \kappa_\nu^{{\rm abs},i} J_\nu \, {\rm d}\nu = \int_0^\infty \kappa_\nu^{{\rm abs},i} B_\nu(T_{{\rm eq},i}) \, {\rm d}\nu, \tag{7.1}$$

where $\kappa_\nu^{{\rm abs},i}$ is the absorption opacity of dust type i, and J_ν is the local radiation intensity. The indicative temperature $T_{\rm cell}$ is then obtained by mass-weighted averaging over dust types as:

$$T_{\rm cell} = \frac{\sum_i \rho_i T_{{\rm eq},i}}{\sum_i \rho_i}, \tag{7.2}$$

where ρ_i is the mass (or number) density of dust type i.

We also include heating by the cosmic microwave background (CMB), whose temperature increases with redshift as $T_{\rm CMB}(z) = (1+z) \times T_{{\rm CMB}(z=0)}$, making its effect non-negligible at high redshift (da Cunha et al., 2015).

7.2.3 Clump identification

We identify [OIII]-bright clumps based on the surface density of the star formation rate as described in Section 6.2.3. The re-constructed grid size Δ, the threshold grouping number $N_{\rm grid}$ are the same as in Section 6.2.3, but only changed the threshold surface SFR density from $\Sigma({\rm SFR}) \geq 1\,M_\odot\,{\rm yr}^{-1}/N_{\rm grids} = 10^{1.5}\,M_\odot\,{\rm yr}^{-1}\,{\rm kpc}^{-2}$ to $\Sigma({\rm SFR}) \geq 0.63\,M_\odot\,{\rm yr}^{-1}/N_{\rm grids} = 10^{1.3}\,M_\odot\,{\rm yr}^{-1}\,{\rm kpc}^{-2}$. The 0.2-dex changing threshold does not change the clumpy fraction as discussed in Chapter 6. We identify clumps based on the above threshold using a dendrogram technique (Rosolowsky et al., 2008).

In Chapter 6, we have also checked the virial parameters of the identified clumps, which are defined as $\alpha_{\rm vir} \equiv 5\sigma_{\rm clump}^2 R_{\rm clump}/(GM)$, where $\sigma_{\rm clump}$ and M are the velocity dispersion within a clump and baryon mass a clump, respectively. Clumps have $\alpha_{\rm vir} \sim 0.2$, indicating that they are gravitationally bound.

7.2.4 Numerical Convergence and Effects of Stochastic Heating and Self-absorption

We have tested the numerical convergence of our radiative transfer (RT) simulations and evaluated the impact of stochastic heating and self-absorption. Table 7.1 summarizes the test configurations. Here, $n_{\rm p}$ denotes the number of photon packets launched per wavelength bin, and n_λ is the number of wavelength bins. Our default setup adopts $(n_{\rm p}, n_\lambda) = (10^7, 150)$.

Figure 7.2 shows the resulting SEDs for the high-resolution cases $(n_{\rm p}, n_\lambda) = (10^8, 150)$ and $(10^7, 300)$. The differences between these and the fiducial setup are less than 30% across all wavelengths, and typically below 10% in both the rest-frame UV and FIR regions. These discrepancies are negligible when integrated over broadband filters and do not affect our conclusions.

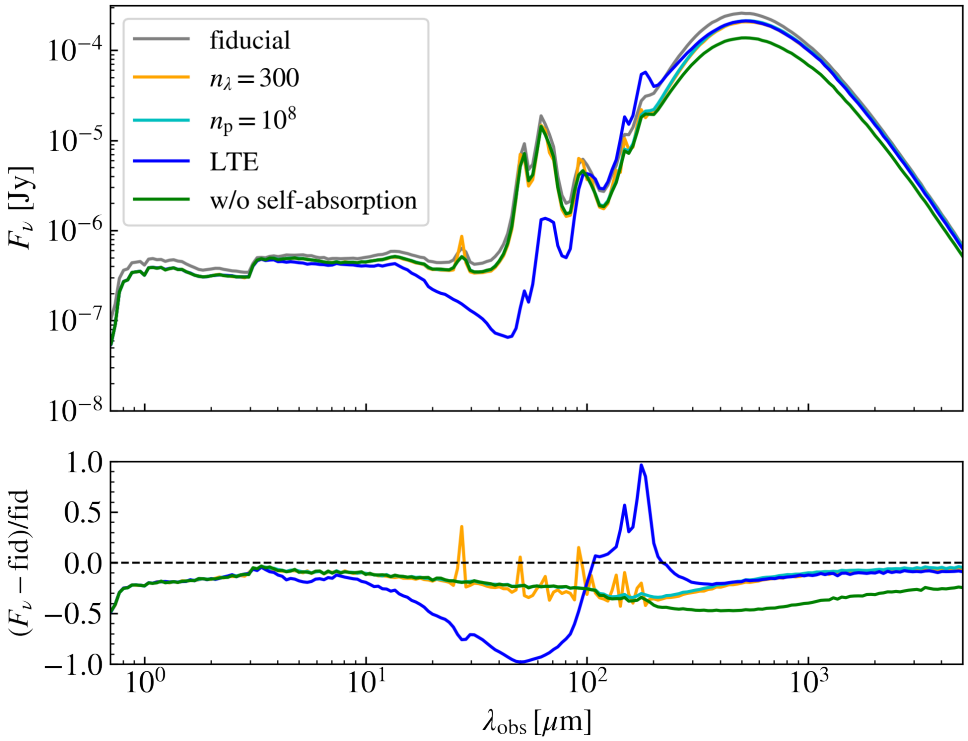

Figure 7.2: SEDs of FL958 at $z = 7.2$ with different SKIRT settings. In the upper panel, we plot the SED for the fiducial case and two runs with more wavelength bins ($n_\lambda = 300$), and more photon packages ($n_\mathrm{p} = 10^8$) launched per wavelength bin. Additionally, we show the outcome of simulations for which stochastic heating or self-absorption is turned off ("LTE", "w/o self-absorption"). The detailed SKIRT settings in each model are described in Table 7.1. In the lower panel, we show the fractional difference between the various runs and the fiducial model.

We also show the result for a model without stochastic heating, i.e., assuming that all dust grains are in thermal equilibrium with the incident radiation field. The resulting SED, shown in blue, lacks significant mid-IR emission that originates from stochastically heated small grains such as PAHs. In this case, the re-emitted flux in the mid-IR is underestimated by up to a factor of two. This wavelength range overlaps with the expected sensitivity window of the proposed instrument PRIMA (Moullet et al., 2023), making it a promising probe of stochastic heating in high-z galaxies.

The green line shows the SED computed without self-absorption of dust emission. This model exhibits a net decrease in flux in both the mid-IR and FIR ranges. In the absence of self-absorption, the re-absorption and subsequent re-emission of radiation within optically thick dust regions are not accounted for, leading to an underestimation of the total luminosity. Consequently, the flux can be underestimated by up to 40% compared to the fiducial simulation.

name	n_p	n_λ	self-absorption	stochastic heating
fiducial	10^7	150	◯	◯
nw300	10^7	300	◯	◯
np1e8	10^8	150	◯	◯
LTE	10^7	150	◯	×
w/o self-absorption	10^7	150	×	◯

Table 7.1: The parameters used in each SKIRT calculation in Section 7.2.4. All cases adopt MW-like dust type (Weingartner and Draine, 2001) and a fixed dust-to-metal ratio of 0.4.

7.2.5 Inclination Effects

Before proceeding to the main results, we investigate how galaxy inclination affects our radiative transfer (RT) calculations. Because observed spectral energy distributions (SEDs) can depend significantly on the line-of-sight (LoS), we performed additional RT calculations using two alternative viewing angles for our fiducial simulation. Figure 7.3 presents the resulting SEDs for a merger-induced clumpy galaxy (left panel) and a VDI-induced clumpy galaxy (right panel). In the merger-induced clumpy galaxy, clumps are distributed three-dimensionally and are not confined to a specific plane. Consequently, inclination effects on the SEDs are relatively minor. We find a maximum deviation of approximately 20% in the rest-frame UV flux, accompanied by a corresponding increase in re-emitted IR flux up to about 20%. In contrast, the VDI-induced clumpy galaxy exhibits more pronounced inclination effects, as the clumps predominantly lie in the xy-plane. Figure 7.3 illustrates that edge-on orientations (xz- and yz-planes) experience significantly higher dust attenuation compared to the face-on orientation (xy-plane), due to increased optical depth along the line-of-sight. This result is consistent with observations of dust lanes commonly seen in edge-on galaxies in the local Universe (e.g., Xilouris et al., 1999; Bianchi, 2007). For edge-on views, UV flux is suppressed by up to 50% relative to the face-on orientation. Moreover, IR emission in edge-on views is partially absorbed by optically thick dust layers, reducing the flux by up to 30% relative to the face-on orientation.

Throughout the subsequent results section, we present the xy-plane orientation as the face-on view for ex-situ (merger-induced) clumpy galaxies, and we use the xy-plane (yz-plane) as the face-on (edge-on) view for in-situ (VDI-induced) clumpy galaxies.

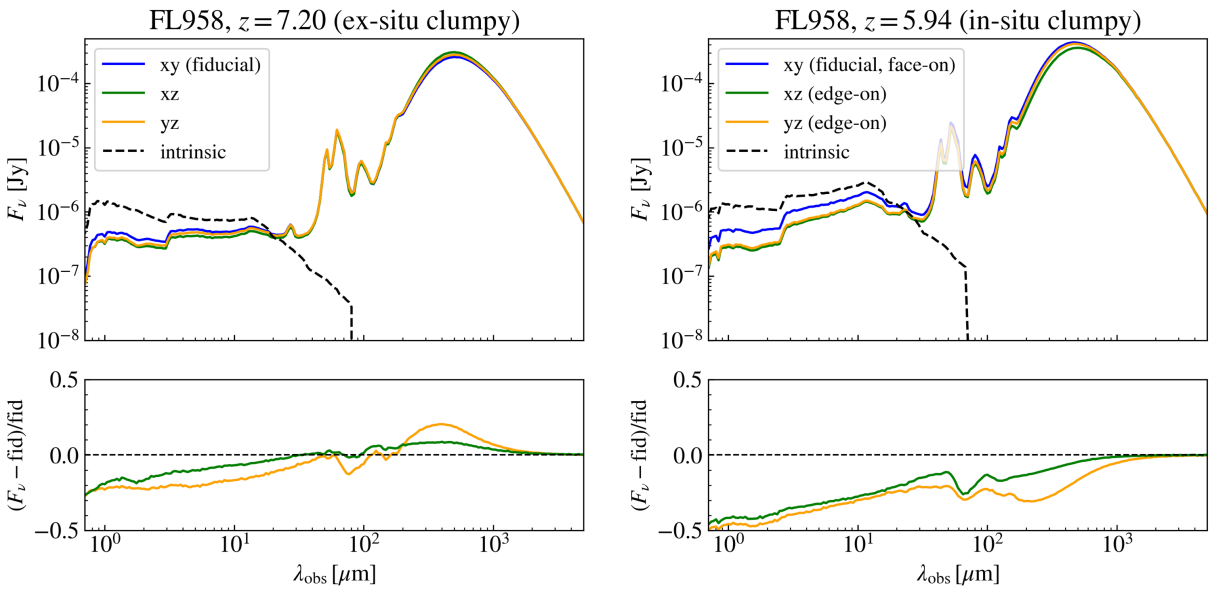

Figure 7.3: Left: The top panel shows SEDs of an ex-situ (merger-induced) clumpy galaxy for the fiducial orientation (xy-plane, face-on; blue) compared to alternative lines-of-sight (xz-plane, yz-plane). The black solid line shows the intrinsic (dust-free) SED. The bottom panel shows fractional differences in flux between each alternative orientation (xz, yz) and the fiducial xy-plane. The black solid line is an intrinsic SED. The bottom panel shows the fractional difference between each LoS and the fiducial xy-plane. Right: Same as the left panels, but for an in-situ (violent disk instability-induced) clumpy galaxy. Here, the fiducial xy-plane corresponds to the face-on view, while the xz- and yz-planes represent edge-on views.

7.3 Result

7.3.1 General Properties of FL958

Among the 62 massive galaxies in our simulations, we select one representative galaxy named FL958, which experienced both ex-situ and in-situ clump formation. FL958 underwent a major merger between $z = 7.33$ and $z = 6.69$, during which clumps formed in the merging system, particularly triggered by tidal tails created at the first pericentric passage. We trace the evolution of FL958 across 66 snapshots from $z = 9.5$ to $z = 5.25$, with intervals of approximately 7–10 Myr.

Figure 7.4 presents the evolutionary history of FL958. In the left panel, we plot the total masses of gas, stars, and dust, while the right panel shows the star formation rate (SFR) averaged over 10 and 100 Myr, both as functions of redshift. The halo merger event occurred at $z = 7.33$, and additional clumps subsequently formed at $z = 7.2$ (indicated by the vertical gray dotted line in Figure 7.4). Based on our clump identification procedure, we detect three distinct clumps within the galaxy system, as illustrated in Figure 7.5.

During the merger, the masses of gas, stars, and dust all increased by approximately a factor of two. The corresponding 10 Myr-averaged SFR rose from $17\,M_\odot\,\mathrm{yr}^{-1}$ at $z = 7.62$ to $85\,M_\odot\,\mathrm{yr}^{-1}$ at $z = 7.13$. Subsequently, the gas mass decreased by a factor of about 1.5 due to rapid consumption through merger-induced star formation. This was followed by a brief quenching (mini-quench) lasting approximately 12 Myr at $z = 6.6$. After $z < 6.5$, the gas mass gradually increased again through cold gas accretion (e.g., Dekel et al., 2009a), leading to renewed star formation and corresponding growth in stellar and dust masses.

Throughout the merger and subsequent gas accretion phases, the galaxy acquired substantial angular momentum, eventually forming a cold gas disk. This evolution resembles recent observations of rotationally-supported cold disks traced by [CII] emission at $z = 7.2$ (Rowland et al., 2024). At $z = 5.94$, the sustained cold accretion triggered violent disk instabilities (VDI), leading to the formation of multiple in-situ clumps (see Figure 7.5). Such a VDI-driven scenario is consistent with several other cosmological simulations (e.g., Dekel et al., 2009b; Ceverino et al., 2010; Mandelker et al., 2014, 2025; Ceverino et al., 2023).

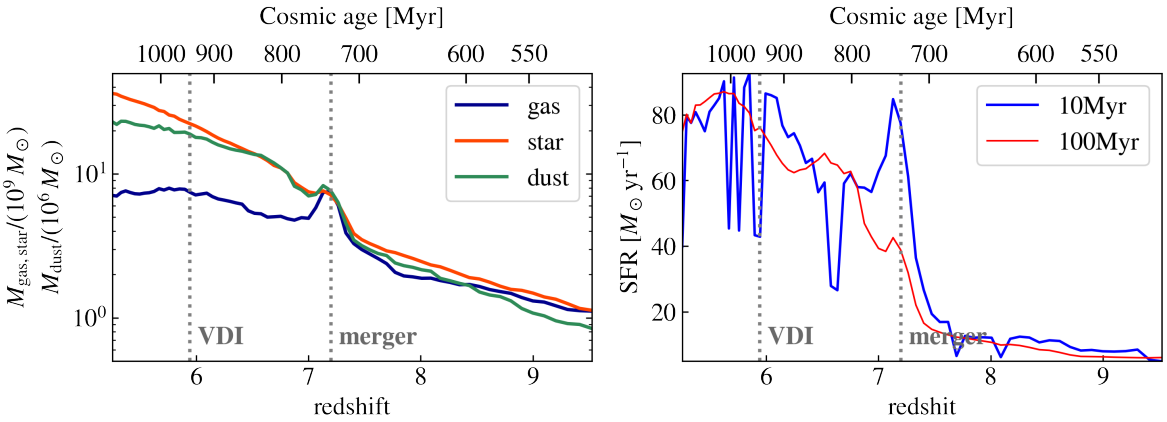

Figure 7.4: Masses (left panel) and SFRs (right panel) as functions of cosmic age. In the left panel, the blue, red, and green lines represent the masses of gas ($T < 5{\times}10^5$ K and $n > 0.1\,\mathrm{cm}^{-3}$), stars, and dust (assumed to be $= 0.4\times$ gas-phase metal mass), respectively. Vertical gray dotted lines at $z = 7.2$ and $z = 5.94$ mark the timings of a major merger and violent disk instabilities (VDI). In the right panel, the blue and red lines represent SFRs averaged over 10 and 100 Myr, respectively, computed as the stellar mass formed over the past X Myr divided by X Myr, where X = 10 or 100.

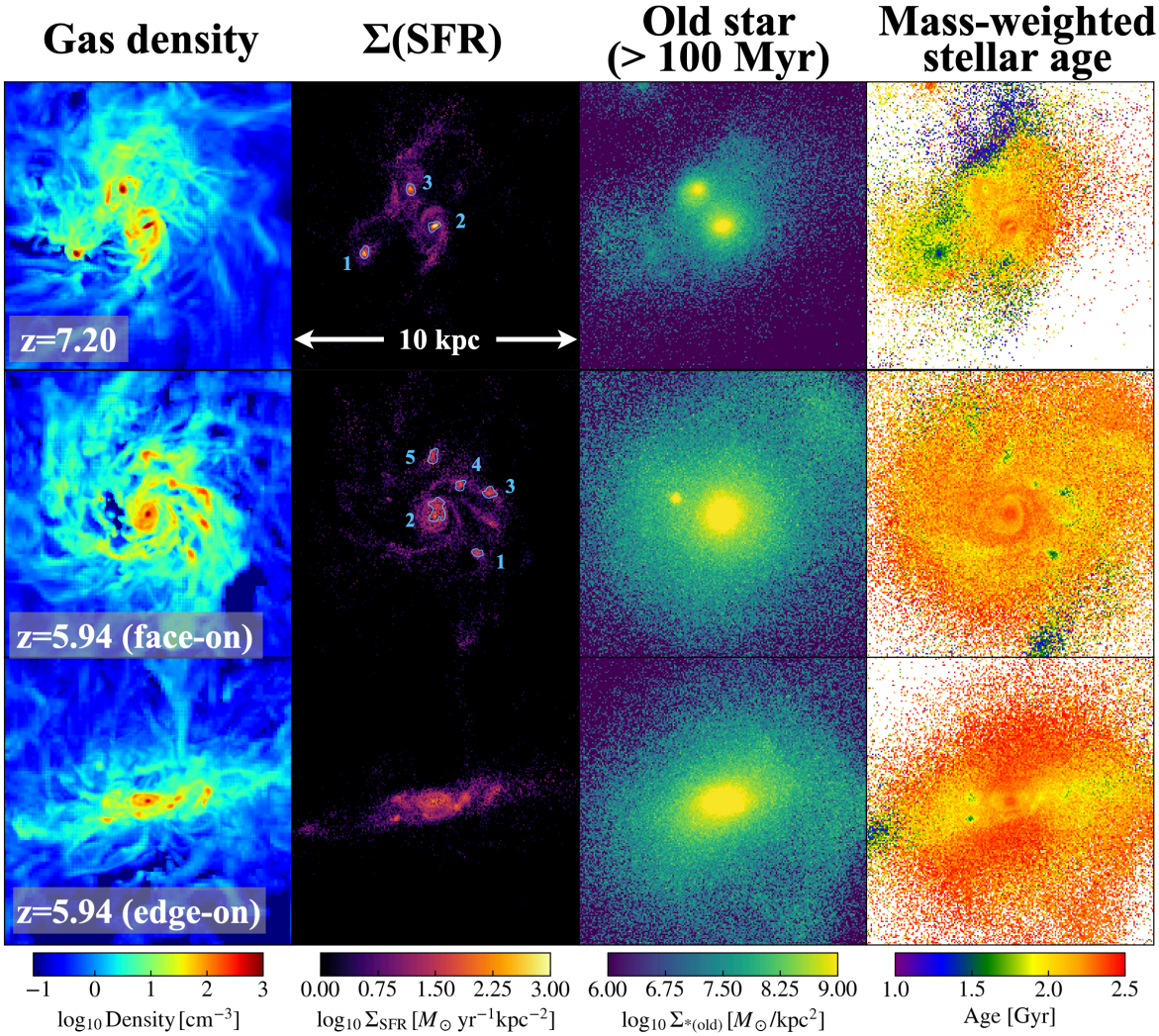

Figure 7.5: Projected distribution of our galaxy at $z = 7.2$ (top) and $z = 5.94$ (middle for face-on, and bottom for edge-on), where the merger and VDI-driven clump formation occurs. From left to right, we plot gas number density, surface SFR, surface mass distributions of stars older than 100 Myrs, and mass-weighted stellar age. One side length of the panel and the projected depth of each panel is 10 kpc. The identified clumps are labeled in light blue in the second column.

Table 7.2: Properties of identified clumps.

	$\langle\Sigma_\star\,(\mathrm{SFR})\rangle$ $[M_\odot\,\mathrm{yr}^{-1}\,\mathrm{kpc}^{-2}]$	$\langle n_{\mathrm{gas}}\rangle$ $[\mathrm{cm}^{-3}]$	Age [Myr]	$M_\star$ $[M_\odot]$	sSFR $[\mathrm{Gyr}^{-1}]$	R_{clump} [pc]
merger-1	107	369	26	1.40×10^8	45	138
merger-2	287	1021	139	2.00×10^9	8	132
merger-3	89	478	83	2.40×10^8	20	132
VDI-1	33	87	42	6.10×10^7	22	113
VDI-2 (proto-bulge)	42	152	214	3.90×10^9	2	231
VDI-3	40	134	52	4.40×10^7	56	141
VDI-4	38	94	71	3.90×10^7	39	113
VDI-5	32	86	58	3.50×10^7	58	141

To qualitatively confirm this scenario, we show the face-on Toomre-Q map of FL958 at $z = 5.94$ in Figure 7.6. The Toomre-Q parameter is defined as: $Q \equiv \frac{\sigma_{\rm r}\kappa}{AG\Sigma}$, where $\sigma_{\rm r}$, κ, and Σ are the radial velocity dispersion, the epicyclic frequency of the disk, and the surface density, respectively. Here, A is a numerical factor depending on the disk component: $A = \pi$ for a purely gaseous disk and $A \simeq 3.36$ for a purely stellar disk (Toomre, 1964; Elmegreen, 2011; Inoue et al., 2016b). A disk is stable against gravitational collapse if $Q \gg 1$, whereas gravitational instabilities occur when $Q < 1$, leading to clump formation and subsequent fragmentation. We compute the Toomre-Q parameter assuming a two-component disk consisting of gas and stars, following the methods described in previous works (e.g., Romeo and Wiegert, 2011; Romeo and Falstad, 2013; Inoue et al., 2016b). In Figure 7.6, we clearly see disk-like structures with $Q > 1$ and distinct clumps with $Q < 1$, supporting the scenario of clump formation via violent disk instability. Note, however, that some initial proto-clumps may have $Q > 1$, indicating that a low Toomre-Q value alone does not exclusively indicate disk-instability origin (Inoue et al., 2016b).

The overall morphology evolution from $z = 9.5$ to $z = 5.25$ is obtained through the movie [1].

Interestingly, during the VDI phase at $z = 6 - 5.25$, the 10 Myr-averaged SFR exhibits fluctuations on intervals of approximately 7–10 Myr, driven primarily by variations in gas inflow (left panel of Figure 7.4). Correspondingly, the number of clumps also varies between $N_{\rm clumps} = 0$ and 5. Hereafter, we refer to the 10 Myr-averaged SFR simply as "SFR".

Figure 7.4 also shows the 100 Myr-averaged SFR as a red line, since stellar populations younger than 100 Myr contribute predominantly to UV radiation, while populations younger than 10 Myr dominate nebular emission from HII regions. Although the 10 Myr-averaged SFR exhibits large fluctuations around the merger and during the VDI phase, the 100 Myr-averaged SFR steadily increases throughout the entire evolution from $z = 9.5$ to $z = 5.25$.

Figure 7.5 shows the projected maps of physical properties at $z = 7.2$ and $z = 5.94$, where the merger and VDI-driven clump formation occur. For FL958 at $z = 5.94$, we show both face-on and edge-on maps. The corresponding gas, stellar, and dust masses are $M_{\rm gas} = 7.55 \times 10^9\,M_\odot$, $M_* = 7.15 \times 10^9\,M_\odot$, $M_{\rm d} = 7.66 \times 10^6\,M_\odot$ at $z = 7.2$ and $M_{\rm gas} = 7.44 \times 10^9\,M_\odot$, $M_* = 2.23 \times 10^{10}\,M_\odot$, $M_{\rm d} = 1.88 \times 10^7\,M_\odot$ at $z = 5.94$, respectively. Each panel of Figure 7.5 shows the distributions of gas number density, surface star formation rate density, surface stellar mass of stars older than 100 Myrs, and mass-weighted stellar age. The top row of Figure 7.5 is the same as the bottom row of Figures 6.7 and 6.8 in Chapter 6. Table 7.2 summarizes physical properties of clumps identified in $z = 7.2$ (three clumps) and $z = 5.94$ (five clumps).

In the top panels, we present FL958 at $z = 7.2$. Clump 1 forms within a tidal tail produced by the interaction between clumps 2 and 3, indicating an ex-situ origin. The gas surrounding clumps 2 and 3 is diffuse, appearing as tidal or extended components. Clumps 1, 2, and 3 each exhibit gas densities exceeding $\sim 350\,{\rm cm}^{-3}$, triggering intense star formation with surface densities $\gtrsim 90\,M_\odot\,{\rm yr}^{-1}\,{\rm kpc}^{-2}$. The distribution of stars older than 100 Myr shows that clumps 2 and 3 contain substantial pre-existing stellar populations with surface densities $\Sigma_{*,\rm old} \simeq 10^9\,M_\odot\,{\rm kpc}^{-2}$, whereas clump 1 lacks such an older component. This result is consistent with its shorter formation timescale of approximately 50 Myr, as discussed in Chapter 6. The rightmost column of Figure7.8 further highlights this age contrast: clump 1 is dominated by younger stars ($\lesssim 30\,{\rm Myr}$), while clump 2 primarily hosts older stellar populations ($\sim 300\,{\rm Myr}$).

In the middle panels, we show FL958 at $z = 5.94$ in a face-on view. The galaxy exhibits a clear disk structure containing multiple clumps formed via violent disk instability (VDI; i.e., in-situ origin), as confirmed by the Toomre-Q map shown in Figure 7.6. Regions of high gas density closely coincide with enhanced surface star formation rates, while older stars are centrally concentrated in the emerging proto-bulge. Interestingly, a small overdensity of older stars appears just to the left of the bulge, lacking corresponding features in either gas-density or SFR maps. This particular clump originated from micro-mergers with mass ratios of $q > 10$ (also see the dark matter distributions in the animation). The stellar age map confirms that

[1]The link is here. The animation shows the time evolution of gas (left) and dark matter (right) densities.

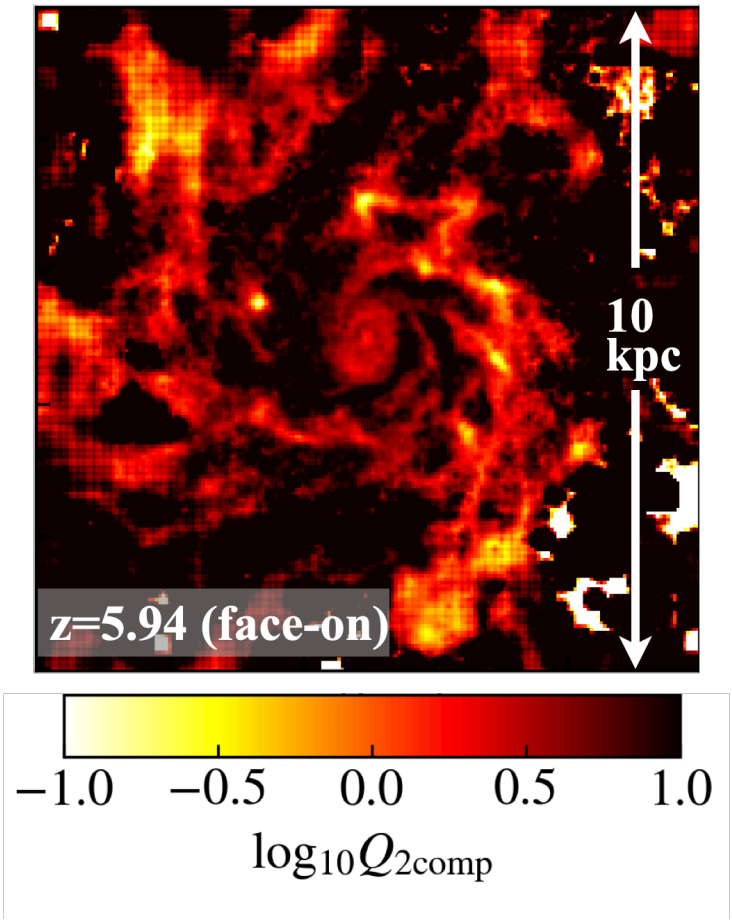

Figure 7.6: Toomre-Q map for FL958 at $z = 5.94$. One side length is 10 kpc. The value of Q is computed assuming a two-component disk. The regions with $Q < 1$ are gravitationally unstable for axisymmetric modes. The larger regions where $1 < Q < 2$ can be subject to higher modes of instability.

the VDI-driven clumps predominantly host younger stellar populations ($\sim 50\,\mathrm{Myr}$), whereas the proto-bulge consists primarily of older stellar populations ($\sim 200\,\mathrm{Myr}$) as shown in Table 7.2.

The bottom panels show an edge-on view at $z = 5.94$. In this projection, the apparent separations between clumps become narrow, making individual clumps difficult to identify. Such projection effects are especially significant for VDI-driven clumpy systems, as we discuss in the next section.

7.3.2 Radiation map

In Figure 7.7, we present the projected spatial distributions of dust properties for FL958 at $z = 7.2$ and $z = 5.94$. The four columns, from left to right, show the dust column density (Σ_{dust}), massweighted dust temperature ($T_{\mathrm{d,mw}}$), restframe V-band attenuation at 5500 Å (A_V), and dusttogas ratio (DTG). The spatial distribution of dust column density closely resembles the gas density structure shown in Figure 7.5.

The mass-weighted dust temperature ($T_{\mathrm{d,mw}}$) is systematically higher at $z = 7.2$ than at $z = 5.94$, consistent with a more bursty star formation at higher redshift (see Figure 7.4). Massive young stars emit strong UV radiation (e.g., Xiao et al., 2018), which efficiently heats the dust. The three clumps at $z = 7.2$ exhibit relatively moderate temperatures of $T_{\mathrm{d,mw}} \simeq 40\,\mathrm{K}$, whereas the surrounding diffuse gas reaches higher temperatures of $T_{\mathrm{d,mw}} > 50\,\mathrm{K}$. This inversion occurs because low-density gas surrounding the clumps is directly exposed to UV radiation, whereas dust within the clumps is self-shielded due to their higher column densities.

The distribution of A_V closely traces the dust column density. In the edge-on projection, the maximum attenuation reaches approximately $A_V \sim 3\,\mathrm{mag}$, while individual clumps formed via VDI show $A_V \sim 1\,\mathrm{mag}$ in the face-on view. Since the clumps and the central bulge align nearly along the same line of sight, the total observed attenuation is roughly a sum of their individual contributions.

The rightmost column displays the DTG distribution. Regions dominated by older stellar populations, specifically merger-induced clump 2 at $z = 7.2$ and VDI-induced clump 2 (i.e., the central proto-bulge) at $z = 5.94$, reach DTG values of ~ 0.01. These values are in good agreement with recent spatially resolved ALMA measurements at $z \sim 4$, which inferred a similar DTG from the surfacebrightness ratio of the [CI] line and the restframe 380 μm dust continuum (Birkin et al., 2023).

Figure 7.8 presents the dustprocessed emission of FL958 at $z = 7.2$ (top) and $z = 5.94$ (bottom). From left to right, each row shows: rest-frame UV surface brightness at 1600 Å, total IR (TIR) surface brightness (integrated over 8–1000 μm), RGB composite without dust attenuation, and RGB composite with dust attenuation.

The UV maps are noticeably more extended than the TIR maps, reflecting the fact that a fraction of UV photons is scattered to large distances. This scattering effect is reflected as a noisy image in Figure 7.8. Although the intrinsic UV luminosity is highest within the clumps, the observed UV surface brightness in both clumps and their surroundings is comparable. This is because the clumps have high dust columns that heavily attenuate UV radiation, whereas the surrounding diffuse gas has less attenuation. The contrast between the third and fourth columns (RGB composites) illustrates this effect.

In contrast, the TIR surface brightness closely traces the dust column density, and regions with strong UV absorption re-emit more power in the IR. In the rightmost two columns, we show mock JWST/NIRCam RGB images using the F115W, F220W, and F356W filters (third column without dust, fourth with dust). Even without dust attenuation, older stellar populations appear red. Once dust is included, all regions become noticeably redder, and in the edge-on view, the dust heavily attenuates rest-frame optical emission as well as UV emission.

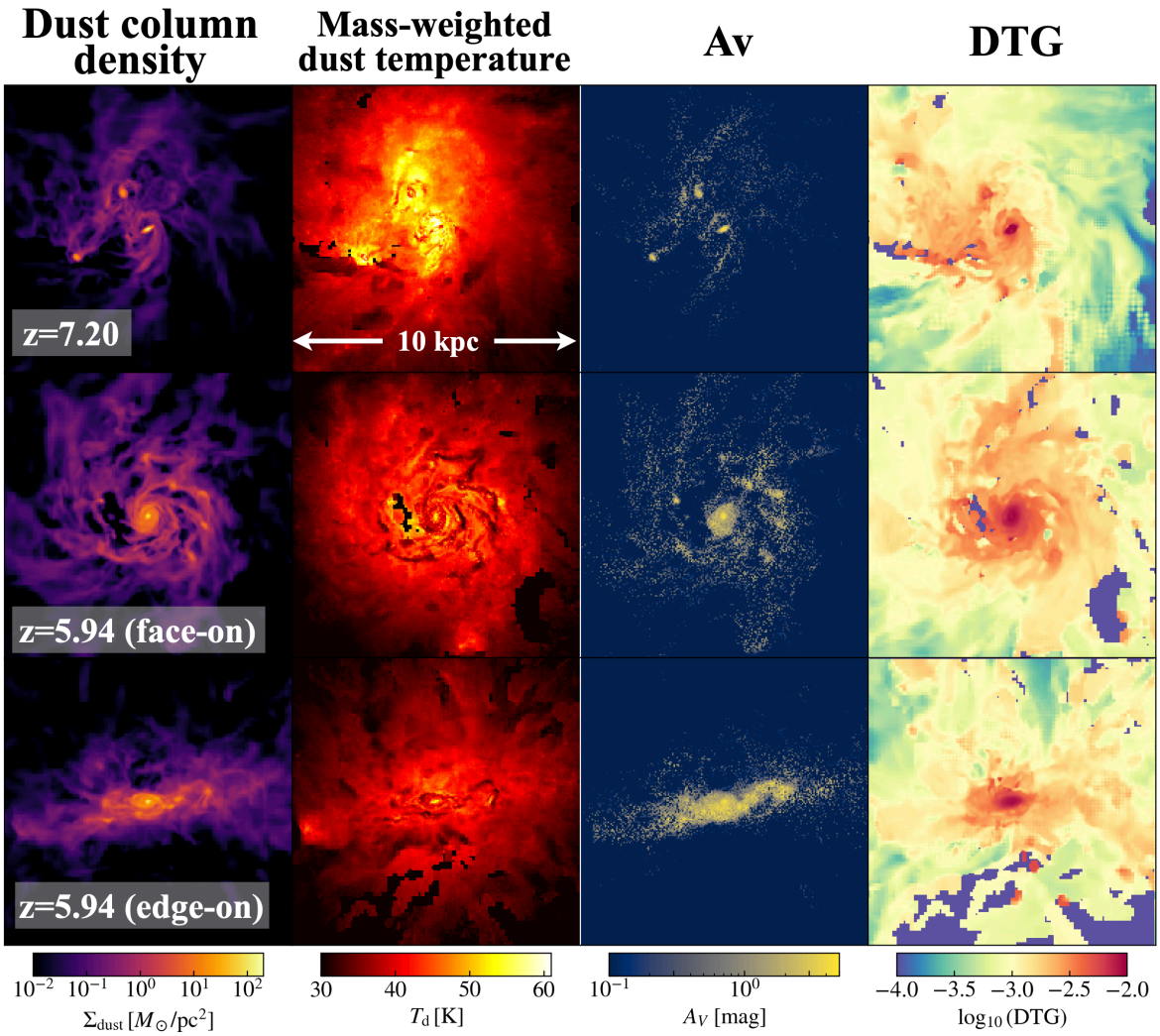

Figure 7.7: Projected distributions of FL958 at $z = 7.2$ and $z = 5.94$ as similar as Figure 7.5 bur for dust properties. From left to right column, we plot dust column density($\Sigma_{\rm dust}$), mass-weighted dust temperature, Av, and dust-to-gas ratio (DTG). For $\Sigma_{\rm dust}$ and DTG, we first calculate surface gas metal mass and projected gas metallicity distribution, and multiply them by dust-to-metal ratio of DTM = 0.4. For dust temperature and Av map, we obtain them as the outputs of RT calculation. The side length and projected depth of each panel are 10 kpc, as in Figure 7.5.

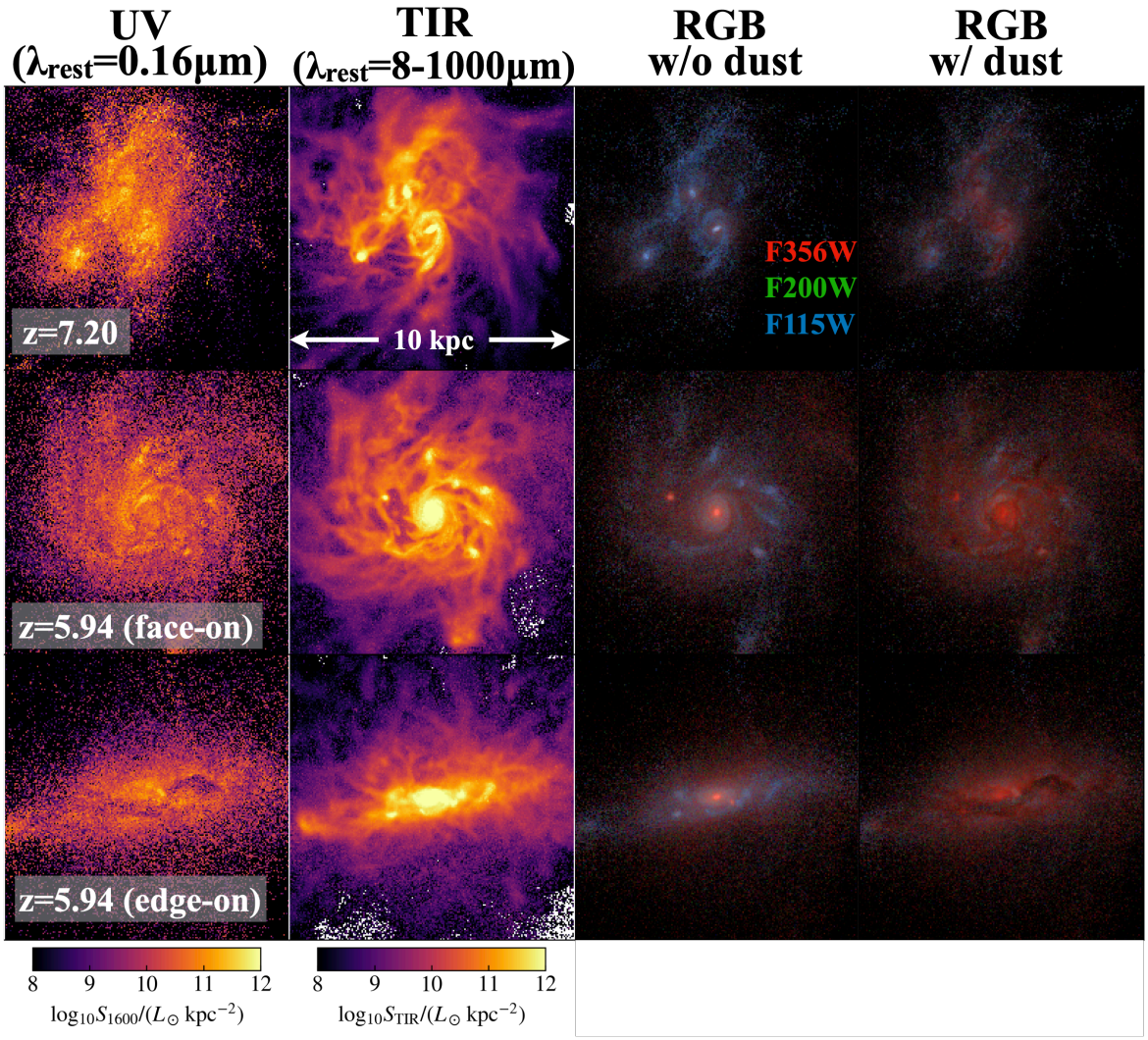

Figure 7.8: Dust emission properties of FL958 at at $z = 7.2$ and $z = 5.94$ as in Figure 7.5 and 7.7. From left to right, we plot the surface brightness in the rest-frame UV (νL_ν at 1600Å), in the total IR emission through $\lambda_{\rm rest} = 8 - 1000\,\mu$m, and mock three-color images (JWST/NIRCam F115W, F200W, and F356W) without / with dust attenuation. The field of view, one side length, and the projection length are the same as Figure 7.5 and 7.7.

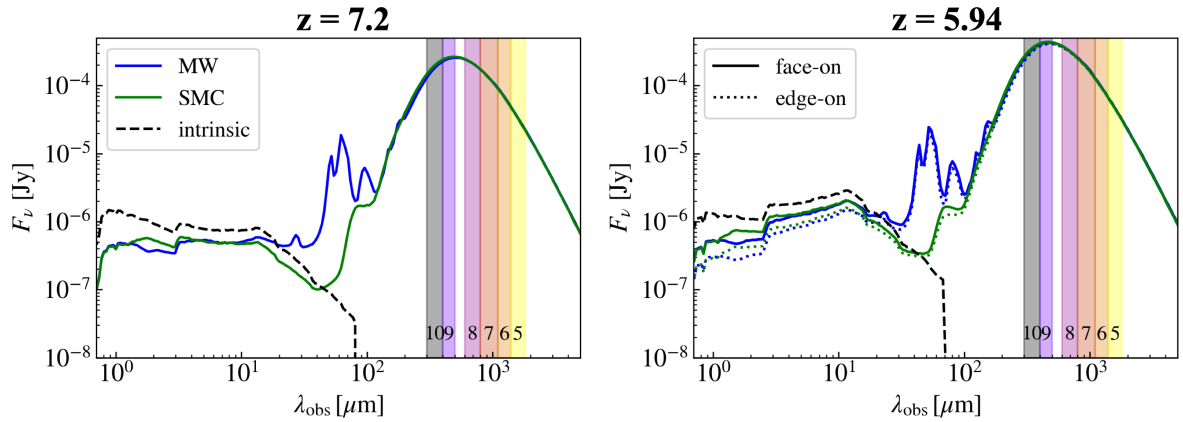

Figure 7.9: SEDs of FL958 at $z = 7.2$ (left) and $z = 5.94$ (right). The solid black lines represent the intrinsic stellar continuum, and the blue and green lines show SKIRT SEDs calculated with MW and SMC-like dust models, respectively. For the right panel, we also plot the edge-on SEDs as dotted lines, which are discussed in detail in Section 7.2.5. Shaded regions indicate the wavelength ranges of ALMA bands 10 to 5.

7.3.3 Integrated Dust Properties of the Systems

In this section, we focus on the integrated dust properties within a 10-kpc radius.

7.3.3.1 SED and Temperature Calculation

Figure 7.9 shows the SEDs of FL958 at $z = 7.2$ (left) and $z = 5.94$ (right), calculated using the SKIRT radiative transfer code. The blue and green lines represent the SEDs computed for MW- and SMC-type dust, respectively. The dashed lines represent the intrinsic stellar emission, i.e., the SEDs without dust attenuation.

The mid-IR SED ($\lambda_{\rm rest} = 6 - 25, \mu$m) differs significantly between the MW- and SMC-type dust models due to the presence of PAH emission in the MW model, a feature that can be probed by future PRIMA[2] observations (also see Section 4.4). The MW-type dust model exhibits a prominent absorption feature at 2175Å, in the near-UV extinction curve, leading to a consistently negative rest-frame UV slope $\beta_{\rm UV}$.

The right panel also includes SEDs for the edge-on orientation. In the edge-on view, UV attenuation is enhanced by up to 50% relative to the face-on view, while the difference in IR re-emission within the ALMA bands is minor, typically less than 20%. The detailed inclination effects are discussed in Section 7.2.5. Using these SEDs, we calculate the UV slope $\beta_{\rm UV}$ and dust temperatures as described below.

The UV continuum slope, $\beta_{\rm UV}$, defined through the relation $f_\lambda \propto \lambda^{\beta_{\rm UV}}$ (Calzetti et al., 1994), is widely used as an indicator of UV-continuum attenuation. Thanks to JWST's unprecedented sensitivity in infrared imaging and spectroscopy extending up to $\lambda_{\rm obs} \sim 5\,\mu$m, robust measurements of the UV slope $\beta_{\rm UV}$ at $z \gtrsim 7$ have recently become available for the first time (e.g., Cullen et al., 2023; Topping et al., 2022; Morales et al., 2024; Cullen et al., 2024; Topping et al., 2024a; Dottorini et al., 2024; Saxena et al., 2024).

We have tested the following two ways to calculate $\beta_{\rm UV}$. Firstly, we calculate $\beta_{\rm UV}$ in the rest-frame wavelength range of $\lambda_{\rm rest} = 1268 - 2580$ A as the same as Calzetti et al. (1994). Although this method is commonly adopted in observational studies (e.g., Sugahara et al., 2025), it can be significantly influenced by the 2175 Å bump in MW-type dust extinction curves, as illustrated in Figure 7.9. Consequently, this systematically leads to underestimations (more negative values)

[2]The PRobe far-Infrared Mission for Astrophysics; Moullet et al. 2023

of the UV slope, typically producing $\beta_{\rm UV} \lesssim -2.0$ for galaxy FL958 (see also Narayanan et al., 2018). We then consider the second way as the same as Liang et al. (2021),

$$\beta_{\rm UV} = \frac{\log_{10}(f_{\lambda,1230{\rm A}}) - \log_{10}(f_{\lambda,3200{\rm A}})}{\log_{10}(\lambda_{1230{\rm A}}) - \log_{10}(\lambda_{3200{\rm A}})}, \tag{7.3}$$

where $f_{\lambda,1230{\rm A}}$ and $f_{\lambda,3200{\rm A}}$ are the flux density at rest-frame 1230 Å and 3200 Å, respectively. We adopt a relatively long wavelength range rather than the first method to avoid the UV bump effect. In the following discussion, we adopt the second method.

Regarding dust temperature, there are different definitions both observationally and theoretically. We calculate the dust temperatures in the following three ways.

(i) Peak Temperature $T_{\rm d,peak}$

The peak dust temperature ($T_{\rm d,peak}$) is obtained from the Wien displacement law from the rest-frame wavelength at which the infrared flux-density (F_ν) peaks ($\lambda_{\rm peak}$). This is defined as

$$T_{\rm d,peak} = \frac{2.898 \times 10^3\,\mu{\rm m\,K}}{\lambda_{\rm peak}}, \tag{7.4}$$

which follows the relation for a greybody[3] with a dust emissivity index $\beta = 2$, i.e., $L_\nu \propto (1 - e^{-\tau_\nu})B_\nu \sim \nu^\beta B_\nu = \frac{\nu^{3+\beta}}{e^{h_{\rm p}\nu/(k_{\rm B}T)} - 1}$[4]. This measure has been used in many observational studies (e.g., Casey et al., 2018; Schreiber et al., 2018; Burnham et al., 2021). A more realistic form is the two-component dust SED model, consisting of a MBB function for old dust and a power-law component for warmer dust (Casey, 2012). Nevertheless, an optically thin MBB function at local equilibrium temperature is still a good approximation for the local dust emissivity at rest-frame $\lambda_{\rm rest} > 30\,\mu$m where non-LTE effects are negligible. Note that $T_{\rm d,peak}$ is only a proxy for $\lambda_{\rm peak}$, and the choice of the normalization is to compare with other theoretical and observational studies.

(ii) Mass-weighted Dust Temperature $T_{\rm d,mw}$

Next, we introduce the mass-weighted dust temperature

$$T_{\rm d,mw} = \frac{\sum_i T_{{\rm cell},i}\rho_{{\rm d},i}V_{{\rm d},i}}{\sum_i \rho_{{\rm d},i}V_{{\rm cell},i}}, \tag{7.5}$$

where $T_{{\rm cell},\,i}$ is the mass-weighted dust temperature for cell i as defined in Eq. (7.2) given by SKIRT. This is the most straightforward one to calculate from dust radiative transfer calculations for simulated galaxies and is adopted by various authors in the literature (e.g., Behrens et al., 2018; Liang et al., 2019; Ma et al., 2019). It is worth noting that the mass-weighted temperature directly relates to the dust SED at Rayleigh-Jeans tail (e.g., Scoville et al., 2016; Liang et al., 2019).

(iii) Luminosity-weighted Dust Temperature $T_{\rm d,lumis}$

Finally, we define the luminosity-weighted dust temperature as

$$T_{\rm d,lumis} = \frac{\sum_i T_{{\rm cell},i}L_{{\rm IR},i}}{\sum_i L_{{\rm IR},i}}, \tag{7.6}$$

where $L_{{\rm IR},i}$ is the bolometric luminosity of dust re-emission per cell that satisfies $L_{{\rm IR},i} \propto M_{{\rm d},i}T_{{\rm d,ind},i}^{4+\beta} = \rho_{{\rm d},i}V_{{\rm cell},i}T_{{\rm d,ind},i}^{4+\beta}$. This $T_{\rm d,lumis}$ is also introduced by Behrens et al. (2018); Lower et al. (2024). Here we adopt $\beta = 1.7$. We note here that neither the mass-weighted nor the

[3]Note that the term greybody is often used interchangeably with modified blackbody (MBB), however the former refers to the condition where the optical depth not wavelength dependent (Casey et al., 2014).

[4]The peak flux density is taken as B_ν, not B_λ.

luminosity-weighted temperatures are necessarily measurable quantities, as radiative transfer effects can bias temperatures measured from dust luminosities (Lower et al., 2024).

We calculate the three temperatures at $z = 7.2$ and $z = 5.94$, and obtain the follows; $T_{\rm d,peak} = 47.5\,{\rm K}$, $T_{\rm d,mw} = 49.7\,{\rm K}$, $T_{\rm d,lumis} = 64.1\,{\rm K}$ at $z = 7.2$ and $T_{\rm d,peak} = 43.9\,{\rm K}$, $T_{\rm d,mw} = 40.9\,{\rm K}\,T_{\rm d,lumis} = 48.5\,{\rm K}$ at $z = 5.94$. In the next section, we will show the redshift evolution of those dust temperatures and explain their correlations in detail.

7.3.3.2 Redshift Evolution of Physical Properties

Figure 7.10 summarizes the evolution of the global dust emission properties from $z = 9.9$ to $z = 5.25$. From top to bottom, the panels show the star formation rate (SFR), UV slope ($\beta_{\rm UV}$), UV magnitude ($M_{\rm UV}$) and UV attenuation ($A_{\rm UV}$), dust temperature ($T_{\rm d}$), and infrared excess (IRX $\equiv L_{\rm TIR}/L_{\rm UV}$). The UV slope $\beta_{\rm UV}$ is defined by Eq. (7.3). The time evolution of $\beta_{\rm UV}$ roughly correlates with that of the 10 Myr-averaged SFR, specifically, when the SFR decreases, the slope becomes redder. The intrinsic UV slope varies approximately in the range $[-2.5, -2.0]$, while the attenuated UV slope ranges between $[-2.1, -1.2]$.

Regarding the UV magnitude ($M_{\rm UV}$), we calculate it from λL_λ at rest-frame $\lambda = 1600\,{\rm Å}$. The fluctuations in both intrinsic and attenuated UV magnitudes correspond closely to those in the 10 Myr-averaged SFR, even though stellar populations with ages up to ~ 100 Myr contribute to UV emission. The UV attenuation ($A_{\rm UV}$) rapidly increases following the merger event at $z \sim 7$, and subsequently, the global $A_{\rm UV}$ remains above 1 mag.

For dust temperatures, we consider the three types of temperatures as introduced in Section 7.3.3.1. The luminosityweighted temperatures $T_{\rm d,lumis}$ always exceed the massweighted temperatures $T_{\rm d,mass}$ by 10–25 K, reflecting that the most luminous dust is warm, whereas most of the dust mass is cold (e.g., Behrens et al., 2018; Lower et al., 2024; Sommovigo et al., 2021; Liang et al., 2019). The time fluctuation of peak temperatures $T_{\rm d,peak}$ is complex. At $z \gtrsim 8$, when UV attenuation and dust mass are small, $T_{\rm d,peak}$ can exceed $T_{\rm d,mass}$; during the merger at $z \sim 7$, it sits $\sim$5 K above $T_{\rm d,mass}$. This behavior arises primarily from radiativetransfer effects and the finite optical depth in the restFIR. Thermal dust emission in the restFIR is often assumed to be optically thin, or to transition from thick to thin around 100–200 μm . This assumption underpins both the modeling of FIR SEDs for UV and submillimeterselected galaxy samples (Swinbank et al., 2014; Harikane et al., 2020; Sommovigo et al., 2022) and the definition of $T_{\rm d,peak}$ (Eq.7.4). However, in dense clumps this assumption breaks down. For instance, the global SED in Figure 7.9 peaks at $\lambda_{\rm rest,peak} = 60\,\mu{\rm m}$. From Figure 7.1, the restFIR opacity is

$$\kappa_\lambda = 0.5 \left(\frac{\lambda}{870\,\mu{\rm m}}\right)^{-\beta}\ {\rm cm^2\,g^{-1}} \tag{7.7}$$

$$\therefore \kappa_{60\mu{\rm m}} = 105\,{\rm cm^2\,g^{-1}}\ \ ({\rm for}\ \beta = 2). \tag{7.8}$$

According to Figure 7.7, clumps typically have dust columns of $\sim 100\,M_\odot\,{\rm pc^{-2}} = 2.1{\times}10^{-2}\,{\rm g\,cm^{-2}}$, implying $\tau_{60\,\mu{\rm m}} \simeq 2.2$. Thus, in clumps the FIR emission is optically thick, and even as heating increases $T_{\rm d,mass}$, the large optical depth prevents an increase in $T_{\rm d,peak}$. A similar trend has been reported in several theoretical studies (e.g., Ma et al., 2019; Liang et al., 2019; Lower et al., 2024).

In the bottom panel of Figure 7.10, we show the evolution of IRX, the UV luminosity $L_{\rm UV}$, and the total IR luminosity $L_{\rm TIR}$. We define IRX as

$${\rm IRX} \equiv \frac{L_{\rm TIR}}{L_{\rm UV}} = \frac{\int_{8\,\mu{\rm m}}^{1000\,\mu{\rm m}} L_\lambda\,{\rm d}\lambda}{\lambda_{1600{\rm Å}} L_{\lambda,1600}}, \tag{7.9}$$

where all wavelengths are in the rest frame. The temporal variation of IRX closely tracks that of UV attenuation $A_{\rm UV}$, indicating that changes in dust absorption and reemission govern IRX.

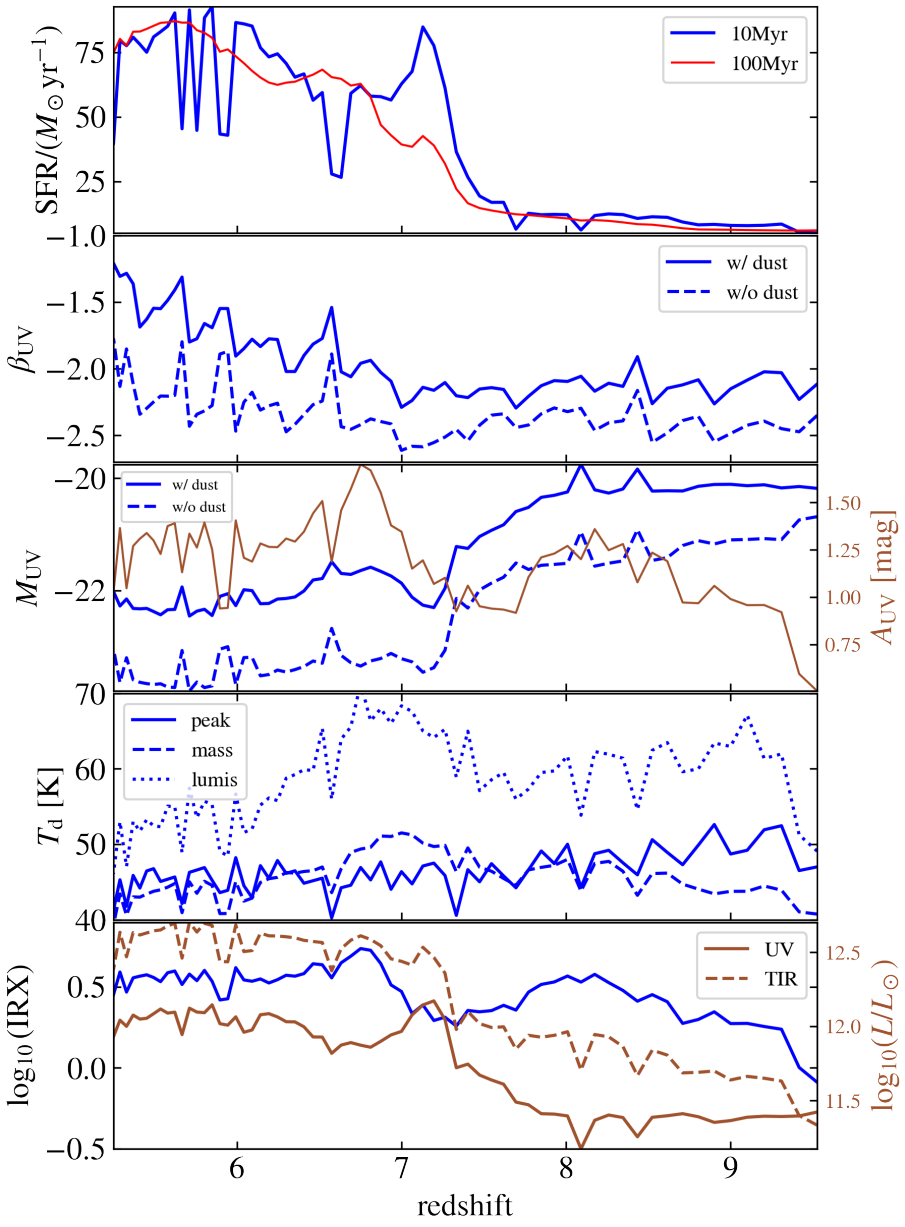

Figure 7.10: Redshift evolution of physical properties within 10 kpc regions. The top panel shows the SFR averaged over 10 Myr (blue) and 100 Myr (red), as in Figure 7.4. The second panel represents UV slopes before and after dust attenuation as dashed and solid lines, respectively. The UV slopes are calculated using Eq. (7.3). The third panel shows UV magnitude, and $A_{\rm UV}$. The fourth panel shows three different dust temperatures. The solid, dashed, and dotted blue lines are peak dust temperature, mass-weighted, and luminosity-weighted dust temperatures, respectively, as detailed in the text. The bottom panel represents IRX in the blue line, and UV /total-IR luminosities in the brown lines.

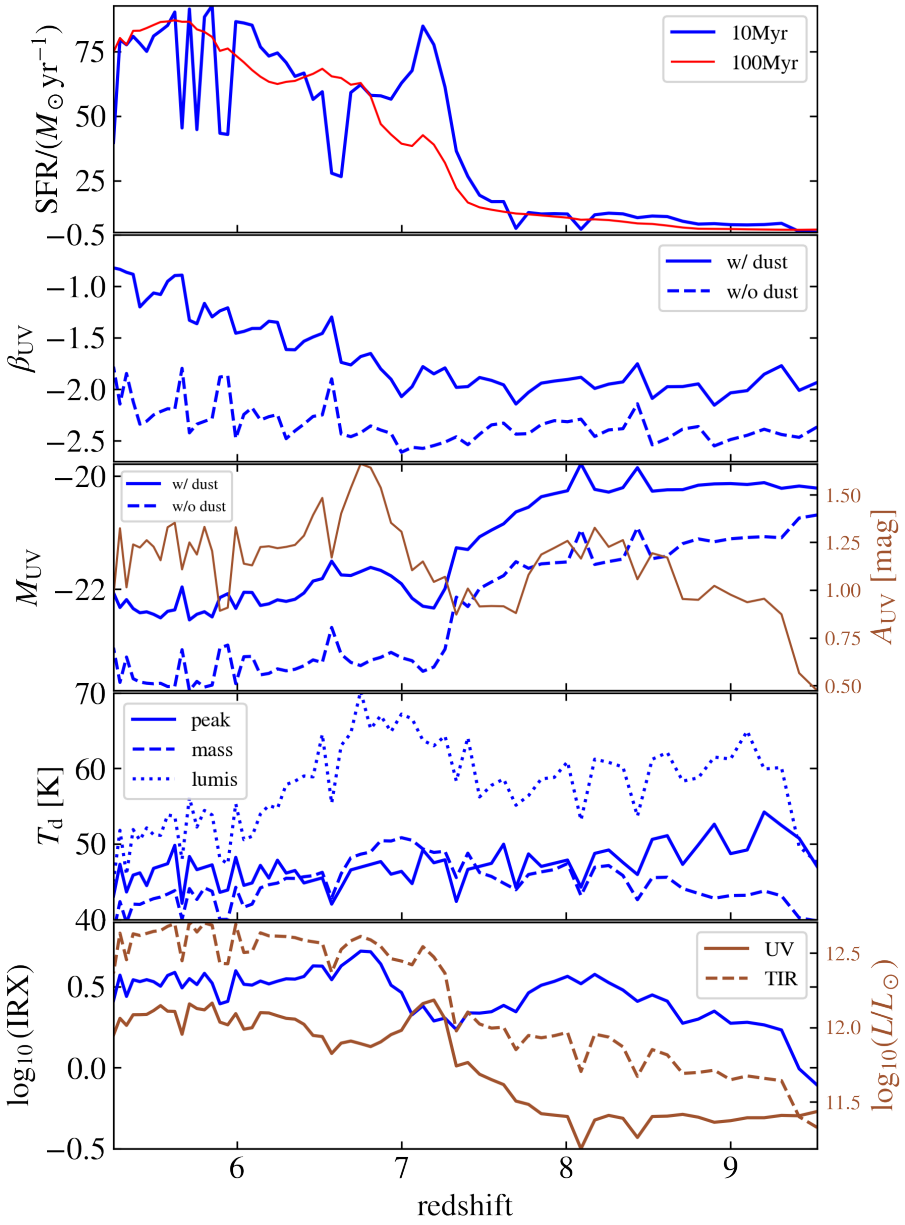

Figure 7.11: The same as Figure 7.10 but for SMC-like grains.

In contrast, the fluctuations of $L_{\rm TIR}$ and $L_{\rm UV}$ trace the time evolution of the 10 Myr–averaged SFR, demonstrating that both the dustreprocessed IR output and the intrinsic UV emission respond on similar timescales to bursts in star formation.

Figure 7.11 shows the time evolution of dust properties as the same as Figure 7.10, but for SMC-like dust grains. The main difference is the attenuated UV-slope. As shown in Figure 3.18, SMC has steeper extinction curves than MW and is expected to have steeper attenuation curves as well (Behrens et al., 2018). Then the UV-slope is redder than that of MW by $\Delta\beta_{\rm UV} \simeq 0.5$. However, the extinction cross-sections at $\lambda_{\rm rest} = 1600$ are almost the same, and the values of $M_{\rm UV}$ and $A_{\rm UV}$ are almost the same as MW case. As shown in Figure 7.9, the IR emission does not change largely between dust types, and the IRX values are almost the same. Although differences in grain size distribution can affect dust temperatures, all three temperatures have almost the same values as those for the MW.

7.3.4 Dust Properties of Individual Clumps

Figures 7.12 and 7.13 summarize the intrinsic and attenuated SEDs of each clump, identified as described in Section 7.2.3. We immediately see that both the unreddened slope ($\beta_{\rm UV,0}$) and the dustreddened slope ($\beta_{\rm UV,MW}$) vary significantly from clump to clump.

In the $z = 7.2$ major-merger system, clumps 2 and 3 correspond to the central and companion galaxies, respectively, while clump 1 traces the tidal tail formed during the peri-center passage. As shown in Figure 7.5 and Table 7.2, clump 1 is dominated by young stars and exhibits steep intrinsic UV slopes ($\beta_{\rm UV,0} < -2.5$). In contrast, clump 2 hosts the oldest stellar population among the three clumps and already contains dust from pre-merger star formation, resulting in the reddest observed UV slope ($\beta_{\rm UV,MW} = -1.65$).

Figure 7.13 shows the VDI-driven system at $z = 5.94$. Here, clump 2 corresponds to the central proto-bulge, whereas clumps 1, 3, 4, and 5 form via disk instabilities (see Figure 7.6). Clump 2 has the reddest UV slope in both intrinsic and attenuated cases. However, the VDI-driven clumps exhibit a wide range of UV slopes and IRX values, despite having similar stellar ages (Figure 7.5). Notably, clump 5 exhibits a very blue UV slope ($\beta_{\rm UV,MW} = -2.36$) and a low IRX (0.56). These features suggest that clump 5 is a newly formed VDI fragment, while the others are older VDI-driven clumps.

Figure 7.14 shows the IRX–β relationship for our simulated galaxy (FL958). The gray points represent the integrated properties of FL958 across the entire simulation from $z = 9.5$ to $z = 5.25$. The red and blue circles indicate snapshots at $z = 7.2$ (merger-driven) and $z = 5.94$ (VDI-driven), respectively, highlighting epochs of distinctly clumpy morphologies. For reference, we overlay theoretical IRX–β relations calculated assuming two intrinsic UV slopes ($\beta_{\rm UV,0}$): the local calibration by Meurer et al. (1999) ($\beta_{\rm UV,0} = -2.23$) and the high-redshift calibration by Reddy et al. (2018) ($\beta_{\rm UV,0} = -2.62$). Both reference curves assume the Calzetti attenuation law (Calzetti et al., 2000).

The integrated galaxy properties (gray points) closely follow the high-z Calzetti IRX–β curve (Reddy et al., 2018). As cosmic time progresses, the galaxy moves toward redder UV slopes (larger $\beta_{\rm UV}$), while maintaining relatively constant IRX values (≈ 0.5). However, the IRX–β relations for individual clumps deviate significantly from these integrated values. Both ex-situ (merger-driven) and in-situ (VDI-driven) clumps show systematically higher IRX values compared to the integrated system. Notably, the VDI-driven clumps follow closely the high-z Calzetti curve, whereas the merger-driven clumps lie 1–2 dex above the reference curves. This result indicates that merger-driven clumps have bluer intrinsic UV slopes than VDI-driven clumps but suffer substantially stronger dust attenuation. We discuss possible explanations for this discrepancy, specifically related to the geometry of dust and star distributions, by introducing a toy model in Section 7.4.1.

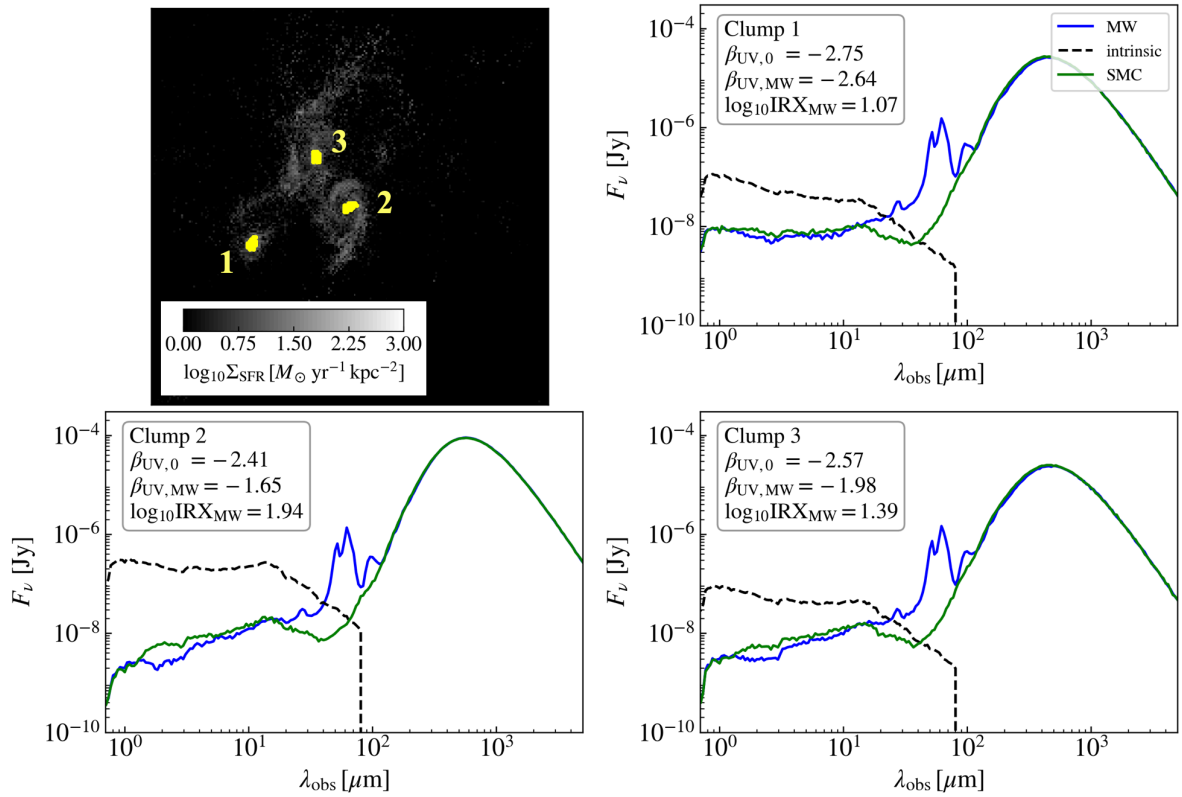

Figure 7.12: SEDs for the three clumps identified in FL958 at $z = 7.2$. The upper-left panel shows the SFR surface-density map (as in Figure 7.5), with pixels exceeding the clump-identification threshold highlighted in yellow and each clump labeled. The remaining panels display the SED of each clump. The solid blue and green lines denote the attenuated SEDs assuming Milky Way and SMC-like dust, respectively, while the dashed black line shows the intrinsic stellar continuum. Each panel also reports the UV–$\beta_{\rm UV}$ slopes (with and without dust) and the infrared excess (IRX).

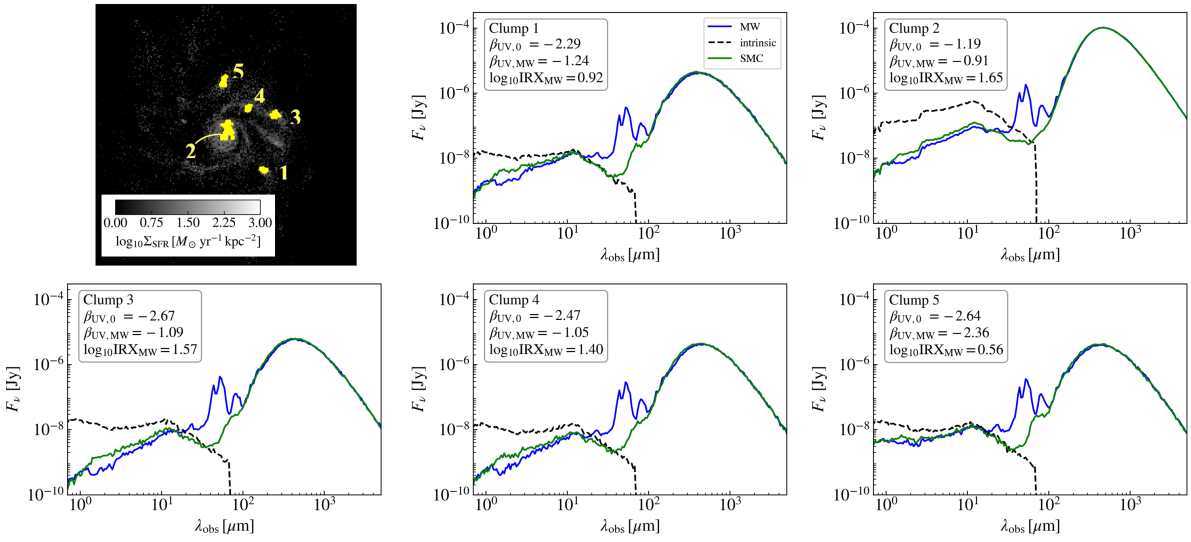

Figure 7.13: Same as in Figure 7.12, but for FL958 at $z = 5.94$.

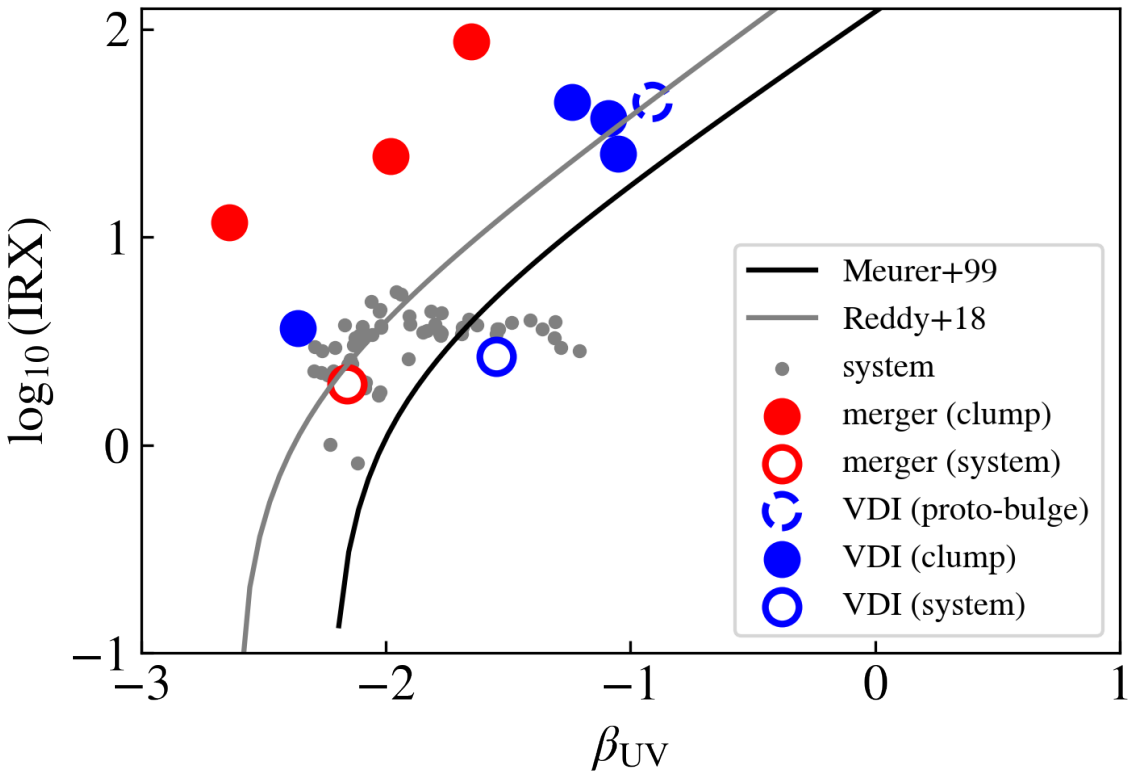

Figure 7.14: IRX–$\beta_{\rm UV}$ relation assuming a Milky Way–like dust type. The gray points show the integrated properties of FL958 within a 10 kpc region from $z = 9.5$ to $z = 5.25$. The red and blue points correspond to individual clumps at $z = 7.2$ (merger-driven) and $z = 5.94$ (VDI-driven), respectively. The sizes of the red and blue markers are scaled by the peak dust temperatures of the clumps. For reference, we show the IRX–$\beta_{\rm UV}$ relations from Meurer et al. (1999) (black) and Reddy et al. (2018) (gray), both of which adopt the Calzetti attenuation law.

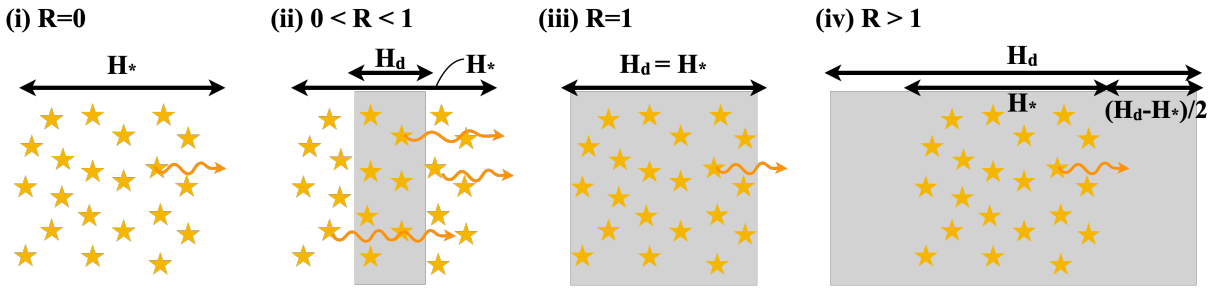

Figure 7.15: Illustration of the four simplified dust-star geometry models characterized by different dust-to-star scale height ratios ($R \equiv H_{\rm d}/H_*$). Stars represent the stellar layer with scale height H_*, and gray shaded areas indicate the uniform dust layer with scale height $H_{\rm d}$. Orange arrows schematically represent escaping UV radiation. The escape probability for each geometry type is derived explicitly in the main text.

7.4 Discussion

7.4.1 Ex-situ vs. In-situ Dust Properties

In Section 7.3.4, we found different IRX–β relations between integrated galaxy results and individual clumps. Even among clumps, ex-situ and in-situ populations exhibit distinct IRX–β relationships. To interpret these differences, we construct a simple toy model of dust and star distributions and demonstrate how differences can be explained by variations in dust-star geometry, parametrized by two physical quantities.

We assume star and dust layers with scale heights H_* and $H_{\rm d}$, respectively. The geometry is symmetric, and the dust layer has a uniform dust density, $n_{\rm d}$. We define two important parameters: the dust-to-star scale height ratio $R \equiv H_{\rm d}/H_*$, and the fiducial optical depth $\tau_\lambda^{\rm fid} = \sigma\lambda n_{\rm d} H_{\rm d}$, where σ_λ is the dust cross-section, uniquely determined by the chosen dust extinction curve. We introduce the escape probability at wavelength λ as $P_{{\rm esc},\lambda} \equiv L_{{\rm obs},\lambda}/L_{{\rm int},\lambda}$, where $L_{{\rm obs},\lambda}$ and $L_{{\rm int},\lambda}$ are the observed and intrinsic luminosities, respectively.

The dust geometry is categorized into four types based on the scale-height ratio R, as schematically illustrated in Figure 7.15:

(i) $R = 0$: There is no dust layer, and therefore the observed luminosity is equal to the intrinsic luminosity, i.e., $P_{{\rm esc},\lambda} = 1$.

(ii) $0 < R < 1$: This corresponds to the *sandwich* geometry (Xu and Buat, 1995), with an escape probability given by

$$P_{{\rm esc},\lambda} = \frac{1-R}{2}(1+e^{-\tau_\lambda^{\rm fid}}) + \frac{R}{\tau_\lambda^{\rm fid}}(1-e^{-\tau_\lambda^{\rm fid}}). \tag{7.10}$$

(iii) $R = 1$: This corresponds to a well-mixed geometry, and the escape probability is given by

$$P_{{\rm esc},\lambda} = \frac{1-e^{-\tau_\lambda^{\rm fid}}}{\tau_\lambda^{\rm fid}}. \tag{7.11}$$

Cases (ii) and (iii) can be considered as a continuous transition.

(iv) $R > 1$: This corresponds to a combination of well-mixed and screen geometries. The escape probability is then given by

$$P_{{\rm esc},\lambda} = \frac{1-e^{-\tau_\lambda^{\rm mix}}}{\tau_\lambda^{\rm mix}} e^{-\tau_\lambda^{\rm screen}}, \tag{7.12}$$

where we define optical depths for the well-mixed and screen components as

$$\tau_\lambda^{\rm mix} = \sigma_\lambda n_{\rm d} H_* = \sigma_\lambda n_{\rm d} H_{\rm d} \frac{H_*}{H_{\rm d}} = \frac{\tau_\lambda^{\rm fid}}{R} \tag{7.13}$$

$$\tau_\lambda^{\rm screen} = \sigma_\lambda n_{\rm d} \frac{H_{\rm d} - H_*}{2} = \frac{\tau_\lambda^{\rm fid}}{2}\left(1 - \frac{1}{R}\right). \tag{7.14}$$

Next, we derive expressions for IRX and $\beta_{\rm UV}$ from this toy model. We introduce an effective optical depth defined as $\tau_{{\rm eff},\lambda} = -\log_{\rm e}(P_{{\rm esc},\lambda})$. Assuming the intrinsic UV luminosity is balanced by the observed UV and re-emitted IR luminosities, IRX is expressed as

$${\rm IRX} = \frac{L_{\rm TIR}}{L_{\rm obs,UV}} = \frac{1 - e^{-\tau^{\rm eff,UV}}}{e^{-\tau^{\rm eff,UV}}} = \frac{1 - P_{\rm esc,UV}}{P_{\rm esc,UV}}. \tag{7.15}$$

We consider a wavelength of 1600 Åas representative of UV radiation.

To define the UV slope, we select two wavelengths consistent with Section 7.3.3: $\lambda_1 = 1230$, and $\lambda_2 = 3200,$. The observed UV slope is then

$$\beta_{\rm UV} = \frac{\log_{10}(f_{\lambda_1}) - \log_{10}(f_{\lambda_2})}{\log_{10}(\lambda_1) - \log_{10}(\lambda_2)} \tag{7.16}$$

$$= \frac{\log_{10}(f^0_{\lambda_1}) - \log_{10}(f^0_{\lambda_2}) - (\log_{10} e) \times (\tau_{{\rm eff},\lambda_1} - \tau_{{\rm eff},\lambda_2})}{\log_{10}(\lambda_1) - \log_{10}(\lambda_2)} \tag{7.17}$$

$$= \frac{\log_{10}(f^0_{\lambda_1}) - \log_{10}(f^0_{\lambda_2})}{\log_{10}(\lambda_1) - \log_{10}(\lambda_2)} + \frac{-0.43(\tau_{{\rm eff},\lambda_1} - \tau_{{\rm eff},\lambda_2})}{\log_{10}(\lambda_1) - \log_{10}(\lambda_2)} \tag{7.18}$$

$$= \beta_{\rm UV,0} + \Delta\beta, \tag{7.19}$$

where f_λ (f^0_λ) denotes the observed (intrinsic) flux density at wavelength λ.

Finally, we derive the fiducial optical depth at $\lambda = \lambda_1$ as

$$\tau_{\lambda_1}^{\rm fid} = \tau_{\rm UV}^{\rm fid}\left(\frac{A_{\lambda_1}}{A_{\rm UV}}\right), \tag{7.20}$$

where the attenuation ratio is uniquely set by the adopted extinction curve. The intrinsic UV slope $\beta_{\rm UV,0}$ depends on the intrinsic SED, specifically stellar population age (star formation history) and metallicity. According to Eq. (7.19), $\Delta\beta$ is independent of the intrinsic SED and depends only on the dust geometries, provided that the dust type is fixed.

We now construct theoretical grids on the IRX–$\beta_{\rm UV}$ plane by parametrizing dust-star geometry through R and the fiducial optical depth $\tau^{\rm fid}$UV. The left panel of Figure 7.16 shows IRX–βUV grids obtained by varying these two parameters, assuming an intrinsic UV slope of $\beta_{\rm UV,0} = -2.5$. This intrinsic value is chosen based on typical star-forming galaxy populations, as indicated by Figure 7.10, though it fluctuates between approximately -2.5 and -2.0.

In the case of $R = 0$, the position on the IRX–$\beta_{\rm UV}$ plane is fixed at $(\beta_{\rm UV,0}, {\rm IRX}) = (-2.5, 0)$. As $R \to 0$, the toy model represents a scenario with a very thin dust sheet placed symmetrically at the center of the stellar distribution. In the optically thick regime ($\tau \gg 1$), radiation from behind this central dust sheet is absorbed and re-emitted in the IR, whereas radiation from the front side escapes directly as UV emission. These two contributions become equal, causing IRX to asymptotically approach 1. For $R < 1$, the grid curves exhibit a characteristic inverted-C shape because escaping radiation includes reddened contributions from the obscured backside. When $R = 1$ (fully well-mixed), the UV slope remains nearly constant with increasing optical depth ($\tau_{\rm UV}^{\rm fid} \gtrsim 1$), and IRX simply increases vertically. For large R values ($R \gtrsim 3$), the geometry approaches a screen model as shown in the solid black line.

In simulations, intrinsic physical properties such as the intrinsic UV slope ($\beta_{\rm UV,0}$) are readily available, and the dust-type can be consistently fixed (MW-type dust is assumed throughout

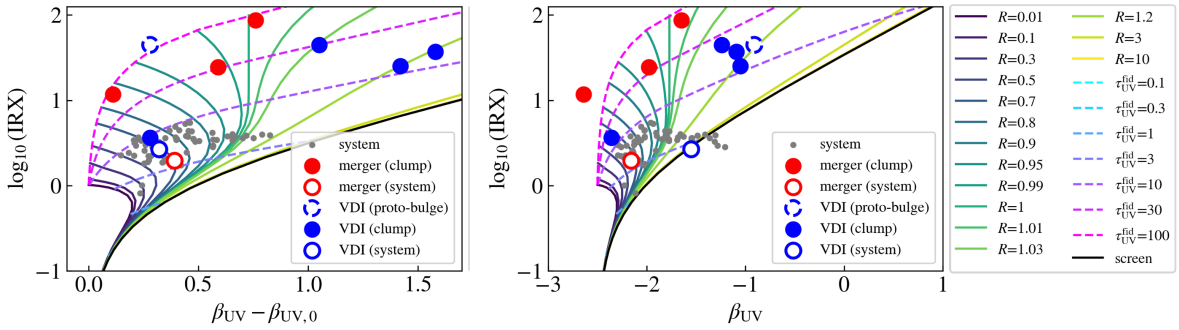

Figure 7.16: IRX–$\beta_{\rm UV}$ (left) and IRX–$\Delta\beta$ (right) relations calculated with varying dust-star geometry parameters R and fiducial UV optical depth $\tau_{\rm UV}^{\rm fid}$. The solid black lines represent theoretical curves assuming a screen geometry. Gray points show the integrated galaxy results for each snapshot of FL958 measured within a 10 kpc region, identical to those presented in Figure 7.14. Red and blue circles denote results for individual clumps, categorized into ex-situ (merger-driven; red) and in-situ (VDI-driven; blue) scenarios, respectively, as also shown in Figure 7.14. All simulation data points assume MW-type dust, and the toy-model grids adopt an MW dust extinction curve with $R_V = 3.1$ (Cardelli et al., 1989).

Figure 7.16). As introduced in Equation (7.19), this allows us to directly compute the intrinsic slope difference, defined as $\Delta\beta = \beta_{\rm UV} - \beta_{\rm UV,0}$. Consequently, the distribution of simulated galaxies on the IRX–$\Delta\beta$ plane (right panel of Figure 7.16) exclusively reflects variations in dust geometry. In what follows, we therefore utilize the IRX–$\Delta\beta$ plane to interpret the dust geometry in our simulated galaxies. The right panel of Figure7.16 shows our simulated galaxies on the IRX–$\Delta\beta$ plane, enabling direct interpretation of dust-star geometry. The interpretation of grid distribution here parallels that of the left panel. System-integrated results at $z < 6$ predominantly fall within $0.5 < R < 1$ and $0 < \tau_{\rm UV}^{\rm fid} < 3$, indicating a sandwich-like geometry. This reflects the coexistence of dense, optically thick star-forming regions obscured by dust layers and diffuse, UV-bright stellar regions. VDI-driven clumps show slightly higher optical depth ($\tau_{\rm UV}^{\rm fid} \sim 3$–4) and scale-height ratios around $R \sim 1.3$. This geometry suggests that VDI-clumps form from gravitational instabilities in gas-rich, metal-enriched disks, with clumps collapsing on timescales set by disk gas density.

However, Merger-driven clumps exhibit significantly different geometries, clustering around $R = 0.8$–1 (nearly well-mixed) with much higher optical depths ($\tau_{\rm UV}^{\rm fid} = 30$–100). Despite their large optical depths, the escape probability for well-mixed geometry scales as $P_{\rm esc,UV} \sim {\tau_{\rm UV}^{\rm fid}}^{-1}$, allowing 1–3% UV photons to escape. This high optical depth results from gas compression during interactions with companion galaxies, significantly enhancing local dust column densities.

Thus, given a known dust-type (extinction curve), the IRX–β (or IRX–$\Delta\beta$) plane effectively diagnoses dust-star geometry.

7.4.2 Application to Observations

Next, we apply our theoretical grids to interpret recent high-redshift observations. Some recent studies have begun exploring IRX–β relationships at the clump level in high-z galaxies (Sugahara et al., 2025; Lines et al., 2025, Mawatari et al. in prep.), although most available results are integrated values. Unlike simulations, dust-type (extinction curves) in observed galaxies is generally unknown. Nevertheless, overlaying observational points onto the IRX–β plane with toy-model geometry grids allows us to test consistency with MW- or SMC-like dust types. Figure 7.17 shows observational results for $z > 5$ galaxies plotted against grids calculated assuming MW-like (left) and SMC-like (right) dust.

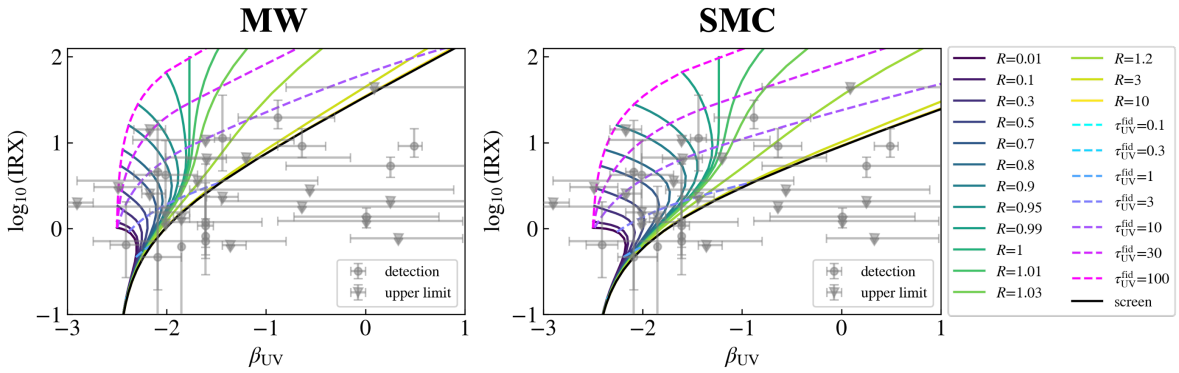

Figure 7.17: IRX–β relation with theoretical grids adopting MW-like (left) and SMC-like (right) dust extinction curves. Both panels also show observational data for galaxies at $z > 5$ as gray points with error bars, compiled from Mitsuhashi et al. (2024), Harikane et al. (2020), Hashimoto et al. (2019), Bakx et al. (2021), Akins et al. (2022), Witstok et al. (2022), and Algera et al. (2023). Observational data points shown as gray circles correspond to galaxies with dust continuum detections, while gray triangles represent non-detections (upper limits on IRX). The theoretical grids are computed adopting the MW extinction curve with $R_V = 3.1$ (Cardelli et al., 1989) and the SMC-bar extinction curve with $R_V = 2.74$ (Gordon et al., 2003), respectively.

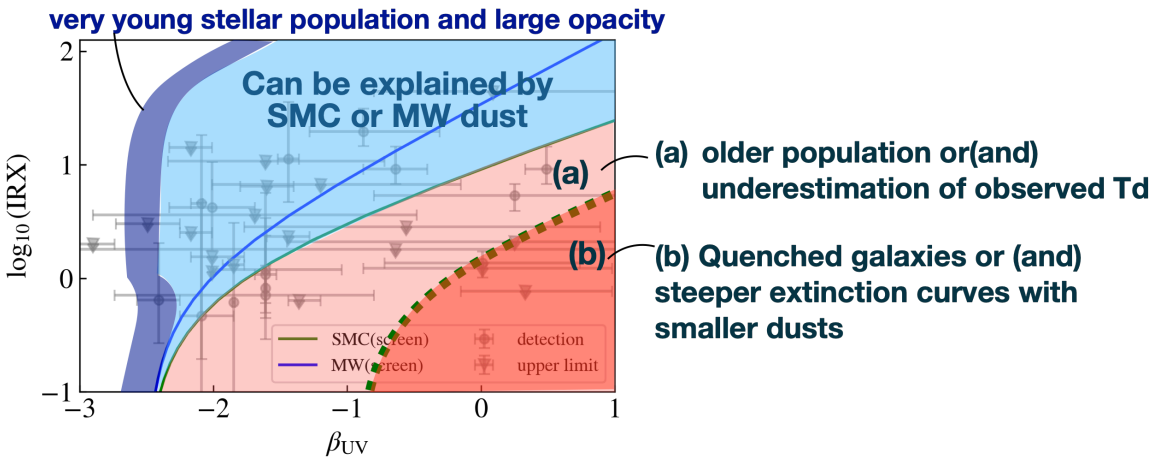

Figure 7.18: A schematic figure summarizing our interpretation of observed high-redshift galaxies in the IRX–$\beta_{\rm UV}$ plane. Gray points represent observed galaxies at $z > 5$, identical to those shown in Figure 7.17. The light-blue shaded region indicates the parameter space that can be explained by toy-model geometries assuming MW- or SMC-type dust. The dark-blue region corresponds to galaxies hosting very young stellar populations (younger than ~ 10 Myr) with significant UV opacity ($\tau_{\rm UV}^{\rm fid} \sim 100$). The light-red region suggests older stellar populations than typical star-forming galaxies or (and) potential underestimations of dust temperature. Finally, the dark-red region may indicate quenched galaxies or (and) galaxies having steeper extinction curves with smaller grain sizes than those of the SMC dust model.

Since the SMC extinction curve is steeper at UV wavelengths compared to MW extinction, this suggests smaller dust grains dominate in the SMC (Weingartner and Draine, 2001), shifting the IRX–β relation to redder slopes at fixed IRX. Observed galaxies located to the right of the MW screen geometry curve can thus be partially explained by SMC-type dust.

An additional important consideration is the intrinsic UV slope ($\beta_{\rm UV,0}$), which was set to -2.5 in the previous plots. In reality, older stellar populations yield redder intrinsic slopes, effectively shifting the curves toward larger (redder) β values. As an example, we computed $\beta_{\rm UV,0}$ for a galaxy whose star formation ceased 100 Myr prior, adopting a BPASS SED with $0.1, Z_{\odot}$, and found $\beta_{\rm UV,0} = -0.85$. Such shifts toward older populations allow galaxies beyond the SMC screen geometry curve to be explained naturally. Figure 7.18 schematically summarizes these interpretations. The light-blue region highlights galaxies explained by typical MW- or SMC-type dust geometries. Recent JWST observations have begun characterizing attenuation curves in high-z galaxies(e.g., Markov et al., 2023, 2025), thus potentially identifying dust types. With dust types constrained by JWST, our framework allows direct inferences about dust geometry.

The dark-blue region corresponds to galaxies hosting very young stellar populations combined with significant UV opacity ($\tau^{\rm fid}{\rm UV} \sim 100$). Recent JWST observations of UV slopes have indeed identified numerous dust-free galaxies at high-z characterized by intrinsically very blue UV slopes (e.g., Cullen et al., 2024). If stellar populations are younger than 10 Myr, the intrinsic slope ($\beta{\rm UV}, 0$) becomes even bluer than our default assumption of -2.5, effectively shifting the theoretical grid lines toward the left. This scenario naturally explains a few observed galaxies in the IRX–β diagram, as they can be characterized by very young stellar populations and thin dust layers with large UV opacity.

The area to the right of the standard SMC screen geometry curve (assuming $\beta_{\rm UV,0} = -2.5$) is shaded in red. Within this region, we further subdivide based on a curve representing a quenched galaxy population that ceased star formation 100 Myr prior, i.e., $\beta_{\rm UV,0} = -0.85$ (green dotted line). This divides the region into two distinct subregions: region (a), shaded in light red, and region (b), shaded in dark red.

Region (a) corresponds to galaxies with somewhat older stellar populations than typical star-forming galaxies, or galaxies in which the dust continuum emission is undetected, leading to a potential underestimation of dust temperature ($T_{\rm d}$). Non-detection scenarios force continuum fitting based on upper limits, which can significantly underestimate the intrinsic dust temperature. Since total IR luminosity scales roughly as $L_{\rm IR} \propto T_{\rm d}^{4+\beta_{\rm IR}}$ assuming a gray-body spectrum, this underestimation would result in artificially lowered IRX values. Correcting for this, these galaxies might move into the canonical region (light-blue).

Finally, region (b) could represent either fully quenched galaxies, whose star formation has halted for over 100 Myr, or galaxies that contain stellar populations intermediate in age (older than typical star-forming galaxies, but younger than fully quenched galaxies) combined with a dust population dominated by grains even smaller than those found in SMC-type dust. This would produce a steeper extinction curve in the UV, thus explaining the galaxies' position in region (b). Future JWST observations of the rest-frame UV and optical continua will be crucial to discriminating among these proposed scenarios.

Overall, the IRX–β diagram provides a powerful diagnostic tool, capable of categorizing observed galaxies by their dust geometries, intrinsic stellar populations, and dust grain properties.

7.4.3 Caveates

There are several caveats to our study. First, we have adopted a fixed dust–to–metal ratio of 0.4. According to Dayal et al. (2022), DTM keeps the constant value of 0.37 when considering only stellar-path production. However, in reality, processes such as astration and destruction act to reduce the DTM, while ejection (which preferentially removes gas-phase metals) and grain growth act to increase it. Moreover, the efficiency of grain growth depends on the accretion timescale for gas-phase metals to stick onto dust grains, which scales as $t_{\rm acc} \propto n^{-1}T^{-1/2}Z^{-1}$.

The equation implies that higher-density, lower-temperature, higher-metallicity environments such as molecular clouds favor collisions and subsequent sticking between gas-phase metals and grains (Dwek, 1998; Zhukovska et al., 2008). In practice, one often writes $t_{\rm acc} = t_{\rm acc,\odot}\left(Z/Z_\odot\right)^{-1}$, and Dayal et al. (2022) shows that adopting $t_{\rm acc,\odot} = 30\,$Myr causes the DTM to decline from 0.6 at $z \simeq 12$ to 0.47 by $z \simeq 7$, whereas shortening $t_{\rm acc,\odot}$ to 0.3 Myr raises the DTM by a factor of ~ 2.7. In future work we will therefore implement a fully time-dependent DTM obtained from semi-analytic models (e.g., Dayal et al., 2022; Tsuna et al., 2023; Toyouchi et al., 2025) and cosmological simulations (e.g., Aoyama et al., 2017; Graziani et al., 2020; Kannan et al., 2025).

Second, we have assumed a fixed dust composition and size distribution: Milky Way–and SMC-like mixtures. The high-redshift dust is believed to form predominantly in core-collapse supernovae (Mancini et al., 2015) and to be processed by shocks in such a way that small grains are preferentially destroyed, biasing the population toward larger particles (Makiya and Hirashita, 2022). Because grains whose radii exceed the photon wavelength λ scatter and absorb nearly independently of λ under Mie theory, a distribution dominated by large grains produces a gray (flat) attenuation curve. We therefore plan to explore evolving dust yields, shattering, coagulation, and ISM growth in a self-consistent framework that allows both composition and size distribution to vary with redshift.

Third, we investigate a single simulated galaxy, even though Nakazato et al. (2024) estimates that about 10–20 % of $M_* \gtrsim 10^9\,M_\odot$ galaxies in the Epoch of Reionization appear as merger-driven clumpy systems. To assess the diversity of clumpy-galaxy dust properties more robustly, it will be necessary to extend our analysis to a statistically representative sample. Since the FirstLight simulations contain the 62 zoom-in halos in the 40 cMpch^{-1} (see Section 7.2), we plan to perform statistical analysis in future work.

Finally, we identify clumps using a fixed [OIII] –brightness threshold in SFR surface density as the same as Nakazato et al. (2024), which by construction excludes *dormant* clumps lacking ongoing star formation. For example, at $z = 5.94$ a small component immediately adjacent to a disk-galaxy bulge is bright in rest-optical / near-IR continuum but dark in [OIII] and would therefore be missed in our identification. Indeed, clump identification in real observations is also difficult since it depends sensitively on filter choice, exposure time, point-spread function, and detection limits. We will in future quantify how the number, sizes, and inferred properties of clumps vary in a statistical, filter-dependent manner across multiple bands and observational setups (e.g., Punyasheel et al., 2025).

7.5 Conclusion and Summary

In this chapter, we have investigated dust properties at sub-galactic scales in high-redshift galaxies using cosmological zoom-in simulations combined with three-dimensional, post-processed dust radiative transfer calculations. We traced the detailed time evolution of a simulated galaxy undergoing both ex-situ (merger-driven) and in-situ (VDI-driven) clumpy phases, identifying clumps based on their star formation rate surface densities.

We first examined the time evolution of integrated dust properties and found that the merger-driven clumpy phase at $z \sim 7.2$ triggered highly bursty star formation, generating strong UV radiation with an intrinsic magnitude of $M_{\rm UV,0} = -23.5$ and the bluest UV slope of $\beta_{\rm UV,0} = -2.6$. The IRX peaked shortly after the merger, reaching $\log_{10}({\rm IRX}) = 0.74$. In contrast, during the VDI-driven phase at $z \sim 5.9$–5.5, the intrinsic UV slope became redder in response to variability in the 10 Myr-averaged star formation rate, while the IRX remained relatively constant around $\log_{10}({\rm IRX}) \simeq 0.5$.

Focusing on two representative snapshots: $z = 7.2$ for merger-driven clumps and $z = 5.94$ for VDI-driven clumps, we found that both types of clumps exhibit IRX values that are approximately 0.5-1.7 dex higher than their respective integrated galaxy values. Moreover, over 50% of the clumps had redder UV slopes compared to the integrated galaxy, a discrepancy attributed

to the significant contribution of diffuse stellar components around clumps, which lead to overall bluer integrated UV slopes. These results indicate that the IRX–β relation for spatially resolved clumps differs from that for integrated systems. Consequently, observations of clumpy systems may underestimate the total star formation rate if the IRX–β relation calibrated for single (or unresolved) systems is applied.

To interpret the observed scatter in the IRX-$\beta_{\rm UV}$ plane, we introduced a toy model parameterized by the scale-height ratio of dust to stars ($R \equiv H_{\rm d}/H_*$) and UV optical depth in the dust layer (represented by $\tau_{\rm UV}^{\rm fid}$). We found that VDI-driven clumps possess optical depths similar to their host galaxies ($\tau_{\rm UV}^{\rm fid} \sim 3$), whereas merger-driven clumps show significantly higher optical depths ($\tau_{\rm UV}^{\rm fid} \sim 30 - 100$), resulting from gas compression due to galaxy-galaxy interactions. This enhances the dust column density and leads to higher attenuation. Furthermore, we found that merger-driven clumps predominantly exhibit well-mixed dust-star geometries, while some VDI-driven clumps are better described by combinations of well-mixed and screen-like geometries.

Finally, we applied our toy model to observed galaxies and demonstrated the potential of the IRX-$\beta_{\rm UV}$ relation as a diagnostic tool for distinguishing between different dust-star geometries, particularly when dust-type information can be constrained observationally.

In the near future, detailed analyses of dust attenuation curves from JWST are expected to place strong constraints on dust types. Upcoming observations with PRIMA (the PRobe far-Infrared Mission for Astrophysics; Moullet et al., 2023), which will probe rest-frame mid-infrared emission, are anticipated to further improve our understanding of dust properties. Moreover, combining high-spatial-resolution data from JWST and ALMA will ultimately provide deeper insights into the distinct stellar and dust properties associated with different clump-formation pathways. These synergetic observations will enable direct constraints on spatially resolved IRX–β relations and facilitate more accurate estimates of total star formation rates.

Chapter 8

Physical Origins of [OIII]/[CII] Line Ratios of High-Redshift Galaxies

8.1 Introduction

The interstellar medium (ISM) is fundamentally important for galaxy formation and evolution, as it governs star formation activity, influences chemical enrichment processes, and mediates various forms of feedback. While local galaxy observations have established the foundational understanding of ISM physics, investigating the properties and behavior of the ISM at $z > 6$ is critical to comprehensively explore the early stages of galaxy formation occurring during and before the Epoch of Reionization (EoR) as introduced in Chapter 4. Galaxies at such high redshifts typically exhibit extreme physical conditions, including significantly lower metallicities and more intense radiation fields compared to local galaxies, potentially leading to substantial changes in physical state and chemical composition of the USM.

Among the various ISM tracers, the far-infrared (FIR) lines [OIII] 88μm and [CII] 158μm have been used most significantly for high-redshift studies. The [OIII] line traces ionized gas surrounding massive star-forming regions, whereas the [CII] line originates both in neutral photodissociation regions (PDRs) and mildly ionized gas, although it is thought to mostly originate in PDRs (Stacey et al., 2010; Gullberg et al., 2015; Vallini et al., 2015; Lagache et al., 2018; Cormier et al., 2019). Observations of these FIR lines with the Atacama Large Millimeter/Submillimeter Array (ALMA) have opened a new era for investigating the physical conditions in star-forming regions of $z > 6$ galaxies.

Recent ALMA observations have succeeded in detecting the rest FIR emission lines [OIII] 88μm and [CII] 158μm from galaxies at $z > 6$ (e.g., Inoue et al., 2016a), and have extended these detections even beyond $z > 10$ for some spectroscopically confirmed galaxies identified by JWST (Schouws et al., 2024; Carniani et al., 2025; Zavala et al., 2024). Notably, these high-redshift galaxies exhibit elevated [OIII] /[CII] line ratios ranging from approximately 1 to 20, significantly higher than the typical ratios of 0.04–1 observed in local galaxies (Howell et al., 2010; De Looze et al., 2014; Díaz-Santos et al., 2017) as shown in Figure 4.2 of Chapter 4. Furthermore, the non-detection of [CII] emission in GS-z14-0—the highest-redshift galaxy observed to date constrains a lower limit for the line ratio of [OIII] /[CII] > 3.5 (Schouws et al., 2025).

These findings suggest that high-redshift galaxies might host unique ISM conditions. Several explanations have been proposed, such as lower PDR covering fractions, higher ionization parameters, lower metallicities, and an enhanced oxygen-to-carbon abundance ratio (e.g., Harikane et al., 2020; Katz et al., 2022; Nyhagen et al., 2024). However, the origin of the observed line ratios remains under debate.

Theoretical efforts have aimed to interpret these puzzling observational results using various modeling approaches, including semi-analytic methods for line emission (Lagache et al., 2018; Popping et al., 2019), cosmological zoom-in simulations focused on relatively small sam-

ples (individual galaxy snapshots) (e.g., Vallini et al., 2015, 2017; Katz et al., 2019; Olsen et al., 2017; Pallottini et al., 2019; Arata et al., 2020; Schimek et al., 2024; Nyhagen et al., 2024), and larger-scale simulations encompassing statistically significant galaxy samples (Katz et al., 2022; Pallottini et al., 2022; Ramos Padilla et al., 2023). However, most current simulations do not incorporate fully coupled, on-the-fly radiative transfer (RT) calculations alongside chemical reaction networks, thus requiring numerous assumptions when modeling the multi-phase ISM. Although some simulations perform on-the-fly RT calculations, they typically have spatial resolutions on the order of 10–20 pc, potentially neglecting small-scale ISM structures critical for accurately determining the ionization state of gas. Despite the diverse range of theoretical modeling approaches explored so far, reproducing the observed high [OIII] /[CII] line ratios at $z > 6$ has proven challenging for many of these models.

Indeed, the characteristic scale of an HII region surrounding a single OB-type star can be described by the Strömgren radius,

$$R_{\rm S} \;=\; 1.85\,{\rm pc}\left(\frac{n_{\rm HII}}{500\,{\rm cm^{-3}}}\right)^{-2/3}\left(\frac{Q({\rm H})}{5\times10^{49}\,{\rm s^{-1}}}\right)^{1/3}, \tag{8.1}$$

where $n_{\rm HII}$ and Q(H) are the gas number density of HII region and the ionizing photon number per unit time emitted from the source stars, respectively. Eq. (8.1) shows that for typical densities observed in the ISM at high-z, sub-pc resolution simulations are needed to resolve the multi-phase ISM accurately.

In this study, we introduce a novel suite of cosmological zoom-in simulations reaching spatial resolutions down to 0.1 pc and incorporating on-the-fly radiative transfer (RT), allowing us to realistically model the multi-phase ISM and accurately predict emission lines spanning from the rest-frame UV to FIR wavelengths. We specifically target galaxies at redshifts $z > 10$ to investigate the physical mechanisms driving the elevated [OIII] /[CII] line ratios observed in high-redshift sources. Our analysis covers the spatial variations and temporal evolution of the [OIII] /[CII] ratio, complemented by an analytical toy model designed to interpret the multi-phase nature of the gas. Furthermore, by exploring the interplay between ALMA-observed rest-FIR lines ([OIII] , [CII]) and JWST-observed rest-optical lines (e.g., Hβ, [OIII] 4959, 5007Å), we demonstrate how observational data can be used to derive constraints on multi-phase gas properties, thereby providing insights into the physical conditions and feedback processes shaping galaxies in the early Universe.

This chapter is structured as follows. In Section 8.2, we describe our simulation setup and line calculation methods. Section 8.3 presents the resulting emission line properties and compare these results with observations and other theoretical works. In Section 8.4, we discuss the redshift evolution of [OIII] /[CII] from high-z to low-z and investigate the synergy with JWST rest-frame optical lines. Finally, Section 8.5 summarizes our conclusions and outlines future prospects.

8.2 Methods

8.2.1 Zoom-in Cosmological Simulations

The simulation suite used in this study was initially presented in Garcia et al. (2023, 2025) and Sugimura et al. (2024) (hereafter S24). S24 run cosmological zoom-in radiation-hydrodynamics simulations focused on a dwarf galaxy, utilizing the RAMSES-RT code (Teyssier, 2002; Rosdahl et al., 2013), which employs adaptive mesh refinement (AMR) techniques and solves radiative transfer equations based on the M1 closure scheme (Rosdahl et al., 2013).

We begin with a low-resolution, dark-matter-only simulation within a comoving volume of $35\,h^{-1}$ Mpc on a side. The initial conditions are generated at $z = 127$ with MUSIC (Hahn and Abel, 2011). From this simulation, we select a dark matter halo with $M_{\rm vir} = 8.8\times10^9\,M_\odot$ at $z = 0$. This halo grows to a mass of $10^8\,M_\odot$ by $z \sim 10$, eventually becoming a dwarf galaxy in the Local Group by $z = 0$ (Ricotti et al., 2022).

We subsequently perform a zoom-in simulation targeting this specific halo. The refined simulation volume extends approximately $300\,h^{-1}$, ckpc on each side, achieving an initial spatial resolution of $2\,h^{-1}$, ckpc, and employs dark matter particles with a mass of $800\,M_\odot$. Halos are identified using the ROCKSTAR halo finder (Behroozi et al., 2013), with a minimum requirement of 300 particles per halo. This particle-count threshold corresponds to resolving halos down to a mass of $2.4\times10^5\,M_\odot$, comparable to the minihalos expected to host the formation of the first stars (e.g., Yoshida et al., 2003). We evolve the simulation until $z = 9.5$.

AMR refinement takes place on the fly. A cell is flagged for refinement if it contains more than eight dark matter or star particles. Additionally, the Jeans length must be resolved by $N_{\rm J}$ cells. Truelove et al. (1997) argued that the Jeans length should be resolved by at least four cells ($N_{\rm J} = 4$) to prevent artificial fragmentation. Specifically, for cells with $2.4\,{\rm pc}[(1+z)/10]^{-1} \leq \Delta x \leq 77\,{\rm pc}[(1+z)/10]^{-1}$, we set $N_{\rm J} = 8$, and for cells with $0.3\,{\rm pc}[(1+z)/10]^{-1} \leq \Delta x \leq 1.2\,{\rm pc}[(1+z)/10]^{-1}$, we set $N_{\rm J} = 4$. At the highest refinement level ($l = 25$), the minimum physical cell size is therefore $\Delta x_{\rm min} = 0.15\,{\rm pc}[(1+z)/10]^{-1}$.

We categorize the radiation field into four different energy bins: the Lyman-Werner band (FUV, 11.2–13.6 eV), hydrogen(H)-ionizing radiation (EUV1, 13.6–24.6 eV), helium(He)-ionizing radiation (EUV2, 24.6–54.4 eV), and He^+-ionizing radiation (EUV3, 54.4–200 eV). To account for dust attenuation, we adopt a cross-section that scales linearly with metallicity, $\sigma_{\rm d,eff} = 4\times10^{-21}\,(Z/Z_\odot){\rm cm}^2$, based on the assumption of a fixed dust-to-metal mass ratio (Katz et al., 2017).

Photoionization and photoheating are modeled using a seven-species, non-equilibrium chemical network that tracks H, H^+, e^-, H_2, He, He^+, He^{++}, following Park et al. (2021). We assume that H^- remains in equilibrium with these species. We additionally include the absorption of FUV radiation in self-shielded regions following Park et al. (2021), as well as dust photoelectric heating according to the prescription of Kimm et al. (2017). The self-shielding of Lyman-Werner photons in dense gas is modeled using the analytic fitting function provided by Draine and Bertoldi (1996). Metal and dust cooling/heating rates are calculated following Katz et al. (2017), employing the cooling tables provided by GRACKLE (Smith et al., 2017). However, unlike Katz et al. (2017), we do not adopt a sub-grid clumping factor to model dust-catalyzed H_2 formation, assuming instead that our spatial resolution explicitly resolves this process.

Star formation occurs in cells at the maximum refinement level ($l = 25$) whose gas density satisfies

$$n \;>\; n_{\rm crit} = 5.0\times10^4\,{\rm cm}^{-3}\left(\frac{T}{100\,{\rm K}}\right)\left(\frac{1+z}{10}\right)^2\left(\frac{N_{\rm cr}}{4}\right), \tag{8.2}$$

which is derived from the Jeans criterion expressed in physical units, $\Delta x_{\rm min} < \lambda_{\rm J}/N_{\rm cr}$. This criterion corresponds to densities of approximately $10^{4-5}\,{\rm cm}^{-3}$, sufficiently high to accurately capture the gravitational collapse of star-forming gas (see the density–temperature phase diagram in Fig. 9 of S24). Once a cell meets the star formation condition, star particles are generated according to the procedure described below.

If the metallicity is below the critical threshold $Z_{\rm crit} = 10^{-5}\,Z_\odot$, we generate a single PopIII star particle representing a binary of $40\,M_\odot$ and $80\,M_\odot$ stars. This choice is motivated by recent radiation-hydrodynamics simulations, which indicate that Pop III stars preferentially form in massive binary configurations (Sugimura et al., 2020, 2023). Both stars emit UV photons following Schaerer (2002) for 4 Myr. The $40\,M_\odot$ star eventually explodes as a hypernova, releasing 3×10^{52} erg of thermal energy and leaving a $20\,M_\odot$ black hole (Woosley et al., 2002; Wise et al., 2012). The $80\,M_\odot$ star collapses directly into a black hole without an explosion, resulting in the formation of a $100\,M_\odot$ black hole binary modeled as a single sink particle. We track subsequent black hole growth via Bondi-Hoyle-Lyttleton accretion but neglect mechanical and X-ray feedback from these BHs.

If $Z > Z_{\rm crit}$, we instead form PopII star clusters by spawning multiple $100\,M_\odot$ PopII star particles.Each particle represents an unresolved stellar population following a Salpeter initial

mass function (IMF) (Salpeter, 1955) spanning 1–100 $M_\odot$. The total mass of a new cluster $M_{\rm cluster}$, is calculated as $M_{\rm cluster} = f_* M_{\rm cloud}$, where $M_{\rm cloud}$ is the gas mass in cells with $n > 10^{-3} n_{\rm peak}$ around the density peak ($n_{\rm peak}$ is the peak density). The star formation efficiency f_* is given by

$$f_* = \min[0.8, 0.004 \left(\frac{Z_{\rm cloud}}{10^{-3} Z_\odot}\right)^{0.25} \left(\frac{M_{\rm cloud}}{10^4\, M_\odot}\right)^{0.4} \times \left(1 + \frac{n_{\rm cloud}}{100\,{\rm cm^{-3}}}\right)^{0.91}], \tag{8.3}$$

where $Z_{\rm cloud}$ and $n_{\rm cloud}$ are the average metallicity and density of the cloud. This formulation of star formation efficiency is motivated by radiation-hydrodynamics simulations of star cluster formation conducted by He et al. (2019). For radiation from PopII stars, we use the stellar population synthesis models of Bruzual and Charlot (2003). Each PopII star particle (of 100 $M_\odot$) contains approximately one massive star ($\gtrsim 8\, M_\odot$), which eventually explodes as a supernova (SN). We assign the SN event randomly between 4 Myr and 40 Myr (Leitherer et al., 1999), with an ejecta mass of 10 $M_\odot$, a thermal energy of 10^{51} erg, and a metal mass $M_{\rm metal,II} = 0.5\, M_\odot$ (Kimm et al., 2015). Further details of our simulation setup and methodology are described in S24.

8.2.2 Emission Line Calculations

We calculate metal line luminosities using the CLOUDY spectral synthesis code (v23.02; Ferland et al., 2017; Chatzikos et al., 2023). Each simulation cell provides information about temperature, density, metallicity, and the local radiation field. Ideally, CLOUDY simulations would be performed individually for every cell, incorporating the local spectral energy distribution (SED) derived from our four radiation energy bins, the absolute radiation intensity, gas density, gas temperature, metallicity, and slab thickness. However, since each snapshot contains over 10^5 cells and our simulation includes roughly 200 snapshots (from $z \sim 20$ to $z \sim 9$), performing individual CLOUDY calculations for all $\sim 2 \times 10^7$ cells would be computationally infeasible. To address this, we instead generate precomputed lookup tables separately for two cell categories: photodissociation region (PDR) cells and HII cells. Cells are classified into these categories based on whether their hydrogen ionization fraction is below or above a threshold value $y_{\rm HII,thres}$.

Figure 8.1(a) shows the histogram of the ionization fraction $y_{\rm HII}$ for snapshot 208 ($z = 10.5\,, t_{\rm Univ} = 462$ Myr), where the strongest burst of star formation begins ($z = 10.5$). We find that the distribution is clearly bimodal: ionized cells are concentrated at $y_{\rm HII} \gtrsim 0.9$, whereas non-ionized cells are predominantly located at $y_{\rm HII} \lesssim 0.2$. We observe a similar trend in other snapshots and thus adopt a threshold fraction of $y_{\rm HII,thres} = 0.8$. The overall distribution does not change significantly when we choose a threshold in the range $y_{\rm HII,thres} = 0.5 - 0.9$.

Figure 8.1(b) and (c) show histograms of the gas number density and temperature, respectively. From these histograms, we determine the parameter ranges for $n_{\rm H}$ and T, as summarized in Table 8.1. Although snapshot 208 does not include gas cells at densities reaching the critical threshold for star formation ($\sim 10^4\,{\rm cm^{-3}}$), we nevertheless extend our parameter space up to this density to ensure completeness.

Figure 8.1(d) shows the metallicity histogram. We find that both HII and PDR cells span similar metallicity ranges, so we adopt the same parameter range for both in Table 8.1. Figure 8.1(e) shows the histogram of gas column density of each cell, revealing that both HII and PDR cells lie within $\log_{10}(N_{\rm H}/{\rm cm^{-2}}) = 17$-$22$. The upper limit is consistent with the star formation criterion described in Section 8.2.1, $\sim 0.1\,{\rm pc} \times 10^4\,{\rm cm^{-3}} = 3 \times 10^{21}\,{\rm cm^{-2}}$. Figure 8.1(f) shows the histogram of FUV radiation fields, where each field is normalized to the Milky Way value $G_0 = 3.024 \times 10^{-4}\,{\rm erg\,s^{-1}\,cm^{-2}}$, calculated over 11.2-13.6 eV using the fitting function of Mathis et al. (1983). The value G_0 corresponds to $J_{21} = 8$, where J_{21} is the specific FUV

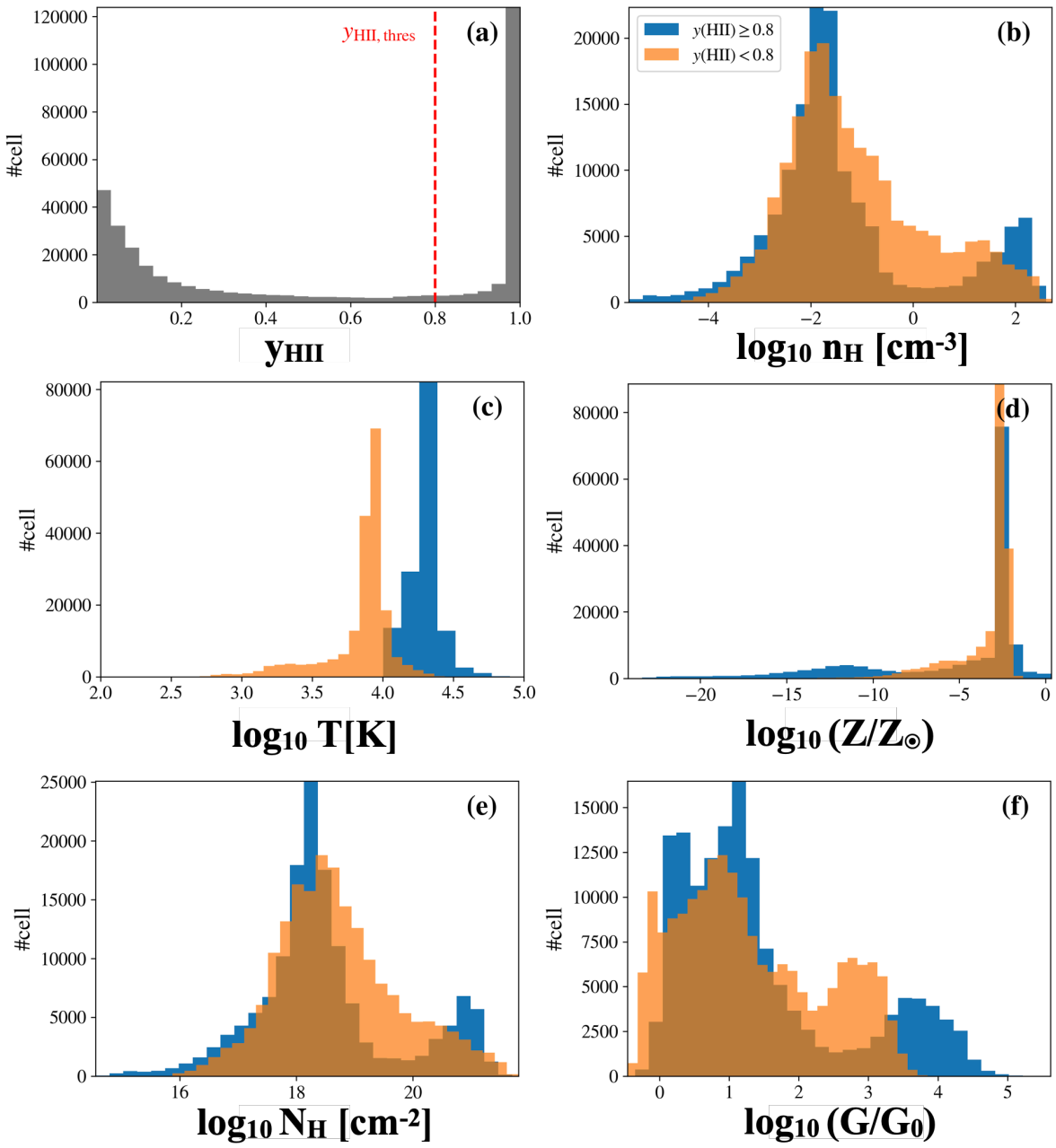

Figure 8.1: Histograms of various physical properties of simulated cells at $z = 10.5$ (snapshot 208), which marks the largest SFR during the burst of star formation. Panels show (a) ionization fraction, (b) gas number density, (c) gas temperature, (d) gas-phase metallicity, (e) gas column density, and (f) FUV radiation field. For panels (b)–(f), the orange histograms correspond to PDR cells ($y_{\rm HII} < 0.8$), and the blue histograms correspond to HII cells ($y_{\rm HII} \geq 0.8$). This figure is taken from Nakazato et al. (2025).

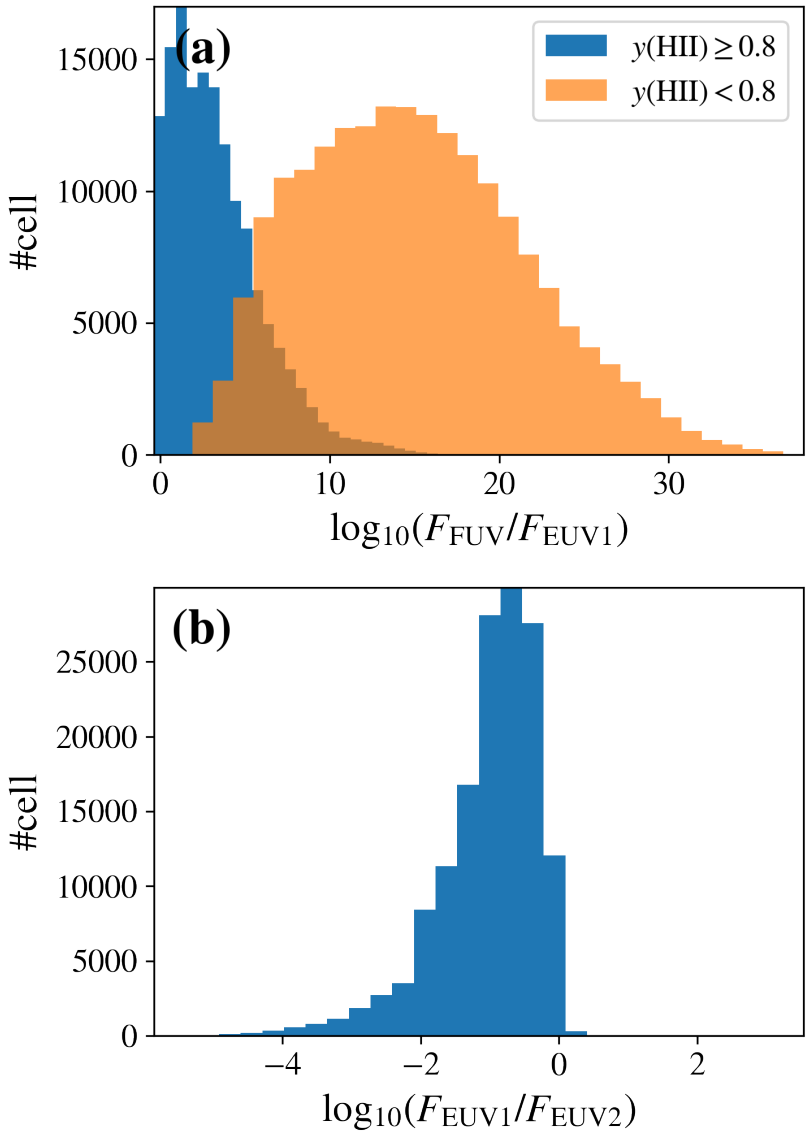

Figure 8.2: Histograms of the radiation field at $z = 10.5$ (snapshot 208). (a) The flux ratio of FUV to EUV1. Orange and blue histograms correspond to PDR and HII cells, respectively. We find that the FUV flux in PDR cells exceeds the EUV flux by ~ 20 orders of magnitude, making the EUV component negligible. (b) The flux ratio of EUV1 to EUV2 for HII cells. This figure is taken from Nakazato et al. (2025).

intensity in units of $10^{-21}\,\mathrm{erg\,s^{-1}cm^{-2}sr^{-1}Hz^{-1}}$. The figure indicates that HII and PDR cells exhibit different FUV distributions, and we set the parameter ranges accordingly in Table 8.1.

To run CLOUDY, we must first specify the shape of the input SED. For PDR cells, we consider only the radiation within the FUV energy bin, since the ionizing photon density is roughly 20 orders of magnitude lower than the FUV photon density in these regions. We therefore adopt a power-law SED with slope ν^{-1}, approximating a nearly constant flux across the narrow energy range 11.2–13.6 eV. In principle, the FUV radiation field slope can vary spatially. For example, cells near stars may exhibit steeper stellar SED slopes (e.g., $\beta_{\rm UV} \sim -2.5$; Yanagisawa et al. 2024), whereas more distant cells often experience background radiation characterized by a slope of $\nu^{-4.41}$ (Mathis et al., 1983). Nevertheless, given the narrow energy range involved, our results are insensitive to the exact choice of slope. For HII cells, we characterize the SED shape using two flux ratios: FE1 $\equiv$ FUV/EUV1 and E12 $\equiv$ EUV1/EUV2. We again assume a power-law spectrum with slope ν^{-1} across these three energy bins (FUV, EUV1, EUV2). Figure 8.2 presents histograms of these flux ratios, computed from photon number densities using the median photon energy of each bin. Guided by these distributions, we select appropriate parameter values as summarized in Table 8.1. In this work, we neglect EUV3 photons ($h\nu > 54.4\,\mathrm{eV}$). Since our primary focus is on the [OIII] and [CII] emission lines, whose ionization potentials are 35.12 eV and 11.26 eV respectively, the exclusion of EUV3 radiation is not expected to influence their emissivities. However, lines from species with higher ionization potentials, such as HeII 1640 Å, would require inclusion of the EUV3 bin. We will explore this additional parameter space in future studies.

To summarize, we construct a lookup table using seven parameters: gas density $n_{\rm H}$, gas metallicity $Z_{\rm gas}$, FUV radiation field G, gas temperature T, gas column density $N_{\rm H}$, and (for HII cells) the two flux ratios (FE1, E12), as listed in Table 8.1.

Table 8.1: Parameter ranges for PDR cells ($y_{\rm HII} < 0.8$) and HII cells ($y_{\rm HII} \geq 0.8$) used in the CLOUDY calculations. The table is taken from Nakazato et al. (2025).

	PDR cells ($y_{\rm HII} < 0.8$)	**HII cells** ($y_{\rm HII} \geq 0.8$)
$\log(G/G_0)$	0, 1, 2, 3, 4	1, 2, 3, 4, 5
$\log(n/\mathrm{cm^{-3}})$	-2, -1, 0, 1, 2, 3, 4	-2, -1, 0, 1, 2, 3
$\log(Z/Z_\odot)$	-4, -3, -2, -1, 0	-4, -3, -2, -1, 0
$\log(T/\mathrm{K})$	2, 2.5, 3, 3.5, 4	4, 4.5, 5
$\log(N_{\rm H}/\mathrm{cm^{-2}})$	17, 18, 19, 20, 21, 22	17, 18, 19, 20, 21, 22
$\log(F_{\rm FUV}/F_{\rm EUV1})$	(considered only FUV radiation)	0, 1, 2, 3, 4, 5
$\log(F_{\rm EUV1}/F_{\rm EUV2})$	(considered only FUV radiation)	-2, -1, 0, 1

In our CLOUDY calculations, we adopt a gas slab in an open geometry, assuming uniform density, temperature, metallicity, FUV flux, and SED shape. Accordingly, we create input SEDs parametrized by FE1 and E12, and use the "grid" command to vary $G, Z, n_{\rm H}, T$ and $N_{\rm H}$. We include an isotropic background from the cosmic microwave background (CMB) at $z = 10$ and assume that the abundance ratios of individual elements follow solar values (GASS command; Grevesse et al., 2010). The calculations are iterated until convergence and then stopped when the slab reaches the column density $N_{\rm H}$. The flux of each line is then extracted as the emergent emissivity.

We determine the line emissivity of each cell by interpolating from the pre-computed emissivity lookup table. For HII and PDR cells, the interpolation is conducted in the seven- and five-dimensional parameter spaces, respectively, using the nearest 2^7 and 2^5 grid points surrounding the cell's parameters.

The above emission calculations are conducted within the virial radius of the halo, which ranges from $R_{\rm vir} \sim 0.2\,\mathrm{kpc}$ at $z = 20$ to $R_{\rm vir} \sim 1.5\,\mathrm{kpc}$ at $z = 9$. We include all gases within this

region because strong SN feedback can expand HII regions out to the halo scale (see Figure 2 in S24).

8.3 Results

8.3.1 Galaxy Formation Histories

Figure 8.3 presents the formation history of our simulated galaxy. In the left panel, we show the evolution of gas mass, dark matter halo mass, and stellar mass. In the right panel, we display the star formation rate (SFR), averaged over timescales of 3, 10, and 100 Myr, as functions of cosmic age.

Pop III star formation begins at $z = 24$. At $z \sim 17$, the EUV feedback and subsequent Pop III hypernova explosion sweep out gas to halo scales, reducing the gas mass by 0.3 dex. After Pop III SNe, metal-enriched gas re-accumulates, and Pop II star formation begins at $z \sim 13$.

Although the newly formed Pop II stars stochastically explode as supernovae (SNe) throughout 4–40 Myr, the gravitational potential of the host halo is sufficiently deep to prevent these SN explosions from driving gas outflows on a halo scale. However, star formation is continuously suppressed by FUV radiation and SN feedback, primarily through photodissociation of H_2 and heating of the gas to temperatures around $T \sim 10^4$ K. This hot, pressurized gas resists gravitational collapse, delaying further star formation. During this suppression period, gas clouds continue to grow via accretion of surrounding material and cool predominantly through Lyman-alpha emission. Eventually, the cloud becomes gravitationally unstable at $z \sim 10.5$, triggering rapid star formation characterized by relatively high star formation efficiencies (f_* defined by Eq. 8.3) of approximately 10% (S24).

The right-hand panel of Figure 8.3 presents the star formation rate (SFR) averaged over three distinct timescales. The SFR averaged over 3 Myr closely follows the 10 Myr average, though the 3 Myr average reveals finer-scale fluctuations reflecting highly stochastic starburst events occurring roughly every ~ 1, Myr. In contrast, the 100 Myr–averaged SFR (shown in red) displays a step-like growth pattern up to $z \simeq 9.1$. Although three brief episodes of suppressed star formation called *mini-quenching* occur at $z \sim 12$, 11, 10, each persists for less than 100 Myr. Consequently, these short-term quiescent phases are smoothed out in the 100 Myr–averaged SFR, giving the appearance of a nearly constant SFR during those intervals.

In observational work, star-formation histories (SFHs) are usually inferred from SED fitting of the stellar continuum, and thus the shape of SFH tends to similar to our 100 Myr–averaged behavior. Short-timescale burstiness can still be probed observationally through indicators such as the Hα-to-UV luminosity ratio (e.g. Asada et al., 2024; Endsley et al., 2024), which is sensitive to SFR variations on $\sim$10 Myr scales.

From the next section, we primarily analyze emission lines associated with the PopII star formation phase at $z = 9$–13, since the star formation rate during the earlier PopIII phase ($z = 14$–24) is relatively low and highly intermittent (see also Figure4 in S24). Emission lines from the PopIII phase may be essential for detecting signatures of PopIII stellar populations to compare with the recently observed extremely metal-poor galaxies (e.g., Fujimoto et al., 2025; Nakajima et al., 2025). We defer a detailed analysis of this early epoch to future work. In this chapter, we present results based on 137 simulation snapshots covering the PopII formation period.

8.3.2 Structural Properties during the Pop II Bursty Phase

Figure 8.4 shows the projected maps of physical properties at $z = 10.45$, where the SFR (specific SFR; sSFR) reaches a maximum value of 0.051 $M_\odot \mathrm{yr}^{-1}$ (74.5 Gyr^{-1}). The corresponding stellar and gas masses are $M_* = 6.9{\times}10^5\ M_\odot$, $M_{\mathrm{gas(total)}} = 1.39{\times}10^7\ M_\odot$, $M_{\mathrm{HI}} = 7.72{\times}10^6\ M_\odot$, $M_{\mathrm{HII}} =$

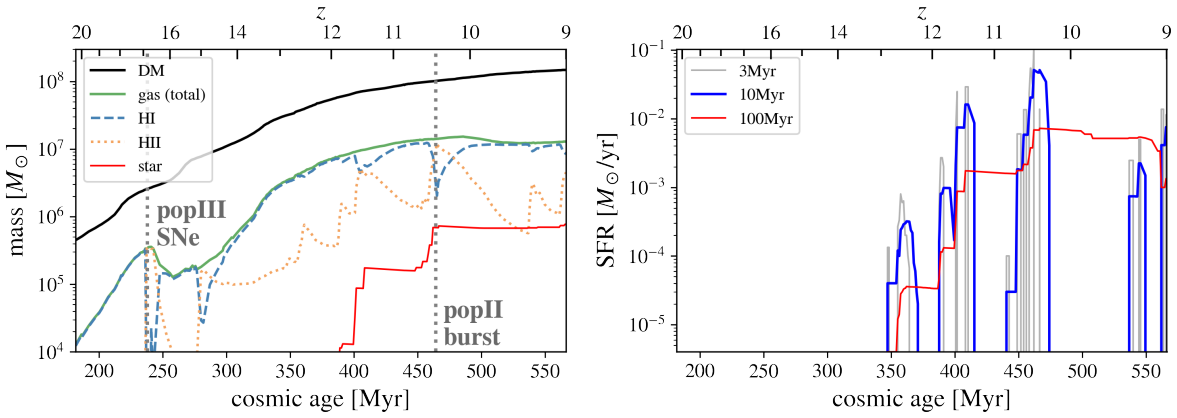

Figure 8.3: Mass (left panel) and SFR (right panel) as a function of the cosmic age. In the left panel, the black, green, blue dashed, orange dotted, and thin red lines are masses of dark matter (DM), total gas, neutral hydrogen, ionized gas, and stars, respectively. The vertical gray dotted lines at $t_{\rm Univ} \sim 240$ Myr (~ 460 Myr) represent the timing of popIII hypernovae (popII bursty star formation). In the right panel, thin gray, blue, and red lines show SFRs averaged over 3, 10, and 100 Myrs. They are computed by summing the stellar mass formed over the past X Myr and dividing by X Myr, where $X = 3, 10,$ or 100. This figure is taken from Nakazato et al. (2025).

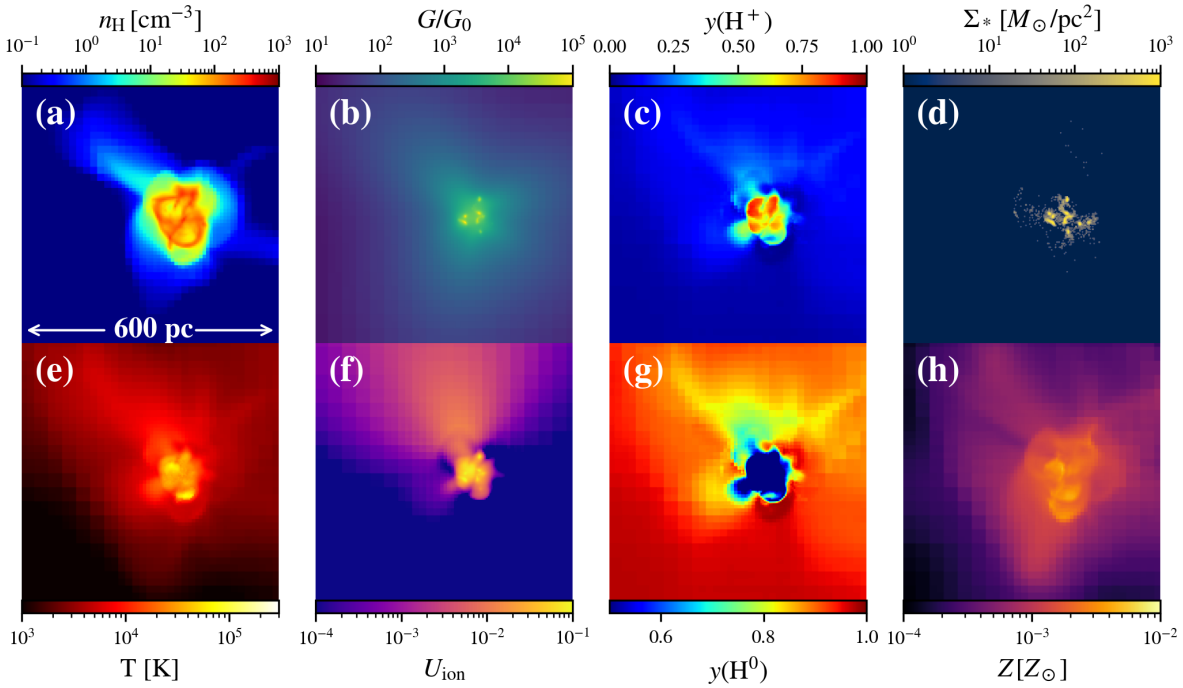

Figure 8.4: Projected distributions of our galaxy at $z = 10.45$ ($t_{\rm Univ} = 462$ Myr), where the largest bursty star formation proceeds with sSFR $= 74.5\,{\rm Gyr}^{-1}$. In the upper row, we plot gas number density ($n_{\rm H}$), FUV radiation field (G), ionization fraction ($y(H^+)$), and surface stellar mass density (Σ_*). In the bottom row, we show gas temperature (T), ionization parameter ($U_{\rm ion}$), neutral hydrogen fraction ($y(H^0)$), and gas-phase metallicity (Z). Note that all $n_{\rm H}, T, y(H^+), y(H^0), U_{\rm ion}$, and Z are gas density-weighted averaged along the selected line of sight. The FUV radiation field G is a photon number density-weighted average. One side length of the panel and the projected depth of each panel is 600 pc. This figure is taken from Nakazato et al. (2025).

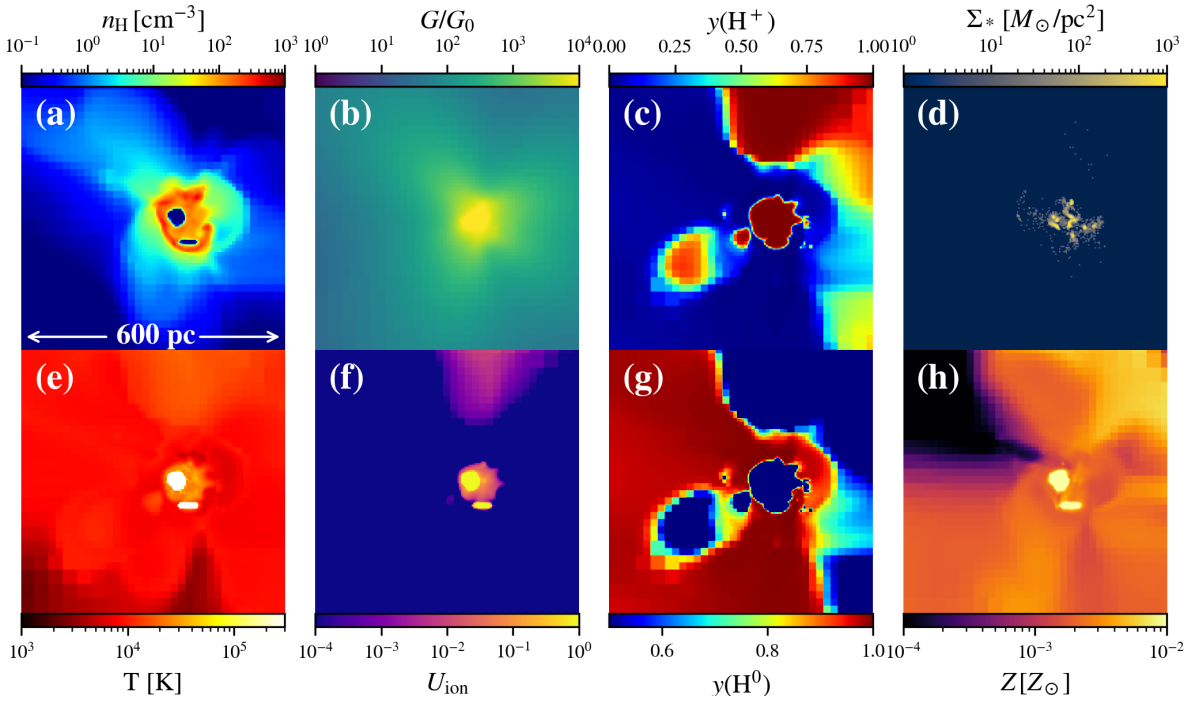

Figure 8.5: Same as Figure 8.4 but sliced maps at $z = 10.45$. Only Σ_* is a projected map. This figure is taken from Nakazato et al. (2025).

$6.22 \times 10^6\ M_\odot$, and $M_{H_2} = 0.19\ M_\odot$, respectively. Here, M_{HI}, M_{HII} and M_{H_2} are gas masses of neutral atomic hydrogen gas, hydrogen ionized gas, and hydrogen molecular gas. Each panel of Figure 8.4 illustrates projected distributions of gas density, FUV radiation field strength (G), hydrogen ionization fraction, stellar mass surface density, gas temperature, ionization parameter (U_{ion}), neutral gas fraction, and gas metallicity. The ionization parameter is defined as the ratio of the ionizing photon number density to the gas number density.

In panel (a) of Figure 8.4, we identify two central cavities surrounded by dense gas with typical densities of $n_H \simeq 500\,cm^{-3}$ within the ∼100 pc scale star-forming cloud. These cavities are fully ionized (panel (a)) and spatially correlated with regions of enhanced metallicity (panel (d)), indicating they have been created by supernova (SN) explosions. Regions exhibiting an apparent ionization fraction of $y(H^+) \simeq 0.5$ are primarily the result of projection effects. To clarify these projection effects, we also plot sliced maps as shown in Figure 8.5. We see that individual cells generally have ionization fractions very close to either fully ionized ($y(H^+) = 1$) or fully neutral ($y(H^+) = 0$). The sliced maps also confirm that the two central cavities exhibit very high temperatures ($T > 5 \times 10^5\,K$) and increased metallicities ($Z \sim 10^{-2}\,Z_\odot$), strongly supporting their origin from SN explosions. Additionally, the sliced views reveal several other ionized bubbles in the upper and left regions, which are not as prominent in the projected maps.

Panel (g) in Figure 8.4 confirms that the gas surrounding the cavities is neutral. This dense cloud is gravitationally unstable and is collapsing to form stars.

While SNe occur in the center, some stellar clusters remain bound (Garcia et al., 2023, 2025). Panel (d) presents the surface stellar mass density, which peaks at $\Sigma_* \sim 3 \times 10^3\ M_\odot\ pc^{-2}$. The distribution of stellar clusters and their high surface density are interestingly consistent with the recently observed stellar clusters at $z \gtrsim 6$ (Vanzella et al., 2023b; Welch et al., 2023; Bradley et al., 2024; Mowla et al., 2024), while Adamo et al. (2024b) reported 1 dex-larger surface density.

The temperature map in panel (e) illustrates that the central regions are heated to around $2 \times 10^4\,K$ due to photoionization by EUV photons emitted from massive stars. Additionally, localized hot spots reaching temperatures above $T \gtrsim 5 \times 10^5\,K$ are visible, which originate from SN explosions that initially produce gas as hot as $T \sim 10^8\,K$. Both photoionized regions and

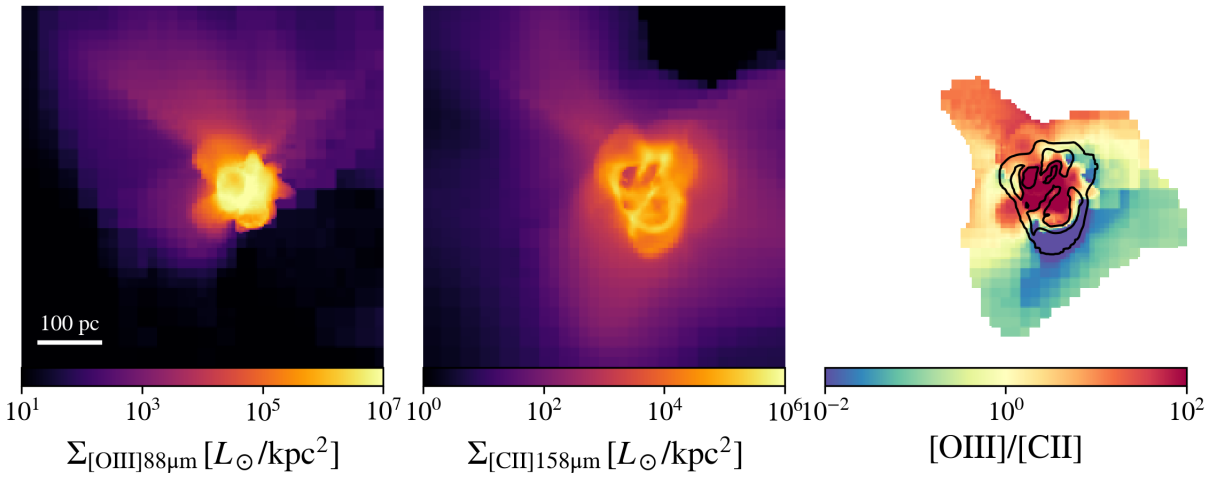

Figure 8.6: FIR emission line distributions of our galaxy at $z = 10.45$, at the same time as in Figure 8.4. The left and middle panels show the surface brightness of [OIII] 88 μm and [CII] 158 μm , respectively. The right panel presents the line ratio of [OIII] 88 μm to [CII] 158 μm . Pixels with low surface brightness ($\Sigma_{[CII]158\mu m} > 10^2\,L_\odot/kpc^2$) are masked. The black contours represent the [CII] flux $10^4, 10^5\,L_\odot/kpc^2$, respectively. The side length and projected depth of each panel are 600 pc, as in Figure 8.4. A movie showing the time evolution of emission map is available (link). This figure is taken from Nakazato et al. (2025).

collisionally ionized SN-driven bubbles contribute to the ionization structure. However, since the recombination timescale typically exceeds the gas cooling timescale, these ionized regions persist for extended periods (Hartley and Ricotti, 2016). Outside the ionized bubbles, the neutral gas remains warm, maintaining temperatures of approximately $T \sim (5-8) \times 10^3$ K. This elevated neutral-gas temperature results from strong FUV radiation penetrating beyond the ionized regions, characterized by intensities of $G/G_0 \sim 10^3$ (equivalently, $J_{21} \sim 10^4$). Such intense radiation effectively suppresses H_2 cooling in low-metallicity gas environments (with metallicities of a few $\times 10^{-3}\,Z_\odot$; see panel (h)). As a result, cooling is dominated by Lyman-alpha emission under these conditions (Omukai et al., 2008; S24, see also Figure 8.7). This intense FUV field is also consistent with recent observational evidence from high-redshift galaxies at $z > 6$ (Fudamoto et al., 2025).

The UV radiation emitted by these stars creates ionized regions that are highly anisotropic and inhomogeneous, as shown by the maps of the ionization fraction (panel (c)) and the ionization parameter (panel (f)). There are ionizing bubbles in the center with ~ 100 pc scale and the ionization parameter peaks in the bubbles with $\log U_{\rm ion} \sim -1$, which are co-located with recent star formation events.

Interestingly, the FUV distribution differs from the $U_{\rm ion}$ map. The brightest central regions, with $G/G_0 \sim 10^4$, coincide spatially with the ionized regions. However, EUV radiation drops rapidly outside the HII regions while FUV radiation extends over 600 pc, maintaining a high value of $G/G_0 \sim 10^2$. These EUV and FUV radiation distributions largely affect the [OIII] and [CII] distributions, as explained in Section 8.3.3.

8.3.3 FIR Line Properties during the Pop II Bursty Phase

8.3.3.1 Luminosity Maps

In Figure 8.6, we show the emission maps of [OIII] 88μm and [CII] 158 μm , as well as the emission ratio of [OIII] /[CII] at $z = 10.5$. Their luminosities are $L_{[OIII]} = 3.73 \times 10^4\,L_\odot$ and $L_{[CII]} = 1.59 \times 10^3\,L_\odot$, respectively.

As shown by Nakazato et al. (2023), the [OIII] emission traces the $U_{\rm ion}$ map with $U_{\rm ion} \gtrsim 10^{-2}$. It is concentrated within a compact area of ~ 100 pc, while the extended component in the upper region is 100 times fainter.

In contrast, the spatial distribution of [CII] emission differs notably from that of the [OIII] emission, closely resembling instead the gas density distribution shown in Figure 8.4. The most intense [CII] emission originates from dense gas regions with $n_{\rm H} \sim 500\,{\rm cm}^{-3}$, which envelop the SN-driven cavities. Additionally, diffuse [CII] emission at levels around $10^3\,L_\odot{\rm kpc}^{-2}$ traces more tenuous gas with densities of $n_{\rm H} \sim 1\,{\rm cm}^{-3}$. The overall [CII]-emitting structure exhibits an asymmetric morphology, extending out to scales of approximately 250 pc.

For quantitative analysis, we compute the half light radii of [OIII] and [CII] [1], and obtain $r_{\rm e}$[OIII] $= 75$ pc, $r_{\rm e}$[CII] $= 90$ pc, and the ratio between the radii is $r_{\rm e}$[CII] $/r_{\rm e}$[OIII] $= 1.2$. These values should be interpreted with caution because [CII] is predominantly emitted from shell-like regions offset from the [OIII] region and both the [CII] and [OIII] distributions are anisotropic and extended (Figure 8.6 and the accompanying movie). Nevertheless, we track the size ratio throughout the bursty phase at $z \approx 10.5$ and find that it fluctuates between $r_{\rm e}$[CII] $/r_{\rm e}$[OIII] $= 1-2$.

Emission line ratios are commonly used diagnostics for probing galaxy properties. In particular, the ratio of the [OIII] 88 μm and [CII] 158 μm emission lines is of special interest because these two bright FIR lines originate from gas in distinct phases, allowing us to constrain the physical conditions of the ISM in high-redshift galaxies. The right-hand panel of Figure 8.6 displays the spatial distribution of the [OIII] /[CII] line ratio, calculated from the ratio of surface brightness between [OIII] and [CII] emission in each pixel. We observe extremely high line ratios of approximately 100 in the central ionized regions dominated by [OIII] emission, whereas the ratio sharply decreases to values of 0.01–0.1 in the dense neutral gas surrounding these regions. Averaging over the entire halo within the virial radius $R_{\rm vir}$, we derive a global line ratio of [OIII] /[CII] $= 23.4$.

Observations of [OIII] /[CII] have been made in several galaxies at $z \geq 6$, as introduced in Section 8.1, but most of these ratios are measured as a whole-galaxy average. Currently, only the $z = 7.13$ galaxy A1689-zD1 shows the spatial variation of [OIII] /[CII] , as reported in Wong et al. (2022). They found that the central region has a ratio ~ 3.5 times higher than the galaxy-wide average, which is consistent with our result. Other theoretical studies (Schimek et al., 2024; Nyhagen et al., 2024) have also presented [OIII] /[CII] maps for $z \sim 6$ galaxies. They reproduced the line ratio of [OIII] /[CII] $\sim$ 1-10 partially, but most regions have [OIII] /[CII] $\sim$ 0.1-0.01, resulting in the low total ratio of [OIII] /[CII] $= 0.17$. This could be because these observations probe large-scale structures ($\sim$ 10 kpc), including circumgalactic medium (CGM) gas and gas bridges formed during galaxy mergers, where significant reservoirs of neutral gas contribute prominently to the [CII] emission. Indeed, recent ALMA observations have identified strong [CII] emission originating from bridge-like gas structures connecting merging galaxies, providing observational support for this scenario (Izumi et al., 2024; Zanella et al., 2024, Fudamoto et al. in prep.).

Overall, our simulations with a high-spatial resolution of 0.1 pc can precisely capture the difference between [OIII] and [CII] distributions and reproduce high [OIII] /[CII] ratios.

8.3.3.2 Physical Conditions of Gas Emitting [OIII] 88 μm and [CII] 158 μm Lines

Figure 8.7 shows the density–temperature phase diagram of gas at z=10.5, with colorbars indicating the hydrogen ionization fraction, as well as the luminosities of [OIII] and [CII] emission. The gray contours represent the gas mass distribution within each phase-space bin. The hot gas at $T \gtrsim 3 \times 10^5$ K originates predominantly from supernova feedback, whereas radiative feedback from young stars heats gas to temperatures around 2×10^4 K. The left-hand panel demonstrates

[1] We take the center as the brightest point of [OIII] .

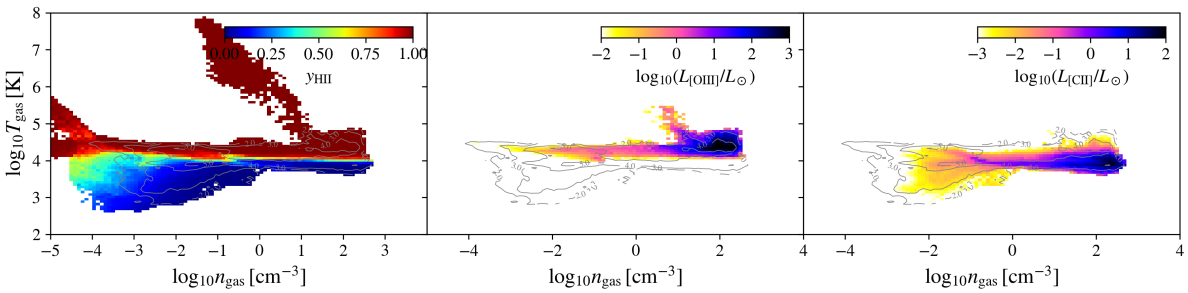

Figure 8.7: Phase-space diagrams of gas number density versus temperature for all cells within $2R_{\rm vir}(= 3.0\,{\rm kpc})$ at $z = 10.45$. The left panel shows the ionization fraction in the phase space. The middle (right) panel presents the luminosities of [OIII] 88μm ([CII] 158 μm) in each bin. In the middle panel, we omit the hot gas with $T > 3 \times 10^5\,{\rm K}$ produced by SN heating. The gray contours indicate four levels of gas mass in each bin: $\log M_{\rm gas}\,[M_\odot] = 2, 3, 4, 5$. The bin sizes are $\Delta \log n_{\rm H}\,[{\rm cm^{-3}}] = 0.09$ and $\Delta \log T\,[{\rm K}] = 0.065$ in all panels. This figure is taken from Nakazato et al. (2025).

that gas heated to these temperatures is fully ionized.

In the middle panel, we show the physical state of the gas that emits the [OIII] line, which originates entirely from ionized cells, as the ionizing energy of O^+ is 35.1 eV. We find that the ionized gas spans a wide range of densities, from $0.1\,{\rm cm^{-3}}$ to $500\,{\rm cm^{-3}}$, and contributes to the [OIII] emission. Such diffused ionized gas originates from HII bubbles in the upper part in panel (f) of Figure 8.4. We also compute the ionized-gas density weighted by mass and by the [OIII] 88μm luminosity, obtaining $\langle n_{\rm HII}\rangle = 37$ and 120 ${\rm cm^{-3}}$, respectively. Intriguingly, the latter value matches the very recent measurements of Harikane et al. (2025b), who derive electron densities for EoR galaxies from the [OIII] 88μm line and find values lower than those inferred from rest-UV/optical line ratios. The luminosity-weighted average ionized gas density $\langle n_{\rm HII}\rangle$ is discussed further in Section 8.4.2.

The hot SN-heated gas with temperatures $T = 5 \times 10^5 - 10^8\,{\rm K}$ exceeds the maximum temperature of our CLOUDY calculation grid ($T_{\rm max} = 10^5\,{\rm K}$). Thus, the [OIII] emission from this extremely hot gas is artificial, since oxygen under these conditions is typically collisionally ionized to OIV or OV (Osterbrock and Ferland, 2006). However, we have verified that this artificial [OIII] emission from SN-heated cells accounts for only about 0.2% of the total emission, making its impact negligible.

The right panel shows the same type of diagram but for the [CII] line, indicating that 80% of the emission comes from a neutral gas. In particular, gas with $n_{\rm H} \gtrsim 100\,{\rm cm^{-3}}$ is the main contributor (70% of the total luminosity: 14% from HII and 56% from PDR) to the [CII] emission. We derive neutralgas densities weighted by mass and by the PDR-[CII] 158μm luminosity, in the same way as for $\langle n_{\rm HII}\rangle$. The resulting values are $\langle n_{\rm HI}\rangle = 36$ and 168 ${\rm cm^{-3}}$, respectively. Notice that even though our simulation follows higher gas densities up to $n_{\rm H} \simeq 10^4\,{\rm cm^{-3}}$, these gases are converted into stars immediately, and are not seen in most snapshots (see Fig. 9 of S24 for a snapshot where gases reach $n_{\rm H} \gtrsim 10^4\,{\rm cm^{-3}}$).

Observationally, the ionization state of gas responsible for [CII] emission can be probed using the line ratio of [CII] 158 μm and [NII] 205 μm . This diagnostic is effective because the ionization potentials of neutral carbon (11.3eV) and nitrogen (14.5 eV) lie just below and above that of hydrogen (13.6 eV), respectively. Consequently, [NII] emission originates exclusively from ionized (HII) regions, whereas [CII] emission arises from both ionized and neutral (PDR) regions. Additionally, the similarity in ionization potentials makes this line ratio relatively insensitive to variations in the ionization parameter (e.g., Nagao et al., 2012). Using the [NII] /[CII] ratio, Cormier et al. (2015) analyzed local metal-poor dwarf galaxies and concluded that approximately 85% of their [CII] emission arises from neutral gas. Similarly, Witstok et al. (2022) examined

[CII]-emitting gas in galaxies observed at $z > 6$, and found that the majority of observed [CII] emission originates in PDR regions.

PDRs in high-metallicity environments ($\sim Z_\odot$) typically consist of a two-phase medium: warm neutral medium (WNM) and cold neutral medium (CNM) (Wolfire et al., 1995) as explained in Section 3.1.2. However, our $z \gtrsim 10$ galaxy has almost only WNM due to the strong FUV radiation from massive stars and the low abundance of metals and dust that work as coolants ($\sim 10^{-3} Z_\odot$). A decline in the CNM fraction in galaxies at high redshift has also been argued in previous theoretical studies (e.g., Vallini et al., 2013).

8.3.4 Time Evolution of Global Emission Properties

Figure 8.8 presents the time evolution of global emission properties of our simulated galaxy over the redshift range from $z = 13$ to $z = 9$. The individual panels display the evolution of the star formation rate (SFR), the FUV radiation field (G) and ionization parameter ($U_{\rm ion}$), the emission line luminosities of [OIII] and [CII], the mass ratio between ionized and neutral hydrogen gas ($M_{\rm HII}/M_{\rm HI}$), the [OIII]/[CII] line ratio, and metallicity. We compute the global values of G and $U_{\rm ion}$ as photon-number-weighted and gas-number-density-weighted averages, respectively.

In the left-middle panel, we show the [OIII] and [CII] luminosities. The [OIII] evolution follows that of the SFR averaged over 10 Myr, because O^{2+} ions exist in HII regions produced by young ($\lesssim 10$ Myr), massive stars. The ionizing photon production rate Q(H) [s^{-1}] decreases rapidly when stellar ages exceed 10 Myr. Xiao et al. (2018) show that Q(H) at 3, 10, 30, and 100 Myr for a single stellar population with $M_* = 10^6\,M_\odot$ and $Z = 10^{-5}$ are log Q(H) [s^{-1}] = 52.5, 51.2, 49.1, and 47.1, respectively. The upper-right panel shows the evolution of $U_{\rm ion}$ and G. The $U_{\rm ion}$ peaks at the $z \sim 10.5$ bursty phase with $\log U_{\rm ion} \simeq -1.5$ suddenly decreases to $\log U_{\rm ion} = -5$ within 50 Myrs. The time fluctuation is consistent with that of 10 Myr-averaged SFR and [OIII].

Meanwhile, the [CII] emission persists even during the "mini-quench" phases, closely tracking the evolution of the FUV radiation field. This correlation arises because the [CII] line predominantly originates from neutral gas illuminated by FUV photons (as illustrated in the right-middle panel). To quantify this, we calculated the FUV luminosity for a stellar population of $M_* = 10^6\,M_\odot$, metallicity $Z = 10^{-5}$, and ages of 3, 10, 30, and 100 Myr using BPASS *single* stellar population SEDs (Stanway and Eldridge, 2018; Byrne et al., 2022)[2]. We found $\log L_{\rm FUV}\,[L_\odot] = 8.1$, 7.7, 7.1, and 6.3, respectively. Over the period from 3 Myr to 30 Myr, the FUV luminosity decreases by only one order of magnitude, whereas the ionizing photon production rate drops by approximately 3.5 orders of magnitude. The decrease in [CII] luminosity observed during mini-quench phases is consistent with this moderate decline in the FUV flux shown in the upper-right panel of Figure 8.8. Due to our simulation's short snapshot interval of 1 Myr, compared with previous galaxy simulations (e.g., Arata et al., 2020; Katz et al., 2019), we are uniquely able to investigate this temporal evolution in greater detail.

The orange dotted line indicates the [CII] emission originating from HII regions. Its time evolution also tracks the 10 Myr-averaged SFR, but it contributes less than 1% most of the time as shown in Section 8.3.3.2. Only at the cosmic age of 472-479 Myr does [CII] from HII regions contribute about 56-66%.

The bottom-left panel illustrates the redshift evolution of the [OIII]/[CII] line ratio. As discussed previously, the relatively smooth evolution of [CII] luminosity indicates that fluctuations in the line ratio primarily trace variations in [OIII] luminosity, $\log U_{\rm ion}$, and the 10 Myr-averaged SFR, which are recently reported by Kohandel et al. (2025). The highest starburst phases exhibit peak line ratios of [OIII]/[CII] ~ 50 at the onset of intense star formation activity ($t_{\rm Univ} \sim 460$ Myr). Subsequently, the ratio rapidly declines to ~ 0.2 at the onset of a mini-quench episode, then slightly rebounds to ~ 0.4 around $t_{\rm Univ} \sim 500$ Myr due to the different

[2]Our RT calculations employ the BC03 model. However, according to Eldridge et al. (2017), BPASS *single* SEDs at ages younger than 1 Gyr closely resemble other models such as STARBURST99 (Leitherer et al., 1999), GALAXEV (Bruzual and Charlot, 2003), and Maraston (2005).

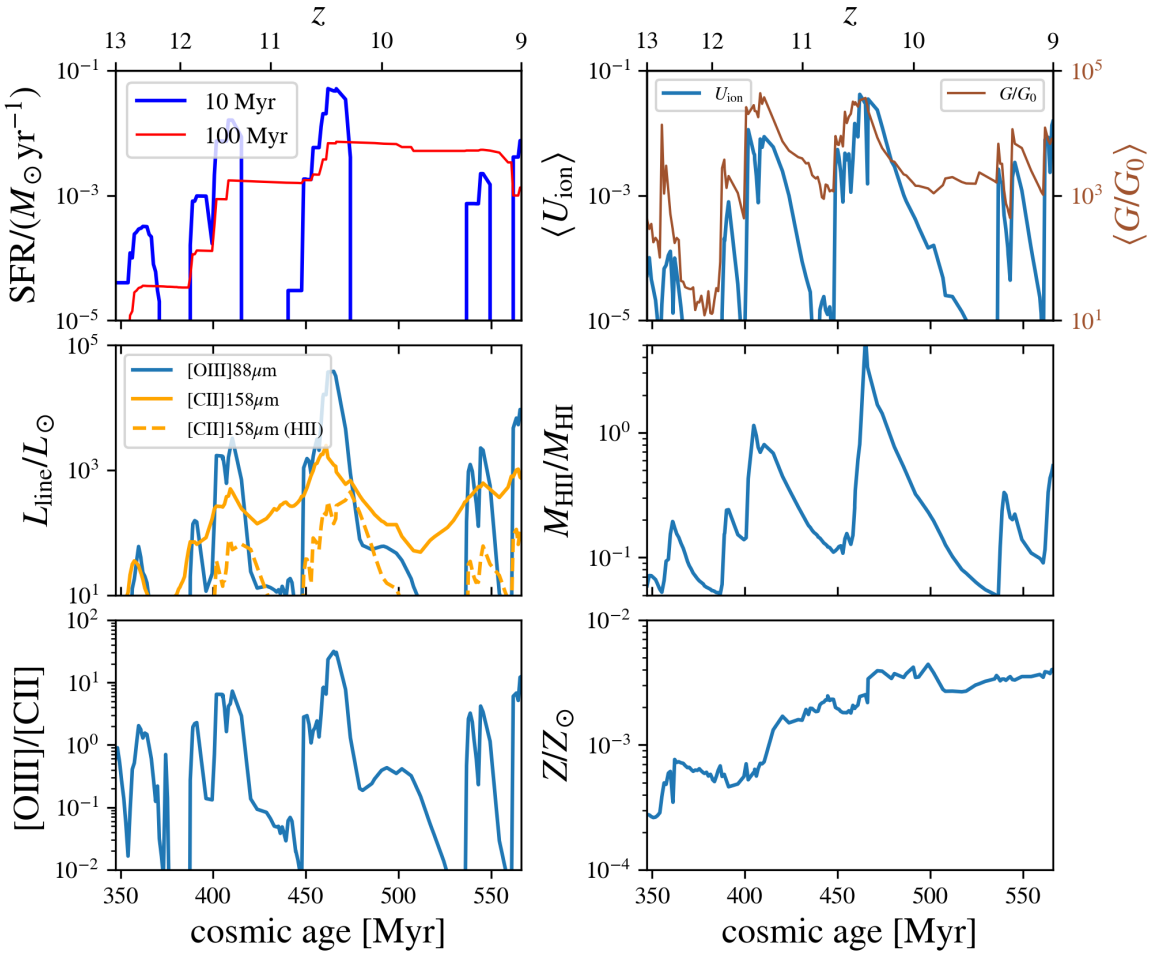

Figure 8.8: Redshift evolution of physical properties within $2R_{\rm vir}$. In the left column, the top panel shows the SFR averaged over 10 Myr (blue) and 100 Myr (red), as in Figure 8.3 (right). The middle panel presents line luminosities of [OIII] 88 μm (blue) and [CII] 158 μm (orange). The orange dashed line shows the contribution of [CII] luminosity from HII regions. The bottom panel is the line ratio of [OIII] /[CII] . In the right column, the ionization parameter and FUV radiation field (top), the ratio of the HI mass to the HII mass (middle), and gas metallicity (bottom) are plotted. The ionization parameter and FUV radiation field are calculated as averages weighted by gas number densities and FUV photon numbers, respectively. This figure is taken from Nakazato et al. (2025).

decreasing timescales of [OIII] and [CII] luminosities. Interestingly, the temporal fluctuations of the [OIII] /[CII] ratio closely resemble those of the gas mass ratio ($M_{\rm HII}/M_{\rm HI}$), despite the latter exhibiting an amplitude roughly one order of magnitude smaller. We will further examine the correlation between the [OIII] /[CII] ratio and the $M_{\rm HII}/M_{\rm HI}$ mass ratio in Section 8.4.1.

Finally, we show the redshift evolution of the metallicity in the bottom-right panel, motivated by previous theoretical studies that suggest a correlation between the [OIII] /[CII] line ratio and metallicity (e.g., Arata et al., 2020). We find that the metallicity fluctuation is not very large compared to radiation fluctuations. Since accelerated gas by SNe remains bound within the halo at $z \lesssim 13$, the metallicity gradually increases with time even during the mini-quenched phase. Therefore, the redshift evolution of FIR luminosity does not trace gas metallicity very much in comparison to other properties (SFR, EUV/FUV radiation fields). However, the luminosity would be correlated with the metallicity when we compare galaxies with the same SFR (e.g., Inoue et al., 2014).

8.3.5 Comparison with Observations

There are empirical correlations between FIR lines and SFR in galaxies, which have been extensively investigated through both observations and simulations. These are widely used to validate theoretical predictions against observational constraints.

In Figure 8.9, we show the [OIII]-SFR (left) and [CII]-SFR (right) relationships for our simulated galaxy at $z = 9 - 13$. Following previous theoretical studies (e.g., Pallottini et al., 2019; Katz et al., 2019; Nakazato et al., 2023), we adopt the 10 Myr-averaged SFR defined in Figure 8.3. For comparison, we also show the local empirical relationships for starburst and metal-poor dwarf galaxies from De Looze et al. (2014), as well as the relation derived by Harikane et al. (2020) for observed galaxies at $z \gtrsim 6$. Note that the Harikane et al. (2020) relation is based on galaxies with SFR $\simeq 4 - 220\,M_\odot\,{\rm yr}^{-1}$, while the local relations from De Looze et al. (2014) cover SFR ranges of SFR $\simeq 10^{-3} - 30\,M_\odot\,{\rm yr}^{-1}$ (metal-poor dwarfs) and $(1 - 1000), M_\odot, {\rm yr}^{-1}$ (starbursts). We extrapolate these empirical relations to the lower SFR regime of our simulations. The gray points with error bars represent observational data from galaxies at $z \gtrsim 6$, and their references are cited in the caption of Figure 8.9.

For the [OIII]-SFR relation, nearly all of our simulated points lie 1-2 dex above the local starburst galaxies with the same SFR due to high-ionization states with $\log U_{\rm ion} \sim [-1.5, -2]$, whereas the local galaxies typically have $\log U_{\rm ion} \sim -3$ (Harikane et al., 2020). However, our [OIII] luminosities are about 1-2 dex below the local metal-poor or $z \gtrsim 6$ observed relations. The offset is readily explained by metallicity: the simulations have gas metallicities of only $(0.5 - 5) \times 10^{-3}\,Z_\odot$, roughly two orders of magnitude lower than the $\sim 0.25\,Z_\odot$ typical of local metal-poor systems. Because the [OIII] emissivity scales nearly linearly with metallicity in this regime (see Figure 1 of Inoue et al., 2014), the predicted [OIII] luminosities are correspondingly reduced by a factor of ~ 100, yielding the observed 1–2 dex deficit.

For the [CII] –SFR relation, our simulation results lie approximately 1–2 dex below the local empirical relations derived from starburst and metal-poor dwarf galaxies, but are closer to the observed relation for galaxies at $z \gtrsim 6$. We suggest two primary reasons for this offset: (i) negligible contributions from strongly ionized HII regions, where carbon is largely ionized to C^{++} (e.g., Liang et al., 2024), and (ii) significantly lower gas-phase metallicity. Indeed, Liang et al. (2024) have shown that $L_{\rm [CII]}/{\rm SFR}$ scales approximately linearly with gas metallicity, a trend consistent with our simulation results. Interestingly, the slope of the [CII] –SFR relation in our simulations is shallower than that of the corresponding [OIII] –SFR relation. This difference arises because the [OIII] luminosity closely tracks the 10 Myr-averaged SFR used in both the [OIII] –SFR and [CII] –SFR analyses, whereas the [CII] luminosity exhibits only a weak dependence on the same averaged SFR, as demonstrated in Section 8.3.4. Both relations exhibit significant scatter at a given SFR. The [OIII] –SFR relation shows a scatter of 1–2 dex. Roughly one dex of this dispersion is attributable to differences in metallicities, while additional scatter

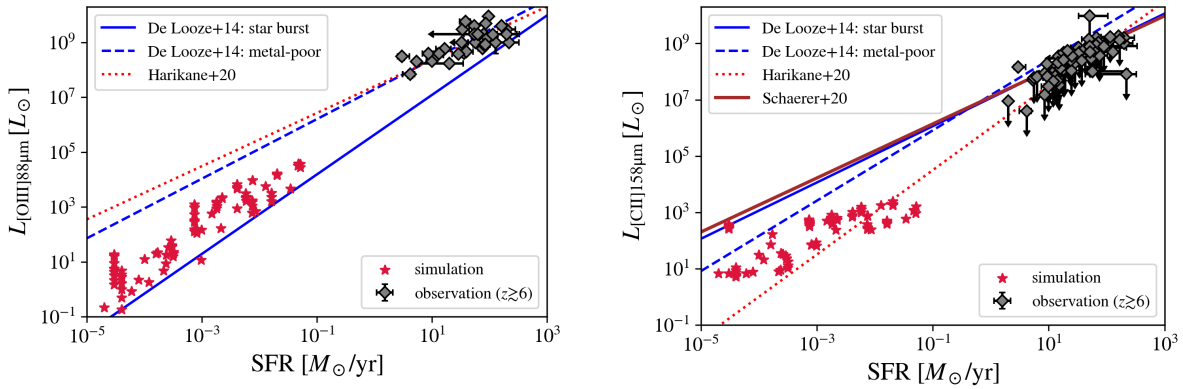

Figure 8.9: (Left) The [OIII] 88 μm luminosity versus SFR. We adopt 10 Myr-averaged SFR. The red stars represent our simulation snapshots ($z = 9 - 13$). For comparison, we show the [OIII]-SFR relations derived from observations of local galaxies by De Looze et al. (2014) and $z \gtrsim 6$ galaxies by Harikane et al. (2020). Gray points are the observational results of high-z ($z > 6$) galaxies from Hashimoto et al. (2018); Tamura et al. (2019); Inoue et al. (2016a); Hashimoto et al. (2019); Carniani et al. (2017); Harikane et al. (2020); Wong et al. (2022); Witstok et al. (2022); Zavala et al. (2024); Algera et al. (2024); Schouws et al. (2024); Bakx et al. (2024); Fujimoto et al. (2024b). (Right) The [CII] 158 μm luminosity versus SFR. The red stars again represent our simulation snapshots ($z = 9 - 13$). For comparison, we show the [CII]-SFR relations derived from observations of local galaxies (De Looze et al., 2014), ALPINE survey for $z \sim 5$ galaxies (Schaerer et al., 2020), and $z \gtrsim 6$ galaxies (Harikane et al., 2020). Gray points are the observational results of high-z ($z > 6$) galaxies from Laporte et al. (2019); Bakx et al. (2020); Hashimoto et al. (2019); Maiolino et al. (2015); Harikane et al. (2020); Wong et al. (2022); Witstok et al. (2022); Algera et al. (2024); Schouws et al. (2025); Bakx et al. (2024); Schaerer et al. (2015); Watson et al. (2015); Pentericci et al. (2016); Ota et al. (2014); Smit et al. (2018); Bradač et al. (2017); Matthee et al. (2017); Carniani et al. (2017, 2018); Kanekar et al. (2013); Matthee et al. (2019); Knudsen et al. (2016); Fujimoto et al. (2019); Capak et al. (2015); Sommovigo et al. (2022); Fudamoto et al. (2024). This figure is taken from Nakazato et al. (2025).

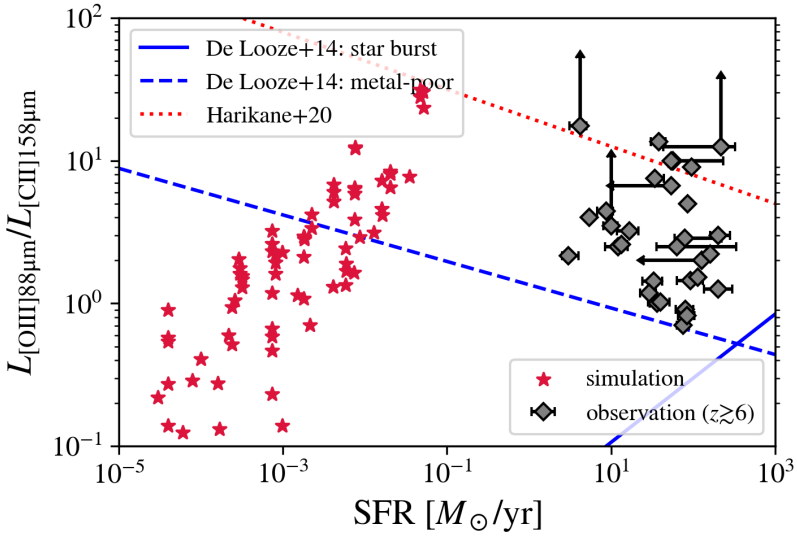

Figure 8.10: Total [OIII] /[CII] line luminosity ratio as a function of SFR for our simulated galaxy at $z = 9 - 13$ (red stars). The gray points show the observations of $z \gtrsim 6$ galaxies where both [OIII] and [CII] lines are targeted. Some [CII] lines are upper-limits, and the ratio is plotted accordingly. The blue and red lines are relationships for local galaxies (De Looze et al., 2014) and $z \gtrsim 6$ galaxies (Harikane et al., 2020), respectively, as in Figure 8.9. This figure is taken from Nakazato et al. (2025).

arises from spatial and temporal fluctuations in the gas density. Similar mechanisms can explain the scatter observed in the [CII] –SFR relation.

Hashimoto et al. (2019) and Harikane et al. (2020) have pointed out that there exists a negative correlation between the ratio of [OIII] /[CII] and the bolometric luminosity of the host. The bolometric luminosity is expected to scale with the SFR of the galaxy (i.e., $L_{\rm bol} \propto L_{\rm UV} \propto$ SFR). Figure 8.10, we plot [OIII] /[CII] -SFR relation for our galaxy at $z = 9 - 13$ as red stars. We see that there is a roughly positive correlation between [OIII] /[CII] but with the large scatter of ratios with 1-2 dex at a fixed SFR, which reflects stochastic bursty star formation. We will discuss this correlation in Section 8.3.6. Our galaxy has a variety of [OIII] /[CII] $= 0.1 - 50$ at $z = 9 - 13$. Recently, Schouws et al. (2025) targeted $z = 14.2$ galaxy JADES-GS-z14-0 and reported non-detection of [CII] , which constrained a lower limit [OIII] /[CII] > 3.5. Our galaxy successfully reproduces such a high line ratio during the bursty star formation phase (Figure 8.8).

8.3.6 Comparison with Simulations

In addition to the comparison to observations in the previous subsection, we compare our results with other cosmological simulations at $z \gtrsim 6$ in Figure 8.11 (references are in the caption). Note that, except for the PONOS simulation (Schimek et al., 2024), the other simulations analyze multiple galaxies at a fixed redshift, while our study tracks a single galaxy through time. Therefore, scatter in the other simulations arises from galaxy-to-galaxy variation, whereas in our case, it reflects temporal variability. Furthermore, our simulation explores a much lower mass (lower SFR) regime than previous studies, complicating direct comparisons. Nonetheless, our approach provides valuable insights into the FIR line–SFR relationship for high-z galaxies over a wide range of masses and star formation rates.

For [OIII] -SFR, some simulations of Moriwaki et al. (2018); Arata et al. (2020); Pallottini et al. (2022); Nakazato et al. (2023) are located on the relationships of local metal-poor and $z > 6$ galaxies and have more luminous [OIII] 88μm than the other ones (Olsen et al., 2017; Schimek et al., 2024; Katz et al., 2022), which are around the local star-burst relations.

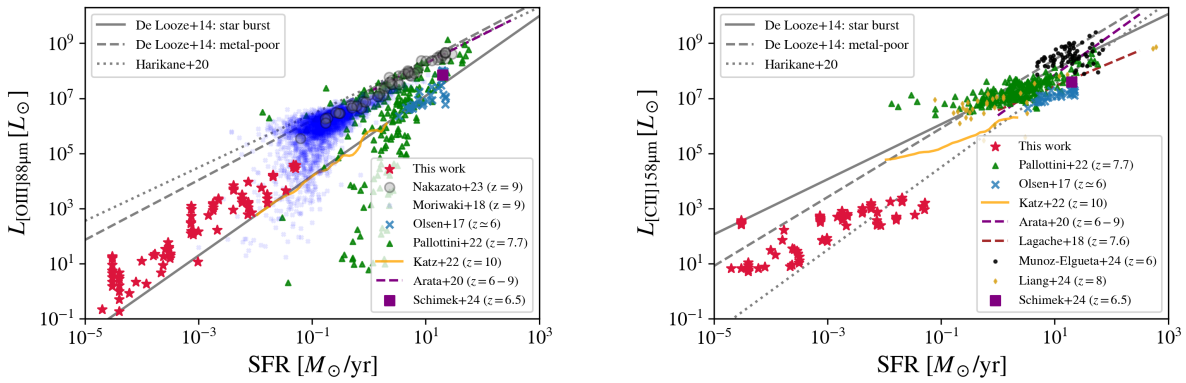

Figure 8.11: Same as Figure 8.9 but comparison with $z \gtrsim 6$ galaxy simulations. We compare our results with FirstLight (Nakazato et al., 2023), Moriwaki et al. (2018), SERRA (Pallottini et al., 2022), SIGAME (Olsen et al., 2017), Katz et al. (2022), Arata et al. (2020), TNG(Muñoz-Elgueta et al., 2024). FIRE-box(Liang et al., 2024), and PONOS(Schimek et al., 2024). We also plot the semi-analytical model of Lagache et al. (2018) in the right panel. This figure is taken from Nakazato et al. (2025).

As mentioned in Section 8.3.5, our simulated galaxy is consistent with the relation of local metal-poor galaxies rather than that of local star-burst because of its very low-metallicity of $\log(Z/Z_\odot) = [-3.5, -2.7]$.

For [CII] -SFR, the slope of our data is shallower than that of [OIII] -SFR, again as mentioned in Section 8.3.5. This trend is similar to the other simulations with on-the-fly RT (Pallottini et al., 2022; Katz et al., 2022).

Figure 8.12 shows the relationship between [OIII] /[CII] and SFR in our simulation compared with other theoretical studies at $z \gtrsim 6$. We find a positive correlation consistent with the results of Olsen et al. (2017), Pallottini et al. (2022), and Katz et al. (2022), although an anti-correlation was reported by Arata et al. (2020). The differences among simulation trends, as well as the absence of a clear observational correlation, can be interpreted in terms of galaxy mass and associated star formation variability. Low-mass galaxies have shallow gravitational potentials, allowing stellar feedback to strongly regulate star formation and thus produce large, stochastic variations in SFR. In such galaxies, the [OIII] /[CII] ratio closely tracks fluctuations in the 10 Myr-averaged SFR and ionization parameter $U_{\rm ion}$ (see Section 8.3.4; also Kohandel et al. 2025). As galaxies grow and their gravitational potentials deepen, the amplitude of SFR fluctuations diminishes and the correlation weakens. Current observational samples at $z \gtrsim 6$, detected simultaneously in [OIII] and [CII] , tend to represent relatively massive systems ($M_* \gtrsim 10^9\, M_\odot$), whose comparatively smooth star-formation histories may obscure the relationship predicted by simulations of lower-mass galaxies.

The main difference with respect to previous studies is the values of the line ratios. Our simulation reaches values as high as [OIII] /[CII] ~ 50, whereas other simulations typically find lower ratios in the range $0.1 - 3$ and fail to reproduce the high observed ratios shown in Figure 8.10. The exact reasons behind this discrepancy are difficult to pinpoint, as star formation and feedback prescriptions vary considerably across simulations. One possibility is our exceptionally short snapshot interval, especially around the intense starburst phase at $z \approx 10.5$, during which we output snapshots every 1 Myr. This high temporal resolution allows us to capture transient peaks in the [OIII] /[CII] ratio, which can reach up to ~ 30 at the peak of star formation bursts. In contrast, many other simulations analyze data from single snapshots or use coarser time intervals, potentially missing these short-lived extreme episodes.

Another potential factor is the spatial resolution of radiative transfer (RT) calculations. Many previous simulations employ RT at resolutions of 10 pc or coarser, which may not ac-

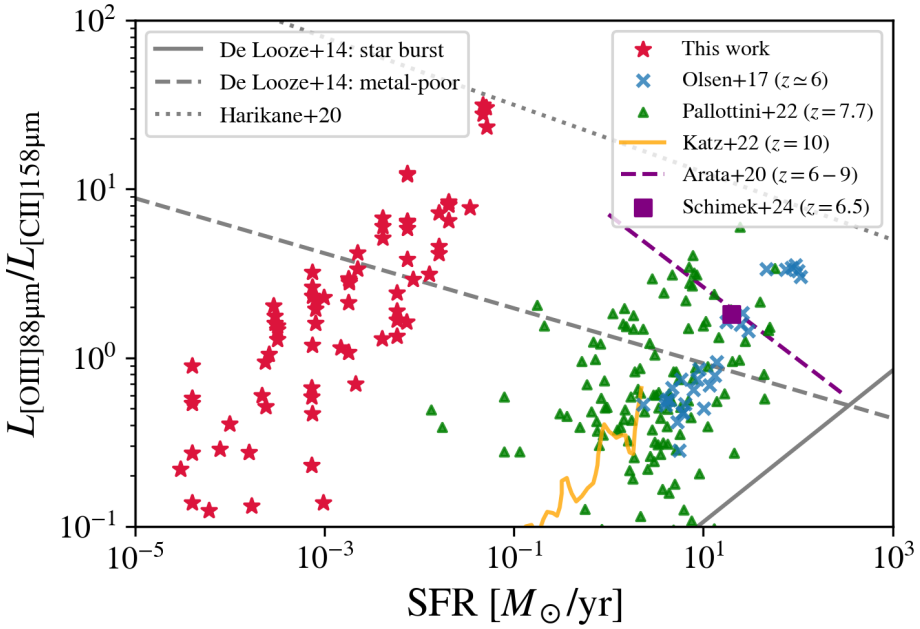

Figure 8.12: Same as Figure 8.10 but comparison with previous theoretical works at $z \gtrsim 6$ that investigated both [OIII] and [CII] lines. References are in the caption of Figure 8.11. This figure is taken from Nakazato et al. (2025).

curately trace the ionization structure within dense gas. For instance, Pallottini et al. (2019) noted that their simulation with a resolution of 28 pc could not adequately resolve ionized gas at densities $n_{\mathrm{HII}} \gtrsim 1, \mathrm{cm}^{-3}$, potentially leading to underestimated [OIII] luminosities and overestimated [CII] luminosities. By contrast, our simulations, with a much finer resolution of 0.1 pc, accurately resolve high-density ionized regions ($n_{\mathrm{HII}} \sim 500\,\mathrm{cm}^{-3}$), resulting in stronger [OIII] emission (which scales as $\propto n_{\mathrm{HII}}^2$). We further discuss the impact of RT resolution on simulated line ratios in Section8.4.3.

8.4 Discussion

8.4.1 Physical Origins of the High [OIII]/[CII] Ratio

Several possible explanations have been proposed for the high [OIII]/[CII] ratios observed in high-redshift galaxies. For instance, Harikane et al. (2020) and Katz et al. (2022) examined eight potential contributing factors: (A) elevated ionization parameters, (B) lower gas metallicities, (C) higher electron densities, (D) enhanced O/C abundance ratios, (E) reduced PDR covering fractions, (F) attenuation by the cosmic microwave background (CMB), (G) spatially extended halos, and (H) inclination effects. However, these factors often interact in complex ways, complicating the identification of the dominant physical mechanism driving high [OIII]/[CII] ratios. Therefore, we return to the basic physical parameters and focus our analysis on three fundamental properties: gas density, gas temperature, and ion fractions.

8.4.1.1 Toy Model for Intrinsic Line Luminosities

Here we derive emission line luminosities from a simple model assuming constant temperature and density in each gas phase. The intrinsic luminosities of forbidden lines (i.e., collisionally

excited lines) can be written as

$$\begin{aligned} L_{\rm int} &= \Lambda(n_{\rm gas}, T) n_{\rm gas} n_{\rm ion} V_{\rm gas} \\ &= \Lambda(T) n_{\rm gas}^2 X_{\rm ion} V_{\rm gas} \quad (\text{for } n_{\rm gas} < n_{\rm crit}), \end{aligned} \tag{8.4}$$

where $\Lambda, V_{\rm gas}$, and $X_{\rm ion}$ are cooling rate [erg s^{-1}cm^3], gas volume, and the fraction of a target ion, respectively. Here, $n_{\rm gas}$ denotes the number density of each gas phase and is written as $n_{\rm gas} = n_{\rm HII}$ in HII regions and $n_{\rm gas} = n_{\rm HI}$ in PDRs. The main collision partners in HII regions and PDR are electrons and neutral hydrogen atoms, and their densities are $n_{\rm c} = n_{\rm e} \simeq n_{\rm HII}$ for HII regions and $n_{\rm c} = n_{\rm HI}$ for PDR. The observed luminosity is decreased to some extent via several effects such as aperture and inclination effect, which will be discussed in Section 8.4.3:

$$L_{\rm obs} = f_{\rm obs}\, L_{\rm int} \;\; (0 < f_{\rm obs} < 1)\,, \tag{8.5}$$

where $f_{\rm obs}$ is the suppression factor related to observations. The intrinsic [OIII] and [CII] luminosities and their ratio are given as [3]

$$L_{\rm [OIII],int} = \Lambda_{\rm [OIII]}(T_{\rm e}) n_{\rm HII}^2 X_{\rm O^{++}} V_{\rm HII}\,, \tag{8.6}$$

$$\begin{aligned} L_{\rm [CII],int} &= \Lambda_{\rm [CII]}(T_{\rm e}) n_{\rm HII}^2 X_{\rm C^+}^{\rm (HII)} V_{\rm HII} \\ &\quad + \Lambda_{\rm [CII]}(T_{\rm HI}) n_{\rm HI}^2 X_{\rm C^+}^{\rm (HI)} V_{\rm HI}\,, \end{aligned} \tag{8.7}$$

$$\begin{aligned} \therefore \frac{L_{\rm [CII],int}}{L_{\rm [OIII],int}} &= \frac{\Lambda_{\rm [CII]}(T_{\rm e})}{\Lambda_{\rm [OIII]}(T_{\rm e})} \cdot \frac{X_{\rm C^+}^{\rm (HII)}}{X_{\rm O^{++}}} \\ &\quad + \frac{\Lambda_{\rm [CII]}(T_{\rm HI})}{\Lambda_{\rm [OIII]}(T_{\rm e})} \frac{n_{\rm HI}^2}{n_{\rm HII}^2} \frac{X_{\rm C^+}^{\rm (HI)}}{X_{\rm O^{++}}} \frac{V_{\rm HI}}{V_{\rm HII}}\,, \end{aligned} \tag{8.8}$$

where $T_{\rm HI}$ is the gas temperature in the PDRs, and $T_{\rm e}(= T_{\rm HII})$ is the electron (gas) temperature in HII regions. In this analysis, we neglect [CII] emission from molecular gas, since its mass fraction remains below 1% even during the intense starburst phases in our simulation. Such dominance of atomic hydrogen gas in high-redshift galaxies has also been reported by other simulation studies (Casavecchia et al., 2025). Furthermore, the FIRE simulations (Liang et al., 2024) reports that the molecular gas contributes less than 10% of the total [CII] emission at $z = 0 - 8$.

8.4.1.2 Cooling Rates of [OIII] and [CII] Lines

From here, we will calculate the cooling rate of collisionally excited lines in HII regions. A cooling rate for a collisionally excited line in the case of low-density and no stimulated emission is expressed as:

$$\Lambda_{21} = h\nu_{21} q_{12}, \tag{8.9}$$

where ν is the frequency of the emission line and q_{12} is the collisional excitation rate per unit time per unit volume [cm^{3}s^{-1}]. The cooling rate is defined to calculate volume emissivity as

$$\epsilon_{21} = n_{\rm c} n_1 \Lambda_{21}, \tag{8.10}$$

where n_1 is the number density of lower levels. Since [OIII] and [CII] transitions are $^3P_1 \rightarrow ^3P_0$ and $^2P_{3/2} \rightarrow ^2P_{1/2}$, n_1 correspond to the base levels of their ions. From Eq. (3.34), the collisional

[3] The critical densities of [OIII] 88μm and [CII] 158μm in HII regions with $T_{\rm HII} = 10^4$ K are 510 and 50 cm^{-3}, respectively (Osterbrock and Ferland, 2006) The critical density of [CII] 158μm in PDR with $T_{\rm HI} = 5000(100)$ K is $1.5(2.7) \times 10^3$ cm^{-3} (Draine, 2011).

de-excitation rate q_{21} due to electron collisions is given by

$$q_{21} = \frac{8.629 \times 10^{-6}}{T^{-1/2}} \frac{\Upsilon_{(1,2)}}{g_2} \, [\mathrm{cm^3 s^{-1}}], \tag{8.11}$$

$$\Upsilon_{(1,2)[\mathrm{OIII}]} = 0.55, \tag{8.12}$$

$$\Upsilon_{(1,2)[\mathrm{CII}]} = 2.15. \tag{8.13}$$

Here $\Upsilon_{(1,2)}$ is the collision strength (dimensionless) and the temperature is expressed in kelvin [K]. From eq. (8.33), we obtain $q_{12} = q_{21} g_2/g_1 \exp(-T_*/T)$, and the equivalent temperatures for [OIII] 88μm and [CII] 158μm are 163 K and 91.2 K, respectively. Finally, eq. (8.9) can be written as

$$\Lambda_{21} = h\nu_{21} \frac{8.629 \times 10^{-6}}{T^{-1/2}} \frac{\Upsilon_{(1,2)}}{g_1} \exp\left(-\frac{T_*}{T}\right) \tag{8.14}$$

$$\simeq h\nu_{21} \frac{8.629 \times 10^{-6}}{T^{-1/2}} \frac{\Upsilon_{(1,2)}}{g_1}. \tag{8.15}$$

The approximated eq. (8.15) can be satisfied when we consider FIR emission lines from HII regions, i.e., $T_* \ll T_\mathrm{e}$ and $\exp(-T_*/T) \to 1$. The cooling rates for [OIII] 88μm and [CII] 158 μm are

$$\Lambda_{[\mathrm{OIII}]}(T_\mathrm{e}) = 1.07 \times 10^{-19} {T_\mathrm{e}}^{-1/2} \ \mathrm{erg\,s^{-1} cm^3} \tag{8.16}$$

$$\Lambda_{[\mathrm{CII}]}(T_\mathrm{e}) = 1.17 \times 10^{-19} {T_\mathrm{e}}^{-1/2} \ \mathrm{erg\,s^{-1} cm^3}. \tag{8.17}$$

From above discussion, we obtain $\Lambda_{[\mathrm{CII}]}(T_\mathrm{e})/\Lambda_{[\mathrm{OIII}]}(T_\mathrm{e}) \simeq 1$ in HII regions. Stellar radiation in high-redshift galaxies tends to be dominated by young and low-metallicity populations and to have hard SEDs (= high U_ion). Consequently, $X_{\mathrm{C+}}^{(\mathrm{HII})}$ is much smaller than that of local galaxies: $X_{\mathrm{C+}}^{(\mathrm{HII})} \ll X_{\mathrm{O++}}$, and the first term in Eq. (8.8) can be negligible. The cooling rate of [CII] ([OIII]) is calculated considering collisions with atomic hydrogen (electrons) in PDR (HII regions). They are approximated as follows:

$$\Lambda_{[\mathrm{CII}]}(T_\mathrm{HI}) = 10^{-24} \exp\left(-\frac{91.2}{T_\mathrm{HI}}\right) \times (16 + 0.344\sqrt{T_\mathrm{HI}} - 47.7/T_\mathrm{HI}) \, \mathrm{erg\,cm^3 s^{-1}}, \tag{8.18}$$

$$\Lambda_{[\mathrm{OIII}]}(T_\mathrm{e}) = 10^{-19} T_\mathrm{e}^{-1/2} \, \mathrm{erg\,cm^3 s^{-1}}. \tag{8.19}$$

Eq. (8.18) is taken from Barinovs et al. (2005) and Eq. (8.19) is obtained from Eq. (8.16). The temperature T_HI in Eq. (8.18) and T_e in Eq. (8.19) are expressed in Kelvin. Note that Eq. (8.18) does not include the effect of CMB attenuation. We derive the attenuation factor in the next paragraph.

8.4.1.3 Impact of Cosmic Microwave Background (CMB) Attenuation

In our CLOUDY setup, we include attenuation by the cosmic microwave background (CMB), as detailed in Section 8.2. Below, we quantify its impact, following Goldsmith et al. (2012), Arata et al. (2020), and Liang et al. (2024).

For [CII] emission, we consider two-level populations and define level 1 (2) as the lower (upper) level. The volume emissivity of [CII] emission $\epsilon_{[\mathrm{CII}]}$ [$\mathrm{erg\,s^{-1} cm^3}$]is

$$\epsilon_{[\mathrm{CII}]} = [A_{21} n_2 + B_{21} n_2 J_\nu(T_\mathrm{b}) - B_{12} n_1 J_\nu(T_\mathrm{b})] \, h\nu_{[\mathrm{CII}]}, \tag{8.20}$$

where A_{21}, B_{21}, B_{12} are Einstein's coefficients, and they have the following relationship:

$$B_{12} = \frac{g_2}{g_1} B_{21} \tag{8.21}$$

$$\frac{A_{21}}{B_{21}} = \frac{8\pi h \nu_{[\mathrm{CII}]}^3}{c^2}. \tag{8.22}$$

The value of A_{21} is $A_{21} = 2.29 \times 10^{-6}\,\mathrm{s}^{-1}$ (Nussbaumer and Storey, 1981). The statistical weight for level 1 (2) is $g_1 = 2 (g_2 = 4)$. Here $J_\nu(T_\mathrm{b})$ is the background radiation at temperature of T_b, i.e., Blackbody radiation at CMB temperature;

$$J_\nu(T_\mathrm{b}) = \frac{4\pi}{c} B_\mathrm{bb}(T_\mathrm{CMB}) = \frac{8\pi h \nu^3}{c^2} \frac{1}{\exp(T_*/T_\mathrm{CMB}) - 1}, \tag{8.23}$$

where T_* is an equivalent temperature, $T_* \equiv h\nu_{[\mathrm{CII}]}/k_\mathrm{B} = 91.2\,\mathrm{K}$. The excitation temperature of the transition is defined to satisfy the following relationship;

$$\frac{n_2}{n_1} = \frac{g_2}{g_1} \exp\left(-\frac{T_*}{T_\mathrm{ex}}\right). \tag{8.24}$$

By substituting eq.(8.24) into eq.(8.20), we obtain

$$\epsilon_{[\mathrm{CII}]} = n_2 A_{21} h\nu \left[1 - \frac{\exp(T_*/T_\mathrm{ex}) - 1}{\exp(T_*/T_\mathrm{b}) - 1}\right] \equiv n_2 A_{21} h\nu \eta \tag{8.25}$$

The η is the correction term for background radiation. To calculate this term, we derive $\exp(T_*/T_\mathrm{ex})$ from the rate equation;

$$n_2 \left[A_{21} + B_{21} J_\nu + C_{21}\right] = n_1 \left[B_{12} J_\nu + C_{12}\right]. \tag{8.26}$$

From eq. (8.26), we get

$$\frac{n_2}{n_1} = \frac{B_{12} J_\nu + C_{12}}{A_{21} + B_{21} J_\nu + C_{21}} \tag{8.27}$$

$$\therefore \frac{g_2}{g_1} \exp\left(-\frac{T_*}{T_\mathrm{ex}}\right) = \frac{B_{12} J_\nu + n_\mathrm{c} q_{12}^\mathrm{c}}{A_{21} + B_{21} J_\nu + n_\mathrm{c} q_{21}^\mathrm{c}}, \tag{8.28}$$

where n_c and $q_{12}^\mathrm{c}(q_{21}^\mathrm{c})$ are the number density of a collision partner and collision rate efficiency for the partner. The partners for HII region, PDR, and molecular gas are electrons, neutral hydrogen atoms, and hydrogen molecules, respectively. The corresponding collision rate efficiencies are (Goldsmith et al., 2012)

$$q_{21}^e = 8.7 \times 10^{-8}\,\mathrm{cm}^3\mathrm{s}^{-1} (T/2000)^{-0.37} \tag{8.29}$$

$$q_{21}^\mathrm{HI} = 4.0 \times 10^{-11}\,\mathrm{cm}^3\mathrm{s}^{-1} (16 + 0.35 T^{0.5} + 48 T^{-1}) \tag{8.30}$$

$$q_{21}^{\mathrm{H}_2} = 3.8 \times 10^{-10}\,\mathrm{cm}^3\mathrm{s}^{-1} (T/100)^{0.14}, \tag{8.31}$$

where the temperature T is expressed in kelvin [K]. We define G as the same as Goldsmith et al. (2012); Liang et al. (2024), $G \equiv 1/[\exp(T_*/T_\mathrm{b}) - 1]$, and rewrite eq. (8.23) as

$$B_{21} J_\nu = A_{21} G. \tag{8.32}$$

From the detailed balance, we obtain

$$\frac{q_{12}^\mathrm{c}}{q_{21}^\mathrm{c}} = \frac{g_2}{g_1} \exp\left(-\frac{T_*}{T_\mathrm{kin}}\right). \tag{8.33}$$

Inserting eq. (8.32) and eq. (8.33) into eq.(8.28), we get

$$\exp\left(\frac{T_*}{T_{\rm ex}}\right) = \frac{A_{21}(1+G) + n_{\rm c} q_{21}^{\rm c}}{G A_{21} + n_{\rm c} q_{21}^{\rm c} \exp\left(-\frac{T_*}{T_{\rm kin}}\right)}. \tag{8.34}$$

In the case without CMB radiation, G reaches zero and $T_{\rm ex} \to T_{\rm kin}$. When the second term in the numerator of eq.(8.34) is weak, i.e., diffuse gas $n_{\rm c} \ll A_{21}/q_{21}^{\rm c}$, the CMB effect ($G > 0$) becomes large to the excitation temperature $T_{\rm ex}$, decreasing η.

To calculate eq. (8.34) for [CII] emission, we need to consider multi-phase gas; HII , HI , and molecular gas. For HII region, the typical gas temperature is $\sim 10^4$ K, and we can approximate $\exp(-T_*/T_{\rm kin}) \to 0$, obtaining

$$\exp\left(\frac{T_*}{T_{\rm ex}}\right) = \frac{(1+G)A_{21} + n_{\rm e} q_{21}^{\rm c}}{G A_{21}}. \tag{8.35}$$

We will obtain the cooling rate from HII regions by inserting eq.(8.35) into eq.(8.20). For PDR (molecular gas), we replace $n_{\rm c}$ and $q_{21}^{\rm c}$ as $n_{\rm HI}(n_{\rm H_2})$ and $q_{21}^{\rm HI}(q_{21}^{\rm H_2})$, respectively. We then obtain the cooling rate $\Lambda_{\rm HI}(\Lambda_{\rm H_2})$. The total luminosity is the sum of the luminosity from each region ($L_{\rm [CII]} = L_{\rm [CII]}^{\rm (HII)} + L_{\rm [CII]}^{\rm (HI)} + L_{\rm [CII]}^{\rm (H_2)}$), but we can approximate $L_{\rm [CII]} \approx L_{\rm [CII]}^{\rm (HI)}$ since the most [CII] emission comes from PDR. Then we can evaluate the CMB effect as

$$\begin{aligned}
\frac{L_{\rm [CII]}(T_{\rm CMB})}{L_{\rm [CII]}(T_{\rm b}=0)} &\sim \frac{L_{\rm [CII]}^{\rm (HI)}(T_{\rm CMB})}{L_{\rm [CII]}^{\rm (HI)}(T_{\rm b}=0)} \\
&= \frac{\epsilon_{\rm [CII]}^{\rm (HI)}(T_{\rm CMB})}{\epsilon_{\rm [CII]}^{\rm (HI)}(T_{\rm b}=0)} = \eta^{\rm HI} \\
&= 1 - \frac{\exp(T_*/T_{\rm ex}) - 1}{\exp(T_*/T_{\rm b}) - 1}.
\end{aligned} \tag{8.36}$$

Figure 8.13 shows how much [CII] emission is suppressed by CMB at $z = 10.0$. Here, we only consider collisions of neutral hydrogen atoms. For diffused gas with $n_{\rm H} \lesssim 30\,{\rm cm}^{-3}$, the CMB effect becomes significant, resulting in a reduction of luminosity over 80%. The threshold diffuse gas number density is lower at lower-redshift (e.g., $n_{\rm H} \lesssim 10(1)\,{\rm cm}^{-3}$ at $z = 7(4)$). If the gas number density is higher than the critical density $n_{\rm crit}$, the rate equation is dominated by the collision terms, and the CMB effect becomes negligible. We also plot the contours for [CII] emission as the same as the right panel of Figure 8.7 and [CII] mainly comes from dens and warm gas with $n_{\rm H} = 10^{2-3}\,{\rm cm}^{-3}$ and $T = 5000 - 10^4$ K. In this region, the CMB at $z = 10(7)$ affects 10-20 (~ 5)%.

Notice that the cosmic microwave background (CMB) at $z = 0$ can hinder detectability by adding background noise that obscures the line signal (da Cunha et al., 2013; Kohandel et al., 2019). We do not account for this effect here because our focus is on the intrinsic luminosity of high-redshift galaxies. However, it could become significant when making detailed comparisons of line profiles between simulations and observations.

In summary, although the CMB at $z = 10\,(z = 7)$ suppresses [CII] luminosities by roughly 10–20% (∼5%), this effect does not significantly alter the derived scaling relationship in the next section (Section 8.4.1.4).

8.4.1.4 Scaling Relationship for the Intrinsic [OIII]/[CII] Ratio

From Figures 8.1 and 8.7, the typical temperatures of PDR and HII regions are $T_{\rm HI} \sim 5000$ K and $T_{\rm e} \sim 2 \times 10^4$ K, and the corresponding cooling rates are $\Lambda_{\rm [CII]} = 3.96 \times 10^{-23}\,{\rm erg\,cm^3 s^{-1}}$ and $\Lambda_{\rm [OIII]} = 7.58 \times 10^{-22}\,{\rm erg\,cm^3 s^{-1}}$, respectively. For $X_{\rm C^+}^{\rm (HI)}/X_{\rm O^{++}}$, we can approximate

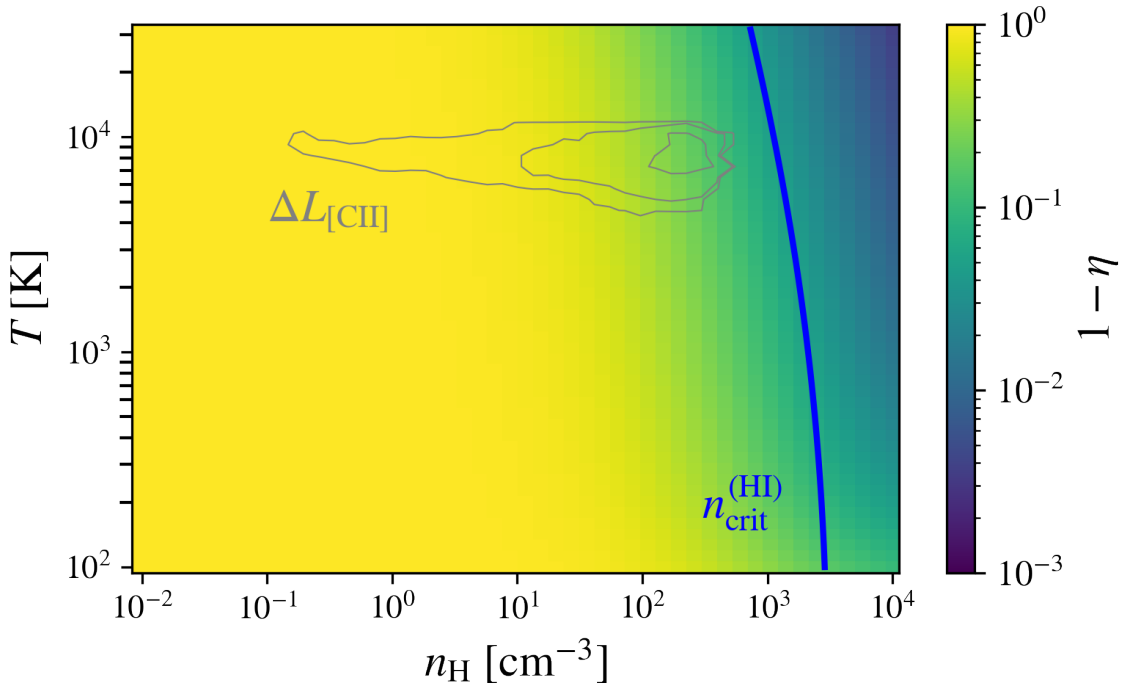

Figure 8.13: The CMB effect to [CII] 158μm luminosity at $z = 10$ as a function of hydrogen nuclei density and temperature. The color scale indicates the reduction strength $1 - \eta$, where η is the luminosity ratio of [CII] with (without) the CMB stimulated emission and absorption. The blue solid line represents the critical density of hydrogen atoms. The gray contours show the [CII] luminosity in the phase-diagram with $\log L_{[\mathrm{CII}]}/[L_\odot/\Delta \log n_{\mathrm{H}}/\Delta \log T]) = -0.5, 0.5, 1.5$, where $\Delta \log n_{\mathrm{H}} = 0.12$ and $\Delta \log T = 0.05$. Note that the contoured [CII] luminosities are calculated by considering the CMB effect in CLOUDY. This figure is taken from Nakazato et al. (2025).

as the element abundance ratio $A(\mathrm{C})/A(\mathrm{O})$ because $X^{(\mathrm{HI})}_{\mathrm{C}^+}/X^{(\mathrm{HI})}_{\mathrm{C,tot}} \sim 1$ in a neural gas and $X_{\mathrm{O}^{++}}/X^{(\mathrm{HII})}_{\mathrm{O,tot}} \sim 1$ in HII regions are satisfied. Here $X^{(\mathrm{HI})}_{\mathrm{C,tot}}$ and $X^{(\mathrm{HII})}_{\mathrm{O,tot}}$ denote the total fraction of carbon and oxygen, summed over all ionization states in each region. We then rewrite Eq. (8.8) as

$$\begin{aligned}\frac{L_{[\mathrm{OIII}],\mathrm{int}}}{L_{[\mathrm{CII}],\mathrm{int}}} &= \frac{\Lambda_{[\mathrm{OIII}]}(T_\mathrm{e})}{\Lambda_{[\mathrm{CII}]}(T_\mathrm{HI})}\frac{M_\mathrm{HII}}{M_\mathrm{HI}}\frac{n_\mathrm{HII}}{n_\mathrm{HI}}\frac{A(\mathrm{O})}{A(\mathrm{C})} \\ &= 5.7\left(\frac{M_\mathrm{HII}/M_\mathrm{HI}}{0.3}\right)\left(\frac{n_\mathrm{HII}/n_\mathrm{HI}}{0.5}\right)\frac{(\mathrm{O/C})}{(\mathrm{O/C})_\odot},\end{aligned} \tag{8.37}$$

where M_HII (M_HI) is ionized (neutral hydrogen) gas mass and $\mathrm{O/C} \equiv A(\mathrm{O})/A(\mathrm{C})$ is the abundance ratio. We adopted typical values for the gas mass ratio from the middle-right panel in Figure 8.8 and for the density ratio from Figure 8.7. Since the above derivation assumes constant temperature and density in each phase, the density ratio that appears in Eq. (8.37), $n_\mathrm{HII}/n_\mathrm{HI}$, should be considered a global luminosity-weighted ratio: n_HII is the average weighted by the [OIII] 88μm line luminosity and n_HI is the average weighted by the [CII] 158μm line luminosity. This ratio is time dependent and varies between 0.3-1 during bursts of star formation, to 10^{-2}-10^{-3} during quiescence periods between starbursts. Eq. (8.37) shows that line ratios of about 5-6 can be obtained assuming typical values of $M_\mathrm{HII}/M_\mathrm{HI} \sim 0.3$ and $n_\mathrm{HII}/n_\mathrm{HI} \sim 0.5$. During star-formation bursts, the ionized gas mass can be larger than the neutral gas mass, as shown in Figure 8.3, leading to even more extreme values of the line ratio (> 10).

8.4.2 Redshift Evolution of [OIII]/[CII]

Here, we discuss how the [OIII] /[CII] ratio evolves with redshift based on Eq. (8.37). Observations suggest that [OIII] /[CII] ratios are higher at $z \gtrsim 6$ than in local star-forming galaxies (see Sections 8.1 and 8.3.5). To unveil the origin of this redshift evolution, we examine the redshift dependence of four key factors that influence the line ratio: cooling rates, gas masses, gas densities, and elemental abundances.

Cooling Rates. As the metallicity increases, both the PDRs and the HII regions cool to lower temperatures through metal/dust cooling (e.g., Omukai et al., 2005). PDRs can cool to $\sim 100\,\mathrm{K}$, while HII regions cool to $\sim 8000\,\mathrm{K}$ (e.g., Osterbrock and Ferland, 2006). Correspondingly, the cooling rates change to $\Lambda_{[\mathrm{CII}]} = 7.62 \times 10^{-24}\,\mathrm{erg\,s^{-1}\,cm^3}$[4] and $\Lambda_{[\mathrm{OIII}]} = 1.2 \times 10^{-21}\,\mathrm{erg\,s^{-1}\,cm^3}$. Interestingly, the [OIII] 88 μm cooling rate increases slightly, whereas that of [CII] 158 μm decreases.[5] Consequently, the ratio $\Lambda_{[\mathrm{OIII}]}/\Lambda_{[\mathrm{CII}]}$ increases from about 19 to 157 as one moves from high-z to lower-z. However, the impact of cooling rates is reversed by the three other effects discussed below, and the [OIII] /[CII] ratio turns out to be higher in high-z galaxies.

Gas Mass. From Figure 8.8, our simulated galaxies typically show a high ionized-to-neutral gas mass ratio, $M_\mathrm{HII}/M_\mathrm{HI} > 0.3$, when the line ratio is large, [OIII] /[CII] > 3. Such high mass ratios are also found in other high-redshift galaxies, as we will discuss in Section 8.4.4. In contrast, local galaxies, including the Milky Way, typically show much lower values, $M_\mathrm{HII}/M_\mathrm{HI} \approx 0.01$ (Tielens, 2005), suggesting a significantly lower ionized gas fraction relative to neutral gas at low-z. This effect is therefore expected to reduce the line ratio at low-z.

[4]Here we assume that [CII] emission from CNM dominates at lower redshifts since the gas density is over 10 times higher than that of WNM.

[5]However, rest-optical [OIII] cooling rates rise with temperature (see Figure 3.2 of Osterbrock and Ferland, 2006).

Density. In our simulation, we have computed the [OIII] 88μm - and [CII] 158μm -luminosity-weighted gas densities separately for ionized (HII) and neutral (PDR) gas. During bursty star formation episodes, the simulated galaxy exhibits ionized gas densities of $\langle n_{\rm HII}\rangle = 20$–$200\,{\rm cm}^{-3}$ and neutral gas densities of $\langle n_{\rm HI}\rangle = 70$–$600\,{\rm cm}^{-3}$, with their ratio fluctuating in the range $\langle n_{\rm HII}\rangle/\langle n_{\rm HI}\rangle = 0.3$–$1.0$. Recently, Harikane et al. (2025b) estimated electron densities of galaxies during the Epoch of Reionization using the FIR [OIII] 88μm emission line, obtaining values $n_{\rm e} \lesssim 500\,{\rm cm}^{-3}$, with some galaxies even below $100\,{\rm cm}^{-3}$. These estimates, while systematically lower than those derived from optical ([OII]-based) or UV (CIII]-based) emission lines, interestingly match the [OIII] 88μm -weighted ionized gas densities derived in our simulations.

For local galaxies, Nakazato et al. (2023) and Harikane et al. (2025b) derived FIR-[OIII]-weighted electron densities using the [OIII] 88μm /52μm line ratio, based on observational data from Fernández-Ontiveros et al. (2016) and Brauher et al. (2008). Their estimated electron densities are typically around $100\,{\rm cm}^{-3}$. Meanwhile, neutral gas densities of local star-forming galaxies have been estimated by Malhotra et al. (2001), typically yielding $n_{\rm HI} \sim 10^3\,{\rm cm}^{-3}$. Thus, we expect that the gas density ratio $n_{\rm HII}/n_{\rm HI}$ decreases systematically from approximately 0.5 at high redshift to roughly 0.1 in local star-forming galaxies.

Elemental Abundances. Since we adopt solar abundance ratios in our current model, the O/C ratio remains constant. In reality, however, high-redshift galaxies may be enriched primarily by Type II SNe, possibly elevating O/C above the solar value (Nomoto et al., 2006; Stark et al., 2017). For instance, Type II SNe yields at $1/20\,Z_\odot$ could lead to O/C ratios up to eight times higher than the solar values. Some observations of $z > 6$ galaxies also suggest about twice the solar O/C ratio (Stark et al., 2017), which can linearly decrease [CII] luminosity with respect to [OIII] luminosity and thus boost [OIII] /[CII] . In lower-redshift galaxies, O/C would converge closer to the solar ratio.[6]

Considering these four factors and Eq. (8.37), we estimate that the [OIII] /[CII] ratio could decrease from approximately 5.7 (or 11.2, if O/C is significantly enhanced) at high redshift to roughly 0.3 at lower redshift. This is consistent with the [OIII] /[CII] $\sim 0.04 - 1$ values observed in local starburst galaxies (De Looze et al., 2014).

8.4.3 Role of Numerical Resolution and $f_{\rm obs}$ in Reproducing High [OIII]/[CII] Ratios at $z > 6$

In Figure 8.10, our simulated galaxies achieve the high [OIII] /[CII] ratios ($\sim$ 3–30), reproducing the values observed at $z > 6$. In contrast, Figure 8.12 shows that other simulations yield lower [OIII] /[CII] values, falling short of the high observed ratios at $z > 6$. A likely reason for this discrepancy is our exceptionally high spatial resolution, which is sufficient to resolve dense HII regions whose typical size is estimated by the Strömgren radius with 1 pc order (Eq. (8.1)). Previous on-the-fly RT simulations (e.g., Pallottini et al., 2019; Katz et al., 2019) employed cell sizes an order of magnitude larger than these HII regions[7]. Consequently, their simulations can produce partially ionized cells where ionizing photons are absorbed within under-resolved volumes, whereas our higher resolution allows cells to be either predominantly neutral ($x_{\rm HII} \approx 0$) or ionized ($x_{\rm HII} \approx 1$) (see Figure 8.1). Insufficient resolution can lead to an underestimate of both the ionized gas mass and its density, suppressing [OIII] /[CII] to below unity according to Equation (8.37).

[6] We note that a fraction of both carbon and oxygen is locked up in solid grains. Because carbon is more heavily depleted onto dust than oxygen (Draine, 2011), the gas-phase O/C ratio can be up to ~ 2.5 times higher than the solar value.

[7] Strictly speaking, the size of an individual HII region around each star particle depends on Q(H), which scales with the star-particle mass. For reference, Katz et al. (2022) employ stellar particles of $400\,M_\odot$, while Pallottini et al. (2019) use $1.2 \times 10^4\,M_\odot$. The corresponding Strömgren radii are ~ 3 pc and ~ 9 pc, respectively—both are below the spatial resolution of their simulations.

In the previous section, we focused on physical parameters affecting the intrinsic emission line ratios. However, observational factors also influence the measured line luminosities through the factor $f_{\rm obs}$ in Eq. (8.5). For instance, extended [CII] emission may be missed when using small observational apertures, and a large velocity width (FWHM) could lower the peak flux below detection limits. Harikane et al. (2020) adopted relatively large apertures ($\sim 2''$) to fully capture halo-scale [CII] emission, yet still reported high [OIII] /[CII] ratios of approximately 3.4–8.8. They also showed that applying an extended [CII] spatial profile (Fujimoto et al., 2019) to data obtained with smaller apertures (Inoue et al., 2016a; Laporte et al., 2019) increases the recovered [CII] flux by at most ~ 0.6 dex, keeping the [OIII] /[CII] ratio high. Another factor, large velocity widths due to edge-on views, might also reduce the observed flux density (Kohandel et al., 2019). However, Katz et al. (2022) analyzed simulated galaxies viewed from different angles and found that [CII] emission lines are not systematically broader than [OIII] . We therefore conclude that aperture losses and velocity–width effects can lower $f_{\rm obs}$ for [CII] luminosities, thereby increasing [OIII] /[CII] ratios in certain sources, but are unlikely to be the primary cause of the observed high ratios. This figure is taken from Nakazato et al. (2025).

8.4.4 Synergy of JWST-detected Lines

In Section 8.4.1, we have shown [OIII] /[CII] $\propto (M_{\rm HII}/M_{\rm HI})(n_{\rm HII}/n_{\rm HI})$. To examine the validity of this relation, we derive the mass ratio $M_{\rm HII}/M_{\rm HI}$ observationally for the first time by combining JWST and ALMA observations.

The ionized gas mass $M_{\rm HII}$ can be calculated using Hβ luminosity (Finkelman et al., 2010):

$$\begin{aligned} M_{\rm HII} &= \frac{L_{\rm H\beta} m_{\rm H}/n_{\rm e}}{4\pi j_{\rm H\beta}/(n_{\rm e} n_{\rm p})} \\ &= 1.01\times10^{6}\,M_{\odot}\left(\frac{L_{\rm H\beta}}{10^{40}\,{\rm erg/s}}\right)\left(\frac{n_{\rm e}}{100\,{\rm cm^{-3}}}\right)^{-1}, \end{aligned} \tag{8.38}$$

where $m_{\rm H}$ and $j_{\rm H\beta}$ are the proton mass and Hβ emission coefficient, respectively. The value of $j_{\rm H\beta}$ can be changed by electron temperatures, but its temperature dependency is insignificant (Osterbrock and Ferland, 2006; Draine, 2011). For $M_{\rm HI}$, we use the conversion relation from [CII] luminosity to gas mass derived by Vallini et al. (2025)[8]:

$$M_{\rm HI} = \alpha_{\rm [CII]}\, L_{\rm [CII]}\ , \tag{8.39}$$

where

$$\log\left(\alpha_{\rm [CII]}/M_{\odot}L_{\odot}^{-1}\right) = -0.39\log(Z/Z_{\odot}) + 0.67. \tag{8.40}$$

Figure 8.14 shows the relation between [OIII] /[CII] and $M_{\rm HII}/M_{\rm HI}$. We plot every $z > 6$ object for which [OIII] 88 μm, [CII] 158 μm, Hβ, and gas-phase metallicity are currently available (references are in the caption of Figure 8.14). We successfully obtain the positive correlation between [OIII] /[CII] and $M_{\rm HII}/M_{\rm HI}$, as expected from Eq. (8.37), albeit with large scatter. The theoretical relation given by Eq. (8.37) is plotted in Figure 8.14) as colored bands corresponding to different density ratios. The width of the bands, corresponding to a factor of $\lesssim 1.5$ difference,

[8]We do not adopt the conversion factor derived from our own simulations, because we track only a single galaxy whose bursty star–formation history at $z > 10$ produces a much larger scatter in the metallicity–$\alpha_{\rm [CII]}$ relation than that reported by Vallini et al. (2025). Once galaxies grow sufficiently massive, their SFR fluctuations should subside and the scatter is expected to converge. We therefore apply the calibration of Vallini et al. (2025) to the observed systems, assuming that the inferred gas mass is dominated by neutral atomic hydrogen, $M_{\rm HI}$. A conversion between $L_{\rm [CII]}$ and the neutral–gas mass ($M_{\rm HI}$) has also been investigated by Heintz et al. (2021, 2025) using GRB afterglows and damped–Lyα spectrum. Because those methods can include large amounts of circumgalactic gas, we do not employ their relations here and instead focus on the multi-phase ISM in star-forming regions.

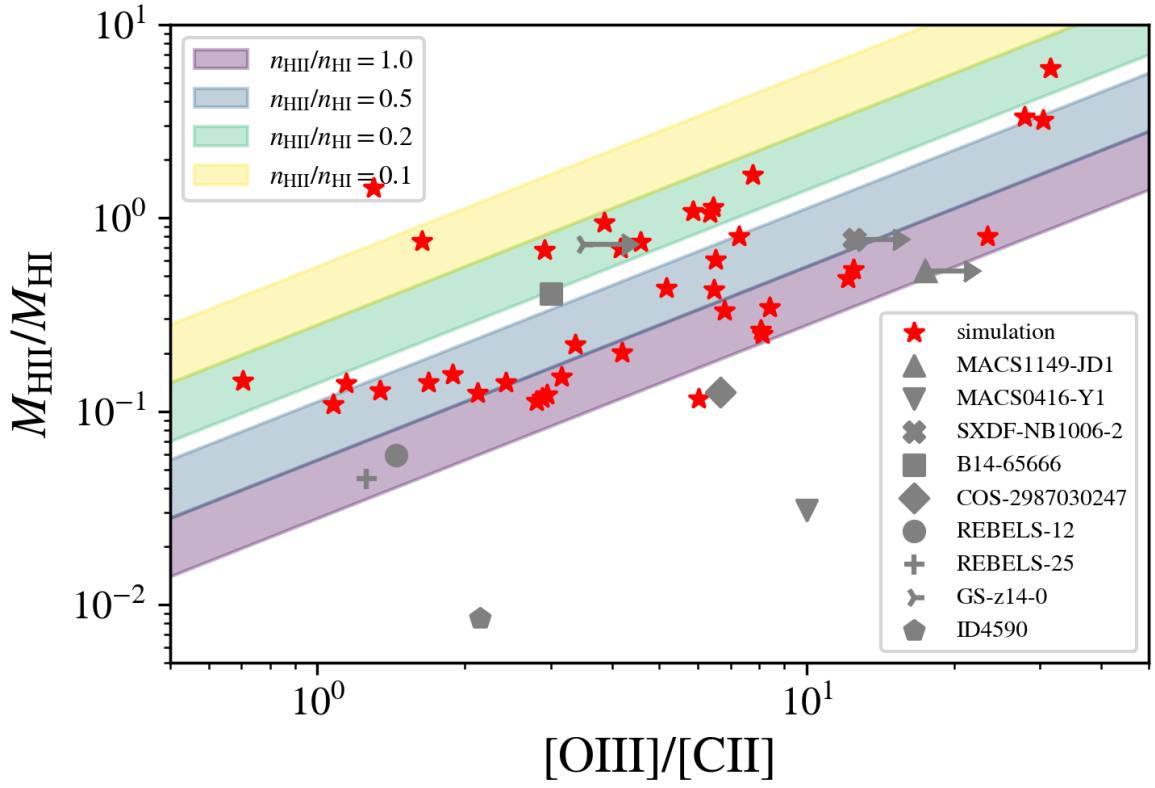

Figure 8.14: The relationship between [OIII] /[CII] and $M_{\rm HII}/M_{\rm HI}$. The red stars are our simulation results with SFR $> 10^{-3}\,M_\odot{\rm yr}^{-1}$ and gray plots are observational results at $z \gtrsim 6$. The information of $L_{[\rm OIII]\,88\mu m}$, $L_{[\rm CII]\,158\mu m}$, $L_{\rm H\beta}$, and $12 + \log({\rm O/H})$ are from the following references; MACS1149-JD1 (Hashimoto et al., 2018; Laporte et al., 2019; Stiavelli et al., 2023), MACS0416-Y1 (Tamura et al., 2019; Bakx et al., 2020; Harshan et al., 2024), SXDF-NB1006 (Inoue et al., 2016a, , Ren et al. submitted), B14-65666 (Hashimoto et al., 2019; Jones et al., 2024a), COS2987030247 (Witstok et al., 2022, , Usui et al. in prep., Mawatari et al. in prep,), REBELS-12 and REBELS-25 (Algera et al., 2024; Rowland et al., 2025), GS-z14-0 (Schouws et al., 2024, 2025; Helton et al., 2025), ID4590 (Fujimoto et al., 2024b; Heintz et al., 2023). We calculate $M_{\rm HII}$ assuming $n_{\rm HII} = 100\,{\rm cm}^{-3}$. The colorband shows the different density ratio cases with $n_{\rm HII}/n_{\rm HI} = 0.1 - 1.0$, with different neutral gas temperatures of $T_{\rm HI} = 500 - 5000\,{\rm K}$. This figure is taken from Nakazato et al. (2025).

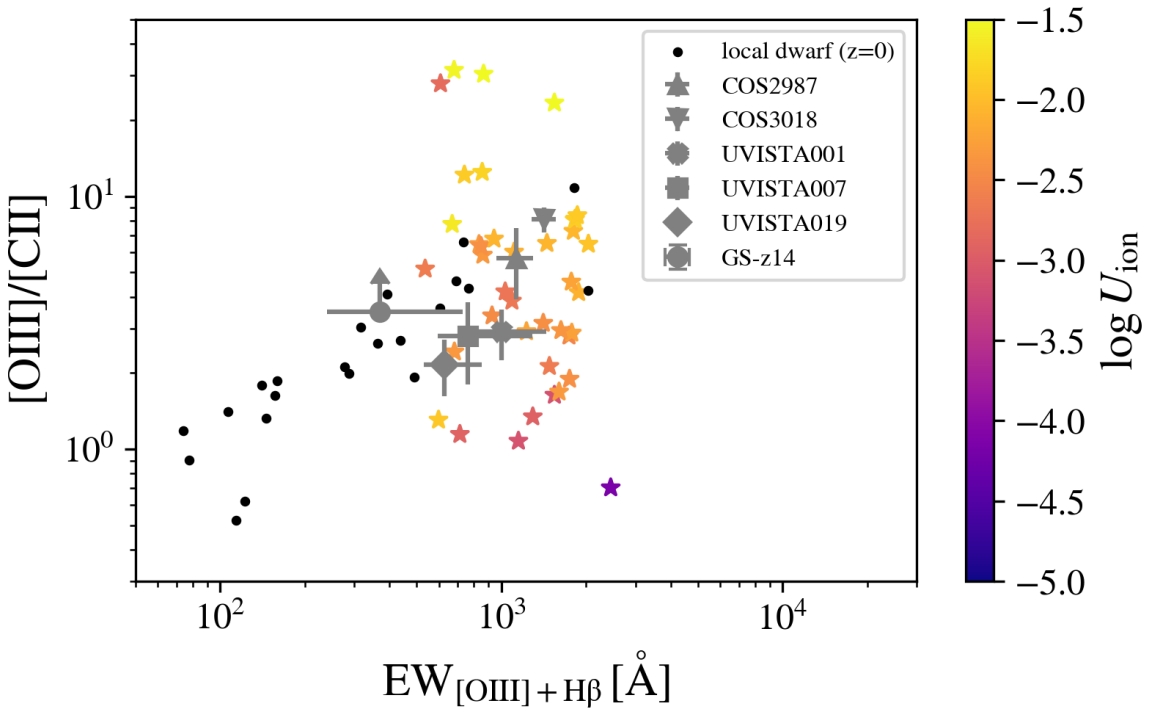

Figure 8.15: [OIII] /[CII] ratio as a function of [OIII] $_{4959,5007}$ + Hβ equivalent width. Star plots are our simulation results at $z = 9-13$ with SFR $> 10^{-3}\,M_\odot \mathrm{yr}^{-1}$, and a colorbar represents the averaged ionization parameters. Gray and black plots are $z > 6$ galaxies (Witstok et al., 2022; Schouws et al., 2025) and local dwarf galaxies from the Dwarf Galaxy Survey (Kumari et al., 2024), respectively. This figure is taken from Nakazato et al. (2025).

indicates the impact of varying the cooling-rate ratio by changing neutral-gas temperatures in $T_{\rm HI} = 500$–5000 K. We also plots our simulation results with SFR $> 10^{-3}\,M_\odot \mathrm{yr}^{-1}$, which exhibit a clear positive correlation between [OIII] /[CII] and $M_{\rm HII}/M_{\rm HI}$. The physical conditions of large $M_{\rm HII}/M_{\rm HI}$ environments are similar to density-bounded ISM, implying low PDR covering fractions and large escape fractions. Our results show GS-z14-0, MACS1149-JD1, SXDF-NB1006-2, and B14-65666 have relatively high mass ratio of $M_{\rm HII}/M_{\rm HI} \gtrsim 0.3$, and might have large escape fractions.

We also investigate another synergetic diagnostic enabled by the combination of JWST and ALMA, the relation between the [OIII] /[CII] ratio and equivalent width of [OIII] $_{4959,5007}$ + Hβ (EW([OIII] +Hβ)). Recent observations suggest that the [OIII] /[CII] line ratio correlates with the EW([OIII] +Hβ), because bursty star formation not only elevates the [OIII] /[CII] line ratio (see Section 8.3.4) but also enhances the the emission lines ([OIII] +Hβ) relative to the underlying stellar continuum. Figure 8.15 presents the relation between the [OIII] /[CII] ratio and EW([OIII] +Hβ) for our simulation results with SFR $> 10^{-3}\,M_\odot \mathrm{yr}^{-1}$. We have calculated the stellar continuum by applying BPASS *single* SED to each stellar particle as a function of age, stellar mass, and metallicity. The EW of an emission line is defined as Inoue (2011)

$$\mathrm{EW}_{\rm line} \equiv \frac{L_{\rm line}}{L_{*,\lambda \rm line}}, \tag{8.41}$$

where $L_{\rm line}$ is the line luminosity and $L_{*,\lambda \rm line}$ is the stellar luminosity density at the line wavelength $\lambda_{\rm line}$. Although we neglect the nebular continuum contribution to the continuum, which would reduce the EW, the effect is expected to be modest, at most a factor of 3 (Inoue, 2011).

The [OIII] $_{4959,5007}$ + Hβ EW is obtained as

$$\begin{aligned}\mathrm{EW}([\mathrm{OIII}]_{4959,5007} + \mathrm{H}\beta) = \mathrm{EW}([\mathrm{OIII}]_{4959}) \\ + \mathrm{EW}([\mathrm{OIII}]_{5007}) + \mathrm{EW}(\mathrm{H}\beta).\end{aligned} \tag{8.42}$$

Our simulated galaxy exhibits large equivalent widths of 500-2000 Å, reflecting its very young stellar populations with ages less than 10 Myrs. The distribution of our simulation results also encompasses recent high-redshift observations, which report EW([OIII] $_{4959,5007}$ + Hβ) = 500 − 1300 Å and [OIII] /[CII] ≃ 3-10 (Witstok et al., 2022; Schouws et al., 2025). In this regime, our simulation results exhibit high ionization parameters, with $\log U_{\rm ion} \gtrsim -2$.

8.4.5 Caveats

Several caveats should be considered in interpreting the results of this study. First, our analysis is based on a single galaxy simulated across multiple redshifts. Although our simulation achieves high resolution (0.1 pc) and includes on-the-fly radiative transfer, the computational cost restricts our sample size. Therefore, it remains uncertain whether the conclusions drawn from this single galaxy can be generalized to the broader galaxy population.

Second, our simulated galaxy is less massive than typical observed high-redshift galaxies, which have stellar masses of $M_* \gtrsim 10^8, M_\odot$. Our galaxy, destined to evolve into a dwarf galaxy by $z = 0$, has a stellar mass of $M_* \sim 10^{5-6}, M_\odot$ at $z > 10$, comparable to stellar clusters rather than massive galaxies. However, gravitational lensing can enable observations of such low-mass galaxies at high redshifts. Recently, several proto-stellar clusters with $M_* \sim 10^{5-6}, M_\odot$ have indeed been gravitationally magnified and detected at $z = 6 - 10$ (e.g., Vanzella et al., 2023b; Adamo et al., 2024b). Given upcoming JWST observations targeting similarly low-mass systems in gravitational lensing fields (e.g., GO5119, GO6882, GO7049), direct comparisons of the ISM properties with our simulation results will soon be feasible. For massive high-z galaxies with $M_* \gtrsim 10^8\, M_\odot$, recent stellar mass functions indicate their number densities are $\phi \lesssim 10^{-3}\,\mathrm{cMpc}^{-3}$ at $z = 9$ and $\phi \lesssim 10^{-4}\,\mathrm{cMpc}^{-3}$ at $z = 11$ (e.g., Harvey et al., 2025; Weibel et al., 2024; Ceverino et al., 2024; Shuntov et al., 2025). Identifying representative samples of such massive galaxies at z>10 thus requires simulations with cosmological volumes $V_{\rm vol} \gtrsim (20\,\mathrm{cMpc})^3$. However, current zoom-in simulations cannot simultaneously achieve both 0.1 pc spatial resolution and on-the-fly radiative transfer for such large simulation volumes.

In summary, this study lacks statistics and massive samples. However, our sub-parsec resolution and on-the-fly RT simulations can reveal the most detailed ISM structures and ionizing states at high-z for the first time, and explain the physical origins of the observed emission line ratios.

8.5 Conclusion and Summary

We have presented detailed emission-line calculations applied to a cosmological zoom-in simulation at 0.1 pc resolution, incorporating on-the-fly radiative transfer. By combining CLOUDY with seven physical parameters, we computed multi-wavelength emission lines from the rest-frame UV to IR. Using 137 simulation snapshots at 1 Myr intervals, we analyzed the emission properties of a galaxy at redshifts $z = 9 - 13$, with particular focus on the [OIII] 88μm and [CII] 158μm lines.

We found that the [OIII] emission primarily originates from central HII regions with a high ionization parameter ($\log(U_{\rm ion}) \approx -1$), whereas the [CII] emission is mainly produced in dense surrounding PDRs that trace the overall gas distribution. This difference leads to a sharp spatial contrast in the [OIII] /[CII] ratio: values exceed 100 in the central ∼100 pc but drop to ∼0.01 just outside the ionized region. Regarding to luminosity time evolution, the [OIII] luminosity closely tracks the 10 Myr-averaged SFR and ionization parameter, while the [CII] emission evolves more

gradually, reflecting the FUV radiation field from longer-lived stars (10–100 Myr). As a result, variations in the [OIII] /[CII] ratio are mainly driven by changes in [OIII] luminosity, and only during the peak starburst phase at $z \sim 10$ does the ratio exceed 10.

When examining emission-line v.s. SFR relations, we found that the [OIII] –SFR correlation is steeper than local analogs, while the [CII] –SFR relation is flatter. These trends are consistent with recent ALMA observations and theoretical studies. Our simulations reproduce high [OIII] /[CII] ratios without assuming non-standard O/C abundances. We demonstrate that the [OIII] /[CII] ratio approximately scales with the ratios of gas masses ($M_{\rm HII}/M_{\rm HI}$), gas densities ($n_{\rm HII}/n_{\rm HI}$), and elemental abundances (A(O)/A(C)).

To test this scaling relation, we estimated $M_{\rm HII}/M_{\rm HI}$ for observed galaxies at $z > 6$ using Hβ and [CII] emission lines, finding a positive correlation with the observed [OIII] /[CII] ratios. The scatter around this relation is primarily driven by variations in gas density and cooling efficiency. We also explored the connection between the [OIII] /[CII] ratio and the optical equivalent width of EW([OIII] $_{4959,5007}$ + Hβ). We found that galaxies with high [OIII] /[CII] ratios ($\gtrsim 3$) also exhibit large equivalent widths of 500–2000Å, both quantities reflecting high-ionization conditions. Since $M_{\rm HII}/M_{\rm HI}$ is expected to be positively correlated with the Lyman continuum escape fraction ($f_{\rm esc,LyC}$), the observed galaxies with high [OIII] /[CII] ratios may also have large $f_{\rm esc,LyC}$ values, potentially contributing to cosmic reionization.

The highest priority for future work is to reproduce the high [OIII] /[CII] ratios in massive simulated galaxies with stellar masses comparable to observed systems ($M_* \simeq 10^{8-10}\,M_\odot$), such as those in the FirstLight simulations used in Chapters 6 and 7. Ideally, cosmological simulations with on-the-fly radiative transfer and sub-pc resolution would be performed for these massive targets down to $z \sim 5$. However, this remains computationally infeasible with current resources. Therefore, sub-grid modeling of multi-phase gas is required. Sub-grid models for emission lines originating in HII regions have been developed in Chapter 6 (see also Nakazato et al., 2023), while the remaining sub-grid treatment for PDRs can proceed as follows.

First, we need to investigate the dependence of [CII] emissivity on the radiation field strength (G), gas number density ($n_{\rm H}$), gas column density ($N_{\rm H}$), and metallicity (Z), and prepare look-up tables as a function of these four parameters. Second, UV radiation fields should be computed using the post-processing radiative transfer approach employed in Chapter 7, and the [CII] luminosity can then be calculated on a grid-by-grid basis. Since the physical properties are averaged within each grid and cannot resolve the internal structure of the multi-phase ISM, the initial [CII] luminosities are expected to be underestimated. To address this, the gas column density (or gas volume density) will need to be adjusted by a multiplicative factor as a sub-grid correction, informed by the results presented in this chapter.

While sub-grid modeling will improve theoretical predictions, complementary observations are equally essential. In the near future, upcoming synergetic observations with ALMA and JWST will provide spatially resolved information on electron densities and the relative masses of ionized and neutral gas, enabling detailed studies of ISM conditions and star formation processes in high-redshift galaxies.

Chapter 9

Conclusions

Understanding the nature of galaxies formed within the first billion years of the Universe is crucial to unravel the processes of cosmic reionization and the formation and evolution of the first galaxies. Recent JWST observations have spectroscopically identified abundant high-redshift galaxies via rest-frame UV and optical emission lines. In particular, JWST has opened up galaxy science at $z > 10$, continually pushing the frontier of the most distant known galaxies. To date, more than 1,300 galaxies at $z > 6$ (cosmic age <1 Gyr) have been confirmed, enabling statistical investigations of their physical properties. Simultaneously, the Atacama Large Millimeter/submillimeter Array (ALMA) has allowed detections of rest-frame far-infrared (FIR) emission lines and dust re-emission from these high-redshift galaxies. Multi-wavelength emission characteristics thus hold crucial insights into star formation (mass assembly) histories and galaxy kinematics.

To provide theoretical interpretations and complementary insights for these cutting-edge observations, this study employs cosmological galaxy formation simulations combined with comprehensive multi-wavelength emission modeling. In this thesis, we focus on galaxy dynamics, dust physics, and ISM properties through the following topics: (i) the formation mechanism of clumpy galaxies, (ii) the internal distribution of dust attenuation and re-emission associated with dynamical events such as mergers and rotating disks, and (iii) the physical origins of high [OIII] /[CII] ratios observed in $z > 6$ galaxies. We develop multi-wavelength emission models for nebular lines and continuum emission from the rest-frame UV to FIR. We then apply these models to zoom-in cosmological simulations and compare our predictions to the latest observations from JWST and ALMA.

JWST's high spatial resolution has unveiled previously unresolved internal structures in galaxies at $z > 6$, revealing clumpy morphologies. While local galaxy clumps primarily form through violent disk instabilities or minor mergers, the formation mechanisms for clumps in high-redshift galaxies, which often lack well-developed disks, remain unclear. To clarify this, we used large-scale, high-resolution cosmological zoom-in simulations (FirstLight), investigating the nature and formation of clumps during the epoch of reionization ($z = 5.5 - 9$). In order to directly compare the observed clumpy galaxies, we focus on 100 pc-scale sub-galactic clumps that are bright in the [OIII] 5007Åline with flux greater than $\sim 10^{-18}\,\mathrm{erg\,s^{-1}\,cm^{-2}}$, to be detected by JWST with a reasonable exposure times of $\sim 10^4$ sec. For 62 simulated galaxies that have stellar masses of $(0.5-6)\times10^{10}\,M_\odot$ at $z = 5$, we find clumps in 1828 snapshots. The clumps are identified by the SFR surface densities from the relationships of [OIII] 5007Åand SFR. About one-tenth of the snapshots show the existence of clumpy systems with two or more components. Most of the clumps are formed by mergers and can be characterized by their ages: central clumps dominated by stellar populations older than 50 Myr, and off-centered clumps dominated by younger stellar populations with specic SFRs of $\sim 50\,\mathrm{Gyr^{-1}}$. The latter type of young clumps is formed from gas debris in the tidal tails of major mergers with baryonic mass ratios of $1 \leq q < 4$. The merger-induced clumps are short-lived and merge within a dynamical time

of several tens of million years. The number density of the clumpy systems is estimated to be $\sim 10^{-5}\,\mathrm{cMpc}^{-3}$, which is consistent with major merger frequencies at $z = 6 - 9$. This merger-driven clumpy formation scenario can interpret several features of observed clumpy systems at $z > 6$, such as bursty star formation activity occurring a few tens of Myr before the observed epoch, Lyα emitters that may significantly contribute to cosmic reionization, and large cold disk galaxies during the epoch of reionization (EoR).

In addition to the formation and dynamical evolution of clumpy systems, understanding their dust properties is essential for accurately tracing star formation histories in the early universe. To this end, we performed spatially resolved dust analyses by combining JWST's capability to probe rest-UV/optical dust attenuation with ALMA's ability to measure rest-FIR dust re-emission. Such analyses are critical for accurately reconstructing dust-obscured star formation histories in the early Universe. In Chapter 7, we investigate differences in dust properties between integrated galaxies and individual clumps formed through merger-driven and violent disk instability (VDI)-driven processes. Utilizing the same FirstLight simulation framework from Chapter 6, we performed post-processed three-dimensional dust radiative transfer calculations, tracking a simulated galaxy from $z = 9.5$ to $z = 5.25$ and identifying clumps based on star formation rate surface densities. For integrated properties, the merger-driven phase at $z \sim 7.2$ triggers highly bursty star formation, generating intense UV radiation with intrinsic magnitudes reaching $M_{\mathrm{UV},0} = -23.5$ and blue UV slopes ($\beta_{\mathrm{UV}} \simeq -2.3$). The infrared excess (IRX) peaks shortly after mergers at $\log_{10}(\mathrm{IRX}) = 0.74$. During the VDI phase ($z \sim 5.9 - 5.2$), UV slopes become redder with $\beta_{\mathrm{UV}} \simeq -1.7$ to -1.3, while IRX remains nearly constant $\log_{10}(\mathrm{IRX}) \sim 0.5$. Comparing clumps and integrated galaxy properties, both merger-driven and VDI-driven clumps show IRX values elevated by 0.5–1.7 dex relative to the integrated galaxy. More than half the clumps exhibit redder UV slopes compared to the integrated galaxy, whose bluer slope is dominated by diffuse stellar emission. We further introduce a toy model explaining IRX–β_{UV} scatter by using two parameters: dust optical depth and the dust-to-star scale-height ratio. Merger-driven clumps exhibit well-mixed geometries with optical depths approximately ten times higher than VDI-driven clumps, which show optical depths similar to the integrated galaxy and predominantly screen-like geometries. We finally propose that combining JWST attenuation curve analyses with our toy model turns the IRX–β_{UV} relation into an effective geometry diagnostic. The partially resolved IRX–β_{UV} relation enables us to accurately estimate the total SFR (UV + IR) of observed galaxies, while using system-integrated IRX–β_{UV} relations may lead to underestimates of both the total SFR and the dust-obscured fraction.

In addition to continuum-based diagnostics such as IRX–β_{UV}, emission line ratios like [OIII] 88μm/[CII] 158μm serve as powerful probes of the ISM phases and ionization conditions in high-redshift galaxies. While JWST primarily traces emission from ionized gas, ALMA captures lines from both ionized and neutral gas ([OIII] 88μm, [CII] 158μm). The synergy between JWST and ALMA thus enables a comprehensive view of the multi-phase interstellar medium (ISM) in star-forming regions at high redshift. Observational studies have reported [OIII] 88μm/[CII] 158μm line ratios at high redshift exceeding those of local star-forming galaxies by factors of 10–100. Although various simulations attempted to reproduce these ratios, insufficient spatial resolution and simplified radiation modeling have typically prevented successful explanations. In Chapter 8, we investigate the origin of rest-frame far-infrared [OIII] 88μm and [CII] 158μm emission by performing zoom-in cosmological simulations (RAMSES-RT) of dwarf-galaxy progenitors at $z = 9 - 13$. Our simulations incorporate on-the-fly radiative transfer at sub-pc (~ 0.1 pc) resolution, allowing us to resolve the multi-phase ISM. We compute emission lines on a cell-by-cell basis, taking into account local temperature, density, metallicity, radiation field strength, column density, and spectral hardness of radiation bins. We find that [OIII] predominantly arises from centrally located ionizing bubbles with temperatures of $\sim (1 - 5) \times 10^4\,\mathrm{K}$ and high ionization parameters of $\log U_{\mathrm{ion}} \simeq -1.5$. In contrast, [CII] is produced in the surrounding dense neutral regions at $\sim 5 \times 10^3\,\mathrm{K}$, which are heated by strong

FUV radiation from the central stellar clusters. This spatial arrangement leads to large local variations in [OIII] /[CII] , ranging from $\sim$ 100 to 0.01. Our galaxy reproduces the global ratio [OIII] /[CII] $\sim 5-30$, consistent with recent ALMA detections at $z > 6$ without invoking enhanced O/C abundance ratios. We further derive that [OIII] /[CII] linearly scales with the mass and density ratios of ionized to neutral gas, $M_{\rm HII}/M_{\rm HI}$ and $n_{\rm HII}/n_{\rm HI}$ and show that the [OIII] /[CII] ratio typically changes from 5.7 to 0.3 from high-z to low-z. We quantitatively explain the redshift evolution of this line ratio for the first time. For future synergies of JWST and ALMA, we derived $M_{\rm HII}/M_{\rm HI}$ for observed $z > 6$ galaxies using Hβ and [CII] and show the validity of our scaling relations. This detailed emission line modeling for multi-phase gas, along with sub-pc spatially resolved emission maps, can be incorporated as a sub-grid model into simulations of more massive galaxies that are comparable to observed systems.

Our multi-wavelength modeling framework provides valuable tools for next-generation telescopes. For instance, the PRIMA Space Telescope, anticipated to launch in 2031, will probe wavelengths not accessible by ALMA or JWST. This wavelength coverage enables the observation of small grain dust emissions, PAH emissions, and mid-infrared lines from HII regions invisible to ALMA. Applying SEDs derived from our dust radiative transfer models, we can predict the detectability of these emissions. Furthermore, HII region line emission models established in this thesis directly support future PRIMA observations. In addition, by incorporating our [CII] emission line modeling in RAMSES-RT simulations into the FirstLight simulations, it will become possible to reproduce the spatially extended [CII] emission maps of neutral gas around clumpy galaxies. Although FirstLight simulations provide a sample of observable massive galaxies, radiative transfer and chemistries are not incorporated, making it difficult to model [CII] emission maps accurately. By integrating subgrid models derived from our RAMSES-RT simulations, such as the Habing radiation field strength and gas column densities in neutral gas cells, we can now enable [CII] emission line modeling within the FirstLight framework.

In this thesis, we have investigated gas dynamics, dust physics, and ISM properties of high-z galaxies at $z > 6$ by combining multi-wavelength emission modeling with zoom-in cosmological simulations. Our results will serve as valuable theoretical predictions that can be directly tested against panchromatic observations conducted by JWST, ALMA, and next-generation telescopes, thus deepening our understanding of the formation and evolution of the first galaxies and cosmic star formation histories.

Acknowledgement

Words cannot fully express my gratitude to my supervisor, Professor Naoki Yoshida, for his invaluable support, sincere guidance, and generous funding, all of which made my Ph.D. life truly fruitful. His inspiring ideas, innovative feedback, and critical comments greatly improved the quality of my research. Every discussion with him motivated me to investigate thoroughly and work diligently. He also provided me with wonderful opportunities to study high-redshift galaxies and to join the JWST observational team, collaborating closely with researchers from Japan and Spain. Through five years of intensive research, I was able to explore the formation and evolution of high-redshift galaxies across a broad wavelength range from rest-UV to rest-FIR.

Next, I would like to thank my closest collaborator, Professor Daniel Ceverino, who provided the FirstLight simulation data and always gave me insightful comments and valuable suggestions on my research. Even though our collaboration was conducted mostly remotely, I learned many essential skills from him, ranging from analyzing simulation data to effectively writing scientific papers and clearly discussing the physics behind our results. Without his generous help and support, it would not have been possible to complete my research successfully.

I am also grateful to my research collaborator, Professor Andrea Ferrara, who warmly welcomed me as a visiting student in Pisa for four months. The period I spent in Italy was one of the most rewarding experiences of my Ph.D. life. During that time, I was able to start a new project involving analytical calculations, an approach I had never used before. It was an invaluable experience to learn how to approach analytical work from him, and his dedication toward research greatly inspired me to continue my own studies. I also wish to express my sincere gratitude to my colleagues at Scuola Normale Superiore for their kindness and hospitality. I had a truly wonderful time with them.

I would like to express my gratitude to my research collaborators, Professor Kazuyuki Sugimura, Professor Akio Inoue, and Professor Massimo Ricotti, who collaborated with me on the analysis of the [OIII] /[CII] line ratio. Thanks to our insightful discussions, I was able to prepare a thorough and detailed paper on the physics of radiation. I am also very thankful to Kosei Matsumoto, a Ph.D. student at Ghent University, who generously provided guidance on using the radiative transfer code SKIRT. Without his invaluable help, I would not have been able to successfully carry out my research on dusty galaxies.

My thanks also go to Professor Takuya Hashimoto, Professor Luis Colina, Professor Javier Álvarez-Márquez, and all the members of the RIOJA collaboration for warmly welcoming me into observational collaborations for the first time. Through my interactions with them, I gained invaluable insights into observational techniques and was inspired by numerous ideas to explore further with simulations. I also express my gratitude to all my collaborators for providing me the opportunities to contribute to their excellent research projects.

I would like to express my sincere gratitude to the dissertation committee members, Professor Katsuaki Asano, Professor Masahiro Takada, Professor Hideyuki Tagoshi, Professor Aya Bamba, Professor Masahiro Kawasaki, and Professor Michiko Fujii, for their insightful comments and valuable suggestions.

I would like to express my gratitude to Dr. Daichi Tsuna, who invited me to join the dusty outflow collaboration and shared insightful discussions about high-redshift galaxies, and to Dr.

Yici Zhong, who offered valuable career advice as well as enjoyable conversations. I also thank all members of the Theoretical Astrophysics Group and the Research Center for the Early Universe at the University of Tokyo for numerous fruitful discussions. Additionally, I am grateful to all members of the *zemi* groups I have participated in.

Special thanks to my best friend, Hiroka, who has always been there to listen, whether I'm feeling happy or down, and who has stood by my side for more than ten years. Every time I return to our hometown, Okinawa, we enjoy wonderful vacations together. I deeply admire her vibrant personality and boundless enthusiasm, and I'm truly proud to have such a dear friend in my life. I would also like to thank my best friend, Risshin Okabe. We've been together since freshman year, having first met through a part-time job, studied in the same department during our undergraduate years, and eventually become close Ph.D. buddies. We supported each other through the tough times during undergraduate studies. He always made me laugh, and thanks to him, my student life has been truly enjoyable and memorable.

Finally, I would like to express my deepest gratitude to my parents, brothers, and grandmother for always believing in me, understanding me, and providing unwavering support throughout my life. Your encouragement has continuously motivated me to pursue my goals and guided me in my career beyond my Ph.D. I was deeply touched by your genuine efforts to understand my research, such as watching astronomy documentaries and reading relevant books. Without your constant love and support, none of my achievements would have been possible.

I acknowledge the support from the International Graduate Program for Excellence in Earth-Space Science (IGPEES) of the University of Tokyo and JSR fellowship. The work made use of v2.3 of the Binary Population and Spectral Synthesis (BPASS) models as described in Byrne et al. (2022) and Stanway and Eldridge (2018). I acknowledge funding from JSPS KAKENHI Grant Number 23KJ0728 and support from JSPS International Leading Research 23K20035. Parts of the calculations in this work were carried out on Cray XC50/XD2000 and analysis servers at Center for Computational Astrophysics, National Astronomical Observatory of Japan.

Bibliography

Abdurro'uf, Coe, D., Jung, I., Ferguson, H. C., Brammer, G., Iyer, K. G., Bradley, L. D., Dayal, P., Windhorst, R. A., Zitrin, A., Meena, A. K., Oguri, M., Diego, J. M., Kokorev, V., Dimauro, P., Adamo, A., Conselice, C. J., Welch, B., Vanzella, E., Hsiao, T. Y.-Y., Xu, X., Roy, N., and Mulcahey, C. R. (2023). Spatially Resolved Stellar Populations of $0.3 < z < 6.0$ Galaxies in WHL 0137-08 and MACS 0647+70 Clusters as Revealed by JWST: How Do Galaxies Grow and Quench over Cosmic Time? ApJ, 945(2):117.

Abdurro'uf, Larson, R. L., Coe, D., Hsiao, T. Y.-Y., Álvarez-Márquez, J., Gómez, A. C., Adamo, A., Bhatawdekar, R., Bik, A., Bradley, L. D., Conselice, C. J., Dayal, P., Diego, J. M., Fujimoto, S., Furtak, L. J., Hutchison, T. A., Jung, I., Killi, M., Kokorev, V., Mingozzi, M., Norman, C., Resseguier, T., Ricotti, M., Rigby, J. R., Vanzella, E., Welch, B., Windhorst, R. A., Xu, X., and Zitrin, A. (2024). JWST NIRSpec High-resolution Spectroscopy of MACS0647–JD at $z = 10.167$: Resolved [O II] Doublet and Electron Density in an Early Galaxy. ApJ, 973(1):47.

Adamo, A., Atek, H., Bagley, M. B., Bañados, E., Barrow, K. S. S., Berg, D. A., Bezanson, R., Bradač, M., Brammer, G., Carnall, A. C., Chisholm, J., Coe, D., Dayal, P., Eisenstein, D. J., Eldridge, J. J., Ferrara, A., Fujimoto, S., de Graaff, A., Habouzit, M., Hutchison, T. A., Kartaltepe, J. S., Kassin, S. A., Kriek, M., Labbé, I., Maiolino, R., Marques-Chaves, R., Maseda, M. V., Mason, C., Matthee, J., McQuinn, K. B. W., Meynet, G., Naidu, R. P., Oesch, P. A., Pentericci, L., Pérez-González, P. G., Rigby, J. R., Roberts-Borsani, G., Schaerer, D., Shapley, A. E., Stark, D. P., Stiavelli, M., Strom, A. L., Vanzella, E., Wang, F., Wilkins, S. M., Williams, C. C., Willott, C. J., Wylezalek, D., and Nota, A. (2024a). The First Billion Years, According to JWST. *arXiv e-prints*, page arXiv:2405.21054.

Adamo, A., Bradley, L. D., Vanzella, E., Claeyssens, A., Welch, B., Diego, J. M., Mahler, G., Oguri, M., Sharon, K., Abdurro'uf, Hsiao, T. Y.-Y., Messa, M., Zackrisson, E., Brammer, G., Coe, D., Kokorev, V., Ricotti, M., Zitrin, A., Fujimoto, S., Inoue, A. K., Resseguier, T., Rigby, J. R., Jiménez-Teja, Y., Windhorst, R. A., and Xu, X. (2024b). The discovery of bound star clusters 460 Myr after the Big Bang. *arXiv e-prints*, page arXiv:2401.03224.

Agertz, O., Kravtsov, A. V., Leitner, S. N., and Gnedin, N. Y. (2013). Toward a Complete Accounting of Energy and Momentum from Stellar Feedback in Galaxy Formation Simulations. ApJ, 770(1):25.

Agertz, O., Teyssier, R., and Moore, B. (2009). Disc formation and the origin of clumpy galaxies at high redshift. MNRAS, 397(1):L64–L68.

Akins, H. B., Fujimoto, S., Finlator, K., Watson, D., Knudsen, K. K., Richard, J., Bakx, T. J. L. C., Hashimoto, T., Inoue, A. K., Matsuo, H., Michałowski, M. J., and Tamura, Y. (2022). ALMA Reveals Extended Cool Gas and Hot Ionized Outflows in a Typical Star-forming Galaxy at $Z = 7.13$. ApJ, 934(1):64.

Algera, H. S. B., Inami, H., Oesch, P. A., Sommovigo, L., Bouwens, R. J., Topping, M. W., Schouws, S., Stefanon, M., Stark, D. P., Aravena, M., Barrufet, L., da Cunha, E., Dayal, P., Endsley, R., Ferrara, A., Fudamoto, Y., Gonzalez, V., Graziani, L., Hodge, J. A., Hygate, A. P. S., de Looze, I., Nanayakkara, T., Schneider, R., and van der Werf, P. P. (2023). The ALMA REBELS survey: the dust-obscured cosmic star formation rate density at redshift 7. MNRAS, 518(4):6142–6157.

Algera, H. S. B., Inami, H., Sommovigo, L., Fudamoto, Y., Schneider, R., Graziani, L., Dayal, P., Bouwens, R., Aravena, M., da Cunha, E., Ferrara, A., Hygate, A. P. S., van Leeuwen, I., De Looze, I., Palla, M., Pallottini, A., Smit, R., Stefanon, M., Topping, M., and van der Werf, P. P. (2024).

Cold dust and low [O III]/[C II] ratios: an evolved star-forming population at redshift 7. MNRAS, 527(3):6867–6887.

Allamandola, L. J., Tielens, A. G. G. M., and Barker, J. R. (1985). Polycyclic aromatic hydrocarbons and the unidentified infrared emission bands: auto exhaust along the milky way. ApJ, 290:L25–L28.

Álvarez-Márquez, J., Colina, L., Crespo Gómez, A., Rinaldi, P., Melinder, J., Östlin, G., Annunziatella, M., Labiano, A., Bik, A., Bosman, S., Greve, T. R., Wright, G., Alonso-Herrero, A., Boogaard, L., Azollini, R., Caputi, K. I., Costantin, L., Eckart, A., GarcÍa-MarÍn, M., Gillman, S., Hjorth, J., Iani, E., Ilbert, O., Jermann, I., Langeroodi, D., Meyer, R., Peissker, F., Pérez-González, P., Pye, J. P., Tikkanen, T., Topinka, M., van der Werf, P., Walter, F., Henning, T., and Ray, T. (2023). Spatially-resolved Hα and ionizing photon production efficiency in the lensed galaxy MACS1149-JD1 at a redshift of 9.11. *arXiv e-prints*, page arXiv:2309.06319.

Anders, E. and Grevesse, N. (1989). Abundances of the elements: Meteoritic and solar. Geochim. Cosmochim. Acta, 53(1):197–214.

Aoyama, S., Hirashita, H., and Nagamine, K. (2020). Galaxy simulation with the evolution of grain size distribution. MNRAS, 491(3):3844–3859.

Aoyama, S., Hou, K.-C., Hirashita, H., Nagamine, K., and Shimizu, I. (2018). Cosmological simulation with dust formation and destruction. MNRAS, 478(4):4905–4921.

Aoyama, S., Hou, K.-C., Shimizu, I., Hirashita, H., Todoroki, K., Choi, J.-H., and Nagamine, K. (2017). Galaxy simulation with dust formation and destruction. MNRAS, 466(1):105–121.

Arata, S., Yajima, H., Nagamine, K., Abe, M., and Khochfar, S. (2020). Starbursting [O III] emitters and quiescent [C II] emitters in the reionization era. MNRAS, 498(4):5541–5556.

Arata, S., Yajima, H., Nagamine, K., Li, Y., and Khochfar, S. (2019). Radiative properties of the first galaxies: rapid transition between UV and infrared bright phases. MNRAS, 488(2):2629–2643.

Arrabal Haro, P., Dickinson, M., Finkelstein, S. L., Kartaltepe, J. S., Donnan, C. T., Burgarella, D., Carnall, A. C., Cullen, F., Dunlop, J. S., Fernández, V., Fujimoto, S., Jung, I., Krips, M., Larson, R. L., Papovich, C., Pérez-González, P. G., Amorín, R. O., Bagley, M. B., Buat, V., Casey, C. M., Chworowsky, K., Cohen, S. H., Ferguson, H. C., Giavalisco, M., Huertas-Company, M., Hutchison, T. A., Kocevski, D. D., Koekemoer, A. M., Lucas, R. A., McLeod, D. J., McLure, R. J., Pirzkal, N., Seillé, L.-M., Trump, J. R., Weiner, B. J., Wilkins, S. M., and Zavala, J. A. (2023). Confirmation and refutation of very luminous galaxies in the early Universe. Nature, 622(7984):707–711.

Arribas, S., Perna, M., Rodríguez Del Pino, B., Lamperti, I., D'Eugenio, F., Pérez-González, P. G., Jones, G. C., Crespo Gómez, A., Curti, M., Lim, S., Álvarez-Márquez, J., Bunker, A. J., Carniani, S., Charlot, S., Jakobsen, P., Maiolino, R., Übler, H., Willott, C. J., Böker, T., Chevallard, J., Circosta, C., Cresci, G., Kumari, N., Parlanti, E., Scholtz, J., Venturi, G., and Witstok, J. (2024). GA-NIFS: The core of an extremely massive protocluster at the epoch of reionisation probed with JWST/NIRSpec. A&A, 688:A146.

Asada, Y., Sawicki, M., Abraham, R., Bradač, M., Brammer, G., Desprez, G., Estrada-Carpenter, V., Iyer, K., Martis, N., Matharu, J., Mowla, L., Muzzin, A., Noirot, G., Sarrouh, G. T. E., Strait, V., Willott, C. J., and Harshan, A. (2024). Bursty star formation and galaxy-galaxy interactions in low-mass galaxies 1 Gyr after the Big Bang. MNRAS, 527(4):11372–11392.

Asada, Y., Sawicki, M., Desprez, G., Abraham, R., Bradač, M., Brammer, G., Harshan, A., Iyer, K., Martis, N. S., Mowla, L., Muzzin, A., Noirot, G., Ravindranath, S., Sarrouh, G. T. E., Strait, V., Willott, C. J., and Zabl, J. (2023). JWST catches the assembly of a z 5 ultra-low-mass galaxy. MNRAS, 523(1):L40–L45.

Asano, R. S., Takeuchi, T. T., Hirashita, H., and Inoue, A. K. (2013). Dust formation history of galaxies: A critical role of metallicity* for the dust mass growth by accreting materials in the interstellar medium. *Earth, Planets and Space*, 65(3):213–222.

Asplund, M., Grevesse, N., Sauval, A. J., and Scott, P. (2009). The Chemical Composition of the Sun. ARA&A, 47(1):481–522.

Baes, M., Verstappen, J., De Looze, I., Fritz, J., Saftly, W., Vidal Pérez, E., Stalevski, M., and Valcke, S. (2011). Efficient Three-dimensional NLTE Dust Radiative Transfer with SKIRT. ApJS, 196(2):22.

Baker, W. M., Tacchella, S., Johnson, B. D., Nelson, E., Suess, K. A., D'Eugenio, F., Curti, M., de Graaff, A., Ji, Z., Maiolino, R., Robertson, B., Scholtz, J., Alberts, S., Arribas, S., Boyett, K., Bunker, A. J., Carniani, S., Charlot, S., Chen, Z., Chevallard, J., Curtis-Lake, E., Danhaive, A. L., DeCoursey, C., Egami, E., Eisenstein, D. J., Endsley, R., Hausen, R., Helton, J. M., Kumari, N., Looser, T. J., Maseda, M. V., Puskás, D., Rieke, M., Sandles, L., Sun, F., Übler, H., Williams, C. C., Willmer, C. N. A., and Witstok, J. (2023). Inside-out growth in the early Universe: a core in a vigorously star-forming disc. *arXiv e-prints*, page arXiv:2306.02472.

Bakx, T. J. L. C., Algera, H. S. B., Venemans, B., Sommovigo, L., Fujimoto, S., Carniani, S., Hagimoto, M., Hashimoto, T., Inoue, A. K., Salak, D., Serjeant, S., Vallini, L., Eales, S., Ferrara, A., Fudamoto, Y., Imamura, C., Inoue, S., Knudsen, K. K., Matsuo, H., Sugahara, Y., Tamura, Y., Taniguchi, A., and Yamanaka, S. (2024). Gas conditions of a star-formation selected sample in the first billion years. MNRAS, 532(2):2270–2288.

Bakx, T. J. L. C., Sommovigo, L., Carniani, S., Ferrara, A., Akins, H. B., Fujimoto, S., Hagimoto, M., Knudsen, K. K., Pallottini, A., Tamura, Y., and Watson, D. (2021). Accurate dust temperature determination in a z = 7.13 galaxy. MNRAS, 508(1):L58–L63.

Bakx, T. J. L. C., Tamura, Y., Hashimoto, T., Inoue, A. K., Lee, M. M., Mawatari, K., Ota, K., Umehata, H., Zackrisson, E., Hatsukade, B., Kohno, K., Matsuda, Y., Matsuo, H., Okamoto, T., Shibuya, T., Shimizu, I., Taniguchi, Y., and Yoshida, N. (2020). ALMA uncovers the [C II] emission and warm dust continuum in a z = 8.31 Lyman break galaxy. MNRAS, 493(3):4294–4307.

Barinovs, Ğ., van Hemert, M. C., Krems, R., and Dalgarno, A. (2005). Fine-Structure Excitation of C^+ and Si^+ by Atomic Hydrogen. ApJ, 620(1):537–541.

Barisic, I., Faisst, A. L., Capak, P. L., Pavesi, R., Riechers, D. A., Scoville, N. Z., Cooke, K., Kartaltepe, J. S., Casey, C. M., and Smolcic, V. (2017). Dust Properties of C II Detected z $\sim$ 5.5 Galaxies: New HST/WFC3 Near-IR Observations. ApJ, 845(1):41.

Barrow, K. S. S., Wise, J. H., Norman, M. L., O'Shea, B. W., and Xu, H. (2017). First light: exploring the spectra of high-redshift galaxies in the Renaissance Simulations. MNRAS, 469(4):4863–4878.

Barrufet, L., Oesch, P. A., Weibel, A., Brammer, G., Bezanson, R., Bouwens, R., Fudamoto, Y., Gonzalez, V., Gottumukkala, R., Illingworth, G., Heintz, K. E., Holden, B., Labbe, I., Magee, D., Naidu, R. P., Nelson, E., Stefanon, M., Smit, R., van Dokkum, P., Weaver, J. R., and Williams, C. C. (2023). Unveiling the nature of infrared bright, optically dark galaxies with early JWST data. MNRAS, 522(1):449–456.

Begley, R., Cullen, F., McLure, R. J., Shapley, A. E., Dunlop, J. S., Carnall, A. C., McLeod, D. J., Donnan, C. T., Hamadouche, M. L., and Stanton, T. M. (2024). Connecting the escape fraction of Lyman-alpha and Lyman-continuum photons in star-forming galaxies at z âLČ 4-5. MNRAS, 527(2):4040–4051.

Behrens, C., Pallottini, A., Ferrara, A., Gallerani, S., and Vallini, L. (2018). Dusty galaxies in the Epoch of Reionization: simulations. MNRAS, 477(1):552–565.

Behroozi, P. S., Wechsler, R. H., and Wu, H.-Y. (2013). The ROCKSTAR Phase-space Temporal Halo Finder and the Velocity Offsets of Cluster Cores. ApJ, 762(2):109.

Bertoldi, F. and McKee, C. F. (1992). Pressure-confined Clumps in Magnetized Molecular Clouds. ApJ, 395:140.

Bianchi, L., Clayton, G. C., Bohlin, R. C., Hutchings, J. B., and Massey, P. (1996). Ultraviolet Extinction by Interstellar Dust in External Galaxies: M31. ApJ, 471:203.

Bianchi, S. (2007). The dust distribution in edge-on galaxies. Radiative transfer fits of V and K'-band images. A&A, 471(3):765–773.

Bik, A., Álvarez-Márquez, J., Colina, L., Crespo Gómez, A., Peissker, F., Walter, F., Boogaard, L. A., Östlin, G., Greve, T. R., Wright, G., Alonso-Herrero, A., Caputi, K. I., Costantin, L., Eckart, A., Gillman, S., Hjorth, J., Iani, E., Jermann, I., Labiano, A., Langeroodi, D., Melinder, J., Pérez-González, P. G., Pye, J. P., Rinaldi, P., Tikkanen, T., van der Werf, P., Güdel, M., Henning, T., Lagage, P. O., Ray, T., and van Dishoeck, E. F. (2023). Clumpy star formation and an obscured nuclear starburst in the luminous dusty z=4 galaxy GN20 seen by MIRI/JWST. *arXiv e-prints*, page arXiv:2312.03074.

Birkin, J. E., Hutchison, T. A., Welch, B., Spilker, J. S., Aravena, M., Bayliss, M. B., Cathey, J., Chapman, S. C., Gonzalez, A. H., Gururajan, G., Hayward, C. C., Khullar, G., Kim, K. J., Mahler, G., Malkan, M. A., Narayanan, D., Olivier, G. M., Phadke, K. A., Reuter, C., Rigby, J. R., Smith, J. D. T., Solimano, M., Sulzenauer, N., Vieira, J. D., Vizgan, D., and Weiss, A. (2023). JWST's TEMPLATES for Star Formation: The First Resolved Gas-phase Metallicity Maps of Dust-obscured Star-forming Galaxies at z $\sim$ 4. ApJ, 958(1):64.

Birkin, J. E., Spilker, J. S., Herrera-Camus, R., Davies, R. L., Lee, L. L., Aravena, M., Assef, R. J., Barcos-Muñoz, L., Bolatto, A., Diaz-Santos, T., Faisst, A. L., Ferrara, A., Fisher, D. B., González-López, J., Ikeda, R., Knudsen, K., Li, J., Li, Y., de Looze, I., Lutz, D., Mitsuhashi, I., Posses, A., Relaño, M., Solimano, M., Tadaki, K.-i., and Villanueva, V. (2025). The ALMA-CRISTAL survey: weak evidence for star-formation driven outflows in $z \sim 5$ main-sequence galaxies. *arXiv e-prints*, page arXiv:2504.17877.

Blaauw, A. (1961). On the origin of the O- and B-type stars with high velocities (the "run-away" stars), and some related problems. Bull. Astron. Inst. Netherlands, 15:265.

Boley, A. C., Hayfield, T., Mayer, L., and Durisen, R. H. (2010). Clumps in the outer disk by disk instability: Why they are initially gas giants and the legacy of disruption. Icarus, 207(2):509–516.

Bournaud, F. and Elmegreen, B. G. (2009). Unstable Disks at High Redshift: Evidence for Smooth Accretion in Galaxy Formation. ApJ, 694(2):L158–L161.

Bournaud, F., Perret, V., Renaud, F., Dekel, A., Elmegreen, B. G., Elmegreen, D. M., Teyssier, R., Amram, P., Daddi, E., Duc, P.-A., Elbaz, D., Epinat, B., Gabor, J. M., Juneau, S., Kraljic, K., and Le Floch', E. (2014). The Long Lives of Giant Clumps and the Birth of Outflows in Gas-rich Galaxies at High Redshift. ApJ, 780(1):57.

Bouwens, R. J., Aravena, M., Decarli, R., Walter, F., da Cunha, E., Labbé, I., Bauer, F. E., Bertoldi, F., Carilli, C., Chapman, S., Daddi, E., Hodge, J., Ivison, R. J., Karim, A., Le Fevre, O., Magnelli, B., Ota, K., Riechers, D., Smail, I. R., van der Werf, P., Weiss, A., Cox, P., Elbaz, D., Gonzalez-Lopez, J., Infante, L., Oesch, P., Wagg, J., and Wilkins, S. (2016). ALMA Spectroscopic Survey in the Hubble Ultra Deep Field: The Infrared Excess of UV-Selected z = 2-10 Galaxies as a Function of UV-Continuum Slope and Stellar Mass. ApJ, 833(1):72.

Bouwens, R. J., Illingworth, G., Ellis, R. S., Oesch, P., and Stefanon, M. (2022a). z 2-9 Galaxies Magnified by the Hubble Frontier Field Clusters. II. Luminosity Functions and Constraints on a Faint-end Turnover. ApJ, 940(1):55.

Bouwens, R. J., Illingworth, G. D., Franx, M., Chary, R. R., Meurer, G. R., Conselice, C. J., Ford, H., Giavalisco, M., and van Dokkum, P. (2009). UV Continuum Slope and Dust Obscuration from z $\sim$6 to z $\sim$2: The Star Formation Rate Density at High Redshift. ApJ, 705(1):936–961.

Bouwens, R. J., Illingworth, G. D., Franx, M., and Ford, H. (2007). UV Luminosity Functions at z$\sim$4, 5, and 6 from the Hubble Ultra Deep Field and Other Deep Hubble Space Telescope ACS Fields: Evolution and Star Formation History. ApJ, 670(2):928–958.

Bouwens, R. J., Smit, R., Schouws, S., Stefanon, M., Bowler, R., Endsley, R., Gonzalez, V., Inami, H., Stark, D., Oesch, P., Hodge, J., Aravena, M., da Cunha, E., Dayal, P., de Looze, I., Ferrara, A., Fudamoto, Y., Graziani, L., Li, C., Nanayakkara, T., Pallottini, A., Schneider, R., Sommovigo, L., Topping, M., van der Werf, P., Algera, H., Barrufet, L., Hygate, A., Labbé, I., Riechers, D., and Witstok, J. (2022b). Reionization Era Bright Emission Line Survey: Selection and Characterization of Luminous Interstellar Medium Reservoirs in the z > 6.5 Universe. ApJ, 931(2):160.

Bowler, R. A. A., Bourne, N., Dunlop, J. S., McLure, R. J., and McLeod, D. J. (2018). Obscured star formation in bright z âĽČ 7 Lyman-break galaxies. MNRAS, 481(2):1631–1644.

Bowler, R. A. A., Cullen, F., McLure, R. J., Dunlop, J. S., and Avison, A. (2022). The discovery of rest-frame UV colour gradients and a diversity of dust morphologies in bright z âĽČ 7 Lyman-break galaxies. MNRAS, 510(4):5088–5101.

Bowler, R. A. A., Dunlop, J. S., McLure, R. J., and McLeod, D. J. (2017). Unveiling the nature of bright z âĽČ 7 galaxies with the Hubble Space Telescope. MNRAS, 466(3):3612–3635.

Bowler, R. A. A., Inami, H., Sommovigo, L., Smit, R., Algera, H. S. B., Aravena, M., Barrufet, L., Bouwens, R., da Cunha, E., Cullen, F., Dayal, P., De Looze, I., Dunlop, J. S., Fudamoto, Y., Mauerhofer, V., McLure, R. J., Stefanon, M., Schneider, R., Ferrara, A., Graziani, L., Hodge, J. A., Nanayakkara, T., Palla, M., Schouws, S., Stark, D. P., and van der Werf, P. P. (2024). The ALMA REBELS survey: obscured star formation in massive Lyman-break galaxies at z= 4-8 revealed by the IRX-β and $M_\star$ relations. MNRAS, 527(3):5808–5828.

Bradač, M., Garcia-Appadoo, D., Huang, K.-H., Vallini, L., Quinn Finney, E., Hoag, A., Lemaux, B. C., Borello Schmidt, K., Treu, T., Carilli, C., Dijkstra, M., Ferrara, A., Fontana, A., Jones, T., Ryan, R., Wagg, J., and Gonzalez, A. H. (2017). ALMA [C II] 158 μm Detection of a Redshift 7 Lensed Galaxy behind RXJ1347.1-1145. ApJ, 836(1):L2.

Bradač, M., Strait, V., Mowla, L., Iyer, K. G., Noirot, G., Willott, C., Brammer, G., Abraham, R., Asada, Y., Desprez, G., Estrada-Carpenter, V., Harshan, A., Martis, N. S., Matharu, J., Muzzin, A., Rihtaršič, G., Sarrouh, G. T. E., and Sawicki, M. (2023). Star Formation at the Epoch of Reionization with CANUCS: The ages of stellar populations in MACS1149-JD1. *arXiv e-prints*, page arXiv:2308.13288.

Bradley, L. D., Adamo, A., Vanzella, E., Sharon, K., Brammer, G., Coe, D., Diego, J. M., Kokorev, V., Mahler, G., Oguri, M., Abdurro'uf, Bhatawdekar, R., Christensen, L., Fujimoto, S., Hashimoto, T., Y. -Y Hsiao, T., Inoue, A. K., Jiménez-Teja, Y., Messa, M., Norman, C., Ricotti, M., Tamura, Y., Windhorst, R. A., Xu, X., and Zitrin, A. (2024). Unveiling the Cosmic Gems Arc at $z \sim 10.2$ with JWST. *arXiv e-prints*, page arXiv:2404.10770.

Brauher, J. R., Dale, D. A., and Helou, G. (2008). A Compendium of Far-Infrared Line and Continuum Emission for 227 Galaxies Observed by the Infrared Space Observatory. ApJS, 178(2):280–301.

Bromm, V. and Yoshida, N. (2011). The First Galaxies. ARA&A, 49(1):373–407.

Bruzual, G. and Charlot, S. (2003). Stellar population synthesis at the resolution of 2003. MNRAS, 344(4):1000–1028.

Buck, T., Macciò, A. V., Obreja, A., Dutton, A. A., Domínguez-Tenreiro, R., and Granato, G. L. (2017). NIHAO XIII: Clumpy discs or clumpy light in high-redshift galaxies? MNRAS, 468(3):3628–3649.

Bunker, A. J., Saxena, A., Cameron, A. J., Willott, C. J., Curtis-Lake, E., Jakobsen, P., Carniani, S., Smit, R., Maiolino, R., Witstok, J., Curti, M., D'Eugenio, F., Jones, G. C., Ferruit, P., Arribas, S., Charlot, S., Chevallard, J., Giardino, G., de Graaff, A., Looser, T. J., Lützgendorf, N., Maseda, M. V., Rawle, T., Rix, H.-W., Del Pino, B. R., Alberts, S., Egami, E., Eisenstein, D. J., Endsley, R., Hainline, K., Hausen, R., Johnson, B. D., Rieke, G., Rieke, M., Robertson, B. E., Shivaei, I., Stark, D. P., Sun, F., Tacchella, S., Tang, M., Williams, C. C., Willmer, C. N. A., Baker, W. M., Baum, S., Bhatawdekar, R., Bowler, R., Boyett, K., Chen, Z., Circosta, C., Helton, J. M., Ji, Z., Kumari, N., Lyu, J., Nelson, E., Parlanti, E., Perna, M., Sandles, L., Scholtz, J., Suess, K. A., Topping, M. W., Übler, H., Wallace, I. E. B., and Whitler, L. (2023). JADES NIRSpec Spectroscopy of GN-z11: Lyman-α emission and possible enhanced nitrogen abundance in a z = 10.60 luminous galaxy. A&A, 677:A88.

Burnham, A. D., Casey, C. M., Zavala, J. A., Manning, S. M., Spilker, J. S., Chapman, S. C., Chen, C.-C., Cooray, A., Sanders, D. B., and Scoville, N. Z. (2021). The Physical Drivers of the Luminosity-weighted Dust Temperatures in High-redshift Galaxies. ApJ, 910(2):89.

Byrne, C. M., Stanway, E. R., Eldridge, J. J., McSwiney, L., and Townsend, O. T. (2022). The dependence of theoretical synthetic spectra on α-enhancement in young, binary stellar populations. MNRAS, 512(4):5329–5338.

Calura, F., Lupi, A., Rosdahl, J., Vanzella, E., Meneghetti, M., Rosati, P., Vesperini, E., Lacchin, E., Pascale, R., and Gilli, R. (2022). Sub-parsec resolution cosmological simulations of star-forming clumps at high redshift with feedback of individual stars. MNRAS, 516(4):5914–5934.

Calura, F., Pascale, R., Agertz, O., Andersson, E., Lacchin, E., Lupi, A., Meneghetti, M., Nipoti, C., Ragagnin, A., Rosdahl, J., Vanzella, E., Vesperini, E., and Zanella, A. (2025). SIEGE: III. The formation of dense stellar clusters in sub-parsec resolution cosmological simulations with individual star feedback. A&A, 698:A207.

Calzetti, D., Armus, L., Bohlin, R. C., Kinney, A. L., Koornneef, J., and Storchi-Bergmann, T. (2000). The Dust Content and Opacity of Actively Star-forming Galaxies. ApJ, 533(2):682–695.

Calzetti, D., Kinney, A. L., and Storchi-Bergmann, T. (1994). Dust Extinction of the Stellar Continua in Starburst Galaxies: The Ultraviolet and Optical Extinction Law. ApJ, 429:582.

Cameron, A. J., Katz, H., Rey, M. P., and Saxena, A. (2023). Nitrogen enhancements 440 Myr after the big bang: supersolar N/O, a tidal disruption event, or a dense stellar cluster in GN-z11? MNRAS, 523(3):3516–3525.

Cameron, A. J., Katz, H., Witten, C., Saxena, A., Laporte, N., and Bunker, A. J. (2024). Nebular dominated galaxies: insights into the stellar initial mass function at high redshift. MNRAS, 534(1):523–543.

Camps, P. and Baes, M. (2015). SKIRT: An advanced dust radiative transfer code with a user-friendly architecture. *Astronomy and Computing*, 9:20–33.

Camps, P. and Baes, M. (2020). SKIRT 9: Redesigning an advanced dust radiative transfer code to allow kinematics, line transfer and polarization by aligned dust grains. *Astronomy and Computing*, 31:100381.

Capak, P. L., Carilli, C., Jones, G., Casey, C. M., Riechers, D., Sheth, K., Carollo, C. M., Ilbert, O., Karim, A., Lefevre, O., Lilly, S., Scoville, N., Smolcic, V., and Yan, L. (2015). Galaxies at redshifts 5 to 6 with systematically low dust content and high [C II] emission. Nature, 522(7557):455–458.

Cardelli, J. A., Clayton, G. C., and Mathis, J. S. (1989). The Relationship between Infrared, Optical, and Ultraviolet Extinction. ApJ, 345:245.

Carniani, S., D'Eugenio, F., Ji, X., Parlanti, E., Scholtz, J., Sun, F., Venturi, G., Bakx, T. J. L. C., Curti, M., Maiolino, R., Tacchella, S., Zavala, J. A., Hainline, K., Witstok, J., Johnson, B. D., Alberts, S., Bunker, A. J., Charlot, S., Eisenstein, D. J., Helton, J. M., Jakobsen, P., Kumari, N., Robertson, B., Saxena, A., Übler, H., Williams, C. C., Willmer, C. N. A., and Willott, C. (2025). The eventful life of a luminous galaxy at z = 14: metal enrichment, feedback, and low gas fraction? A&A, 696:A87.

Carniani, S., Hainline, K., D'Eugenio, F., Eisenstein, D. J., Jakobsen, P., Witstok, J., Johnson, B. D., Chevallard, J., Maiolino, R., Helton, J. M., Willott, C., Robertson, B., Alberts, S., Arribas, S., Baker, W. M., Bhatawdekar, R., Boyett, K., Bunker, A. J., Cameron, A. J., Cargile, P. A., Charlot, S., Curti, M., Curtis-Lake, E., Egami, E., Giardino, G., Isaak, K., Ji, Z., Jones, G. C., Kumari, N., Maseda, M. V., Parlanti, E., Pérez-González, P. G., Rawle, T., Rieke, G., Rieke, M., Del Pino, B. R., Saxena, A., Scholtz, J., Smit, R., Sun, F., Tacchella, S., Übler, H., Venturi, G., Williams, C. C., and Willmer, C. N. A. (2024). Spectroscopic confirmation of two luminous galaxies at a redshift of 14. Nature, 633(8029):318–322.

Carniani, S., Maiolino, R., Pallottini, A., Vallini, L., Pentericci, L., Ferrara, A., Castellano, M., Vanzella, E., Grazian, A., Gallerani, S., Santini, P., Wagg, J., and Fontana, A. (2017). Extended ionised and clumpy gas in a normal galaxy at z = 7.1 revealed by ALMA. A&A, 605:A42.

Carniani, S., Maiolino, R., Smit, R., and Amorín, R. (2018). ALMA Detection of Extended [C II] Emission in Himiko at z = 6.6. ApJ, 854(1):L7.

Casavecchia, B., Maio, U., Péroux, C., and Ciardi, B. (2025). Atomic and molecular gas as traced by [C II] emission. A&A, 693:A119.

Casey, C. M. (2012). Far-infrared spectral energy distribution fitting for galaxies near and far. MNRAS, 425(4):3094–3103.

Casey, C. M., Narayanan, D., and Cooray, A. (2014). Dusty star-forming galaxies at high redshift. Phys. Rep., 541(2):45–161.

Casey, C. M., Zavala, J. A., Spilker, J., da Cunha, E., Hodge, J., Hung, C.-L., Staguhn, J., Finkelstein, S. L., and Drew, P. (2018). The Brightest Galaxies in the Dark Ages: Galaxies' Dust Continuum Emission during the Reionization Era. ApJ, 862(1):77.

Cesarsky, D., Lequeux, J., Abergel, A., Perault, M., Palazzi, E., Madden, S., and Tran, D. (1996). Infrared spectrophotometry of NGC 7023 with ISOCAM. A&A, 315:L305–L308.

Ceverino, D., Dekel, A., and Bournaud, F. (2010). High-redshift clumpy discs and bulges in cosmological simulations. MNRAS, 404(4):2151–2169.

Ceverino, D., Glover, S. C. O., and Klessen, R. S. (2017). Introducing the FirstLight project: UV luminosity function and scaling relations of primeval galaxies. MNRAS, 470(3):2791–2798.

Ceverino, D., Hirschmann, M., Klessen, R. S., Glover, S. C. O., Charlot, S., and Feltre, A. (2021). FirstLight IV: diversity in sub-L_* galaxies at cosmic dawn. MNRAS, 504(3):4472–4480.

Ceverino, D., Klessen, R. S., and Glover, S. C. O. (2018). FirstLight - II. Star formation rates of primeval galaxies from z=5-15. MNRAS, 480(4):4842–4850.

Ceverino, D., Klessen, R. S., and Glover, S. C. O. (2019). FirstLight III: rest-frame UV-optical spectral energy distributions of simulated galaxies at cosmic dawn. MNRAS, 484(1):1366–1377.

Ceverino, D. and Klypin, A. (2009). The Role of Stellar Feedback in the Formation of Galaxies. ApJ, 695(1):292–309.

Ceverino, D., Klypin, A., Klimek, E. S., Trujillo-Gomez, S., Churchill, C. W., Primack, J., and Dekel, A. (2014). Radiative feedback and the low efficiency of galaxy formation in low-mass haloes at high redshift. MNRAS, 442(2):1545–1559.

Ceverino, D., Mandelker, N., Snyder, G. F., Lapiner, S., Dekel, A., Primack, J., Ginzburg, O., and Larkin, S. (2023). Effects of feedback on galaxies in the VELA simulations: elongation, clumps, and compaction. MNRAS, 522(3):3912–3925.

Ceverino, D., Nakazato, Y., Yoshida, N., Klessen, R. S., and Glover, S. C. O. (2024). Redshift-dependent galaxy formation efficiency at z = 5 âĂŚ 13 in the FirstLight Simulations. A&A, 689:A244.

Chabrier, G. (2005). The Initial Mass Function: From Salpeter 1955 to 2005. In Corbelli, E., Palla, F., and Zinnecker, H., editors, *The Initial Mass Function 50 Years Later*, volume 327 of *Astrophysics and Space Science Library*, page 41.

Chatzikos, M., Bianchi, S., Camilloni, F., Chakraborty, P., Gunasekera, C. M., Guzmán, F., Milby, J. S., Sarkar, A., Shaw, G., van Hoof, P. A. M., and Ferland, G. J. (2023). The 2023 Release of Cloudy. Rev. Mexicana Astron. Astrofis., 59:327–343.

Chen, Z., Stark, D. P., Endsley, R., Topping, M., Whitler, L., and Charlot, S. (2023). JWST/NIRCam observations of stars and H II regions in z âĽČ 6-8 galaxies: properties of star-forming complexes on 150 pc scales. MNRAS, 518(4):5607–5619.

Chiaki, G. and Yoshida, N. (2022). Disc fragmentation and oligarchic growth of protostellar systems in low-metallicity gas clouds. MNRAS, 510(4):5199–5219.

Choustikov, N., Katz, H., Saxena, A., Garel, T., Devriendt, J., Slyz, A., Kimm, T., Blaizot, J., and Rosdahl, J. (2024). The great escape: understanding the connection between Ly α emission and LyC escape in simulated JWST analogues. MNRAS, 532(2):2463–2484.

Claeyssens, A., Adamo, A., Messa, M., Dessauges-Zavadsky, M., Richard, J., Kramarenko, I., Matthee, J., and Naidu, R. P. (2025). Tracing star formation across cosmic time at tens of parsec-scales in the lensing cluster field Abell 2744. MNRAS, 537(3):2535–2558.

Claeyssens, A., Adamo, A., Richard, J., Mahler, G., Messa, M., and Dessauges-Zavadsky, M. (2023). Star formation at the smallest scales: a JWST study of the clump populations in SMACS0723. MNRAS, 520(2):2180–2203.

Cochrane, R. K., Anglés-Alcázar, D., Cullen, F., and Hayward, C. C. (2024). Disappearing Galaxies: The Orientation Dependence of JWST-bright, HST-dark, Star-forming Galaxy Selection. ApJ, 961(1):37.

Cochrane, R. K., Hayward, C. C., Anglés-Alcázar, D., Lotz, J., Parsotan, T., Ma, X., Kereš, D., Feldmann, R., Faucher-Giguère, C. A., and Hopkins, P. F. (2019). Predictions for the spatial distribution of the dust continuum emission in $1 < z < 5$ star-forming galaxies. MNRAS, 488(2):1779–1789.

Colina, L., Crespo Gómez, A., Álvarez-Márquez, J., Bik, A., Walter, F., Boogaard, L., Labiano, A., Peissker, F., Pérez-González, P., Östlin, G., Greve, T. R., Nørgaard-Nielsen, H. U., Wright, G., Alonso-Herrero, A., Azollini, R., Caputi, K. I., Dicken, D., García-Marín, M., Hjorth, J., Ilbert, O., Kendrew, S., Pye, J. P., Tikkanen, T., van der Werf, P., Costantin, L., Iani, E., Gillman, S., Jermann, I., Langeroodi, D., Moutard, T., Rinaldi, P., Topinka, M., van Dishoeck, E. F., Güdel, M., Henning, T., Lagage, P. O., Ray, T., and Vandenbussche, B. (2023). Uncovering the stellar structure of the dusty star-forming galaxy GN20 at $z = 4.055$ with MIRI/JWST. A&A, 673:L6.

Conroy, C. and Gunn, J. E. (2010). The Propagation of Uncertainties in Stellar Population Synthesis Modeling. III. Model Calibration, Comparison, and Evaluation. ApJ, 712(2):833–857.

Conroy, C., Gunn, J. E., and White, M. (2009). The Propagation of Uncertainties in Stellar Population Synthesis Modeling. I. The Relevance of Uncertain Aspects of Stellar Evolution and the Initial Mass Function to the Derived Physical Properties of Galaxies. ApJ, 699(1):486–506.

Conselice, C. J., Rajgor, S., and Myers, R. (2008). The structures of distant galaxies - I. Galaxy structures and the merger rate to $z \sim 3$ in the Hubble Ultra-Deep Field. MNRAS, 386(2):909–927.

Cormier, D., Abel, N. P., Hony, S., Lebouteiller, V., Madden, S. C., Polles, F. L., Galliano, F., De Looze, I., Galametz, M., and Lambert-Huyghe, A. (2019). The Herschel Dwarf Galaxy Survey. II. Physical conditions, origin of [C II] emission, and porosity of the multiphase low-metallicity ISM. A&A, 626:A23.

Cormier, D., Lebouteiller, V., Madden, S. C., Abel, N., Hony, S., Galliano, F., Baes, M., Barlow, M. J., Cooray, A., De Looze, I., Galametz, M., Karczewski, O. Ł., Parkin, T. J., Rémy, A., Sauvage, M., Spinoglio, L., Wilson, C. D., and Wu, R. (2012). The nature of the interstellar medium of the starburst low-metallicity galaxy Haro 11: a multi-phase model of the infrared emission. A&A, 548:A20.

Cormier, D., Madden, S. C., Lebouteiller, V., Abel, N., Hony, S., Galliano, F., Rémy-Ruyer, A., Bigiel, F., Baes, M., Boselli, A., Chevance, M., Cooray, A., De Looze, I., Doublier, V., Galametz, M., Hughes, T., Karczewski, O. Ł., Lee, M. Y., Lu, N., and Spinoglio, L. (2015). The Herschel Dwarf Galaxy Survey. I. Properties of the low-metallicity ISM from PACS spectroscopy. A&A, 578:A53.

Costantin, L., Pérez-González, P. G., Vega-Ferrero, J., Huertas-Company, M., Bisigello, L., Buitrago, F., Bagley, M. B., Cleri, N. J., Cooper, M. C., Finkelstein, S. L., Holwerda, B. W., Kartaltepe, J. S., Koekemoer, A. M., Nelson, D., Papovich, C., Pillepich, A., Pirzkal, N., Tacchella, S., and Yung, L. Y. A. (2023). Expectations of the Size Evolution of Massive Galaxies at $3 \leq z \leq 6$ from the TNG50 Simulation: The CEERS/JWST View. ApJ, 946(2):71.

Cueto, E. R., Hutter, A., Dayal, P., Gottlöber, S., Heintz, K. E., Mason, C., Trebitsch, M., and Yepes, G. (2024). ASTRAEUS. IX. Impact of an evolving stellar initial mass function on early galaxies and reionisation. A&A, 686:A138.

Cullen, F., McLeod, D. J., McLure, R. J., Dunlop, J. S., Donnan, C. T., Carnall, A. C., Keating, L. C., Magee, D., Arellano-Cordova, K. Z., Bowler, R. A. A., Begley, R., Flury, S. R., Hamadouche, M. L., and Stanton, T. M. (2024). The ultraviolet continuum slopes of high-redshift galaxies: evidence for the emergence of dust-free stellar populations at $z > 10$. MNRAS, 531(1):997–1020.

Cullen, F., McLure, R. J., McLeod, D. J., Dunlop, J. S., Donnan, C. T., Carnall, A. C., Bowler, R. A. A., Begley, R., Hamadouche, M. L., and Stanton, T. M. (2023). The ultraviolet continuum slopes (β) of galaxies at z âĽČ 8-16 from JWST and ground-based near-infrared imaging. MNRAS, 520(1):14–23.

Curti, M., Cresci, G., Mannucci, F., Marconi, A., Maiolino, R., and Esposito, S. (2017). New fully empirical calibrations of strong-line metallicity indicators in star-forming galaxies. MNRAS, 465(2):1384–1400.

Curti, M., D'Eugenio, F., Carniani, S., Maiolino, R., Sandles, L., Witstok, J., Baker, W. M., Bennett, J. S., Piotrowska, J. M., Tacchella, S., Charlot, S., Nakajima, K., Maheson, G., Mannucci, F., Amiri, A., Arribas, S., Belfiore, F., Bonaventura, N. R., Bunker, A. J., Chevallard, J., Cresci, G., Curtis-Lake, E., Hayden-Pawson, C., Jones, G. C., Kumari, N., Laseter, I., Looser, T. J., Marconi, A., Maseda, M. V., Scholtz, J., Smit, R., Übler, H., and Wallace, I. E. B. (2023). The chemical enrichment in the early Universe as probed by JWST via direct metallicity measurements at z $\sim$ 8. MNRAS, 518(1):425–438.

Curti, M., Mannucci, F., Cresci, G., and Maiolino, R. (2020). The mass-metallicity and the fundamental metallicity relation revisited on a fully T_e-based abundance scale for galaxies. MNRAS, 491(1):944–964.

Curtis-Lake, E., Carniani, S., Cameron, A., Charlot, S., Jakobsen, P., Maiolino, R., Bunker, A., Witstok, J., Smit, R., Chevallard, J., Willott, C., Ferruit, P., Arribas, S., Bonaventura, N., Curti, M., D'Eugenio, F., Franx, M., Giardino, G., Looser, T. J., Lützgendorf, N., Maseda, M. V., Rawle, T., Rix, H.-W., Rodríguez del Pino, B., Übler, H., Sirianni, M., Dressler, A., Egami, E., Eisenstein, D. J., Endsley, R., Hainline, K., Hausen, R., Johnson, B. D., Rieke, M., Robertson, B., Shivaei, I., Stark, D. P., Tacchella, S., Williams, C. C., Willmer, C. N. A., Bhatawdekar, R., Bowler, R., Boyett, K., Chen, Z., de Graaff, A., Helton, J. M., Hviding, R. E., Jones, G. C., Kumari, N., Lyu, J., Nelson, E., Perna, M., Sandles, L., Saxena, A., Suess, K. A., Sun, F., Topping, M. W., Wallace, I. E. B., and Whitler, L. (2023). Spectroscopic confirmation of four metal-poor galaxies at z = 10.3-13.2. *Nature Astronomy*, 7:622–632.

da Cunha, E., Groves, B., Walter, F., Decarli, R., Weiss, A., Bertoldi, F., Carilli, C., Daddi, E., Elbaz, D., Ivison, R., Maiolino, R., Riechers, D., Rix, H.-W., Sargent, M., and Smail, I. (2013). On the Effect of the Cosmic Microwave Background in High-redshift (Sub-)millimeter Observations. ApJ, 766(1):13.

da Cunha, E., Walter, F., Smail, I. R., Swinbank, A. M., Simpson, J. M., Decarli, R., Hodge, J. A., Weiss, A., van der Werf, P. P., Bertoldi, F., Chapman, S. C., Cox, P., Danielson, A. L. R., Dannerbauer, H., Greve, T. R., Ivison, R. J., Karim, A., and Thomson, A. (2015). An ALMA Survey of Submillimeter Galaxies in the Extended Chandra Deep Field South: Physical Properties Derived from Ultraviolet-to-radio Modeling. ApJ, 806(1):110.

Davé, R., Anglés-Alcázar, D., Narayanan, D., Li, Q., Rafieferantsoa, M. H., and Appleby, S. (2019). SIMBA: Cosmological simulations with black hole growth and feedback. MNRAS, 486(2):2827–2849.

Davies, R. L., Förster Schreiber, N. M., Genzel, R., Shimizu, T. T., Davies, R. I., Schruba, A., Tacconi, L. J., Übler, H., Wisnioski, E., Wuyts, S., Fossati, M., Herrera-Camus, R., Lutz, D., Mendel, J. T., Naab, T., Price, S. H., Renzini, A., Wilman, D., Beifiori, A., Belli, S., Burkert, A., Chan, J., Contursi, A., Fabricius, M., Lee, M. M., Saglia, R. P., and Sternberg, A. (2021). The KMOS^{3D} Survey: Investigating the Origin of the Elevated Electron Densities in Star-forming Galaxies at $1 \lesssim z \lesssim 3$. ApJ, 909(1):78.

Dayal, P. and Ferrara, A. (2018). Early galaxy formation and its large-scale effects. Phys. Rep., 780:1–64.

Dayal, P., Ferrara, A., Sommovigo, L., Bouwens, R., Oesch, P. A., Smit, R., Gonzalez, V., Schouws, S., Stefanon, M., Kobayashi, C., Bremer, J., Algera, H. S. B., Aravena, M., Bowler, R. A. A., da Cunha, E., Fudamoto, Y., Graziani, L., Hodge, J., Inami, H., De Looze, I., Pallottini, A., Riechers, D., Schneider, R., Stark, D., and Endsley, R. (2022). The ALMA REBELS survey: the dust content of z 7 Lyman break galaxies. MNRAS, 512(1):989–1002.

De Looze, I., Cormier, D., Lebouteiller, V., Madden, S., Baes, M., Bendo, G. J., Boquien, M., Boselli, A., Clements, D. L., Cortese, L., Cooray, A., Galametz, M., Galliano, F., Graciá-Carpio, J., Isaak, K., Karczewski, O. Ł., Parkin, T. J., Pellegrini, E. W., Rémy-Ruyer, A., Spinoglio, L., Smith, M. W. L., and Sturm, E. (2014). The applicability of far-infrared fine-structure lines as star formation rate tracers over wide ranges of metallicities and galaxy types. A&A, 568:A62.

Dekel, A., Birnboim, Y., Engel, G., Freundlich, J., Goerdt, T., Mumcuoglu, M., Neistein, E., Pichon, C., Teyssier, R., and Zinger, E. (2009a). Cold streams in early massive hot haloes as the main mode of galaxy formation. Nature, 457(7228):451–454.

Dekel, A. and Krumholz, M. R. (2013). Steady outflows in giant clumps of high-z disc galaxies during migration and growth by accretion. MNRAS, 432(1):455–467.

Dekel, A., Sari, R., and Ceverino, D. (2009b). Formation of Massive Galaxies at High Redshift: Cold Streams, Clumpy Disks, and Compact Spheroids. ApJ, 703(1):785–801.

Dekel, A., Sarkar, K. C., Birnboim, Y., Mandelker, N., and Li, Z. (2023). Efficient formation of massive galaxies at cosmic dawn by feedback-free starbursts. MNRAS, 523(3):3201–3218.

D'Eugenio, F., Maiolino, R., Carniani, S., Chevallard, J., Curtis-Lake, E., Witstok, J., Charlot, S., Baker, W. M., Arribas, S., Boyett, K., Bunker, A. J., Curti, M., Eisenstein, D. J., Hainline, K., Ji, Z., Johnson, B. D., Kumari, N., Looser, T. J., Nakajima, K., Nelson, E., Rieke, M., Robertson, B., Scholtz, J., Smit, R., Sun, F., Venturi, G., Tacchella, S., Übler, H., Willmer, C. N. A., and Willott, C. (2024). JADES: Carbon enrichment 350 Myr after the Big Bang. A&A, 689:A152.

Di Matteo, P., Bournaud, F., Martig, M., Combes, F., Melchior, A. L., and Semelin, B. (2008). On the frequency, intensity, and duration of starburst episodes triggered by galaxy interactions and mergers. A&A, 492(1):31–49.

Díaz-Santos, T., Armus, L., Charmandaris, V., Lu, N., Stierwalt, S., Stacey, G., Malhotra, S., van der Werf, P. P., Howell, J. H., Privon, G. C., Mazzarella, J. M., Goldsmith, P. F., Murphy, E. J., Barcos-Muñoz, L., Linden, S. T., Inami, H., Larson, K. L., Evans, A. S., Appleton, P., Iwasawa, K., Lord, S., Sanders, D. B., and Surace, J. A. (2017). A Herschel/PACS Far-infrared Line Emission Survey of Local Luminous Infrared Galaxies. ApJ, 846(1):32.

Dinerstein, H. L., Lester, D. F., and Werner, M. W. (1985). Far-infrared line observations of planetary nebulae. I. The (O III) spectrum. ApJ, 291:561–570.

Dopita, M. A. and Sutherland, R. S. (1996). Spectral Signatures of Fast Shocks. I. Low-Density Model Grid. ApJS, 102:161.

Dopita, M. A. and Sutherland, R. S. (2003). *Astrophysics of the diffuse universe*.

Dottorini, D., Calabrò, A., Pentericci, L., Mascia, S., Llerena, M., Napolitano, L., Santini, P., Roberts-Borsani, G., Castellano, M., Amorín, R., Dickinson, M., Fontana, A., Hathi, N., Hirschmann, M., Koekemoer, A., Lucas, R. A., Merlin, E., Morales, A., Pacucci, F., Wilkins, S., Arrabal Haro, P., Bagley, M., Finkelstein, S., Kartaltepe, J., Papovich, C., and Pirzkal, N. (2024). Evolution of the UV slope of galaxies at cosmic morning ($z > 4$): the properties of extremely blue galaxies. *arXiv e-prints*, page arXiv:2412.01623.

Draine, B. T. (2011). *Physics of the Interstellar and Intergalactic Medium*.

Draine, B. T., Aniano, G., Krause, O., Groves, B., Sandstrom, K., Braun, R., Leroy, A., Klaas, U., Linz, H., Rix, H.-W., Schinnerer, E., Schmiedeke, A., and Walter, F. (2014). Andromeda's Dust. ApJ, 780(2):172.

Draine, B. T. and Bertoldi, F. (1996). Structure of Stationary Photodissociation Fronts. ApJ, 468:269.

Draine, B. T. and Li, A. (2007). Infrared Emission from Interstellar Dust. IV. The Silicate-Graphite-PAH Model in the Post-Spitzer Era. ApJ, 657(2):810–837.

Duan, Q., Conselice, C. J., Li, Q., Austin, D., Harvey, T., Adams, N. J., Duncan, K. J., Trussler, J., Ferreira, L., Westcott, L., Harris, H., Windhorst, R. A., Holwerda, B. W., Broadhurst, T. J., Coe, D., Cohen, S. H., Du, X., Driver, S. P., Frye, B., Grogin, N. A., Hathi, N. P., Jansen, R. A., Koekemoer, A. M., Marshall, M. A., Nonino, M., Ortiz, R., Pirzkal, N., Robotham, A., Ryan, R. E., Summers, J., D'Silva, J. C. J., Willmer, C. N. A., and Yan, H. (2025). Galaxy Mergers in the Epoch of Reionization I: A JWST Study of Pair Fractions, Merger Rates, and Stellar Mass Accretion Rates at $z = 4.5$ - 11.5. MNRAS.

Dwek, E. (1998). The Evolution of the Elemental Abundances in the Gas and Dust Phases of the Galaxy. ApJ, 501:643.

Dwek, E., Arendt, R. G., Bouchet, P., Burrows, D. N., Challis, P., Danziger, I. J., De Buizer, J. M., Gehrz, R. D., Kirshner, R. P., McCray, R., Park, S., Polomski, E. F., and Woodward, C. E. (2008). Infrared and X-Ray Evidence for Circumstellar Grain Destruction by the Blast Wave of Supernova 1987A. ApJ, 676(2):1029–1039.

Eldridge, J. J., Stanway, E. R., Xiao, L., McClelland, L. A. S., Taylor, G., Ng, M., Greis, S. M. L., and Bray, J. C. (2017). Binary Population and Spectral Synthesis Version 2.1: Construction, Observational Verification, and New Results. PASA, 34:e058.

Elmegreen, B. G. (2011). Gravitational Instabilities in Two-component Galaxy Disks with Gas Dissipation. ApJ, 737(1):10.

Elmegreen, B. G., Elmegreen, D. M., Sánchez Almeida, J., Muñoz-Tuñón, C., Dewberry, J., Putko, J., Teich, Y., and Popinchalk, M. (2013). Massive Clumps in Local Galaxies: Comparisons with High-redshift Clumps. ApJ, 774(1):86.

Elmegreen, D. M., Elmegreen, B. G., Ravindranath, S., and Coe, D. A. (2007). Resolved Galaxies in the Hubble Ultra Deep Field: Star Formation in Disks at High Redshift. ApJ, 658(2):763–777.

Endsley, R., Chisholm, J., Stark, D. P., Topping, M. W., and Whitler, L. (2024). The Burstiness of Star Formation at $z \sim 6$: A Huge Diversity in the Recent Star Formation Histories of Very UV-faint Galaxies. *arXiv e-prints*, page arXiv:2410.01905.

Enßlin, T. A., Pfrommer, C., Springel, V., and Jubelgas, M. (2007). Cosmic ray physics in calculations of cosmological structure formation. A&A, 473(1):41–57.

Esmerian, C. J. and Gnedin, N. Y. (2022). Modeling Dust Production, Growth, and Destruction in Reionization-era Galaxies with the CROC Simulations: Methods and Parameter Exploration. ApJ, 940(1):74.

Faisst, A. L., Capak, P. L., Yan, L., Pavesi, R., Riechers, D. A., Barišić, I., Cooke, K. C., Kartaltepe, J. S., and Masters, D. C. (2017). Are High-redshift Galaxies Hot? Temperature of z > 5 Galaxies and Implications for Their Dust Properties. ApJ, 847(1):21.

Fakhouri, O. and Ma, C.-P. (2009). Environmental dependence of dark matter halo growth - I. Halo merger rates. MNRAS, 394(4):1825–1840.

Faure, B., Bournaud, F., Fensch, J., Daddi, E., Behrendt, M., Burkert, A., and Richard, J. (2021). Hierarchical fragmentation in high redshift galaxies revealed by hydrodynamical simulations. MNRAS, 502(3):4641–4657.

Feldmann, R., Boylan-Kolchin, M., Bullock, J. S., Çatmabacak, O., Faucher-Giguère, C.-A., Hayward, C. C., Kereš, D., Lazar, A., Liang, L., Moreno, J., Oesch, P. A., Quataert, E., Shen, X., and Sun, G. (2025). Elevated UV luminosity density at Cosmic Dawn explained by non-evolving, weakly mass-dependent star formation efficiency. MNRAS, 536(1):988–1016.

Fensch, J., Renaud, F., Bournaud, F., Duc, P. A., Agertz, O., Amram, P., Combes, F., Di Matteo, P., Elmegreen, B., Emsellem, E., Jog, C. J., Perret, V., Struck, C., and Teyssier, R. (2017). High-redshift major mergers weakly enhance star formation. MNRAS, 465(2):1934–1949.

Ferland, G. J., Chatzikos, M., Guzmán, F., Lykins, M. L., van Hoof, P. A. M., Williams, R. J. R., Abel, N. P., Badnell, N. R., Keenan, F. P., Porter, R. L., and Stancil, P. C. (2017). The 2017 Release Cloudy. Rev. Mexicana Astron. Astrofis., 53:385–438.

Ferland, G. J., Korista, K. T., Verner, D. A., Ferguson, J. W., Kingdon, J. B., and Verner, E. M. (1998). CLOUDY 90: Numerical Simulation of Plasmas and Their Spectra. PASP, 110(749):761–778.

Ferland, G. J., Porter, R. L., van Hoof, P. A. M., Williams, R. J. R., Abel, N. P., Lykins, M. L., Shaw, G., Henney, W. J., and Stancil, P. C. (2013). The 2013 Release of Cloudy. Rev. Mexicana Astron. Astrofis., 49:137–163.

Fernández-Ontiveros, J. A., Spinoglio, L., Pereira-Santaella, M., Malkan, M. A., Andreani, P., and Dasyra, K. M. (2016). Far-infrared Line Spectra of Active Galaxies from the Herschel/PACS Spectrometer: The Complete Database. ApJS, 226(2):19.

Ferrara, A. (2024). Super-early JWST galaxies, outflows, and Lyα visibility in the Epoch of Reionization. A&A, 684:A207.

Ferrara, A., Pallottini, A., and Dayal, P. (2023). On the stunning abundance of super-early, luminous galaxies revealed by JWST. MNRAS, 522(3):3986–3991.

Ferrara, A., Pallottini, A., and Sommovigo, L. (2025). Blue monsters at z > 10: Where all their dust has gone. A&A, 694:A286.

Finkelman, I., Brosch, N., Funes, J. G., Kniazev, A. Y., and Väisänen, P. (2010). Ionized gas in E/S0 galaxies with dust lanes. MNRAS, 407(4):2475–2500.

Finkelstein, S. L., Bagley, M. B., Arrabal Haro, P., Dickinson, M., Ferguson, H. C., Kartaltepe, J. S., Papovich, C., Burgarella, D., Kocevski, D. D., Huertas-Company, M., Iyer, K. G., Koekemoer, A. M., Larson, R. L., Pérez-González, P. G., Rose, C., Tacchella, S., Wilkins, S. M., Chworowsky, K., Medrano, A., Morales, A. M., Somerville, R. S., Yung, L. Y. A., Fontana, A., Giavalisco, M., Grazian, A., Grogin, N. A., Kewley, L. J., Kirkpatrick, A., Kurczynski, P., Lotz, J. M., Pentericci, L., Pirzkal, N., Ravindranath, S., Ryan, R. E., Trump, J. R., Yang, G., Almaini, O., Amorín, R. O., Annunziatella, M., Backhaus, B. E., Barro, G., Behroozi, P., Bell, E. F., Bhatawdekar, R., Bisigello, L., Bromm, V., Buat, V., Buitrago, F., Calabrò, A., Casey, C. M., Castellano, M., Chávez Ortiz, Ó. A., Ciesla, L., Cleri, N. J., Cohen, S. H., Cole, J. W., Cooke, K. C., Cooper, M. C., Cooray, A. R., Costantin, L., Cox, I. G., Croton, D., Daddi, E., Davé, R., de La Vega, A., Dekel, A., Elbaz, D., Estrada-Carpenter, V., Faber, S. M., Fernández, V., Finkelstein, K. D., Freundlich, J., Fujimoto, S., García-Argumánez, Á., Gardner, J. P., Gawiser, E., Gómez-Guijarro, C., Guo, Y., Hamblin, K., Hamilton, T. S., Hathi, N. P., Holwerda, B. W., Hirschmann, M., Hutchison, T. A., Jaskot, A. E., Jha, S. W., Jogee, S., Juneau, S., Jung, I., Kassin, S. A., Le Bail, A., Leung, G. C. K., Lucas, R. A., Magnelli, B., Mantha, K. B., Matharu, J., McGrath, E. J., McIntosh, D. H., Merlin, E., Mobasher, B., Newman, J. A., Nicholls, D. C., Pandya, V., Rafelski, M., Ronayne, K., Santini, P., Seillé, L.-M., Shah, E. A., Shen, L., Simons, R. C., Snyder, G. F., Stanway, E. R., Straughn, A. N., Teplitz, H. I., Vanderhoof, B. N., Vega-Ferrero, J., Wang, W., Weiner, B. J., Willmer, C. N. A., Wuyts, S., Zavala, J. A., and Ceers Team (2022). A Long Time Ago in a Galaxy Far, Far Away: A Candidate z $\sim$ 12 Galaxy in Early JWST CEERS Imaging. ApJ, 940(2):L55.

Fiore, F., Ferrara, A., Bischetti, M., Feruglio, C., and Travascio, A. (2023). Dusty-wind-clear JWST Super-early Galaxies. ApJ, 943(2):L27.

Fisher, R., Bowler, R. A. A., Stefanon, M., Rowland, L. E., Algera, H. S. B., Aravena, M., Bouwens, R., Dayal, P., Ferrara, A., Fudamoto, Y., Gulis, C., Hodge, J. A., Inami, H., Ormerod, K., Pallottini, A., Phillips, S. G., Sartorio, N. S., Schouws, S., Smit, R., Sommovigo, L., Stark, D. P., and van der Werf, P. P. (2025). REBELS-IFU: dust attenuation curves of 12 massive galaxies at z âLČ 7. MNRAS, 539(1):109–126.

Fitzpatrick, E. L. (1999). Correcting for the Effects of Interstellar Extinction. PASP, 111(755):63–75.

Fitzpatrick, E. L. and Massa, D. (1986). An Analysis of the Shapes of Ultraviolet Extinction Curves. I. The 2175 Angstrom Bump. ApJ, 307:286.

Fudamoto, Y., Inoue, A. K., Bouwens, R., Inami, H., Smit, R., Stark, D., Aravena, M., Pallottini, A., Hashimoto, T., Oguri, M., Bowler, R. A. A., da Cunha, E., Dayal, P., Ferrara, A., Fujimoto, S., Heintz, K. E., Hygate, A. P. S., van Leeuwen, I. F., De Looze, I., Rowland, L. E., Stefanon, M., Sugahara, Y., Witstok, J., and van der Werf, P. P. (2025). ALMA Observations of [OI]145um and [NII]205um Emission lines from Star-Forming Galaxies at $z \sim 7$. *arXiv e-prints*, page arXiv:2504.03831.

Fudamoto, Y., Inoue, A. K., Coe, D., Welch, B., Acebron, A., Ricotti, M., Mandelker, N., Windhorst, R. A., Xu, X., Sugahara, Y., Bauer, F. E., Bradač, M., Bradley, L. D., Diego, J. M., Florian, M., Frye, B., Fujimoto, S., Hashimoto, T., Henry, A., Mahler, G., Oesch, P. A., Ravindranath, S., Rigby, J., Sharon, K., Strait, V., Tamura, Y., Trenti, M., Vanzella, E., Zackrisson, E., and Zitrin, A. (2024).

The Extended [C II] under Construction? Observation of the Brightest High-z Lensed Star-forming Galaxy at z = 6.2. ApJ, 961(1):71.

Fudamoto, Y., Inoue, A. K., and Sugahara, Y. (2023). Estimating dust temperature and Far-IR luminosity of high-redshift galaxies using ALMA single-band continuum observations. MNRAS, 521(2):2962–2968.

Fudamoto, Y., Oesch, P. A., Faisst, A., Béthermin, M., Ginolfi, M., Khusanova, Y., Loiacono, F., Le Fèvre, O., Capak, P., Schaerer, D., Silverman, J. D., Cassata, P., Yan, L., Amorin, R., Bardelli, S., Boquien, M., Cimatti, A., Dessauges-Zavadsky, M., Fujimoto, S., Gruppioni, C., Hathi, N. P., Ibar, E., Jones, G. C., Koekemoer, A. M., Lagache, G., Lemaux, B. C., Maiolino, R., Narayanan, D., Pozzi, F., Riechers, D. A., Rodighiero, G., Talia, M., Toft, S., Vallini, L., Vergani, D., Zamorani, G., and Zucca, E. (2020a). The ALPINE-ALMA [CII] survey. Dust attenuation properties and obscured star formation at z $\sim$ 4.4-5.8. A&A, 643:A4.

Fudamoto, Y., Oesch, P. A., Magnelli, B., Schinnerer, E., Liu, D., Lang, P., Jiménez-Andrade, E. F., Groves, B., Leslie, S., and Sargent, M. T. (2020b). A3COSMOS: the dust attenuation of star-forming galaxies at z = 2.5-4.0 from the COSMOS-ALMA archive. MNRAS, 491(4):4724–4734.

Fudamoto, Y., Oesch, P. A., Schinnerer, E., Groves, B., Karim, A., Magnelli, B., Sargent, M. T., Cassata, P., Lang, P., Liu, D., Le Fèvre, O., Leslie, S., Smolčić, V., and Tasca, L. (2017). The dust attenuation of star-forming galaxies at z $\sim$ 3 and beyond: New insights from ALMA observations. MNRAS, 472(1):483–490.

Fudamoto, Y., Oesch, P. A., Schouws, S., Stefanon, M., Smit, R., Bouwens, R. J., Bowler, R. A. A., Endsley, R., Gonzalez, V., Inami, H., Labbe, I., Stark, D., Aravena, M., Barrufet, L., da Cunha, E., Dayal, P., Ferrara, A., Graziani, L., Hodge, J., Hutter, A., Li, Y., De Looze, I., Nanayakkara, T., Pallottini, A., Riechers, D., Schneider, R., Ucci, G., van der Werf, P., and White, C. (2021). Normal, dust-obscured galaxies in the epoch of reionization. Nature, 597(7877):489–492.

Fudamoto, Y., Smit, R., Bowler, R. A. A., Oesch, P. A., Bouwens, R., Stefanon, M., Inami, H., Endsley, R., Gonzalez, V., Schouws, S., Stark, D., Algera, H. S. B., Aravena, M., Barrufet, L., da Cunha, E., Dayal, P., Ferrara, A., Graziani, L., Hodge, J. A., Hygate, A. P. S., Inoue, A. K., Nanayakkara, T., Pallottini, A., Pizzati, E., Schneider, R., Sommovigo, L., Sugahara, Y., Topping, M., van der Werf, P., Bethermin, M., Cassata, P., Dessauges-Zavadsky, M., Ibar, E., Faisst, A. L., Fujimoto, S., Ginolfi, M., Hathi, N., Jones, G. C., Pozzi, F., and Schaerer, D. (2022). The ALMA REBELS Survey: Average [C II] 158 μm Sizes of Star-forming Galaxies from z 7 to z 4. ApJ, 934(2):144.

Fujii, M. S., Saitoh, T. R., Hirai, Y., and Wang, L. (2021). SIRIUS project. III. Star-by-star simulations of star cluster formation using a direct N-body integrator with stellar feedback. PASJ, 73(4):1074–1099.

Fujimoto, S., Naidu, R. P., Chisholm, J., Atek, H., Endsley, R., Kokorev, V., Furtak, L. J., Pan, R., Liu, B., Bromm, V., Venditti, A., Visbal, E., Sarmento, R., Weibel, A., Oesch, P. A., Brammer, G., Schaerer, D., Adamo, A., Berg, D. A., Bezanson, R., Chemerynska, I., Claeyssens, A., Dessauges-Zavadsky, M., Frebel, A., Korber, D., Labbe, I., Marques-Chaves, R., Matthee, J., McQuinn, K. B. W., Muñoz, J. B., Natarajan, P., Saldana-Lopez, A., Suess, K. A., Volonteri, M., and Zitrin, A. (2025). GLIMPSE: An ultra-faint $\simeq 10^5$ $M_\odot$ Pop III Galaxy Candidate and First Constraints on the Pop III UV Luminosity Function at $z \simeq 6-7$. *arXiv e-prints*, page arXiv:2501.11678.

Fujimoto, S., Ouchi, M., Ferrara, A., Pallottini, A., Ivison, R. J., Behrens, C., Gallerani, S., Arata, S., Yajima, H., and Nagamine, K. (2019). First Identification of 10 kpc [C II] 158 μm Halos around Star-forming Galaxies at z = 5-7. ApJ, 887(2):107.

Fujimoto, S., Ouchi, M., Kohno, K., Valentino, F., Giménez-Arteaga, C., Brammer, G. B., Furtak, L. J., Kohandel, M., Oguri, M., Pallottini, A., Richard, J., Zitrin, A., Bauer, F. E., Boylan-Kolchin, M., Dessauges-Zavadsky, M., Egami, E., Finkelstein, S. L., Ma, Z., Smail, I., Watson, D., Hutchison, T. A., Rigby, J. R., Welch, B. D., Ao, Y., Bradley, L. D., Caminha, G. B., Caputi, K. I., Espada, D., Endsley, R., Fudamoto, Y., González-López, J., Hatsukade, B., Koekemoer, A. M., Kokorev, V., Laporte, N., Lee, M., Magdis, G. E., Ono, Y., Rizzo, F., Shibuya, T., Shimasaku, K., Sun, F., Toft, S., Umehata, H., Wang, T., and Yajima, H. (2024a). Primordial Rotating Disk Composed of $\geq$15 Dense Star-Forming Clumps at Cosmic Dawn. *arXiv e-prints*, page arXiv:2402.18543.

Fujimoto, S., Ouchi, M., Nakajima, K., Harikane, Y., Isobe, Y., Brammer, G., Oguri, M., Giménez-Arteaga, C., Heintz, K. E., Kokorev, V., Bauer, F. E., Ferrara, A., Kojima, T., Lagos, C. d. P., Laura, S., Schaerer, D., Shimasaku, K., Hatsukade, B., Kohno, K., Sun, F., Valentino, F., Watson, D., Fudamoto, Y., Inoue, A. K., González-López, J., Koekemoer, A. M., Knudsen, K., Lee, M. M., Magdis, G. E., Richard, J., Strait, V. B., Sugahara, Y., Tamura, Y., Toft, S., Umehata, H., and Walth, G. (2024b). JWST and ALMA Multiple-line Study in and around a Galaxy at z = 8.496: Optical to Far-Infrared Line Ratios and the Onset of an Outflow Promoting Ionizing Photon Escape. ApJ, 964(2):146.

Fukushima, H. and Yajima, H. (2021). Radiation hydrodynamics simulations of massive star cluster formation in giant molecular clouds. MNRAS, 506(4):5512–5539.

Fukushima, H. and Yajima, H. (2024). Impacts of stellar wind and supernovae on star cluster formation: Origins of extremely high N/O ratios and multiple stellar populations. PASJ, 76(5):1122–1130.

Fukushima, H., Yajima, H., Sugimura, K., Hosokawa, T., Omukai, K., and Matsumoto, T. (2020). Star cluster formation and cloud dispersal by radiative feedback: dependence on metallicity and compactness. MNRAS, 497(3):3830–3845.

Furusawa, H., Kashikawa, N., Kobayashi, M. A. R., Dunlop, J. S., Shimasaku, K., Takata, T., Sekiguchi, K., Naito, Y., Furusawa, J., Ouchi, M., Nakata, F., Yasuda, N., Okura, Y., Taniguchi, Y., Yamada, T., Kajisawa, M., Fynbo, J. P. U., and Le Fèvre, O. (2016). A New Constraint on the Lyα Fraction of UV Very Bright Galaxies at Redshift 7. ApJ, 822(1):46.

Garaldi, E., Kannan, R., Smith, A., Borrow, J., Vogelsberger, M., Pakmor, R., Springel, V., Hernquist, L., Galárraga-Espinosa, D., Yeh, J. Y. C., Shen, X., Xu, C., Neyer, M., Spina, B., Almualla, M., and Zhao, Y. (2024). The THESAN project: public data release of radiation-hydrodynamic simulations matching reionization-era JWST observations. MNRAS, 530(4):3765–3786.

Garcia, F. A. B., Ricotti, M., and Sugimura, K. (2025). Seeding Cores: A Pathway for Nuclear Star Clusters from Bound Star Clusters in the First Billion Years. *arXiv e-prints*, page arXiv:2503.08779.

Garcia, F. A. B., Ricotti, M., Sugimura, K., and Park, J. (2023). Star cluster formation and survival in the first galaxies. MNRAS, 522(2):2495–2515.

Gardner, J. P., Mather, J. C., Clampin, M., Doyon, R., Greenhouse, M. A., Hammel, H. B., Hutchings, J. B., Jakobsen, P., Lilly, S. J., Long, K. S., Lunine, J. I., McCaughrean, M. J., Mountain, M., Nella, J., Rieke, G. H., Rieke, M. J., Rix, H.-W., Smith, E. P., Sonneborn, G., Stiavelli, M., Stockman, H. S., Windhorst, R. A., and Wright, G. S. (2006). The James Webb Space Telescope. Space Sci. Rev., 123(4):485–606.

Gelli, V., Mason, C., and Hayward, C. C. (2024). The impact of mass-dependent stochasticity at cosmic dawn. *arXiv e-prints*, page arXiv:2405.13108.

Gelli, V., Salvadori, S., Ferrara, A., Pallottini, A., and Carniani, S. (2021). Dwarf Satellites of High-z Lyman Break Galaxies: A Free Lunch for JWST. ApJ, 913(2):L25.

Gelli, V., Salvadori, S., Ferrara, A., Pallottini, A., and Carniani, S. (2023). Quiescent Low-mass Galaxies Observed by JWST in the Epoch of Reionization. ApJ, 954(1):L11.

Gelli, V., Salvadori, S., Pallottini, A., and Ferrara, A. (2020). The stellar populations of high-redshift dwarf galaxies. MNRAS, 498(3):4134–4149.

Genel, S., Genzel, R., Bouché, N., Naab, T., and Sternberg, A. (2009). The Halo Merger Rate in the Millennium Simulation and Implications for Observed Galaxy Merger Fractions. ApJ, 701(2):2002–2018.

Genel, S., Genzel, R., Bouché, N., Sternberg, A., Naab, T., Förster Schreiber, N. M., Shapiro, K. L., Tacconi, L. J., Lutz, D., Cresci, G., Buschkamp, P., Davies, R. I., and Hicks, E. K. S. (2008). Mergers and Mass Accretion Rates in Galaxy Assembly: The Millennium Simulation Compared to Observations of z $\approx$ 2 Galaxies. ApJ, 688(2):789–793.

Genel, S., Naab, T., Genzel, R., Förster Schreiber, N. M., Sternberg, A., Oser, L., Johansson, P. H., Davé, R., Oppenheimer, B. D., and Burkert, A. (2012). Short-lived Star-forming Giant Clumps in Cosmological Simulations of z ≈ 2 Disks. ApJ, 745(1):11.

Genel, S., Vogelsberger, M., Springel, V., Sijacki, D., Nelson, D., Snyder, G., Rodriguez-Gomez, V., Torrey, P., and Hernquist, L. (2014). Introducing the Illustris project: the evolution of galaxy populations across cosmic time. MNRAS, 445(1):175–200.

Genzel, R., Burkert, A., Bouché, N., Cresci, G., Förster Schreiber, N. M., Shapley, A., Shapiro, K., Tacconi, L. J., Buschkamp, P., Cimatti, A., Daddi, E., Davies, R., Eisenhauer, F., Erb, D. K., Genel, S., Gerhard, O., Hicks, E., Lutz, D., Naab, T., Ott, T., Rabien, S., Renzini, A., Steidel, C. C., Sternberg, A., and Lilly, S. J. (2008). From Rings to Bulges: Evidence for Rapid Secular Galaxy Evolution at z ∼2 from Integral Field Spectroscopy in the SINS Survey. ApJ, 687(1):59–77.

Genzel, R., Newman, S., Jones, T., Förster Schreiber, N. M., Shapiro, K., Genel, S., Lilly, S. J., Renzini, A., Tacconi, L. J., Bouché, N., Burkert, A., Cresci, G., Buschkamp, P., Carollo, C. M., Ceverino, D., Davies, R., Dekel, A., Eisenhauer, F., Hicks, E., Kurk, J., Lutz, D., Mancini, C., Naab, T., Peng, Y., Sternberg, A., Vergani, D., and Zamorani, G. (2011). The Sins Survey of z ∼2 Galaxy Kinematics: Properties of the Giant Star-forming Clumps. ApJ, 733(2):101.

Genzel, R., Tacconi, L. J., Eisenhauer, F., Förster Schreiber, N. M., Cimatti, A., Daddi, E., Bouché, N., Davies, R., Lehnert, M. D., Lutz, D., Nesvadba, N., Verma, A., Abuter, R., Shapiro, K., Sternberg, A., Renzini, A., Kong, X., Arimoto, N., and Mignoli, M. (2006). The rapid formation of a large rotating disk galaxy three billion years after the Big Bang. Nature, 442(7104):786–789.

Gieles, M., Erkal, D., Antonini, F., Balbinot, E., and Peñarrubia, J. (2021). A supra-massive population of stellar-mass black holes in the globular cluster Palomar 5. *Nature Astronomy*, 5:957–966.

Giménez-Arteaga, C., Fujimoto, S., Valentino, F., Brammer, G. B., Mason, C. A., Rizzo, F., Rusakov, V., Colina, L., Prieto-Lyon, G., Oesch, P. A., Espada, D., Heintz, K. E., Knudsen, K. K., Dessauges-Zavadsky, M., Laporte, N., Lee, M., Magdis, G. E., Ono, Y., Ao, Y., Ouchi, M., Kohno, K., and Koekemoer, A. M. (2024). Outshining in the spatially resolved analysis of a strongly lensed galaxy at z = 6.072 with JWST NIRCam. A&A, 686:A63.

Giménez-Arteaga, C., Oesch, P. A., Brammer, G. B., Valentino, F., Mason, C. A., Weibel, A., Barrufet, L., Fujimoto, S., Heintz, K. E., Nelson, E. J., Strait, V. B., Suess, K. A., and Gibson, J. (2023). Spatially Resolved Properties of Galaxies at 5 < z < 9 in the SMACS 0723 JWST ERO Field. ApJ, 948(2):126.

Ginolfi, M., Jones, G. C., Béthermin, M., Fudamoto, Y., Loiacono, F., Fujimoto, S., Le Févre, O., Faisst, A., Schaerer, D., Cassata, P., Silverman, J. D., Yan, L., Capak, P., Bardelli, S., Boquien, M., Carraro, R., Dessauges-Zavadsky, M., Giavalisco, M., Gruppioni, C., Ibar, E., Khusanova, Y., Lemaux, B. C., Maiolino, R., Narayanan, D., Oesch, P., Pozzi, F., Rodighiero, G., Talia, M., Toft, S., Vallini, L., Vergani, D., and Zamorani, G. (2020). The ALPINE-ALMA [C II] survey: Star-formation-driven outflows and circumgalactic enrichment in the early Universe. A&A, 633:A90.

Gnat, O. and Sternberg, A. (2007). Time-dependent Ionization in Radiatively Cooling Gas. ApJS, 168(2):213–230.

Gnedin, N. Y. and Kravtsov, A. V. (2011). Environmental Dependence of the Kennicutt-Schmidt Relation in Galaxies. ApJ, 728(2):88.

Goldader, J. D., Meurer, G., Heckman, T. M., Seibert, M., Sanders, D. B., Calzetti, D., and Steidel, C. C. (2002). Far-Infrared Galaxies in the Far-Ultraviolet. ApJ, 568(2):651–678.

Goldsmith, P. F., Langer, W. D., Pineda, J. L., and Velusamy, T. (2012). Collisional Excitation of the [C II] Fine Structure Transition in Interstellar Clouds. ApJS, 203(1):13.

Gordon, K. D., Calzetti, D., and Witt, A. N. (1997). Dust in Starburst Galaxies. ApJ, 487(2):625–635.

Gordon, K. D., Clayton, G. C., Misselt, K. A., Landolt, A. U., and Wolff, M. J. (2003). A Quantitative Comparison of the Small Magellanic Cloud, Large Magellanic Cloud, and Milky Way Ultraviolet to Near-Infrared Extinction Curves. ApJ, 594(1):279–293.

Gould, R. J. and Salpeter, E. E. (1963). The Interstellar Abundance of the Hydrogen Molecule. I. Basic Processes. ApJ, 138:393.

Granato, G. L., Lacey, C. G., Silva, L., Bressan, A., Baugh, C. M., Cole, S., and Frenk, C. S. (2000). The Infrared Side of Galaxy Formation. I. The Local Universe in the Semianalytical Framework. ApJ, 542(2):710–730.

Graziani, L., Schneider, R., Ginolfi, M., Hunt, L. K., Maio, U., Glatzle, M., and Ciardi, B. (2020). The assembly of dusty galaxies at z $\geq$ 4: statistical properties. MNRAS, 494(1):1071–1088.

Grevesse, N., Asplund, M., Sauval, A. J., and Scott, P. (2010). The chemical composition of the Sun. Ap&SS, 328(1-2):179–183.

Grevesse, N. and Sauval, A. J. (1998). Standard Solar Composition. Space Sci. Rev., 85:161–174.

Gullberg, B., De Breuck, C., Vieira, J. D., Weiß, A., Aguirre, J. E., Aravena, M., Béthermin, M., Bradford, C. M., Bothwell, M. S., Carlstrom, J. E., Chapman, S. C., Fassnacht, C. D., Gonzalez, A. H., Greve, T. R., Hezaveh, Y., Holzapfel, W. L., Husband, K., Ma, J., Malkan, M., Marrone, D. P., Menten, K., Murphy, E. J., Reichardt, C. L., Spilker, J. S., Stark, A. A., Strandet, M., and Welikala, N. (2015). The nature of the [C II] emission in dusty star-forming galaxies from the SPT survey. MNRAS, 449(3):2883–2900.

Guo, Y., Ferguson, H. C., Bell, E. F., Koo, D. C., Conselice, C. J., Giavalisco, M., Kassin, S., Lu, Y., Lucas, R., Mandelker, N., McIntosh, D. H., Primack, J. R., Ravindranath, S., Barro, G., Ceverino, D., Dekel, A., Faber, S. M., Fang, J. J., Koekemoer, A. M., Noeske, K., Rafelski, M., and Straughn, A. (2015). Clumpy Galaxies in CANDELS. I. The Definition of UV Clumps and the Fraction of Clumpy Galaxies at 0.5 < z < 3. ApJ, 800(1):39.

Gutiérrez, L. and Beckman, J. E. (2008). The physics of the HII regions: the photoionization equilibrium in the HII regions of M51. In *Lecture Notes and Essays in Astrophysics*, volume 3, pages 177–188.

Haardt, F. and Madau, P. (1996). Radiative Transfer in a Clumpy Universe. II. The Ultraviolet Extragalactic Background. ApJ, 461:20.

Hahn, O. and Abel, T. (2011). Multi-scale initial conditions for cosmological simulations. MNRAS, 415(3):2101–2121.

Hainline, K. N., D'Eugenio, F., Jakobsen, P., Chevallard, J., Carniani, S., Witstok, J., Ji, Z., Curtis-Lake, E., Johnson, B. D., Robertson, B., Tacchella, S., Curti, M., Charlot, S., Helton, J. M., Arribas, S., Bhatawdekar, R., Bunker, A. J., Cameron, A. J., Egami, E., Eisenstein, D. J., Hausen, R., Kumari, N., Maiolino, R., Perez-Gonzalez, P. G., Rieke, M., Saxena, A., Scholtz, J., Smit, R., Sun, F., Williams, C. C., Willmer, C. N. A., and Willott, C. (2024a). Searching for Emission Lines at $z > 11$: The Role of Damped Lyman-α and Hints About the Escape of Ionizing Photons. *arXiv e-prints*, page arXiv:2404.04325.

Hainline, K. N., Johnson, B. D., Robertson, B., Tacchella, S., Helton, J. M., Sun, F., Eisenstein, D. J., Simmonds, C., Topping, M. W., Whitler, L., Willmer, C. N. A., Rieke, M., Suess, K. A., Hviding, R. E., Cameron, A. J., Alberts, S., Baker, W. M., Baum, S., Bhatawdekar, R., Bonaventura, N., Boyett, K., Bunker, A. J., Carniani, S., Charlot, S., Chevallard, J., Chen, Z., Curti, M., Curtis-Lake, E., D'Eugenio, F., Egami, E., Endsley, R., Hausen, R., Ji, Z., Looser, T. J., Lyu, J., Maiolino, R., Nelson, E., Puskás, D., Rawle, T., Sandles, L., Saxena, A., Smit, R., Stark, D. P., Williams, C. C., Willott, C., and Witstok, J. (2024b). The Cosmos in Its Infancy: JADES Galaxy Candidates at z > 8 in GOODS-S and GOODS-N. ApJ, 964(1):71.

Harikane, Y., Inoue, A. K., Ellis, R. S., Ouchi, M., Nakazato, Y., Yoshida, N., Ono, Y., Sun, F., Sato, R. A., Ferrami, G., Fujimoto, S., Kashikawa, N., McLeod, D. J., Pérez-González, P. G., Sawicki, M., Sugahara, Y., Xu, Y., Yamanaka, S., Carnall, A. C., Cullen, F., Dunlop, J. S., Egami, E., Grogin, N., Isobe, Y., Koekemoer, A. M., Laporte, N., Lee, C.-H., Magee, D., Matsuo, H., Matsuoka, Y., Mawatari, K., Nakajima, K., Nakane, M., Tamura, Y., Umeda, H., and Yanagisawa, H. (2025a). JWST, ALMA, and Keck Spectroscopic Constraints on the UV Luminosity Functions at z $\sim$ 7–14: Clumpiness and Compactness of the Brightest Galaxies in the Early Universe. ApJ, 980(1):138.

Harikane, Y., Nakajima, K., Ouchi, M., Umeda, H., Isobe, Y., Ono, Y., Xu, Y., and Zhang, Y. (2024). Pure Spectroscopic Constraints on UV Luminosity Functions and Cosmic Star Formation History from 25 Galaxies at z $_{spec}$ = 8.61-13.20 Confirmed with JWST/NIRSpec. ApJ, 960(1):56.

Harikane, Y., Ouchi, M., Inoue, A. K., Matsuoka, Y., Tamura, Y., Bakx, T., Fujimoto, S., Moriwaki, K., Ono, Y., Nagao, T., Tadaki, K.-i., Kojima, T., Shibuya, T., Egami, E., Ferrara, A., Gallerani, S., Hashimoto, T., Kohno, K., Matsuda, Y., Matsuo, H., Pallottini, A., Sugahara, Y., and Vallini, L. (2020). Large Population of ALMA Galaxies at z > 6 with Very High [O III] 88 μm to [C II] 158 μm Flux Ratios: Evidence of Extremely High Ionization Parameter or PDR Deficit? ApJ, 896(2):93.

Harikane, Y., Ouchi, M., Oguri, M., Ono, Y., Nakajima, K., Isobe, Y., Umeda, H., Mawatari, K., and Zhang, Y. (2023). A Comprehensive Study of Galaxies at z 9-16 Found in the Early JWST Data: Ultraviolet Luminosity Functions and Cosmic Star Formation History at the Pre-reionization Epoch. ApJS, 265(1):5.

Harikane, Y., Sanders, R. L., Ellis, R., Jones, T., Ouchi, M., Laporte, N., Roberts-Borsani, G., Katz, H., Nakajima, K., Ono, Y., and Gupta, M. (2025b). JWST & ALMA Joint Analysis with [OII]3726,3729, [OIII]4363, [OIII]88m, and [OIII]52m: Multi-Zone Evolution of Electron Densities at $\mathbf{z \sim 0-14}$ and Its Impact on Metallicity Measurements. *arXiv e-prints*, page arXiv:2505.09186.

Harshan, A., Tripodi, R., Martis, N. S., Rihtaršič, G., Bradač, M., Asada, Y., Brammer, G., Desprez, G., Estrada-Carpenter, V., Matharu, J., Markov, V., Muzzin, A., Mowla, L., Noirot, G., Sarrouh, G. T. E., Sawicki, M., Strait, V., and Willott, C. (2024). Detailed Study of Stars and Gas in a z = 8.3 Massive Merger with Extreme Dust Conditions. ApJ, 977(2):L36.

Hartley, B. and Ricotti, M. (2016). Modelling reionization in a bursty universe. MNRAS, 462(2):1164–1179.

Harvey, T., Conselice, C. J., Adams, N. J., Austin, D., Juodžbalis, I., Trussler, J., Li, Q., Ormerod, K., Ferreira, L., Lovell, C. C., Duan, Q., Westcott, L., Harris, H., Bhatawdekar, R., Coe, D., Cohen, S. H., Caruana, J., Cheng, C., Driver, S. P., Frye, B., Furtak, L. J., Grogin, N. A., Hathi, N. P., Holwerda, B. W., Jansen, R. A., Koekemoer, A. M., Marshall, M. A., Nonino, M., Vijayan, A. P., Wilkins, S. M., Windhorst, R., Willmer, C. N. A., Yan, H., and Zitrin, A. (2025). EPOCHS. IV. SED Modeling Assumptions and Their Impact on the Stellar Mass Function at 6.5 ≤ z ≤ 13.5 Using PEARLS and Public JWST Observations. ApJ, 978(1):89.

Hashimoto, T., Álvarez-Márquez, J., Fudamoto, Y., Colina, L., Inoue, A. K., Nakazato, Y., Ceverino, D., Yoshida, N., Costantin, L., Sugahara, Y., Gómez, A. C., Blanco-Prieto, C., Mawatari, K., Arribas, S., Marques-Chaves, R., Pereira-Santaella, M., Bakx, T. J. L. C., Hagimoto, M., Hashigaya, T., Matsuo, H., Tamura, Y., Usui, M., and Ren, Y. W. (2023). Reionization and the ISM/Stellar Origins with JWST and ALMA (RIOJA): The Core of the Highest-redshift Galaxy Overdensity at z = 7.88 Confirmed by NIRSpec/JWST. ApJ, 955(1):L2.

Hashimoto, T., Inoue, A. K., Mawatari, K., Tamura, Y., Matsuo, H., Furusawa, H., Harikane, Y., Shibuya, T., Knudsen, K. K., Kohno, K., Ono, Y., Zackrisson, E., Okamoto, T., Kashikawa, N., Oesch, P. A., Ouchi, M., Ota, K., Shimizu, I., Taniguchi, Y., Umehata, H., and Watson, D. (2019). Big Three Dragons: A z = 7.15 Lyman-break galaxy detected in [O III] 88 μm, [C II] 158 μm, and dust continuum with ALMA. PASJ, 71(4):71.

Hashimoto, T., Laporte, N., Mawatari, K., Ellis, R. S., Inoue, A. K., Zackrisson, E., Roberts-Borsani, G., Zheng, W., Tamura, Y., Bauer, F. E., Fletcher, T., Harikane, Y., Hatsukade, B., Hayatsu, N. H., Matsuda, Y., Matsuo, H., Okamoto, T., Ouchi, M., Pelló, R., Rydberg, C.-E., Shimizu, I., Taniguchi, Y., Umehata, H., and Yoshida, N. (2018). The onset of star formation 250 million years after the Big Bang. Nature, 557(7705):392–395.

Haslbauer, M., Kroupa, P., Zonoozi, A. H., and Haghi, H. (2022). Has JWST Already Falsified Dark-matter-driven Galaxy Formation? ApJ, 939(2):L31.

Hayes, M., Schaerer, D., Östlin, G., Mas-Hesse, J. M., Atek, H., and Kunth, D. (2011). On the Redshift Evolution of the Lyα Escape Fraction and the Dust Content of Galaxies. ApJ, 730(1):8.

He, C.-C., Ricotti, M., and Geen, S. (2019). Simulating star clusters across cosmic time - I. Initial mass function, star formation rates, and efficiencies. MNRAS, 489(2):1880–1898.

Hebb, M. H. and Menzel, D. H. (1940). Physical Processes in Gaseous Nebulae. X. Collisional Excitation of Nebulium. ApJ, 92:408.

Heintz, K. E., Giménez-Arteaga, C., Fujimoto, S., Brammer, G., Espada, D., Gillman, S., González-López, J., Greve, T. R., Harikane, Y., Hatsukade, B., Knudsen, K. K., Koekemoer, A. M., Kohno, K., Kokorev, V., Lee, M. M., Magdis, G. E., Nelson, E. J., Rizzo, F., Sanders, R. L., Schaerer, D., Shapley, A. E., Strait, V. B., Toft, S., Valentino, F., van der Wel, A., Vijayan, A. P., Watson, D., Bauer, F. E., Christiansen, C. R., and Wilson, S. N. (2023). The Gas and Stellar Content of a Metal-poor Galaxy at z = 8.496 as Revealed by JWST and ALMA. ApJ, 944(2):L30.

Heintz, K. E., Pollock, C., Witstok, J., Carniani, S., Hainline, K. N., D'Eugenio, F., Terp, C., Saxena, A., and Watson, D. (2025). Dissecting the massive pristine, neutral gas reservoir of a remarkably bright galaxy at z = 14.179. *arXiv e-prints*, page arXiv:2502.06016.

Heintz, K. E., Watson, D., Oesch, P. A., Narayanan, D., and Madden, S. C. (2021). Measuring the H I Content of Individual Galaxies Out to the Epoch of Reionization with [C II]. ApJ, 922(2):147.

Helton, J. M., Rieke, G. H., Alberts, S., Wu, Z., Eisenstein, D. J., Hainline, K. N., Carniani, S., Ji, Z., Baker, W. M., Bhatawdekar, R., Bunker, A. J., Cargile, P. A., Charlot, S., Chevallard, J., D'Eugenio, F., Egami, E., Johnson, B. D., Jones, G. C., Lyu, J., Maiolino, R., Pérez-González, P. G., Rieke, M. J., Robertson, B., Saxena, A., Scholtz, J., Shivaei, I., Sun, F., Tacchella, S., Whitler, L., Williams, C. C., Willmer, C. N. A., Willott, C., Witstok, J., and Zhu, Y. (2025). Photometric detection at 7.7 μm of a galaxy beyond redshift 14 with JWST/MIRI. *Nature Astronomy*.

Herrera-Camus, R., Förster Schreiber, N., Genzel, R., Tacconi, L., Bolatto, A., Davies, R. L., Fisher, D., Lutz, D., Naab, T., Shimizu, T., Tadaki, K., and Übler, H. (2021). Kiloparsec view of a typical star-forming galaxy when the Universe was ∼1 Gyr old. I. Properties of outflow, halo, and interstellar medium. A&A, 649:A31.

Hirano, S., Hosokawa, T., Yoshida, N., Omukai, K., and Yorke, H. W. (2015). Primordial star formation under the influence of far ultraviolet radiation: 1540 cosmological haloes and the stellar mass distribution. MNRAS, 448(1):568–587.

Hirano, S., Hosokawa, T., Yoshida, N., Umeda, H., Omukai, K., Chiaki, G., and Yorke, H. W. (2014). One Hundred First Stars: Protostellar Evolution and the Final Masses. ApJ, 781(2):60.

Hirano, S. and Yoshida, N. (2024). Early Structure Formation from Primordial Density Fluctuations with a Blue, Tilted Power Spectrum: High-redshift Galaxies. ApJ, 963(1):2.

Hirashita, H. (1999). Dust-to-Gas Ratio and Metallicity in Dwarf Galaxies. ApJ, 522(1):220–224.

Hirashita, H. and Ferrara, A. (2002). Effects of dust grains on early galaxy evolution. MNRAS, 337(3):921–937.

Hirschmann, M., Charlot, S., Feltre, A., Curtis-Lake, E., Somerville, R. S., Chevallard, J., Choi, E., Nelson, D., Morisset, C., Plat, A., and Vidal-Garcia, A. (2022). Emission-line properties of IllustrisTNG galaxies: from local diagnostic diagrams to high-redshift predictions for JWST. *arXiv e-prints*, page arXiv:2212.02522.

Hirschmann, M., Charlot, S., Feltre, A., Curtis-Lake, E., Somerville, R. S., Chevallard, J., Choi, E., Nelson, D., Morisset, C., Plat, A., and Vidal-Garcia, A. (2023). Emission-line properties of IllustrisTNG galaxies: from local diagnostic diagrams to high-redshift predictions for JWST. MNRAS, 526(3):3610–3636.

Hirschmann, M., Charlot, S., Feltre, A., Naab, T., Choi, E., Ostriker, J. P., and Somerville, R. S. (2017). Synthetic nebular emission from massive galaxies - I: origin of the cosmic evolution of optical emission-line ratios. MNRAS, 472(2):2468–2495.

Hodge, J. A. and da Cunha, E. (2020). High-redshift star formation in the Atacama large millimetre/-submillimetre array era. *Royal Society Open Science*, 7(12):200556.

Hoefner, S., Jorgensen, U. G., Loidl, R., and Aringer, B. (1998). Dynamic model atmospheres of AGB stars. I. Atmospheric structure and dynamics. A&A, 340:497–507.

Hopkins, P. F., Croton, D., Bundy, K., Khochfar, S., van den Bosch, F., Somerville, R. S., Wetzel, A., Keres, D., Hernquist, L., Stewart, K., Younger, J. D., Genel, S., and Ma, C.-P. (2010). Mergers in ΛCDM: Uncertainties in Theoretical Predictions and Interpretations of the Merger Rate. ApJ, 724(2):915–945.

Hopkins, P. F., Kereš, D., Murray, N., Quataert, E., and Hernquist, L. (2012). Stellar feedback and bulge formation in clumpy discs. MNRAS, 427(2):968–978.

Hopkins, P. F., Quataert, E., and Murray, N. (2011). Self-regulated star formation in galaxies via momentum input from massive stars. MNRAS, 417(2):950–973.

Hopkins, P. F., Wetzel, A., Kereš, D., Faucher-Giguère, C.-A., Quataert, E., Boylan-Kolchin, M., Murray, N., Hayward, C. C., Garrison-Kimmel, S., Hummels, C., Feldmann, R., Torrey, P., Ma, X., Anglés-Alcázar, D., Su, K.-Y., Orr, M., Schmitz, D., Escala, I., Sanderson, R., Grudić, M. Y., Hafen, Z., Kim, J.-H., Fitts, A., Bullock, J. S., Wheeler, C., Chan, T. K., Elbert, O. D., and Narayanan, D. (2018). FIRE-2 simulations: physics versus numerics in galaxy formation. MNRAS, 480(1):800–863.

Hosokawa, T., Omukai, K., Yoshida, N., and Yorke, H. W. (2011). Protostellar Feedback Halts the Growth of the First Stars in the Universe. *Science*, 334(6060):1250.

Howell, J. H., Armus, L., Mazzarella, J. M., Evans, A. S., Surace, J. A., Sanders, D. B., Petric, A., Appleton, P., Bothun, G., Bridge, C., Chan, B. H. P., Charmandaris, V., Frayer, D. T., Haan, S., Inami, H., Kim, D.-C., Lord, S., Madore, B. F., Melbourne, J., Schulz, B., U, V., Vavilkin, T., Veilleux, S., and Xu, K. (2010). The Great Observatories All-sky LIRG Survey: Comparison of Ultraviolet and Far-infrared Properties. ApJ, 715(1):572–588.

Hsiao, T. Y.-Y., Álvarez-Márquez, J., Coe, D., Crespo Gómez, A., Abdurro'uf, Dayal, P., Larson, R. L., Bik, A., Blanco-Prieto, C., Colina, L., Pérez-González, P. G., Costantin, L., Prieto-Jiménez, C., Adamo, A., Bradley, L. D., Conselice, C. J., Fujimoto, S., Furtak, L. J., Hutchison, T. A., James, B. L., Jiménez-Teja, Y., Jung, I., Kokorev, V., Mingozzi, M., Norman, C., Ricotti, M., Rigby, J. R., Sharon, K., Vanzella, E., Welch, B., Xu, X., Zackrisson, E., and Zitrin, A. (2024). JWST MIRI Detections of Hα and [O III] and a Direct Metallicity Measurement of the z = 10.17 Lensed Galaxy MACS0647âĂŚJD. ApJ, 973(2):81.

Hsiao, T. Y.-Y., Coe, D., Abdurro'uf, Whitler, L., Jung, I., Khullar, G., Meena, A. K., Dayal, P., Barrow, K. S. S., Santos-Olmsted, L., Casselman, A., Vanzella, E., Nonino, M., Jiménez-Teja, Y., Oguri, M., Stark, D. P., Furtak, L. J., Zitrin, A., Adamo, A., Brammer, G., Bradley, L., Diego, J. M., Zackrisson, E., Finkelstein, S. L., Windhorst, R. A., Bhatawdekar, R., Hutchison, T. A., Broadhurst, T., Dimauro, P., Andrade-Santos, F., Eldridge, J. J., Acebron, A., Avila, R. J., Bayliss, M. B., Benítez, A., Binggeli, C., Bolan, P., Bradač, M., Carnall, A. C., Conselice, C. J., Donahue, M., Frye, B., Fujimoto, S., Henry, A., James, B. L., Kassin, S. A., Kewley, L., Larson, R. L., Lauer, T., Law, D., Mahler, G., Mainali, R., McCandliss, S., Nicholls, D., Pirzkal, N., Postman, M., Rigby, J. R., Ryan, R., Senchyna, P., Sharon, K., Shimizu, I., Strait, V., Tang, M., Trenti, M., Vikaeus, A., and Welch, B. (2023). JWST Reveals a Possible z 11 Galaxy Merger in Triply Lensed MACS0647-JD. ApJ, 949(2):L34.

Huang, H.-L., Jiang, J.-Q., and Piao, Y.-S. (2024). High-redshift JWST massive galaxies and the initial clustering of supermassive primordial black holes. *arXiv e-prints*, page arXiv:2407.15781.

Huertas-Company, M., Iyer, K. G., Angeloudi, E., Bagley, M. B., Finkelstein, S. L., Kartaltepe, J., McGrath, E. J., Sarmiento, R., Vega-Ferrero, J., Arrabal Haro, P., Behroozi, P., Buitrago, F., Cheng, Y., Costantin, L., Dekel, A., Dickinson, M., Elbaz, D., Grogin, N. A., Hathi, N. P., Holwerda, B. W., Koekemoer, A. M., Lucas, R. A., Papovich, C., Pérez-González, P. G., Pirzkal, N., Seillé, L. M., de la Vega, A., Wuyts, S., Yang, G., and Yung, L. Y. A. (2024). Galaxy morphology from z $\sim$ 6 through the lens of JWST. A&A, 685:A48.

Hutter, A., Cueto, E. R., Dayal, P., Gottlöber, S., Trebitsch, M., and Yepes, G. (2025). ASTRAEUS: X. Indications of a top-heavy initial mass function in highly star-forming galaxies from JWST observations at z > 10. A&A, 694:A254.

Ikeda, R., Tadaki, K.-i., Mitsuhashi, I., Aravena, M., De Looze, I., Förster Schreiber, N. M., González-López, J., Herrera-Camus, R., Spilker, J., Barcos-Muñoz, L., Bowler, R. A. A., Calistro Rivera, G., da Cunha, E., Davies, R., Díaz-Santos, T., Ferrara, A., Killi, M., Lee, L. L., Li, J., Lutz, D., Posses, A., Smit, R., Solimano, M., Telikova, K., Übler, H., Veilleux, S., and Villanueva, V. (2025). The ALMA-CRISTAL Survey: Spatial extent of [CII] line emission in star-forming galaxies at z = 4âĂŚ6. A&A, 693:A237.

Inami, H., Algera, H. S. B., Schouws, S., Sommovigo, L., Bouwens, R., Smit, R., Stefanon, M., Bowler, R. A. A., Endsley, R., Ferrara, A., Oesch, P., Stark, D., Aravena, M., Barrufet, L., da Cunha, E., Dayal, P., De Looze, I., Fudamoto, Y., Gonzalez, V., Graziani, L., Hodge, J. A., Hygate, A. P. S., Nanayakkara, T., Pallottini, A., Riechers, D. A., Schneider, R., Topping, M., and van der Werf, P. (2022). The ALMA REBELS Survey: dust continuum detections at z > 6.5. MNRAS, 515(3):3126–3143.

Inayoshi, K., Harikane, Y., Inoue, A. K., Li, W., and Ho, L. C. (2022). A Lower Bound of Star Formation Activity in Ultra-high-redshift Galaxies Detected with JWST: Implications for Stellar Populations and Radiation Sources. ApJ, 938(2):L10.

Inayoshi, K., Kimura, S. S., and Noda, H. (2024). Weakness of X-rays and Variability in High-redshift AGNs with Super-Eddington Accretion. *arXiv e-prints*, page arXiv:2412.03653.

Inayoshi, K. and Maiolino, R. (2025). Extremely Dense Gas around Little Red Dots and High-redshift Active Galactic Nuclei: A Nonstellar Origin of the Balmer Break and Absorption Features. ApJ, 980(2):L27.

Inayoshi, K., Visbal, E., and Haiman, Z. (2020). The Assembly of the First Massive Black Holes. ARA&A, 58:27–97.

Inoue, A. K. (2005). Attenuation law of normal disc galaxies with clumpy distributions of stars and dust. MNRAS, 359(1):171–182.

Inoue, A. K. (2011). Rest-frame ultraviolet-to-optical spectral characteristics of extremely metal-poor and metal-free galaxies. MNRAS, 415(3):2920–2931.

Inoue, A. K., Hashimoto, T., Chihara, H., and Koike, C. (2020). Radiative equilibrium estimates of dust temperature and mass in high-redshift galaxies. MNRAS, 495(2):1577–1592.

Inoue, A. K., Shimizu, I., Tamura, Y., Matsuo, H., Okamoto, T., and Yoshida, N. (2014). ALMA Will Determine the Spectroscopic Redshift z > 8 with FIR [O III] Emission Lines. ApJ, 780(2):L18.

Inoue, A. K., Tamura, Y., Matsuo, H., Mawatari, K., Shimizu, I., Shibuya, T., Ota, K., Yoshida, N., Zackrisson, E., Kashikawa, N., Kohno, K., Umehata, H., Hatsukade, B., Iye, M., Matsuda, Y., Okamoto, T., and Yamaguchi, Y. (2016a). Detection of an oxygen emission line from a high-redshift galaxy in the reionization epoch. *Science*, 352(6293):1559–1562.

Inoue, S., Dekel, A., Mandelker, N., Ceverino, D., Bournaud, F., and Primack, J. (2016b). Non-linear violent disc instability with high Toomre's Q in high-redshift clumpy disc galaxies. MNRAS, 456(2):2052–2069.

Inoue, S. and Yoshida, N. (2019). Clumpy galaxies in cosmological simulations: the effect of ISM model. MNRAS, 488(3):4400–4412.

Ishikawa, Y., Zakamska, N. L., Shen, Y., Liu, X., Chen, Y.-C., Hwang, H.-C., Vayner, A., Rupke, D. S. N., Veilleux, S., Wylezalek, D., Gross, A. C., Sankar, S., and Diachenko, N. (2025). VODKA-JWST: Synchronized Growth of Two Supermassive Black Holes in a Massive Gas Disk? A 3.8 kpc Separation Dual Quasar at Cosmic Noon with the NIRSpec Integral Field Unit. ApJ, 982(1):22.

Isobe, Y., Ouchi, M., Nakajima, K., Harikane, Y., Ono, Y., Xu, Y., Zhang, Y., and Umeda, H. (2023a). Redshift Evolution of the Electron Density in the ISM at $z \sim 0 - 9$ Uncovered with JWST/NIRSpec Spectra and Line-Spread Function Determinations. *arXiv e-prints*, page arXiv:2301.06811.

Isobe, Y., Ouchi, M., Tominaga, N., Watanabe, K., Nakajima, K., Umeda, H., Yajima, H., Harikane, Y., Fukushima, H., Xu, Y., Ono, Y., and Zhang, Y. (2023b). JWST Identification of Extremely Low C/N Galaxies with [N/O] $\gtrsim$ 0.5 at z 6-10 Evidencing the Early CNO-cycle Enrichment and a Connection with Globular Cluster Formation. ApJ, 959(2):100.

Izotov, Y. I., Chisholm, J., Worseck, G., Guseva, N. G., Schaerer, D., and Prochaska, J. X. (2022). Lyman alpha and Lyman continuum emission of Mg II-selected star-forming galaxies. MNRAS, 515(2):2864–2881.

Izumi, T., Matsuoka, Y., Onoue, M., Strauss, M. A., Umehata, H., Silverman, J. D., Nagao, T., Imanishi, M., Kohno, K., Toba, Y., Iwasawa, K., Nakanishi, K., Sawamura, M., Fujimoto, S., Kikuta, S., Kawaguchi, T., Aoki, K., and Goto, T. (2024). Merging Gas-rich Galaxies That Harbor Low-luminosity Twin Quasars at z = 6.05: A Promising Progenitor of the Most Luminous Quasars. ApJ, 972(1):116.

Jenkins, E. B. (2009). A Unified Representation of Gas-Phase Element Depletions in the Interstellar Medium. ApJ, 700(2):1299–1348.

Jeong, T. B., Jeon, M., Song, H., and Bromm, V. (2025). Simulating High-redshift Galaxies: Enhancing UV Luminosity with Star Formation Efficiency and a Top-heavy IMF. ApJ, 980(1):10.

Ji, X., Übler, H., Maiolino, R., D'Eugenio, F., Arribas, S., Bunker, A. J., Charlot, S., Perna, M., Rodríguez Del Pino, B., Böker, T., Cresci, G., Curti, M., Kumari, N., and Lamperti, I. (2024). GA-NIFS: an extremely nitrogen-loud and chemically stratified galaxy at z 5.55. MNRAS, 535(1):881–908.

Joblin, C., Leger, A., and Martin, P. (1992). Contribution of Polycyclic Aromatic Hydrocarbon Molecules to the Interstellar Extinction Curve. ApJ, 393:L79.

Jones, G. C., Bowler, R., Bunker, A. J., Arribas, S., Carniani, S., Charlot, S., Perna, M., Rodríguez Del Pino, B., Übler, H., Willott, C. J., Chevallard, J., Cresci, G., Parlanti, E., Scholtz, J., and Venturi, G. (2024a). GA-NIFS: interstellar medium properties and tidal interactions in the evolved massive merging system B14-65666 at z = 7.152. *arXiv e-prints*, page arXiv:2412.15027.

Jones, G. C., Bunker, A. J., Telikova, K., Arribas, S., Carniani, S., Charlot, S., D'Eugenio, F., Maiolino, R., Perna, M., Rodriguez Del Pino, B., Ubler, H., Willott, C., Aravena, M., Boker, T., Cresci, G., Curti, M., Herrera-Camus, R., Lamperti, I., Parlanti, E., Perez-Gonzalez, P. G., and Villanueva, V. (2024b). GA-NIFS: Witnessing the complex assembly of a massive star-forming system at $z = 5.7$. *arXiv e-prints*, page arXiv:2405.12955.

Jones, G. C., Übler, H., Perna, M., Arribas, S., Bunker, A. J., Carniani, S., Charlot, S., Maiolino, R., Del Pino, B. R., Willott, C., Bowler, R. A. A., Böker, T., Cameron, A. J., Chevallard, J., Cresci, G., Curti, M., D'Eugenio, F., Kumari, N., Saxena, A., Scholtz, J., Venturi, G., and Witstok, J. (2024c). GA-NIFS: JWST/NIRSpec integral field unit observations of HFLS3 reveal a dense galaxy group at z $\sim$ 6.3. A&A, 682:A122.

Jonsson, P., Groves, B. A., and Cox, T. J. (2010). High-resolution panchromatic spectral models of galaxies including photoionization and dust. MNRAS, 403(1):17–44.

Jubelgas, M., Springel, V., Enßlin, T., and Pfrommer, C. (2008). Cosmic ray feedback in hydrodynamical simulations of galaxy formation. A&A, 481(1):33–63.

Jungwiert, B., Combes, F., and Palouš, J. (2001). Continuous stellar mass-loss in N-body models of galaxies. A&A, 376:85–97.

Kageura, Y., Ouchi, M., Nakane, M., Umeda, H., Harikane, Y., Yoshiura, S., Nakajima, K., Yajima, H., and Thai, T. T. (2025). Census of Lyα Emission from $\sim$600 Galaxies at z = 5–14: Evolution of the Lyα Luminosity Function and a Late Sharp Cosmic Reionization. ApJS, 278(2):33.

Kalita, B. S., Silverman, J. D., Daddi, E., Mercier, W., Ho, L. C., and Ding, X. (2024). Near-IR clumps and their properties in high-z galaxies with JWST/NIRCam. *arXiv e-prints*, page arXiv:2402.02679.

Kanekar, N., Wagg, J., Chary, R. R., and Carilli, C. L. (2013). A Search for C II 158 μm Line Emission in HCM 6A, a Lyα Emitter at z = 6.56. ApJ, 771(2):L20.

Kannan, R., Puchwein, E., Smith, A., Borrow, J., Garaldi, E., Keating, L., Vogelsberger, M., Zier, O., McClymont, W., Shen, X., Popovic, F., Tacchella, S., Hernquist, L., and Springel, V. (2025). Introducing the THESAN-ZOOM project: radiation-hydrodynamic simulations of high-redshift galaxies with a multi-phase interstellar medium. *arXiv e-prints*, page arXiv:2502.20437.

Kannan, R., Smith, A., Garaldi, E., Shen, X., Vogelsberger, M., Pakmor, R., Springel, V., and Hernquist, L. (2022). The THESAN project: predictions for multitracer line intensity mapping in the epoch of reionization. MNRAS, 514(3):3857–3878.

Kannan, R., Springel, V., Hernquist, L., Pakmor, R., Delgado, A. M., Hadzhiyska, B., Hernández-Aguayo, C., Barrera, M., Ferlito, F., Bose, S., White, S. D. M., Frenk, C., Smith, A., and Garaldi, E. (2023). The MillenniumTNG project: the galaxy population at z $\geq$ 8. MNRAS, 524(2):2594–2605.

Kashino, D., Lilly, S. J., Matthee, J., Eilers, A.-C., Mackenzie, R., Bordoloi, R., and Simcoe, R. A. (2023). EIGER. I. A Large Sample of [O III]-emitting Galaxies at 5.3 < z < 6.9 and Direct Evidence for Local Reionization by Galaxies. ApJ, 950(1):66.

Kashino, D., Silverman, J. D., Sanders, D., Kartaltepe, J. S., Daddi, E., Renzini, A., Valentino, F., Rodighiero, G., Juneau, S., Kewley, L. J., Zahid, H. J., Arimoto, N., Nagao, T., Chu, J., Sugiyama, N., Civano, F., Ilbert, O., Kajisawa, M., Le Fèvre, O., Maier, C., Masters, D., Miyaji, T., Onodera, M., Puglisi, A., and Taniguchi, Y. (2017). The FMOS-COSMOS Survey of Star-forming Galaxies at z $\approx$ 1.6. IV. Excitation State and Chemical Enrichment of the Interstellar Medium. ApJ, 835(1):88.

Katz, H., Galligan, T. P., Kimm, T., Rosdahl, J., Haehnelt, M. G., Blaizot, J., Devriendt, J., Slyz, A., Laporte, N., and Ellis, R. (2019). Probing cosmic dawn with emission lines: predicting infrared and nebular line emission for ALMA and JWST. MNRAS, 487(4):5902–5921.

Katz, H., Kimm, T., Ellis, R. S., Devriendt, J., and Slyz, A. (2023a). The challenges of identifying Population III stars in the early Universe. MNRAS, 524(1):351–360.

Katz, H., Kimm, T., Haehnelt, M., Sijacki, D., Rosdahl, J., and Blaizot, J. (2018). A Census of the LyC photons that form the UV background during reionization. MNRAS, 478(4):4986–5005.

Katz, H., Kimm, T., Sijacki, D., and Haehnelt, M. G. (2017). Interpreting ALMA observations of the ISM during the epoch of reionization. MNRAS, 468(4):4831–4861.

Katz, H., Rey, M. P., Cadiou, C., Kimm, T., and Agertz, O. (2024). The Impact of Star Formation and Feedback Recipes on the Stellar Mass and Interstellar Medium of High-Redshift Galaxies. *arXiv e-prints*, page arXiv:2411.07282.

Katz, H., Rosdahl, J., Kimm, T., Blaizot, J., Choustikov, N., Farcy, M., Garel, T., Haehnelt, M. G., Michel-Dansac, L., and Ocvirk, P. (2023b). The SPHINX Public Data Release: Forward Modelling High-Redshift JWST Observations with Cosmological Radiation Hydrodynamics Simulations. *The Open Journal of Astrophysics*, 6:44.

Katz, H., Rosdahl, J., Kimm, T., Blaizot, J., Choustikov, N., Farcy, M., Garel, T., Haehnelt, M. G., Michel-Dansac, L., and Ocvirk, P. (2023c). The SPHINX Public Data Release: Forward Modelling High-Redshift JWST Observations with Cosmological Radiation Hydrodynamics Simulations. *The Open Journal of Astrophysics*, 6:44.

Katz, H., Rosdahl, J., Kimm, T., Garel, T., Blaizot, J., Haehnelt, M. G., Michel-Dansac, L., Martin-Alvarez, S., Devriendt, J., Slyz, A., Teyssier, R., Ocvirk, P., Laporte, N., and Ellis, R. (2022). The nature of high [O III]$_{88\mu m}$/[C II]$_{158\mu m}$ galaxies in the epoch of reionization: Low carbon abundance and a top-heavy IMF? MNRAS, 510(4):5603–5622.

Kennicutt, Robert C., J. (1998a). Star Formation in Galaxies Along the Hubble Sequence. ARA&A, 36:189–232.

Kennicutt, Jr., R. C. (1998b). Star Formation in Galaxies Along the Hubble Sequence. ARA&A, 36:189–232.

Kido, D., Ioka, K., Hotokezaka, K., Inayoshi, K., and Irwin, C. M. (2025). Black Hole Envelopes in Little Red Dots. *arXiv e-prints*, page arXiv:2505.06965.

Killi, M., Watson, D., Fujimoto, S., Akins, H., Knudsen, K., Richard, J., Harikane, Y., Rigopoulou, D., Rizzo, F., Ginolfi, M., Popping, G., and Kokorev, V. (2023). A solar metallicity galaxy at z > 7? Possible detection of the [N II] 122 μm and [O III] 52 μm lines. MNRAS, 521(2):2526–2534.

Kim, J.-h., Abel, T., Agertz, O., Bryan, G. L., Ceverino, D., Christensen, C., Conroy, C., Dekel, A., Gnedin, N. Y., Goldbaum, N. J., Guedes, J., Hahn, O., Hobbs, A., Hopkins, P. F., Hummels, C. B., Iannuzzi, F., Keres, D., Klypin, A., Kravtsov, A. V., Krumholz, M. R., Kuhlen, M., Leitner, S. N., Madau, P., Mayer, L., Moody, C. E., Nagamine, K., Norman, M. L., Onorbe, J., O'Shea, B. W., Pillepich, A., Primack, J. R., Quinn, T., Read, J. I., Robertson, B. E., Rocha, M., Rudd, D. H., Shen, S., Smith, B. D., Szalay, A. S., Teyssier, R., Thompson, R., Todoroki, K., Turk, M. J., Wadsley, J. W., Wise, J. H., Zolotov, A., and AGORA Collaboration29, t. (2014). The AGORA High-resolution Galaxy Simulations Comparison Project. ApJS, 210(1):14.

Kimm, T. and Cen, R. (2014). Escape Fraction of Ionizing Photons during Reionization: Effects due to Supernova Feedback and Runaway OB Stars. ApJ, 788(2):121.

Kimm, T., Cen, R., Devriendt, J., Dubois, Y., and Slyz, A. (2015). Towards simulating star formation in turbulent high-z galaxies with mechanical supernova feedback. MNRAS, 451(3):2900–2921.

Kimm, T., Cen, R., Rosdahl, J., and Yi, S. K. (2016). Formation of Globular Clusters in Atomic-cooling Halos Via Rapid Gas Condensation and Fragmentation during the Epoch of Reionization. ApJ, 823(1):52.

Kimm, T., Katz, H., Haehnelt, M., Rosdahl, J., Devriendt, J., and Slyz, A. (2017). Feedback-regulated star formation and escape of LyC photons from mini-haloes during reionization. MNRAS, 466(4):4826–4846.

Kitzbichler, M. G. and White, S. D. M. (2008). A calibration of the relation between the abundance of close galaxy pairs and the rate of galaxy mergers. MNRAS, 391(4):1489–1498.

Kiyota, T., Ouchi, M., Xu, Y., Nakazato, Y., Soga, K., Yajima, H., Fujimoto, S., Harikane, Y., Nakajima, K., Ono, Y., Sun, D., Kusakabe, H., Ceverino, D., Hatsukade, B., Iono, D., Kohno, K., and Nakanishi, K. (2025). Comprehensive JWST+ALMA Study on the Extended Ly Emitters, Himiko and CR7 at $z \sim 7$: Blue Major Merger Systems in Stark Contrast to Submillimeter Galaxies. *arXiv e-prints*, page arXiv:2504.03156.

Klypin, A. and Holtzman, J. (1997). Particle-Mesh code for cosmological simulations. *arXiv e-prints*, pages astro–ph/9712217.

Klypin, A., Yepes, G., Gottlöber, S., Prada, F., and Heß, S. (2016). MultiDark simulations: the story of dark matter halo concentrations and density profiles. MNRAS, 457(4):4340–4359.

Klypin, A. A., Trujillo-Gomez, S., and Primack, J. (2011). Dark Matter Halos in the Standard Cosmological Model: Results from the Bolshoi Simulation. ApJ, 740(2):102.

Knudsen, K. K., Richard, J., Kneib, J.-P., Jauzac, M., Clément, B., Drouart, G., Egami, E., and Lindroos, L. (2016). [C II] emission in z $\sim$ 6 strongly lensed, star-forming galaxies. MNRAS, 462(1):L6–L10.

Kobayashi, C. and Ferrara, A. (2024). Rapid Chemical Enrichment by Intermittent Star Formation in GN-z11. ApJ, 962(1):L6.

Kohandel, M., Ferrara, A., Pallottini, A., Vallini, L., Sommovigo, L., and Ziparo, F. (2023). Interpreting ALMA non-detections of JWST super-early galaxies. MNRAS, 520(1):L16–L20.

Kohandel, M., Pallottini, A., and Ferrara, A. (2025). Synthetic Clones of the Most Distant Galaxies in the Universe. *arXiv e-prints*, page arXiv:2505.07935.

Kohandel, M., Pallottini, A., Ferrara, A., Carniani, S., Gallerani, S., Vallini, L., Zanella, A., and Behrens, C. (2020). Velocity dispersion in the interstellar medium of early galaxies. MNRAS, 499(1):1250–1265.

Kohandel, M., Pallottini, A., Ferrara, A., Zanella, A., Behrens, C., Carniani, S., Gallerani, S., and Vallini, L. (2019). Kinematics of z $\geq$ 6 galaxies from [C II] line emission. MNRAS, 487(3):3007–3020.

Kohandel, M., Pallottini, A., Ferrara, A., Zanella, A., Rizzo, F., and Carniani, S. (2024). Dynamically cold disks in the early Universe: Myth or reality? A&A, 685:A72.

Komatsu, E., Dunkley, J., Nolta, M. R., Bennett, C. L., Gold, B., Hinshaw, G., Jarosik, N., Larson, D., Limon, M., Page, L., Spergel, D. N., Halpern, M., Hill, R. S., Kogut, A., Meyer, S. S., Tucker, G. S., Weiland, J. L., Wollack, E., and Wright, E. L. (2009). Five-Year Wilkinson Microwave Anisotropy Probe Observations: Cosmological Interpretation. ApJS, 180(2):330–376.

Koprowski, M. P., Coppin, K. E. K., Geach, J. E., McLure, R. J., Almaini, O., Blain, A. W., Bremer, M., Bourne, N., Chapman, S. C., Conselice, C. J., Dunlop, J. S., Farrah, D., Hartley, W., Karim, A., Knudsen, K. K., Michałowski, M. J., Scott, D., Simpson, C., Smith, D. J. B., and van der Werf, P. P. (2018). A direct calibration of thtae IRX-β relation in Lyman-break Galaxies at z = 3-5. MNRAS, 479(4):4355–4366.

Kravtsov, A. V. (2003). On the Origin of the Global Schmidt Law of Star Formation. ApJ, 590(1):L1–L4.

Kravtsov, A. V., Klypin, A. A., and Khokhlov, A. M. (1997). Adaptive Refinement Tree: A New High-Resolution N-Body Code for Cosmological Simulations. ApJS, 111(1):73–94.

Kumari, N., Smit, R., Leitherer, C., Witstok, J., Irwin, M. J., Sirianni, M., and Aloisi, A. (2024). A study of extreme C III]1908 & [O III]88/[C II]157 emission in Pox 186: implications for JWST+ALMA (FUV + FIR) studies of distant galaxies. MNRAS, 529(2):781–801.

Kuruvanthodi, A., Schaerer, D., Marques-Chaves, R., Korber, D., Weibel, A., Oesch, P. A., and Roberts-Borsani, G. (2024). Strong Balmer break objects at z $\sim$ 7–10 uncovered with JWST. A&A, 691:A310.

Lagache, G., Cousin, M., and Chatzikos, M. (2018). The [CII] 158 μm line emission in high-redshift galaxies. A&A, 609:A130.

Lamers, H. J. G. L. M. and Cassinelli, J. P. (1999). *Introduction to Stellar Winds*.

Langan, I., Ceverino, D., and Finlator, K. (2020). Weak evolution of the mass-metallicity relation at cosmic dawn in the FirstLight simulations. MNRAS, 494(2):1988–1993.

Laporte, N., Ellis, R. S., Boone, F., Bauer, F. E., Quénard, D., Roberts-Borsani, G. W., Pelló, R., Pérez-Fournon, I., and Streblyanska, A. (2017). Dust in the Reionization Era: ALMA Observations of a z = 8.38 Gravitationally Lensed Galaxy. ApJ, 837(2):L21.

Laporte, N., Katz, H., Ellis, R. S., Lagache, G., Bauer, F. E., Boone, F., Inoue, A. K., Hashimoto, T., Matsuo, H., Mawatari, K., and Tamura, Y. (2019). The absence of [C II] 158 μm emission in spectroscopically confirmed galaxies at z > 8. MNRAS, 487(1):L81–L85.

Larson, R. B. (1969). Numerical calculations of the dynamics of collapsing proto-star. MNRAS, 145:271.

Laseter, I. H., Maseda, M. V., Curti, M., Maiolino, R., D'Eugenio, F., Cameron, A. J., Looser, T. J., Arribas, S., Baker, W. M., Bhatawdekar, R., Boyett, K., Bunker, A. J., Carniani, S., Charlot, S., Chevallard, J., Curtis-lake, E., Egami, E., Eisenstein, D. J., Hainline, K., Hausen, R., Ji, Z., Kumari, N., Perna, M., Rawle, T., Rix, H.-W., Robertson, B., Rodríguez Del Pino, B., Sandles, L., Scholtz, J., Smit, R., Tacchella, S., Übler, H., Williams, C. C., Willott, C., and Witstok, J. (2024). JADES: Detecting [OIII]λ4363 emitters and testing strong line calibrations in the high-z Universe with ultra-deep JWST/NIRSpec spectroscopy up to z $\sim$ 9.5. A&A, 681:A70.

Leger, A. and Puget, J. L. (1984). Identification of the Unidentified Infrared Emission Features of Interstellar Dust. A&A, 137:L5–L8.

Leitherer, C., Schaerer, D., Goldader, J. D., Delgado, R. M. G., Robert, C., Kune, D. F., de Mello, D. F., Devost, D., and Heckman, T. M. (1999). Starburst99: Synthesis Models for Galaxies with Active Star Formation. ApJS, 123(1):3–40.

Lelli, F., Di Teodoro, E. M., Fraternali, F., Man, A. W. S., Zhang, Z.-Y., De Breuck, C., Davis, T. A., and Maiolino, R. (2021). A massive stellar bulge in a regularly rotating galaxy 1.2 billion years after the Big Bang. *Science*, 371(6530):713–716.

Li, A. and Draine, B. T. (2001). Infrared Emission from Interstellar Dust. II. The Diffuse Interstellar Medium. ApJ, 554(2):778–802.

Li, Q., Narayanan, D., and Davé, R. (2019). The dust-to-gas and dust-to-metal ratio in galaxies from z = 0 to 6. MNRAS, 490(1):1425–1436.

Li, Z., Dekel, A., Sarkar, K. C., Aung, H., Giavalisco, M., Mandelker, N., and Tacchella, S. (2024). Feedback-free starbursts at cosmic dawn: Observable predictions for JWST. A&A, 690:A108.

Liang, L., Feldmann, R., Hayward, C. C., Narayanan, D., Çatmabacak, O., Kereš, D., Faucher-Giguère, C.-A., and Hopkins, P. F. (2021). The IRX-β relation of high-redshift galaxies. MNRAS, 502(3):3210–3241.

Liang, L., Feldmann, R., Kereš, D., Scoville, N. Z., Hayward, C. C., Faucher-Giguère, C.-A., Schreiber, C., Ma, X., Hopkins, P. F., and Quataert, E. (2019). On the dust temperatures of high-redshift galaxies. MNRAS, 489(1):1397–1422.

Liang, L., Feldmann, R., Murray, N., Narayanan, D., Hayward, C. C., Anglés-Alcázar, D., Bassini, L., Richings, A. J., Faucher-Giguère, C.-A., Chung, D. T., Chan, J. Y. H., Tolgay, D., Çatmabacak, O., Kereš, D., and Hopkins, P. F. (2024). [C II] 158 μm emission as an indicator of galaxy star formation rate. MNRAS, 528(1):499–541.

Lin, Q., Yang, X., Li, A., and Witstok, J. (2025). Polycyclic aromatic hydrocarbon and the ultraviolet extinction bump at the cosmic dawn. A&A, 694:A84.

Lines, N. E. P., Bowler, R. A. A., Adams, N. J., Fisher, R., Varadaraj, R. G., Nakazato, Y., Aravena, M., Assef, R. J., Birkin, J. E., Ceverino, D., da Cunha, E., Cullen, F., De Looze, I., Donnan, C. T., Dunlop, J. S., Ferrara, A., Grogin, N. A., Herrera-Camus, R., Ikeda, R., Koekemoer, A. M., Killi, M., Li, J., McLeod, D. J., McLure, R. J., Mitsuhashi, I., Pérez-González, P. G., Relano, M., Solimano, M., Spilker, J. S., Villanueva, V., and Yoshida, N. (2025). JWST PRIMER: a lack of outshining in four normal z = 4 âĂŚ 6 galaxies from the ALMA-CRISTAL Survey. MNRAS, 539(3):2685–2706.

Lisenfeld, U. and Ferrara, A. (1998). Dust-to-Gas Ratio and Metal Abundance in Dwarf Galaxies. ApJ, 496(1):145–154.

Liu, B. and Bromm, V. (2022). Accelerating Early Massive Galaxy Formation with Primordial Black Holes. ApJ, 937(2):L30.

Liu, H., Jiang, Y.-F., Quataert, E., Greene, J. E., and Ma, Y. (2025). The Balmer Break and Optical Continuum of Little Red Dots From Super-Eddington Accretion. *arXiv e-prints*, page arXiv:2507.07190.

López-Sanjuan, C., Le Fèvre, O., Tasca, L. A. M., Epinat, B., Amram, P., Contini, T., Garilli, B., Kissler-Patig, M., Moultaka, J., Paioro, L., Perret, V., Queyrel, J., Tresse, L., Vergani, D., and Divoy, C. (2013). MASSIV: Mass Assembly Survey with SINFONI in VVDS. V. The major merger rate of star-forming galaxies at $0.9 < z < 1.8$ from IFS-based close pairs. A&A, 553:A78.

Lovell, C. C., Geach, J. E., Davé, R., Narayanan, D., and Li, Q. (2021a). Reproducing submillimetre galaxy number counts with cosmological hydrodynamic simulations. MNRAS, 502(1):772–793.

Lovell, C. C., Vijayan, A. P., Thomas, P. A., Wilkins, S. M., Barnes, D. J., Irodotou, D., and Roper, W. (2021b). First Light And Reionization Epoch Simulations (FLARES) - I. Environmental dependence of high-redshift galaxy evolution. MNRAS, 500(2):2127–2145.

Lower, S., Narayanan, D., Hu, C.-Y., and Privon, G. C. (2024). Cosmic Sands. II. Challenges in Predicting and Measuring High-z Dust Temperatures. ApJ, 965(2):123.

Lu, S., Frenk, C. S., Bose, S., Lacey, C. G., Cole, S., Baugh, C. M., and Helly, J. C. (2025). A comparison of pre-existing ΛCDM predictions with the abundance of JWST galaxies at high redshift. MNRAS, 536(1):1018–1034.

Ma, X., Hayward, C. C., Casey, C. M., Hopkins, P. F., Quataert, E., Liang, L., Faucher-Giguère, C.-A., Feldmann, R., and Kereš, D. (2019). Dust attenuation, dust emission, and dust temperature in galaxies at $z \geq 5$: a view from the FIRE-2 simulations. MNRAS, 487(2):1844–1864.

Ma, X., Hopkins, P. F., Boylan-Kolchin, M., Faucher-Giguère, C.-A., Quataert, E., Feldmann, R., Garrison-Kimmel, S., Hayward, C. C., Kereš, D., and Wetzel, A. (2018a). Simulating galaxies in the reionization era with FIRE-2: morphologies and sizes. MNRAS, 477(1):219–229.

Ma, X., Hopkins, P. F., Faucher-Giguère, C.-A., Zolman, N., Muratov, A. L., Kereš, D., and Quataert, E. (2016). The origin and evolution of the galaxy mass-metallicity relation. MNRAS, 456(2):2140–2156.

Ma, X., Hopkins, P. F., Garrison-Kimmel, S., Faucher-Giguère, C.-A., Quataert, E., Boylan-Kolchin, M., Hayward, C. C., Feldmann, R., and Kereš, D. (2018b). Simulating galaxies in the reionization era with FIRE-2: galaxy scaling relations, stellar mass functions, and luminosity functions. MNRAS, 478(2):1694–1715.

Ma, X., Hopkins, P. F., Garrison-Kimmel, S., Faucher-Giguère, C.-A., Quataert, E., Boylan-Kolchin, M., Hayward, C. C., Feldmann, R., and Kereš, D. (2018c). Simulating galaxies in the reionization era with FIRE-2: galaxy scaling relations, stellar mass functions, and luminosity functions. MNRAS, 478(2):1694–1715.

Ma, X., Quataert, E., Wetzel, A., Hopkins, P. F., Faucher-Giguère, C.-A., and Kereš, D. (2020). No missing photons for reionization: moderate ionizing photon escape fractions from the FIRE-2 simulations. MNRAS, 498(2):2001–2017.

Madau, P. and Dickinson, M. (2014). Cosmic Star-Formation History. ARA&A, 52:415–486.

Madden, S. C., Rémy-Ruyer, A., Galametz, M., Cormier, D., Lebouteiller, V., Galliano, F., Hony, S., Bendo, G. J., Smith, M. W. L., Pohlen, M., Roussel, H., Sauvage, M., Wu, R., Sturm, E., Poglitsch, A., Contursi, A., Doublier, V., Baes, M., Barlow, M. J., Boselli, A., Boquien, M., Carlson, L. R., Ciesla, L., Cooray, A., Cortese, L., de Looze, I., Irwin, J. A., Isaak, K., Kamenetzky, J., Karczewski, O. Ł., Lu, N., MacHattie, J. A., O'Halloran, B., Parkin, T. J., Rangwala, N., Schirm, M. R. P., Schulz, B., Spinoglio, L., Vaccari, M., Wilson, C. D., and Wozniak, H. (2013). An Overview of the Dwarf Galaxy Survey. PASP, 125(928):600.

Maiolino, R., Carniani, S., Fontana, A., Vallini, L., Pentericci, L., Ferrara, A., Vanzella, E., Grazian, A., Gallerani, S., Castellano, M., Cristiani, S., Brammer, G., Santini, P., Wagg, J., and Williams, R. (2015). The assembly of 'normal' galaxies at z $\sim$ 7 probed by ALMA. MNRAS, 452(1):54–68.

Maiolino, R., Nagao, T., Grazian, A., Cocchia, F., Marconi, A., Mannucci, F., Cimatti, A., Pipino, A., Ballero, S., Calura, F., Chiappini, C., Fontana, A., Granato, G. L., Matteucci, F., Pastorini, G., Pentericci, L., Risaliti, G., Salvati, M., and Silva, L. (2008). AMAZE. I. The evolution of the mass-metallicity relation at z $>$ 3. A&A, 488(2):463–479.

Maji, M., Zhu, Q., Li, Y., Charlton, J., Hernquist, L., and Knebe, A. (2017). The Formation and Evolution of Star Clusters in Interacting Galaxies. ApJ, 844(2):108.

Makiya, R. and Hirashita, H. (2022). Cosmic evolution of grain size distribution in galaxies using the ν^2GC semi-analytical model. MNRAS, 517(2):2076–2087.

Malhotra, S., Kaufman, M. J., Hollenbach, D., Helou, G., Rubin, R. H., Brauher, J., Dale, D., Lu, N. Y., Lord, S., Stacey, G., Contursi, A., Hunter, D. A., and Dinerstein, H. (2001). Far-Infrared Spectroscopy of Normal Galaxies: Physical Conditions in the Interstellar Medium. ApJ, 561(2):766–786.

Mancini, M., Schneider, R., Graziani, L., Valiante, R., Dayal, P., Maio, U., Ciardi, B., and Hunt, L. K. (2015). The dust mass in z $>$ 6 normal star-forming galaxies. MNRAS, 451:L70–L74.

Mandelker, N., Dekel, A., Ceverino, D., DeGraf, C., Guo, Y., and Primack, J. (2017). Giant clumps in simulated high- z Galaxies: properties, evolution and dependence on feedback. MNRAS, 464(1):635–665.

Mandelker, N., Dekel, A., Ceverino, D., Tweed, D., Moody, C. E., and Primack, J. (2014). The population of giant clumps in simulated high-z galaxies: in situ and ex situ migration and survival. MNRAS, 443(4):3675–3702.

Mandelker, N., Ginzburg, O., Dekel, A., Bournaud, F., Krumholz, M. R., Ceverino, D., and Primack, J. (2025). Formation of giant clumps in high-z disc galaxies by compressive turbulence. MNRAS, 538(1):L9–L15.

Mao, Y.-W., Kong, X., and Lin, L. (2014). Characterizing Ultraviolet and Infrared Observational Properties for Galaxies. II. Features of Attenuation Law. ApJ, 789(1):76.

Maraston, C. (2005). Evolutionary population synthesis: models, analysis of the ingredients and application to high-z galaxies. MNRAS, 362(3):799–825.

Marconcini, C., D'Eugenio, F., Maiolino, R., Arribas, S., Bunker, A., Carniani, S., Charlot, S., Perna, M., Rodríguez Del Pino, B., Übler, H., Willott, C. J., Böker, T., Cresci, G., Curti, M., Jones, G. C., Lamperti, I., Parlanti, E., and Venturi, G. (2024). GA-NIFS: the interplay between merger, star formation, and chemical enrichment in MACS1149-JD1 at z = 9.11 with JWST/NIRSpec. MNRAS, 533(2):2488–2501.

Markov, V., Gallerani, S., Ferrara, A., Pallottini, A., Parlanti, E., Mascia, F. D., Sommovigo, L., and Kohandel, M. (2025). The evolution of dust attenuation in z ≈ 2-12 galaxies observed by JWST. *Nature Astronomy*, 9:458–468.

Markov, V., Gallerani, S., Pallottini, A., Sommovigo, L., Carniani, S., Ferrara, A., Parlanti, E., and Di Mascia, F. (2023). Dust attenuation law in JWST galaxies at z ∼ 7-8. A&A, 679:A12.

Marques-Chaves, R., Schaerer, D., Kuruvanthodi, A., Korber, D., Prantzos, N., Charbonnel, C., Weibel, A., Izotov, Y. I., Messa, M., Brammer, G., Dessauges-Zavadsky, M., and Oesch, P. (2024). Extreme N-emitters at high redshift: Possible signatures of supermassive stars and globular cluster or black hole formation in action. A&A, 681:A30.

Marshall, M. A., Wilkins, S., Di Matteo, T., Roper, W. J., Vijayan, A. P., Ni, Y., Feng, Y., and Croft, R. A. C. (2022). The impact of dust on the sizes of galaxies in the Epoch of Reionization. MNRAS, 511(4):5475–5491.

Mason, C. A., Trenti, M., and Treu, T. (2023). The brightest galaxies at cosmic dawn. MNRAS, 521(1):497–503.

Mathis, J. S., Mezger, P. G., and Panagia, N. (1983). Interstellar radiation field and dust temperatures in the diffuse interstellar medium and in giant molecular clouds. A&A, 128:212–229.

Mathis, J. S., Rumpl, W., and Nordsieck, K. H. (1977). The size distribution of interstellar grains. ApJ, 217:425–433.

Matsumoto, K., Hirashita, H., Nagamine, K., van der Giessen, S., Romano, L. E. C., Relaño, M., De Looze, I., Baes, M., Nersesian, A., Camps, P., Hou, K.-c., and Oku, Y. (2024). Observational signatures of the dust size evolution in isolated galaxy simulations. A&A, 689:A79.

Matsuoka, Y., Onoue, M., Kashikawa, N., Iwasawa, K., Strauss, M. A., Nagao, T., Imanishi, M., Lee, C.-H., Akiyama, M., Asami, N., Bosch, J., Foucaud, S., Furusawa, H., Goto, T., Gunn, J. E., Harikane, Y., Ikeda, H., Izumi, T., Kawaguchi, T., Kikuta, S., Kohno, K., Komiyama, Y., Lupton, R. H., Minezaki, T., Miyazaki, S., Morokuma, T., Murayama, H., Niida, M., Nishizawa, A. J., Oguri, M., Ono, Y., Ouchi, M., Price, P. A., Sameshima, H., Schulze, A., Shirakata, H., Silverman, J. D., Sugiyama, N., Tait, P. J., Takada, M., Takata, T., Tanaka, M., Tang, J.-J., Toba, Y., Utsumi, Y., and Wang, S.-Y. (2018). Subaru High-z Exploration of Low-Luminosity Quasars (SHELLQs). II. Discovery of 32 quasars and luminous galaxies at $5.7 < z \leq 6.8$. PASJ, 70:S35.

Matthee, J., Mackenzie, R., Simcoe, R. A., Kashino, D., Lilly, S. J., Bordoloi, R., and Eilers, A.-C. (2023). EIGER. II. First Spectroscopic Characterization of the Young Stars and Ionized Gas Associated with Strong Hβ and [O III] Line Emission in Galaxies at z = 5-7 with JWST. ApJ, 950(1):67.

Matthee, J., Sobral, D., Boogaard, L. A., Röttgering, H., Vallini, L., Ferrara, A., Paulino-Afonso, A., Boone, F., Schaerer, D., and Mobasher, B. (2019). Resolved UV and [C II] Structures of Luminous Galaxies within the Epoch of Reionization. ApJ, 881(2):124.

Matthee, J., Sobral, D., Boone, F., Röttgering, H., Schaerer, D., Girard, M., Pallottini, A., Vallini, L., Ferrara, A., Darvish, B., and Mobasher, B. (2017). ALMA Reveals Metals yet No Dust within Multiple Components in CR7. ApJ, 851(2):145.

Mauerhofer, V., Dayal, P., Haehnelt, M. G., Kimm, T., Rosdahl, J., and Teyssier, R. (2025). Synergising semi-analytical models and hydrodynamical simulations to interpret JWST data from the first billion years. A&A, 696:A157.

Mayer, L., van Donkelaar, F., Messa, M., Capelo, P. R., and Adamo, A. (2025). In Situ Formation of Star Clusters at z > 7 via Galactic Disk Fragmentation: Shedding Light on Ultracompact Clusters and Overmassive Black Holes Seen by JWST. ApJ, 981(2):L28.

McClymont, W., Tacchella, S., Smith, A., Kannan, R., Puchwein, E., Borrow, J., Garaldi, E., Keating, L., Vogelsberger, M., Zier, O., Shen, X., and Popovic, F. (2025a). The THESAN-ZOOM project: central starbursts and inside-out quenching govern galaxy sizes in the early Universe. *arXiv e-prints*, page arXiv:2503.04894.

McClymont, W., Tacchella, S., Smith, A., Kannan, R., Puchwein, E., Borrow, J., Garaldi, E., Keating, L., Vogelsberger, M., Zier, O., Shen, X., Popovic, F., and Simmonds, C. (2025b). The THESAN-ZOOM project: Burst, quench, repeat – unveiling the evolution of high-redshift galaxies along the star-forming main sequence. *arXiv e-prints*, page arXiv:2503.00106.

McGaugh, S. S. (1991). H II Region Abundances: Model Oxygen Line Ratios. ApJ, 380:140.

McLure, R. J., Dunlop, J. S., Cullen, F., Bourne, N., Best, P. N., Khochfar, S., Bowler, R. A. A., Biggs, A. D., Geach, J. E., Scott, D., Michałowski, M. J., Rujopakarn, W., van Kampen, E., Kirkpatrick, A., and Pope, A. (2018). Dust attenuation in 2 < z < 3 star-forming galaxies from deep ALMA observations of the Hubble Ultra Deep Field. MNRAS, 476(3):3991–4006.

Menon, S. H., Federrath, C., and Krumholz, M. R. (2023). Outflows driven by direct and reprocessed radiation pressure in massive star clusters. MNRAS, 521(4):5160–5176.

Menon, S. H., Lancaster, L., Burkhart, B., Somerville, R. S., Dekel, A., and Krumholz, M. R. (2024). The Interplay between the Initial Mass Function and Star Formation Efficiency through Radiative Feedback at High Stellar Surface Densities. ApJ, 967(2):L28.

Meurer, G. R., Heckman, T. M., and Calzetti, D. (1999). Dust Absorption and the Ultraviolet Luminosity Density at z ∼3 as Calibrated by Local Starburst Galaxies. ApJ, 521(1):64–80.

Meštrić, U., Vanzella, E., Zanella, A., Castellano, M., Calura, F., Rosati, P., Bergamini, P., Mercurio, A., Meneghetti, M., Grillo, C., Caminha, G. B., Nonino, M., Merlin, E., Cupani, G., and Sani, E. (2022). Exploring the physical properties of lensed star-forming clumps at $2 \lesssim z \lesssim 6$. MNRAS, 516(3):3532–3555.

Meyer, R. A., Oesch, P. A., Giovinazzo, E., Weibel, A., Brammer, G., Matthee, J., Naidu, R. P., Bouwens, R. J., Chisholm, J., Covelo-Paz, A., Fudamoto, Y., Maseda, M., Nelson, E., Shivaei, I., Xiao, M., Herard-Demanche, T., Illingworth, G. D., Kerutt, J., Kramarenko, I., Labbe, I., Leonova, E., Magee, D., Matharu, J., Prieto Lyon, G., Reddy, N., Schaerer, D., Shapley, A., Stefanon, M., Wozniak, M. A., and Wuyts, S. (2024). JWST FRESCO: a comprehensive census of Hβ+[OIII] emitters at 6.8<z<9.0 in the GOODS fields. *arXiv e-prints*, page arXiv:2405.05111.

Meynet, G. and Maeder, A. (2003). Stellar evolution with rotation. X. Wolf-Rayet star populations at solar metallicity. A&A, 404:975–990.

Mie, G. (1908). Beiträge zur Optik trüber Medien, speziell kolloidaler Metallösungen. *Annalen der Physik*, 330(3):377–445.

Mingozzi, M., James, B. L., Arellano-Córdova, K. Z., Berg, D. A., Senchyna, P., Chisholm, J., Brinchmann, J., Aloisi, A., Amorín, R. O., Charlot, S., Feltre, A., Hayes, M., Heckman, T., Henry, A., Hernandez, S., Kumari, N., Leitherer, C., Llerena, M., Martin, C. L., Nanayakkara, T., Ravindranath, S., Skillman, E. D., Sugahara, Y., Wofford, A., and Xu, X. (2022). CLASSY IV. Exploring UV Diagnostics of the Interstellar Medium in Local High-z Analogs at the Dawn of the JWST Era. ApJ, 939(2):110.

Mitsuhashi, I., Harikane, Y., Bauer, F. E., Bakx, T. J. L. C., Ferrara, A., Fujimoto, S., Hashimoto, T., Inoue, A. K., Iwasawa, K., Nishimura, Y., Imanishi, M., Ono, Y., Saito, T., Sugahara, Y., Umehata, H., Vallini, L., Wang, T., and Zavala, J. A. (2024). SERENADE. II. An ALMA Multiband Dust Continuum Analysis of 28 Galaxies at $5 < z < 8$ and the Physical Origin of the Dust Temperature Evolution. ApJ, 971(2):161.

Mo, H., van den Bosch, F. C., and White, S. (2010). *Galaxy Formation and Evolution*.

Morales, A. M., Finkelstein, S. L., Leung, G. C. K., Bagley, M. B., Cleri, N. J., Dave, R., Dickinson, M., Ferguson, H. C., Hathi, N. P., Jones, E., Koekemoer, A. M., Papovich, C., Pérez-González, P. G., Pirzkal, N., Smith, B., Wilkins, S. M., and Yung, L. Y. A. (2024). Rest-frame UV Colors for Faint Galaxies at $z \sim 9$–16 with the JWST NGDEEP Survey. ApJ, 964(2):L24.

Morishita, T., Roberts-Borsani, G., Treu, T., Brammer, G., Mason, C. A., Trenti, M., Vulcani, B., Wang, X., Acebron, A., Bahé, Y., Bergamini, P., Boyett, K., Bradac, M., Calabrò, A., Castellano, M., Chen, W., De Lucia, G., Filippenko, A. V., Fontana, A., Glazebrook, K., Grillo, C., Henry, A., Jones, T., Kelly, P. L., Koekemoer, A. M., Leethochawalit, N., Lu, T.-Y., Marchesini, D., Mascia, S., Mercurio, A., Merlin, E., Metha, B., Nanayakkara, T., Nonino, M., Paris, D., Pentericci, L., Rosati, P., Santini, P., Strait, V., Vanzella, E., Windhorst, R. A., and Xie, L. (2023). Early Results from GLASS-JWST. XIV. A Spectroscopically Confirmed Protocluster 650 Million Years after the Big Bang. ApJ, 947(2):L24.

Morishita, T., Stiavelli, M., Grillo, C., Rosati, P., Schuldt, S., Trenti, M., Bergamini, P., Boyett, K., Chary, R.-R., Leethochawalit, N., Roberts-Borsani, G., Treu, T., and Vanzella, E. (2024). Diverse Oxygen Abundance in Early Galaxies Unveiled by Auroral Line Analysis with JWST. ApJ, 971(1):43.

Morishita, T., Stiavelli, M., Vanzella, E., Bergamini, P., Boyett, K., Chiaberge, M., Grillo, C., Leethochawalit, N., Messa, M., Roberts-Borsani, G., Rosati, P., and Shajib, A. (2025). Metallicity Scatter Originating from Sub-kiloparsec Starbursting Clumps in the Core of a Protocluster at z=7.88. *arXiv e-prints*, page arXiv:2501.11879.

Moriwaki, K., Yoshida, N., Shimizu, I., Harikane, Y., Matsuda, Y., Matsuo, H., Hashimoto, T., Inoue, A. K., Tamura, Y., and Nagao, T. (2018). The distribution and physical properties of high-redshift [O III] emitters in a cosmological hydrodynamics simulation. MNRAS, 481(1):L84–L88.

Moullet, A., Kataria, T., Lis, D., Unwin, S., Hasegawa, Y., Mills, E., Battersby, C., Roc, A., and Meixner, M. (2023). PRIMA General Observer Science Book. *arXiv e-prints*, page arXiv:2310.20572.

Moustakas, J. and Kennicutt, Jr., R. C. (2006). An Integrated Spectrophotometric Survey of Nearby Star-forming Galaxies. ApJS, 164(1):81–98.

Mowla, L., Iyer, K., Asada, Y., Desprez, G., Tan, V. Y. Y., Martis, N., Sarrouh, G., Strait, V., Abraham, R., Bradač, M., Brammer, G., Muzzin, A., Pacifici, C., Ravindranath, S., Sawicki, M., Willott, C., Estrada-Carpenter, V., Jahan, N., Noirot, G., Matharu, J., Rihtaršič, G., and Zabl, J. (2024). Formation of a low-mass galaxy from star clusters in a 600-million-year-old Universe. Nature, 636(8042):332–336.

Muñoz-Elgueta, N., Arrigoni Battaia, F., Kauffmann, G., Pakmor, R., Walch, S., Obreja, A., and Buhlmann, L. (2024). Simulated [CII] emission in high-z star-forming galaxies. A&A, 690:A392.

Murray, N., Quataert, E., and Thompson, T. A. (2005). On the Maximum Luminosity of Galaxies and Their Central Black Holes: Feedback from Momentum-driven Winds. ApJ, 618(2):569–585.

Murray, N., Quataert, E., and Thompson, T. A. (2010). The Disruption of Giant Molecular Clouds by Radiation Pressure & the Efficiency of Star Formation in Galaxies. ApJ, 709(1):191–209.

Mushtaq, M., Ceverino, D., Klessen, R. S., Reissl, S., and Puttasiddappa, P. H. (2023). Dust attenuation in galaxies at cosmic dawn from the FirstLight simulations. MNRAS, 525(4):4976–4984.

Nagao, T., Maiolino, R., De Breuck, C., Caselli, P., Hatsukade, B., and Saigo, K. (2012). ALMA reveals a chemically evolved submillimeter galaxy at $z = 4.76$. A&A, 542:L34.

Nagao, T., Maiolino, R., and Marconi, A. (2006). Gas metallicity diagnostics in star-forming galaxies. A&A, 459(1):85–101.

Nagele, C. and Umeda, H. (2023). Multiple Channels for Nitrogen Pollution by Metal-enriched Supermassive Stars and Implications for GN-z11. ApJ, 949(1):L16.

Naidu, R. P., Oesch, P. A., Brammer, G., Weibel, A., Li, Y., Matthee, J., Chisholm, J., Pollock, C. L., Heintz, K. E., Johnson, B. D., Shen, X., Hviding, R. E., Leja, J., Tacchella, S., Ganguly, A., Witten, C., Atek, H., Belli, S., Bose, S., Bouwens, R., Dayal, P., Decarli, R., de Graaff, A., Fudamoto, Y., Giovinazzo, E., Greene, J. E., Illingworth, G., Inoue, A. K., Kane, S. G., Labbe, I., Leonova, E., Marques-Chaves, R., Meyer, R. A., Nelson, E. J., Roberts-Borsani, G., Schaerer, D., Simcoe, R. A., Stefanon, M., Sugahara, Y., Toft, S., van der Wel, A., van Dokkum, P., Walter, F., Watson, D., Weaver, J. R., and Whitaker, K. E. (2025). A Cosmic Miracle: A Remarkably Luminous Galaxy at $z_{\rm spec} = 14.44$ Confirmed with JWST. *arXiv e-prints*, page arXiv:2505.11263.

Naidu, R. P., Oesch, P. A., van Dokkum, P., Nelson, E. J., Suess, K. A., Brammer, G., Whitaker, K. E., Illingworth, G., Bouwens, R., Tacchella, S., Matthee, J., Allen, N., Bezanson, R., Conroy, C., Labbe, I., Leja, J., Leonova, E., Magee, D., Price, S. H., Setton, D. J., Strait, V., Stefanon, M., Toft, S., Weaver, J. R., and Weibel, A. (2022). Two Remarkably Luminous Galaxy Candidates at z $\approx$ 10-12 Revealed by JWST. ApJ, 940(1):L14.

Nakajima, K., Ellis, R. S., Robertson, B. E., Tang, M., and Stark, D. P. (2020). The Lyman Continuum Escape Survey. II. Ionizing Radiation as a Function of the [O III]/[O II] Line Ratio. ApJ, 889(2):161.

Nakajima, K. and Ouchi, M. (2014). Ionization state of inter-stellar medium in galaxies: evolution, SFR-M_*-Z dependence, and ionizing photon escape. MNRAS, 442(1):900–916.

Nakajima, K., Ouchi, M., Harikane, Y., Vanzella, E., Ono, Y., Isobe, Y., Nishigaki, M., Tsujimoto, T., Nakamura, F., Xu, Y., Umeda, H., and Zhang, Y. (2025). An Ultra-Faint, Chemically Primitive Galaxy Forming at the Epoch of Reionization. *arXiv e-prints*, page arXiv:2506.11846.

Nakajima, K., Ouchi, M., Isobe, Y., Harikane, Y., Zhang, Y., Ono, Y., Umeda, H., and Oguri, M. (2023). JWST Census for the Mass-Metallicity Star Formation Relations at z = 4-10 with Self-consistent Flux Calibration and Proper Metallicity Calibrators. ApJS, 269(2):33.

Nakazato, Y., Ceverino, D., and Yoshida, N. (2024). A Merger-driven Scenario for Clumpy Galaxy Formation in the Epoch of Reionization: Physical Properties of Clumps in the FirstLight Simulation. ApJ, 975(2):238.

Nakazato, Y. and Ferrara, A. (2024). Radiation-driven dusty outflows from early galaxies. *arXiv e-prints*, page arXiv:2412.07598.

Nakazato, Y., Sugimura, K., Inoue, A. K., and Ricotti, M. (2025). Unveiling the Ionized and Neutral ISM at z $>$ 10 : The Origin of [O III] /[C II] Ratios from a Sub-parsec Resolution Radiative Transfer Simulation. *arXiv e-prints*, page arXiv:2505.12397.

Nakazato, Y., Yoshida, N., and Ceverino, D. (2023). Simulations of High-redshift [O III] Emitters: Chemical Evolution and Multiline Diagnostics. ApJ, 953(2):140.

Nanni, A., Romano, M., Donevski, D., Witstok, J., Shivaei, I., Fioc, M., and Sawant, P. (2025). Origins of Carbon Dust in a JWST-Observed Primeval Galaxy at $z \sim$6.7. *arXiv e-prints*, page arXiv:2505.10701.

Narayanan, D., Davé, R., Johnson, B. D., Thompson, R., Conroy, C., and Geach, J. (2018). The IRX-β dust attenuation relation in cosmological galaxy formation simulations. MNRAS, 474(2):1718–1736.

Narayanan, D., Turk, M. J., Robitaille, T., Kelly, A. J., McClellan, B. C., Sharma, R. S., Garg, P., Abruzzo, M., Choi, E., Conroy, C., Johnson, B. D., Kimock, B., Li, Q., Lovell, C. C., Lower, S., Privon, G. C., Roberts, J., Sethuram, S., Snyder, G. F., Thompson, R., and Wise, J. H. (2021). POWDERDAY: Dust Radiative Transfer for Galaxy Simulations. ApJS, 252(1):12.

Navarro, J. F. and Benz, W. (1991). Dynamics of Cooling Gas in Galactic Dark Halos. ApJ, 380:320.

Neeleman, M., Walter, F., Decarli, R., Drake, A. B., Eilers, A.-C., Meyer, R. A., and Venemans, B. P. (2023). ALMA 400 pc Imaging of a z = 6.5 Massive Warped Disk Galaxy. ApJ, 958(2):132.

Nomoto, K., Tominaga, N., Umeda, H., Kobayashi, C., and Maeda, K. (2006). Nucleosynthesis yields of core-collapse supernovae and hypernovae, and galactic chemical evolution. Nucl. Phys. A, 777:424–458.

Nussbaumer, H. and Storey, P. J. (1981). C II two-electron transitions. A&A, 96(1-2):91–95.

Nyhagen, C. T., Schimek, A., Cicone, C., Decataldo, D., and Shen, S. (2024). A theoretical investigation of far-infrared fine structure lines at $z > 6$ and of the origin of the [OIII]88/[CII]158 enhancement. *arXiv e-prints*, page arXiv:2410.18471.

Oesch, P. A., Brammer, G., van Dokkum, P. G., Illingworth, G. D., Bouwens, R. J., Labbé, I., Franx, M., Momcheva, I., Ashby, M. L. N., Fazio, G. G., Gonzalez, V., Holden, B., Magee, D., Skelton, R. E., Smit, R., Spitler, L. R., Trenti, M., and Willner, S. P. (2016). A Remarkably Luminous Galaxy at z=11.1 Measured with Hubble Space Telescope Grism Spectroscopy. ApJ, 819(2):129.

Okamoto, T., Frenk, C. S., Jenkins, A., and Theuns, T. (2010). The properties of satellite galaxies in simulations of galaxy formation. MNRAS, 406(1):208–222.

Oklopčić, A., Hopkins, P. F., Feldmann, R., Kereš, D., Faucher-Giguère, C.-A., and Murray, N. (2017). Giant clumps in the FIRE simulations: a case study of a massive high-redshift galaxy. MNRAS, 465(1):952–969.

Olsen, K., Greve, T. R., Narayanan, D., Thompson, R., Davé, R., Niebla Rios, L., and Stawinski, S. (2017). SÍGAME Simulations of the [CII], [OI], and [OIII] Line Emission from Star-forming Galaxies at zâĽČ 6. ApJ, 846(2):105.

Omukai, K., Schneider, R., and Haiman, Z. (2008). Can Supermassive Black Holes Form in Metal-enriched High-Redshift Protogalaxies? ApJ, 686(2):801–814.

Omukai, K., Tsuribe, T., Schneider, R., and Ferrara, A. (2005). Thermal and Fragmentation Properties of Star-forming Clouds in Low-Metallicity Environments. ApJ, 626(2):627–643.

Ono, Y., Fujimoto, S., Harikane, Y., Ouchi, M., Vallini, L., Ferrara, A., Shibuya, T., Pallottini, A., Inoue, A. K., Imanishi, M., Shimasaku, K., Hashimoto, T., Lee, C.-H., Sugahara, Y., Tamura, Y., Kohno, K., and Schramm, M. (2022). ALMA Observations of CO Emission from Luminous Lyman-break Galaxies at z = 6.0293-6.2037. ApJ, 941(1):74.

Ono, Y., Harikane, Y., Ouchi, M., Yajima, H., Abe, M., Isobe, Y., Shibuya, T., Wise, J. H., Zhang, Y., Nakajima, K., and Umeda, H. (2023). Morphologies of Galaxies at z $\gtrsim$ 9 Uncovered by JWST/NIRCam Imaging: Cosmic Size Evolution and an Identification of an Extremely Compact Bright Galaxy at z 12. ApJ, 951(1):72.

Oppenheimer, B. D. and Davé, R. (2006). Cosmological simulations of intergalactic medium enrichment from galactic outflows. MNRAS, 373(4):1265–1292.

Ormerod, K., Witstok, J., Smit, R., de Graaff, A., Helton, J. M., Maseda, M. V., Shivaei, I., Bunker, A. J., Carniani, S., D'Eugenio, F., Bhatawdekar, R., Chevallard, J., Franx, M., Kumari, N., Maiolino, R., Rinaldi, P., Robertson, B., and Tacchella, S. (2025). Detection of the 2175Å UV Bump at z>7: Evidence for Rapid Dust Evolution in a Merging Reionisation-Era Galaxy. *arXiv e-prints*, page arXiv:2502.21119.

Osterbrock, D. and Flather, E. (1959). Electron Densities in the Orion Nebula. II. ApJ, 129:26.

Osterbrock, D. E. and Ferland, G. J. (2006). *Astrophysics of gaseous nebulae and active galactic nuclei*.

Ostriker, E. C. and Shetty, R. (2011). Maximally Star-forming Galactic Disks. I. Starburst Regulation Via Feedback-driven Turbulence. ApJ, 731(1):41.

Ota, K., Walter, F., Ohta, K., Hatsukade, B., Carilli, C. L., da Cunha, E., González-López, J., Decarli, R., Hodge, J. A., Nagai, H., Egami, E., Jiang, L., Iye, M., Kashikawa, N., Riechers, D. A., Bertoldi, F., Cox, P., Neri, R., and Weiss, A. (2014). ALMA Observation of 158 μm [C II] Line and Dust Continuum of a z = 7 Normally Star-forming Galaxy in the Epoch of Reionization. ApJ, 792(1):34.

Ouchi, M., Ellis, R., Ono, Y., Nakanishi, K., Kohno, K., Momose, R., Kurono, Y., Ashby, M. L. N., Shimasaku, K., Willner, S. P., Fazio, G. G., Tamura, Y., and Iono, D. (2013). An Intensely Star-forming Galaxy at z ∼7 with Low Dust and Metal Content Revealed by Deep ALMA and HST Observations. ApJ, 778(2):102.

Overzier, R. A. (2016). The realm of the galaxy protoclusters. A review. A&A Rev., 24(1):14.

Overzier, R. A., Heckman, T. M., Wang, J., Armus, L., Buat, V., Howell, J., Meurer, G., Seibert, M., Siana, B., Basu-Zych, A., Charlot, S., Gonçalves, T. S., Martin, D. C., Neill, J. D., Rich, R. M., Salim, S., and Schiminovich, D. (2011). Dust Attenuation in UV-selected Starbursts at High Redshift and Their Local Counterparts: Implications for the Cosmic Star Formation Rate Density. ApJ, 726(1):L7.

Pacucci, F. and Narayan, R. (2024). Mildly Super-Eddington Accretion onto Slowly Spinning Black Holes Explains the X-Ray Weakness of the Little Red Dots. ApJ, 976(1):96.

Pagel, B. E. J., Edmunds, M. G., Blackwell, D. E., Chun, M. S., and Smith, G. (1979). On the composition of H II regions in southern galaxies - I. NGC 300 and 1365. MNRAS, 189:95–113.

Pallottini, A. and Ferrara, A. (2023a). Stochastic star formation in early galaxies: Implications for the James Webb Space Telescope. A&A, 677:L4.

Pallottini, A. and Ferrara, A. (2023b). Stochastic star formation in early galaxies: Implications for the James Webb Space Telescope. A&A, 677:L4.

Pallottini, A., Ferrara, A., Decataldo, D., Gallerani, S., Vallini, L., Carniani, S., Behrens, C., Kohandel, M., and Salvadori, S. (2019). Deep into the structure of the first galaxies: SERRA views. MNRAS, 487(2):1689–1708.

Pallottini, A., Ferrara, A., Gallerani, S., Behrens, C., Kohandel, M., Carniani, S., Vallini, L., Salvadori, S., Gelli, V., Sommovigo, L., D'Odorico, V., Di Mascia, F., and Pizzati, E. (2022). A survey of high-z galaxies: SERRA simulations. MNRAS, 513(4):5621–5641.

Pallottini, A., Ferrara, A., Gallerani, S., Vallini, L., Maiolino, R., and Salvadori, S. (2017). Zooming on the internal structure of zâĽČ6 galaxies. MNRAS, 465(3):2540–2558.

Panuzzo, P., Bressan, A., Granato, G. L., Silva, L., and Danese, L. (2003). Dust and nebular emission. I. Models for normal galaxies. A&A, 409:99–114.

Parashari, P. and Laha, R. (2023). Primordial power spectrum in light of JWST observations of high redshift galaxies. MNRAS, 526(1):L63–L69.

Park, J., Ricotti, M., and Sugimura, K. (2021). Population III star formation in an X-ray background - II. Protostellar discs, multiplicity, and mass function of the stars. MNRAS, 508(4):6193–6208.

Parlanti, E., Carniani, S., Pallottini, A., Cignoni, M., Cresci, G., Kohandel, M., Mannucci, F., and Marconi, A. (2023). ALMA hints at the presence of turbulent disk galaxies at z > 5. A&A, 673:A153.

Parlanti, E., Carniani, S., Venturi, G., Herrera-Camus, R., Arribas, S., Bunker, A. J., Charlot, S., D'Eugenio, F., Maiolino, R., Perna, M., Übler, H., Böker, T., Cresci, G., Curti, M., Jones, G. C., Lamperti, I., Pérez-González, P. G., Del Pino, B. R., and Zamora, S. (2025). GA-NIFS: Multiphase analysis of a star-forming galaxy at z ∼ 5.5. A&A, 695:A6.

Pendleton, Y. J. and Allamandola, L. J. (2002). The Organic Refractory Material in the Diffuse Interstellar Medium: Mid-Infrared Spectroscopic Constraints. ApJS, 138(1):75–98.

Pentericci, L., Carniani, S., Castellano, M., Fontana, A., Maiolino, R., Guaita, L., Vanzella, E., Grazian, A., Santini, P., Yan, H., Cristiani, S., Conselice, C., Giavalisco, M., Hathi, N., and Koekemoer, A. (2016). Tracing the Reionization Epoch with ALMA: [C II] Emission in z ∼ 7 Galaxies. ApJ, 829(1):L11.

Pillepich, A., Nelson, D., Springel, V., Pakmor, R., Torrey, P., Weinberger, R., Vogelsberger, M., Marinacci, F., Genel, S., van der Wel, A., and Hernquist, L. (2019). First results from the TNG50 simulation: the evolution of stellar and gaseous discs across cosmic time. MNRAS, 490(3):3196–3233.

Pillepich, A., Springel, V., Nelson, D., Genel, S., Naiman, J., Pakmor, R., Hernquist, L., Torrey, P., Vogelsberger, M., Weinberger, R., and Marinacci, F. (2018). Simulating galaxy formation with the IllustrisTNG model. MNRAS, 473(3):4077–4106.

Planck Collaboration, Ade, P. A. R., Aghanim, N., Armitage-Caplan, C., Arnaud, M., Ashdown, M., Atrio-Barandela, F., Aumont, J., Baccigalupi, C., Banday, A. J., Barreiro, R. B., Bartlett, J. G., Battaner, E., Benabed, K., Benoît, A., Benoit-Lévy, A., Bernard, J. P., Bersanelli, M., Bielewicz, P., Bobin, J., Bock, J. J., Bonaldi, A., Bond, J. R., Borrill, J., Bouchet, F. R., Bridges, M., Bucher, M., Burigana, C., Butler, R. C., Calabrese, E., Cappellini, B., Cardoso, J. F., Catalano, A., Challinor, A., Chamballu, A., Chary, R. R., Chen, X., Chiang, H. C., Chiang, L. Y., Christensen, P. R., Church, S., Clements, D. L., Colombi, S., Colombo, L. P. L., Couchot, F., Coulais, A., Crill, B. P., Curto, A., Cuttaia, F., Danese, L., Davies, R. D., Davis, R. J., de Bernardis, P., de Rosa, A., de Zotti, G., Delabrouille, J., Delouis, J. M., Désert, F. X., Dickinson, C., Diego, J. M., Dolag, K., Dole, H., Donzelli, S., Doré, O., Douspis, M., Dunkley, J., Dupac, X., Efstathiou, G., Elsner, F., Enßlin, T. A., Eriksen, H. K., Finelli, F., Forni, O., Frailis, M., Fraisse, A. A., Franceschi, E., Gaier, T. C., Galeotta, S., Galli, S., Ganga, K., Giard, M., Giardino, G., Giraud-Héraud, Y., Gjerløw, E., González-Nuevo, J., Górski, K. M., Gratton, S., Gregorio, A., Gruppuso, A., Gudmundsson, J. E., Haissinski, J., Hamann, J., Hansen, F. K., Hanson, D., Harrison, D., Henrot-Versillé, S., Hernández-Monteagudo, C., Herranz, D., Hildebrandt, S. R., Hivon, E., Hobson, M., Holmes, W. A., Hornstrup, A., Hou, Z., Hovest, W., Huffenberger, K. M., Jaffe, A. H., Jaffe, T. R., Jewell, J., Jones, W. C., Juvela, M., Keihänen, E., Keskitalo, R., Kisner, T. S., Kneissl, R., Knoche, J., Knox, L., Kunz, M., Kurki-Suonio, H., Lagache, G., Lähteenmäki, A., Lamarre, J. M., Lasenby, A., Lattanzi, M., Laureijs, R. J., Lawrence, C. R., Leach, S., Leahy, J. P., Leonardi, R., León-Tavares, J., Lesgourgues, J., Lewis, A., Liguori, M., Lilje, P. B., Linden-Vørnle, M., López-Caniego, M., Lubin, P. M., Macías-Pérez, J. F., Maffei, B., Maino, D., Mandolesi, N., Maris, M., Marshall, D. J., Martin, P. G., Martínez-González, E., Masi, S., Massardi, M., Matarrese, S., Matthai, F., Mazzotta, P., Meinhold, P. R., Melchiorri, A., Melin, J. B., Mendes, L., Menegoni, E., Mennella, A., Migliaccio, M., Millea, M., Mitra, S., Miville-Deschênes, M. A., Moneti, A., Montier, L., Morgante, G., Mortlock, D., Moss, A., Munshi, D., Murphy, J. A., Naselsky, P., Nati, F., Natoli, P., Netterfield, C. B., Nørgaard-Nielsen, H. U., Noviello, F., Novikov, D., Novikov, I., O'Dwyer, I. J., Osborne, S., Oxborrow, C. A., Paci, F., Pagano, L., Pajot, F., Paladini, R., Paoletti, D., Partridge, B., Pasian, F., Patanchon, G., Pearson, D., Pearson, T. J., Peiris, H. V., Perdereau, O., Perotto, L., Perrotta, F., Pettorino, V., Piacentini, F., Piat, M., Pierpaoli, E., Pietrobon, D., Plaszczynski, S., Platania, P., and Pointecouteau, E. (2014). Planck 2013 results. XVI. Cosmological parameters. A&A, 571:A16.

Popesso, P., Concas, A., Cresci, G., Belli, S., Rodighiero, G., Inami, H., Dickinson, M., Ilbert, O., Pannella, M., and Elbaz, D. (2023). The main sequence of star-forming galaxies across cosmic times. MNRAS, 519(1):1526–1544.

Popping, G., Narayanan, D., Somerville, R. S., Faisst, A. L., and Krumholz, M. R. (2019). The art of modelling CO, [C I], and [C II] in cosmological galaxy formation models. MNRAS, 482(4):4906–4932.

Posses, A., Aravena, M., González-López, J., Förster Schreiber, N. M., Liu, D., Lee, L., Solimano, M., Díaz-Santos, T., Assef, R. J., Barcos-Muñoz, L., Bovino, S., Bowler, R. A. A., Calistro Rivera, G., da Cunha, E., Davies, R. L., Killi, M., De Looze, I., Ferrara, A., Fisher, D. B., Herrera-Camus, R., Ikeda, R., Lambert, T., Li, J., Lutz, D., Mitsuhashi, I., Palla, M., Relaño, M., Spilker, J., Naab, T., Tadaki, K., Telikova, K., Übler, H., van der Giessen, S., and Villanueva, V. (2024). The ALMA-CRISTAL survey: Extended [CII] emission in an interacting galaxy system at z ∼5.5. *arXiv e-prints*, page arXiv:2403.03379.

Punyasheel, P., Vijayan, A. P., Greve, T. R., Roper, W. J., Algera, H., Gillman, S., Gullberg, B., Irodotou, D., Lovell, C. C., Seeyave, L. T. C., Thomas, P. A., and Wilkins, S. M. (2025). First Light And Reionisation Epoch Simulations (FLARES): XVI. Size evolution of massive dusty galaxies at cosmic dawn from the ultraviolet to infrared. A&A, 696:A234.

Ralegankar, P., Pavičević, M., and Viel, M. (2024). Primordial magnetic fields: consistent initial conditions and impact on high-z structures. J. Cosmology Astropart. Phys., 2024(7):027.

Ramos Padilla, A. F., Wang, L., van der Tak, F. F. S., and Trager, S. C. (2023). Diagnosing the interstellar medium of galaxies with far-infrared emission lines. II. [C II], [O I], [O III], [N II], and [N III] up to z = 6. A&A, 679:A131.

Reddy, N. A., Oesch, P. A., Bouwens, R. J., Montes, M., Illingworth, G. D., Steidel, C. C., van Dokkum, P. G., Atek, H., Carollo, M. C., Cibinel, A., Holden, B., Labbé, I., Magee, D., Morselli, L., Nelson, E. J., and Wilkins, S. (2018). The HDUV Survey: A Revised Assessment of the Relationship between UV Slope and Dust Attenuation for High-redshift Galaxies. ApJ, 853(1):56.

Renaud, F., Boily, C. M., Naab, T., and Theis, C. (2009). Fully Compressive Tides in Galaxy Mergers. ApJ, 706(1):67–82.

Renaud, F., Bournaud, F., and Duc, P.-A. (2015). A parsec-resolution simulation of the Antennae galaxies: formation of star clusters during the merger. MNRAS, 446(2):2038–2054.

Renaud, F., Bournaud, F., Emsellem, E., Elmegreen, B., Teyssier, R., Alves, J., Chapon, D., Combes, F., Dekel, A., Gabor, J., Hennebelle, P., and Kraljic, K. (2013). A sub-parsec resolution simulation of the Milky Way: global structure of the interstellar medium and properties of molecular clouds. MNRAS, 436(2):1836–1851.

Renaud, F., Bournaud, F., Kraljic, K., and Duc, P. A. (2014). Starbursts triggered by intergalactic tides andinterstellar compressive turbulence. MNRAS, 442:L33–L37.

Ribeiro, B., Le Fèvre, O., Cassata, P., Garilli, B., Lemaux, B. C., Maccagni, D., Schaerer, D., Tasca, L. A. M., Zamorani, G., Zucca, E., Amorín, R., Bardelli, S., Hathi, N. P., Koekemoer, A., and Pforr, J. (2017). The VIMOS Ultra-Deep Survey: A major merger origin for the high fraction of galaxies at $2 < z < 6$ with two bright clumps. A&A, 608:A16.

Ricotti, M., Polisensky, E., and Cleland, E. (2022). Ghostly stellar haloes and their relationship to ultrafaint dwarfs. MNRAS, 515(1):302–319.

Rizzo, F., Kohandel, M., Pallottini, A., Zanella, A., Ferrara, A., Vallini, L., and Toft, S. (2022). Dynamical characterization of galaxies up to $z \sim 7$. A&A, 667:A5.

Rizzo, F., Vegetti, S., Fraternali, F., Stacey, H. R., and Powell, D. (2021). Dynamical properties of z 4.5 dusty star-forming galaxies and their connection with local early-type galaxies. MNRAS, 507(3):3952–3984.

Rizzo, F., Vegetti, S., Powell, D., Fraternali, F., McKean, J. P., Stacey, H. R., and White, S. D. M. (2020). A dynamically cold disk galaxy in the early Universe. Nature, 584(7820):201–204.

Roberts-Borsani, G., Treu, T., Shapley, A., Fontana, A., Pentericci, L., Castellano, M., Morishita, T., Bergamini, P., and Rosati, P. (2024). Between the Extremes: A JWST Spectroscopic Benchmark for High-redshift Galaxies Using ∼500 Confirmed Sources at $z \geq 5$. ApJ, 976(2):193.

Rodighiero, G., Enia, A., Bisigello, L., Girardi, G., Gandolfi, G., Kohandel, M., Pallottini, A., Badinelli, N., Grazian, A., Ferrara, A., Vulcani, B., Bianchetti, A., Marasco, A., Sinigaglia, F., Castellano, M., Santini, P., and Cassata, P. (2024a). An optically-dark merging system at z∼6 detected by JWST. *arXiv e-prints*, page arXiv:2405.04572.

Rodighiero, G., Enia, A., Bisigello, L., Girardi, G., Gandolfi, G., Kohandel, M., Pallottini, A., Badinelli, N., Grazian, A., Ferrara, A., Vulcani, B., Bianchetti, A., Marasco, A., Sinigaglia, F., Castellano, M., Santini, P., Cassata, P., Corsini, E. M., and Gruppioni, C. (2024b). An optically dark merging system at $z \sim 6$ detected by JWST. A&A, 691:A69.

Rodríguez Del Pino, B., Perna, M., Arribas, S., D'Eugenio, F., Lamperti, I., Pérez-González, P. G., Übler, H., Bunker, A., Carniani, S., Charlot, S., Maiolino, R., Willott, C. J., Böker, T., Chevallard, J., Cresci, G., Curti, M., Jones, G. C., Parlanti, E., Scholtz, J., and Venturi, G. (2024). GA-NIFS: Co-evolution within a highly star-forming galaxy group at $z \sim 3.7$ witnessed by JWST/NIRSpec IFS. A&A, 684:A187.

Rodriguez-Gomez, V., Genel, S., Vogelsberger, M., Sijacki, D., Pillepich, A., Sales, L. V., Torrey, P., Snyder, G., Nelson, D., Springel, V., Ma, C.-P., and Hernquist, L. (2015). The merger rate of galaxies in the Illustris simulation: a comparison with observations and semi-empirical models. MNRAS, 449(1):49–64.

Rodriguez-Gomez, V., Pillepich, A., Sales, L. V., Genel, S., Vogelsberger, M., Zhu, Q., Wellons, S., Nelson, D., Torrey, P., Springel, V., Ma, C.-P., and Hernquist, L. (2016). The stellar mass assembly of galaxies in the Illustris simulation: growth by mergers and the spatial distribution of accreted stars. MNRAS, 458(3):2371–2390.

Rodríguez-Puebla, A., Behroozi, P., Primack, J., Klypin, A., Lee, C., and Hellinger, D. (2016). Halo and subhalo demographics with Planck cosmological parameters: Bolshoi-Planck and MultiDark-Planck simulations. MNRAS, 462(1):893–916.

Roman-Oliveira, F., Fraternali, F., and Rizzo, F. (2023). Regular rotation and low turbulence in a diverse sample of z $\sim$ 4.5 galaxies observed with ALMA. MNRAS, 521(1):1045–1065.

Romano, L. E. C., Nagamine, K., and Hirashita, H. (2022). Dust diffusion in SPH simulations of an isolated galaxy. MNRAS, 514(1):1441–1460.

Romeo, A. B. and Agertz, O. (2014). Larson's scaling laws, and the gravitational instability of clumpy discs at high redshift. MNRAS, 442(2):1230–1238.

Romeo, A. B., Burkert, A., and Agertz, O. (2010). A Toomre-like stability criterion for the clumpy and turbulent interstellar medium. MNRAS, 407(2):1223–1230.

Romeo, A. B. and Falstad, N. (2013). A simple and accurate approximation for the Q stability parameter in multicomponent and realistically thick discs. MNRAS, 433(2):1389–1397.

Romeo, A. B. and Wiegert, J. (2011). The effective stability parameter for two-component galactic discs: is $Q^{-1} \approx {Q^{-1}}_{stars} + {Q^{-1}}_{gas}$? MNRAS, 416(2):1191–1196.

Roper, W. J., Lovell, C. C., Vijayan, A. P., Marshall, M. A., Irodotou, D., Kuusisto, J. K., Thomas, P. A., and Wilkins, S. M. (2022). First Light And Reionisation Epoch Simulations (FLARES) - IV. The size evolution of galaxies at z $\geq$ 5. MNRAS, 514(2):1921–1939.

Rosdahl, J., Blaizot, J., Aubert, D., Stranex, T., and Teyssier, R. (2013). RAMSES-RT: radiation hydrodynamics in the cosmological context. MNRAS, 436(3):2188–2231.

Rosdahl, J., Blaizot, J., Katz, H., Kimm, T., Garel, T., Haehnelt, M., Keating, L. C., Martin-Alvarez, S., Michel-Dansac, L., and Ocvirk, P. (2022). LyC escape from SPHINX galaxies in the Epoch of Reionization. MNRAS, 515(2):2386–2414.

Rosdahl, J., Katz, H., Blaizot, J., Kimm, T., Michel-Dansac, L., Garel, T., Haehnelt, M., Ocvirk, P., and Teyssier, R. (2018). The SPHINX cosmological simulations of the first billion years: the impact of binary stars on reionization. MNRAS, 479(1):994–1016.

Rosdahl, J., Schaye, J., Teyssier, R., and Agertz, O. (2015). Galaxies that shine: radiation-hydrodynamical simulations of disc galaxies. MNRAS, 451(1):34–58.

Rosolowsky, E. W., Pineda, J. E., Kauffmann, J., and Goodman, A. A. (2008). Structural Analysis of Molecular Clouds: Dendrograms. ApJ, 679(2):1338–1351.

Rowland, L. E., Hodge, J., Bouwens, R., Mancera Piña, P. E., Hygate, A., Algera, H., Aravena, M., Bowler, R., da Cunha, E., Dayal, P., Ferrara, A., Herard-Demanche, T., Inami, H., van Leeuwen, I., de Looze, I., Oesch, P., Pallottini, A., Phillips, S., Rybak, M., Schouws, S., Smit, R., Sommovigo, L., Stefanon, M., and van der Werf, P. (2024). REBELS-25: discovery of a dynamically cold disc galaxy at z = 7.31. MNRAS, 535(3):2068–2091.

Rowland, L. E., Stefanon, M., Bouwens, R., Hodge, J., Algera, H., Fisher, R., Dayal, P., Pallottini, A., Stark, D. P., Heintz, K. E., Aravena, M., Bowler, R., Cescon, K., Endsley, R., Ferrara, A., Gonzalez, V., Graziani, L., Gulis, C., Herard-Demanche, T., Inami, H., Laza-Ramos, A., van Leeuwen, I., de Looze, I., Nanayakkara, T., Oesch, P., Ormerod, K., Sartorio, N. S., Schouws, S., Smit, R., Sommovigo, L., Toft, S., Weaver, J. R., and van der Werf, P. (2025). REBELS-IFU: Evidence for metal-rich massive galaxies at z$\sim$6-8. *arXiv e-prints*, page arXiv:2501.10559.

Rybicki, G. B. and Lightman, A. P. (1986). *Radiative Processes in Astrophysics*.

Salim, S. and Narayanan, D. (2020). The Dust Attenuation Law in Galaxies. ARA&A, 58:529–575.

Salpeter, E. E. (1955). The Luminosity Function and Stellar Evolution. ApJ, 121:161.

Sanders, R. L., Shapley, A. E., Kriek, M., Reddy, N. A., Freeman, W. R., Coil, A. L., Siana, B., Mobasher, B., Shivaei, I., Price, S. H., and de Groot, L. (2016). The MOSDEF Survey: Electron Density and Ionization Parameter at z ∼2.3. ApJ, 816(1):23.

Saxena, A., Cameron, A. J., Katz, H., Bunker, A. J., Chevallard, J., D'Eugenio, F., Arribas, S., Bhatawdekar, R., Boyett, K., Cargile, P. A., Carniani, S., Charlot, S., Curti, M., Curtis-Lake, E., Hainline, K., Ji, Z., Johnson, B. D., Jones, G. C., Kumari, N., Laseter, I., Maseda, M. V., Robertson, B., Simmonds, C., Tacchella, S., Ubler, H., Williams, C. C., Willott, C., Witstok, J., and Zhu, Y. (2024). Hitting the slopes: A spectroscopic view of UV continuum slopes of galaxies reveals a reddening at z > 9.5. *arXiv e-prints*, page arXiv:2411.14532.

Schaerer, D. (2002). On the properties of massive Population III stars and metal-free stellar populations. A&A, 382:28–42.

Schaerer, D., Boone, F., Zamojski, M., Staguhn, J., Dessauges-Zavadsky, M., Finkelstein, S., and Combes, F. (2015). New constraints on dust emission and UV attenuation of z = 6.5-7.5 galaxies from millimeter observations. A&A, 574:A19.

Schaerer, D., Ginolfi, M., Béthermin, M., Fudamoto, Y., Oesch, P. A., Le Fèvre, O., Faisst, A., Capak, P., Cassata, P., Silverman, J. D., Yan, L., Jones, G. C., Amorin, R., Bardelli, S., Boquien, M., Cimatti, A., Dessauges-Zavadsky, M., Giavalisco, M., Hathi, N. P., Fujimoto, S., Ibar, E., Koekemoer, A., Lagache, G., Lemaux, B. C., Loiacono, F., Maiolino, R., Narayanan, D., Morselli, L., Méndez-Hernàndez, H., Pozzi, F., Riechers, D., Talia, M., Toft, S., Vallini, L., Vergani, D., Zamorani, G., and Zucca, E. (2020). The ALPINE-ALMA [C II] survey. Little to no evolution in the [C II]-SFR relation over the last 13 Gyr. A&A, 643:A3.

Schaerer, D., Izotov, Y. I., Worseck, G., Berg, D., Chisholm, J., Jaskot, A., Nakajima, K., Ravindranath, S., Thuan, T. X., and Verhamme, A. (2022). Strong Lyman continuum emitting galaxies show intense C IV λ1550 emission. A&A, 658:L11.

Schaye, J., Crain, R. A., Bower, R. G., Furlong, M., Schaller, M., Theuns, T., Dalla Vecchia, C., Frenk, C. S., McCarthy, I. G., Helly, J. C., Jenkins, A., Rosas-Guevara, Y. M., White, S. D. M., Baes, M., Booth, C. M., Camps, P., Navarro, J. F., Qu, Y., Rahmati, A., Sawala, T., Thomas, P. A., and Trayford, J. (2015). The EAGLE project: simulating the evolution and assembly of galaxies and their environments. MNRAS, 446(1):521–554.

Schaye, J. and Dalla Vecchia, C. (2008). On the relation between the Schmidt and Kennicutt-Schmidt star formation laws and its implications for numerical simulations. MNRAS, 383(3):1210–1222.

Schimek, A., Decataldo, D., Shen, S., Cicone, C., Baumschlager, B., van Kampen, E., Klaassen, P., Madau, P., Di Mascolo, L., Mayer, L., Montoya Arroyave, I., Mroczkowski, T., and Warraich, J. (2024). High resolution modelling of [CII], [CI], [OIII], and CO line emission from the interstellar medium and circumgalactic medium of a star-forming galaxy at z ∼ 6.5. A&A, 682:A98.

Schneider, R. and Maiolino, R. (2024). The formation and cosmic evolution of dust in the early Universe: I. Dust sources. A&A Rev., 32(1):2.

Scholtz, J., Silcock, M. S., Curtis-Lake, E., Maiolino, R., Carniani, S., D'Eugenio, F., Ji, X., Jakobsen, P., Hainline, K., Arribas, S., Baker, W. M., Bhatawdekar, R., Bunker, A. J., Charlot, S., Chevallard, J., Curti, M., Eisenstein, D. J., Isobe, Y., Jones, G. C., Parlanti, E., Pérez-González, P. G., Rinaldi, P., Robertson, B., Tacchella, S., Übler, H., Williams, C. C., Willott, C., and Witstok, J. (2025). JADES: Carbon-enhanced, Nitrogen-normal compact galaxy at z=11.2. *arXiv e-prints*, page arXiv:2507.17809.

Scholtz, J., Witten, C., Laporte, N., Übler, H., Perna, M., Maiolino, R., Arribas, S., Baker, W. M., Bennett, J. S., D'Eugenio, F., Simmonds, C., Tacchella, S., Witstok, J., Bunker, A. J., Carniani, S., Charlot, S., Cresci, G., Curtis-Lake, E., Eisenstein, D. J., Kumari, N., Robertson, B., Rodríguez Del Pino, B., Smit, R., Venturi, G., Williams, C. C., and Willmer, C. N. A. (2024). GN-z11: The environment of an active galactic nucleus at z = 10.603. New insights into the most distant Lyα detection. A&A, 687:A283.

Schouws, S., Bouwens, R. J., Algera, H., Smit, R., Kumari, N., Rowland, L. E., van Leeuwen, I., Sommovigo, L., Ferrara, A., Oesch, P. A., Ormerod, K., Stefanon, M., Herard-Demanche, T., Hodge, J., Fudamoto, Y., Röttgering, H., and van der Werf, P. (2025). Deep Constraints on [CII]158μm in JADES-GS-z14-0: Further Evidence for a Galaxy with Low Gas Content at z=14.2. *arXiv e-prints*, page arXiv:2502.01610.

Schouws, S., Bouwens, R. J., Ormerod, K., Smit, R., Algera, H., Sommovigo, L., Hodge, J., Ferrara, A., Oesch, P. A., Rowland, L. E., van Leeuwen, I., Stefanon, M., Herard-Demanche, T., Fudamoto, Y., Röttgering, H., and van der Werf, P. (2024). Detection of [OIII]88μm in JADES-GS-z14-0 at z=14.1793. *arXiv e-prints*, page arXiv:2409.20549.

Schouws, S., Stefanon, M., Bouwens, R., Smit, R., Hodge, J., Labbé, I., Algera, H., Boogaard, L., Carniani, S., Fudamoto, Y., Holwerda, B. W., Illingworth, G. D., Maiolino, R., Maseda, M., Oesch, P., and van der Werf, P. (2022). Significant Dust-obscured Star Formation in Luminous Lyman-break Galaxies at z 7-8. ApJ, 928(1):31.

Schreiber, C., Elbaz, D., Pannella, M., Ciesla, L., Wang, T., and Franco, M. (2018). Dust temperature and mid-to-total infrared color distributions for star-forming galaxies at $0 < z < 4$. A&A, 609:A30.

Scoville, N., Sheth, K., Aussel, H., Vanden Bout, P., Capak, P., Bongiorno, A., Casey, C. M., Murchikova, L., Koda, J., Álvarez-Márquez, J., Lee, N., Laigle, C., McCracken, H. J., Ilbert, O., Pope, A., Sanders, D., Chu, J., Toft, S., Ivison, R. J., and Manohar, S. (2016). ISM Masses and the Star formation Law at Z = 1 to 6: ALMA Observations of Dust Continuum in 145 Galaxies in the COSMOS Survey Field. ApJ, 820(2):83.

Seaton, M. J. (1954). Electron temperatures and electron densities in planetary nebulae. MNRAS, 114:154.

Seaton, M. J. (1960). Planetary nebulae. *Reports on Progress in Physics*, 23(1):313–354.

Shen, X., Kannan, R., Puchwein, E., Smith, A., Vogelsberger, M., Borrow, J., Garaldi, E., Keating, L., Zier, O., McClymont, W., Tacchella, S., Wang, Z., and Hernquist, L. (2025). The THESAN-ZOOM project: Star-formation efficiencies in high-redshift galaxies. *arXiv e-prints*, page arXiv:2503.01949.

Shen, X., Vogelsberger, M., Borrow, J., Hu, Y., Erickson, E., Kannan, R., Smith, A., Garaldi, E., Hernquist, L., Morishita, T., Tacchella, S., Zier, O., Sun, G., Eilers, A.-C., and Wang, H. (2024). The THESAN project: galaxy sizes during the epoch of reionization. *arXiv e-prints*, page arXiv:2402.08717.

Shen, X., Vogelsberger, M., Boylan-Kolchin, M., Tacchella, S., and Kannan, R. (2023). The impact of UV variability on the abundance of bright galaxies at $z \geq 9$. MNRAS, 525(3):3254–3261.

Shibuya, T., Ito, Y., Asai, K., Kirihara, T., Fujimoto, S., Toba, Y., Miura, N., Umayahara, T., Iwadate, K., Ali, S. S., and Kodama, T. (2024). Galaxy Morphologies Revealed with Subaru HSC and Super-Resolution Techniques II: Environmental Dependence of Galaxy Mergers at z$\sim$2-5. *arXiv e-prints*, page arXiv:2403.06729.

Shibuya, T., Ouchi, M., Kubo, M., and Harikane, Y. (2016). Morphologies of $\sim$190,000 Galaxies at z = 0-10 Revealed with HST Legacy Data. II. Evolution of Clumpy Galaxies. ApJ, 821(2):72.

Shimizu, I., Inoue, A. K., Okamoto, T., and Yoshida, N. (2014). Physical properties of UDF12 galaxies in cosmological simulations. MNRAS, 440(1):731–745.

Shuntov, M., Ilbert, O., Toft, S., Arango-Toro, R. C., Akins, H. B., Casey, C. M., Franco, M., Harish, S., Kartaltepe, J. S., Koekemoer, A. M., McCracken, H. J., Paquereau, L., Laigle, C., Bethermin, M., Dubois, Y., Drakos, N. E., Faisst, A., Gozaliasl, G., Gillman, S., Hayward, C. C., Hirschmann, M., Huertas-Company, M., Jespersen, C. K., Jin, S., Kokorev, V., Lambrides, E., Le Borgne, D., Liu, D., Magdis, G., Massey, R., McPartland, C. J. R., Mercier, W., McCleary, J. E., McKinney, J., Oesch, P. A., Renzini, A., Rhodes, J. D., Rich, R. M., Robertson, B. E., Sanders, D., Trebitsch, M., Tresse, L., Valentino, F., Vijayan, A. P., Weaver, J. R., Weibel, A., Wilkins, S. M., and Yang, L. (2025). COSMOS-Web: Stellar mass assembly in relation to dark matter halos across $0.2 < z < 12$ of cosmic history. A&A, 695:A20.

Smit, R., Bouwens, R. J., Carniani, S., Oesch, P. A., Labbé, I., Illingworth, G. D., van der Werf, P., Bradley, L. D., Gonzalez, V., Hodge, J. A., Holwerda, B. W., Maiolino, R., and Zheng, W. (2018). Rotation in [C II]-emitting gas in two galaxies at a redshift of 6.8. Nature, 553(7687):178–181.

Smith, B. D., Bryan, G. L., Glover, S. C. O., Goldbaum, N. J., Turk, M. J., Regan, J., Wise, J. H., Schive, H.-Y., Abel, T., Emerick, A., O'Shea, B. W., Anninos, P., Hummels, C. B., and Khochfar, S. (2017). GRACKLE: a chemistry and cooling library for astrophysics. MNRAS, 466(2):2217–2234.

Sobral, D., Matthee, J., Darvish, B., Schaerer, D., Mobasher, B., Röttgering, H. J. A., Santos, S., and Hemmati, S. (2015). Evidence for PopIII-like Stellar Populations in the Most Luminous Lyman-α Emitters at the Epoch of Reionization: Spectroscopic Confirmation. ApJ, 808(2):139.

Solimano, M., González-López, J., Aravena, M., Herrera-Camus, R., De Looze, I., Förster Schreiber, N. M., Spilker, J., Tadaki, K., Assef, R. J., Barcos-Muñoz, L., Davies, R. L., Díaz-Santos, T., Ferrara, A., Fisher, D. B., Guaita, L., Ikeda, R., Johnston, E. J., Lutz, D., Mitsuhashi, I., Moya-Sierralta, C., Relaño, M., Naab, T., Posses, A. C., Telikova, K., Übler, H., van der Giessen, S., Veilleux, S., and Villanueva, V. (2024). The ALMA-CRISTAL survey: Discovery of a 15 kpc-long gas plume in a z = 4.54 Lyman-α blob. A&A, 689:A145.

Sommovigo, L., Ferrara, A., Carniani, S., Zanella, A., Pallottini, A., Gallerani, S., and Vallini, L. (2021). Dust temperature in ALMA [C II]-detected high-z galaxies. MNRAS, 503(4):4878–4891.

Sommovigo, L., Ferrara, A., Pallottini, A., Carniani, S., Gallerani, S., and Decataldo, D. (2020). Warm dust in high-z galaxies: origin and implications. MNRAS, 497(1):956–968.

Sommovigo, L., Ferrara, A., Pallottini, A., Dayal, P., Bouwens, R. J., Smit, R., da Cunha, E., De Looze, I., Bowler, R. A. A., Hodge, J., Inami, H., Oesch, P., Endsley, R., Gonzalez, V., Schouws, S., Stark, D., Stefanon, M., Aravena, M., Graziani, L., Riechers, D., Schneider, R., van der Werf, P., Algera, H., Barrufet, L., Fudamoto, Y., Hygate, A. P. S., Labbé, I., Li, Y., Nanayakkara, T., and Topping, M. (2022). The ALMA REBELS Survey: cosmic dust temperature evolution out to z 7. MNRAS, 513(3):3122–3135.

Springel, V. and Hernquist, L. (2003). Cosmological smoothed particle hydrodynamics simulations: a hybrid multiphase model for star formation. MNRAS, 339(2):289–311.

Stacey, G. J., Hailey-Dunsheath, S., Ferkinhoff, C., Nikola, T., Parshley, S. C., Benford, D. J., Staguhn, J. G., and Fiolet, N. (2010). A 158 μm [C II] Line Survey of Galaxies at z $\sim$1-2: An Indicator of Star Formation in the Early Universe. ApJ, 724(2):957–974.

Stanway, E. R. and Eldridge, J. J. (2018). Re-evaluating old stellar populations. MNRAS, 479(1):75–93.

Stark, D. P., Ellis, R. S., Charlot, S., Chevallard, J., Tang, M., Belli, S., Zitrin, A., Mainali, R., Gutkin, J., Vidal-García, A., Bouwens, R., and Oesch, P. (2017). Lyα and C III] emission in z = 7-9 Galaxies: accelerated reionization around luminous star-forming systems? MNRAS, 464(1):469–479.

Steidel, C. C., Adelberger, K. L., Dickinson, M., Giavalisco, M., Pettini, M., and Kellogg, M. (1998). A Large Structure of Galaxies at Redshift Z approximately 3 and Its Cosmological Implications. ApJ, 492(2):428–438.

Stiavelli, M., Morishita, T., Chiaberge, M., Grillo, C., Leethochawalit, N., Rosati, P., Schuldt, S., Trenti, M., and Treu, T. (2023). The Puzzling Properties of the MACS1149-JD1 Galaxy at z = 9.11. ApJ, 957(2):L18.

Storey, P. J. and Zeippen, C. J. (2000). Theoretical values for the [OIII] 5007/4959 line-intensity ratio and homologous cases. MNRAS, 312(4):813–816.

Sugahara, Y., Álvarez-Márquez, J., Hashimoto, T., Colina, L., Inoue, A. K., Costantin, L., Fudamoto, Y., Mawatari, K., Ren, Y. W., Arribas, S., Bakx, T. J. L. C., Blanco-Prieto, C., Ceverino, D., Crespo Gómez, A., Hagimoto, M., Hashigaya, T., Marques-Chaves, R., Matsuo, H., Nakazato, Y., Pereira-Santaella, M., Tamura, Y., Usui, M., and Yoshida, N. (2025). RIOJA. Complex Dusty Starbursts in a Major Merger B14-65666 at z = 7.15. ApJ, 981(2):135.

Sugimura, K., Matsumoto, T., Hosokawa, T., Hirano, S., and Omukai, K. (2020). The Birth of a Massive First-star Binary. ApJ, 892(1):L14.

Sugimura, K., Matsumoto, T., Hosokawa, T., Hirano, S., and Omukai, K. (2023). Formation of Massive and Wide First-star Binaries in Radiation Hydrodynamic Simulations. ApJ, 959(1):17.

Sugimura, K., Ricotti, M., Park, J., Garcia, F. A. B., and Yajima, H. (2024). Violent starbursts and quiescence induced by FUV radiation feedback in metal-poor galaxies at high-redshift. *arXiv e-prints*, page arXiv:2403.04824.

Sun, F., Helton, J. M., Egami, E., Hainline, K. N., Rieke, G. H., Willmer, C. N. A., Eisenstein, D. J., Johnson, B. D., Rieke, M. J., Robertson, B., Tacchella, S., Alberts, S., Baker, W. M., Bhatawdekar, R., Boyett, K., Bunker, A. J., Charlot, S., Chen, Z., Chevallard, J., Curtis-Lake, E., Danhaive, A. L., DeCoursey, C., Ji, Z., Lyu, J., Maiolino, R., Rujopakarn, W., Sandles, L., Shivaei, I., Übler, H., Willott, C., and Witstok, J. (2024). JADES: Resolving the Stellar Component and Filamentary Overdense Environment of Hubble Space Telescope (HST)-dark Submillimeter Galaxy HDF850.1 at z = 5.18. ApJ, 961(1):69.

Sun, G., Faucher-Giguère, C.-A., Hayward, C. C., Shen, X., Wetzel, A., and Cochrane, R. K. (2023). Bursty Star Formation Naturally Explains the Abundance of Bright Galaxies at Cosmic Dawn. ApJ, 955(2):L35.

Swinbank, A. M., Simpson, J. M., Smail, I., Harrison, C. M., Hodge, J. A., Karim, A., Walter, F., Alexander, D. M., Brandt, W. N., de Breuck, C., da Cunha, E., Chapman, S. C., Coppin, K. E. K., Danielson, A. L. R., Dannerbauer, H., Decarli, R., Greve, T. R., Ivison, R. J., Knudsen, K. K., Lagos, C. D. P., Schinnerer, E., Thomson, A. P., Wardlow, J. L., Weiß, A., and van der Werf, P. (2014). An ALMA survey of sub-millimetre Galaxies in the Extended Chandra Deep Field South: the far-infrared properties of SMGs. MNRAS, 438(2):1267–1287.

Tacchella, S., Eisenstein, D. J., Hainline, K., Johnson, B. D., Baker, W. M., Helton, J. M., Robertson, B., Suess, K. A., Chen, Z., Nelson, E., Puskás, D., Sun, F., Alberts, S., Egami, E., Hausen, R., Rieke, G., Rieke, M., Shivaei, I., Williams, C. C., Willmer, C. N. A., Bunker, A., Cameron, A. J., Carniani, S., Charlot, S., Curti, M., Curtis-Lake, E., Looser, T. J., Maiolino, R., Maseda, M. V., Rawle, T., Rix, H.-W., Smit, R., Übler, H., Willott, C., Witstok, J., Baum, S., Bhatawdekar, R., Boyett, K., Danhaive, A. L., de Graaff, A., Endsley, R., Ji, Z., Lyu, J., Sandles, L., Saxena, A., Scholtz, J., Topping, M. W., and Whitler, L. (2023). JADES Imaging of GN-z11: Revealing the Morphology and Environment of a Luminous Galaxy 430 Myr after the Big Bang. ApJ, 952(1):74.

Tadaki, K.-i., Kodama, T., Tanaka, I., Hayashi, M., Koyama, Y., and Shimakawa, R. (2014). The Nature of Hα-selected Galaxies at z > 2. II. Clumpy Galaxies and Compact Star-forming Galaxies. ApJ, 780(1):77.

Tadaki, K.-i., Tsujita, A., Tamura, Y., Kohno, K., Hatsukade, B., Iono, D., Lee, M. M., Matsuda, Y., Michiyama, T., Nagao, T., Nakanishi, K., Nishimura, Y., Saito, T., Umehata, H., and Zavala, J. (2022). Detection of nitrogen and oxygen in a galaxy at the end of reionization. PASJ, 74(3):L9–L16.

Takeuchi, T. T., Yuan, F.-T., Ikeyama, A., Murata, K. L., and Inoue, A. K. (2012). Reexamination of the Infrared Excess-Ultraviolet Slope Relation of Local Galaxies. ApJ, 755(2):144.

Tamburello, V., Rahmati, A., Mayer, L., Cava, A., Dessauges-Zavadsky, M., and Schaerer, D. (2017). Clumpy galaxies seen in H α: inflated observed clump properties due to limited spatial resolution and sensitivity. MNRAS, 468(4):4792–4800.

Tamura, Y., C. Bakx, T. J. L., Inoue, A. K., Hashimoto, T., Tokuoka, T., Imamura, C., Hatsukade, B., Lee, M. M., Moriwaki, K., Okamoto, T., Ota, K., Umehata, H., Yoshida, N., Zackrisson, E., Hagimoto, M., Matsuo, H., Shimizu, I., Sugahara, Y., and Takeuchi, T. T. (2023). The 300 pc Resolution Imaging of a z = 8.31 Galaxy: Turbulent Ionized Gas and Potential Stellar Feedback 600 Million Years after the Big Bang. ApJ, 952(1):9.

Tamura, Y., Mawatari, K., Hashimoto, T., Inoue, A. K., Zackrisson, E., Christensen, L., Binggeli, C., Matsuda, Y., Matsuo, H., Takeuchi, T. T., Asano, R. S., Sunaga, K., Shimizu, I., Okamoto, T.,

Yoshida, N., Lee, M. M., Shibuya, T., Taniguchi, Y., Umehata, H., Hatsukade, B., Kohno, K., and Ota, K. (2019). Detection of the Far-infrared [O III] and Dust Emission in a Galaxy at Redshift 8.312: Early Metal Enrichment in the Heart of the Reionization Era. ApJ, 874(1):27.

Tanaka, T. S., Silverman, J. D., Nakazato, Y., Onoue, M., Shimasaku, K., Fudamoto, Y., Fujimoto, S., Ding, X., Faisst, A. L., Valentino, F., Jin, S., Hayward, C. C., Kokorev, V., Ceverino, D., Kalita, B. S., Casey, C. M., Liu, Z., Kaminsky, A., Fei, Q., Andika, I. T., Lambrides, E., Akins, H. B., Kartaltepe, J. S., Koekemoer, A. M., McCracken, H. J., Rhodes, J., Robertson, B. E., Franco, M., Liu, D., Chartab, N., Gillman, S., Gozaliasl, G., Hirschmann, M., Huertas-Company, M., Massey, R., Roy, N., Sattari, Z., Shuntov, M., Sterling, J., Toft, S., Trakhtenbrot, B., Yoshida, N., and Zavala, J. A. (2024). Crimson Behemoth: A massive clumpy structure hosting a dusty AGN at z=4.91. PASJ, 76(6):1323–1335.

Tasca, L. A. M., Le Fèvre, O., López-Sanjuan, C., Wang, P. W., Cassata, P., Garilli, B., Ilbert, O., Le Brun, V., Lemaux, B. C., Maccagni, D., Tresse, L., Bardelli, S., Contini, T., Charlot, S., Cucciati, O., Fontana, A., Giavalisco, M., Kneib, J. P., Salvato, M., Taniguchi, Y., Vergani, D., Zamorani, G., and Zucca, E. (2014). Evidence for major mergers of galaxies at $2 \lesssim z < 4$ in the VVDS and VUDS surveys. A&A, 565:A10.

Telikova, K., González-López, J., Aravena, M., Posses, A., Villanueva, V., Baeza-Garay, M., Jones, G. C., Solimano, M., Lee, L., Assef, R. J., De Looze, I., Diaz Santos, T., Ferrara, A., Ikeda, R., Herrera-Camus, R., Übler, H., Lamperti, I., Mitsuhashi, I., Relano, M., Perna, M., and Tadaki, K. (2024). The ALMA-CRISTAL Survey: Complex kinematics of the galaxies at the end of the Reionization Era. *arXiv e-prints*, page arXiv:2411.09033.

Teyssier, R. (2002). Cosmological hydrodynamics with adaptive mesh refinement. A new high resolution code called RAMSES. A&A, 385:337–364.

Thompson, T. A., Quataert, E., and Murray, N. (2005). Radiation Pressure-supported Starburst Disks and Active Galactic Nucleus Fueling. ApJ, 630(1):167–185.

Tielens, A. G. G. M. (2005). *The Physics and Chemistry of the Interstellar Medium*.

Toomre, A. (1964). On the gravitational stability of a disk of stars. ApJ, 139:1217–1238.

Topping, M. W., Sanders, R. L., Shapley, A. E., Pahl, A. J., Reddy, N. A., Stark, D. P., Berg, D. A., Clarke, L., Cullen, F., Dunlop, J. S., Ellis, R. S., Förster Schreiber, N. M., Illingworth, G. D., Jones, T., Narayanan, D., Pettini, M., and Schaerer, D. (2025). The AURORA Survey: The Evolution of Multi-phase Electron Densities at High Redshift. *arXiv e-prints*, page arXiv:2502.08712.

Topping, M. W., Stark, D. P., Endsley, R., Plat, A., Whitler, L., Chen, Z., and Charlot, S. (2022). Searching for Extremely Blue UV Continuum Slopes at z = 7-11 in JWST/NIRCam Imaging: Implications for Stellar Metallicity and Ionizing Photon Escape in Early Galaxies. ApJ, 941(2):153.

Topping, M. W., Stark, D. P., Endsley, R., Whitler, L., Hainline, K., Johnson, B. D., Robertson, B., Tacchella, S., Chen, Z., Alberts, S., Baker, W. M., Bunker, A. J., Carniani, S., Charlot, S., Chevallard, J., Curtis-Lake, E., DeCoursey, C., Egami, E., Eisenstein, D. J., Ji, Z., Maiolino, R., Williams, C. C., Willmer, C. N. A., Willott, C., and Witstok, J. (2024a). The UV continuum slopes of early star-forming galaxies in JADES. MNRAS, 529(4):4087–4103.

Topping, M. W., Stark, D. P., Senchyna, P., Plat, A., Zitrin, A., Endsley, R., Charlot, S., Furtak, L. J., Maseda, M. V., Smit, R., Mainali, R., Chevallard, J., Molyneux, S., and Rigby, J. R. (2024b). Metal-poor star formation at $z > 6$ with JWST: new insight into hard radiation fields and nitrogen enrichment on 20 pc scales. MNRAS, 529(4):3301–3322.

Torrey, P., Vogelsberger, M., Marinacci, F., Pakmor, R., Springel, V., Nelson, D., Naiman, J., Pillepich, A., Genel, S., Weinberger, R., and Hernquist, L. (2019). The evolution of the mass-metallicity relation and its scatter in IllustrisTNG. MNRAS, 484(4):5587–5607.

Toyouchi, D., Yajima, H., Ferrara, A., and Nagamine, K. (2025). Bridging Theory and Observations: Insights into Star Formation Efficiency and Dust Attenuation in $z > 5$ Galaxies. *arXiv e-prints*, page arXiv:2502.12538.

Trebitsch, M., Blaizot, J., Rosdahl, J., Devriendt, J., and Slyz, A. (2017). Fluctuating feedback-regulated escape fraction of ionizing radiation in low-mass, high-redshift galaxies. MNRAS, 470(1):224–239.

Treu, T., Calabrò, A., Castellano, M., Leethochawalit, N., Merlin, E., Fontana, A., Yang, L., Morishita, T., Trenti, M., Dressler, A., Mason, C., Paris, D., Pentericci, L., Roberts-Borsani, G., Vulcani, B., Boyett, K., Bradac, M., Glazebrook, K., Jones, T., Marchesini, D., Mascia, S., Nanayakkara, T., Santini, P., Strait, V., Vanzella, E., and Wang, X. (2023). Early Results From GLASS-JWST. XII. The Morphology of Galaxies at the Epoch of Reionization. ApJ, 942(2):L28.

Trinca, A., Schneider, R., Valiante, R., Graziani, L., Ferrotti, A., Omukai, K., and Chon, S. (2024). Exploring the nature of UV-bright z $\gtrsim$ 10 galaxies detected by JWST: star formation, black hole accretion, or a non-universal IMF? MNRAS, 529(4):3563–3581.

Tripodi, R., D'Eugenio, F., Maiolino, R., Curti, M., Scholtz, J., Tacchella, S., Bunker, A. J., Trussler, J. A. A., Cameron, A. J., Arribas, S., Baker, W. M., Bradač, M., Carniani, S., Charlot, S., Ji, X., Ji, Z., Robertson, B., Übler, H., Venturi, G., Willmer, C. N. A., and Witstok, J. (2024). Spatially resolved emission lines in galaxies at $4 \leq z < 10$ from the JADES survey: evidence for enhanced central star formation. *arXiv e-prints*, page arXiv:2403.08431.

Truelove, J. K., Klein, R. I., McKee, C. F., Holliman, John H., I., Howell, L. H., and Greenough, J. A. (1997). The Jeans Condition: A New Constraint on Spatial Resolution in Simulations of Isothermal Self-gravitational Hydrodynamics. ApJ, 489(2):L179–L183.

Tsukui, T. and Iguchi, S. (2021). Spiral morphology in an intensely star-forming disk galaxy more than 12 billion years ago. *Science*, 372(6547):1201–1205.

Tsuna, D., Nakazato, Y., and Hartwig, T. (2023). A photon burst clears the earliest dusty galaxies: modelling dust in high-redshift galaxies from ALMA to JWST. MNRAS, 526(4):4801–4813.

Usui, M., Mawatari, K., Álvarez-Márquez, J., Hashimoto, T., Sugahara, Y., Marques-Chaves, R., Inoue, A. K., Colina, L., Arribas, S., Blanco-Prieto, C., Nakazato, Y., Yoshida, N., Bakx, T. J. L. C., Ceverino, D., Costantin, L., Crespo Gómez, A., Hagimoto, M., Matsuo, H., Osone, W., Ren, Y. W., Fudamoto, Y., Hashigaya, T., Pereira-Santaella, M., and Tamura, Y. (2025). RIOJA. JWST and ALMA unveil the inhomogeneous and complex ISM structure in a star-forming galaxy at $z = 6.81$. *arXiv e-prints*, page arXiv:2507.02054.

Vallini, L., Ferrara, A., Pallottini, A., and Gallerani, S. (2017). Molecular cloud photoevaporation and far-infrared line emission. MNRAS, 467(2):1300–1312.

Vallini, L., Gallerani, S., Ferrara, A., and Baek, S. (2013). Far-infrared line emission from high-redshift galaxies. MNRAS, 433(2):1567–1572.

Vallini, L., Gallerani, S., Ferrara, A., Pallottini, A., and Yue, B. (2015). On the [CII]-SFR Relation in High Redshift Galaxies. ApJ, 813(1):36.

Vallini, L., Pallottini, A., Kohandel, M., Sommovigo, L., Ferrara, A., Bethermin, M., Herrera-Camus, R., Carniani, S., Faisst, A., Zanella, A., Pozzi, F., Dessauges-Zavadsky, M., Gruppioni, C., Veraldi, E., and Accard, C. (2025). Spatially resolved [CII]-gas conversion factor in early galaxies. *arXiv e-prints*, page arXiv:2504.14001.

van der Wel, A., Franx, M., van Dokkum, P. G., Skelton, R. E., Momcheva, I. G., Whitaker, K. E., Brammer, G. B., Bell, E. F., Rix, H. W., Wuyts, S., Ferguson, H. C., Holden, B. P., Barro, G., Koekemoer, A. M., Chang, Y.-Y., McGrath, E. J., Häussler, B., Dekel, A., Behroozi, P., Fumagalli, M., Leja, J., Lundgren, B. F., Maseda, M. V., Nelson, E. J., Wake, D. A., Patel, S. G., Labbé, I., Faber, S. M., Grogin, N. A., and Kocevski, D. D. (2014). 3D-HST+CANDELS: The Evolution of the Galaxy Size-Mass Distribution since z = 3. ApJ, 788(1):28.

Vanni, I., Salvadori, S., Skúladóttir, Á., Rossi, M., and Koutsouridou, I. (2023). Characterizing the true descendants of the first stars. MNRAS, 526(2):2620–2644.

Vanzella, E., Castellano, M., Bergamini, P., Treu, T., Mercurio, A., Scarlata, C., Rosati, P., Grillo, C., Acebron, A., Caminha, G. B., Nonino, M., Nanayakkara, T., Roberts-Borsani, G., Bradac, M., Wang, X., Brammer, G., Strait, V., Vulcani, B., Meštrić, U., Meneghetti, M., Calura, F., Henry, A., Zanella, A., Trenti, M., Boyett, K., Morishita, T., Calabrò, A., Glazebrook, K., Marchesini, D., Birrer, S., Yang, L., and Jones, T. (2022). Early Results from GLASS-JWST. VII. Evidence for Lensed, Gravitationally Bound Protoglobular Clusters at z = 4 in the Hubble Frontier Field A2744. ApJ, 940(2):L53.

Vanzella, E., Claeyssens, A., Welch, B., Adamo, A., Coe, D., Diego, J. M., Mahler, G., Khullar, G., Kokorev, V., Oguri, M., Ravindranath, S., Furtak, L. J., Hsiao, T. Y.-Y., Abdurro'uf, Mandelker, N., Brammer, G., Bradley, L. D., Bradač, M., Conselice, C. J., Dayal, P., Nonino, M., Andrade-Santos, F., Windhorst, R. A., Pirzkal, N., Sharon, K., de Mink, S. E., Fujimoto, S., Zitrin, A., Eldridge, J. J., and Norman, C. (2023a). JWST/NIRCam Probes Young Star Clusters in the Reionization Era Sunrise Arc. ApJ, 945(1):53.

Vanzella, E., Claeyssens, A., Welch, B., Adamo, A., Coe, D., Diego, J. M., Mahler, G., Khullar, G., Kokorev, V., Oguri, M., Ravindranath, S., Furtak, L. J., Hsiao, T. Y.-Y., Abdurro'uf, Mandelker, N., Brammer, G., Bradley, L. D., Bradač, M., Conselice, C. J., Dayal, P., Nonino, M., Andrade-Santos, F., Windhorst, R. A., Pirzkal, N., Sharon, K., de Mink, S. E., Fujimoto, S., Zitrin, A., Eldridge, J. J., and Norman, C. (2023b). JWST/NIRCam Probes Young Star Clusters in the Reionization Era Sunrise Arc. ApJ, 945(1):53.

Venturi, G., Carniani, S., Parlanti, E., Kohandel, M., Curti, M., Pallottini, A., Vallini, L., Arribas, S., Bunker, A. J., Cameron, A. J., Castellano, M., Ferrara, A., Fontana, A., Gallerani, S., Gelli, V., Maiolino, R., Ntormousi, E., Pacifici, C., Pentericci, L., Salvadori, S., and Vanzella, E. (2024). Gas-phase metallicity gradients in galaxies at $z \sim 6 - 8$. *arXiv e-prints*, page arXiv:2403.03977.

Viero, M. P., Sun, G., Chung, D. T., Moncelsi, L., and Condon, S. S. (2022). The early Universe was dust-rich and extremely hot. MNRAS, 516(1):L30–L34.

Vijayan, A. P., Clay, S. J., Thomas, P. A., Yates, R. M., Wilkins, S. M., and Henriques, B. M. (2019). Detailed dust modelling in the L-GALAXIES semi-analytic model of galaxy formation. MNRAS, 489(3):4072–4089.

Vijayan, A. P., Wilkins, S. M., Lovell, C. C., Thomas, P. A., Camps, P., Baes, M., Trayford, J., Kuusisto, J., and Roper, W. J. (2022). First Light And Reionisation Epoch Simulations (FLARES) - III. The properties of massive dusty galaxies at cosmic dawn. MNRAS, 511(4):4999–5017.

Villa-Vélez, J. A., Buat, V., Theulé, P., Boquien, M., and Burgarella, D. (2021). Fitting spectral energy distributions of FMOS-COSMOS emission-line galaxies at z $\sim$ 1.6: Star formation rates, dust attenuation, and [OIII]λ5007 emission-line luminosities. A&A, 654:A153.

Vogelsberger, M., Genel, S., Springel, V., Torrey, P., Sijacki, D., Xu, D., Snyder, G., Nelson, D., and Hernquist, L. (2014). Introducing the Illustris Project: simulating the coevolution of dark and visible matter in the Universe. MNRAS, 444(2):1518–1547.

Vogelsberger, M., Nelson, D., Pillepich, A., Shen, X., Marinacci, F., Springel, V., Pakmor, R., Tacchella, S., Weinberger, R., Torrey, P., and Hernquist, L. (2020). High-redshift JWST predictions from IllustrisTNG: dust modelling and galaxy luminosity functions. MNRAS, 492(4):5167–5201.

Wang, B., Fujimoto, S., Labbé, I., Furtak, L. J., Miller, T. B., Setton, D. J., Zitrin, A., Atek, H., Bezanson, R., Brammer, G., Leja, J., Oesch, P. A., Price, S. H., Chemerynska, I., Cutler, S. E., Dayal, P., van Dokkum, P., Goulding, A. D., Greene, J. E., Fudamoto, Y., Khullar, G., Kokorev, V., Marchesini, D., Pan, R., Weaver, J. R., Whitaker, K. E., and Williams, C. C. (2023). UNCOVER: Illuminating the Early Universe-JWST/NIRSpec Confirmation of z > 12 Galaxies. ApJ, 957(2):L34.

Wang, X., Jones, T., Vulcani, B., Treu, T., Morishita, T., Roberts-Borsani, G., Malkan, M. A., Henry, A., Brammer, G., Strait, V., Bradač, M., Boyett, K., Calabrò, A., Castellano, M., Fontana, A., Glazebrook, K., Kelly, P. L., Leethochawalit, N., Marchesini, D., Santini, P., Trenti, M., and Yang, L. (2022). Early Results from GLASS-JWST. IV. Spatially Resolved Metallicity in a Low-mass z 3 Galaxy with NIRISS. ApJ, 938(2):L16.

Watanabe, K., Ouchi, M., Nakajima, K., Isobe, Y., Tominaga, N., Suzuki, A., Ishigaki, M. N., Nomoto, K., Takahashi, K., Harikane, Y., Hatano, S., Kusakabe, H., Moriya, T. J., Nishigaki, M., Ono, Y., Onodera, M., and Sugahara, Y. (2024). EMPRESS. XIII. Chemical Enrichment of Young Galaxies Near and Far at z $\sim$ 0 and 4–10: Fe/O, Ar/O, S/O, and N/O Measurements with a Comparison of Chemical Evolution Models. ApJ, 962(1):50.

Watson, D., Christensen, L., Knudsen, K. K., Richard, J., Gallazzi, A., and Michałowski, M. J. (2015). A dusty, normal galaxy in the epoch of reionization. Nature, 519(7543):327–330.

Weibel, A., Oesch, P. A., Barrufet, L., Gottumukkala, R., Ellis, R. S., Santini, P., Weaver, J. R., Allen, N., Bouwens, R., Bowler, R. A. A., Brammer, G., Carnall, A. C., Cullen, F., Dayal, P., Dickinson, M., Donnan, C. T., Dunlop, J. S., Giavalisco, M., Grogin, N. A., Illingworth, G. D., Koekemoer, A. M., Labbe, I., Marchesini, D., McLeod, D. J., McLure, R. J., Naidu, R. P., Pérez-González, P. G., Shuntov, M., Stefanon, M., Toft, S., and Xiao, M. (2024). Galaxy build-up in the first 1.5 Gyr of cosmic history: insights from the stellar mass function at z 4-9 from JWST NIRCam observations. MNRAS, 533(2):1808–1838.

Weinberger, R., Springel, V., Pakmor, R., Nelson, D., Genel, S., Pillepich, A., Vogelsberger, M., Marinacci, F., Naiman, J., Torrey, P., and Hernquist, L. (2018). Supermassive black holes and their feedback effects in the IllustrisTNG simulation. MNRAS, 479(3):4056–4072.

Weingartner, J. C. and Draine, B. T. (2001). Dust Grain-Size Distributions and Extinction in the Milky Way, Large Magellanic Cloud, and Small Magellanic Cloud. ApJ, 548(1):296–309.

Welch, B., Coe, D., Zitrin, A., Diego, J. M., Windhorst, R., Mandelker, N., Vanzella, E., Ravindranath, S., Zackrisson, E., Florian, M., Bradley, L., Sharon, K., Bradač, M., Rigby, J., Frye, B., and Fujimoto, S. (2023). RELICS: Small-scale Star Formation in Lensed Galaxies at z = 6-10. ApJ, 943(1):2.

White, S. D. M. and Frenk, C. S. (1991). Galaxy Formation through Hierarchical Clustering. ApJ, 379:52.

Wilkins, S. M., Lovell, C. C., Fairhurst, C., Feng, Y., Di Matteo, T., Croft, R., Kuusisto, J., Vijayan, A. P., and Thomas, P. (2020). Nebular-line emission during the Epoch of Reionization. MNRAS, 493(4):6079–6094.

Wilkins, S. M., Lovell, C. C., Vijayan, A. P., Irodotou, D., Adams, N. J., Roper, W. J., Caruana, J., Matthee, J., Seeyave, L. T. C., Conselice, C. J., Pérez-González, P. G., Turner, J. C., Donnellan, J. M. S., Verma, A., and Trussler, J. A. A. (2023a). First light and reionization epoch simulations (FLARES) XI: [O III] emitting galaxies at 5 $<$ z $<$ 10. MNRAS, 522(3):4014–4027.

Wilkins, S. M., Vijayan, A. P., Lovell, C. C., Roper, W. J., Irodotou, D., Caruana, J., Seeyave, L. T. C., Kuusisto, J. K., Thomas, P. A., and Parris, S. A. K. (2023b). First light and reionization epoch simulations (FLARES) V: the redshift frontier. MNRAS, 519(2):3118–3128.

Wilkins, S. M., Vijayan, A. P., Lovell, C. C., Roper, W. J., Zackrisson, E., Irodotou, D., Seeyave, L. T. C., Kuusisto, J. K., Thomas, P. A., Caruana, J., and Conselice, C. J. (2023c). First Light And Reionization Epoch Simulations (FLARES) VII: The star formation and metal enrichment histories of galaxies in the early Universe. MNRAS, 518(3):3935–3948.

Wise, J. H., Demchenko, V. G., Halicek, M. T., Norman, M. L., Turk, M. J., Abel, T., and Smith, B. D. (2014). The birth of a galaxy - III. Propelling reionization with the faintest galaxies. MNRAS, 442(3):2560–2579.

Wise, J. H., Turk, M. J., Norman, M. L., and Abel, T. (2012). The Birth of a Galaxy: Primordial Metal Enrichment and Stellar Populations. ApJ, 745(1):50.

Wiseman, P., Schady, P., Bolmer, J., Krühler, T., Yates, R. M., Greiner, J., and Fynbo, J. P. U. (2017). Evolution of the dust-to-metals ratio in high-redshift galaxies probed by GRB-DLAs. A&A, 599:A24.

Witstok, J., Jakobsen, P., Maiolino, R., Helton, J. M., Johnson, B. D., Robertson, B. E., Tacchella, S., Cameron, A. J., Smit, R., Bunker, A. J., Saxena, A., Sun, F., Alberts, S., Arribas, S., Baker, W. M., Bhatawdekar, R., Boyett, K., Cargile, P. A., Carniani, S., Charlot, S., Chevallard, J., Curti, M.,

Curtis-Lake, E., D'Eugenio, F., Eisenstein, D. J., Hainline, K. N., Jones, G. C., Kumari, N., Maseda, M. V., Pérez-González, P. G., Rinaldi, P., Scholtz, J., Übler, H., Williams, C. C., Willmer, C. N. A., Willott, C., and Zhu, Y. (2025). Witnessing the onset of reionization through Lyman-α emission at redshift 13. Nature, 639(8056):897–901.

Witstok, J., Shivaei, I., Smit, R., Maiolino, R., Carniani, S., Curtis-Lake, E., Ferruit, P., Arribas, S., Bunker, A. J., Cameron, A. J., Charlot, S., Chevallard, J., Curti, M., de Graaff, A., D'Eugenio, F., Giardino, G., Looser, T. J., Rawle, T., Rodríguez del Pino, B., Willott, C., Alberts, S., Baker, W. M., Boyett, K., Egami, E., Eisenstein, D. J., Endsley, R., Hainline, K. N., Ji, Z., Johnson, B. D., Kumari, N., Lyu, J., Nelson, E., Perna, M., Rieke, M., Robertson, B. E., Sandles, L., Saxena, A., Scholtz, J., Sun, F., Tacchella, S., Williams, C. C., and Willmer, C. N. A. (2023). Carbonaceous dust grains seen in the first billion years of cosmic time. Nature, 621(7978):267–270.

Witstok, J., Smit, R., Maiolino, R., Kumari, N., Aravena, M., Boogaard, L., Bouwens, R., Carniani, S., Hodge, J. A., Jones, G. C., Stefanon, M., van der Werf, P., and Schouws, S. (2022). Dual constraints with ALMA: new [O III] 88 μm and dust-continuum observations reveal the ISM conditions of luminous LBGs at z 7. MNRAS.

Witten, C., Laporte, N., Martin-Alvarez, S., Sijacki, D., Yuan, Y., Haehnelt, M. G., Baker, W. M., Dunlop, J. S., Ellis, R. S., Grogin, N. A., Illingworth, G., Katz, H., Koekemoer, A. M., Magee, D., Maiolino, R., McClymont, W., Pérez-González, P. G., Puskás, D., Roberts-Borsani, G., Santini, P., and Simmonds, C. (2024). Deciphering Lyman-α emission deep into the epoch of reionization. *Nature Astronomy*, 8:384–396.

Witten, C., McClymont, W., Laporte, N., Roberts-Borsani, G., Sijacki, D., Tacchella, S., Simmonds, C., Katz, H., Ellis, R. S., Witstok, J., Maiolino, R., Ji, X., Hayes, B. R., Looser, T. J., and D'Eugenio, F. (2025). Rising from the ashes: evidence of old stellar populations and rejuvenation events in the very early Universe. MNRAS, 537(1):112–126.

Wolfire, M. G., Hollenbach, D., McKee, C. F., Tielens, A. G. G. M., and Bakes, E. L. O. (1995). The Neutral Atomic Phases of the Interstellar Medium. ApJ, 443:152.

Wong, Y. H. V., Wang, P., Hashimoto, T., Takagi, T., Goto, T., Kim, S. J., Wu, C. K. W., On, A. Y. L., Santos, D. J. D., Lu, T.-Y., Kilerci-Eser, E., Ho, S. C. C., and Hsiao, T. Y. Y. (2022). ALMA Detections of [O III] and [C II] Emission Lines From A1689-zD1 at z = 7.13. ApJ, 929(2):161.

Woosley, S. E., Heger, A., and Weaver, T. A. (2002). The evolution and explosion of massive stars. *Reviews of Modern Physics*, 74(4):1015–1071.

Woosley, S. E. and Weaver, T. A. (1995). The Evolution and Explosion of Massive Stars. II. Explosive Hydrodynamics and Nucleosynthesis. ApJS, 101:181.

Wu, X., Davé, R., Tacchella, S., and Lotz, J. (2020). Photometric properties of reionization-epoch galaxies in the SIMBA simulations. MNRAS, 494(4):5636–5651.

Xiao, L., Stanway, E. R., and Eldridge, J. J. (2018). Emission-line diagnostics of nearby H II regions including interacting binary populations. MNRAS, 477(1):904–934.

Xilouris, E. M., Byun, Y. I., Kylafis, N. D., Paleologou, E. V., and Papamastorakis, J. (1999). Are spiral galaxies optically thin or thick? A&A, 344:868–878.

Xu, C. and Buat, V. (1995). Are spiral disks really opaque? A&A, 293:L65–L68.

Xu, H., Wise, J. H., Norman, M. L., Ahn, K., and O'Shea, B. W. (2016). Galaxy Properties and UV Escape Fractions during the Epoch of Reionization: Results from the Renaissance Simulations. ApJ, 833(1):84.

Yajima, H., Choi, J.-H., and Nagamine, K. (2011). Escape fraction of ionizing photons from high-redshift galaxies in cosmological SPH simulations. MNRAS, 412(1):411–422.

Yajima, H., Nagamine, K., Zhu, Q., Khochfar, S., and Dalla Vecchia, C. (2017). Growth of First Galaxies: Impacts of Star Formation and Stellar Feedback. ApJ, 846(1):30.

Yanagisawa, H., Ouchi, M., Nakajima, K., Harikane, Y., Fujimoto, S., Ono, Y., Umeda, H., Nakane, M., Yajima, H., Fukushima, H., and Xu, Y. (2024). A Galaxy with an Extremely Blue UV Slope $= -3$ at $z = 9.25$ Identified by JWST Spectroscopy: Evidence for a Weak Nebular Continuum and Efficient Ionizing Photon Escape? *arXiv e-prints*, page arXiv:2411.19893.

Yang, S., Lidz, A., Smith, A., Benson, A., and Li, H. (2023). Efficient simulations of ionized ISM emission lines: a detailed comparison between the FIRE high-redshift suite and observations. MNRAS, 525(4):5989–6004.

Yoshida, N., Abel, T., Hernquist, L., and Sugiyama, N. (2003). Simulations of Early Structure Formation: Primordial Gas Clouds. ApJ, 592(2):645–663.

Yoshida, N., Hosokawa, T., and Omukai, K. (2012). Formation of the first stars in the universe. *Progress of Theoretical and Experimental Physics*, 2012(1):01A305.

Yoshida, N., Omukai, K., Hernquist, L., and Abel, T. (2006). Formation of Primordial Stars in a ΛCDM Universe. ApJ, 652(1):6–25.

Yung, L. Y. A., Somerville, R. S., Finkelstein, S. L., Wilkins, S. M., and Gardner, J. P. (2024). Are the ultra-high-redshift galaxies at z > 10 surprising in the context of standard galaxy formation models? MNRAS, 527(3):5929–5948.

Zanella, A., Iani, E., Dessauges-Zavadsky, M., Richard, J., De Breuck, C., Vernet, J., Kohandel, M., Arrigoni Battaia, F., Bolamperti, A., Calura, F., Chen, C. C., Devereaux, T., Ferrara, A., Mainieri, V., Pallottini, A., Rodighiero, G., Vallini, L., and Vanzella, E. (2024). Unveiling [C II] clumps in a lensed star-forming galaxy at z ∼ 3.4. A&A, 685:A80.

Zavala, J. and Frenk, C. S. (2019). Dark Matter Haloes and Subhaloes. *Galaxies*, 7(4):81.

Zavala, J. A., Bakx, T., Mitsuhashi, I., Castellano, M., Calabro, A., Akins, H., Buat, V., Casey, C. M., Fernandez-Arenas, D., Franco, M., Fontana, A., Hatsukade, B., Ho, L. C., Ikeda, R., Kartaltepe, J., Koekemoer, A. M., McKinney, J., Napolitano, L., Pérez-González, P. G., Santini, P., Serjeant, S., Terlevich, E., Terlevich, R., and Yung, L. Y. A. (2024). ALMA Detection of [O III] 88 μm at z = 12.33: Exploring the Nature and Evolution of GHZ2 as a Massive Compact Stellar System. ApJ, 977(1):L9.

Zavala, J. A., Casey, C. M., Manning, S. M., Aravena, M., Bethermin, M., Caputi, K. I., Clements, D. L., Cunha, E. d., Drew, P., Finkelstein, S. L., Fujimoto, S., Hayward, C., Hodge, J., Kartaltepe, J. S., Knudsen, K., Koekemoer, A. M., Long, A. S., Magdis, G. E., Man, A. W. S., Popping, G., Sanders, D., Scoville, N., Sheth, K., Staguhn, J., Toft, S., Treister, E., Vieira, J. D., and Yun, M. S. (2021). The Evolution of the IR Luminosity Function and Dust-obscured Star Formation over the Past 13 Billion Years. ApJ, 909(2):165.

Zhang, S., Bromm, V., and Liu, B. (2024). How do Primordial Black Holes change the Halo Mass Function and Structure? *arXiv e-prints*, page arXiv:2405.11381.

Zhukovska, S., Gail, H. P., and Trieloff, M. (2008). Evolution of interstellar dust and stardust in the solar neighbourhood. A&A, 479(2):453–480.

Ziparo, F., Ferrara, A., Sommovigo, L., and Kohandel, M. (2023). Blue monsters. Why are JWST super-early, massive galaxies so blue? MNRAS, 520(2):2445–2450.